Journal of NUCLEAR SCIENCE and TECHNOLOGY, Supplement 5, p. 329–332 (June 2008)

Measurement of (γ, n) Reaction Cross Section for Long-lived β-emitting Radionuclide ^{129}I by using Bremsstrahlung Photons

Abul Kalam Md. Lutfor RAHMAN[1*], Shigeyuki KUWABARA, Kunio KATO[1] , Hidehiko ARIMA[1], Nobuhiro SHIGYO[1], Kenji ISHIBASHI[1], Jun-ichi HORI[2], Ken NAKAJIMA[2], Tetsuo GOTO[3], and Mikio UEMATSU[3]

[1]*Kyushu University, Fukuoka 813-0395 Japan*
[2]*Kyoto University Research Reactor Institute, Osaka 590-0494 Japan*
[3]*Toshiba Corporation, Yokohama 235-8523 Japan*

Many long-lived non-gamma emitting radioactive nuclei such as ^{129}I, ^{14}C and ^{93}Zr are produced as wastes from nuclear fuel cycle facilities. They are called "difficult-to-measure" radio nuclei. Among them ^{129}I is a long-lived β-emitting isotope with a half-life of 1.57 x 10^7 years. Iodine compounds are mobile in the vadose zone and groundwater and increase a significant long-term risk. Transmutation of ^{129}I is a challenging issue in nuclear waste management and disposal. If ^{129}I is transmuted into ^{128}I (half life; 25 minutes), it can easily be measured by a Ge detector. However, the ^{129}I(γ, n) reaction cross section has not been measured so far. In this study we have measured the inclusive ^{129}I(γ, n)^{128}I cross section by using bremsstrahlung photons. The bremsstrahlung photons were produced from a 30-MeV electron linac. Measured average activation cross section agrees with 12% deviation from the evaluated one in the IAEA photonuclear data library. Gamma and neutron fluxes for the (γ, n) and the (n, γ) reaction were also calculated by the EGS and the MCNP codes.

KEYWORDS: non-destructive detection, long-lived β-radionuclide, bremsstrahlung photon, (γ, n) reaction cross section, ^{129}I, transmutation, Ge detector

I. Introduction

Some nuclei in nuclear wastes are seriously hazardous to the environment because of very long decay times of more than million years which is longer than the life of artificial barriers. The concept of partitioning and transmutation of long-lived nuclides is an attractive option to reduce the long-term risk of the storage of high-level waste from nuclear facilities. A number of methods have been presented and discussed involving transmutation by bombardment with neutrons from a reactor or a particle accelerator[1), 2)] and nuclear transmutation by high-brightness gamma-ray generated through laser Compton scattering (LCS)[3), 4)]. Radioactive wastes contain transuranic or fissile nuclides and should be classified according to their radioactivity levels so that they would be properly disposed. The wastes generally include a large amount of long-lived non-gamma emitting "difficult to measure" nuclides such as ^{129}I and ^{14}C. Measurement of the quantity of such radioactive nuclide has been carried out by conventional method like the scaling factor technique (SF)[5)]. However, before applying the technique, the correlation is needed between 'easy-to-measure' nuclides which are readily measured non-destructively and 'difficult-to-measure' ones such as pure β-radioactive nuclide. Since the SF method is carried out by chemical analysis, it takes a long time and much cost. We propose a technique, "non-destructive-detection" for gamma ray measurement. The principal of the 'non-destructive detection' method is illustrated in **Fig. 1**. This method consists of an electron accelerator, a heavy-metal target like a tantalum, a drum containing radioactive waste and a Ge gamma-ray detector. An electron beam strikes on the heavy-metal target and generates high-energy bremsstrahlung photons.

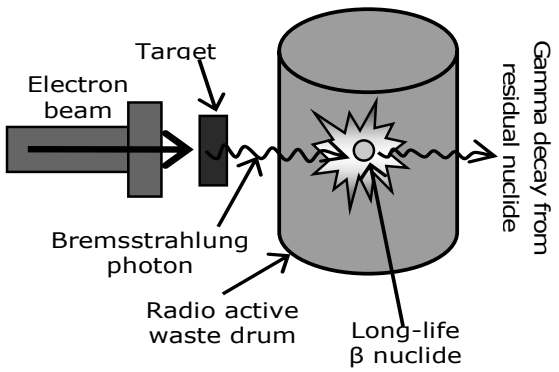

Fig. 1 Concept of non-destructive detection using an electron accelerator.

The β-emitting long-lived radio nuclides in the waste drum are converted into short-lived γ-emitting ones by bombardment of high energy bremsstrahlung photons. After that, their radioactivity is measured non-destructively from the outside of the waste drum with a Ge spectrometer.

Examples of some photonuclear reaction applicable to non-destructive detection method are listed in **Table 1**. Among them ^{129}I is of large amount in the nuclear waste. It decays by beta emission with a half-life of 1.57×10^7 years. 5.54 kg/GWey of ^{129}I together with 1.22 kg/GWey of a stable

*Corresponding Author, Tel. +81-92-802-3484, Fax.+81-92-802-3484, E-mail: akmlr05@kune2a.nucl.kyushu-u.ac.jp

nuclide of ^{127}I are contained in a UO_2 spent fuel of a light water reactor burnt to 60 GWd/t after 5 years cooling[6].

Table 1: Example of photonuclear reactions applicable to non-destructive detection.

Nuclide	Half-life [years]	Reaction	Residual nuclide	Half-life	Decay mode
^{14}C	5.73×10^{3}	(γ, p)	^{13}B	17.4 ms	β^-
^{36}Cl	3.01×10^{5}	(γ, 2n)	^{34m}Cl	32.3 m	β^+
^{59}Ni	7.50×10^{5}	(γ, p)	^{58}Co	70.9 d	EC
^{79}Se	6.50×10^{4}	(γ, p)	^{78}As	1.5 h	β^-
^{99}Tc	2.13×10^{5}	(γ, 3n)	^{96m}Tc	51.5 m	EC
^{129}I	1.57×10^{7}	(γ, n)	^{128}I	25 m	β^-
^{93}Zr	1.53×10^{6}	(γ, p)	^{92}Y	3.54 h	β^-

The ^{129}I is a long-life difficult-to measure nuclide. On the other hand ^{128}I is a short-life one and easily can be measured by gamma counting. So it is necessary to know the cross section of $^{129}I(\gamma, n)^{128}I$ and also the feasibility of non-destructive method. The photonuclear reaction cross section of ^{129}I has not been measured so far. In this work, the inclusive photonuclear reaction cross section of $^{129}I(\gamma, n)$ ^{128}I was measured by using bremsstrahlung photons emitted from a target irradiated by a 30-MeV electron linac. The experimental data were analyzed by the calculation with Monte Carlo codes EGS5[7] and MCNP[8].

II. Experiment and Materials

The irradiation experiment was carried out for a sealed source of radioactive iodine sample (radioactivity of 2.65 MBq) by using a 30-MeV electron linear accelerator at Kyoto University Research Reactor Institute. **Fig. 2** shows the experiment layout.

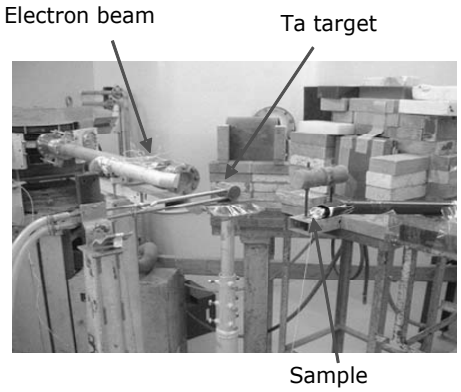

Fig. 2 Irradiation experiment layout

The irradiation time was 30 minutes. The beam current was 27.8 μA. The frequency was 100 Hz and the pulse width was 100 ns. Bremsstrahlung photons were generated from a thick tantalum target 50 mm in diameter and 61 mm long near the extraction port of the accelerator. **Fig. 3** illustrates the geometrical positions in the experiment. The radioactive iodine sample was placed at 33 cm from the target along the beam axis. The iodine sample 27.8 mm in diameter and 2.8 mm thick contains radioactive ^{129}I of 68% and stable ^{127}I of 32%. The sample was irradiated together with ^{197}Au foils placed in front and back of the iodine sample to measure photon and neutron fluxes at the sample position. One of the gold foils was covered by cadmium sheets to get the fast-neutron flux information. The sizes and weights of the gold foils are shown in **Table 2**.

Table 2 Sizes and weights of gold foils.

Sample	Position	Size	Weight
Small gold	Front of iodine	6 mmΦ × 15 μm	8.32 mg
Small gold	Back of iodine	6 mmΦ × 15 μm	8.33 mg
Big gold	Back of iodine	20 mmΦ × 10 μm	76.67 mg
Small gold covered by Cd sheet	Back of iodine	6 mmΦ × 30 μm	17.81 mg

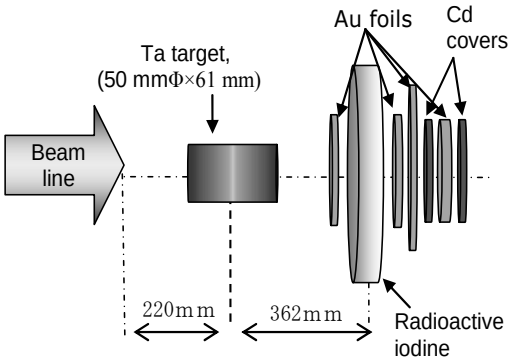

Fig. 3 Sample geometrical position in the experiment

Gamma rays from irradiated gold foils and iodine sample were measured by a Ge detector for 30 minutes. The cooling time for gold foil was 1 hour 4 minutes and for iodine sample was 24 minutes. The gold foils were placed 4 mm and the iodine sample was 170 mm apart from the end cup of the detector surface.

III. Results and Discussion

1. Flux Calculation

The measured photon flux data obtained from the gold foil irradiation were checked by the values from the EGS5 calculation. Gold foils of different sizes were used to know the uniformity of photon flux distribution in the iodine sample. Photon fluxes at the iodine sample position were determined by averaging fluxes on different gold foils in front and back of the iodine. The average fluxes were then used in the iodine sample analysis. The effect of angular distribution of the photon flux was considered and it was evaluated as the experimental error of the average cross section. To know the contribution of ^{127}I (n, γ) ^{128I} reaction to the yield of total ^{128}I, fast neutron flux was calculated by the MCNP code. In addition, slow-neutron flux in the thermal and epithermal regions was derived from the experimental data of gold foils with and without cadmium sheets. The slow neutron flux was assumed to have a Maxwellian distribution with amplitude and a temperature parameters.

The two parameters were determined by the gold activation results with and without cadmium. The neutron transmission through the cadmium sheet was taken into account. The temperature of slow neutron was given as 2.69×10^{-2} keV. The contribution of ^{127}I (n, γ) ^{128}I was obtained mainly through the slow neutron flux.

2. Results of Gold Foil Irradiation

Fig. 4 shows the example of gamma ray spectrum from irradiated gold.

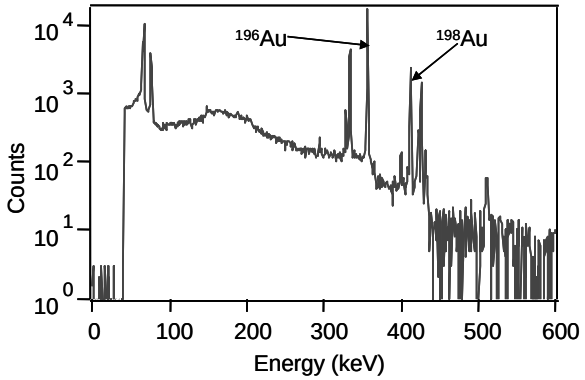

Fig. 4 Gamma spectrum of irradiated gold foil

The peak at 355.73 keV originates from the decaying isotope ^{196}Au through ^{197}Au (γ, n) ^{196}Au reaction and that at 411.80 keV from ^{198}Au through ^{197}Au (n, γ) ^{198}Au. The yields obtained from the irradiation are listed in **Table 3**.

Table 3 Yields obtained from ^{197}Au foil irradiation

Gold foil	Yield (Bq)	
	^{196}Au	^{198}Au
Front of iodine	2.39×10^5	1.39×10^4
Back of iodine	2.32×10^5	1.19×10^4
Back of iodine (big)	2.00×10^6	1.34×10^5
Au covered by Cd	2.17×10^5	5.28×10^3

The photon flux was calculated by the EGS5 code. **Fig. 5** shows the example of photon spectra of the EGS5 code calculation taking the number of particles 8×10^6 per batch.

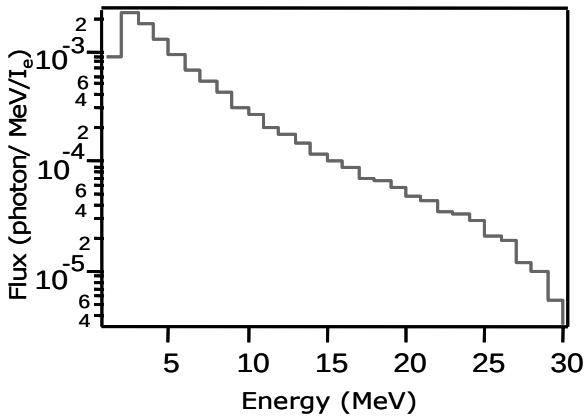

Fig. 5 Photon flux from 30 MeV incident electrons by the EGS5 code.

In the calculation the average statistical error was 4% and at the resonance energy region error was less than 3%. The peak energy at giant dipole resonance is 13.5 MeV for ^{197}Au.

For ^{197}Au (γ, n) ^{196}Au reaction, the intensity of calculated flux deviated by 20% from the experimental one. We suppose that the deviation is in a tolerable level due to such possible situations as sample-position might shift from electron-beam axis. The calculated value was normalized to reproduce the experimental gold foil data at the iodine sample position.

3. Results of Radioactive Iodine Sample Irradiation

Fig. 6 stands for gamma ray spectrum of irradiated iodine sample.

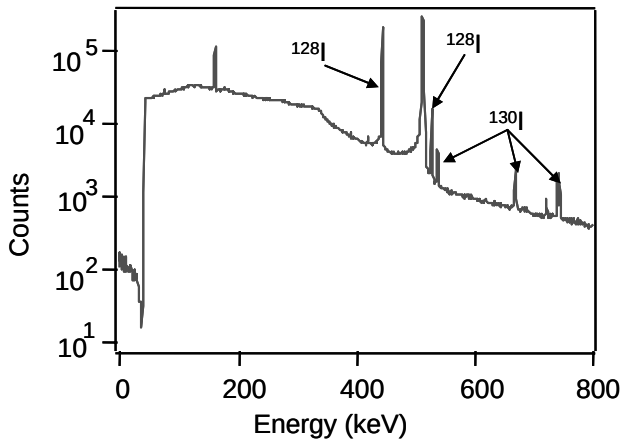

Fig. 6 Gamma ray spectrum of iodine sample

The peaks at 442.9 and 526 keV originate from the decaying isotope ^{128}I through ^{129}I (γ, n) ^{128}I reaction and those at 536, 668.5 and 739.5 keV from ^{130}I through ^{129}I (n, γ) ^{130}I. Since the iodine sample includes ^{127}I at 32 %, ^{127}I (n, γ) ^{128}I reaction may occur simultaneously together with ^{129}I (γ, n) ^{128}I reaction. Therefore the contribution of ^{127}I (n, γ) reaction to the production of ^{128}I was estimated on the basis of the neutron flux. The yields obtained from the irradiation of ^{129}I with the contribution of ^{127}I (n, γ) reaction are listed in **Table 4**. The contribution of ^{127}I (n, γ) was as small as 1.9 % due to minimized use of cooling water inside the target through a coiled channel.

Table 4 Yields obtained from iodine irradiation

Nuclide	Yields (Bq)		
	Total	^{128}I from ^{129}I	^{128}I from ^{127}I
^{128}I	5.19×10^6 ± 3.11×10^5	5.1×10^6 ± 3.06×10^5	9.69×10^4 ± 5.8×10^3

The yield obtained from the measurement can be expressed by the following equation.

Centering activation rate = $\sigma\phi N$, (1)

Yield = Centering activation rate/N = $\sigma\phi$, (2)

where σ = Cross section, ϕ = flux, N= number of nuclide.

The flux was corrected by the gold foil activation and was used in the determination of cross section using the following equation.

$$\frac{\text{Centering activation rate}}{N \times \phi_{\text{corrected}}} = \sigma \quad (3)$$

The average cross sections of ^{129}I (γ, n) ^{128}I reaction are summarized in **Table 5**. The cross section average was taken in the photon energies from 9 to 30 MeV. The ratio of the measured cross section to the evaluated one is 88 %. The evaluated values in the IAEA photo nuclear data library[9] shows an agreement with the experimental one with a deviation of 12%.

Table 5 Average activation cross section of ^{129}I over bremsstrahlung photon spectrum

Average reaction cross section	Measured (barn)	Evaluated (barn)	Ratio Measured/Evaluated
	0.099 (± 0.006)	0.113	0.88 (± 0.05)

The details of systematic and statistical errors were listed in **Table 6**. The systematic error was assigned to be 5.3%, except the error of reference cross section of ^{197}Au (γ, n). The photon flux uncertainty in target was included in the systematic error and was derived from the differential activation values of front and back of gold foils. The uncertainties in the active diameter of ^{129}I target and in the flux energy distribution at 0 to 2 degree angle were also considered in the table. The uncertainty in the concentration of ^{129}I in the iodine sample was set at 5%. The statistical error was evaluated to be 3%, resulting in a total error of 6%.

Table 6 The details of the uncertainty

Uncertainty	Systematic (%)	Statistical (%)
Flux at target position	1.5	
Iodine active area	0.1	
Flux energy distribution (0-2 degree)	0.9	
^{129}I concentration	5	
Total	5.3	3
Total (Syst. and Stat. in %)	6.0	

The result indicates the applicability of non-destructive measurement for the transmutation of ^{129}I in a radioactive waste by bremsstrahlung photon irradiation.

IV. Conclusions

The difficulties in radioactive waste management are the treatment of long-lived radio nuclei with the environmental sustainability. The applicability of non-destructive detection method favourable for the environment for long-lived "difficult-to-measure" ^{129}I isotope was performed using an electron linac. The average inclusive cross section of ^{129}I (γ, n)^{128}I reaction was measured by using continuous energy bremsstrahlung photons. The experimental fluxes were checked by the calculation of Monte Carlo codes EGS5 and MCNP. The measurement needed information about the influence of (n, γ) reaction caused mainly by slow neutrons. The ^{127}I (n, γ) reaction rate in production of ^{128}I with the help of Au (n, γ) reaction was estimated. The result of photo neutron contribution was found to be an admissible level. The measured average ^{129}I (γ, n) ^{128}I cross section gave a deviation of 12% from the evaluated value in the IAEA photonuclear data library.

Acknowledgement

The authors express their gratefulness to staffs of Kyoto University Research Reactor Institute for giving the opportunity to use the facility and other experimental support.

References

1) S.Matsuura, 'Future Perspective of Nuclear Energy in Japan and the OMEGA Program,' Nuclear Physics A 654, 417c (1999).
2) Waclaw Gudowski, 'Accelerator-driven Transmutation Projects. The Importance of Nuclear Physics Research for Waste Transmutation,' Nuclear Physics A 654, 436c (1999).
3) KW D Ledingham, J Magill, P McKenna, et.al, 'Laser-driven photo-transmutation of 129I—a long-lived nuclear waste product,' J. Phys. D: Appl. Phys. 36, L79 (2003).
4) D.Li, K. Imasaki,1 M. Aoki, et.al, 'Experiment on gamma ray generation by laser compton scattering' International Journal of Infrared and Millimeter Waves, Vol. 24, No. 8, August, p1301 (2003).
5) Ki Ha Hwang , Kun Jai Lee, 'Modeling the activity and scaling factor of 129I in the primary coolant and CVCS resin of
6) operating PWR,' Annals of Nuclear Energy, Vol. 32,1898 (2005).
7) Y. Ando, H. Takano, 'Estimation of LWR spent fuel composition,' Japan Atomic Energy Research Institute Report JAERI-Research 99-004, (1999).
8) H. Hirayama, Y. Namito, A.F. Bielajew, S.J. Wilderman and W.R. Nelson, 'The EGS5 Code System,' by SLAC-R-730 (2005) and KEK Report 2005-8 (2005).
9) Lawrence J. Cox, et al. 'MCNP Version 5' LU-UR-02-1527 (2002).
10) Y. Han, Y. O. Lee, NDEL, KAERI, High Energy Photonuclear Library, EVAL-DEC 99.

Journal of NUCLEAR SCIENCE and TECHNOLOGY, Supplement 5, p. 333–336 (June 2008)

On the Use of a Thick Carbon Target in the 90º Compton Spectroscopy for the Measurement of Diagnostic X-rays

A. MOHAMMADI[1*] , M. BABA[1], H. OHUCHI[2], Y. Kaga[3], F. Yamada[3]

[1]*Cyclotron and Radioisotope Center, Tohoku University, Sendai 980-8578, Japan*
[2]*Graduate School of Pharmaceutical sciences, Tohoku University, Sendai 980-8578, Japan*
[3]*Radiation Division, Sendai Kousei Hospital, Sendai 980-0873, Japan*

In order to perform quality assurance (QA) and quality control (QC) of the X-ray radiographic systems, we studied the Compton spectroscopy using different shape and size of scatterer such as columnar carbon rods of 2 cm diameter, which were cut at different angles of 15º, 30º, 45º, 60º and 75º. The appropriate shape of a carbon scatterer was studied in terms of minimum multiple scattering, the energy broadening and easy practical use. Calculated exposure results from our Compton spectroscopy using two scatteres were confirmed by the results of exposure measurement using a calibrated ionization chamber. The Compton spectroscopy of x-ray radiographic systems with a thick carbon scatterer proved to be a useful method for the evaluation of such system performance.

KEYWORDS: diagnostic x-ray, compton spectroscopy, scatterer, thick carbon target

I. Introduction

Radio diagnostic technologies are widely used in medical fields. Assessment of quality assurance and quality control of these systems is getting more important due to the development of diagnostic techniques. In order to evaluate the performance of the systems, knowledge on the primary x-ray spectrum is important.

The Compton spectroscopy technique is used for the measurements of diagnostic x-ray units because direct measurement is very difficult due to an extremely high-photon fluence rate that causes a significant detector pile-up effect. In this technique, scattered photons at 90º from a sample are measured and then the primary energy spectrum is derived using the Compton differential cross-section. The energy resolution of Compton scattering spectrum is influenced by material and shape of the scattering object. Scatterers of low atomic number give rise to small contributions of coherently scattered photons. On the other hand, scatterers of high atomic number produce energy broadening due to the Compton profile because the mean binding energy increases with the increasing atomic number[1)].

The Compton spectroscopy technique was realized by Yaffe et al to measure x-ray spectra from diagnostic x-ray tubes[2)]. In this study, a Lucite foil disc was used as a scattered. Matscheko and Ribberfors determined the optimal combination of some parameters like shape and volume of the scatterer in order to reduce the Compton broadening[3)]. The optimal scatterer shape was a circular rod (diameter less than 5 mm), which lied in a scattering chamber of Compton spectrometer[4), 5)]. Maeda et al measured the diagnostic x-ray spectrum using a carbon scatterer, which was made from a columnar carbon rod of 2 cm diameter x 2 cm height and cut at 45 deg[6)].

It should be noted that the reconstruction algorithm in Compton spectroscopy assumes that only singly scattered photons from the scatterer are detected and others such as the multiply scattered photons and nonzero acceptance angle of the detector introduce errors or uncertainties into the reconstructed results unless they can be accurately corrected for. Therefore, it is necessary to have complete information about fraction of multiple scattering and the angle acceptance in Compton scattered spectrum.

For this purpose, computer simulation is a useful tool to characterize the Compton scattered spectrum. In the present study, The MCNP4C code was used to determine Compton scattered spectrum from different shape of thick scatterers and then the primary spectra under a clinical operating condition were acquired by Compton method using a schottky CdTe detector and two scatterers.

II. Materials and Methods

1. Simulation Method

The MCNP (Monte Carlo N-Particle Transport) code is a powerful simulation program for neutron, photon and electron transport calculations. In the detailed physics treatment for photon interaction, photoelectric absorption can result in fluorescent emission, the Thomson and Klein-Nishina differential cross sections are modified by appropriate form factors taking electron-binding effects into account, and coherent scattering is included. Angular distributions of secondary photons are isotropic for photoelectric effect, fluorescence, and pair production, and come from sampling the well-known Thomson and Klein-Nishina formulas for coherent and incoherent scattering. The energy of an incoherently scattered photon is calculated from the sampled scattering angle. The flux of photons can be

*Corresponding Author, Tel No: +81-22-795-780, E-mail: akram@cyric.tohoku.ac.jp

estimated with either point or ring detector next-event estimators (F5 tally).

The spectrum of Compton scattered photon can be calculated by the MCNP4C. The experimental setup (**Fig. 1** without the detector) was simulated to calculate the Compton scattered photons at 90º after the secondary collimator using the F5 tally.

The x-ray source was simulated as a point source because the focal spot dimension is very small compared with the large distance between the scatterer and the source. Photons are isotropically emitted into a solid angle focused on the scatterer in order to reduce computer time.

Carbon was chosen as our scattering target because of its low-atomic number. The flux of 90º scattered photons was calculated for different shapes of carbon scatterers including, a cylinder with height and diameter of 2 cm and five cylinders with the same diameter of 2 cm, that are cut at 15º, 30º, 45º, 60º and 75º with different height of 0.58, 1.157, 2, 3.46 and 7.46 cm, respectively. The scattering target is made large enough for quick and accurate positioning in a clinical setting.

2. Compton Scattering Measurement

Fig. 1 shows the geometry of our experiment for the 90º Compton scattering measurement. The Compton scattered photon spectra of x-ray tube was measured in this experimental setup.

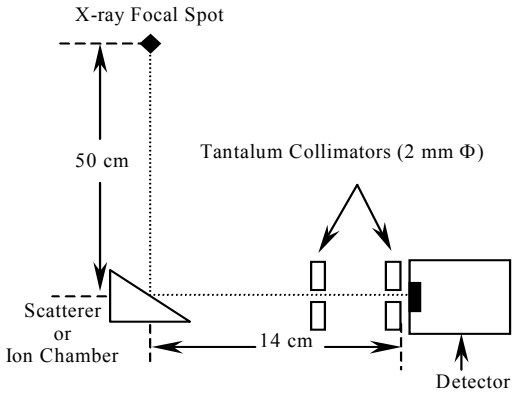

Fig. 1. Experimental setup for Compton scattering measurement

The x-ray unit employed was a Hitachi Medico (Model UH-6GB-11T). The inherent filtration of the x-ray tube was 2.8 mm Al_{eq}. The rotating anode had a tungsten target with 10º angle and two focal spot sizes of 0.6 and 1 mm were available. The irradiation condition of x-ray tube was 70 kV and 10 mA. As shown in **Fig.1**, the scattering targets were placed 50 cm away from the focal spot (source), and the size of x-ray field on the surface of our scatterers was adjusted to be 2 x 2 cm^2.

The collimator system was composed of two 3 mm thick tantalum plates with pinhole diameter 2 mm. They were spaced with a spacing 3.6 cm apart and located in front of the detector. For tight and quick alignment of detector system, the scatterer and the collimators, they were fixed firmly to a common support, which is made of PVC (poly vinyl chloride).

The detector employed in this study was a Schottky CdTe detector using a guard-ring cathode (provided by Clear Pulse Inc.,). It is a planar detector with the crystal size of 6×6 mm^2, active area of 4×4 mm^2 and 0.3 mm thick. The detector bias voltage was 200 V and detector calibration was done by ^{241}Am source with energy bin of 0.2 keV[7].

3. Correction of Measured Spectrum

After measuring the Compton scattered in order to correct the measured spectra for the response of our detector we applied an unfolding method that is known as stripping procedure[6] and it is given by the following equation.

$$N_t(E_0) = \{N_d(E_0) - \sum_{E_0+0.2}^{E_{Max}} R(E_0, E) N_t(E)\} / \varepsilon(E_0) \qquad (1)$$

where $N_t(E_0)$ is the true number of photons of energy E_0, $N_d(E_0)$ is the number of photons detected of energy E_0, E_{max} is the maximum energy of the spectrum, $R(E_0,E)$ is the response function of the detector for monoenergetic photons of energy E_0 and $\varepsilon(E_0)$ is the photo peak efficiency for photons of energy E_0. The stripping procedure is applied step-by-step starting from E_{max} to the minimum energy.

The response functions were obtained using the Monte Carlo simulation code MCNP4C that simulates the photon interactions in a CdTe crystal. The charge carrier trapping in our detector was insignificant and not taken into account for the response function [7]. An example of the detector response function for photon energy of 50 keV and the photo peak efficiency are shown in **Fig. 2**.

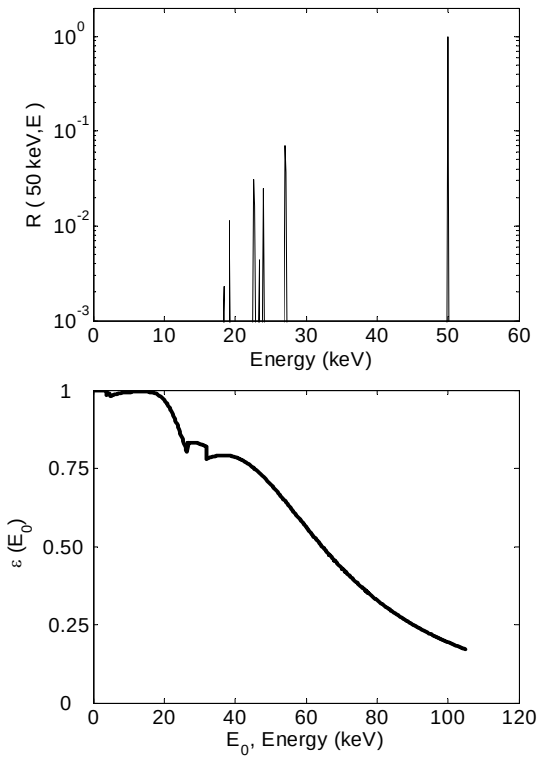

Fig. 2. Response function of the detector for 50 keV (upper), and the photo peak efficiency of the detector (bottom)

4. Reconstruction Procedure

In Compton scattering at 90º the energy of incident photons, E_p, is related to that of scattered photons, E_s, by

$$E_p = E_s/(1 - E_s/511) \quad (2)$$

The intensity of the incident photons is calculated by

$$I(E_p) = S(E_p)/(d\sigma/d\Omega)_{(\theta=\pi/2)} \quad (3)$$

where $I(E_p)$ is the primary photon numbers incident on the carbon scatterer, $S(E_p)$ is the scattered photon numbers after stripping correction and energy correction (equations (1), (2)). The $(d\sigma/d\Omega)_{\theta=\pi/2}$ is Compton differential cross section at 90º which is given by the Klein-Nishina formula. It is the probability that photon will scatter at 90º into solid angle dΩ, in unit of cm^2sr^{-1}per atom. The Klein-Nishina formula is given as follows at 90º scattering.

$$(d\sigma/d\theta)_{(\theta=\pi/2)} = Zr_0^2 \frac{1}{2}\left(\frac{1}{1+\alpha}\right)^2\left(1 + \frac{\alpha^2}{1+\alpha}\right) \quad (4)$$

$$\alpha = E_p/511 \quad (5)$$

where r_0 is the classical radius of the electron and is equal to 2.82×10^{-13} cm, and Z is atomic number of scatterer.

5. Evaluation of Reconstructed Spectra

Validity of reconstructed spectra was evaluated through comparisons with Monte Carlo calculation of x-ray spectra and an exposure measurement. Diagnostic radiology x-ray spectra can be generated successfully by MCNP4C8). The incident photon spectrum for the x-ray tube at 50 cm was simulated by this code. Also the exposure at 50 cm distance was measured using an ion chamber (Radiation Monitor Controller, Model 9015, 6 cc chamber) and was compared with calculated exposure from reconstructed spectra (see section Ⅲ).

III. Result and discussion

1. Compton Scattered Spectrum

The flux of Compton scattered photons were calculated by the MCNP4C code for different scatterers. **Fig. 3** shows scattered photon spectrum at 90º for 100 keV monoenergetic photons at x-ray focal spot from a cylinder and the scatterers with cutting angle of 15º and 30º. The scattered photon spectra includes both single and multiple Compton scattering. It should be noted that the scattering angle is not always exactly 90º for all detected photons because it is spread slightly due to the electron movement in the scattering target and the geometrical irradiation angle. These two effects cause an energy broadening of the Compton scattered photons. Therefore, the best scatterer shape should be chosen on the basis of the minimum energy broadening and the minimum fraction of multiply scattered events.

Fig. 3 indicates calculated flux of Compton scattered photons for primary photons of 100 keV. From this figure the maximum multiply scattered fraction is resulted from a Cylinder, and for other scatterers, the fraction of multiply scattered events decreases by reducing the cutting angle. This is interpreted as a result of effective scattering volume, which increases with cutting angle and it is maximum for cylinder.

The energy broadening is shown in **Fig. 4** for primary photon energy of 100 keV. The minimum broadening is resulted from scatterer with 15º cutting angle and it increases by increasing the cutting angle. This is owing to more angular spread of detected photons due to bigger effective volume of scatterer with increasing the cutting angle.

From **Fig. 3** and **Fig. 4**, it is clear that smaller cutting angle leads to the better results. However, from the viewpoint of fabrication and practical use, this cutting angle is not convenient. Fortunately, these parameters are weak functions of the cutting angle hence we adopted two carbon scatterers with cutting angle of 30º and 45º in our experiments.

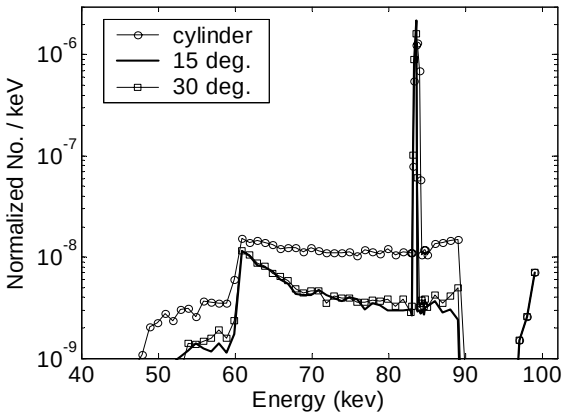

Fig. 3. Calculated spectra of Compton scattered photons for primary photons of 100 keV for three scatterers (see **Fig. 1**)

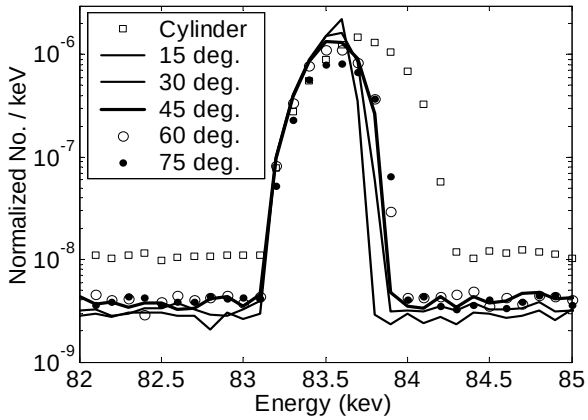

Fig. 4. Energy broadening of Compton scattered photons for primary photons of 100 keV

2. Validation of the Method

For validation of the present method, the spectrum of Compton scattered photons were measured in the experimental setup of **Fig. 1** for two scatteters. **Fig. 5** and **Fig. 6** show the measured and reconstructed spectra for 70 kV tube voltage from scatterers with 30º and 45º cutting angles, respectively. In order to decrease the statistical error we collected the spectra for 20 times irradiation at the same conditions for each experiment. The measured spectra were corrected by stripping method (Eq. (1)) and then the

reconstructed spectra were obtained by applying equations (2), (3), (4) and (5) to the spectra after stripping.

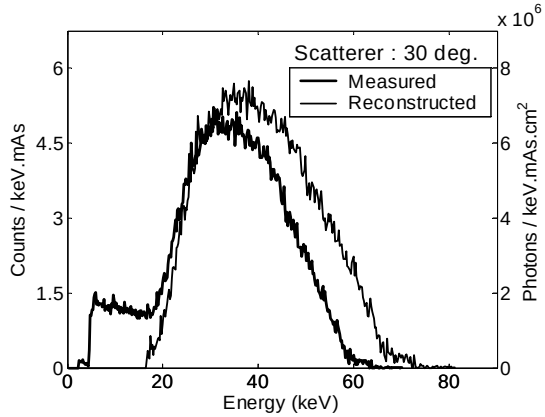

Fig. 5. Measured and reconstructed spectra using a scatterer with 30º cutting angle for 70 kV tube voltage

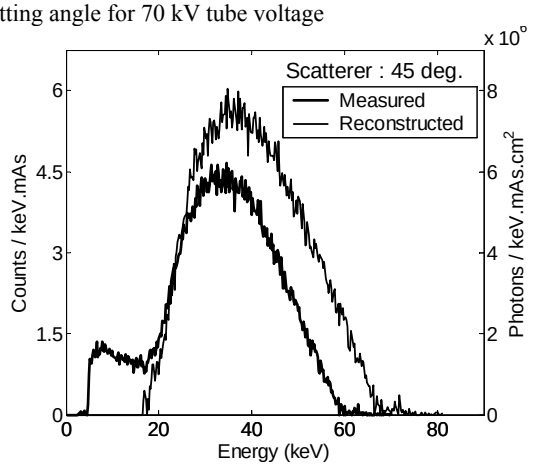

Fig. 6 Measured and reconstructed spectra using a scatterer with 45º cutting angle for 70 kV tube voltage

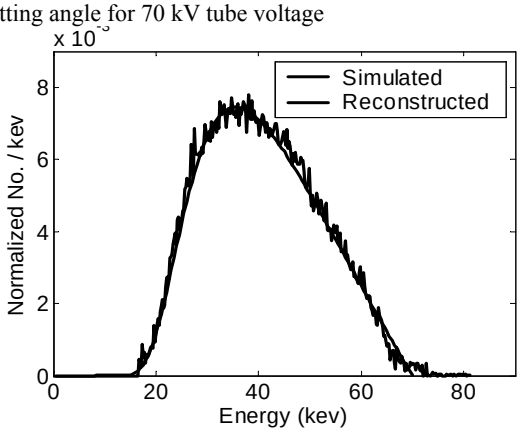

Fig. 7. Comparison of reconstructed spectra from 30º cutting angle with simulated one for 70 kV tube voltage

Table 1. Comparison of measured exposure and calculated exposures for tube voltage of 70 kV

Method	Exposure (mR)
From scatterer with 30º cutting angle	669.9
From scatterer with 45º cutting angle	680.3
Ionization chamber	690.0

Fig. 7 compares reconstructed spectra from 30º cutting angle with the simulated primary spectra using MCNP4C for tube voltage of 70 kV. In **Table 1** calculated exposure from reconstructed spectra (**Fig. 5** and **Fig. 6**) is compared with measured one by ion chamber for tube voltage of 70 kV.

The measured exposure is in good agreement with calculated exposures from the reconstructed spectra (within 3.5%). Also there is a small discrepancy between simulated primary spectra and the reconstructed spectra (**Fig. 7**). These results prove the validity of the present Compton spectrometry using the two mentioned scatterers.

IV. Conclusion

In our study we acquired diagnostic x-ray spectrum by Compton spectroscopy from two thick carbon scatterers. Appropriate thick scatterer shape was studied for Compton scattering measurement using Monte Carlo calculation. The results of the present method were validated by Monte Carlo calculation and exposure measurement.

Therefore, Compton scattering measurements by thick carbon scatterers can be used effectively to evaluate the performance of radio-diagnostic systems.

Acknowledgement

The authors would like to express their gratitude to operating crew of Sendai Kousei hospital for the kind cooperation.

References

1) G.A. Carlsson, C. A. Carlsson, K. Berggren and R. Ribberors, " Calculation of scattering cross sections for increased accuracy in diagnostic radiology. I.energy broadening of Compton-scattered photons," Med. Phys., 9[6], 868 (1982).
2) M. Yaffe, K. W. Taylor, and H.E. Hohns, "Spectroscopy of diagnostic x ray by a Compton-scatter method," Medical Physics, 3[5], 328 (1976).
3) G. Matscheko, G. A. Carlsson and R. Ribberfors, "Compton spectroscopy in the diagnostic x-ray energy range. II. Effects of scattering material and energy resolution," Phys. Med. Biol., 34[2], 199 (1989).
4) G. Matscheko, G. A. Carlsson, "Compton spectroscopy in the diagnostic x-ray energy range. I. Spectrometer design," Phys. Med. Biol., 34[2], 185 (1989).
5) S. Gallardo, J. Rodenas and G. Verdu, "Monte Carlo simulation of the Compton scattering technique applied to characterize diagnostic x-ray spectra," Med. Phys., 31[7], 2082 (2004).
6) K. Maeda, M. Matsumoto, A. Taniguchi, "Compton-scattering measurement of diagnostic x-ray spectrum using high-resolution Schottky CdTe detector," Med. Phys., 32[6], 1542 (2005).
7) A. Mohammadi, M. Baba, H. Ohuchi, "Investigation of the response function of the Schottky CdTe detector with guard-ring cathode through Monte Carlo calculation and measurement," JRSM (in press).
8) M. R. Ay, M. Shahriari, S. Sarkar, M. Adib and H. Zaidi, "Monte Carlo simulation of x-ray spectra in diagnostic radiology and mammography using MCNP4C," Phys. Med. Biol., 49, 4897 (2004).

Journal of NUCLEAR SCIENCE and TECHNOLOGY, Supplement 5, p. 337–339 (June 2008)

Investigation into the Dispersion Coefficients for Natural Rivers by Using a Radiotracer Method

Sung-Hee JUNG[1*], Jong-Bum KIM[1], Jin-Seop KIM[1], Joon-Ha JIN[1], Jae-Hyuk Hyun[2], and Il-won SEO[3]

[1]*Dept. of Radioisotope R&D, Korea Atomic Energy Research Institute, Daejon, Korea*
[2]*Department of Environmental Engineering, Chungnam National University, Daejon, Korea*
[3]*School of Civil, Urban, Geosystem Engineering, Seoul National University, Seoul, Korea*

The mixing characteristics of natural rivers were investigated by analyzing their radioisotope concentration curves for transverse dispersion coefficients. The radioisotope was instantaneously injected into a river as a point source by means of an underwater glass-vial crusher. The detection was made with 60 2inch NaI(Tl) scintillation detectors bound to 6 transverse lines at a downstream position. The multi-channel data acquisition systems, specifically fabricated by the research group for field studies, collected and processed the detection signals transmitted from the detectors. Transverse dispersion coefficient was determined by a moment method on the basis of field measurement data. As a result, the averaged transverse coefficients were 0.25 for S-River and 0.24 for H-River. This result was compared with the conventional values calculated with the empirically proposed formulas and its physical meaning is discussed.

KEYWORDS: transverse dispersion coefficient, natural river, radiotracer, simple moment method

I. Introduction

Industrial development over the last several centuries has caused serious problems. A pollutant is one of those problems, as a result of an increase in the population. When a pollutant has not been processed properly before flowing into rivers, it threatens the environment and the ecosystem. Understanding of hydraulic mixing behaviors is of importance in order to minimize the environmental impact of pollutants and to set up protection plans for rivers.

Pollutants are diluted in rivers mainly by a dispersion that is a spreading out of the particles along a stream or channel due to differences in their velocity. Evaluation of such dispersion characteristics is necessary in terms of the maintenance of a water quality. Especially, a transverse dispersion determines the degree of mixing of pollutants from point sources across the rivers.

The dispersion process in a natural river with many curvatures is so complicated that its dispersion coefficients should be accurately evaluated. Unfortunately, they have seldom been obtained in the field in Korea. In many cases, the dispersion coefficients for simulating the dynamic behaviors of rivers in Korea have cited foreign researches which had been carried out on their own rivers and hydraulic models. This causes a potential risk in that the self purification capacity of a river could be overestimated.

Tracer methods constitute a very convenient means for an observation and examination of effluent dispersion and dilution processes in natural water receivers. Particularly radioisotope tracers provide valuable information with a high accuracy that originates from an in-situ measurement method with no sampling procedure. The mixing characteristics of natural rivers were investigated by analyzing their radioisotope concentration curves for their transverse dispersion coefficients.

II. Experiment

1. Radiotracer Detection Range

Sensors for detecting a radiotracer were submerged under water and the concentration of radiotracer passing around those sensors was measured. The detection range of the radiation sensor was experimentally determined as follows. For the calculation of the experimental linear attenuation coefficient (μ), 2inch NaI detector was placed at 21.8cm distance (x) from the radioisotope and the radiation intensity (I_0) was measured. In turn, the space corresponding to the distance (x) was filled with water and the radiation was measured (I). From the well-known Beer-Lambert equation, the measured intensity as the function of distance from the center of a sensor was derived. As plotted in the **Fig. 1**, more than 90% of the radiation intensity originated from the surrounding volume of 50cm in radius so that the measurement can be assumed as point detections in the consideration of the interval distance between sensors in a transverse line of 5~10m.

$$\mu = \frac{\ln I_0/I}{x} = \frac{\ln 1623/511}{21.8} = 0.053\,cm^{-1}$$

$$dI \propto 4\pi x^2 x^{-2} e^{-0.053(x-3.15)} dx \propto e^{-0.053(x-3.15)} dx$$

$$I = k \cdot \int_{3.15}^{x} e^{-0.053(x-3.15)} dx = k \cdot (1 - 1.28e^{-0.053x})$$

*Corresponding Author, Tel. +82-42-868-8057, Fax. +82-42-862-6980, E-Mail: shjung3@kaeri.re.kr

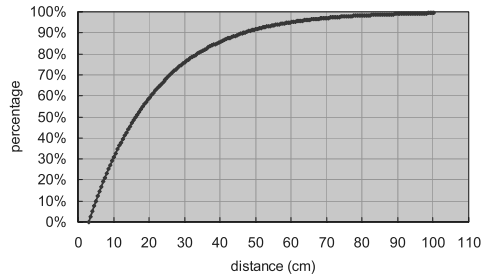

Fig. 1 Calculation of radiation detection measurement in the water

2. Radiotracer Injection and Measurement

The radioisotope, approx. 20mCi of I-131 whose half-life and maximum gamma energy is 8.04days and 0.723MeV respectively, was instantaneously injected as a tracer into the river stream by means of an underwater glass-vial crusher. The tracer measurement was made with 60 2inch NaI(Tl) scintillation detectors bound to 6 transverse lines in the downstream from L1 to L6 as shown in the **Fig. 2**. The detectors were placed in the middle of the water at as low a depth as possible in order to obtain a representative concentration profile. The multi-channel data acquisition systems, specifically fabricated by the research group for radiotracer field studies, collected and processed the detection signals and transmitted them to a portable computer. **Fig. 3** shows the radiotracer measurement results obtained from between S-river and H-river. The basic hydraulic parameters such as a water flow rate and depth profile along the transverse lines were measured just before a radiotracer injection[1].

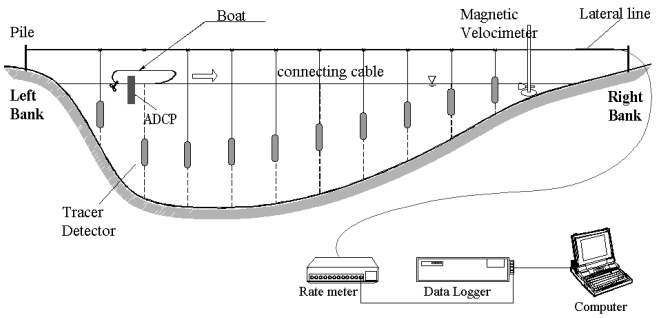

Fig. 2 The installation of radiotracer detection system.

3. Data Conversion into a Tracer Concentration

As the measured radiation data was being recorded as counts per a unit of time, it was converted to its corresponding concentration of a radioisotope by a conversion factor that was evaluated from a radioisotope dilution experiment. It was turned out to be $2.2\times10^{-7}\mu Ci\cdot ml^{-1}$/cps from the lab experiment.

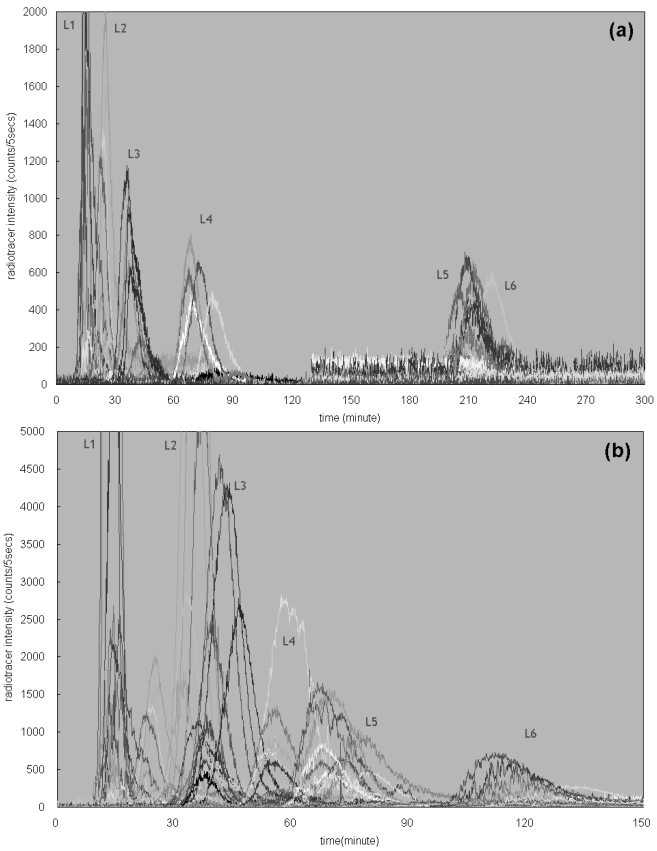

Fig. 3 Radiotracer Measurement Results: (a) S-river, (b) H-river

4. Transverse Dispersion Coefficient by Simple Moment Method

In most cases, the width of a river is much larger than the depth and a pollutant is readily mixed vertically relatively in a short time period rather than transversely. Therefore, the vertical concentration gradients can be neglected thus attention is focused on the transverse and longitudinal changes of the depth-averaged concentrations of the pollutant in this study. The two-dimensional advection-dispersion equation can be expressed as below.

$$\frac{\partial C}{\partial t}+u\frac{\partial C}{\partial x}+v\frac{\partial C}{\partial y}=\frac{1}{h}\frac{\partial}{\partial x}\left(hD_L\frac{\partial C}{\partial x}\right)+\frac{1}{h}\frac{\partial}{\partial y}\left(hD_T\frac{\partial C}{\partial y}\right) \quad (1)$$

where C=depth-averaged concentration; t=time; x= longitudinal distance measured from the injection point; y=transverse distance measured form the left bank; u,v=depth-averaged longitudinal and transverse velocities; h=depth; and D_L, D_T=longitudinal and transverse dispersion coefficients, respectively.

By integrating Eq. (1) with respect to a time from t=0 to ∞, the calculation of the transverse dispersion coefficient can be extended, as Beltaos(1975)[2] presented, to unsteady situations where a radiotracer is injected into water.

$$\int_0^\infty C dt+\int_0^\infty u\frac{\partial C}{\partial x}dt+\int_0^\infty v\frac{\partial C}{\partial y}dt=\frac{1}{h}\int_0^\infty\frac{\partial}{\partial x}(hD_L\frac{\partial C}{\partial x})dt+\frac{1}{h}\int_0^\infty\frac{\partial}{\partial y}(hD_T\frac{\partial C}{\partial y})dt \quad (2)$$

For a steady flow, the quantities (u, v, h, D_L and D_T) are independent of the time. Furthermore, by observing that

$$\int_0^\infty C dt = 0$$

for an instantaneous injection, the equation becomes

$$u\frac{\partial\theta}{\partial x}+v\frac{\partial\theta}{\partial y}=\frac{1}{h}\frac{\partial}{\partial x}\left(hD_L\frac{\partial\theta}{\partial x}\right)+\frac{1}{h}\frac{\partial}{\partial y}\left(hD_T\frac{\partial\theta}{\partial y}\right) \quad (3)$$

where θ = dosage of a tracer which is defined as following

$$\theta \equiv \int_0^\infty C(x,y,t)dt$$

For a steady-state concentration condition, the time variations vanish and the longitudinal dispersion can be negligible. Assuming both the velocity and depth are constant, and the transverse velocity is negligibly small, the above equation can be simplified to

$$u\frac{\partial\theta}{\partial x}=D_T\frac{\partial^2\theta}{\partial y^2} \quad (4)$$

By multiplying y^2 and integrating it, the moment equation for the transverse dispersion coefficient is as follows[3]:

$$D_T=\frac{u}{2}\frac{\partial}{\partial x}\left(\frac{\int_0^W\theta y^2dy}{\int_0^W\theta dy}\right)=\frac{u}{2}\frac{d\sigma_y^2}{dx} \quad (5)$$

where σ^2_y is the variance of the transverse distribution of the depth-averaged concentration. D_T was obtained from the slope of the straight line that was fitted to the data in the plot of σ^2_y versus x.

III. Results and Discussion

From a study in a mildy curved river, Glover(1964) measured the temperature distributions downstream of a heated water discharge from a power plant and analyzed them for the transverse dispersion coefficients (DT/HU*)[4]. It was calculated as 0.72 which is definitely higher than the radiotracer measurement values, 0.25 for S-river and 0.24 for H-river. It is evident that there may be a risk in overestimating a self-purification of a river by simply adopting reference values without confirming their validity by the field measurement.

It was clearly confirmed that radiotracer technique is very useful for obtaining hydraulic parameters from a natural site that is such a vast system to establish measurement data by sampling technologies. This radiotracer technique for hydraulic research can contribute to the sustainable development of natural resources.

Acknowledgement

This study was carried out under the national nuclear research & development project supported by MOST. Special thanks are given to Professor Il-Won Seo and his students of Seoul National University for adapting radiotracer technologies into the environmental resource monitoring research area.

References

1) Il Won SEO, Kyong Oh BAEK, Tae Myong JEON, 'Analysis of transverse mixing in natural streams under slug test', J. Hydraul. Res. 1-13, 2006.
2) Beltaos, S. 'Evaluation of transverse mixing coefficients from slug tests' J. Hydr. Res., IAHR, 13(4), 351-360, 1975.
3) Sayre, W. W., and Chang, F. M., 'A laboratory investigation of open channel dispersion processes for dissolved, suspended, and floating dispersants' Professional Paper No.433-E, U.S. Geological Survey, 1968.
4) Glover, R. E., 'Dispersion of dissolved or suspended materials inflowing streams' Professional Paper No. 433-B, U.S. Geological Survey, 1964.

Journal of NUCLEAR SCIENCE and TECHNOLOGY, Supplement 5, p. 340–343 (June 2008)

A Feasibility Study of X-ray Inspection System Using 90°Compton Scattering

Chang-Ho SHIN[1], Ji Sung PARK[2], Soon Young KIM[1], and Jong Kyung KIM[2*]

[1]*Innovative Technology Center for Radiation Safety, Hanyang University, Seoul 133-791 Korea*
[2]*Department of Nuclear Engineering, Hanyang University, Seoul 133-791, Korea*

A X-ray inspection system, a 90° Compton scattering inspection system coupled with a dual energy method, has been studied, which can directly give the effective atomic number of an unknown object. The 90° scattered signals by irradiating dual energy X-ray beams are measured and used to identify the unknown object hidden among other objects. Many simulations were carried out to verify the feasibility of this work with the illicit materials hidden in many kinds of sample geometries. From the simulation results, the dual energy beam method proposed in this study can find out the effective atomic numbers of the illicit materials. In the cases having simple geometry, all the relative differences between the calculated effective atomic number and the true value are shown to be less than 6.5 %. The feasibility of the dual energy beam method is also verified by scattering experiments using many kinds of sample geometries with TNT simulant. X-ray beams filtered by the ISO standard are used as the radiation source. A narrow detector collimator is employed in front of the detector for an accurate measurement of 90° Compton scattering signals. In the simple geometries containing TNT simulant, it was found that the relative differences between the reference and calculation results were less than 10%. According to the simulation and experiment results, the 90° Compton scattering inspection method coupled with a dual energy method will be effective to find the properties of unknown objects.

KEYWORDS: Compton scattering, inspection system, dual energy method, effective atomic number, explosive detection

I. Introduction

In recent years, as air terrorism has increased rapidly, the importance of an inspection system is becoming more emphasized as well. Several countries that have advanced techniques for the inspection system have been developing new inspection methods, but the inspection system that can identify even the properties of illicit materials has not yet been developed despite their constant efforts.

As the new inspection technique to overcome the weak points of current inspection systems, scattering methods with X-ray source have been being considered because scattering methods provide other factors compared with the transmission factors. Nowadays the well-known commercialized scattering methods are the Back-scattering method[1)] and the coherent scattering method[2)]. These methods have the advantage that they can identify a specific organic material such as explosives or drugs, but they also have the disadvantage that they cannot identify suspicious materials located in a deep position of the luggage. To improve the inspection capability, a 90° Compton scattering method is suggested.[3)] It is known that this method can be useful to inspect explosives and other contraband materials in passenger luggage. Because it uses higher X-ray energy than the other scattering methods, the X-ray can reach suspicious materials located in luggage therefore, it can detect the signals in a deep position. Additionally, since this method requires only the conventional X-ray machine and basic detection system, it does not need to cost as much as the coherent scattering method.

Among these studies, the 90° Compton scattering method has been studied at Hanyang University since 2002.[4] In this paper, to improve the ability of material identification of the 90° Compton scattering method, an approach, called the dual energy beam method, was suggested. MCNP[5)] simulation has been performed to demonstrate the dual energy beam method, and then experimental studies have been carried out to verify the feasibility of this method.

II. Methodology

In this work, the relation between an effective atomic number and the ratio of attenuation coefficients for two energies was studied and various energy pairs are suggested. Then energy pairs that have shown a high gradient between the effective atomic number and the ratio of attenuation coefficient are determined, which were 70/100 keV, 70/120 keV, and 70/150keV.

According to XCOM (Photon Cross Section Database)[6)], the mass attenuation coefficient was calculated by Eq (1), which is expressed in terms of the photon mass attenuation in compound material.

$$\mu_{t,comp}/\rho = \sum_i \omega_i \left(\mu_{t,i}/\rho_i \right) \quad (1)$$

where $\mu_{t,comp}/\rho$ is mass attenuation coefficient of atom *i*,
ω_i is the mass ratio of atom *i*.

* Corresponding Author, Tel. +82-2-2220-0464, Fax. +82-2-2294-4800, E-mail: jkkim1@hanyang.ac.kr

$R_{E1/E2}$ which is the attenuation coefficient ratio for high energy, E_1, and low energy, E_2, is expressed in Eq (2).

$$R_{E_1/E_2} = \frac{\mu_t(Z_{eff}, E_1)/\rho}{\mu_t(Z_{eff}, E_2)/\rho} \quad (2)$$

where $\mu_t(Z_{eff}, E_1)/\rho$ is the mass attenuation coefficient for high energy, E_1, $\mu_t(Z_{eff}, E_2)/\rho$ is the mass attenuation coefficient for low energy, E_2.

Then by using Eq (2) the fitting equation that expresses the relation between the atomic number and the attenuation coefficient is developed as shown in Eq (3). Eq (3) is the polynomial fitting equation which is based on the relation between the atomic number and the attenuation coefficient. The constant 'a_n'is the polynomial fitting constant, and 'i' is the polynomial fitting order.

$$R_{E_1/E_2} = \sum_{n=0}^{i} a_n (Z_{eff})^n \quad (3)$$

where a_n is the coefficient of i-th term.

Finally, to verify the dual energy beam method using Eq (3), simulation studies and scattering experiments were performed for simple geometries as shown in **Fig. 1.**

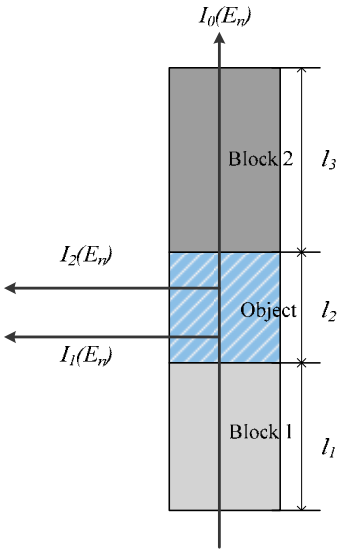

Fig. 1 Simple Geometry for Verifying the Dual Energy Beam Inspection Method (E_1=70 keV, E_2=120 keV, $I_i(E_n)$ = Scattered Response of Initial Source($I_0(E_n)$) at i-th position in Scattering Object)

III. MCNP Calculation

1. Material and Geometry

Many simulation studies using illicit materials hidden in innocuous materials were performed for the demonstration of the dual energy beam method. Scattering objects of 3 cm in length are enclosed by two kinds of innocuous materials. Three simple geometry cases of 4 cm - 3 cm - 5 cm, 7 cm - 3 cm - 5 cm, and 10 cm - 3 cm - 5 cm respectively for the l_1 - l_2 - l_3 parameters in **Fig. 1** were considered for the calculation. The scattering materials used in this study include two kinds of drugs and five kinds of explosives, and neighboring materials consist of ten kinds of sample pairs. Various combinations of illicit and neighboring materials for simulation are considered as shown in **Table 1**.

Table. 1 Various Combinations of Illicit and Neighboring Materials for Simulation Experiment: 70 Different Cases in Total

Object
Hydrochloride form Cocaine
Hydrochloride form Morphine
TNT
Nitro Cellulose
Nitro Glycerine
C-4
RDX

Case	Neighboring Materials	
	Block 1	Block 2
1	Polyethylene	Acetal
2	Polyethylene	Aluminum
3	Wood	Polyethylene
4	ABS	Sugar
5	ABS	Polyester
6	Polyester	Teflon
7	Teflon	Urethane
8	PVC	ABS
9	Polyurethane	PVC
10	Polyester	PVC

2. Results and Discussions

The effective atomic numbers were calculated in the simple geometry by eq (3). As a result, in the case of drug, the relative difference of the effective atomic number between the reference value and the calculated value is less than 3 %, compared with XCOM data. In the case of explosive, the computed value is less than by 6 %, compared with XCOM data. Therefore the method can estimate the effective atomic number of the illicit material, and it was demonstrated that the method is more accurate than the conventional inspection system [7]. The calculation results are shown in **Table 2**.

Table. 2 Computed Effective Atomic Numbers for Various Sample Sets by Simulation (E_1/E_2=70/120, l_1= 4 cm, l_2=3 cm, l_3=5 cm)

Neighboring material (Block 1, 2)	Cocain		Morphine		C4		TNT	
	Z_{eff}	Error (%)	Z_{eff}	Error (%)	Z_{eff}	Error (%)	Z_{eff}	Error (%)
	9.59	Ref.	9.44	Ref.	7.30	Ref.	7.25	Ref.
Polyethylene-Acetal	9.67	0.83	9.39	0.54	7.25	0.64	7.20	0.76
Polyethylene-Aluminum	9.42	1.74	9.24	2.03	7.04	3.58	7.03	3.14
Wood-Polyethylene	9.69	1.09	9.36	0.8	7.23	1.01	7.2	0.69
ABS-Sugar	9.67	0.8	9.37	0.66	7.27	0.42	7.18	1.01
ABS-Polyester	9.63	0.44	9.35	0.87	7.18	1.65	7.14	1.61
Polyester-Teflon	9.43	1.68	9.3	1.45	7.02	3.86	7.19	0.91
Teflon-Urethane	9.47	1.24	9.27	1.73	7.27	0.41	7.19	0.94
PVC-ABS	9.59	0.01	9.31	1.36	7.06	3.37	7.06	2.66
Polyurethane-PVC	9.64	0.49	9.37	0.74	7.20	1.45	7.16	1.35
Polyester-PVC	9.51	0.79	9.34	1.02	7.11	2.59	7.23	0.35
RMS Error		1.1		1.27		2.29		1.59

IV. Scattering Experiment

1. Materials and Configuration

The feasibility of the developed method was verified by scattering experiment using many kinds of sample cases with TNT simulant.

To secure the high count rate for scattering measurements, a 450 kV industrial X-ray tube (Xylon MG450[8]) with a tungsten target) was used as a radiation source. To measure the weak scattering signal, CsI(Tl) scintillator which has high detection efficiency was chosen. For the shielding device to obstruct the background signal simultaneously, the detector collimator was manufactured. Also, some filters, which produces a uniform distribution at the specific energy band, were fabricated. As a result, two standards N80 and N150 x-ray source[9] were manufactured. The effective energies of N80 and N150 x-ray source are 69 keV and 120 keV, respectively.

A scattering sample was TNT simulant which has the same composition and material properties but does not explode. All experiment devices and configuration are shown in **Fig. 2**, and the experiment for diary-TNT-6nylon sample is shown in **Fig. 3**.

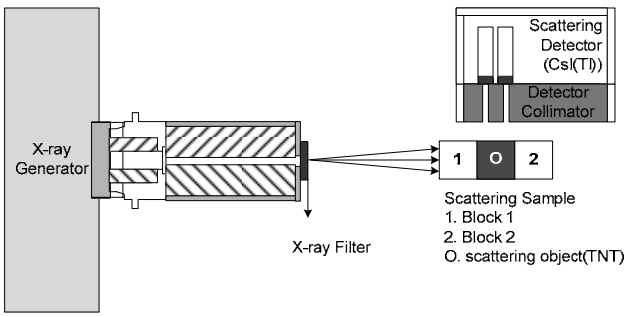

Fig. 2. 90° Compton Scattering Experiment Configuration

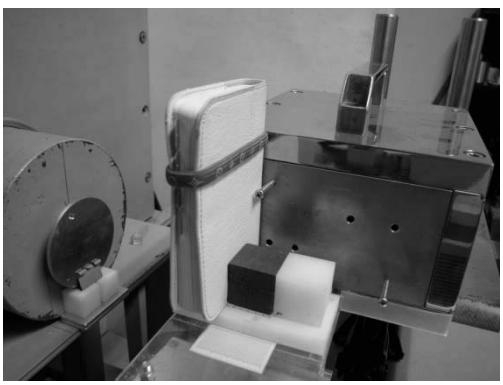

Fig. 3 Scattering Experiment for Diary-TNT-6Nylon Sample Set

2. Results and Discussions

Using the 90° Compton scattering measurement system, the scattering signals were obtained. In this study, for the calculation of the effective atomic number, the two kinds of scattering spectra are required, which are measured using N80 and N150 X-ray sources. The detection time for each experiment was 30 min, and the X-ray intensity was 5 mA for N150 experiments, 10 mA for N80 experiments.

As the experiment results, scattering spectra of TNT simulant for the various sample pairs were obtained. **Fig. 4** shows the measured scattering spectra for N150 X-ray beam.

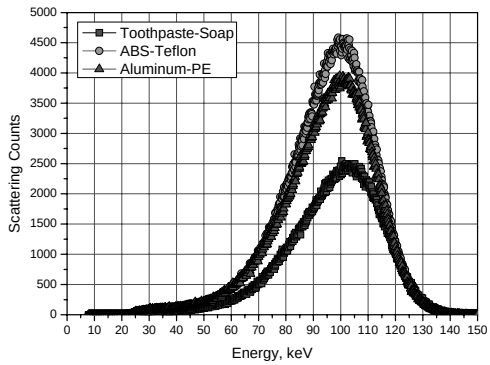

Fig. 4 Scattering Spectra for Various Sample Sets (N150)

To obtain scattering counts, ROI(Region of Interest) was ~~is~~ determined as in **Eq (4)**.

$$ROI = P_0 \pm FWHM,\ C_{Total} = \frac{\sum_{n}^{n+m}(C_n \times E_n)}{\sum_{n}^{n+m} E_n} \qquad (4)$$

where P_o is the peak center channel, C_{Total} is total counts of ROI, n is the left channel of ROI, En is energy of channel n

The effective atomic numbers for each illicit material were calculated using the scattered signals. The calculation results are presented in **Table 3**. From the experiment results, it is found that the relative differences were less than 10 % for all the sample sets. In case of the Polyethylene-TNT-Aluminum sample set, the relative difference of the effective atomic number was 0.86 %. Considering the average error, 30 %, of conventional inspection system for material identifications, the result is shown to be quite accurate.

Table. 3 Computed Effective Atomic Numbers for Various Sample Sets by Experiment

Sample Set	$Z_{eff,TNT}$		Relative Difference (%)
	Reference Value *	Calculated Value	
Toothpaste-TNT-Soap	7.25	7.8456	-10.26
Diary-TNT-6Nylon		7.4236	-4.34
ABS-TNT-Teflon		7.3963	-3.95
Al-TNT-PE		7.176	-0.86

* The reference value are based on XCOM data fitting fuction

V. Conclusions

In this study, a 90° Compton scattering inspection method has been introduced and validated by simulation and experiment studies.

Relative difference between calculation and experiment were less than 10% for all of the samples. The dual energy beam method can accurately estimate the effective atomic number of an unknown object regardless of its location inside the samples.

As a future work, research for complex sample geometries will be carried out for this method to be applied to practical use.

Acknowledgement

This study was performed under the long-term nuclear research and development program sponsored by Ministry of Science and Technology of Korea (M20505080001-05A0908-00110), and supported by the Innovative Technology Center for Radiation Safety (R11-2000-067-01001-0)

References

1) P. Zhu, P. Duvauchelle, G. Peix, and D. Babot, X-ray Compton Backscattering Techniques for Process Tomography: Imaging and Characterization of materials, Meas, Sci. Technol., 7, 281, 1996.
2) H. Strecker, G. Harding, H. Bomsdorf, J. Kanzenback, R. Linde, and G. Martens, Detection of Explosives in Airport Baggage Using Coherent X-ray Scatter, SPIE, 2092, 299, 1993.
3) N. V. Arendtsz and E. M. A. Hussein, Compton Scattering for Density Imaging, Proceedings of the Second International Symposium on Explosive Detection Technology, 137, 1996.
4) T.K. Tuan, S.H. Park, and J.K. Kim, Development of a New Reconstruction Algorithm for Compton Scattering Imaging, Journal of Nuclear Science and Technology, supplement 4, 283, 2004.
5) D.B. Pelowitz, editer, MCNPXTM User's Manual, Version 2.5.0," LA-CP-05-0369, 2005.
6) M. J. Berger, J. H. Hubbell, S, M. Seltzer, J. Chang, J. S. Coursey, E. Sukumar, and D. S. Zucker, XCOM: Photon Cross Section Database (Version 1.3), National Institute of Standards and Technology, Gaithersburg, MD, USA, 2005.
7) Assessment of the Practicality of Pulsed Fast Neutron Analysis for Aviation Security, Panel on Assessment of the Practicality of Pulsed Fast Neutron Analysis for Aviation Security, National Research Council, 16 pages, 2002.
8) Technical description of MG450/D02, Copies obtainable from Yxlon International, http://www.yxlon.com. 2004.
9) Table VIII.6. ISO X-Ray Beam Quality Parameters Offered at NIST, http://physics.nist.gov/Divisions/Div846/Gp2/tab86.html.

Journal of NUCLEAR SCIENCE and TECHNOLOGY, Supplement 5, p. 344–347 (June 2008)

A Performance and an Imaging Result of Silicon Strip Detector

Youngim KIM[1], Sangsu RYU[1], Heedong KANG[1]
Hongjoo KIM[1], Hwanbae PARK[1*], Jungho SO[1], Dohee Son[1] and Kyeryung KIM[2]

[1] *Department of Physics, Kyungpook National University, Daegu 702-701, Korea*
[2] *Proton Engineering Frontier Project, Korea Atomic Energy Research Institute, Daejeon 305-600, Korea*

Since capacitively coupled readout has an advantage of shielding the readout electronics from sensor leakage current, we fabricated an AC-coupled single-sided silicon strip sensor on 5-in. 380 μm-thick wafer and its active area is 3.2 × 3.2 cm^2. It has 64 implanted and readout strips with a strip pitch of 500 μm. Two silicon strip sensors were mounted perpendicularly one another to get two-dimensional position information with a 5 mm space gap. Two low noise analog ASICs, VA1 chips, were used for signal readout of the strip sensor. The single-sided silicon strip detector (SSSD) consists of the two AC-coupled single-sided strip sensors and readout electronics. The SSSD was housed in an Al light-tight box. A CsI(Tl) scintillation crystal and a 2-in. photomultiplier tube were used to trigger signal events. The data acquisition systems were based on a 64 MHz FADC and control softwares for the PC-Linux platform. Experiments were performed at room temperature and silicon sensors were fully depleted. The SNRs were measured to be 29.1 ± 2.2 and 26.4 ± 0.3, respectively, for a 45 MeV proton beam and a ^{90}Sr radioactive source. Imaging tests were performed using a Pb phantom with a ^{90}Sr radioactive source and a 45 MeV proton beam, respectively. From the two-dimensional hit distribution, the phantom images were obtained and the position resolution was estimated to be about 240 μm.

KEYWORDS: silicon strip detector, proton imaging, phantom image, signal-to-noise ratio, cyclotron

I. Introduction

The silicon is the most widely used basic semiconductor material for the radiation detector and the silicon strip detector technology has been used to obtain position measurement. Due to high intrinsic precision and high speed properties of the strip detector, it has been used as positioning detectors in space science and experimental nuclear and particle physics.

A pixel-type detector provides very good position resolution but has very high occupancy in radiation hard environment. This problem can be resolved by having strip-type detector. The number of readout channels is reduced by dividing the diode into strips and position sensitivity is obtained by creating a situation in which the signal charge is split amongst more than one readout electrodes with the ratio of charges depending on the position. The direct coupling can lead to pedestal shifts, a reduction of the dynamic range, and may even drive the electronics into saturation. Since capacitively coupled readout shields the readout electronics from sensor leakage current, the AC-coupled single-sided silicon strip sensors were designed and fabricated. For signal readout, the front-end electronics and DAQ system were developed.

The purposes of this research are to analyze the signal-to-noise ratios of the silicon strip detector, and to demonstrate phantom images by using a radioactive source and a proton beam.

*Corresponding Author, Tel. +82-53-950-7351, Fax. +82-53-953-7351, E-mail: sunshine@knu.ac.kr

II. Silicon Strip Detector

1. Concept and Principle

The silicon sensor is fully depleted by applying a reverse bias voltage.[1)] One of advantages for the full depletion is that silicon bulk can be used as the active sensor volume. When charged particles pass through silicon bulk, electron-hole pairs are produced and electrons are collected in electrodes by the electric field. The high resolution of the silicon strip detector is achieved by dividing large area diode into many small strips and reading charge signals out separately. The position of the charged particle is then determined by the location of the strip showing signal.

Table 1 A specification of the fabricated AC-coupled single-sided silicon strip sensor.

high resistivity (> 5 kΩ·cm), <100>-oriented, and n-type silicon wafers	
sensor area (μm^2)	35,000 × 35,000
sensor thickness (μm)	380
strip pitch (μm)	500
implanted strip width (μm)	400
Readout strip width (μm)	420
Number of implanted strips	64

The silicon strip sensors were fabricated on a 5-in. n-type silicon wafer which has an <100> orientation, high resistivity (>5 kΩ·cm) and a thickness of 380 μm. A specification of the fabricated silicon strip sensors is shown in **Table 1**. They are single-sided and have 64 channels with a 500 μm pitch, and the active area is 3.2 × 3.2 cm^2 with a thickness of 380 μm.

To be considered as a good sensor[2], we required the leakage current of the sensor should be less than 10 nA/strip at the full depletion voltage. The leakage current of a single strip was measured to be about 1.4 nA at 60 volts and the capacitance value showed flatness from above 40 volts.

The designed and fabricated AC-coupled silicon strip sensor has capacitively coupled readout structure which provides the advantage of shielding the electronics from sensor leakage current. In AC-coupled sensor design, capacitances of a sensor were made by separating implantation and metallization of the strips. Meanwhile, biasing resistors of a sensor were made in polysilicon. A thickness of the SiO_2 layer, width and thickness of the polysilicon were optimized to provide required capacitance and biasing resistance, respectively. The DC pads were also built for leakage current measurement.

Design, fabrication process and electrical characteristics measurements of the fabricated AC-coupled silicon strip sensors are described in detail by Kah et al.[3]

2. Performance Tests

This experiment was performed with a 45 MeV proton beam from the MC-50 cyclotron at the Korea Institute of Radiological and Medical Science (KIRAMS) in Seoul, Korea.[4] Two AC-coupled silicon strip sensors, each of them has 64 readout channels, were used for the experiment. Experiment was done at room temperature and sensors were biased at 46 V to fully deplete sensors. They were mounted perpendicularly one another to provide two-dimensional position information with a 5 mm space gap and the silicon strip sensor assembly is shown in **Fig. 1**.

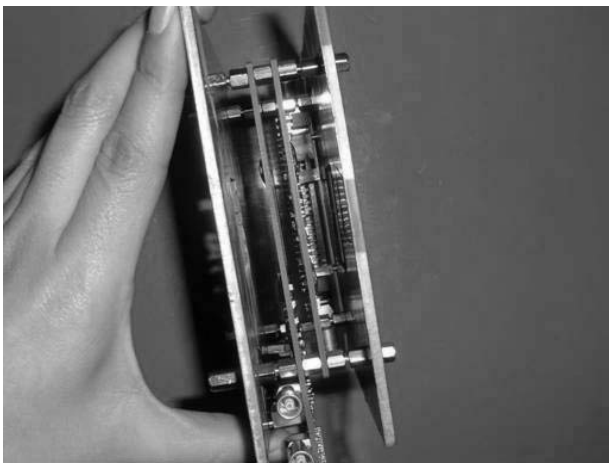

Fig. 1 Two AC-coupled strip sensors are mounted perpendicularly one another to provide two-dimensional position information.

Two low noise analog ASICs, VA1 chips, were used for analog signal readout. We used our VA-hybrid board, Interface board, and VA-control board[5] to read sensor signal out. The serially clocked signals of 64 channels were read out for each event with a 12-bit 64 MHz Flash analog-to-digital converter (FADC).[6] The FADC was located in a VME crate and was read out by the Linux-operating PC through the VME-USB2 interface. The DAQ system and analysis program were written in the framework of ROOT[7] package. The experimental set up is shown in **Fig. 2**.

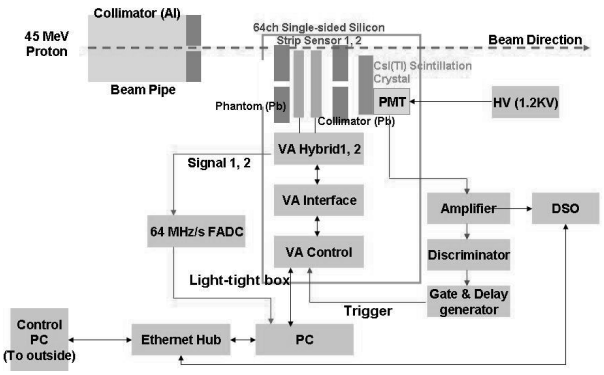

Fig. 2 Experimental setup for performance tests of the manufactured silicon strip detector with a proton beam at the KIRAMS. Sensor assembly is placed intentionally off the beam axis to protect it from radiation damage.

A CsI(Tl) scintillation crystal and a 2-in. photomultiplier tube were used to trigger signal events. The silicon strip sensors, readout electronics and a CsI(Tl) crystal are all assembled in an aluminum light-tight box to shield light and reduce electromagnetic interference. The silicon strip sensor assembly and developed readout electronics were located just behind of the phantom. **Fig. 3** is signal-to-noise ratio of all 64 channels and the average value was measured to be 29.1 $\pm$ 2.2 for a minimum ionizing particle (MIP).

The active sensor area is 3.2 × 3.2 cm^2 and the phantom size is smaller so first and last strip of sensor didn't have the signal.

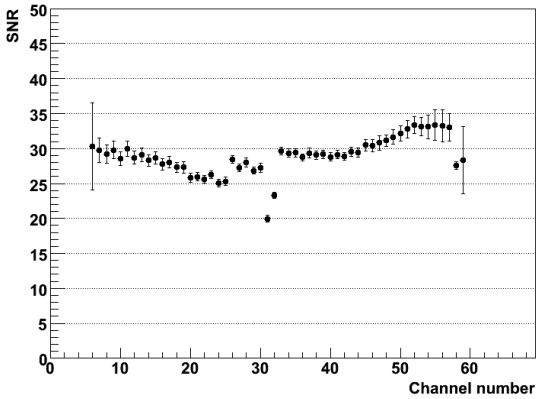

Fig. 3 Signal-to-noise ratios of all channels in the first sensor measured with a 45 MeV proton beam at the KIRAMS.

Two VA chips were used to read signals, each of them controlled 32 channels. A thickness of the lead phantom was 3 mm to absorb the proton beam energy. The phantom was 3.0 x 3.0 cm^2 in size. The first few (1 ~ 4) and the last few (60 ~ 64) channels did not have any signals because the size of the phantom was smaller than that of the active sensor area.

To assess the imaging capability of the silicon strip detector we built a phantom with a 3-mm-thick lead. A size

of the phantom is 30 × 30 mm^2 to fully cover the active area for the silicon detector and to absorb the proton beam energy. Sensor signals from the FADC were recorded in the PC and were analyzed. The two-dimensional plot of hit maps from the first (x-axis) and the second (y-axis) silicon strip detectors is shown in **Fig. 4**.

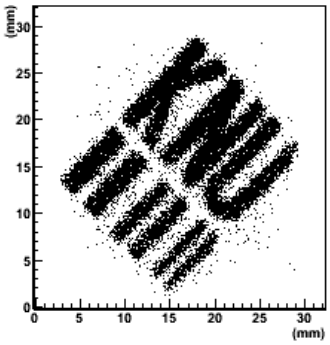

Fig. 4 Hit maps from the first (x-axis) and the second (y-axis) silicon detectors with a 45 MeV proton beam at the KIRAMS.

The width of these small rectangles ranges from 1 mm to 2 mm and the position resolution from hit distributions is estimated to be about 240 μm.

We also performed the sensor test using a ^{90}Sr radioactive source with the same experimental setup for the proton beam test. **Fig. 5** shows the pulse height spectrum measurement of a single strip channel and a signal-to-noise is measured. The signal-to-noise was measured to be 26.4 ± 0.3 for a MIP and this result is consistent with the proton beam test result.

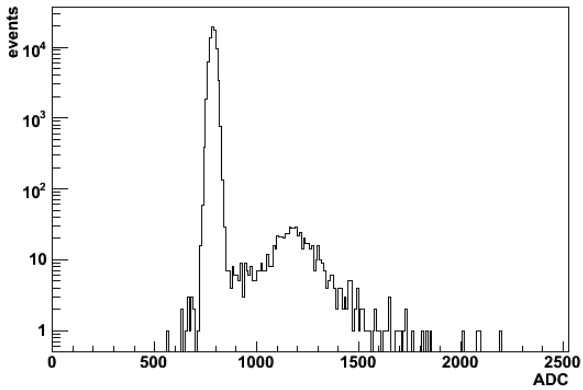

Fig. 5 Pulse height spectrum of a single strip channel measured with a ^{90}Sr radioactive source.

The image of the phantom was also obtained using a ^{90}Sr radioactive source. **Fig. 6** is the two-dimensional plot of hit maps from the first and the second silicon strip detectors. It showed many stray hits due to multiple scattering in silicon materials and space gap between the first and the second silicon detectors.

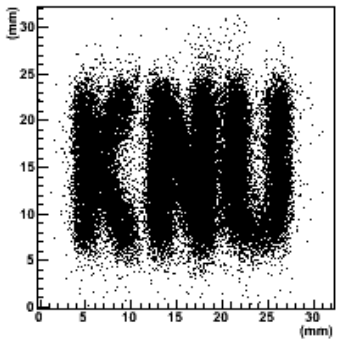

Fig. 6 Hit maps from the first (x-axis) and the second (y-axis) silicon detectors with a ^{90}Sr radioactive source by using the same experimental setup which was used for the proton beam.

III. Discussion

The measurement results of the signal-to-noise ratio of the silicon detector and electronics assembly provides the feasibility of using it as an X-ray imaging sensor. Many stray hits were observed for the radioactive source compared to the proton beam due to multiple scattering in silicon materials and the space gap between the first and the second silicon strip detectors. To avoid multiple scattering effect, achieve better position resolution and have self-triggering capability, we are currently fabricating double-sided silicon strip sensors and developing front-end readout electronics for an X-ray imaging.[8)]

IV. Conclusion

The AC-coupled single-sided silicon strip sensors were designed and fabricated on the 5-in. silicon wafers. The front-end electronics was built for sensor signal readout and assembled with the fabricated silicon strip sensors in the Al light-tight box.

The signal-to-noise ratio (SNR) of the silicon strip sensors with readout electronics was measured to be better than 25 for a MIP with a 45 MeV proton beam at the KIRAMS and a ^{90}Sr radioactive source, respectively. These results show that the developed strip detector with the AC-coupled strip sensors and the front-end electronics was performed well because it is considered to be good detector for SNR > 10. The performance tests as an imaging detector were carried out with an 3-mm-thick lead phantom by using a ^{90}Sr radioactive source and a 45 MeV proton beam, respectively, and the images of the phantom were obtained from the two-dimensional plot of hit maps from the two silicon strip detectors. The phantom images by using a radioactive source and a proton beam were demonstrated and the estimated position resolution from hit distributions is to be about 240 μm.

Acknowledgement

We acknowledge the support by Korea Science and Engineering Foundation under the Basic Atomic Energy Research Institute (BAERI) program, by a Korea Research

Foundation grant funded by the Korean Government (MOEHRD) (KRF-2005-070-C00032), and by the user program of the Proton Engineering Frontier Project. Y.I. Kim would like to thank Seoul Metropolitan Government for Seoul Fellowship.

References

1) Gerhard. Lutz, Semiconductor Radiation Detector, Springer, New York, pp110, (1999).
2) H. Park, H.J. Hyun, D.H. Kah, H.D. Kang, H.J. Kim, Y.I. Kim, Y.J. Kim, D.H. Shim, Y.I. Choi, Y.K. Choi, J. Lee, J.M. Park, K.S. Park, J. Korean Phys. Soc., 49[4], 1401-1406 (2006).
3) D.H. Kah, J.B. Bae, H.D. Kang, H.J. Kim, H. Park, J.M. Park, K.S. Park, "Fabrication and Measurement Result of Silicon Strip Sensors," The Fourth International Symposium on Radiation Safety and Detection Technology, Hanyang University, Seoul, Korea, July 18-20, 2007.
4) http://www.kirams.re.kr/kirams eng/index asp.
5) H.J. Hyun, S.W. Jung, D.H. Kah, H.D. Kang, H.J. Kim, H. Park, "Performance Tests of Developed Silicon Strip Detector by Using a 150GeV Electron Beam," The Fourth International Symposium on Radiation Safety and Detection Technology, Hanyang University, Seoul, Korea, July 18-20, 2007.
6) http://www.noticekorea.com
7) http://root.cern.ch
8) S. Ryu, J.B. Bae, H.J. Hyun, D.H. Kah, Y.I. Kim, H.D. Kang, H.J. Kim, H. Park, K.Y. Kim, J. Korean Phys. Soc., 50[5], 1477-1481 (2007).

Journal of NUCLEAR SCIENCE and TECHNOLOGY, Supplement 5, p. 348–351 (June 2008)

Fabrication of CZT Planar-Type Detectors and Comparison of their Performance

Se-Hwan PARK[1], Jang-Ho HA[1], Jae-Hyung LEE[1], Yoon-Ho CHO[1,2], Han-Soo KIM[1], Sang-Mook KANG[1,2], and Yong-Kyun KIM[2*]

[1] *Korea Atomic Energy Research Institute, Dukjin-dong, Yuseong-gu, Daejeon, Korea*
[2] *Hanyang University, Haengdang-dong, Seongdong-gu, Seoul, Korea*

CZT is one of the most promising materials for X-ray and γ-ray radiation detectors operated at room temperature. We have studied the fabrication process of the CZT planar-type detector, which includes the physical and chemical surface treatment, the fabrication of metal contact, and the surface passivation. CZT planar-type detectors with various metal-semiconductor contacts were made. The dark current and the γ-rays from ^{241}Am were measured with each detector, and they were compared. From the above studies, the effective fabrication method of CZT detector could be deduced. Our work could be helpful to fabricate the high resolution CZT detector, which could be used in various application areas such as nuclear medicine, radiation safety, X-ray and γ-ray astronomy and homeland security

KEYWORDS: CZT detector, Planar-type detector, Indium, Gold, Metal-semiconductor contact

I. Introduction

Cadmium Zinc Telluride (CZT) is one of the most promising materials for high resolution X-ray and γ-ray energy spectroscopy at room temperature[1)]. Since the energy bandgap of the CZT crystal is large enough that the CZT detector can be used for X-ray and γ-ray measurement without cooling system. Because of the high atomic numbers of composite materials of CZT (Cd, Zn, Te), the efficiency of CZT detector is higher than that of Si or Ge detector. Although the CZT detector has been plagued by material problems for a long time, the recent rapid progress in the crystal growing technique makes the application of CZT detector wider.

CZT planar-type detector has metal/CZT/metal structure. The general procedure to make the CZT planar-type detector is as follows; A CZT crystal is cut, the crystal surface is polished with mechanical and chemical method, and metal contacts are made on CZT surface. After that, the CZT crystal surface is passivated to make the detector performance stable.

Previously many researchers studied the fabrication process of CZT detector. The relation between the surface roughness and the detector performance was studied with various chemical etching methods[2)]. The dependency of the detector's performance on the chemical composition of the metal-semiconductor contact was studied [3)].

In most of the previous works, the data about the fabrication process of CZT detector were obtained with the high quality crystals. However, the CZT crystals with lower grade, which means the crystal has a large number of defects, were used in our work. The CZT is known to have many advantages as radiation detector. However, the CZT detector could not be used widely at present because of its high price. Since the CZT crystal with lower grade could be obtained more easily, the study on the fabrication process of CZT detector with lower grade crystal is also very important.

We made various CZT planar-type detectors. CZT detectors with Indium(In)/CZT/In and Gold(Au)/CZT/Au structure were fabricated, and the dependency of the detector performance on the crystal surface and the crystal quality was studied. Au contact on the CZT crystal was made with two different methods, which include high-vacuum evaporation method and electroless deposition method[4)]. CZT detector with Au/CZT/In structure was made to see the Schottky contact effect on the detector's performance. The CZT detector with capacitive Frisch grid was made to reduce the tail of the peak in the energy spectrum.

II. Experiment and Analysis

1. Detectors with In/CZT/In and Au/CZT/Au Structure

CZT detectors with In/CZT/In and Au/CZT/Au structure were made. Two CZT crystals were used in the experiment; one crystal was slight n-type material with low grade (Saint-Gorbain Inc.) and the other crystal was p-type material with discriminator grade (eV Products Inc.). The geometrical dimension of n-type CZT crystal was 9×9×8 mm^3, and that of the p-type crystal was 10×10×5 mm^3. A number of defects such as Te-inclusion could be found easily on surface of n-type crystal. **Fig. 1** shows the detectors made in our work.

When metal with high work function such as gold is in contact with n-type semiconductor, the contact can be Schottky contact. When metal with low work function such as indium is in contact with n-type semiconductor, it can be Ohmic contact.

*Corresponding Author, Tel. +82-2-2220-2354, Fax. +82-2-2296-2354, E-mail: ykkim4@hanyang.ac.kr, ex-spark@kaeri.re.kr

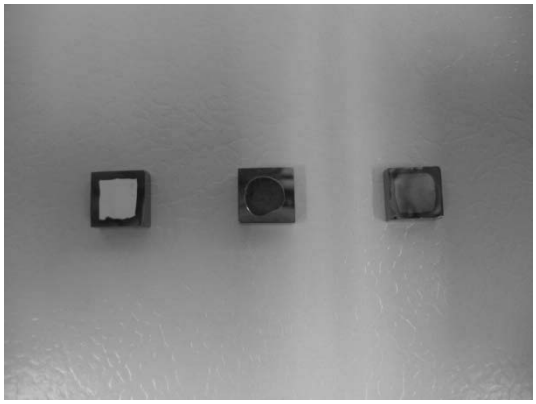

Fig. 1 CZT planar-type detectors made with discriminator grade crystals.

The CZT crystal was grinded with SiC paper and polished finally with 0.05-μm alumina powder. The crystal was chemically etched with 1 % bromine/methanol solution for 1 min. It is known that the bromine/methanol etchant could remove the scratches due to the mechanical polishing. Also, when the CZT crystal is etched with bromine/methanol solution, the CZT surface remains Te-rich[5]. With the inspection of the low grade CZT crystal with microscope, one could find the increase of the Te-rich defects after the chemical etching with bromine/methanol solution.

Four different planar-type detectors were made with low grade CZT crystal. One was In/CZT/In-structured detector with un-etched crystal surface, the second was In/CZT/In structured detector with etched crystal surface, the third was Au/CZT/Au structured detector with un-etched crystal surface, and the last was Au/CZT/Au structured detector with etched crystal surface. Here, the gold contact was made with the electroless deposition method.

The I-V curve and the energy spectrum of 60-keV γ-ray was obtained with each CZT detector. High voltage of 100 V was biased between the electrodes to measure the energy spectrum. The signals from the detector were passed through a pre-amplifier and an amplifier. Finally, the energy spectrum was stored with Multi Channel Analyzer (MCA).

From **Fig. 2**, one could see that the energy resolution of the detector with In contact became worse when the crystal was etched, and the energy resolution of the detector with gold contact became better when the crystal was etched. Here, the energy resolution of the detector was the Full-Width-Half-Maximum (FWHM) of the peak. Indium could make Ohmic contact with n-type semiconductor. When the low grade CZT was etched with the bromine/methanol solution, the Te-rich defects got bigger. And it deteriorated the In/CZT contact, and make the energy resolution worse.

Gold chloride solution was used to make the gold contact on the CZT surface. It was known that the reaction of gold chloride on CZT was supposed to be a transfer of Cd ions toward the $AuCl_3$ solution, leaving a tellurium layer on CZT and gold ions precipitating on this layer[6]. The gold could be placed to make chemical equilibrium in the Te-rich defects, which became larger due to the chemical etching. It could explain why the energy resolution of the detector with gold contact was getting better when the crystal was etched.

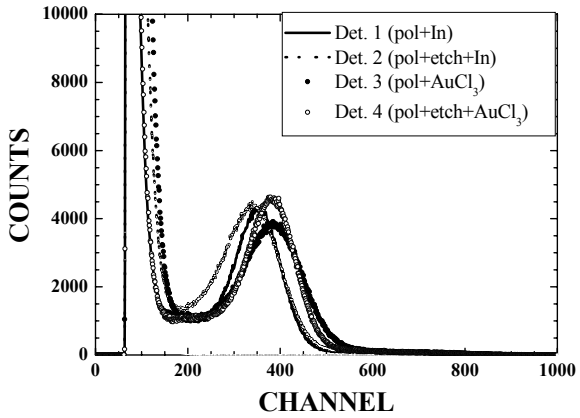

Fig. 2 Energy spectra measured with CZT Planar-type detectors with four different fabrication processes. The detectors were made with a low grade CZT crystal. FWHM of each spectrum was as follows; 34. 5 % (Det. 1), 44.6 % (Det. 2), 40.2 % (Det. 3), and 33.5 % (Det. 4).

CZT detectors with In/CZT/In and Au/CZT/Au structure were also made with discriminator-grade p-type CZT crystals. The number of Te-rich defects on the p-type crystal was smaller than that of the low grade n-type crystal.

In/p-type CZT crystal can be Schottky contact, and Au/p-type CZT crystal can be Ohmic contact. When In was evaporated on both sides of the CZT crystal, the dark current of the detector was too large to measure the energy spectrum. When Au contact was made on the crystal with the electroless deposition method, the energy spectrum could be measured successfully. One could assume that the property of In contact on p-type CZT crystal is similar to that of Au contact on n-type CZT crystal. However, while one could measure the energy spectrum with the detector with Au/CZT(n-type)/Au structure, one could not measure the energy spectrum with the detector with In/CZT(p-type)/In structure. It could be from the deposition method of the metal contact. The indium was deposited with the evaporation method (physical) and the gold was deposited with the electroless deposition method (chemical).

2. Detectors with Au/CZT/Au Structure

Au contact was made on p-type low grade CZT crystal. It is very important to make Ohmic contact on p-type CZT crystal. Two different methods were used to make the gold contact. One was the evaporation method, and the other was the electroless deposition method. Although both methods could be used to make metal contact on CZT crystal, the contact property from both methods is different as explained in the previous discussion.

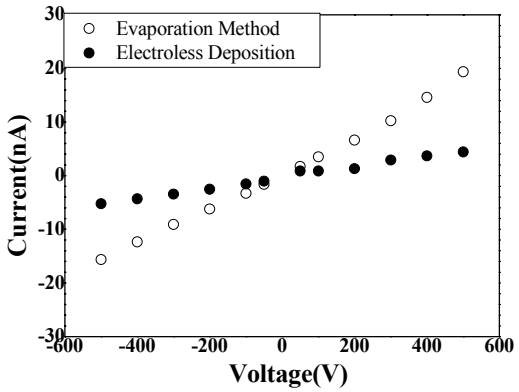

Fig. 3 Leakage currents of Au/CZT/Au detectors. One was made with the evaporation method, and the other was made with the electroless deposition method.

The CZT crystal surface was mechanically polished and chemically etched with 1 % bromine/methanol solution. In the first method, the gold contact was deposited with the evaporation method. Thermal evaporator was used to make gold contact on CZT crystal. The vaccum in the evaporation chamber was kept at around 10^{-5} Torr during the evaporation, and the deposition rate was kept at around 10 n/min. In the second method, the gold contact was made with the electroless deposition method.

Fig. 3 shows the leakage currents of the CZT detectors. As one could see, the leakage current became lower when the gold contact was made with the electroless deposition method. Measurement of 60 keV γ-ray were made with the CZT detectors. The characteristics of the energy spectra measured with the two detectors were similar. However, the energy spectrum of CZT detector made with the evaporation was deteriorated at polarization voltage higher than 200 V. It could be from the increase of the leakage current. **Fig. 4** shows the energy spectrum measured with the CZT detector with gold/CZT/gold structure, where the electrode was deposited with evaporation method.

When gold contact was made with the electroless deposition method, the cadmium layer could be found on the surface of the gold contact. It was found that the passivation with the NH_4/H_2O_2 solution could remove the cadmium layer on the gold contact. When the γ-ray was measured with the detector, which was passivated with the NH_4/H_2O_2 solution, the energy spectrum was enhanced comparing with the energy spectrum measured with the detector before the passivation. The energy resolution of the detector was similiar, however the full peak efficiency was increased after the passivation. The enhancement of the energy spectrum after the passivation was from the removal of the cadmium layer on the gold contact[7]. Fig. 5 shows the energy spectra before and after the surface passivation.

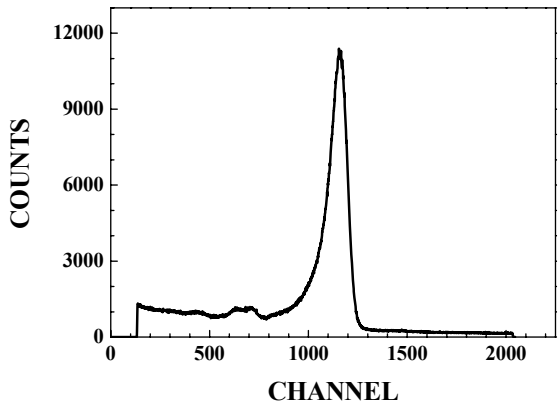

Fig. 4 Energy spectrum measured with CZT detector, where the gold contact was made with the evaporation method. The polarization voltage on the detector was 200 V and the shaping time was 3 μ sec. The FWHM of the peak was 9.4 %.

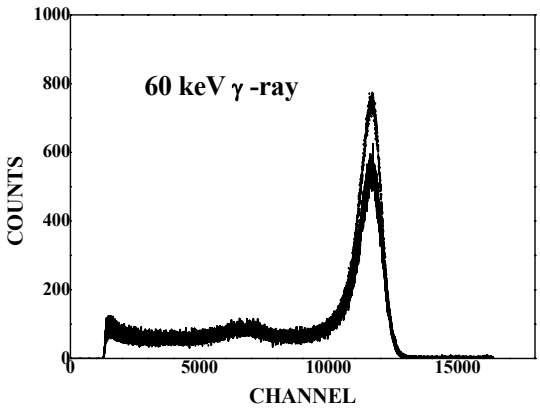

Fig. 5 Passivation effect on the energy spectrum measured with CZT detector. The solid line is from the detector before NH_4/H_2O_2 treatment and the dotted line is from the detector after NH_4/H_2O_2 treatment. The FWHM of the peak was 7.8 % before the surface passivation, and the FWHM of the peak was 7.4 % after the surface passivation.

3. Detectors with In/CZT/Au Structure

CZT Schottky detector was made with In/CZT/Au structure. A p-type CZT crystal was used to make the Schottky detector. Indium contact was deposited with the evaporation method, and gold contact was deposited on the opposite side of the detector with the electroless deposition method. I-V curve and the γ-ray energy spectrum were measured. **Fig. 6** shows the I-V curve of the Schottky detector.

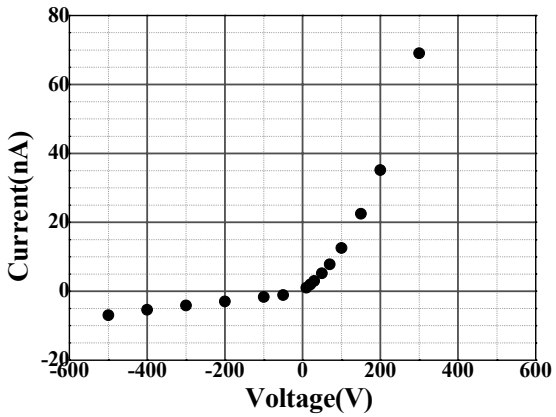

Fig. 6 I-V curve of the CZT Schottky detector.

The energy spectrum of 60 keV γ-ray was measured with the detector and it was compared with the energy spectrum measured with CZT detector with Ohmic contacts. **Fig. 7** shows the energy spectra measured with the CZT Schottky detector and the CZT detector with Ohmic contacts. One could see the slight enhancement of the energy resolution when γ-ray was measured with the CZT Schottky detector.

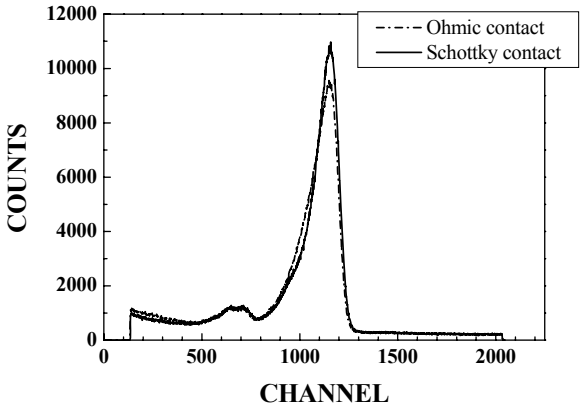

Fig. 7 Energy spectra measured with CZT detector with Ohmic contact, and CZT Schottky detector. The FWHM of peak from the detector with Ohmic contact was 14.6 %, and the FWHM of peak from CZT Schottky was 12.2 %.

It is known that the energy spectrum could be enhanced when the CZT detector with capacitive Frisch grid structure was used for the measurement [8]. The study about the fabrication and measurement of the CZT capacitive grid detector is underway.

III. Conclusion

CZT is very promising material for room temperature γ-ray spectroscopy and radiation imaging. The detector performance depends on the crystal quality, the surface condition, the type of the metal-semiconductor contact, and the electrode design. We studied the dependency of the CZT detector characteristics on the type of metal-semiconductor contact. In most of our study, the CZT crystals with lower grade, which could be used more widely than the high grade crystal, were used. Au layer, made with the electroless deposition method, could be metal contact for CZT detector with p-type crystal. The gold contact on the CZT detectors were made with the evaporation method and the electroless deposition method, and the detector characteristics were compared. The CZT Schottky detector was made, and the γ-ray energy spectrum was successfully measured, and the detector characteristics were compared with the CZT detector with Ohmic contacts. Our work would be helpful to fabricate the CZT detector for high-resolution γ-ray spectroscopy.

Acknowledgement

This work was performed under the nuclear research and development program sponsored by Ministry of Science and Technology of Korea, and supported by the Innovative Technology Center for Radiation Safety (iTRS).

References

1) O. Limousine, 'New trends in CdTe and CdZnTe detectors for X-ray and gamma-ray applications', Nucl. Instr. Meth. A 504, 24, 2003.
2) H. Chen et al., 'Low-temperature photoluminescence of detector grade Cd1-xZnxTe crystal treated by different chemical etchants", J. Appl. Phys. 80, 3509, 1996.
3) G. Wright et al., 'The effect of chemical etching on the charge collecting efficiency of {111} oriented $Cd_{0.9}Zn_{0.1}Te$ nuclear radiation detectors", IEEE Trans. Nucl. Soc. 49, 2521, 2002
4) M.A. George et al., 'Study of electroless Au film deposition on ZnCdTe crystal surface', J. Appl. Phys. 77, 3134, 1995.
5) Y.H. Kim et al, 'Photoluminescence study on the effects of the surface of CdTe by surface passivation', J. Appl. Phys. 85, 7370, 1999.
6) A. Musa et al., 'Properties of electroless gold contacts on p-type cadmium telluride', J. Appl. Phys. 54, 3260, 1983.
7) S.H. Park et al., 'Surface passivation effect on CZT-metal contacts', Trans. Nucl. Sci., submitted.
8) A. Kargar, 'CdZnTe Frich collar detectors for ɣ-ray spectroscopy', Nucl. Instr. Meth. A, 558, 497, 2006.

Journal of NUCLEAR SCIENCE and TECHNOLOGY, Supplement 5, p. 352–355 (June 2008)

6H-SiC Solid State Detector Development for a Neutron Measurement

Jang Ho HA[1], Sang Mook KANG [1,2], Se Hwan PARK [1], Han Soo KIM [1], and Yong Kyun KIM [2*]

[1]*Korea Atomic Energy Reseach Institute, Dukjin-dong, Yuseong-gu, Daejon,, Korea*
[2] *Department of Nuclear Engineering, Hanyang University, Haengdang-dong, Seongdong-gu, Seoul, Korea*

A new solid state detector based on 6H-SiC is one of the promising devices in the nuclear industry for high-level radiation applications in a harsh high-temperature environment. SiC is a semi-conductor with a 3.03-eV band gap energy, and known as a radiation-resistance material. SiC detectors were fabricated by using a 6H-SiC wafer. The properties of the 6H-SiC wafer were over a 10^6 ohm-cm resistivity, a 380 μm thickness, and a (0001)-oriented type. The 6H-SiC detector was prepared by the processes of a dicing, etching, removal of an oxidation layer and a mounting on an alumina substrate. SiC detector was 10×10 mm^2 with a 19.6mm^2 active area. The circular metal contacts consisted of a Si-face/Ni/Au and a C-face/Ni/Au structure. Thin LiF and B film was coated onto the SiC detector surface for a neutron converter. The electrical current-voltage performances of the detectors were measured by using the Keithley 4200-SCS parameter analyzer with self voltage sources. Neutron responses were measured by using a ^{252}Cf source.

KEYWORDS: solid state detector, semiconductor, silicon carbide, neutron measurement, surface barrier detector

I. Introduction

Solid state radiation detectors have been investigated for many applications within various environments. The harsh radiation environments such as a nuclear reactor core, high energy physics experiments, or outer space can cause radiation damage to detectors[1)]. A radiation damage which deteriorates the performance of the devices is a serious and important problem for semiconductor radiation detectors [2)].

The SiC semiconductor has recently emerged as an attractive material for an ionization radiation detection[3)]. A SiC is known as a useful material for the harsh environments needed for a radiation-resistance[4)], a high-temperature operation and a high-critical breakdown voltage, and a high thermal conductivity. Radiation detectors based on semiconductors like SiC, AlN, and BN with a large band energy gap are the most promising for an ionizing detector. For the purposes of a fabrication of a radiation hard detector, a large band gap and a low leakage current are important parameters. SiC has over 170 polytypes. The commercially available single crystals are the hexagonal 4H and 6H. Large diameter single crystals are grown by a physical vapor transport (PVT) process which is based on a modification of the original SiC sublimation method[5)]. In the metal/semiconductor Schottky device the current is induced by the major carrier. Therefore the switching time is faster than that of the p-n junction device[6)]. However, the characteristics of the Schottky device are sensitive to the interface property on the semiconductor's surface. The surface treatments with an oxidation/HF etching and a boiling water immersion during the fabrication of the metal/6H-SiC Schottky device decreased the Schottky barrier heights by about 0.3 to 0.5 eV with respect to that of a 5% HF etching[7)]. It means that a surface treatment is a major parameter for the electrical property of the Schottky device.

Present study is focused on the fabrication and performance of a radiation hard SiC neutron detector which is applicable in air and at a high temperature. Detection principle is shown in **Fig. 1**. The incident neutron was converted into charged particles by a nuclear reaction and the energetic charged particles were absorbed in the SiC sensor. The absorbed mechanism generated electron-hole pairs proportional to the incident charged particle energy.

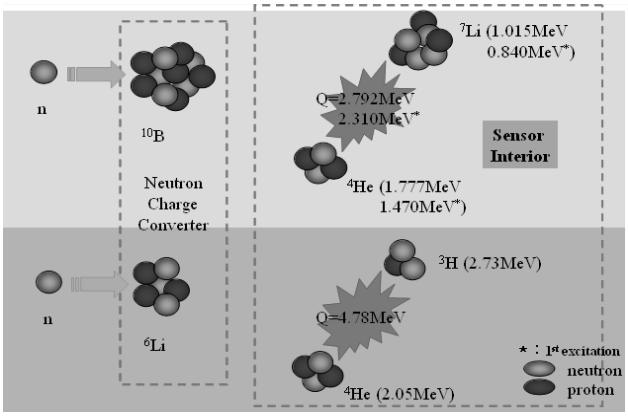

Fig. 1 Neutron detection mechanism in semiconductor detector with neutron conversion film

II. Detector Fabrication Process

We used a 6H-SiC wafer of 2 inch diameter supplied by the Dow Corning Co. The properties of the 6H-SiC wafer are an upper 10^6 ohm-cm resistivity, 380 μm thickness, and a (0001)-oriented type. We prepared 10×10 mm^2 samples by using a semiconductor diamond saw. Generally, a cutting process uses a wax to fix the wafer onto the working table of

*Corresponding Author, Tel. +82-2-2220-2354, Fax. +82-2-2296-2354, E-mail : ykkim4@hanyang.ac.kr

the diamond saw devise. After the cutting process, the wax is removed by an organic solvent or acetone from the wafer's surface. The surface of a SiC wafer was generally etched by using the standard process with H_2SO_4 and H_2O_2 solutions and rinsed with de-ionized (DI) water, and the removal of an oxidation layer by a HCl solution was performed for the metal/semiconductor contacts on the surface which were fabricated by using a thermal evaporator in a vacuum condition. The metallization process was performed under the following conditions; 1.2×10^{-5} Torr, 80 ℃ heating, and a 180°/min rotation speed of the SiC samples holder. The metal contact of the Si-face was Ni(300 Å) and Au(2000 Å), and C-face was Ti(300 Å) and Au(2000 Å). The metal contact shape was a circle with a diameter of 5 mm. To convert the neutron into a charged particle a ^{6}LiF conversion film was evaporated onto an Au metal contact. The thickness was about 10 μm. The LiF(B) film did not have a good contact with the Au layer, so the LiF(B) layer was positioned between another thick Au layer just like a sandwich type.

As a result of process we obtained metal/semiconductor Schottky barrier detectors for neutron detection with a neutron conversion layer.

III. Detector Performance and Results

1. I-V Characteristics Measurement

A major electric detector property is obtained by leakage current measurement with respect to a baised voltage. The SiC detectors were mounted by a conducting epoxy onto the PCB substrate and connected by a wire for the electrical signal readout. The wire terminal was connected to a signal readout and a biased voltage, and the electrical contact pad on PCB substrate was grounded. The current-voltage characteristics of the 6H-SiC radiation detector were measured by using the Keithley 4200-SCS semiconductor characteristics system with a self voltage supply by adjusting the internal biased voltage within -100 V to 100 V. Electric characteristics measurements were carried out at room temperature in a box shielded from the light. The measured I-V characteristics were determined that the detector was a type of metal/semiconductor surface barrier device.

High breakdown voltage is concerned with the maximum operating electric field inside a detector and a charge collection efficiency. We observed that the breakdown voltage was over 100 V.

2. High Dose γ -ray Irradiation test

High neutron field always contains a high γ-ray dose. One of the important characteristics is a γ-ray resistance. SiC samples with 10x10 mm were irradiated by Co-60 γ-ray up to 120 kGy. The irradiation was performed at a γ-ray irradiation facility at the Korea Atom Energy Research Institute (KAERI) with a dose rate of 5 kGy/hour and 15 kGy/hour for 8 hours. A dose rate of 15 kGy/hour is the maximum capacity of the Co-60 γ-ray source at KAERI. The total doses were 40 kGy and 120 kGy, respectively.

We measured the band gap property by using a photon absorption spectroscopy. The difference of the band gap result before and after an irradiation was 0.01eV which was placed in the error ranges of the measurement and the determination.

The radiation-induced damage can be classified into two categories of bulk and surface effects. The most fundamental type of a bulk radiation damage is the Frenkel defect, produced by the displacement of an atom of the semiconductor material from its normal lattice site. The vacancy left behind, together with the original atom now at an interstitial position, constitutes a trapping site for normal charged carriers. These are called as point defects to distinguish them from the more complex "clusters" of a crystalline damage. The γ–rays can create only point defects. When these defects have been formed enough, a carrier lifetime is reduced. The leakage currents of the non-irradiated sample and two 40 kGy, 120 kGy-irradiated samples with the Si-face/Ni/Au interface were measured in the range from 0 to 100 V. We did not find any remarkable differences between before and after an irradiation at 40 kGy and the leakage current was increased at 120 kGy as shown in **Fig. 2**.

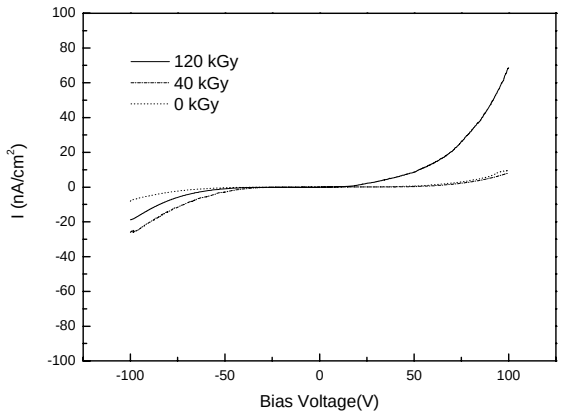

Fig. 2 Typical I-V curve before and after γ-ray irradiation

3. Schottky Barrier Height Determination

The fabricated detector type is one of the Schottky barrier ones. The current transport in the metal-semiconductor Schottky contacts is mainly due to majority carriers, in contrast to p-n junctions, where the minority carriers are responsible. For high-mobility semiconductors the transport can be adequately described by the thermionic emission theory [8].

According to the thermionic emission theory, the flow is limited by the rate at which carriers try to cross the barrier and the Schottky barrier height (SBH) was determined by using the forward current-voltage characteristics of the metal/semiconductor Schottky contacts. The total current density over a potential barrier is analyzed within the framework of the thermionic emission model originally described by Bethe [9] :

$$J_n = J_{ST}\,[\exp(qV/kT) - 1]$$

$J_{ST} = A^*T^2\exp[-(q\Phi_{Bn}/kT)]$,

where J_{ST} is the saturation current density, k is the Boltzman constant, q is the carrier charge, T is the temperature and A* is the effective Richardson constant A* = 194 A/cm^{2}K^2 for a thermionic emission, by neglecting the effects of a optical phonon scattering and quantum mechanical reflection[10].

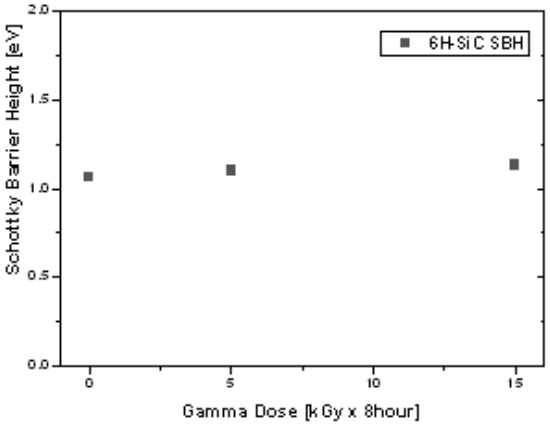

Fig. 3 Schottky bairrier heights with respect to γ -ray dose

The 6H-SiC semiconductor showed similar Schottky barrier heights independent of the different dose rates of the irradiation with Co-60 γ–rays as shown in **Fig. 3**. The SBHs of the C-side of the non-irradiation, 40 kGy and 120 kGy samples are 1.06 eV, 1.11 eV and 1.13 eV, respectively. The SBHs for the 6H-SiC with an orientation (0001) were known to be placed between approximately 0.8 and 1.25eV for the Si-terminated face and between 1.0 and 1.6 eV for the C-terminated face.

3. α-ray Response Measurement

Our detector adapted a neutron to charged particle conversion film. Detector performance was highly dependent on the charge particle detection efficiency. The α–ray responses were measured by a Pu-238 plate-type source with 5.5-MeV at room temperature in a 1-atm air pressure[11]. The α–ray particle was confirmed by using a thin Al plate which is sufficient enough to stop the α–rays. The Al absorber thickness was determined by a charged particle range simulation code (TRIM) which is sufficient enough to stop the α–rays. The energy moderation effect of the 5.5 MeV The α–rays in air was measured by adjusting the distance between the Pu-238 source and the SiC detector. The energy moderation and the simulated deposition energy were used to calculate the energy calibration to determine the energy resolution of the detector operating in room temperature and a 1-atm normal air pressure. Pulse height spectra were obtained by ORTEC and eV-products preamplifiers, as well as a shaping amplifier, and a multi-channel analyzer. **Fig. 4** is the α-ray spectra with different biased voltages. As bias voltage increases, the 5.5 MeV α-ray peak centroid increases because the charge collection efficiency increases.

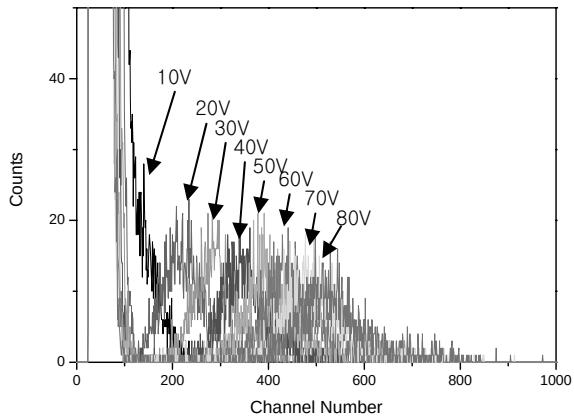

Fig. 4 α-ray responses at 5.5 MeV with respect to different biased voltages

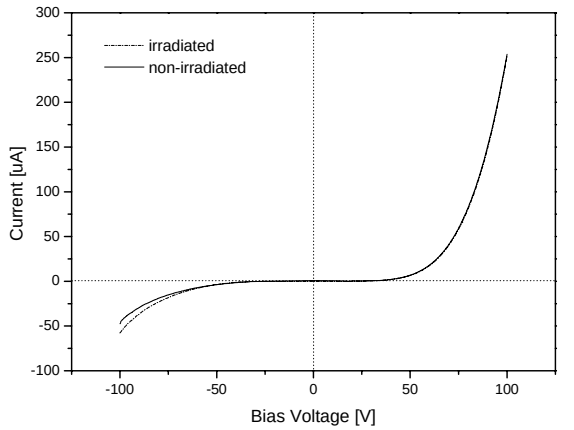

Fig. 5 Typical I-V curve before and after neutron irradiation

In order to investigate the origin of the low energy contribution which is the lowest energy region less than channel no 100 in **Fig. 4**, we compared our results with a silicon surface barrier (SSB) detector purchased from EG&G ORTEC, which can be used at a 1-atm air pressure. From this investigation, the low energy contribution seems to consist of mainly electrical noises originating from the connector and ground loop, and partially from a γ-ray and light leakage contribution.

4. Neutron Response Measurement

Neutron Detection response was performed by using a ^{252}Cf neutron source in air. Neutron damage evaluation was performed by an irradiation of the neutron source up to the 10^8 n/cm^2. **Fig. 5** is the I-V characteristics before and after the neutron irradiation. I-V curves showed almost similar tendencies. As a result SiC detectors were resistant to the neutron damage up to the 10^8 n/cm^2.

One of the effective neutron conversion materials are ^{10}B and ^{6}Li. We fabricated two types of conversion films with a 10 micron thickness. The energy losses of the neutron

conversion film and metal contact structure were simulated by TRIM code. The energy losses were 149, 155, 162 keV for secondary α-rays with energies of 2050, 1777 and 1470 keV, respectively, from (n, α) reaction, and 289 keV for 2730 keV from (n, t) reaction. **Fig. 6** and **7** are the neutron spectra of the ^{10}B and ^{6}Li conversion films. The neutron detection efficiency was expected to be 2.8% as a result of the MCNP and TRIM codes calculation, and measured as 2.5% efficiency.

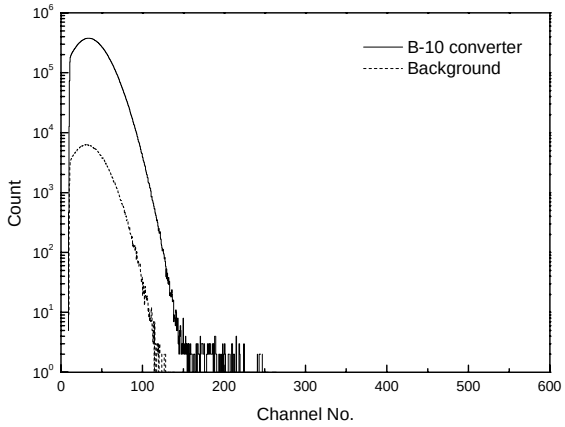

Fig. 6 Neutron detection spectrum measured using by B-10 convert film detector

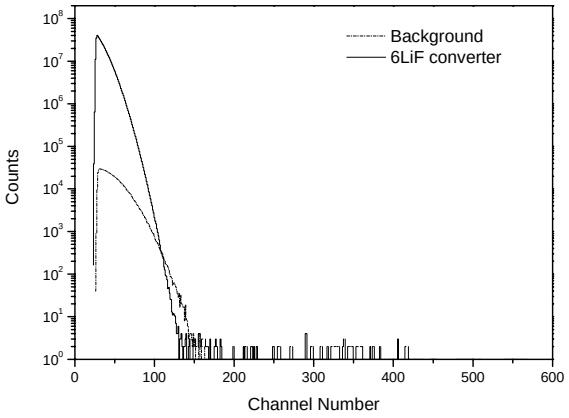

Fig. 7 Neutron detection spectrum measured using by ^{6}LiF convert film detector

The ^{6}LiF converter was 10 micron thickness and the incident Neutron produced from ^{252}Cf was moderated by using high density polyethylene slabs with 30mm thickness. **Fig. 6 and 7** showed neutron spectra. ^{6}Li was known that produced more energetic charge particles compared to ^{10}B converter. It means ^{6}Li gives better neutron discrimination than ^{10}B by energy threshold level from noise and background.

IV. Conclusions

Neutron SiC detectors were fabricated and measured its performances. I-V measurement revealed that this detector was a Schottky barrier type. High dose of γ-rays were irradiated up to 120 kGy and could not find any changes of its electrical properties. Neutron damage was tested by a ^{252}Cf source up to a 10^{8} n/cm^{2}. Neutron responses were measured with two different types of neutron to charge particle converters based on ^{6}Li and ^{10}B materials. The neutron detection efficiency was in good agreement with the calculated result. As a result, the SiC detectors showed a good performance for neutron detection.

Acknowledgement

This work was performed under the mid- and long-term nuclear research and development program sponsored by Ministry of Science and Technology of Korea, and supported by the Innovative Technology Center for Radiation Safety (iTRS).

References

1) A. Larry et al., Nucl. Inst. Meth. A **428**, 95 (1999).
2) F. Nava et al., Nucl. Inst. Meth. A **437**, 354 (1999).
3) A. R. Powell and L. B. Rowland, proceedings of the IEEE, **90**(6), 943 (2003).
4) M. Rogalla et al., Nucl. Phys. B (Proc. Suppl.) **78**, 516S (1999). G. R. Fisher and P. Barnes, Phil. Mag. B. **61**(2), 677 (1990).
5) R. A. Stein et al., Mater. Sci. Eng. **B11**, 69 (1992).
6) D. A. Neamen, "Semiconductor Physics and Devices; basic principles", 2nd ed. (McGrow-Hill, Korea) ch. 8, (2001).
7) T. Teraji, S. Hara, H. Okushi, K. Kajimura, Appl. Phys. Lett. **71**(5), 4 (1997).
8) M. Cze, Physics of semiconductor device, 2nd ed. (Wiley-Interscience, New York) 353-409, (1981).
9) H. A. Bethe, MIT Radiat. Lab. Rep. 43-12, 1942.
10) L. M. Porter, R. F. Davis, J. S. Bow, M. J. Kim , R. W. Carpenter, J. Mater. Res., **10**, 26 (1995).
11) J.H. Ha et al., Nucl. Inst. Meth. A **580**, 416, 2007.

Journal of NUCLEAR SCIENCE and TECHNOLOGY, Supplement 5, p. 356–359 (June 2008)

Large Size $CdWO_4$ Crystal for Energetic X- and γ-Ray Detection

H.J. KIM[1], Hee Dong KANG[1*], H. PARK[1], Shi-hong DOH[2], Sung Hwan Kim[3], and Sang Jun KANG[4]

[1] *Kyungpook National University, Daegu 702-701, Korea*
[2] *Pukyong National University, Busan 608-737, Korea*
[3] *Daegu Health College, Daegu 702-722, Korea*
[4] *School of Liberal Art, Semyung University, Jechon 390-711, Korea*

A Large size of Φ70 mm × 71 mm (2.1 kg) $CdWO_4$ crystal with excellent quality was studied for the energy response of the crystal to the γ-rays. The large crystal was coupled with a green-extended Photomultiplier tube (PMT) and tested at room temperature. We measured light yield and energy resolution of the crystal using various radioactive sources. The energy resolutions of the $CdWO_4$ crystal were obtained to be 9.5 % and 5.3% for 662 keV and 2614 keV, respectively. Linearity of the crystal in different γ-ray energy was also measured. In the environmental background spectrum, well defined peaks of 1461 keV by ^{40}K decay and 2614 keV by ^{208}Tl decay were identified. A simulation study with GEANT4 package was performed for the efficiency comparison with commonly used NaI(Tl) crystal scintillators. The study showed that the $CdWO_4$ crystal is the promising candidate for the boarder control and energetic X-and γ-ray detection equipment.

KEYWORDS: $CdWO_4$, scintillation properties, efficiency, energy resolution, number of photoelectron, linearity

I. Introduction

Scintillation detectors are widely used in the detection and spectroscopy of X-rays or γ-rays at room temperature. The detectors are commonly used in nuclear and high-energy physics, medical imaging, diffraction, non-destructive testing, homeland security, geological exploration, and astrophysics [1].

Important requirements for the scintillation crystals used in these applications include high light output, high stopping power, fast response, low cost, good energy resolution, good linearity, and minimal afterglow. These all requirements can not be met by any of the commercially available scintillators and it should be application specific to choose the best scintillation crystal.

During the last decay high-Z crystal scintillators have been developed for medical imaging such as computer tomography (CT) or positron emission tomography (PET). They include BGO, GSO, LSO and $CdWO_4$ and others, whose distinguished property is high detection efficiency for X- and γ-rays, as well as excellent operational characteristics. These scintillators can be used for medical imaging, radiation detection and board control applications.

Cadmium tungstate ($CdWO_4$, CWO) crystal is one of the candidate for such application since it has high effective Z number, high density, higher light yield than BGO, and very low afterglow [2]. Radiation hardness of CWO crystal is as high as 10^5 rad. Because of such advantage, CWO scintillator is being used extensively in X-ray CT [2]. The main characteristics of $CdWO_4$ crystal are summarized in **Table 1**. Large CWO crystal can be used for the board control, γ-ray spectrometer for well logging [3], planetary lander missions [4], and γ-rays detection for radiation monitoring [5]. S. Ph. Burachas et al. reported 13.8% energy resolution at the energy of 662 keV with a Φ54 mm × 95 mm (1.7 kg) crystal [6].

We report a study of response to the γ-ray of a large Φ70 mm × 71 mm (2.1 kg) CWO crystal with an excellent quality. Also a simulation study with GEANT4 package was done for the efficiency comparison with commonly used NaI(Tl) crystal scintillator.

Table. 1 Properties of $CdWO_4$ crystal scintillator [2].

Properties and characteristics [units]	Value
Effective atomic number	64
Density [g/cm3]	7.9
Melting point [K]	1598
Cleavage plane	<010>
Mohs' hardness	4-4.5
Hygroscopicity	No
Luminescence maximum [nm]	470/540
Index of refraction	2.3
Average decay time [□s]	5 and 20
Light yield [% of NaI(Tl)]	25-40
Afterglow after 3 ms [%]	0.1
Radiation hardness [rad]	10^5

II. Experiment

A 7.0 cm diameter by 7.1 cm thick cylindrical CWO scintillation crystal (2.1 kg) as shown in **Fig. 1** was prepared for the test. The CWO was produced by Novosbisk, Russia and it is so transparent that quality of crystal is better than previously studied one[5),6)] which showed a slight color suggesting self-absorption of the light. The CWO was wrapped with the Teflon followed by the black tape. The crystal is attached with a 3 inch Photomultiplier tube (PMT) with RbCs photocathode (Electron tube). The RbCs photocathode enhances quantum efficiency in the green wavelength region and gives more photoelectron yield for

*Correspinding Author, Tel. +82-53-320-1319, Fax. +82-53-320-1449, E-mail; hongjoo@knu.ac.kr

the CWO crystal than a normal bialkali PMT. The high voltage of -1350 V was applied to the PMT.

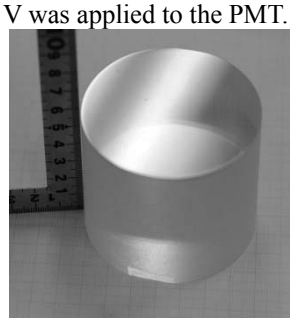

Fig. 1 Φ70 mm × 71 mm of $CdWO_4$ produced by Novosbisk

A 25 MHz USB2 based Flash Analog to Digital Converter (FADC) board was used for the analog signal digitization [7]. An analog signal from the PMT attached to the CWO is connected into the analog input of the FADC board via an ORTEC 576 shaping amplifier. A software threshold setting was applied to trigger an event by a self-trigger algorithm on Field Programmable Gate Array (FPGA) chip of the FADC board. The FADC output was recorded into the personal computer and the recorded data were analyzed with a C^{++} data analysis program. **Fig. 2** shows a schematic diagram of the experimental setup for the radiation measurement.

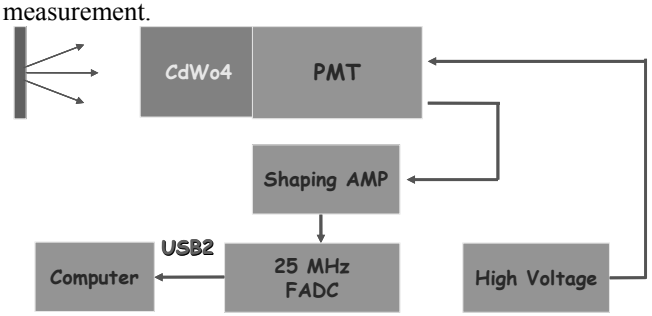

Fig. 2 A Schematic diagram of data acquisition system (DAQ).

For the cross checking purpose, signals from the PMT were also amplified using a home-made amplifier with a low noise and high slew rate. The output signals were then fed into a 400 MHz FADC (flash analog-to-digital converter) [7]. The trigger was formed in the FPGA (field programmable gate array) chip on the FADC board. The FADC was located in the VERSA module eurocard bus (VME) crate and was read out by using a Linux operating PC through the VME-USB2 interface. The module is designed to sample the pulse every 2.5 ns for duration up to 32 μs so that one can fully reconstruct each pulse as shown in **Fig. 3**. We investigated scintillation characteristics of the crystal using single photoelectron (SPE) counting method in 24 μs window since the trigger point is set to be 8 μs. In SPE counting method, it needs to identify SPE signal to reduce the effect coming from the noise to improve energy resolution because the information for the scintillation light from the detector is included only in the SPE signal. We used a clustering algorithm to identify SPEs. If decay time of scintillator is long, the SPE counting method is useful for the characterization of the scintillator [8].

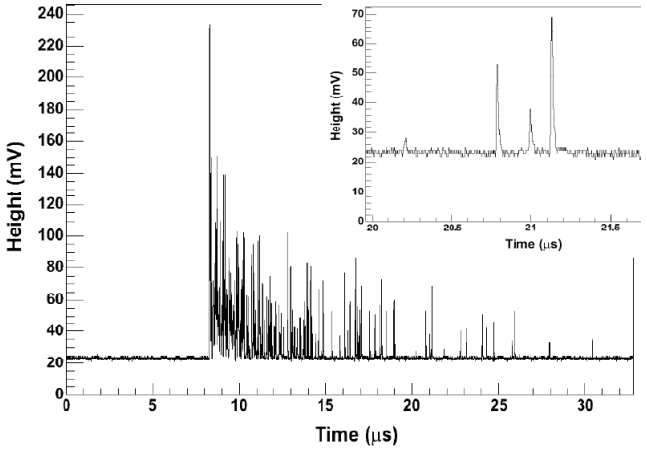

Fig. 3 Typical pulse spectra of the CWO by 400 MHz FADC and SPEs are also shown.

III. Results and Discussion

1. Number of Photoelectron

As described in previous section, SPE can be identified by using a 400 MHz FADC and a clustering algorithm. The number of photoelectrons per keV can be obtained by counting each peak in one event since single photoelectrons are clearly separated one another at low energy as shown in **Fig. 3**. That is, a low energy event can be identified as a set of single photoelectrons above a threshold cut within a timing window of 24 μs. As shown in **Fig. 4**, average number of photoelectons per keV was obtained with low energy events after calibration with 662 keV γ-rays from a ^{137}Cs radioactive source. The average number of photoelectrons of the CWO crystal is obtained to be 2.4 photoelectrons/keV. Taking account only statistical fluctuation, 6.4% of energy resolution could be obtained with 662 keV γ-rays.

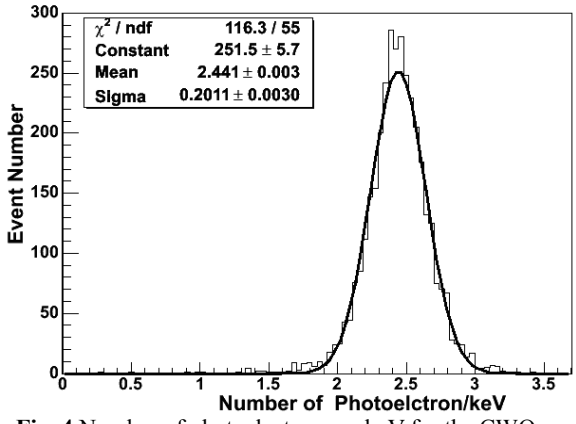

Fig. 4 Number of photoelectron per keV for the CWO crystal.

2. Energy Resolution

The energy response of CWO crystal to γ-rays from ^{137}Cs, ^{22}Na, ^{60}Co radioactive source and natural KCl, thorium oxide powders were used for the energy resolution determination. These results were obtained with a shaping time of 10 μs. The Gaussian fit was applied each identified γ-ray peak and energy resolution is determined by the fitted mean value.

The **Fig. 5** shows the energy resolution of CWO crystal from 511 keV to 2614 keV. The resolution of 9.5% and 5.2% is obtained with 662 keV and 2614 keV γ– rays, respectively. These results are better than previously reported one with similar size of crystal by S. Ph. Burachas et al [6].

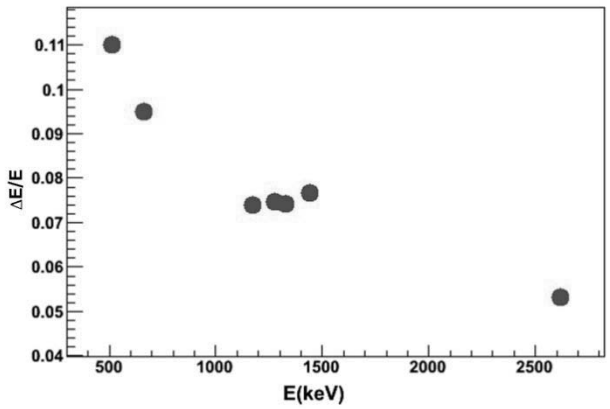

Fig. 5 Energy resolution of the CWO crystal with various γ-ray sources.

3. Linearity

The CWO crystal was irradiated with various radioactive sources with the energy range from 88 keV to 2614 keV for the linearity study. Each γ-ray peak is identified with a Gaussian fit. As shown in **Fig. 6**, the energy response of CWO crystal to γ-ray is linear in the energy range from 100 keV to 2600 keV.

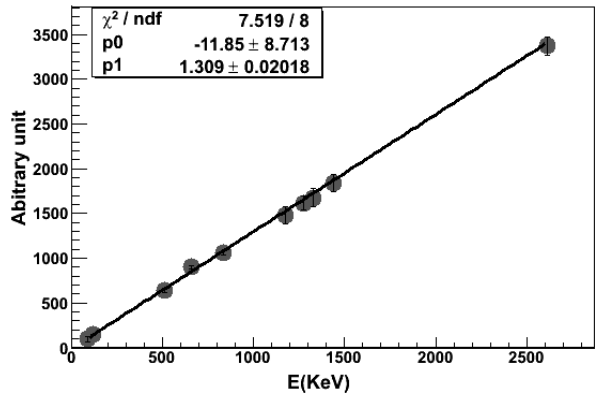

Fig. 6 Linearity distribution of CWO with various γ-ray sources. The solid line shows the linear fit to data.

4. Efficiency Comparison between CWO and NaI(Tl)

A Monte Carlo simulation was performed to compare full peak efficiencies of γ-ray between CWO and NaI(Tl) crystal in the energy range from 0 to 10000 keV. The GEANT4 package with low energy model was used for the simulation[9].

The size of CWO and NaI(Tl) crystals are assumed to be a 7.0 cm diameter by 7.1 cm thick cylindrical shape and each γ-ray is entered in the center of the crystals. The full peak efficiencies are estimated with total energy deposition in the crystal. The efficiency curves of CWO and NaI(Tl) are shown in **Fig. 7**. The full peak efficiencies of the crystals at low energy are not 100% because of backscattering and X-ray emission. Since effective atomic number of CWO crystal is higher than NaI(Tl), full peak efficiencies of CWO at high energy is expect to be much higher than NaI(Tl). The simulation study shows that CWO full peak efficiencies is about 3 and 10 times higher than that of NaI(Tl) in the energy of 2600 keV and 10000 keV, respectively.

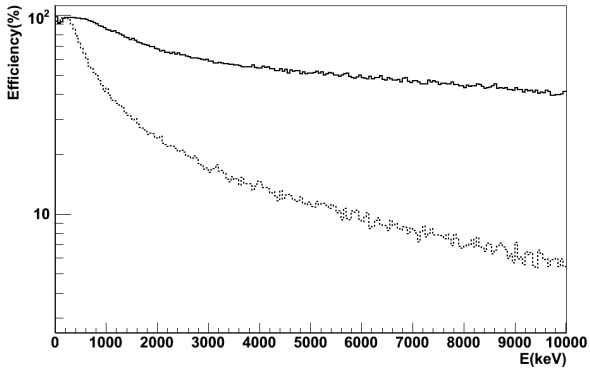

Fig. 7 Efficiency curve of γ-ray by GEANT4 simulation for a) CWO (solid histogram) and b) NaI(Tl) (dashed histogram.

For the full peak efficiency comparison between CWO and NaI(Tl) crystal, similar size of NaI(Tl) crystal was used with 2 inch bi-alkali PMT and 2 μs pulse shaping time. Both CWO and NaI(Tl) was irradiated with natural thorium oxide powder and pulse height spectra are recorded. **Fig. 8** shows energy spectra of the CWO and the NaI(Tl) normalized at low energy. Several γ-ray peaks produced by ^{232}Th decay chain are identified. It confirmed that the full peak efficiency of CWO crystal at 2614 keV is about 3 times higher than that of NaI(Tl) crystal.

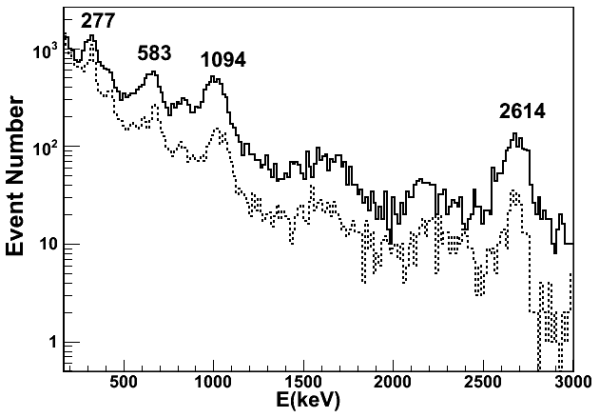

Fig. 8 Pulse height spectra by natural Thorium oxide powder for a) CWO (solid histogram) and b) NaI(Tl) (dashed histogram)

5. Background Energy Spectra of the CWO

The natural background in the experimental hall was measured with the CWO crystal. The energy of recorded pulse height spectrum was calibrated with the energy of 662 keV γ-rays from ^{137}Cs radioactive source. As shown in **Fig. 9**, 511 keV annihilation peak, 583 keV by ^{208}Tl, 1461 keV by ^{40}K and 2614 keV by ^{208}Tl are clearly identified.

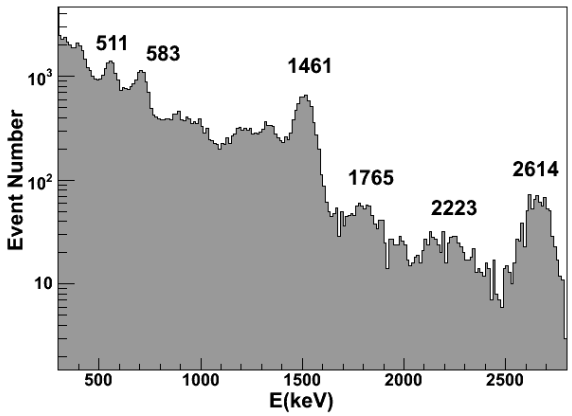

Fig. 9 Background energy spectrum of the CWO crystal.

IV. Conclusions

In this work, we described a study of 7.0 cm diameter by 7.1 cm thick cylindrical CWO scintillation crystal coupled with 3 inch green extended PMT. We determined good energy resolution of 9.5% for 662 keV γ-rays by ^{137}Cs and 5.2% for 2614 keV γ-rays by ^{208}Tl decay, respectively. These values were obtained with a shaping time of 10 μs. The number of photoelectron per keV is obtained to be 2.4 with 400 MHz FADC. Good energy linearity was obtained from 100 keV to 2600 keV.

We also demonstrated in this study the advantages of the large CWO crystal as efficient energetic X-ray or γ-ray detection and compared its efficiency with the NaI(Tl) crystal. The environmental background energy spectra for the CWO crystal show the capability of high energy γ-ray tagging such as 2614 keV produced by ^{208}Tl decay.

The large excellent quality of CWO scintillation crystal studied here confirmed the high efficiency for γ-rays detection and the high potential of CWO crystals for application of the border monitoring equipment and energetic X- and γ-ray detection.

Acknowledgement

This work was supported by the SRC/ERC program of MOST/KOSEF (R11-2000-067-02002-0) and by the Korea Science and Engineering Foundation under the BAERI program.

References

1) G. F. Knoll, *Radiation Detection and Measurement,* John Willey and Sons, New York, (1999).
2) M. Gloubs, B. Grinyov and Jong Kying Kim, L. "Inorganic Scintillators for Modern and Traditional Applications," Institute for Single Crystals, Kharkiv, Ukraine, (2005).
3) C. L. Melcher, R. A. Manente, and J.S. Schweitzer, "Applicability of Barium fluoride and cadmium tungstate scintillators for well logging," *IEEE Trans. Nucl. Sci.,* **41**, 505-517 (1989).
4) Y. Eisen, L.G. Evans, R. Starr and J. I. Trombka, "$CdWO_4$ scintillator as a compact gamma ray spectrometer for planetary lander missions," *Nucl. Instr. and Meth.* A, **490**, 505-517 (2002).
5) M. Moszyński *et al.*, "$CdWO_4$ crystal in gamma-ray spectrometry," *IEEE Trans. Nucl. Sci.,* **52**, 3124-3128 (2005).
6) S. Ph. Burachas *et al.*, "Large volume $CdWO_4$ crystal scintilators," *Nucl. Instr. and Meth.* A **369**, 164-168 (1996).
7) Notice Korea Co., http://noticekorea.com.
8) H. S. Lee, "Dark Matter Search with CsI(Tl) Crystals," *Ph. D. dissertation, School of Phys., Seoul National Univ., Korea*, (2007).
9) S. Agostinelli *et al.*, "GEANT4 –a simulation toolkit," *Nucl. Instr. Meth.*, A **250**, 250-303 (2003)

Journal of NUCLEAR SCIENCE and TECHNOLOGY, Supplement 5, p. 360–363 (June 2008)

Averaged Currents Induced by Alpha Particles in an InSb Compound Semiconductor Detector

Ikuo KANNO[1*], Shigeomi HISHIKI[1#], Yoshitaka KOGETSU[1], Tatsuya NAKAMURA[2], and Masaki KATAGIRI[2]

[1]*Graduate School of Engineering, Kyoto University, Kyoto, Japan*
[2]*Japan Atomic Energy Agency, Ibaraki, Japan*

Very fast pulses due to alpha particle incidence were observed by an undoped-type InSb Schottoky detector. This InSb detector was operated without applying bias voltage and its depletion layer thickness was less than the range of alpha particles. The averaged current induced by alpha particles was analyzed as a function of operating temperature and was shown to be proportional to the Hall mobility of InSb.

KEYWORDS: InSb, compound semiconductor, Hall mobility, cryogenic detector, alpha particle measurement

I. Introduction

X-ray fluorescence (XRF) analysis is a very powerful tool for the investigation of elements contained in commercial products. The technique is applied to ensure shipped products do not contain toxic elements such as Cd and Pb. The K-x rays of Pb, however, are not easily detected by XRF because a Si detector is employed in commercial XRF devices; the absorption coefficient of Si for K-x rays of Pb, with the energy of 88 keV, is very small. Furthermore, the Si detector is not suitable for light elements such as Li and B in view of energy resolution.

This paper discusses the development of photon detectors made of compound semiconductor InSb; InSb has high atomic numbers (In:49, Sb:51) and density (5.78 gcm^{-3}), and the smallest band gap energy (0.165 eV) among developed semiconductors. The photon absorption efficiency is 400-1000 times and 7-10 times greater than those of Si and Ge, respectively. The energy resolution is twice as high as those of conventional semiconductor detectors. Furthermore, InSb has high mobility of electrons and holes: 78000 and 750 $cm^2V^{-1}s^{-1}$ at 77 K for electrons and holes, respectively, which are 50 and 5 times greater than those of Si. A fast charge collection time and high counting rate can be expected when using InSb detectors.[1)]

To date, *pn* junction detectors have been fabricated from *p*-type InSb substrate,[2)] and Schottky detectors have been made from both *p*-type[3)] and undoped-type InSb substrates[4)] using commercially available InSb wafers. Recently, a Schottky detector was made from a commercial undoped-type InSb wafer, which has a lower impurity concentration than those of previously used InSb wafers. The output pulse of this InSb detector showed too fast rise time for conventional charge sensitive and for current sensitive preamplifiers to amplify the pulses properly.[5)] Although the fast pulses were not amplified nominally, the induced charge should be proportional to the deposited energy by alpha particles. To verify this, the output pulses of a current sensitive preamplifier were analyzed.

II. Experiments

1. Detector Fabrication

The InSb wafer was an undoped-type with a thickness of 0.5 mm and diameter of 2 in., manufactured by Wafer Technology (England). According to the results of the Hall effect, the conductivity of the InSb wafer was shown to be slightly *n*-type. The InSb wafer was cut into pieces with dimensions of approximately 12 x 15 mm^2. Both sides of the InSb substrate were etched with thinned HF. One side of the substrate was coated with a photo-resist. A Schottky electrode region was then defined by photolithography with

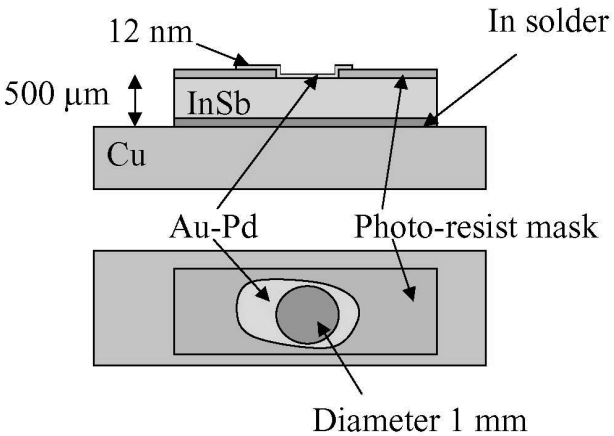

Fig. 1 Schematic drawing of an InSb detector.

a diameter of 1 mm. As a Schottky electrode, Au-Pd (40%) was evaporated with a thickness of 12 nm. The other side of the substrate was soldered to a Cu plate with In solder to form an Ohmic contact. A schematic drawing of the detector is shown in **Fig. 1**.

*Corresponding Author, Tel. +81-774-38-4894, Fax. +81-774-38-3972, E-Mail; kanno@nucleng.kyoto-u.ac.jp
#Present address: Japan Atomic Energy Agency, Gunma, Japan.

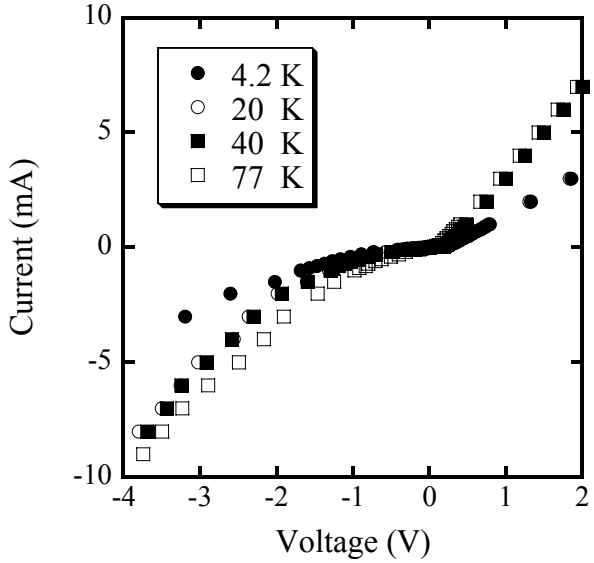

Fig. 2 Current-voltage curves of the InSb detector at various operating temperatures.

Current-voltage (*I-V*) curves were measured over a range of temperature as shown in **Fig. 2**. The resistivity of the InSb detector at 4.2 K was estimated as 4.4 kΩ with the gradient of the *I-V* curve at zero voltage. After *I-V* measurements, the detector was mounted on the cold stage of a cryostat (Infrared Co.), together with an alpha particle source, ^{241}Am.

2. Alpha Particle Measurement

SA-430F5 (NF Corp., Japan) was employed as a current sensitive preamplifier. The bandwidth of the preamplifier was 110 MHz. The obtained typical output pulse is shown in **Fig. 3**. The fast rise time of nearly 3 ns is due to the contribution of electrons. The slower voltage change following the electron contribution is attributed to the holes. The total time from rise to decay was about 20 ns. A bandwidth of 117 MHz is necessary to amplify such very fast pulses. As a result, the obtained pulses have a smaller gain than the nominal pulses.

III. Discussion

1. Electron Contribution

In **Fig. 3**, the electron contribution to the rise of the pulse could be defined as a ratio with respect to the highest voltage. In the same way, an averaged electron contribution was estimated for nearly 1000 pulses at each operating temperature, as shown in **Fig. 4**. In the lower temperature region, from 4.2 K to 40 K, the electron contribution was nearly 80%. The electron contribution decreased at higher temperature. This is understood to be the increase in the contribution of holes due to the release of holes at higher temperature.

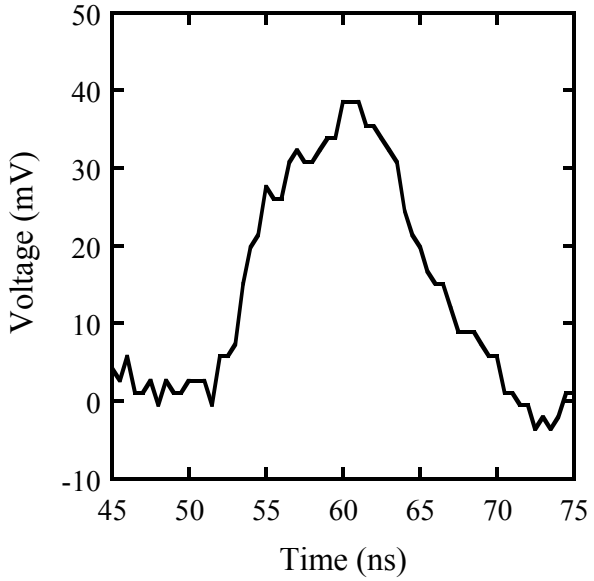

Fig. 3 Typical rise time of alpha particle measured by current preamplifier at 20 K

2.Averaged Current

The time integral of the output pulse measured by the current sensitive preamplifier is regarded as being proportional to the charge created in the depletion layer of the InSb detector.

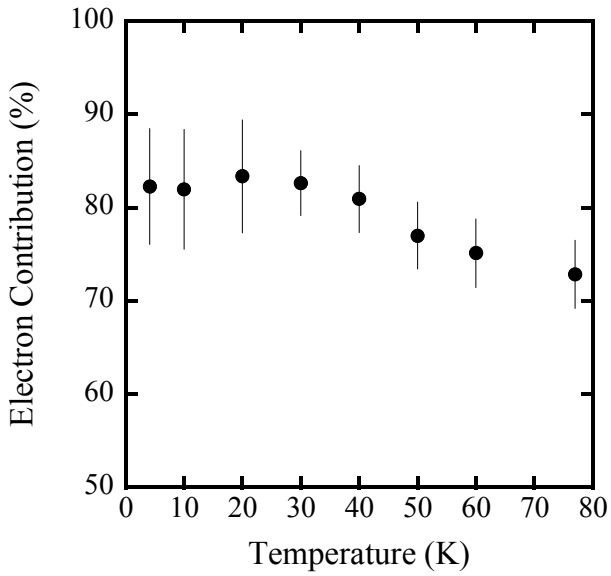

Fig. 4 Electron contribution in preamplifier output pulses as a function of temperature.

The charge divided by the pulse width is taken as an averaged current. In **Fig. 5**, the averaged current is shown as a function of operating temperature. Error bars of each result show the standard deviations of nearly 1000 events.

Taking the effective depletion layer thickness at a zero bias voltage to be 3 μm,[6] and the range of alpha particles with 5.5 MeV in energy to be about 20 μm, alpha particles

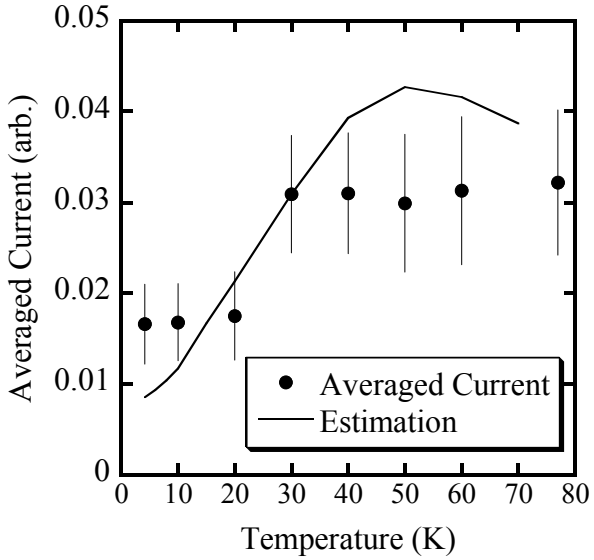

Fig. 5 Averaged current and its estimation.

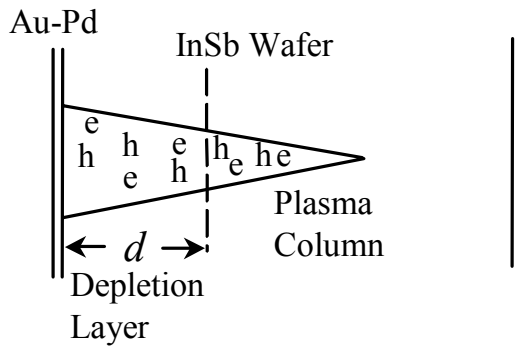

Fig. 6 Schematic drawing of the plasma column created by an incident alpha particle and the thickness of depletion layer. "e" and "h" denote electron and hole created by an alpha particle.

were found to penetrate the depletion layer. As shown in **Fig. 6**, the deposited energy by alpha particles, E, and the created charge, Q, are regarded as being proportional to the depletion layer thickness, d:

$$E \propto Q \propto d \ . \tag{1}$$

The averaged current I is proportional to the product of the charge quantity, Q, and averaged velocity of charges, v. The averaged velocity, v, is given as the product of Hall mobility, μ, and the averaged electric field strength, F.

The electric field strength, $F(x)$, in the depletion layer of an n-type Schottky detector is given as[7)]

$$F(x) = \frac{d-x}{\mu_e \tau} \cdot \tag{2}$$

Here, μ_e is electron mobility, τ is the charge collection time, which is proportional to the resistivity of the substrate, and x is the position of the charge measured from the Schottky barrier. The averaged electric field strength in the depletion layer, F, is obtained as V/d, using the relationship

$$d = \sqrt{2\mu_e \tau V} \ . \tag{3}$$

Here, V is the bias voltage. In this experiment, however, V is taken as an intrinsic voltage, because no bias voltage was applied.

As a result, the averaged current is given as the product of the charge quantity, Q, the Hall mobility, μ, and the averaged electric field strength, F,

$$I \propto Q \cdot \mu \cdot \frac{V}{d} \propto d \cdot \mu \cdot \frac{V}{d} = \mu V . \tag{4}$$

With the assumption that the intrinsic voltage does not change greatly in the temperature range of 4.2 K to 80 K, the averaged current is only dependent on the Hall mobility.

The estimated averaged current, i.e., the Hall mobility, is plotted in **Fig. 5**. The result is normalized to the experimental data at 30 K. Fairly good agreement is obtained. This agreement shows that the amplification by the current amplifier was properly performed, although the gain might be smaller than the nominal value.

IV. Conclusions

For the substrate of high energy resolution, high efficiency photon detectors, InSb is a promising compound semiconductor. Due to the high mobility of electron, high counting rate could be expected with InSb substrate. The conventional preamplifiers, both charge sensitive and current sensitive, are not able to cope with the fast pulses of InSb detector, however, the pulses are shown being amplified properly, although not nominally. For the full use of InSb detectors, the development of faster preamplifiers is expected.

Acknowledgement

This work was supported by Grant-in-Aid for Scientific Research funding from the Japan Society for Promotion of Science, and the Iketani Science and Technology Foundation.

References

1) Wm. C. McHarris, "InSb as a γ–ray detector", *Nucl. Instrum. Methods Phys. Res*., **A 242**, 373 (1986).
2) I. Kanno, F. Yoshihara, R. Nouchi, O. Sugiura, Y. Murase, T. Nakamura, M. Katagiri, "Radiation measurements by a cryogenic *pn* junction InSb detector with operating temperature up to 115 K", *Rev. Sci. Instrum*., **74**, 3968 (2003).
3) I. Kanno, F. Yoshihara, R. Nouchi, O. Sugiura, T. Nakamura, M. Katagiri, "Cryogenic InSb detector for radiation measurements", *Rev. Sci. Instrum*., **73**, 2533 (2002).
4) I. Kanno, S. Hishiki, O. Sugiura, R. Xiang, T. Nakamura, M. Katagiri, "Photon detection by a cryogenic InSb detector", *Rev. Sci. Instrum*., **76**, 023102 (2005).
5) I. Kanno, S. Hishiki, Y. Kogetsu, T. Nakamura, M. Katagiri, "Fast response of InSb Schottky detector", *Rev. Sci. Instrum*.,

78, 056103 (2007).
6) S. Hishiki, Y. Kogetsu, I. Kanno, T. Nakamura, M. Katagiri, "First detection of gamma-ray peaks by an undoped InSb Schottky detector", *Nucl. Instrum. Methods Phys. Res.* **A 559**, 558 (2006).
7) G. F. Knoll, "Radiation Detection and Measurement", 3rd., John Wiley & Sons, New York (2000).

Journal of NUCLEAR SCIENCE and TECHNOLOGY, Supplement 5, p. 364–366 (June 2008)

Explosives Detection Using Deuterium-Deuterium Neutron Generator

Hee-Jung IM[1*], Byoung Chul SONG[1], Yong Joon PARK[1], Young Gu CHEUN[2], Kyuseok SONG[1], and Won-Ho KIM[1]

[1] *Nuclear Chemistry Research Division, Korea Atomic Energy Research Institute, 150 Deokjin-dong, Yuseong-gu, Daejeon 305-353, Republic of Korea*
[2] *Agency for Defense Development, Jochiwongil 462, Yuseong-gu, Daejeon 305-152, Republic of Korea*

Gamma spectra of general and explosive materials were obtained by using the developed neutron induced prompt gamma-ray spectrometry system containing a neutron generator, where the neutron source was created from a deuterium-deuterium reaction, and they were examined to establish whether the samples were explosives or not by using the pattern recognition method. When the gamma spectra of real explosives (or general materials) were projected into the already prepared training set for the pattern recognition, they were placed in the categories of explosives (or general materials) properly.

KEYWORDS: explosives detection, neutron generator, prompt gamma-ray neutron activation analysis, neutron induced prompt gamma-ray spectrometry system, pattern recognition

I. Introduction

In our previously published papers[1), 2)], we have evaluated and discussed the analytical capability of explosives detection by a prompt gamma-ray neutron activation analysis (PGNAA) through the use of relative elemental compositions at a research nuclear reactor and by using an isotopic neutron source, ^{252}Cf. Now, for non-destructive and in-situ measurement with advantages regarding its size, compactness, and safety compared to the other neutron sources, we set up a neutron induced prompt gamma-ray spectrometry (NIPS) system by introducing an accelerator-based neutron generator for illicit material detection in our laboratory in collaboration with a group from the Lawrence Berkley National Laboratory (LBNL) U.S.A[3)].

Pattern recognition of principal components analysis (PCA) is the result of a linear transformation of the used data, and it can often provide a similarity or difference between samples very effectively [4)]. The training set for the pattern recognition of the suitable discriminant classes between illicit and innocuous materials was prepared and developed with the nuclear reactor data. The gamma spectra of real explosives and general materials obtained from our NIPS system were projected into the training set, and it was observed that those materials could essentially be placed in the categories of their groups.

II. Experimental

The gamma spectra collected by using the PGNAA facility of the HANARO research reactor (neutron fluence rate of about 1.4×10^8 $cm^{-2} \cdot s^{-1}$) at the Korea Atomic Energy Research Institute (KAERI)[2)] for a training set were from general materials {melamine [$C_3H_6N_6$, sample No. 9~18], urea [CH_4N_2O, No. 19~21], sulfur powder [S, No. 22~24], di-phosphorpentoxid [P_2O_5, No. 25~27], blank [empty Teflon container, No. 28~30], 1,1,1,5,5,5-hexafluoro-2,4-pentanedione [$C_5H_2F_6O_2$, No. 34~36], and ammonium dihydrogen phosphate [H_6NO_4P, No. 37~39]}, simulated explosives {4-nitrophenol [$C_6H_5NO_3$, sample No. 1], aminobenzoic acid [$C_7H_7NO_2$, No. 2~4] and pentaerythritol tetranitrate [$C_5H_8N_4O_{12}$, No. 5]}, and simulated chemical warfare agents {triethyl phosphate [$C_6H_{15}O_4P$, No. 6~8], o-methoxybenzoyl chloride [$C_8H_7NaClO_2$, No. 31~33], bis-(2-chloroethyl)ethylamine [$C_6H_{13}Cl_2N$, No. 40~42], and 1,2-bis(2-chloroethylthio)ethane [$C_6H_{12}Cl_2S_2$, No. 43~45]}. The general materials were selected from the chemicals which include similar relative concentrations of carbon (C), nitrogen (N), hydrogen (H), oxygen (O), sulfur (S), phosphorous (P), and/or fluorine (F) in their formula as in explosives and chemical warfare agents. The simulated explosives or chemical warfare agents were prepared by mixing several chemicals to produce the same relative concentrations of C, N, H, O, S, P, and/or F as in the real ones[5)]. Each sample (about 0.1 g) was irradiated for 1,000 s, and some samples were measured several times to check on their reproducibility.

Real explosives of HMX (1,3,5,7-tetranitro-1,3,5,7-tetrazacyclooctane; $C_4H_8N_8O_8$), TNT (2,4,6-trinitrotoluene; $C_7H_5N_3O_6$), PETN (pentaerythritol tetranitrate; $C_5H_8N_4O_{12}$), and RDX (hexahydro-1,3,5-trinitro-1,3,5-triazine; $C_3H_6N_6O_6$) were obtained from the Agency for Defense Development (ADD) and were kept safe in ceramic bags with 30 wt % of water and isopropyl alcohol mixture (1 vs. 1 ratio). Around 1,000 g of each explosives and general materials (potassium chloride and melamine) was irradiated for 10,000 s to produce gamma spectra for an application to a pattern recognition test. The software package of MATLAB 7.0.4 (Release 14, The MathWorks) was used for a performance of the pattern recognition.

*Corresponding Author, Tel. +82-42-868-4740, Fax. +82-42-868-8148, E-Mail; imhj@kaeri.re.kr

III. Results and Discussion

The evaluation of a dose rate of the neutron for the radiation shields were carried out by Monte Carlo calculation (MCNP-4C) as well as the evaluation of the thermal neutron concentration effect by the various reflectors to design the NIPS system.

(a)

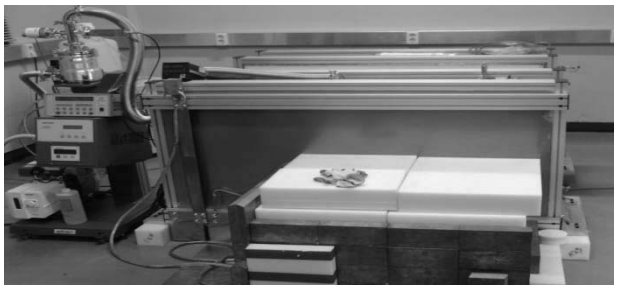

(b)

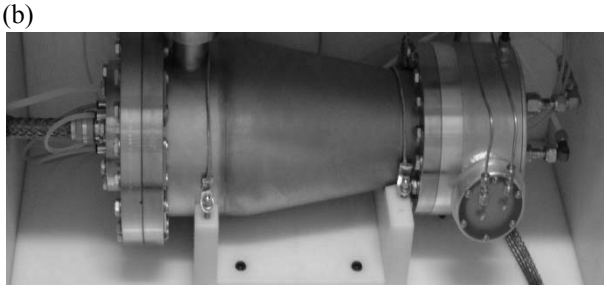

Fig. 1 (a) NIPS System containing (b) Deuterium-Deuterium (D-D) Neutron Generator Installed in Our Laboratory

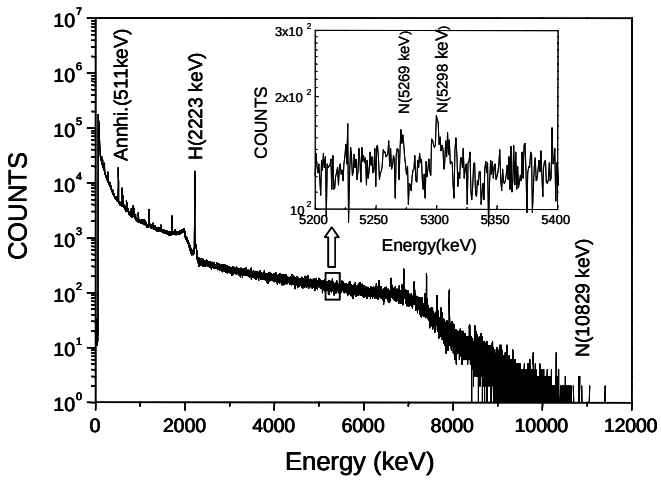

Fig. 2 Prompt Gamma Spectrum of Melamine by Using the NIPS System Including D-D Neutron Generator

Based on all of the calculations and evaluations, the optimized NIPS system equipped with the neutron generator and a high-purity germanium (HPGe) detector based on the NIM (Nuclear Instrumentation Modules) spectrometric modules in association with data acquisition and spectral analysis systems was set up as shown in **Fig. 1**. The D-D neutron generator was located at the center of lower-self, inside of a polyethylene canister. The total neutron fluence rate emitted by the generator is about 1.18 X 10^7 s^{-1} at 5.06 mA of an ion current and 70 kV of a high voltage and obtained by a calibration using a helium detector[6]. Its lifetime is almost semi-permanent as long as deuterium is consistently supplied while the commercial neutron generators consisted of a sealed tube with a limited lifetime as ca. 2,000 h[7].

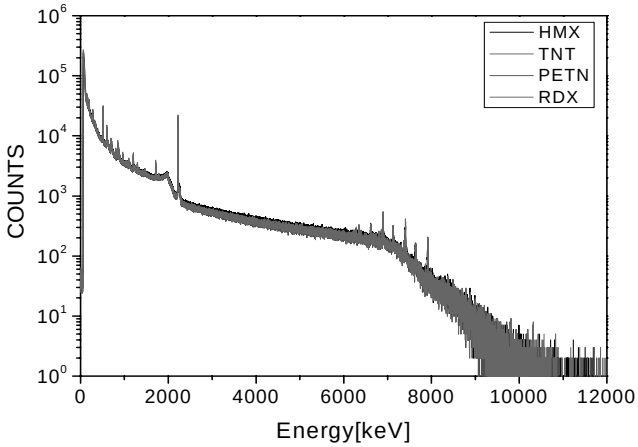

Fig. 3 Prompt Gamma Spectra of Explosives by Using the NIPS System Including D-D Neutron Generator

Fig. 2 and **3** show the gamma spectra of the general (melamine) and the real explosive (HMX, TNT, PETN, and RDX) materials obtained from our NIPS system containing a D-D neutron generator. It was not easy to find the differences between the spectra of melamine and explosives due to similar concentrations of nitrogen, hydrogen, and carbon in their compositions, so PCA was performed to discriminate the illicit materials from general materials easily.

Fig. 4, **5**, and **6** show the three dimensional score plot using three dominant principal components (PC) - PC1, PC2, and PC3. The PCA result of the pattern recognition using gamma spectra obtained by the PGNAA facility of the HANARO research reactor is shown in **Fig. 4**. It provides a good separation of the explosives and chemical warfare agents from the innocuous materials, but there were also considerable overlaps between illicit and general materials.

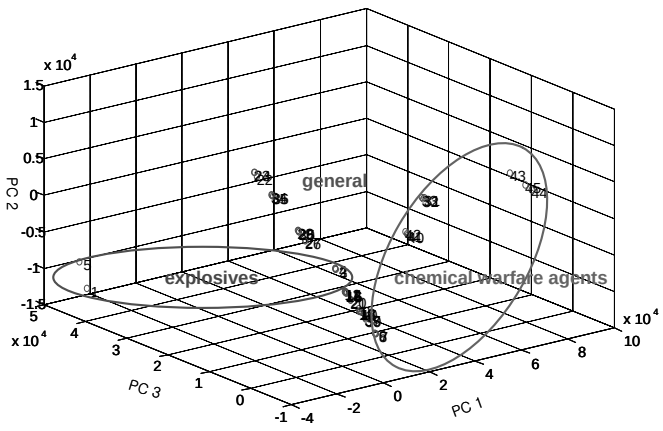

Fig. 4 PCA Result of Pattern Recognition for Training Set

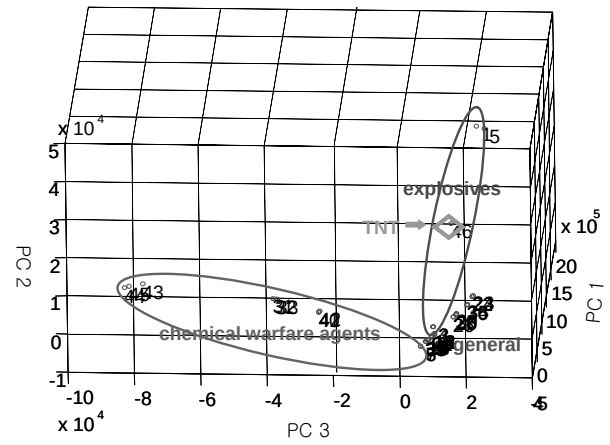

Fig. 5 PCA Result of Pattern Recognition for TNT

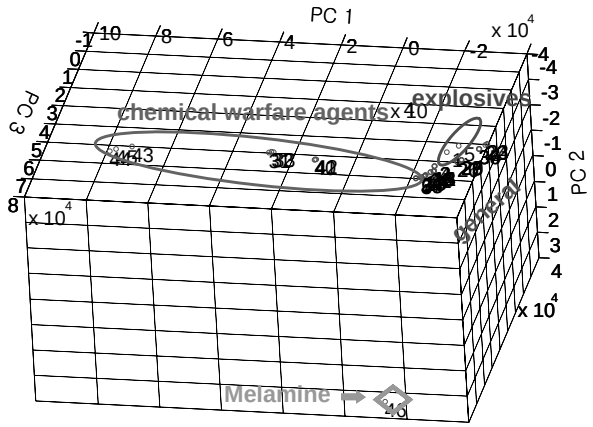

Fig. 6 PCA Result of Pattern Recognition for Melamine

As shown in **Fig. 5**, when the gamma spectrum of TNT was projected into the already prepared training set for the pattern recognition shown in **Fig.4**, it was placed in the category of explosives properly. Other explosives of HMX, PETN, and RDX were all found in a similar position as TNT, and they resulted in the category of explosives.

The general materials of potassium chloride and melamine (**Fig. 6**) were also found in the category of general materials when they were projected into the training set, but a little far from the grouping of general materials. If the training set for the projection of the samples had also been prepared by using the NIPS system, the distance would be reduced and perfectly placed in the category of general materials. Further pre-processing to prepare the proper training set will be attempted for a better pattern recognition by PCA in the future.

IV. Conclusions

Neutrons are penetrating probes, and a signature radiation is also a penetrating probe. Therefore, the NIPS system developed for the bulk detection of hidden explosives and chemical warfare agents in KAERI could be applied to a security check for screening luggage in airports by complementing the pattern recognition of a training set and further study.

Acknowledgement

This work has been accomplished under the fund of the Mid- and Long-Term Nuclear Research and Development Program by the Ministry of Science and Technology, Republic of Korea. We thank Dr. M.-W. Shin and J.-S. Jung for help with the Mont Carlo calculations.

References

1) H.-J. Im, H.-J. Cho, B. C. Song, Y. J. Park, Y.-S. Jung, W.-H. Kim 'Analytical Capability of an Explosives Detection by a Prompt Gamma-ray Neutron Activation Analysis,' Nucl. Instr. and Meth. A, 566[2], 442-447 (2006).
2) H.-J. Im, Y.-H. Lee, Y. J. Park, B. C. Song, JH. Cho, W.-H. Kim 'Noise Reduction in Prompt Gamma Spectra Acquired in Short Times,' Nucl. Instr. and Meth. A, 574[2], 272-279 (2007).
3) J. Reijonen, 'Neutron generators developed at LBNL for homeland security and imaging applications', Nucl. Instr. and Meth. B, 261[1-2], 272-276 (2007).
4) K. R. Beebe, R. J. Pell, M. B. Seasholtz, 'Chemometrics: A Practical Guide', John Wiley & Sons, New York, 56-182, 1998.
5) B. M. Dobratz, P. C. Crawford, 'LLNL Explosives Handbook-Properties of Chemical Explosives and Explosive Simulants', Lawrence Livermore National Laboratory, 1985.
6) R. E. Marshak, J. L. Fowler, Ed., 'Interscience Monographs and Texts in Physics and Astronomy – Helium-3 Neutron Spectrometers', Interscience publishers, New York, Vol. 4, 413-439, 1960.
7) D. L. Chichester, J. D. Simpson, 'Compact Accelerator Neutron Generators', The Industrial Physics, 22-25 (Dec. 2003/Jan. 2004).

Journal of NUCLEAR SCIENCE and TECHNOLOGY, Supplement 5, p. 367–370 (June 2008)

Novel Fast Neutron Detectors for Environmental and Security Applications

Nikolai Z. GALUNOV[1*], Boris V. GRINYOV[1], Jong Kyung KIM[2], Yong Kyun KIM[2],
Oleg A. TARASENKO[1], Natalya V. KARAVAEVA[1], and Sergey V. BUDAKOVSKY[1]

[1]*Institute for Scintillation Materials of Scientific Technology Centre "Institute for Single Crystals", NASU, Kharkov, Ukraine,*
[2]*Innovative Technology Center for Radiation Safety Hanyang University, Seoul, Korea*

Two new types of organic scintillation materials for spectrometry of fast neutrons are studied. Firstly, it is stilbene polycrystalline scintillators obtained by the technology of cold- and hot-pressing and organic. Secondly, it is composite scintillators based on grains of a stilbene single crystal introduced into an optically transparent organosilicone matrix. The influence of a grain size, a chosen type and concentration of grains in a polymer matrix on the scintillation characteristics of proposed materials are discussed.

KEYWORDS: organic scintillator, polycrystal, composite material, fast neutron detector

I. Introduction

The problem of spectrometry of a low intensity flux of fast neutrons is of a great deal in today's ecological, geological, biological, medical tasks, custom survey, etc. The radiation-weighting factor w_R is the value expressing the long-term risk (primarily cancer, leukaemia, etc.) of low-level chronic exposure. It depends upon the type of radiation and other factors. E.g. for photons of γ- radiation $w_R = 1$, but for fast neutrons with energies $E_n \leq 2$ MeV the $w_R = 20$. The same huge value of w_R is correct only for the case of alpha particles or heavy nuclei irradiation.[1)] The main part of a neutron spectrum of natural fission materials is the same range of E_n. To prevent their smuggling through the customs area, the detection of this part (0.1 MeV < E_n < 2 MeV) of neutron spectrum is of a primary importance.

To obtain sensitive and convenient detection technique it is necessary to obtain a large area non-hygroscopic detector, which has a high efficiency of fast neutrons detection and allows to discriminate fast neutron scintillations from background signals (e.g. from gamma scintillations). Hydrogen-containing organic scintillation materials give the most promising way to design such scintillators.

According to the received opinion organic single crystals, plastics, and liquids are the only representatives of the organic scintillators.[2,3)] On the other hand, none of these types of scintillators is so good for solution the problem discussed. Really, organic polymers do not allow separating the signals from neutrons and gamma background, liquid scintillators like plastic scintillators have lower light yield than single crystals. Liquid scintillators mainly are toxic and often inflammable. If we mean the material, organic single crystals are the best choice for fast neutron detection, but even in the case of using modern technologies of crystal growth[4)] the nature of their growing process ties up to obtain the crystals of large diameters. Therefore, the design of new types of organic scintillators with polycrystal structure becomes necessary.

Previously we proposed and realized the idea[4-6)] to obtain new type of organic scintillators, namely, polycrystals, as detectors of ultraviolet and short-range radiation with characteristics close to ones of organic single crystals but without such a limitation on the dimension of their input window. The technologies of cold-pressing and hot-pressing are the base for obtaining of polycrystals.

Another new type of fast neutron detectors under discussion is composite scintillators. Proposed scintillator is based on grains of stilbene introduced into an optically transparent organosilicone matrix. We varied a type of the matrix and a concentration of grains in the matrix to obtain optimal characteristics of the new material.

In this paper we are studying the possibilities to use new organic scintillators based on stilbene not only as detectors of short-range radiation, but as detectors of fast neutrons.

II. Proposed Technologies

New scintillation materials were obtained on the base of cryogenic crushed down structure perfect single crystals grown from a melt. A single crystal boule is crushed at a low temperature. After that the grains of the single crystal of the necessary size is selected by calibrated sieves. Such a process gives the row material for preparation of a new scintillator. It is important that the size of such a grain has to be comparable or to be larger than the range of an ionizing particle. In the case of indirect ionizing radiation, it has to be comparing with the range of corresponding recoil particles.

1. Organic Polycrystals

Proposed scintillator is a hot-pressed or a cold-pressed polycrystal based on grains (with grain size L) of stilbene.

The cold-pressed polycrystals were obtained by single-axial pressing (100…800 MPa) of single crystalline powder in a rigid mould at the room temperature. The hot-pressed polycrystals were obtained during the annealing at the

*Corresponding Author, Tel.: +380-57-341-01-52, Fax: +380-57-340-93-41, E-mail: galunov@isc.kharkov.com

melting temperature and hydrostatic compression about 150 MPa. So, in the latter case, solid state recrystallization is an additional step in the preparation of the crystal.

In our experiments we used 5 mm thick and 30 mm in diameter cold-pressed and hot-pressed stilbene polycrystals. We chose three grain size ranges with the following L-values: from 0.5 to 1 mm, from 1 to 2 mm, and more than 2 mm.

2. Composite Organic Scintillators

Proposed composite scintillator is based on grains (with grain size L) of stilbene introduced into an optically transparent polymer. To prepare composite scintillators we have chosen the same three bands over the range of L- values as in the case of polycrystals, namely, $L < 0.5$ mm, $L \sim 1…2$ mm, and $L > 2$ mm.

So, the method of preparation of such a composite detector included the following operations:[7)]

- obtaining of single crystals by the Bridgman-Stockbarger method,[5,6)]
- grinding of crystalline boules at a low temperature with subsequent sieving through sieves with different cell size (0.5…2.5 mm),
- choice of the optimum dimension of stilbene crystal grains (from 0.5 to 2.5 mm),
- preparation of the organosilicone base,
- introduction of crystalline stilbene grains into the organosilicone base,
- introduction of the composition into a light guide housing,
- vacuum treatment of the composition,
- hermetic sealing of the scintillation detector.

It should be noted that the grains in this system are separated. Therefore, the task of improvement of the structure perfection of a composite scintillator in contrast to the case of a polycrystal does not appear. For composite scintillators it is important to understand the optimal concentration of crystal grains inside the glue. Therefore to choose a base of composite scintillators we studied optical and physical-chemical characteristics of such silicone composite materials as a "silicone rubber for medical purposes" (SKTN-med, St. Petersburg, Russia), Silgard-186, Silgard-527 (Dow Corning Corporation, USA), optical thixotropic silicone lubricants and epoxy optically transparent adhesives.

III. Results and Discussion

1. Short-range Radiation Measurements

The results of the short-range radiation measurements give initial information about scintillation characteristics of the proposed materials.

For the measurements of the light yield of Ø30 mm×5 mm stilbene polycrystals, we used a ^{137}Cs source of 0.622 MeV conversion electrons and a ^{239}Pu source of 5.15 MeV α- particles. An Ø50 mm × 5 mm stilbene single crystal was taken as the reference scintillator. The **Fig. 1** demonstrates the scintillation amplitude spectra for cold-pressed stilbene polycrystals (**Fig. 1**, **a**), as well as for hot-pressed stilbene polycrystals (**Fig. 1**, **b**) irradiated by α-particles from a ^{239}Pu radionuclide source.

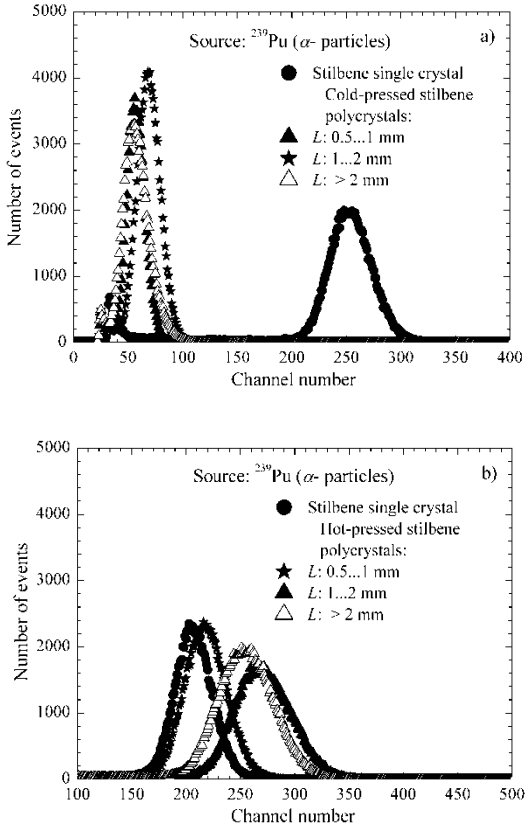

Fig. 1 The scintillation amplitude spectra for cold-pressed (**Fig. 1**, a) and hot-pressed (**Fig. 1**, b) stilbene polycrystals irradiated by α-particles from a ^{239}Pu isotope.

Table 1 The values of relative light yield J for Ø30 mm × 5 mm cold-pressed and hot-pressed stilbene polycrystals

Type of pressing	L, mm	J, %	
		0.622 MeV conversion electrons	5.15 MeV α-particles
Cold	0.5 to 1	60	21.5
Cold	1 to 2	99	30.5
Cold	> 2	97	21
Hot	0.5 to 1	102	104
Hot	1 to 2	117	126
Hot	> 2	115	122

Table 1 summarizes the results of the relative light yield measurement for the Ø30 mm × 5 mm cold-pressed and hot-pressed stilbene polycrystals with different grain size ranges L. For hot-pressed polycrystals, the best results were obtained when L was from 1 mm to 2 mm. The hot-pressed polycrystals have the better parameters than cold-pressed polycrystals. These results are typical for the scintillators discussed. One can see a big difference in J-values between hot-pressed and cold-pressed polycrystals for the case of α-excitation as well as for the case of β-excitation. In the same

time for β-excitation there is no hot-pressed polycrystal with light yield comparable with a single crystal. The range of the 0.622 MeV electron paths can be estimated as 1.75 mm, and the length of alpha particle track as 0.03 mm only.[3)] It means that the influence of light collection process on scintillation light when it passes through a scintillator is more important for the case of α-excitation than for β-excitation. Therefore, the hot-pressed polycrystals have to have the efficiency more close to single crystals because they are more transparent for the emitted light than cold-pressed ones. For cold-pressed polycrystals, both of above-mentioned characteristics have to be worse.

2. Neutron Measurements

We used a ^{239}Pu-Be radionuclide source for both fast neutrons and of photons of γ-radiation. To separate the neutron and background gamma scintillations the special set-up of our design is used.[8)]

Our previous investigations[3,8,9)] of the discriminating ability of stilbene and *p*-terphenyl single crystals indicated that detectors on the base of stilbene scintillators more effective for the modern tasks of neutron spectrometry. Therefore, a stilbene was taken as the base for development of new large area detectors of fast neutrons.

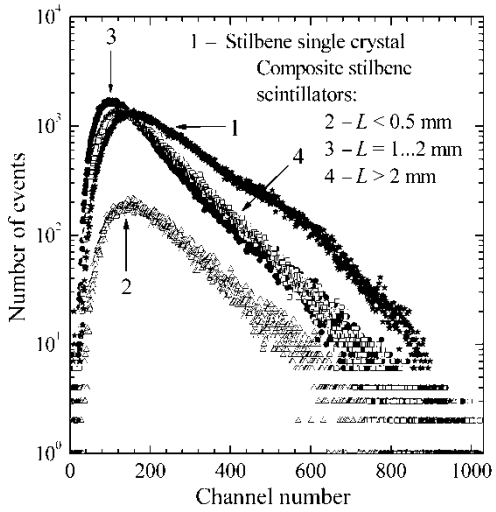

Fig. 2 Recoil proton spectra of a ^{239}Pu-Be source for the reference stilbene single crystal (curve 1) and for a series of scintillators on a base of stilbene grains of size *L* introduced in a silicone matrix (curves 2-4).

We have studied the scintillation properties of composite stilbene scintillators obtained by the above-described method. The investigations were aimed at search for organosilicone base of a composite scintillator, optimal construction of the detector in the context of conditions of light collection, optimal content of stilbene and size of its grains in a silicone base. **Fig. 2** shows as an example the recoil proton spectra generated by fast neutrons of ^{239}Pu-Be source in the reference stilbene single crystal (curve 1) and in composite scintillators on a base of stilbene grains of size *L* introduced in a silicone matrix (curves 2-4). The time and conditions of such a spectrum accumulation was the same for all the measurements.

The relative efficiency χ of fast neutron detection by proposed composite scintillators was calculated as follows. We calculated the total number of events under the curve of a recoil proton spectrum of a composite scintillator and compared this result with the analogous calculation for the reference scintillator (the stilbene single crystal). It allows us to estimate the relative averaged efficiency χ of fast neutron detection by a composite scintillator. If N_n and R_n, is the number of pulses accumulated in channel n for a composite scintillator and for the reference scintillator, respectively, then the relative efficiency of neutron detection by such a composite scintillator is:

$$\chi = \sum_n N_n \Big/ \sum_n R_n . \qquad (1)$$

For the reference scintillator χ- value is taken as 100 %.

Table 2 presents values of χ for composite stilbene scintillators obtained from stilbene grains with linear dimensions *L* from 1 to 2 mm and different organosilicone bases. **Table 2** shows that the relative efficiency χ of fast neutron detection is the best for the scintillator with a grain size *L* from 1 to 2 mm and Sylgard-527 organosilicone base.

Table 2 Values of χ for composite scintillators on the base of stilbene grains and organosilicone compounds

Sample number	Grain size *L*, mm	Organosilicone base and it viscosity, poises	χ, %
1	1…2	SKTN η=110	40
2	1…2	Sylgard-527 η=230	48
3	1…2	Sylgard-186 η=1100	31

Table 3 Values of χ for composite stilbene scintillation detector with different linear dimensions of stilbene grains

Sample number	Grain size *L*, mm	Organosilicone base and it viscosity, poises	χ, %
1	0.5…1	Sylgard-527 η=230	80
2	1…2	Sylgard-527 η=230	83
3	> 2	Sylgard-527 η=230	78

Table 3 presents the values of χ for composite stilbene scintillators (see **Fig. 2**) with different linear dimensions of stilbene grains and a Sylgard-527 organosilicone base. **Table 3** shows that with the increase of the linear dimensions of the grains from 0.5 mm to 2.5 mm the scintillation characteristics improve. The value of χ for the scintillation detector that contains composite scintillation material with *L*= 1…2 mm (the sample No. 2) and is cited by **Table 3** is

higher then χ - value for the scintillator with the same L in **Table 2** (the sample No. 2). In the later case (**Table 2**) it is the scintillator without housing and in the former case (**Table 3**) it is the scintillator in housing with light reflection coating that ensures the better light collection processes in such a construction.

Table 4 shows the values of χ for the detectors with different content of stilbene in the organosilicone base. The increase of the stilbene content in the organosilicone base leads to the growth of the relative efficiency χ of fast neutron detection. So, the technology proposed gives the reproductive results and allows us to obtain detectors with characteristics that approach to ones of single crystals.

Table 4 Values of χ for composite stilbene scintillation detectors with different content of stilbene in the organosilicone base

Sample number	Grain size L, mm	Content of stilbene single crystal, %	χ, %
1	0.5…2	50.4	80
2	0.5…2	63.9	82
3	0.5…2	73.2	95

IV. Conclusions

The basis of technologies of preparation of large area polycrystals and composite organic scintillators as well as the methods of their investigation as fast neutron detectors has been designed.

Results been obtained show that:

i) composite materials and polycrystals in range of neutron energies about units of MeV have the scintillation characteristics close to those of single crystals;

ii) comparison of results of measurements took place for alpha-, beta-, gamma- , and neutron excitations showed that the nontrivial correlation between a grain size and properties of a proposed scintillator exists;

iii) light collection in thin and large diameter, but structurally imperfect scintillators can become the process of primary importance, and its investigation is the separate interesting task because light collection is the real process able to limit the dimensions of scintillators designed;

iv) the second in order of importance factor that can limit the dimensions of scintillators designed is a mechanical strength of scintillation material.

References

1) ICRP Publication 60. 1990 Recommendations of the International Commission on Radiological Protection, 21**,** No. 1–3, Ann. ICRP, (1991).
2) J. B. Birks, The Theory and Practice of Scintillation Counting, Pergamon Press, London, 662 p (1967).
3) N. Z. Galunov, V. P. Seminozhenko, Theory and Practice of the Radioluminescence of Organic Condensed Media, Naukova Dumka, Kiev, 384 p. (1997), [in Russian].
4) N. Z. Galunov, "New generation of highly effective organic scintillators and their process technologies", In abstracts of International Technology Transfer Conference, Iowa State University, June 23-24, 1998, p.124 (1998).
5) S. V. Budakovsky, N. Z. Galunov, V. P. Seminozhenko, "Some new approaches to obtain the organic crystals with high quality", Book of Lecture Notes of First International School on Crystal Growth Technology, Beatenberg, Switzerland, Sept. 21-25, 1998, p.777 (1998).
6) N. Z. Galunov, "The study of the properties of organic bulk materials based on the new knowledge of their radioluminescence mechanism", Mol. Cryst. Liq. Cryst., **252**, 135 (1994).
7) S. V. Budakovsky, N. Z. Galunov, J. -K. Kim et al, "New effective organic scintillators for fast neutron and short-range radiation detection", In 2006 IEEE Nuclear Science Symposium Conference Record, N29-3, p.935 (2006).
8) J. H. Baker, N. Z. Galunov, A. M. Stepanenko, O. A. Tarasenko, "Some aspects of discrimination techniques for the measurement of neutrons and photons of gamma radiation in geological applications", Radiat. Meas., **38**, 817 (2004).
9) N. Z. Galunov, E. V. Martynenko, "Ionizing radiation energy exchange in the regions of high activation density of organic scintillators", Radiat. Meas., **42**, 715 (2007).

Journal of NUCLEAR SCIENCE and TECHNOLOGY, Supplement 5, p. 371–374 (June 2008)

Study on the Influence of the Scattered Radiation in the Industrial Transmission Gamma Tomography

Jongbum KIM[1*], Sunghee JUNG[1], Jinseop KIM[1], Nayoung LEE[1], and Gyuseong CHO[2]

[1] *Korea Atomic Energy Research Institute, Dukjin-dong, Yuseong-gu, Daejon, Korea*
[2] *Korea Advanced Institute of Science and Technology, Seoul, Korea*

The effect of scattered radiation on the transmitted gamma ray signal should be carefully taken into account because it certainly affects the quality of reconstructed tomography images. Therefore this effect was evaluated with different counting modes and gamma energies. For less dense objects such as wood and plastics, the build-up effect can be ignored and ^{137}Cs can yield the better result than ^{60}Co. On the contrary, for the relatively heavy material such as oil and metal the scattered radiation effect of ^{137}Cs source should be considered because the build-up effect is more serious than ^{60}Co. It was also found that the image quality gets better when the count data of photo-peak were used rather than the total counts from the full spectrum. The image improvement technique using precise weight matrix calculation method was suggested to remove the influence of the scattered radiation on the reconstructed image quality. From the experiment, it was concluded that the effect of scattered radiation on the image quality is varied depending on the material composition and radiation energy. Before the implementation in the field, normally the information of the process material is available so the optimal measurement condition can be predetermined on the basis of this study. The additional data processing method is also expected to improve the reconstructed image quality further.

KEYWORDS: scattered radiation, industrial, gamma ray, computed tomography, transmission, single source, single detector

I. Introduction

Since computer tomography technologies have already been developed for medical purpose, industrial process tomography using gamma emitting radioisotopes is being studied in order to investigate large industrial process units during their operation. The industrial process gamma tomography is applied in a wide range of petrochemical and refinery industries[1]. ^{60}Co and ^{137}Cs are preferentially used as gamma radiation source due to their high penetration power into large objects[2]. The influence of scattered radiation on the transmitted gamma ray signal should be carefully taken into account because it certainly affects the quality of reconstructed tomography images. Therefore this effect was evaluated with different counting modes and gamma energies. The parallel beam gamma ray CT with single source and detector pair has been used as an experimental set-up for this study. And the EM (Expectation Maximization) method[3] which is based on statistical model was used for image reconstruction. The details on the hardware and image reconstruction algorithm used here were introduced in reference 3 and 7

II. The Scattered Radiation

The attenuation of radiation in material is denoted as **Eq. 1** without considering build-up of scattered radiation[5].

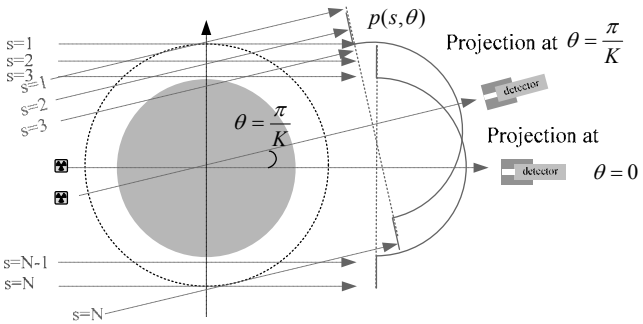

Fig.1 Single source and detector parallel beam CT

$$I = I_0 e^{-\int \mu(x,y)du} \tag{1}$$

where I_0 is the incident beam intensity of the radiation beam and $\mu(x,y)$ represents the linear attenuation coefficient at the x, y point. **Eq. 1** can be rearranged as **Eq. 2**.

$$\ln \frac{I_0}{I} = \int \mu(x,y)du \tag{2}$$

The right side of **Eq. 2** is the line integral of attenuation coefficient function along the path of u, that is defined as the ray-sum. If one ray-sum is measured at certain angle θ and detector bin s, the ray-sum denoted as P(s,θ) as in **Fig.1.**

$$P(s,\theta) = \ln \frac{I_0(s,\theta)}{I(s,\theta)} \tag{3}$$

where $I_0(s,\theta)$ is counts measured without object and $I(s,\theta)$ is counts measured for object at a certain angle θ and detector

*Corresponding Author, Tel No: +82-42-868-8050, Fax No: +82-42-862-6980, E-mail: jong@kaeri.re.kr

bin s. In homogeneously mixed material, the ideal ray-sum is written as **Eq. 4**

$$\mu x = P(s,\theta) \tag{4}$$

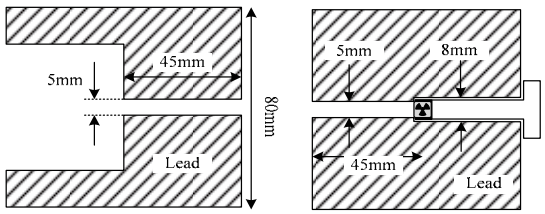

Fig. 2 Cross section image of detector collimator (left) and source collimator (right)

In the photon interaction with the matters, photon does not disappear in Compton scattering. Even in the photoelectric effect and in pair production, although the incident photon is absorbed, X rays are usually produced after subsequent to the photoelectric effect, and annihilation radiation inevitably follows after pair production. As a result, mono-energetic beam incident on a object emerges with continuous spectrum.

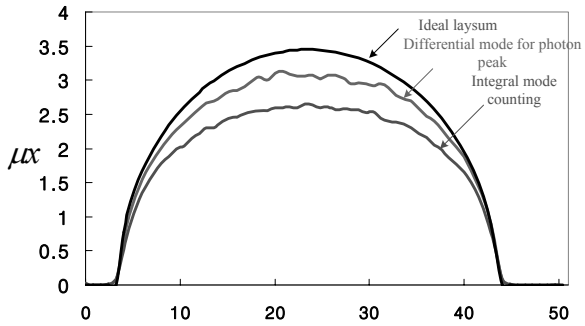

Fig. 3 A projection for uniformly distributed round disk

The build up of the scattered radiation results in the increase of measured counts. In a density measurement by using gamma ray, it can result in lower density than the real one. The **Fig. 3** shows the one projection of water pillar of 40cm measured with ^{137}Cs at integral and differential mode counting for photon peak energy.

In radiation measurement, a collimator reduces the build-up of scattered radiation. But still we can see influence of the scattered radiation from the **Fig. 3**. Even though the detector was shielded as in **Fig. 2**, there are still many scattered radiation.

The cross-section image of **Fig. 4** can be obtained from 64 projections and 64 detector bins at each projection. By applying the EM algorithm, we can get result as in **Fig. 4** for integral mode counting with ^{137}Cs. The result shows the low density in center by the build up of scattered radiation.

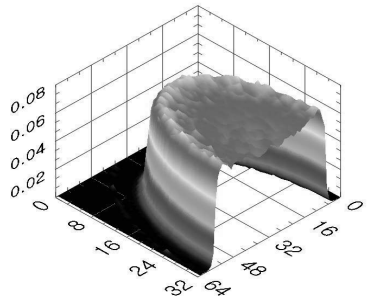

Fig. 4 Slice view of cross section image with integral mode counting

III. Image Improvement Techniques

1. Correction of Artifact from the Scattered Radiation by Experimental Curve

In industrial process gamma tomography, the many cases is to measure the density distribution in a reactor vessel[2]. In gamma process tomography, the object is used to be a vessel including hydrocarbon whose density of 0.8~0.95. Build up factor for hydrocarbon is similar to that of water at around 1MeV. If the composition of material inside a vessel not varies significantly and is hydrocarbon, the compensation of density loss equation is experimentally determined as **Eq. 5**. The **Eq. 5** is determined from the trend curve in **Fig. 3**.

$$\mu x(s,\theta) = 0.12 \times [\ln(\frac{I_0(s,\theta)}{I(s,\theta)})]^2 + \ln(\frac{I_0(s,\theta)}{I(s,\theta)}) \tag{5}$$

2. Correction by Weight Matrix Calculation of Precise Beam Interaction Model

The trajectory of gamma ray of photon peak energy can be regarded as direct line between source and detector in narrow beam collimation. But in normal cases, the beam has a certain width which is determined by source and detector collimation aperture. Although in collimated situation, there are considerable direct photons detected through the collimator unless the collimation depth is substantially thick. When the projection beam has a certain width, the radiation detected through imperfect collimation can be compensated by precise beam interaction model in weight matrix calculation[8]. If the number of total ray-sums from projection and detector bin is M, then the notation of ray-sum denoted as **Eq. 6**

$$p_i = \ln \frac{I_{0i}}{I_i} \tag{6}$$

where i=1~M

When the number of pixel in display image is N, the matrix equation as in **Eq. 7** characterizes the beam interaction in tomography system where H is weighted matrix and μ is linear attenuation coefficient to be determined

$$p_i = \ln \frac{I_{0i}}{I_i} = \sum_{j=1}^{N} H_{ij} \cdot \mu_j \tag{7}$$

where j=1~M

The several weight matrix calculation methods have been introduced in reference 8. One of them is "measurement area of pixel". We modified the above method by adopting more precise beam interaction model. We consider the beam as three regions. The direct photons detected through imperfect collimation can be corrected by adopting the weighted factor determined from the beam interfacing area and attenuation coefficient of collimation material. We divided weighted matrix into H1, H2 and H3 in the measurement area inside the pixel to the each beam where μ_{col} is linear attenuation coefficient and d is thickness of collimator.

$$\ln\frac{I_{0i}}{I_i}=\sum_{j=1}^{N}[H2_{ij}+\frac{1}{\mu_{col}\cdot d}(H1_{ij}+H3_{ij})]\cdot\mu_j \qquad (8)$$

If $\mu_{col}\times d$ is sufficiently large, the measurement system considered as perfect collimation and noted simply as **Eq. 9**.

$$\ln\frac{I_{0i}}{I_i}=\sum_{j=1}^{N}H2_{ij}\cdot\mu_j \qquad (9)$$

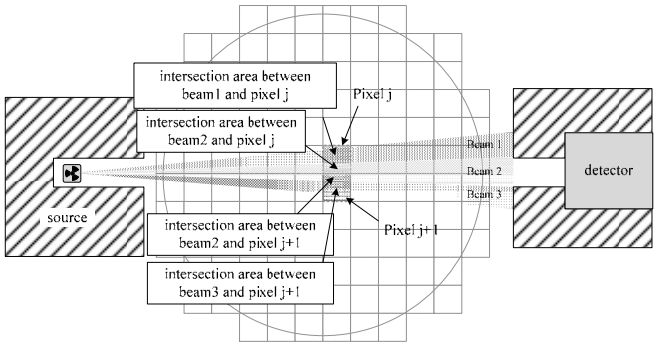

Fig. 5 beam regions and their intersection with pixels

IV. Experimental Result

The energy of source affects the result because the build up of scattered radiation is a function of photon energy. For less dense object such as wood and plastics, the build up can be ignored and ^{137}Cs can yield the better result than ^{60}Co as in **Fig. 6**. Contrarily, for the relatively heavy material such as liquid and metal, the scattered radiation effect of ^{137}Cs source can be more serious than that of ^{60}Co.

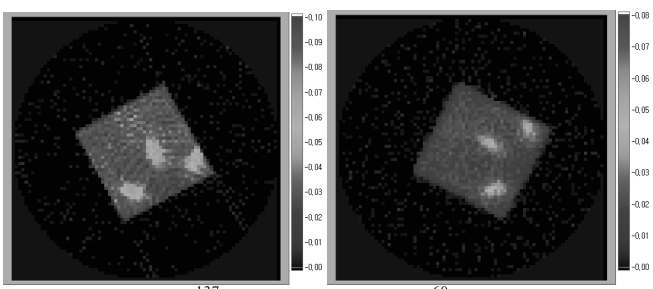

a. ^{137}Cs b. ^{60}Co

Fig. 6 The image of wood timber from different energy sources

Fig. 7 shows the cross section image which is consist of water, oil and air. Linear attenuation coefficient of liquid water is known as 0.0862cm^{-1}. The light oil whose density is 0.815cm^{-1} and linear attenuation coefficient is 0.0702cm^{-1} is filled into the middle layer of the phantom. The result from the integral mode counting shows the low contrast of the materials.

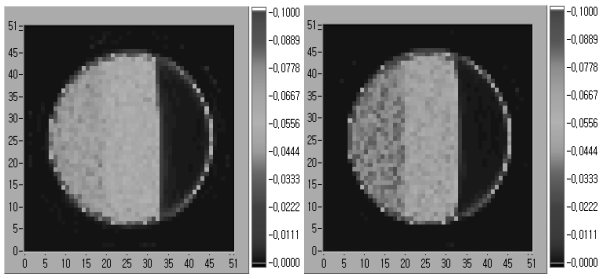

a. integral mode counting **b.** differential mode counting

Fig. 7 The comparison image of water-oil-air layer

Fig. 8 shows the slice view of corrected image by Eq. 5 where uncorrected image has shown in **Fig. 4**. This result shows that the artifact due to the integral mode counting can be reduced by Eq. 5.

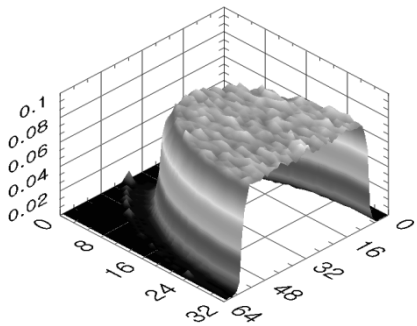

Fig. 8 The slice view of corrected image by Eq5

While Eq. 5 contributes to reduce the discrepancy of overall density distribution, the precise interaction model of Eq. 8 increases the sharpness of an image as in **Fig. 9**. The phantom was made of different size of PE, Teflon, Al and Fe and their density are 0.91, 1.4, 2.7 and 7.6 respectively. The **Fig. 10** shows the crop image of Fe from the **Fig. 9** in which the artifact reduced by adopting the precise beam interaction model.

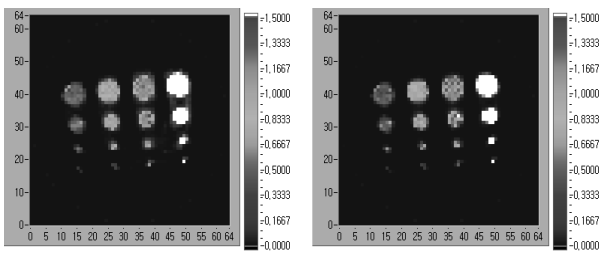

(a) (b)

Fig.9 The images of phantom consisting of PE, Teflon, Al, and Fe (from the left) reconstructed by (a) normal beam interaction model and (b) precise beam interaction model.

The artifact of empty region is dominant in normal beam interaction model than in proposed beam interaction model.

It can be also calculated quantitatively by Eq. 10. The RMS errors for empty region of crop image is 0.013 in normal beam interaction model while 0.0071 in precise beam interaction model

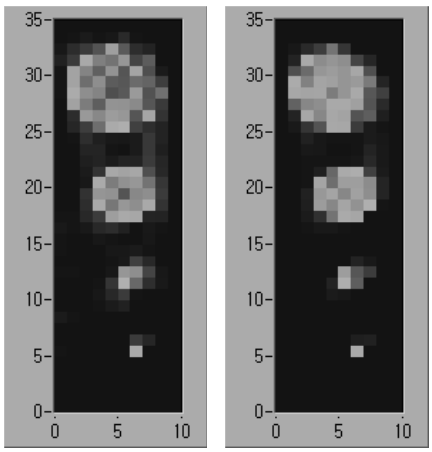

(a) (b)

Fig. 10 The crop images of Fe in **Fig. 9**.

$$RMSE_N = \sqrt{\frac{\sum_{i=1}^{i=N}(\mu_{true,i} - \mu_{reconstructed,i})^2}{N^2}} \qquad (10)$$

V. Conclusions and Remark

The compensation of density loss is of importance in terms of investigation of internal media distribution. If it is not calibrated properly, it can give ambiguous result. In a packed bed type reactor, reaction zone can be determined indirectly[2] by measuring the density distribution. Before the gamma ray tomographic scanning in the field, normally the information of the process material is available so the optimal compensation parameter can be predetermined on the basis of this study. The additional data processing methods which were proposed in this paper can give more accurate result on industrial reactor operation. In addition to the application of transmission tomography, there are many cases that need to detect radiotracer for the behavior of either multi-phase or non–compressible single phase. If we select proper radioisotope tracer which goes selectively to a certain reaction then we can get the functional image of the chemical reactor vessel by industrial SPECT[9] Tomography[10]. For example, if there is a phase transition of a chemical component in multi phase flow, we can apply a proper tracer to investigate its reaction mechanism.

Acknowledgement

This research has been carried out under the Nuclear R&D program by MOST .

References

1) Jamal Chaouki, Faical Larachi, and Milorad P. Dudukovic, "Noninvasive Tomographic and Velocimetric Monitoring of Multiphase Flows," Ind. Eng. Chem. Res., 36[11], 4476(1997).
2) C. Boyer, B. Fanget, "Measurement of liquid flow distribution in trickle bed reactor of large diameter with a new gamma-ray tomographic system," Chemical Engineering Science, 57, 1079(2002).
3) Kenneth Lange and Richard Carson,"EM Reconstruction Algorithms for Emission and Transmission Tomography," Journal of Computer Assisted Tomography, 8[2], 306, (1984)
4) Sailesh B. Kumar, Davood Moslemian and Milorad P. Dudukovic, "A γ-ray tomographic scanner for imaging voidage distribution in two-phase flow systems," Flow Meas. Instrument, 6[1], 61(1995).
5) Avinash C. Kak, Malcolm Slaney, "Principles of Computerized Tomographic Imaging," Electric Copy: IEEE PRESS, 329(1999).
6) Johansen G A and Jackson P, "Radioisotope gauges for industrial process measurements", John Wiley&Sons Ltd, (2004)
7) Jong Bum Kim, Sung Hee Jung and Jin seop Kim "A study on Industrial gamma ray CT with a single Source and detector Pair", Journal of Korean Nuclear Society, 38[4], 50(2006)
8) G.A Johansen, "Gamma ray tomography software and image reconstruction" IAEA/RCA Regional training course on Industrial Process Gamma Tomography , Korea, October 11-15, (2004)
9) S. LEGOUPIL, G. PASCAL, D. CHAMBELLAN, D BLOYET, "An Experimental Single Photon Emission Computed Tomograph Method for Dynamic 2D Fluid Flow Analysis", Applied Radiation and Isotopes, 48,1507(1997)
10) Miles N. Wernick, John N. Aarsvold, "EMISSION TOMOGRAPHY :The Fundamentals of PET and SPECT", ELSEVIER ACADMIC PRESS,472(2004)

Journal of NUCLEAR SCIENCE and TECHNOLOGY, Supplement 5, p. 375–378 (June 2008)

Development of Pile-up Separation Method Using Digital Signal Processing

Takuji OISHI* and Mamoru BABA

Cyclotron and Radioisotope Center, Tohoku University,
6-3, Aoba, Aramaki, Aoba, Sendai, Miyagi, 980-0845, Japan

A new method was developed for separation of pile-up signals by means of pulse shape fitting for the signals which were acquired using a digital signal processing technique. The technique was applied for a high purity germanium (HPGe) detector but can be applied various radiation detectors. In the present method, in addition to linear amplifiers for spectrum measurement, another amplifier with short shaping time is used to derive information on the number of pulses piled up and their timing sequences. Since most of the pulse shapes from HPGe proved to be reproduced with the same pulse shape, we could fit the pile-up signals on the basis of pulse shape, number and the timing between pulses. The method can reconstruct each pulse even for multiple pile-up events without count loss with short analysis time. It enables to correct distortion of an energy spectrum of the HPGe detector and improve the energy resolution.

KEYWORDS: pile-up separation, digital signal processing, HPGe detector, multiple pile-up event

I. Introduction

High purity germanium (HPGe) detectors are used very widely from basic to application areas owing to very high energy resolution. To achieve high energy resolution, usually linear amplifiers are used with long shaping time of several micro-seconds in order to enhance the signal to noise ratio. The long shaping time amplifier leads to a wider output pulse and easily induces overlap between signals, i.e., signal pile-up. The pile-up causes the spectrum distortion and masks sometimes low intensity gamma-rays. It is a serious problem in high count rate measurements.

For this reason, the pile-up correction method has been studied and developed actively[1]**.** Most of the methods, however, eliminate all the signals overlapped within some duration (pile-up rejection). In this method, pile-up signals are rejected but the dead time of the measurement becomes longer and the counting efficiency decreases by the correction. Thus the energy resolution and the efficiency are of trade-off in this method. In order to improve the energy resolution and the efficiency in experiment using HPGe detector, it is highly desirable to manage the energy resolution and the count rate concurrently. For the purpose, pile-up signals should be not rejected but recovered by separation between pile-up pulses, by acquiring pulse shape data for each signals.

In recent years, pulse shape data of signals can be acquired in a reasonable count rate by use of the digital signal processing (DSP) technique, and can be applied to realize this method. In the DSP technique, signals are digitized by a high speed flash-type analog-to-digital converter and the digitized signal waveform data is stored and processed by a computer. This technique enables us to carry out complex and flexible processing because the full signal waveform is acquired[2].

The signal separation method using the DSP technique has already been developed by some researchers including our group[3,4,5]. Most of the developed methods adopt the pulse fitting technique with appropriate function that describes the pulse shape. The parameters to search were time, amplitude, and shape parameters like width. The separation was successful, but two problems remain to be solved: First, it is difficult to separate signals which are very close because identification of pile-up signal is done in view of fitting results. Under the noisy environment, validity of the identification becomes low further. Second, multiple pile-up event could not be considered because there are infinite solutions for the deconvolution without a constraints on the number of pile-up pulses and thereby it is not possible to determine the number of pulses only form fitting. In fact, however, there are, multiple pile-up event.

This difficulty is eliminated if we have information on the number of pulses included in pile-up event, and the timing sequences between pile-up pulses. In this paper, we describe a new method of pile-up correction using timing signal which provide information on the number and timing of pulses. The technique could be applied successfully for a HPGe gamma-ray detector. In the following, principle, method and results are shown taking HPGe cases as an example. The method can be applied to almost all radiation detectors.

II. Principle

To overcome these problems, we newly introduce “a timing pulse” which is obtained from an amplifier with short time constant. As the output signal of the short time amplifier goes back to the baseline much faster than that of the long shaping time, the probability of pile-up occurrence is much lower. Therefore, short shaping time amplifier gives

*Corresponding Author, Tel No: +81-22-795-7806 Fax No: +81-22-795-7809, E-mail: oishit@cyric.tohoku.ac.jp

us the correct information about timing and the number of pulses even if the signal of the long shaping time amplifier is piled up closely. This signal will clearly indicates the number and timing of overlapping pulses as shown in **Fig. 1**.Then, by use of the timing signal, the number and timing can be determined unambiguously except for extreme cases in which signals are very small or close than a few hundred of nano-seconds. In the case of the multiple pile-up event, the fitting is difficult without the timing information since it is too many variables to conduct the deconvolution.

Furthermore, in the case of HPGe detector, we observed that almost all signals are described with the same signal shape as shown in **Fig. 2**. This will be due to long shaping time compared with signal rise time although the shape of preamplifier is different depending on the incident position. The output pulse shape looks to be dominated by integration in amplifier. Under the condition, fitting with functions can be done with the shape parameter fixed and fitting procedure becomes easy and quick.

III. Method

1. Equipment

We acquired the digitized signal from the HPGe detector by data acquiring system shown in **Fig. 3**. Our HPGe detector is coaxial p-type and equipped with a charge sensitive preamplifier. Output of the preamplifier was divided and connected to a research amplifier (ORTEC 450) and a timing filter amplifier (TFA, ORTEC 474). The shaping time of research amplifier was set long enough in order to exhibit inherent energy resolution (differential: 3 μsec, integral: 3 μsec). On the other hand, the shaping time of TFA was as short as 20 ns to obtain timing signal. With this shaping time, the energy resolution of the system is much inferior to inherent one because of incomplete charge collection and high noise levels as shown later, but narrow pulse width are obtained with low probability of pile-up and good timing performance.

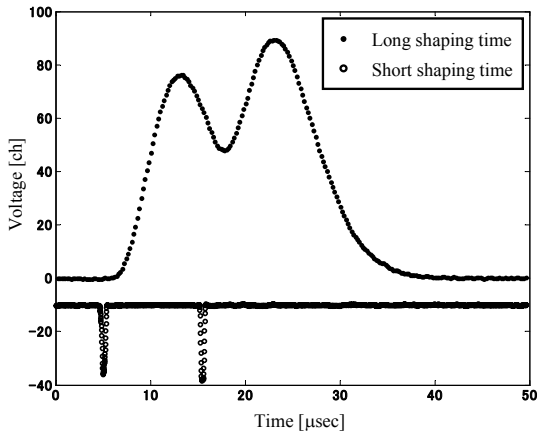

Fig. 1 Different shaping time signals

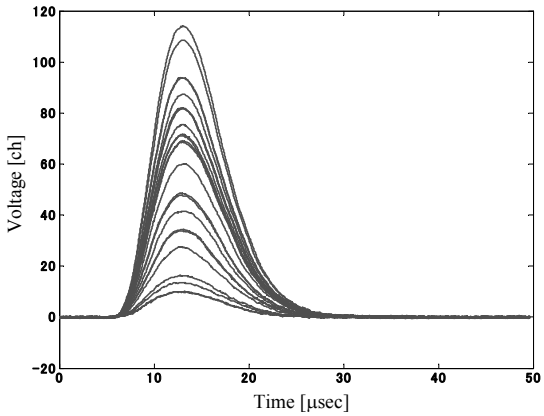

Fig.2 Pulse shape of HPGe with long shaping time

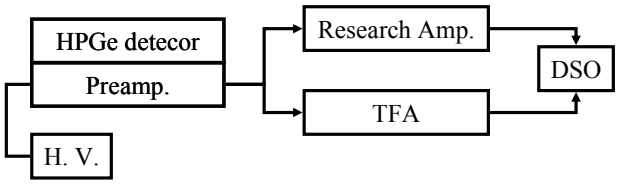

Fig. 3 Data acquisition system TFA: timing filter amplifier DSO: digital storage oscilloscope

Finally, the outputs of the amplifier and the TFA were sent to a digital storage oscilloscope (DSO, LeCroy Wavepro 7000) which was used as a flash analog-to-digital converter and data storage device. The amplitude resolution of the DSO is 8 bits and the maximum sampling rate is 10 GS/sec. In this measurement, the sampling rate of both channels was set 50 MS/sec to be appropriate for fast signal, namely the TFA. The triggering of DSO was done in a self-trigger mode in this measurement. By the DSO the signal waveform of input signal is converted into digital data and stored in the HDD (hard disc drive) of DSO.

2. Signal Fitting Method

The pulse shape of the research amplifier was found to be fitted with an appropriate function based on the CR-$(RC)^n$ shaping[6]. The amplifier is composed by differentiation circuits (CR) and integration circuits (RC). Therefore, from a differential equation, the voltage pulses after the amplifier E_{out} is expressed as described below

$$E_{out}(t) = E\left(\frac{t-x-t_0}{\tau}\right)^n e^{-(t-x-t_0)/\tau} \qquad t \geq x + t_0 \tag{1}$$

$$E_{out}(t) = 0$$

$$t < x + t_0 \tag{2}$$

where E is a pulse height (normalization constant), t is time, τ is a time constant, x is a time offset between the research amplifier and the TFA, n is number of steps of the RC circuit and, t_0 is an origin of time. Each parameter is adjusted by fitting technique.

The parameters related on pulse shape (τ, x, and n) were derived by fitting a pair of waveforms of research amplifier and TFA with good S/N ratio and no pile-up.

The timing signal which is used as the origin of the time was picked up from the TFA signal, by using digital CFD (constant fraction discrimination) method[7] after smoothing. The parameters of the function were as follows: τ=1.487 μsec, x=-0.66 μsec and, n=6.361. Primarily, n should be an integer in the ideal case, but a decimal will be permitted for better fitting accuracy.

Pulse fitting can be performed to all acquired events from a single pulse to multiple pile-up event seamlessly. Accordingly the fitting procedure can be done routinely. At first, the number of pulses in TFA signal was counted and the timing of each pulse is picked up to determine the start point of each pulse. The acquired pulse E_{acq} is described as eq. (3) with superposition of single pulse:

$$E_{acq}(t) = E_{out,1}(t) + E_{out,2}(t) + \cdots + E_{out,i}(t), \quad (3)$$

where i is the number of pulse of TFA signal. Because the calculated pulse shape parameters were fixed and the timing parameter t_0 for each E_{out} was determined by the CFD technique, only E should be determined for each pulse. Therefore, we can apply a liner least square technique, and thereby each E is obtained easily and accurately by the matrix method. Additionally, the fitting improves the pulse height resolution, i.e., the energy resolution because the white noise is smoothed by the fitting. Finally, the separated waveforms were obtained by substituting obtained E and t_0 of each pulse into eq. (1).

Fig. 4 shows an example of pile-up event which looks like a single pulse without pile-up. It is difficult to recognize as the pile-up signal and imagine the number of pulses without the TFA signal (circle). Applying the present method, the acquired amplifier signal (dot) is separated into two signals (broken line) and a sum of the separated pulses is also shown (solid line) to confirm the accuracy of the separation method. The sum of the separated pulses agrees with the amplifier signal very well. Furthermore, each pulse height of separated pulses and TFA pulses are consistent in spite of the fact that the pulse height of TFA is not used in this method. Therefore, the separation is successful. **Fig. 5** shows another example which is a multiple pile-up event.

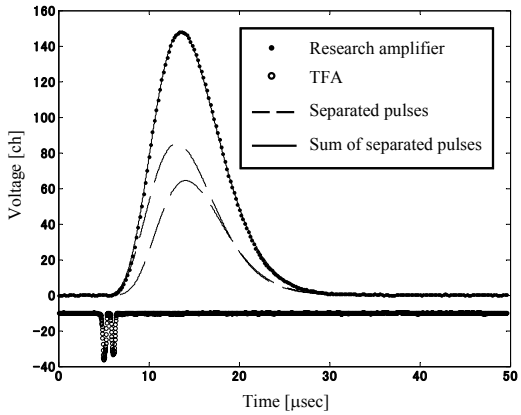

Fig. 4 Separation of very close pulses

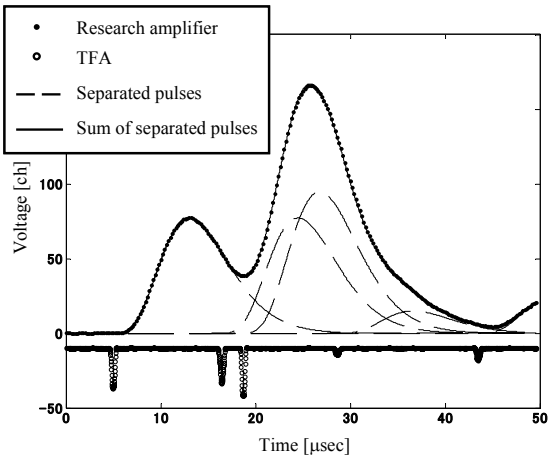

Fig. 5 Separation of multiple pile-up event

The separation can be carried out successfully even in such a case of many pulses involved. In this case, one pulse is separated into four pulses. Such complex separation becomes possible only by the introduction of the timing signal. Therefore, the separation method is very effective even for the multiple pile-up event.

IV. Application

A test experiment was carried out using a ^{137}Cs source placed in front of the HPGe detector enclosed with lead blocks. **Fig. 6** shows the energy spectrum of 1) raw data by a conventional MCA method, 2) analyzed one by the separation method. The spectrum from TFA is also shown for reference. They are normalized by total counts.

In the separation method, the pile-up events which are observed above 662 keV (higher energy than the photopeak) are completely eliminated by the separation. However, the pile-up peak around 1324 keV cannot be eliminated because the TFA signal itself overlapped.

On the other hand, the count in the continuous part due to the Compton scattering and the photo peak are increased in the spectrum after separation. Especially, the photo peak in the spectrum after the separation is about 1.5 times as high as the normal method. This means that after separation procedure, it will become easy to find a small peak existing in this energy region masked with pile-up events.

As noted above, the energy resolution of TFA spectrum is much poor compared with the separated one as shown by a broad photo peak, although the fraction of pile-up events is much fewer. In view of the energy resolution, the separation method has 0.47 %, the normal method has 0.75 %, and the TFA has 4.4 % in FWHM. Thus, the energy resolution is also improved by the fitting procedure, although the photo peak shape of separation spectrum is not the Gaussian distribution. We can see from the comparison of the spectra that the separation method can correct the distortion and improve the resolution.

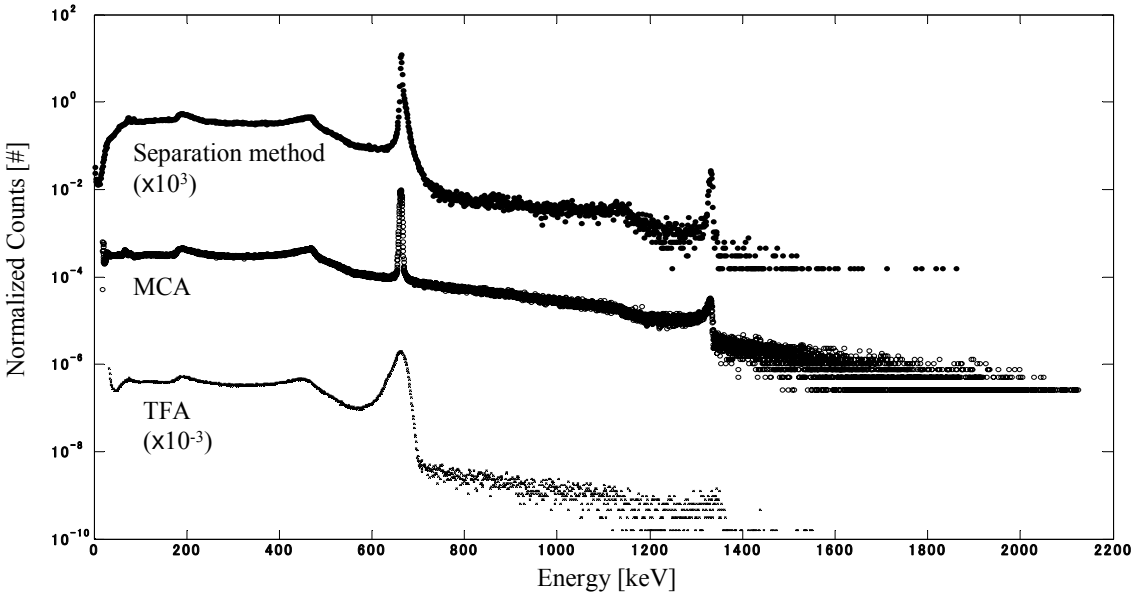

Fig. 6 Distorted and corrected spectrum of ^{137}Cs

V. Conclusion

A new pile-up correction method was developed and applied to high purity germanium detector. In this method, pile-up signals are not rejected but separated into each pulses using the pulse fitting technique to the pulse shape data obtained with the digital signal processing method.

The point of the present method is the employment of the pile-up indicator which gives information on the number of pulses and their timing sequence between pile-up pulses. The timing signal is obtained by shaping pre-amplifier signal with short time constant. On the basis of the fact that the pulse shape of long shaping time amplifier is described with same shape parameters, and the information on the number and timing of pile-up pulses, the pile-up signals can be separated.

The advantage of this method are 1) no count loss, 2) applicability to very close pulses which looks as a single pulse, and multiple pile-up event, 3) fast performance and practicality owing to its simplicity, 4) ability of improvement pulse height resolution. The method was applied to a HPGe detector. As a result, the distortion which was caused by pile-up was corrected without significant count loss.

Moreover, it is possible to realize the real-time processing using the pulse shape parameters (τ, x, and n) obtained due to small amount of calculation. The present technique will be applicable to recently developed ultra fast response detector for measurement in high counting rate situation[8]. The present method will be used to achieve both the fast timing and high energy resolution concurrently to compensate inferior energy resolution of fast response detector by use of coincidence measurement.

References

1) S. L. Blatt, J. Mahieux, and D. Kohler, "Elimination of pulse pileup distortion in nuclear radiation spectra", Nucl. Instr. and Meth., 60, 221, (1968)
2) T. Oishi, T. Yamauchi, M. Hagiwara, H. Yuki, J. Hori, M. Baba, T. Otsuki, "Noise elimination in lead-slowing down neutron spectrometer using digital signal processing", Proceedings of Science, FNDA2006, 067, (2006)
3) T. Itoga, M. Ishikawa, M. Baba, T. Okuji, T. Oishi, M. Nakhostin and Takeo Nishitani, "Fast response neutron emission monitor for fusion reactor using stilbene scintillator and flash-ADC", Radiation Protection Dosimetry, NEUDOS-10 SPECIAL ISSUE, doi:10.1093/rpd/ncm141, (2007)
4) R. J. Komar and H. –B. Mak, "Digital signal processing for BGO detectors", Nucl. Instr. and Meth., A336, 246, (1993)
5) S. Marrone, "A new method for signal acquisition and analysis in high radiation environment", Nucl. Instr. and Meth., B213, 246, (2004)
6) G. F. Knoll, Radiation Detection and Measurement, Third ed., Wiley, New York, (2000)
7) Mark A. Nelson, Brian D. Rooney, Derek R. Dinwiddie and Glen S. Brunson, "Analysis of digital timing methods with BaF_2 scintillators", Nucl. Instr. and Meth., A505, 324, (2003)
8) M. Nakhostin, M. Baba, T. Oishi, T. Itoga and M. Hagiwara, "An ultra fast radiation-resistant fast neutron detector", Radiation Protection Dosimetry, NEUDOS-10 SPECIAL ISSUE, doi:10.1093/rpd/ncm040, (2007)

Journal of NUCLEAR SCIENCE and TECHNOLOGY, Supplement 5, p. 379–382 (June 2008)

Double-stage Low-pressure Parallel Plate Avalanche Counter: A High Count Rate Charged Particle Detector

Mohammad NAKHOSTIN*, Mamoru BABA, and Takuji OISHI

Cyclotron and Radioisotope Center, Tohoku University, Sendai, 980-8578, Japan

This paper investigates the properties of a double-stage parallel plate avalanche counter (PPAC), operated at low gas pressures (5-20 Torr). Substantial improvement in the detector response to light particles, rate capability (~1 MHz/mm^2) and energy resolution were observed in comparison with those of conventional PPACs. The detector is a very attractive option for charged particles detection in intense accelerators.

KEYWORDS: avalanche counter, charged particle detector, high count rate

I. Introduction

Parallel plate avalanche counters (PPACs) have been shown to be well suited as large area, radiation-hard detectors[1,2]. Their easy construction and reliable operation make them very convenient for heavily ionizing particles detection. However, due to low density of the detector sensitive volume, the use of PPAC for low specific ionization (e.g. the light particles at intermediate energy) has been restricted by the difficulty of obtaining large enough output signals in stable condition and without breakdown. Moreover, low-pressure avalanche counters suffer from poor energy resolution, imposed mainly by the fluctuations in the charged particles energy-loss [3].

In principle, the above-mentioned limitations are improved by increasing the amount of primary ionization. However, increasing the amount of primary ionization through the gas pressure or detector gap thickness limits the attainable gas amplification and also drastically raises the required supply voltage[4].

In this paper, we have studied a modified structure of low-pressure avalanche counter in which ionization space is separated from the amplification gap. The idea behind our attempt is to increase the amount of primary ionization by increasing the length of ionization space. In the following sections, after describing the principle of detector operation, the results of investigation on the detector properties such as energy resolution and rate capability are discussed.

II. The Detector Principle

The detector principle is shown in **Fig. 1**. It consists of a large gap for ionization collection and a small gap for charge amplification. The two gaps are delimited with a thin crossed wire mesh. The electric fields inside these gaps are maintained by the voltages applied on the wire mesh plane (HV_1) and the drift electrode (HV_2). When charged particles travel through the detector, due to small size of the amplification gap, the primary ionization is mainly produced in the ionization space. As a result of the electric field maintained along the ionization space, the released electrons are forced to drift into the amplification gap. These drifting electrons initiate avalanches when crossing the very high electric field applied on the amplification gap. The resulting charge that is proportional to the initial number of the drifting electrons induces a signal on the detector electrodes.

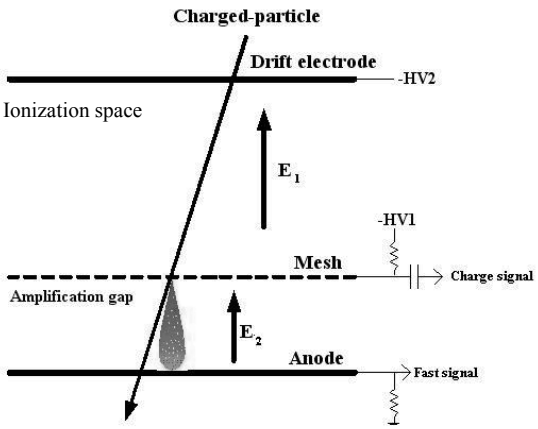

Fig. 1 Principle of double-stage avalanche counter.

The driving force for the electron migration from the ionization space into the amplification gap is induced by the electric field component that is perpendicular to the wire mesh plane. **Fig. 2** shows the calculated values of this component along the detector gap. The calculation has been carried out by using the Maxwell electric field calculation code[5]. The calculation has been performed for the case of equal voltages on the drift electrode and the wire mesh plane. As seen, the very high electric field in the amplification gap is accompanied with a low electric field in the ionization space which is sufficient for the electrons to pass through the openings of the wire mesh and enter to the amplification gap.

The number of primary ionization is determined by both the length of ionization space and the operating gas pressure. Therefore, for a given application, a compromise should be made between the operating gas pressure and the length of ionization space. Regarding to the size of amplification gap,

*Corresponding Author, Tel No: + 81 22 795 7806; Fax No: + 81 22 795 7809, E-mail: nakhostin@cyric.tohoku.ac.jp

small gaps are favorable because it allows a short path for the positive ions produced in the avalanche, thus reducing the collection time of the positive ions and increasing the rate capability of the detector. However, very small amplification gaps may cause mechanical or electrical instability in the counter.

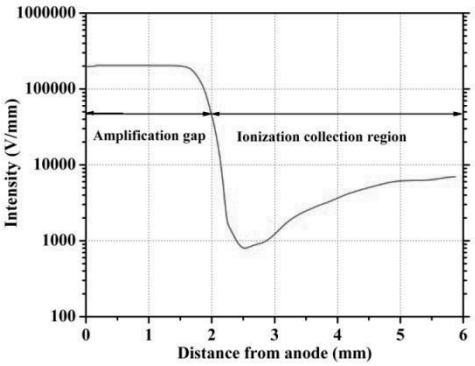

Fig. 2 The electric field intensity along the detector gap. The amplification and ionization gaps are 2 and 4-mm, respectively. The supply voltage is 400 V on both the electrodes.

III. Experiments

Our experiments were carried out with a test chamber in which the mesh plane identified as HV_1 in **Fig. 1**, is made from a solid stainless steel wire mesh with 50-μm diameter and a pitch of 500-μm.

The two other electrodes, identified as anode and drift electrodes, were made of aluminized Mylar foil (7-μm). The electrodes are mounted parallel to each other by means of two replaceable spacers. This allowed the accomplishment of investigation at various ionization and amplification gaps from 0.5 to 10-mm. The anode plane is grounded and negative voltages are applied on the drift and mesh electrodes. The detector active area is 5×5-cm^2.

The detector is placed inside a gas-tight aluminum chamber and operated in the gas flow mode using a two-stage mechanical pumping system. The gas pressure was regulated with a mass flow controller system (MKS mass flow controller) and measured with a calibrated capacitor type pressure gauge. The measurements were performed with isobutane (i-C_4H_{10}) gas at pressure values of 5-25 Torr.

The detector was operated with an ^{241}Am α-source, placed inside the chamber, which emits 5.6 MeV α-particle perpendicular to the detector surface.

As shown in **Fig. 1**, the charge signals induced on the wire mesh are obtained with a conventional charge-sensitive preamplifier (ORTEC 142 PC or ORTEC 142B) and fast signals are read out by means of a fast preamplifier with a rise-time less than 1 ns (FUJI Preamplifier).

IV. Experimental Results

Fig. 3 illustrates the process of charge transfer from the ionization space to the amplification gap. The amplification gap is maintained in the avalanche region by applying a negative voltage on the wire mesh (HV_1= - 350 volt) and the drift electrode voltage (HV_2) has been slowly increased. It is seen that as long as the HV_2 is less than the HV_1, the pulse height is constant corresponding to the small signals originated from the ionization released in the thin amplification gap. As soon as the value of HV_2 reaches to the value of HV_1, a drastic rise in the detector pulse height is observed as a result of an efficient electron transfer from the ionization space to the amplification gap.

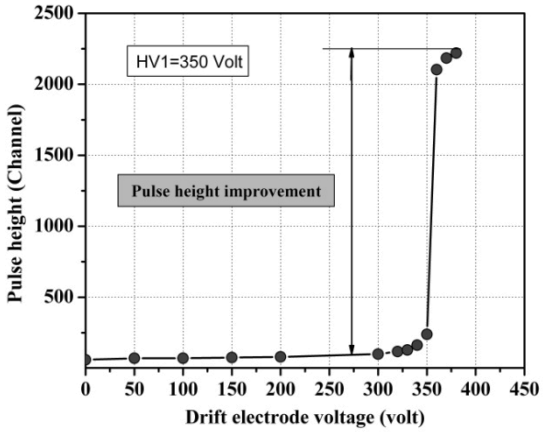

Fig. 3 The dependence of the charge transfer process on the drift electrode voltage (HV_2). The ionization space has been 4-mm and the avalanche region 1-mm deep. The charge transfer takes place at $HV_2 \geq HV_1$ = 350 volt. The operating pressure is 10 Torr.

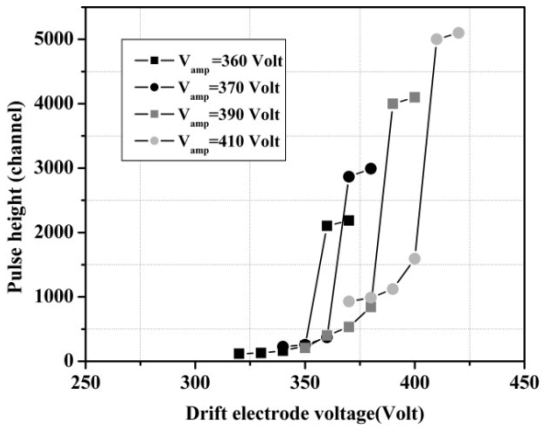

Fig. 4 The dependence of the detector pulse height on the voltage of amplification gap. It is seen that larger amplification fields lead to larger rises in the output signals.

Fig. 4 represents the detector performance for different values of the amplification fields (or HV_1). It is seen that in all the cases the charge transfer takes places when the HV_2 exceeds the HV_1 value and, despite of the constant amount of primary ionization, the detector pulse heights grow up with raising the amplification field. This is actually due to the fact that at higher voltages on the drift electrode the electric field near the openings of the wire mesh becomes rather high so that the primary electrons before entering to the

amplification gap undergo some pre-amplification inside the mesh holes (see **Fig. 2**).

The effect of operating gas pressure on the pulse height growth is shown in **Fig. 5**. It is seen that at the lower gas pressures, in spite of lower amount of primary ionization, the rise in the pulse heights is more significant. This is due to the fact that higher reduced electric fields and accordingly higher gaseous amplification are reached at lower gas pressures.

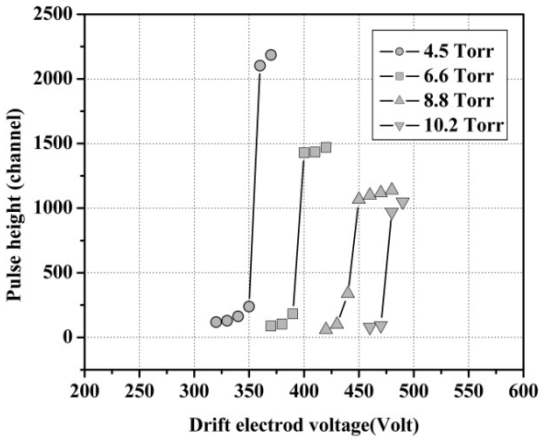

Fig. 5 Illustration of the detector pulse height growth at different gas pressures. The detector has been operated with amplification and ionization gaps of 2-mm and 4-mm, respectively.

In the modified version of the low-pressure avalanche counter, owing to the increased width of the ionization collection space, adequate amount of ionization can be collected and hence large signals are obtained with lower charge amplifications. This significantly improves the long-term stability of the counter because in the avalanche counters operating at high gas amplifications, the spontaneous breakdowns or sparks can damage the detector.

Generally, the energy resolution of a transmission avalanche counter is limited mainly by the fluctuations in the energy-loss of traversing charged particles[3]. As a result of these fluctuations, the energy resolution of PPAC is rather poor, about 30% for the α-particles emitted from ^{241}Am [6]. In the present version of PPAC, owing to larger amount of primary ionization, statistical fluctuations in the energy-loss of the traversing particles are significantly suppressed and therefore considerable improvement in the detector energy resolution is observed. In fact, an energy resolution of better than 14 % was achieved by employing an ionization space of 7-mm and an amplification gap of 0.5-mm at gas pressures as low as 8 Torr. **Fig. 6** shows a typical pulse height distribution of a double-stage PPAC together with a pulse height distribution obtained with a conventional PPAC. It is apparent that the double-stage PPAC has a Gaussian distribution while the conventional PPAC shows a Landau-shape distribution, indicating larger fluctuations in the charged particles energy-loss.

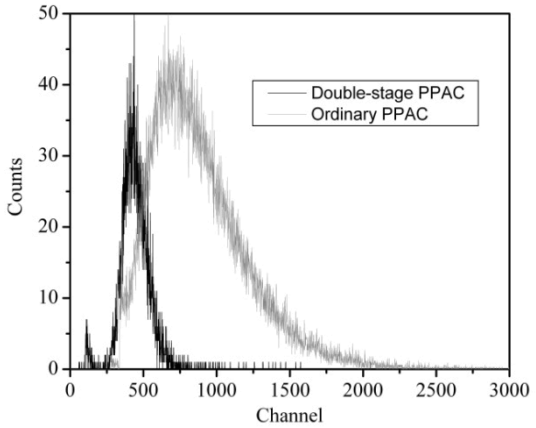

Fig. 6 A typical example of the detector pulse height distribution as compared with that of a conventional PPAC. The double-stage detector consists of 7-mm ionization gap and 0.5-mm amplification gap. The single gap PPAC is 3-mm thick.

In a conventional PPAC, output signal is composed of a fast component due to electrons and a much longer induced signal, typically of some microseconds duration corresponding to the drift of the positive ion cloud (see **Fig. 7-A**). In the case of double-stage PPAC, signal shows different characteristics with that in conventional PPAC. Typical signal waveform of a double-stage PPAC (amplification gap=0.5 mm), as observed with a current sensitive preamplifier has been depicted in **Fig. 7-B**: The signal duration, which is equal with the time required for total charge collection, is about 400 ns. This means that ~400 ns after the detection of a particle the detector gap is cleared of any charge, so that detector can accept a new particle. Considering that the diameter of an avalanche at low gas pressure is around 1-2 mm, one can roughly estimate that the count rate of this detector is at least ~1MHz/mm^2. Such a high rate detector is well suited for charged particle detection in the intense particle accelerators. With respect to the signal rise-time, the rise-time of signal is rather poor. This stems from the spread of primary electrons inside the ionization space and their slow drift velocity (a few cm/μs) at the low electric field of this region. Nevertheless, we observed that when the electric field in the ionization space is

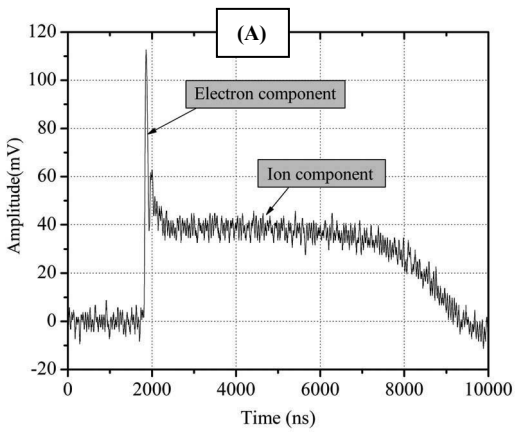

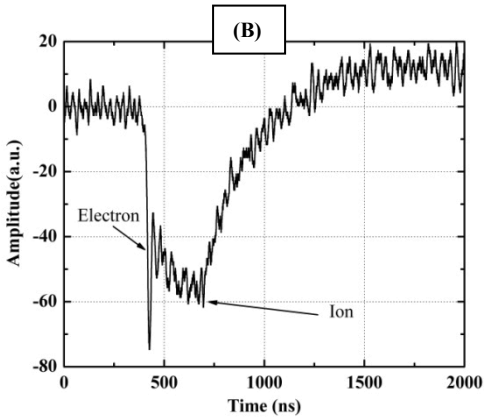

Fig.7 (A) PPAC signal waveform, as obtained with a current-sensitive preamplifier. The electronic and ionic components of the signal are clearly distinguishable. (B) The current signals of a double-stage PPAC including 5-mm of ionization gap and 0.5-mm of amplification gap. The signal duration is ~ 400-ns.

sufficiently high, corresponding with the operation in the avalanche mode, the electrons mobility and consequently signal rise-time is considerably improved (~20 ns), permitting time-of-flight measurements.

VI. Conclusion

We have shown that the modified version of PPAC operates satisfactorily at low gas pressures. The detector structure enables to compensate the lack of ionization by the particles with low specific ionization. This extends the PPAC applicability to the light particles experiments. Furthermore, the following advantages are obtained as compared with that of conventional avalanche counters:

- Detector can withstand very high count rates (~MHz/mm^2),
- Energy resolution is considerably better than that of conventional PPACs.
- Detector shows much better stability in terms of sparks.

Although the performance of the detector associated with the signal rise-time is rather poor, it may be improved by optimizing the detector characteristics in terms of applied electric fields, wire grid shape, thickness of gaps, etc.

References

1) J. Christiansen, Z. Angew Physik 4(1952) 326.
2) J. E. Draper, "*A new fast transmission detector of charged particles*." Nucle. Instr. and Meth. 30 (1964) 148.
3) M. Nakhostin. and M. Baba, "Comment on spectrometric properties of transmission avalanche counters at moderate specific ionization" Nucl. Instr. and Meth A 578(2007)453-454.
4) M. Nakhostin, M. Baba, T. Ohtsuki, T. Okuji, T. Itoga, Nucl. Inst. and Meth. "*Precise measurement of first Townsend coefficient using parallel plate avalanche chamber*" A572 (2007) 999-1003.
5) Ansoft Co, Maxwell Pittsburg, PA, USA.
6) J. Sernicki, "On spectrometric properties of transmission avalanche counters at moderate specific ionization" Nucl. Instr and Meth A572 (2007) 817.

Journal of NUCLEAR SCIENCE and TECHNOLOGY, Supplement 5, p. 383–386 (June 2008)

Development of a High Pressure Xe Ionization Chamber for Environmental Radiation Spectroscopy

Han Soo KIM[1], Yong Kyun KIM[2*], Se Hwan PARK[1], Jang Ho HA[1], Jong Kyung KIM[2], Sang Mook KANG[2], Seung Yeon CHO[3], Do Hyun KIM[3], and Eui Kwon CHUNG[3]

[1]*Korea Atomic Energy Research Institute, Daejeon, Korea*
[2]*Department of Nuclear Engineering, Hanyang University, Seoul, Korea*
[3]*Department of Environmental Engineering, Yonsei University, Wonju, Korea*

A High Pressure Xenon ionization chamber is a promising radiation detector for environmental radiation measurement due to its radiation hardness, its physical rigidity, and its capability of operation at a high temperature up to about 170 ℃. A cylindrical high pressure xenon ionization chamber, which was configured with a shielding mesh to improve its energy resolution, was designed on the basis of an electron transfer simulation code (EGSnrc) to extract an optimal density of Xe gas and a thickness of the chamber wall. An electron drift simulation code, Garfield, which was coupled with a Maxwell electric filed calculator, was also employed for the electron drift simulations due to the geometry of the shielding mesh. Shielding inefficiency was also calculated. A spherical ionization chamber was also designed and fabricated to monitor environmental radiation. A noble gas system was constructed to create a noble gas with a high purity and to inject the noble gas up to 60 atm. The combination of an oxygen absorbent (Oxisorb), a molecular sieve, and a high temperature getter can minimize the electro-negative impurities, such as the O_2 and N_2 gas, to below about several ppb levels. Preliminary tests such as leakage currents, saturation currents, and gas leak test were performed. The performance of the two fabricated ionization chambers at a low dose rate was tested by using a conventional shadow technique with a NIST certified 33.52 MBq ^{226}Ra source in the calibration room at KAERI.

KEY WORDS: high-pressure Xe, ionization chamber, environmental radiation, shadow shielding technique, EGSnrc, Garfield, shielding mesh

I. Introduction

An ionization chamber is still widely used in many fields such as environmental radiation monitoring and industrial application due to its operational stability for a long period and its simple design for its applications[1)]. Pressurized ionization chambers, which are usually made of metal such as stainless steel, have radiation hardness for a long period of time in a comparison with other radiation detectors. Ionization chambers for environmental radiation monitoring are requested to detect a low dose rate at below several μSv/h.

High-pressure xenon (HPXe) gas is attractive gamma-ray detection medium due to its physical and nuclear properties. HPXe has a large detection efficiency for gamma-ray energies, due to its large atomic number (Z = 54), which translates into a high photoelectric absorption and Compton scattering cross sections. In addition, the Fano factor for HPXe is quite good, measured near 0.13 to 0.1[2)]. HPXe ionization chambers are ideal for use in uncontrolled environments, as this detector's response has been shown to be uniform over large temperature ranges up to 170 ℃. Unlike solid detection media that derive their radiation detection capabilities from their crystal structure, the HPXe performance is not degraded by high radiation fluences.

An HPXe ionization chamber, which was equipped with a shielding mesh, was designed on the basis of the results from EGSnrc, a Maxwell electric field calculator and a Garfield electron drift simulator. Shielding inefficiency was also calculated.

A spherical ionization chamber, which was pressurized with Ar up to 25 atm, was also constructed to apply it to environmental radiation monitoring. A gas system was constructed to eliminate the electro-negative impurities and to inject the noble gas up to 60 atm. A conventional shadow shielding technique was incorporated to test the performance of the two ionization chambers at a low dose rate.

II. Experimental

1. Gas Purification and Injection System

The purity of Xe is essential in an HPXe ionization chamber due to the electron attachment by electro-negative gases, which become negative ions after the liberated free electrons being attached. The purification and injection system was designed and constructed to eliminate the electro-negative impurities such as O_2, N_2 and hydro-carbon gases. The combination of an Oxisorb, a molecular sieve, and a high temperature getter can minimize these impurities. The circulation of Xe gas was based on the difference in the temperature of a liquid nitrogen and a high temperature getter (about 350℃). **Fig. 1** shows a diagram of the gas system. Two gas cylinders were incorporated to improve the electron drift velocity of Xe by an addition of 17 % of helium gas[3)]. Xenon and helium mixture will be stored in a reservoir and circulated for several days to reach several ppb

*Corresponding Author, Tel. +82-2-2220-2354, Fax. +82-2-2296-2354, E-Mail: ykkim4@hanyang.ac.kr

impurity levels.

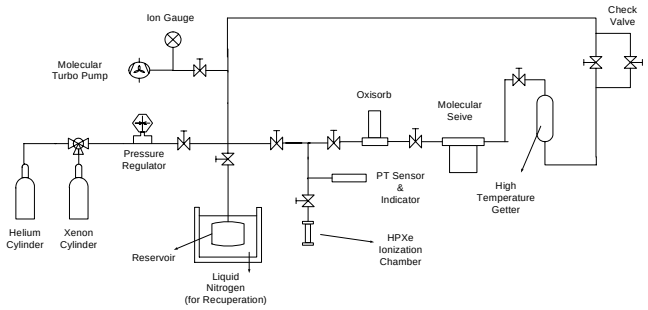

Fig. 1 The gas purification and injection system for an HPXe ionization chamber

2. Design of a cylindrical HPXe Ionization Chamber

A cylindrical HPXe ionization chamber was designed on the basis of the results of the EGSnrc simulation code[4]. A dosrznrc, which simulates the passage of an electron or photon beam in a finite, right cylindrical geometry, was used in the simulation. The considered parameters were the densities of the xenon gas, the thicknesses of an outer shell, and the initial gamma energies. The calculated efficiencies versus the considered parameters are shown in **Table 1**. The simulated energy spectrum at 662 keV is also shown in **Fig. 2**.

Table 1. The calculated percentile efficiency attainable with the given detector parameters by using the EGSnrc code

Initial Energy	Thickness of outer shell	Density of Xenon gas		
		0.4 g/cm^3	0.55 g/cm^3	0.65 g/cm^3
60 keV	1 mm	77.72	78.90	79.38
	2 mm	76.61	77.73	78.38
	3 mm	75.89	76.85	77.27
145 keV	1 mm	72.62	76.22	77.91
	2 mm	68.56	72.24	73.93
	3 mm	65.46	69.02	70.69
662 keV	1 mm	11.24	13.56	14.89
	2 mm	10.30	12.49	13.74
	3 mm	9.53	11.53	12.70
1.17 MeV	1 mm	3.60	5.00	5.86
	2 mm	3.37	4.61	5.44
	3 mm	3.08	4.29	5.08
1.33 MeV	1 mm	2.68	3.85	4.63
	2 mm	2.53	3.64	4.37
	3 mm	2.33	3.45	4.10

The efficiencies throughout the initial energies can be improved when the xenon density is high. Thin outer shells also contribute to higher peak efficiencies. But the density of the xenon gas conflicts with the outer shell thickness. For a cylindrical shape, allowable thickness of an outer shell to endure the pressure is expressed by

$$t = \frac{Dps}{\sigma\eta\times 100} + C \qquad (1)$$

where D represents the diameter of a cylinder in mm, p is the pressure in kg/mm^2, σ is the tension intensity in kg/mm^2, s is 1 as the safety rate, η and C are 0.8 and 1 in Korea. When the material of an outer shell is stainless-steel and the diameter of a cylinder is 76 mm, the thickness of an outer shell must be over 2 mm at a 60 atm pressure for a safe operation.

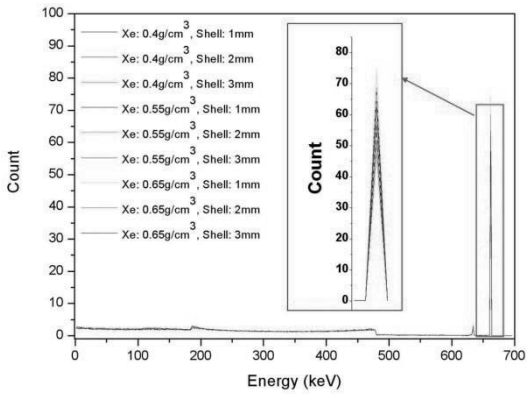

Fig. 2 The 662 keV gamma spectrum obtained by simulation of a dosrznrc of EGSnrc code.

The design of a cylindrical ionization chamber is shown in **Fig. 3**. The diameter and the total length of the ionization chamber were 76 and 170 mm, respectively. The active volume was 450.5 cm^3. Ceramic was chosen for the insulators. The use of a shielding mesh to screen the collecting electrode from the effect of positive ions was suggested by O. R. Frish[5]. A shielding mesh, which eliminates the charge contribution of the slow positive ions, was inserted between the collecting electrode and the potential electrode to increase the energy resolution. Three feed-through connectors were welded onto the flange of the ionization chamber to connect the electrodes. To extract the optimal parameters for the shielding mesh such as the mesh thicknesses, mesh diameters, and the distance from the anode, a Maxwell electric field calculator and a Garfield electron drift simulation were incorporated. The applied voltages of the shielding mesh and the potential electrode were set at -2500V and -5000V, respectively. Mesh spacing was also set at 1 mm. Mesh thicknesses of 0.5, 0.2 and 0.1 mm were simulated. And the distances from the anode was either 7.5 or 5.5 mm. Electron drift lines were not distorted when the mesh thickness and distance from the anode were 0.5 mm and 7.5 mm, respectively. The simulated drift lines are shown in **Fig. 4**. Shielding inefficiency was calculated by using these parameters. In order to purge any gases emanated from the chamber materials, the chamber was kept at 100℃ in vacuum for two weeks before a gas filling. High purity Ar gas was injected by using the constructed gas system up to 40 atm after purification for the preliminary tests.

3. Design of a Spherical Ionization Chamber

A Pressurized Ionization Chamber (PIC) was designed in consideration of an isotropy for an incident radiation and

consideration of an isotropy for an incident radiation and compared with the HPXe ionization chamber. A drawing and a picture are shown in **Fig. 5**. The tri-axial connector, welded on the chamber surface, serves as a terminal for the potential electrode, collector and guard electrode.

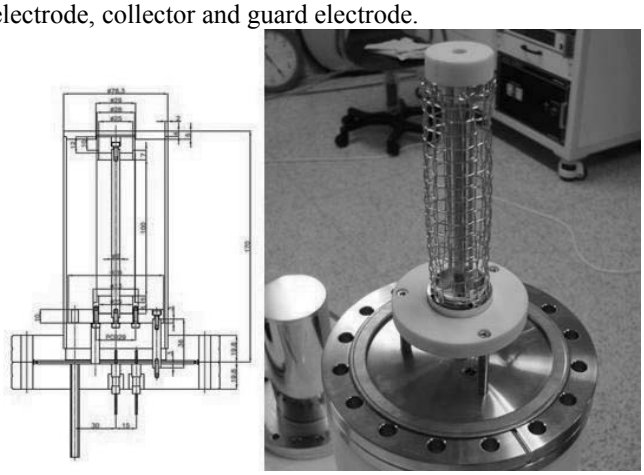

Fig. 3 The designed HPXe ionization chamber for environmental radiation monitoring and spectroscopy (left). And the inner view of the fabricated HPXe ionization chamber with a shielding mesh (right)

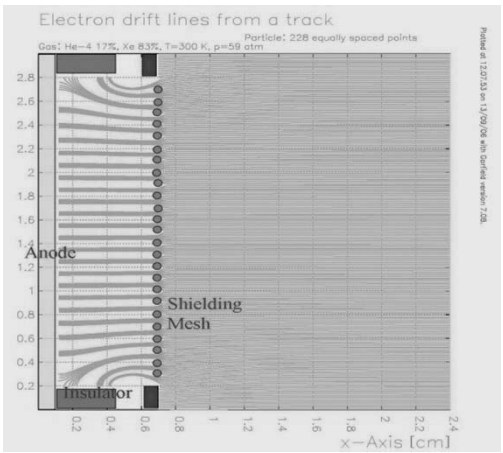

Fig. 4 The simulated shielding mesh by using a Maxwell electric field calculator and a Garfield electron drift simulation when mesh thickness and the distance from the anode were 0.5 and 7.5 mm, respectively

The chamber was fabricated by welding together two 304 stainless steel hemisphere. Purified argon gas was injected up to the pressure of 25 atm. The wall thickness was 0.12 inch. The ionization charge was collected by a spherical aluminum electrode with 2 inch diameter. The sphere was held in place at the center of the chamber shell by a thin aluminum rod. Electrodes were fused to the shell by a metal-to-ceramic tri-axial seal in which the outmost electrode was connected to the chamber shell. The middle or guard electrode was connected to the inner collecting sphere. The center or collecting electrode was completely isolated from the high voltage chamber by a ceramic insulator, which had a minimum resistance of 10^{18} ohms. The assembled chambers were baked in a vacuum at 100 ℃ for four hours and then filled to a known pressure with high purity argon.

4. Measurements of the Fabricated Ionization Chambers at a Low Dose Rate

A Keithley 6517A, an Ortec 673 high voltage supplier, and the LabVIEW program were incorporated to test the performance of the fabricated ionization chambers at a low dose rate. The leakage currents throughout the experiments were kept in the range of 200 fA and the plateaus were observed.

Calibration was also performed by using a conventional shadow technique[6] in a calibration room. Schematic view of the experiments is shown in **Fig. 6**. Linearity against low dose rates was also measured. The source was placed in a low mass holder at a height of about 1 m above the floor and at a distance of 4, 5, 6 m from the ionization chambers, which were at the same height on a low mass stand. A 30-cm thick lead shield with a cross section measuring 10-x-10 cm was interposed on a low mass stand so as to intercept all the primary rays from the source to all parts of the ionization chambers through a full thickness of the shield. Alignment was checked with a string with a dummy source in place. Slight over-shielding in the order of 1-2 cm was used as these results in a negligible error as opposed to an under-shielding which could produce a significant error.

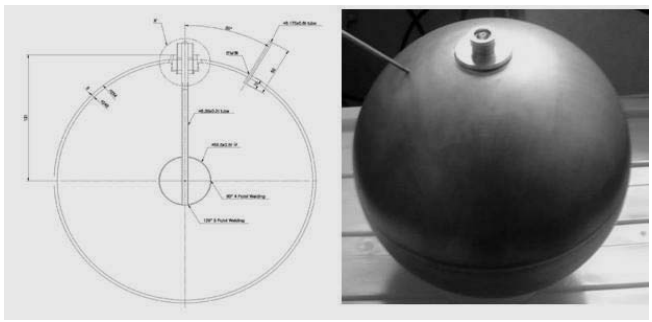

Fig. 5 A spherical ionization chamber for environmental radiation monitoring

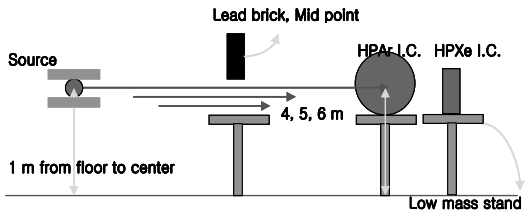

Fig. 6 Experimental setup for the measurement of ionization currents of the fabricated ionization chambers at a low dose rate

The source was placed in its holder and the output signal of the PIC was averaged over a 10- to 30-min time period. The lead shield was removed and the ionization chamber output signal was averaged again over a 10- to 30-min time period. The difference between the average signals was divided by the exposure rate delivered by the source at that a distance to yield the ^{226}Ra primary beam calibration factor.

Fig. 7 and **8** show the linearity of the chamber current change with respect to the dose rate, as measured with the HPXe ionization chamber and the spherical ionization chamber, respectively. Root-mean-square linearities were 0.991 and 0.995, respectively.

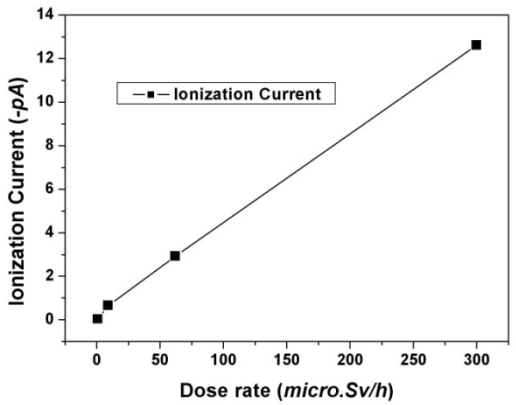

Fig. 7 linearity of ionization currents from the HPXe ionization chamber against low dose rates. Root-mean square linearity was 0.991.The error bars are smaller than the sizes of symbols

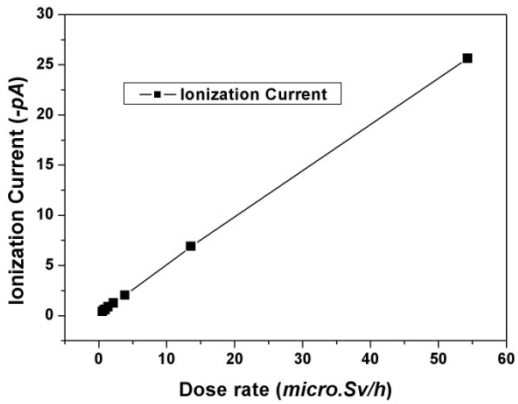

Fig. 8 Linearity between the ionization currents from the PIC and the low dose rates. Root-mean square linearity was 0.995. The error bars are smaller than the sizes of symbols

III. Results and Discussion

The two fabricated ionization chambers for environmental radiation monitoring revealed a linear response against low dose rates from the results by using a conventional shadow shielding technique.

The efficiency of the shielding mesh is measured by the extent to which the charge is induced on the collecting electrode. The shielding inefficiency can be calculated as a function of two geometrical ratios[7]. The electrostatic field and induced charge inside a cylindrical ionization chamber can be calculated by using the expressions obtained for a parallel plate chamber from Bunemann[7] and making logarithmic transformations to a cylindrical geometry. From this transformation, the shielding inefficiency can be estimated by[8]:

$$\delta_0 = 1 - (1/N)\ln(R_g / Nr_0)/\ln(R_g / R_a) \quad (2)$$

where R_a and R_g are the radii of the anode and the shielding mesh, respectively. N and r_0 are the number of wires and the radius of the wires. From this formula, the shielding inefficiency of the fabricated HPXe ionization chamber, which had a 0.5 mm mesh thickness ($2r_0$) and a 7.5 mm radius of a shielding mesh, was 6.8 %.

IV. Conclusions

In this study, two types of pressurized ionization chambers were fabricated and tested with a ^{226}Ra source in a low gamma ray dose range. These two ionization chambers, in current mode operation, showed an excellent linear relationship between the chamber current and the dose rate. The good performance in the low dose range of the ionization chambers suggests that they can be successfully used for low-dose environmental radiation measurement. The shielding inefficiency of an HPXe ionization chamber, which was configured with a shielding mesh to measure an energy spectrum, was calculated. In a future work, energy spectra with the fabricated HPXe ionization chamber will be compared with the simulated energy spectra.

Acknowledgement

This work has been carried out under the nuclear R&D program of the Ministry of Science and Technology (MOST) of Korea. And we are also supported by the iTRS Science Research Center / Engineering Research Center program of MOST / Korea Science and Engineering Foundation (grant # R11-2000-067-02002-0) and partially supported by the BK21 program of Korea Research Foundation(KRF).

References

1) G. F. Knoll., 'Radiation Detection and Measurements,' 3rd Ed., John Wiley & Sons, New York, Chap. 5 (1999).
2) C. Levin et al., 'Charge collection and energy resolution studies in compressed xenon gas near its critical point', Nucl. Instrum. and Meth., 332, 206 (1993)
3) A.E. Bolontnikov et al., 'The spectroscopic properties of high-pressure xenon', Nucl. Instrum. and Meth., 396, 360 (1997)
4) www.irs.inms.nrc.ca/EGSnrc/EGSnrc.html.
5) O.R. Frisch, Unpublished report, BR-49, Isotope analysis of uranium samples by means of their α-ray groups, British Atomic Energy Project.
6) Joshep A. Decampo et al., 'High pressure argon ionization chamber systems for the measurement of environmental radiation exposure rates,' U.S. Atomic Energy Commission, New York, HASL-260 (1972.)
7) O. Bunemann et al., 'Design of grid ionization chambers', Can. J. Research A, 27, 191 (1948.)
8) A. Bolontnikov et al., 'Improving the energy resolution of high pressure Xe cylindrical ionization chambers', IEEE Trans. Nucl. Sci., 44, 3 (1997)

Journal of NUCLEAR SCIENCE and TECHNOLOGY, Supplement 5, p. 387–390 (June 2008)

Operational Characteristics of Ionization Chambers for a Radiation Monitoring

Han Soo KIM[1], Se Hwan PARK[1], Jang Ho HA[1], Yong Kyun KIM[2*], Jong Kyung KIM[2], Seung Yeon CHO[3], Do Hyun KIM[3], and Eui Kwon CHUNG[3]

[1]*Korea Atomic Energy Research Institute, Daejeon, Korea*
[2]*Department of Nuclear Engineering, Hanyang University, Seoul, Korea*
[3]*Department of Environmental Engineering, Yonsei University, Wonju, Korea*

Ionization chambers for a Radiation Monitoring System (RMS) are required to cover a wide range of dose rates from 10^{-1} μSv/h to 10^{6} μSv/h. For a RMS, two cylindrical ionization chambers, which had active volumes of 11.8 L and 1L, were fabricated in consideration of an electronic equilibrium and a guard electrode structure. Preliminary tests such as saturation currents and leakage currents were performed with and without a 925 MBq ^{241}Am gamma source. Linearity against low dose rates was also performed by using a conventional shadow shielding technique with NIST certified 33.52 MBq ^{226}Ra source in a calibration room. A field test with 11.8 L was also performed at the Yong-kwang power plant. A Parallel Plate Ionization Chamber (PPIC) was also developed not only to measure the proton beam intensity but also to derive relevant parameters with other reference ionization chambers aimed at assisting in the quality control of a proton accelerator. Operational characteristics were investigated at high dose rates by using the X-ray generator located at the Korea Research Institute of Standards and Science (KRISS). Ion recombination, which is one of the characteristics of an ionization chamber, was evaluated with the experimental results and a theoretical model. The collection efficiencies of a PPIC were calculated by a experimental two-voltage method when the filling gases and the distance of the two electrodes were varied.

KEY WORDS: ionization chamber, radiation monitoring system (RMS), shadow shielding technique, two-voltage method

I. Introduction

Ionization chambers are still widely used in many fields such as environmental radiation monitoring and measurement of the accelerator beam intensity due to their simple designs and long operational stability[1)].

Ionization chambers for RMS are required to be capable of measuring the dose rates from 10^{-1} to 10^{6} μSv/h. Ionization chambers were designed with different configurations to meet the purpose of a radiation safety and a radiation monitoring. Two cylindrical ionization chambers, which have active volumes of 11.8 L and 1 L, were designed and fabricated as radiation sensors of a RMS. The operational characteristics such as the leakage currents, saturation curve were measured. And linearity against low dose rates and high dose rates were performed by using a conventional shadow shielding technique[2)] and in a standard high radiation field. The preliminary field test was also performed for a month at Young-kwang power plant in Korea.

A PPIC was developed to assist in the quality control of a proton accelerator. Before installing a proton beam line, a fabricated PPIC must be experimentally certified for its linearity and saturation characteristics in a standard radiation field. Operational characteristics of a PPIC were evaluated in terms of a saturation curve[3)], its collection efficiency, and its linearity against low dose rates even if it is used for other specific purposes.

When measuring a dose rate with an ionization chamber, the observed current is always lower than the saturation current due to an ion recombination. An extrapolation method is required to obtain a saturation current, and it depends on the type of recombination inside an ionization chamber. Three different processes for the disappearance of ions can be distinguished in theory[4)]. These are an initial recombination, the general recombination and a diffusion loss. An initial recombination is a recombination of the positive and negative particles formed within the track of a single ionizing particle. A general recombination refers to a process where the positive and negative particles formed by different ionizing particles meet and recombine. A diffusion loss is a process in which ions cannot reach the electrode due to their diffusion. Among these processes, only a general recombination depends on the dose rate. We considered and evaluated the recombination processes with a fabricated PPIC.

II. Experimental

1. Performance of the Cylindrical Ionization Chambers

Two cylindrical ionization chambers, which had an active volume of 11.8 L and 1 L, were designed in consideration of an electronic equilibrium. A guard electrode was inserted to minimize the leakage current flowing from the potential electrode to the collecting electrode. A potential electrode and a collecting electrode were made of carbon coated polyethylene. Insulators were made of Teflon. Two quick gas

*Corresponding Author, Tel. +82-2-2220-2354, Fax. +82-2-2296-2354, E-Mail: ykkim4@hanyang.ac.kr

connectors were installed to fill the gas such as dry air and Ar. A picture of the fabricated ionization chambers equipped with electronics is shown in **Fig. 1**.

A Keithley 6517A, an Ortec 673 high voltage supplier, and the LabVIEW program were incorporated to measure the signal of the ionization chambers. Leakage currents of the two cylindrical ionization chambers were fluctuated in the range of 30 *f*A. In order to determine the operating voltage for the 1L ionization chamber, a 925 MBq ^{241}Am gamma source was used to measure the ionization current. **Fig. 2** shows the variation of the ionization current as a function of the applied voltage, as obtained with the chamber filled with the air and Ar gas, respectively. When filled with Ar, ionization currents were about 5 times larger than when filled with air. Sensitivity of an ionization chamber can be increased by the use of a dense gas, from this result.

Fig. 1 Two cylindrical ionization chambers equipped with electronics. Active volumes are 11.8 L (left) and 1 L (right), respectively

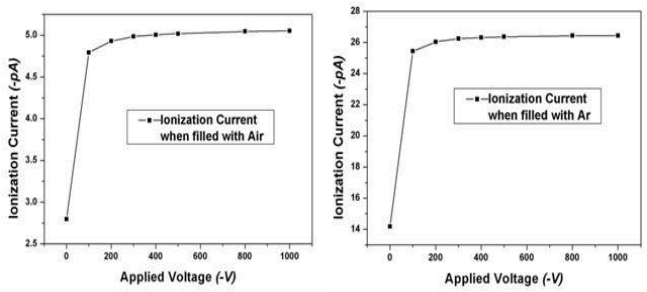

Fig. 2 Saturation curves of 1 L ionization chambers when filled with air and Ar. Distance between the 925 MBq ^{241}Am source and the center of an ionization chamber was 200 mm. The error bars are smaller than the sizes of the symbols

A current's linearity variation with the 11.8 L ionization chamber at high dose rates was measured at the voltage of a plateau region with a standard ^{137}Cs source in a calibration room at KRISS. **Fig. 3** depicts the linearity of the output current variation with respect to the dose rate. The calculated root-mean-square was 1. In low dose range, the chamber current variation was measured with a NIST-certified 33.52 MBq ^{226}Ra source using a conventional shadow shielding technique[2]. The linearity was depicted in **Fig. 3**, and the root-mean-square linearity was calculated as 0.99.

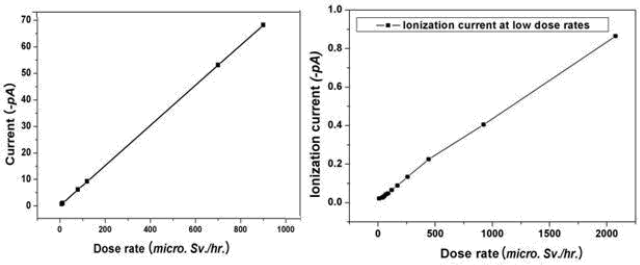

Fig. 3 Linearity against high dose rates (left) and low dose rates (right) with a 11.8 L ionization chamber when filled with air. The root-mean-square linearties were 1 and 0.99, respectively. The error bars are smaller than the sizes of the symbols

2. Performance of the Parallel Plate Ionization Chamber for Proton Beam Monitoring

A schematic of a fabricated parallel plate ionization chamber (PPIC) for a proton beam monitoring is shown in **Fig. 4**. The main considerations for designing the PPIC were reducing the leakage current to increase the sensitivity and minimizing the beam loss because the proton beams must pass through the active area of the PPIC.

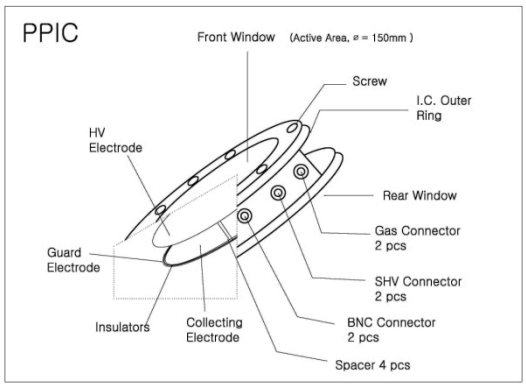

Fig. 4 Schematic of the fabricated PPIC. Double BNCs, SHVs, and gas-quick connectors were installed. Spacers were inserted between the two electrodes

The two electrodes were composed of 50-μm-thick aluminized Mylar fixed on a G-10 ring. Spacers were inserted between the two electrodes to adjust the distance of them. When a 230-MeV proton beam was passed through the PPIC, the proton beam attenuation rate due to the windows and the electrodes was 0.045% from a calculation of the stopping range of the protons in matter by using the SRIM code[5].

The leakage currents throughout the experiments were kept in the range of 20 *f*A. Saturation curves at both polarities of an applied voltage at a high dose rate and a linearity of the current are plotted against the dose rates are shown in **Fig. 5**. Saturation curves at a relatively low dose rate when the filling gas and the distance between the two electrodes were different are shown in **Fig. 6**.

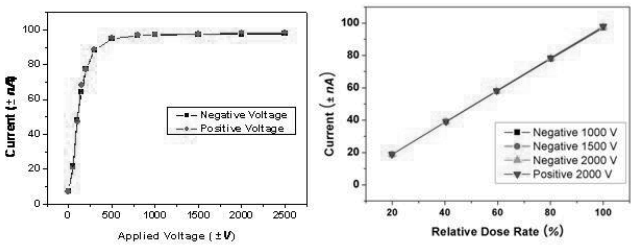

Fig. 5 Saturation curves at both polarities of an applied voltage at a high dose rate produced by the X-ray generator located at KRISS and linearity of the current plotted against the high dose rate. Dose rates were relatively varied. The error bars are smaller than the sizes of the symbols

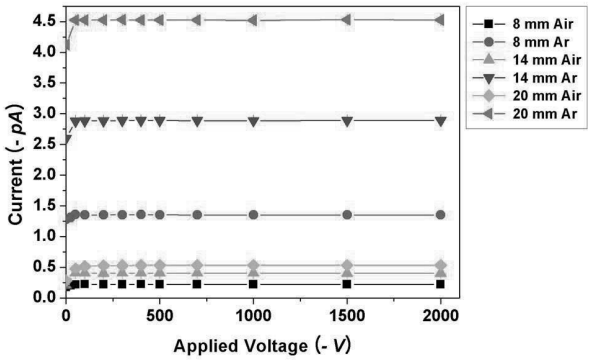

Fig. 6 Saturation curves at a low dose rate when the filling gas and the distance between the two electrodes were different. 925 MBq ^{241}Am was used. The error bars are smaller than the sizes of the symbols

III. Results and Discussion

At constant radiation intensity, the current observed in an ionization chamber is always lower than a complete saturation current mainly due to an ion recombination. Ion recombination processes are distinguished as initial and general recombinations. Initial recombination depends on the ion density along each separate track of an ionizing particle. General recombination depends on the dose rate, and refers to a recombination of the positive and negative ions formed along different ionizing particle tracks. X- and gamma-ray beams at a high dose rate, a general recombination dominates the total recombination losses. If the collection efficiency is to be evaluated, these two different recombinations must be extrapolated by using proper evaluating methods[6)- 7)].

To evaluate the charge collection efficiency, we used a PPIC and extrapolated two different recombination processes. An empirical procedure formerly used to distinguish between initial and general recombinations in continuously irradiated chambers was used to plot the reciprocal of the measured ionization current i against a suitable function of the applied voltage, V, in the chamber. If an initial recombination is dominant, $1/i$ and $1/V$ in the near-saturation region have a linear relationship:

$$1/i = 1/i_0 + \text{constant}/V. \quad (1)$$

If only a general recombination is present, the relationship is:

$$1/i = 1/i_0 + \text{constant}/V^2. \quad (2)$$

At a high dose rate, a general recombination is known to be the dominant process and $1/i$ against $1/V^2$ has a linear relationship. At a low dose rate with a 925 MBq ^{241}Am source, the dominant recombination process must be determined by using an empirical extrapolation method. Plots of $1/i$ against $1/V$ and $1/V^2$ are given in **Fig. 7**.

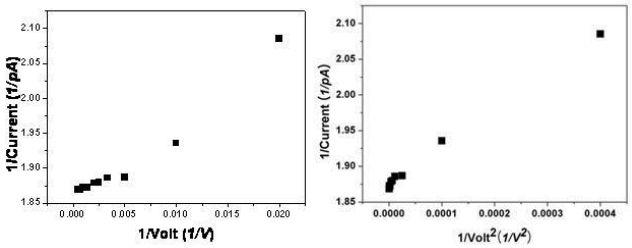

Fig. 7 Plot of i against $1/V$ and $1/V^2$ at relatively low dose rate. From these plots, the initial recombination is negligible for the total recombination

To quantify the ion recombination losses of an ionization chamber, Almond[8)] describe the use of an experimental two-voltage method when a general recombination is dominant. The collection efficiency can be derived form the ion recombination losses. The collection efficiency f at a bias voltage V is defined as $f = 1/i_{sat}$, where i_{sat} is the saturation current which can be determined when $i=\infty$. i_{sat} can be obtained from only two data sets, i and V. Thus, the collection efficiency can be calculated by using an experimental two-voltage method:

$$f = \frac{1}{i_{sat}} - \left(\frac{(V_1/V_2)^2 - (i_1/i_2)}{(V_1/V_2)^2 - 1}\right) \quad (3)$$

where i_1 is the measured ionization current at a normal operating bias voltage V_1 and i_2 is that at a much lower voltage V_2. Almond established the reliability of a two-voltage method for $i_2/i_{sat} > 7$ and $V_1/V_2 < 5$. This means that a voltage ratio V_1/V_2 from three to five allows a two-voltage method to be adequate enough for use in dosimetric protocols[9)]. **Table 1** shows the calculated collection efficiencies and operating voltages for various dose rates and filling gases.

At a high dose rate, the case of the Ar filling was not measured because the current from the air filled ionization chamber was so large, that filling the chamber with Ar was not necessary to obtain a large current.

A preliminary field test with the 11.8L ionization chamber was performed for a month in the reserve radioactive source room at the Young-kwang power plant in Korea. The mean dose rate and the fluctuation for a day were 6.23 μSv/h and 0.07 μSv/h, respectively. This is shown in **Fig. 8**.

Table. 1 Calculated collection efficiencies and operating voltages for various dose rates and filling gases

Dose rate	Distance between the two electrodes	Filling gas	Collection efficiency	Operating voltage set
High	20 mm	Air	99%	2500 V
Low	20 mm	Air	99%	700 V
Low	20 mm	Ar	99%	700 V
Low	14 mm	Air	99%	400 V
Low	14 mm	Ar	99%	400 V
Low	8 mm	Air	99%	200 V
Low	8 mm	Ar	99%	200 V

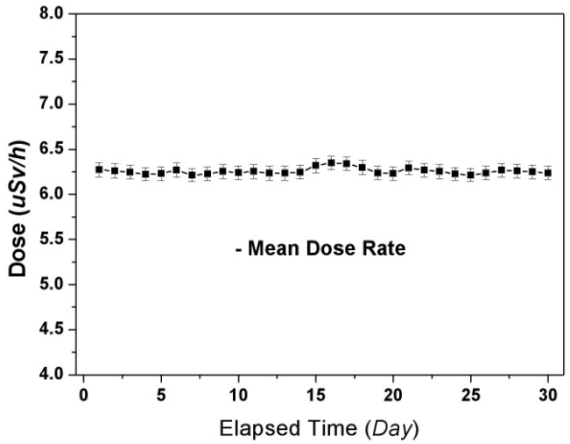

Fig. 8 A preliminary field test in the reserve RI source room at the Young-kwang power plant in Korea

IV. Conclusions

In this study, the performance of two different types of ionization chambers was tested to see if their basic characteristics meet the requirements of their intended usage. All the fabricated ionization chambers had linearity against the applied dose rates. An experimental two voltage method, which can be applied when a general recombination is dominant, was used to evaluate the operational characteristics of the PPIC in both the air filling case and the Ar filling case.

This paper will be helpful in designing and evaluating ionization chambers. Also, all the fabricated ionization chambers in this study are ready to be applied to their application fields, especially the ionization chambers for a RMS.

Acknowledgement

This work has been carried out under the nuclear R&D program of the Ministry of Science and Technology (MOST) of Korea. And we are also supported by the iTRS Science Research Center / Engineering Research Center program of MOST / Korea Science and Engineering Foundation (grant # R11-2000-067-02002-0) and partially supported by the BK21 program of Korea Research Foundation(KRF).

References

1) G. F. Knoll, Radiation Detection and Measurements, 3rd Ed., John Wiley & Sons, New York, Chap. 5 (1999).
2) A. Decampo et al., "High pressure argon ionization chamber systems for the measurement of environmental radiation exposure rates," US. Atomic Energy Commission, New York, HASL-260 (1972).
3) J. Bohm et al., "Saturation corrections for plane-parallel ionization chambers," Phys. Med. Biol. 21, 754 (1976).
4) S.H. Park et al., "Saturation characteristics of the ionization chamber at a low dose rate", Radiation Physics and Chemistry, 73, 248 (2005).
5) J. Ziegler, www.srim.org.
6) J. R. Greening et al., "Saturation characteristics of parallel-plate ionization chambers," Phys. Med. Biol. 9, 143 (1964).
7) A. Piermattei et al., "Ion-recombination correction factor ksat for spherical ion chambers irradiated by continuous photon beams," Phys. Med. Biol. 41, 1025 (1996).
8) P. R. Almond et al., "Use of a Victoreen 500 electrometer to determine ionization chamber collection efficiencies," Med. Phys. 8, 901 (1981).
9) IAEA Technical Report Series No. 277 (1987).

Journal of NUCLEAR SCIENCE and TECHNOLOGY, Supplement 5, p. 391–394 (June 2008)

Development of Layered Type Single Crystalline Diamond Radiation Detector as an Energy Spectrometer

Junichi H. KANEKO[1*], Tokuyuki TERAJI[2], Takahiro IMAI[3], Yuuki HIRAI[1], Satoshi YOSHIZAKI[2], Kei SATOU[1], Souhan KAWAMURA[1], Yusuke OSHIKI[1], Fumiyuki FUJITA[1], Akira HOMMA[1], Toshimichi ITO[2], and Michihiro FURUSAKA[1]

[1]*Graduate School of Engineering, Hokkaido University, N13, W8, Kita-ku, Sapporo, Japan*
[2]*Graduate School of Engineering, Osaka University, 2-1 Yamadaoka, Suita, Osaka, Japan*
[3]*Sumitomo Electric Industries, Ltd., 1-1-1, Koyokita, Itami, Hyogo, Japan*

Radiation detectors were fabricated with layered structure diamonds comprising several micrometers of a boron-doped single crystal diamond and 20 μm of insulating single crystal diamond layers grown on a HP/HT-type Ib diamond single crystal substrate. To improve the yield rate of CVD diamond radiation detectors this approach was adopted. The detectors had rectification characteristics because of their boron-doped diamond contact and aluminum Schottky contact. The leakage current of one detector was less than 0.2 pA at reversed bias voltage of +50 V. Energy resolutions of 2.6% and 2.8% for alpha particles from ^{241}Am were achieved using these detectors. The rise time of a leading edge of an output signal from one detector was less than 20 ns, which was the fastest rise time of the measurement system; drift velocities of charge carriers were estimated to be faster than 1×10^5 cm/s. In addition, cathode luminescence spectra of insulating diamond layers were measured; peaks caused by free exciton recombination and 'band A' were observed. Improved crystallinity of the boron-doped diamond layer helps realization of a layered-type diamond radiation detector with higher energy resolution.

KEYWORDS: Radiation detector, CVD diamond single crystal film, Layered structure, alpha energy spectrum

I. Introduction

A diamond radiation detector presents several beneficial features: high radiation resistance[1)], high-temperature operation[2)], high-speed response, near tissue equivalence, etc. For those reasons, a practical diamond radiation detector is desired in several fields, including nuclear engineering, space engineering, high-energy physics, and radiology. Especially, much research and development have been carried out in the field of health physics. Although a pre-annealing process is required for its production, a dosimeter using a natural diamond for radiation treatment has been commercialized. Recently, several developments using polycrystalline chemical vapor deposition (CVD) diamonds were carried out [3), 4)]. Moreover, a commercial diamond UV detector has been realized. Also, in the 1970s, a Russian group revealed several beneficial features of the diamond radiation detector described above using very high-quality natural type IIa diamond for energy spectrometers. However, the yield rate of spectrometer-grade natural diamond was quite low, and their applications were very limited.

The authors developed diamond radiation detectors made of high-pressure and high-temperature (HP/HT) type IIa diamond single crystals to resolve this situation in spectrometer-grade diamond radiation detectors; these detectors achieved high-energy resolution of better than 0.4%[5), 6)]. However, this high performance is limited to situations in which output signals were mainly caused by motion of holes. Charge trapping of electrons remains as an issue that should be resolved. Accordingly, studies of the charge trapping mechanism were carried out through examination of charge carriers' transportation in diamond[7)]. In addition, to reduce impurities in the diamond crystal, a CVD single diamond crystal was synthesized and adopted for use in a radiation detector; the detector achieved high energy resolution of 0.4% for alpha particles[8)]. However, to synthesize a high-quality diamond single crystal using CVD method, the growth rate must be limited to a lower level. In addition, to fabricate a planar detector, a self-standing thick single crystal that requires a long synthesis time is required. Consequently, it became difficult to maintain a steady synthesis condition. Moreover, the yield rate of high-quality diamond became very low.

As one solution for the low yield rate of CVD diamond radiation detectors, a detector composed of a thin 20-μm-thick sensitive layer, which is sufficient for alpha particle detection, was developed. The detector was made of a stack of thin diamond layers grown on a HP/HT type Ib diamond substrate. This structure was adopted to reduce charge trapping and synthesis time. The detector was used as an energy spectrometer for 14 MeV neutrons[9)]. This article describes the fabrication and evaluation of basic characteristics of the detectors, including those of the diamond crystals themselves.

II. Experimental

1. Crystal Growth and Detector Fabrication

As a first trial, an insulating CVD diamond single crystal was grown on a heavily boron-doped, ca. 500 ppm, HP/HT-

*Corresponding Author, Tel No: +81-11-706-6681, Fax No: ++81-11-706-6681, E-mail: kin@qe.eng.hokudai.ac.jp

type Ib diamond single crystal using plasma-assisted CVD method. A diamond LED with a similar structure was reported elsewhere; a phosphorus-doped diamond layer was grown on the boron-doped diamond substrate instead of an insulating diamond layer. In this structure, a conductive diamond substrate served as an electrode. Although the morphology of the insulating diamond observed using an optical microscope was very smooth, a leakage current on the order of nanoamperes was measured at the bias voltage of several volts. Boron contamination from the substrate made resistivity of the sensitive layer relatively low. Large leakage current harmed operation as a radiation detector. Several samples were fabricated; unfortunately, the results were the same.

The detector structure shown in **Fig. 1** was designed to reduce the boron contamination from a substrate. A HP/HT-type Ib single crystal diamond substrate of 3×3×0.5 mm, whose (100) surface was mechanically polished, was used. Influences of scars caused by polishing and defects in the substrate were expected. Therefore, a 1-μm-thickness buffer layer was grown on the substrate using a main synthesis reactor (AX5250; Sekiteknotron). The buffer layer was evaluated by observation using an optical microscope and cathode luminescence (CL) spectra measurement. Substrates were selected according to CL results. Then a 1–2-μm-thick boron-doped layer was grown using a low-power reactor with a quartz chamber; the boron concentration was ca. 500 ppm. This layer served as an electrode. Finally, an insulating diamond single crystal layer was grown. A fast growth rate of 2 μm/h was adopted; the substrate temperature was 960°C and the methane concentration was 2%. After crystal growth, one part of the insulating diamond layer was removed by oxygen plasma etching. Then the Ti/Au contact was fabricated by evaporation at this part. The contact directly touched the boron doped diamond layer. In addition, the aluminum Schottky contact was fabricated on the insulating diamond layer. **Fig. 2** shows an optical photograph of two layered type diamond radiation detectors designated as #1 and #2. Bias voltage was applied to the aluminum contact; the output signal was also measured through this

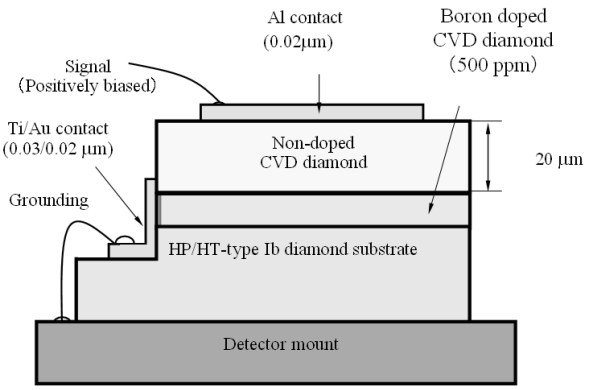

Fig. 1 Schematic drawing of cross section of a layered type single crystalline diamond radiation detector.

contact. Many hillocks were observed in the surface of detector #1.

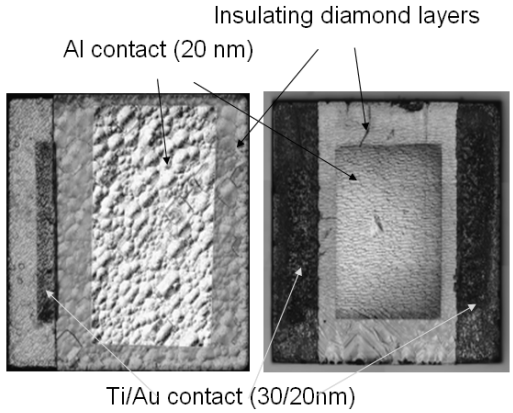

Fig. 2 Photos of the fabricated detectors. left: detector #1, right: detector #2.

2. Experimental Setup

For I-V characteristic measurements, a source measue unit (237; Keithley Instruments) was used. The induced charge distribution, namely the alpha energy spectra of detectors, and output signals were measured using a charge–sensitive preamplifier (142A; Ortec), a linear amplifier (2025; Canberra), a digital storage oscilloscope (9384M; LeCroy Corp.) and a multi channel analyzer (2100C; Labo Inc.).

III. Experimental Results

1. I-V Characteristics

Detectors #1 and #2 showed typical rectification properties, as shown in **Fig. 3**. The leakage current of detector #2 to the aluminum contact at 50 V, a reversed bias condition, was ca. 0.15 pA. For the forward bias, a leakage current of several microamperes was observed at a bias voltage of 20 V. Although there is an influence of interface between an insulating diamond layer, a boron-doped diamond electrode usually functions as a hole injecting electrode[6].

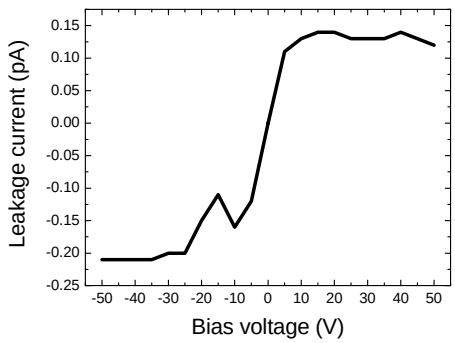

Fig. 3 Curve of I-V characteristics for detector #1. Strong rectification properties were observed; these properties were caused by combination of a boron-doped diamond contact and an aluminum Schottky contact.

2. Alpha energy spectroscopy and observation of output signals from the detector

Fig. 4 shows changes in the distribution of the induced charge on bias voltage obtained using detector #1. As shown in **Fig. 4**, the detector exhibited response to alpha particles even without bias voltage; the boron-doped diamond electrode and the aluminum Schottky contact produced an electric potential gradient in the detector[6]. Energy resolutions changed according to the bias voltage as follows: 0 V, 14%; +10 V, 11.9%; +15 V, 2.6%. As described above, the leakage current in the reverse direction was less than 1 pA at +50 V. However, when the detector measured alpha particles, the detector was not steady, with bias voltage greater than +15 V.

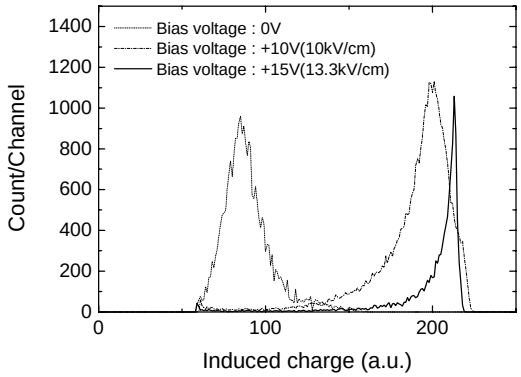

Fig. 4 Alpha energy spectrum obtained by the detector #1. Bias voltage of 15 V was applied to the aluminum Schottky contact. The measurement was carried out in vacuum at room temperature.

At first, detector #2 was fabricated to reduce the leakage current and to improve the bias voltage by adoption of a guard ring electrode. After crystal growth, it was confirmed that the leakage current was sufficiently small compared with detector #1. For that reason, a guard ring was not used. Only structural changes that made a certain connection to the boron-doped diamond electrode were adopted. Although no change was observed in the synthetic condition, a great difference in morphology was apparent between detectors #1 and #2. No hillock was observed in detector #2, probably because of the different thickness of substrates; the thinner substrate, namely 0.3 mm, produced a lower temperature of substrate surface. Consequently, detector #2 accepted bias voltage of +35 V, even under alpha-particle measurement.

Detector #2 collected 7 times the induced charge of that collected by detector #1, as calculated from peak positions in the distribution spectra of the induced charge and gains of the amplifier. Although more than two-times better energy resolution was anticipated from this result, it was 2.8%, which was almost the same value as that of detector #1. No great difference was found in the thicknesses of sensitive layers between detector #1 and #2; it was confirmed through response function measurements for 14 MeV neutrons[9].

Fig. 5 shows a leading edge of an output signal from detector #2 connected with the charge sensitive preamplifier. The rise time of output signals from detector #2 was 10 times faster than that of detector #1. The fastest rise time that was measurable using the measurement system was 20 ns; it was mainly limited by parasitic capacitance between the detector and the preamplifier. The rise time of the output signal shown in **Fig. 5** was 20 ns, reaching the upper limit. The thickness of the sensitive layer, the insulating layer, was 20 μm. The range of 5.486 MeV alpha particles in diamond was ca. 14 μm; therefore, the contributions of motions of holes and electrons to the output signal were 60% and 40%, respectively. Rough estimation shows that drift velocities of electrons and holes were faster than 1×10^5 cm/s. Charge trapping and de-trapping effect on holes were observed slightly, as shown in **Fig. 5**; consequently, shallow trapping center(s) were inferred to exist for holes. Compared to a radiation detector made of a HP/HT-type IIa diamond that had perfect charge collection for holes, only 70% of the induced charge was collected, even for detector #2. Therefore, existence of charge trapping centers for electrons was also expected.

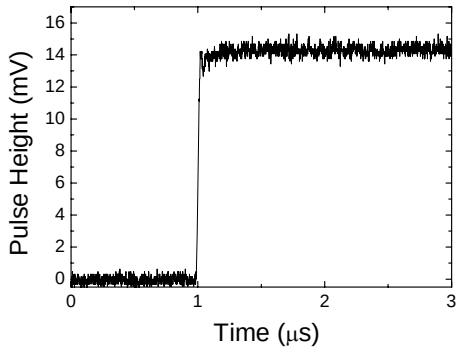

Fig. 5 An example of leading edge of an output signal from the detector #2 connected with a charge sensitive preamplifier. The rise time of this signal was faster than the upper limit of rise time measurement of this system.

IV. Discussion

As shown in **Fig. 2**, the morphology of the insulating diamond layer of detector #2 was superior to that of detector #1. However, the crystalline quality of the insulating layer of detector #1, judging from CL spectrum measurements, was superior to that of detector #2. **Fig. 6** shows CL spectra obtained with the insulating diamond layer after deposition to 20-μm thickness. In **Fig. 6a),** showing detector #1, a free exciton recombination peak is visible at 235 nm; the existence of this peak indicated high total crystalline quality. In addition, there is a peak designated as 'band A' at 430 nm, which is related to structural defects. On the other hand, the CL spectrum obtained with detector #2, as depicted in **Fig. 6b),** mainly shows the 'band A' peak; the free excition recombination peak is very small. Enhancement of surface

defects of the substrate and in the boron-doped layer was expected.

Considering all of the information described above, an induction for the detectors was carried out as follows. Detector #1 showed bad morphology, along with several grain boundaries; the leakage current increased and the bias voltage was limited to a lower level. Therefore, the charge collection efficiency was low because drift velocities of charge carriers were slow. However, the crystalline quality

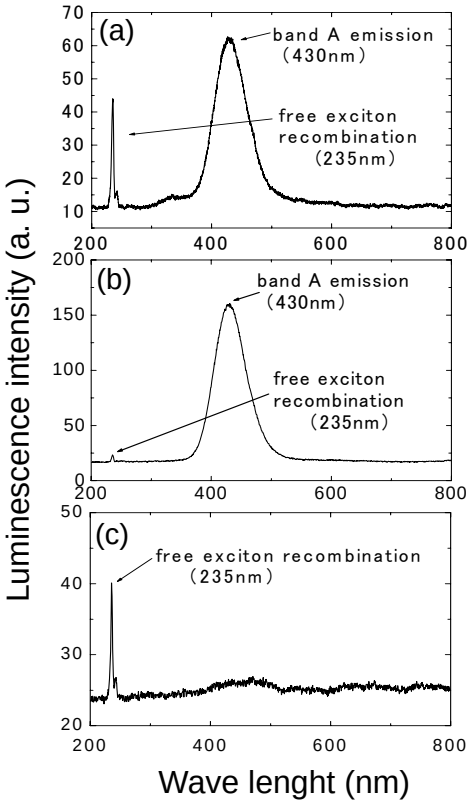

Fig. 6 Cathode luminescence spectra of insulating layers of a) detector #1, b) detector #2, c) insulating diamond grown on a type IIa diamond substrate.

of each grain was superior. For that reason, there was little scattering in charge collection and energy resolution of 2.8% was achieved. In contrast, detector #2 had good morphology and only good, not excellent, crystalline quality. Its charge collection efficiency was improved drastically by the higher bias voltage because charge carriers moved a longer distance. However, scattering in charge collection and energy resolution was not improved much. Further investigation into the relation between synthesis condition, i.e., surface conditions and crystallinity of the substrate and the boron-doped layer, substrate temperature, methane concentration, etc., and examination of crystalline quality based on more samples are indispensable. Moreover, to optimize the detector performance, comparison between crystalline quality and charge transport characteristics should be carried out.

The first improvement should be made for the crystallinity of the boron-doped layer. The reactor used for fabrication of the boron-doped layer mainly caused this problem. **Fig. 6a)** shows a free exciton recombination peak at 235 nm and a 'band A' peak at 430 nm. **Fig. 6c)** shows a CL spectrum obtained with an insulating single diamond layer that was synthesized in completely the same condition as detector #1. The only difference was a diamond substrate: a HP/HT type IIa high-quality diamond substrate was used. As shown in **Fig. 6c),** there was only a free exciton recombination peak. Moreover, even for boron-doped CVD diamond, very high-quality film has been fabricated[10]. Results show that the detector performance will be improved by the combination of these techniques.

V. Conclusions

The prototype layered type CVD diamond radiation detector achieved energy resolution of 2.6% and 2.8%, respectively, for 5.486 MeV alpha particles. Although those energy resolutions were not excellent, these two detectors functioned as an energy spectrometer. This fabrication technique will be more reliable and bring improvement in the yield rate of detectors. In addition, this technique used an inexpensive HP/HT type Ib substrate of ca. 150 US$, and synthesis time were shortened drastically. For those reasons, this technique will contribute to suppression of the fabrication costs of diamond energy spectrometers.

This research was supported by the Grants-in-Aid for Scientific Research (15360498, 17044001, 18035001).

References

1) S. F. Kozlov, R. Stuck, M. Hage-ali, P. Siffert, "Preparation and characteristics of natural diamond nuclear radiation detectors,"IEEE Trans. Nucl. Sci., NS-22 160 (1975).
2) Y. Tanimura et al., "High-temperature operation of a radiation detector made of a type IIa diamond single crystal synthesized by a HP/HT method," Nucl. Instrum. Meth., A443 325 (2000).
3) P. Bergonzo et al., "High collection efficiency CVD diamond alpha detectors," IEEE Trans. Nucl. Sci., NS-45 370 (1998).
4) J.H. Kaneko, T. Tanaka et al., "Radiation detector made of a high-quality polycrystalline diamond,"Diamond and Related Materials, 14 2027 (2005).
5) J. Kaneko et al.,"Diamond radiation detector using a synthetic IIa type mono-crystal," Nucl. Instrum. Meth., A383 547 (1996).
6) J. Kaneko, M. Katagiri et al., "Development of a synthetic diamond radiation detector with a boron doped CVD diamond contact," Nucl. Instrum. Meth., A422 211 (1999).
7) J. H. Kaneko, T. Tanaka et al., "Measurement of behavior of charge carriers and investigation into charge-trapping mechanisms in high-purity type-IIa diamond single crystals grown by high-pressure and high-temperature synthesis,"New Diamond Frontier Carbon Tech., 14(5) 299 (2004).
8) J. H. Kaneko, T. Tanaka, T. Imai et al., "Radiation detector made of a diamond single crystal grown by a chemical vapor deposition method," Nucl. Instrum. Meth., A505 187 (2003).
9) J. H. Kaneko et al., "Response function measurement of layered type CVD single crystal diamond radiation detectors for 14 MeV neutrons," Rev. Sci. Instrum., 75(10) 3581 (2004).
10) Y. G. Chen et al., "Temperature dependence on current-voltage characteristics of nickel/diamond Schottky diodes on high quality boron-doped homoepitaxial diamond film," Appl. Phys. Lett., 82 4367 (2003)

Journal of NUCLEAR SCIENCE and TECHNOLOGY, Supplement 5, p. 395–398 (June 2008)

Performance Characteristics of a CdTe-Based Digital Gamma Imaging System with a ^{75}Se Radioisotope

H. S. CHO[1*], S. I. CHOI[1], K. Y. KIM[1], S. Y. LEE[1], J. E. OH[1], B. S. LEE[2], and S. KIM[3]

[1]*Department of Radiological Science, Yonsei University, Wonju 220-710, Korea*
[2]*School of Biomedical Engineering, Konkuk University, Chunju 380-701, Korea*
[3]*Department of Nuclear and Energy Engineering, Cheju National University, Cheju 690-756, Korea*

As a continuation of our digital radiographic sensor R&D, we have developed a digital gamma imaging system based upon the cadmium-telluride (CdTe) photoconductor for the applications of industrial gamma-imaging. The imaging system consists of a commercially-available CMOS pixel array of a 100 x 100 μm^2 pixel size and a 5.4 x 151.0 mm^2 active area, coupled with a 750-μm-thick CdTe photoconductor, and a collimated selenium (^{75}Se) radioisotope of an about 2.3 x 10^{12} Bq activity and a physical size of 3.0 mm in diameter. In this study, we, for the first time, succeeded in obtaining useful gamma images of several test phantoms with the ^{75}Se radioisotope from the imaging system and evaluated its imaging performance in terms of the line spread function (LSF), the modulation transfer function (MTF), the noise power spectrum (NPS), and the detective quantum efficiency (DQE). For comparison, we also tested its X-ray imaging performance with a microfocus X-ray tube of an about 5 μm focal spot size at an operation condition of 90 kV$_p$ and 100 μA. According to our test results, the designed imaging system seems to be promising for our ongoing application of nondestructive testings, provided that the effective source size of the ^{75}Se radioisotope can be further limited.

KEYWORDS: digital radiographic imaging, CdTe photoconductor, ^{75}Se radioisotope, microfocus X-ray tube

I. Introduction

Since digital radiographic systems offer several advantages over conventional analog film-based systems such as high dynamic range, linear response with the exposure, real-time image acquisition, easy image storage and retrieval, etc., large efforts have been made in research and development of digital radiographic sensors both in the fields of medicine and industry. Commercial state-of-the-art large area systems typically rely on flat panel technology and apply either indirect conversion of X-ray energy with a CsI(Tl) or a Gd_2O_2S(Tb) scintillator or direct conversion with an amorphous selenium (a-Se)[1)-3)]. Direct conversion systems generally yield higher spatial resolution compared to indirect systems due to no optical blurring. In addition, high X-ray energies and gamma imagings require a conversion material of high atomic number (Z) for high absorption efficiency, which offers advantages also in real-time and scanning imaging or generally in any application where the image acquisition speed or radiation dose is critical. Studies on GaAs or HgI_2 have been performed but the most promising high Z material seems to be cadmium-telluride (CdTe) which has been proposed to be used, for example, in medical gamma imaging instead of scintillators in order to improve both the spatial and energy resolution of gamma cameras[4)]. In this study, we have developed a digital gamma imaging system based upon the CdTe photoconductor for our ongoing application of nondestructive testings, and evaluated its imaging performance with ^{75}Se γ-ray and microfocus X-ray sources.

*Corresponding Author, Tel No: +82-33-760-2428, Fax No: +82-33-760-2815, E-mail: hscho1@yonsei.ac.kr

II. Methods and Test Results

1. Digital Gamma Imaging System

Fig. 1 shows photographs of (a) the CdTe-based digital gamma imaging system and (b) a ^{75}Se γ-ray source we used. It consists of a commercially-available CMOS pixel array of a 100 x 100 μm^2 pixel size and a 5.4 (in the scan direction) x 151.0 (in the vertical direction) mm^2 active area, coupled with a 750-μm-thick CdTe photoconductor, a collimated ^{75}Se radioisotope of an about 2.3 x 10^{12} Bq activity and a physical size of 3.0 mm in diameter, and a microstep motor for linear scanning. Here the thick CdTe photo- conductor was incorporated in our imaging system for high absorption efficiency and removal of the significant optical blurring, inherent in the indirect conversion imaging systems. The CMOS pixel array operates in a time-delayed-integration (TDI) mode, as typically required for high scan speed, to improve the signal-to-noise ratio (SNR). **Fig. 2** shows the fractional absorption characteristics for 3 different photon converters of CdTe (100 and 750 μm thick), CsI:Tl (100 μm

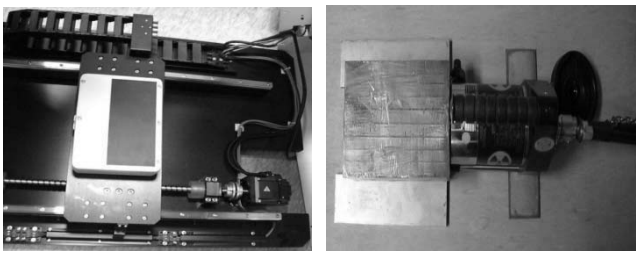

(a) (b)

Fig. 1 Photographs of (a) the CdTe-based digital gamma imaging system we developed and (b) the ^{75}Se γ-ray source.

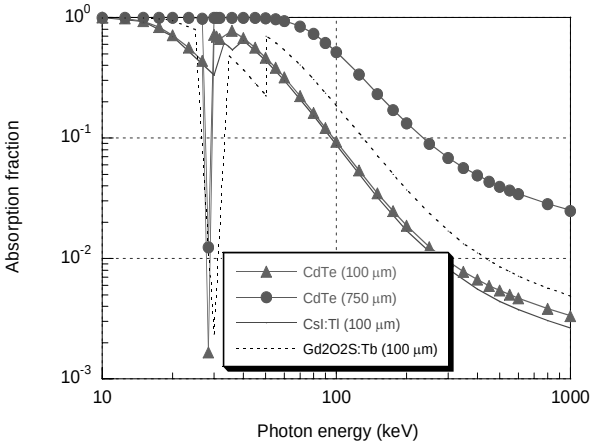

Fig. 2 Fractional absorption curves for three photon converters with different thicknesses as a function of photon energy.

thick), and Gd_2O_2S:Tb (100 μm thick) as a function of photon energy[5]. The absorption fraction for a 750-μm-thick CdTe photoconductor at a photon energy of 100 keV is about 0.52, about 5.9 times higher than for a 100-μm-thick CsI:Tl scintillator. The ^{75}Se radioisotope emits γ-rays in the energy range of 66-401 keV (average energy ~ about 217 keV) and its half-life is about 120 days.

2. Experimental Setup

Fig. 3 shows a schematic illustration of the experimental setup for the gamma image acquisition and its performance testing with the ^{75}Se radioisotope. A mechanical support was designed to maintain a fixed source-to-detector distance (SDD) of 400 mm. The guide tube had a lead (Pb) collimator at the end to shield out radiation, except for that in the direction necessary to make exposure. At the end of the exposure the source was cranked back into a shielding device. The CMOS pixel array was scanned at a speed of 10 mm/sec during the image acquisition. For comparison, we also tested its X-ray imaging performance by acquiring X-ray images with a microfocus X-ray tube (Hamamatsu Corp., L7901-01-1) of an about 5 μm focal spot size at an operation condition of 90 kV_p and 100 mA. **Fig. 4** shows examples of (a) a gamma image of a cellular phone and (b) an X-ray image of an encapsulated IC chip, acquired with the imaging system. In this paper, we presented the imaging performance of the designed system with the ^{75}Se γ-ray and the microfocus X-ray sources in terms of the line spread function (LSF), the modulation transfer function (MTF), the noise power spectrum (NPS), and the detective quantum efficiency (DQE).

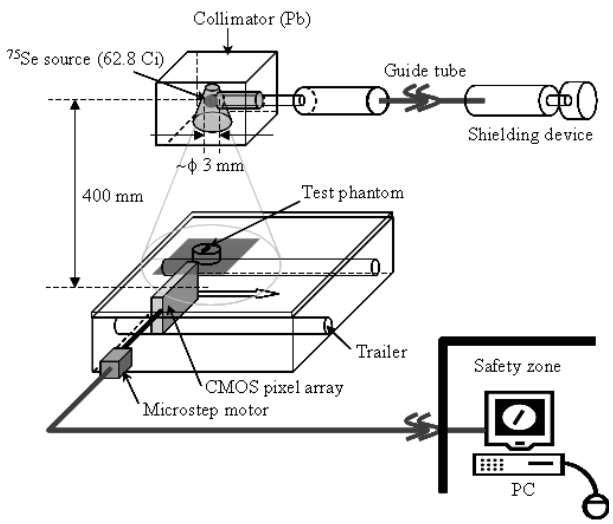

Fig. 3 Schematic illustration of the experimental setup for the gamma image acquisition with the ^{75}Se radioisotope.

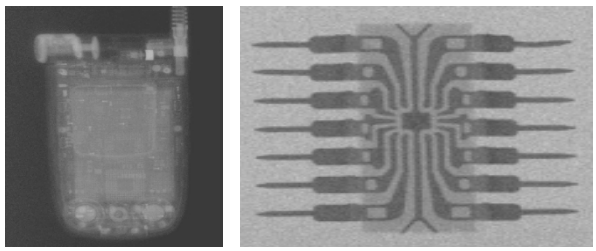

(a) (b)

Fig. 4 Examples of (a) a gamma image of a cellular phone and (b) an X-ray image of an encapsulated IC chip, acquired with the imaging system.

3. Line Spread Function (LSF)

Fig. 5 shows (a) a slit camera with a 10 μm width (Nuclear Associate Corp., 07-624-1) for the measurement of spatial resolution and its (b) γ-ray image and (c) X-ray image acquired at a given test conditions. As shown in **Fig. 3**, the slit camera was placed on the imaging sensor surface and exposed to the γ-ray and the X-ray sources to obtain the line spread function (LSF) which is the system response to a delta (δ) signal. **Fig. 6** shows the measured LSF curves, which spread out and have full-width-at-half-maximums (FWHM) of about 0.86 mm and 0.14 mm, respectively. The spatial resolution with the ^{75}Se γ-ray source was more than 6 times worse than with the microfocus X-ray source, which may be due to the finite source size (i.e., ϕ 3.0 mm) of the ^{75}Se radioisotope. Compared to the LSF measured with the microfocus X-ray source, it will be significantly improved, provided that the effective source size can be further limited.

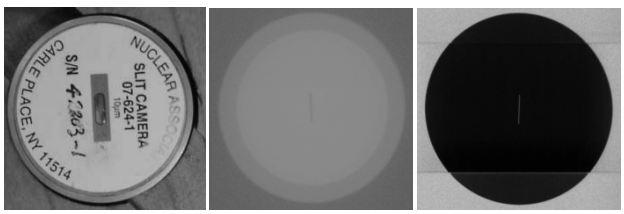

(a) (b) (c)

Fig. 5 (a) a slit camera with a 10 μm width and its (b) γ-ray image and (c) X-ray image.

4. Modulation Transfer Function (MTF)

The modulation transfer function (MTF) is a measure of signal transfer over a range of spatial frequencies and quantifies image sharpness. It is defined as the modulus of

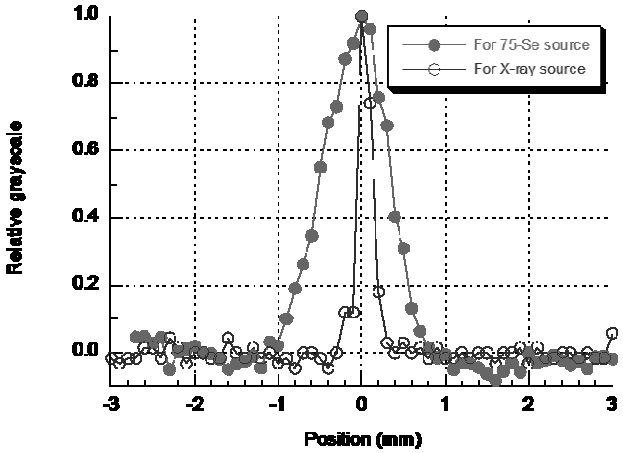

Fig. 6 Line spread functions (LSF) measured with the slit camera by using the ^{75}Se γ-ray and the microfocus X-ray sources.

the Fourier Transform (FT) of the LSF and is always scaled to unity at a zero frequency:

$$MTF(u) = \left| FT\{LSF(x)\} \right| = \left| \frac{1}{\sqrt{2\pi}} \int_{-\infty}^{\infty} LSF(x) e^{i2\pi ux} dx \right| . \qquad (1)$$

The theoretical limit of the MTF is determined by the pixel size of an imaging system. Since the sharpest response of the imaging system to a delta (δ) signal is as wide as one pixel, the *pixel aperture* MTF is the FT of a rectangular function with a width (w) of one pixel[6]:

$$MTF_{pixel.aperture}(u) = \frac{1}{w} \left| \int_{-w/2}^{w/2} e^{i2\pi ux} dx \right| = \frac{\sin \pi uw}{\pi uw} . \qquad (2)$$

Fig. 7 shows the measured presampled MTF curves of the system with the ^{75}Se γ-ray and the microfocus X-ray sources. Note that the pixel aperture (or *ideal*) MTF based upon the *sinc* function of the pixel pitch is also indicated for comparison. The spatial frequency measured at 10% MTF with the ^{75}Se γ-ray source was about 0.87 lp/mm, about three times lower than with the microfocus X-ray source.

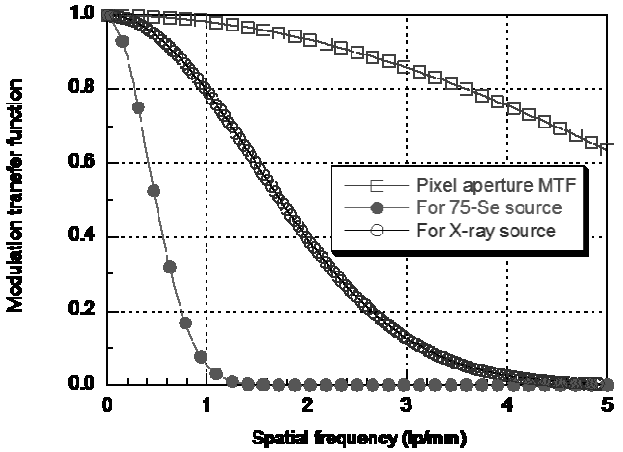

Fig. 7 Presampled modulation transfer functions (MTF) calculated from the measured LSF.

5. Noise Power Spectrum (NPS)

Noise characteristics of an imaging system is quantified as the noise power spectrum (NPS), which expresses the average area occupied by individual photons per unit area (mm^2), and is measured as the following equations[7]:

$$NPS_{raw}(u,v) = \lim_{X,Y\to\infty} \frac{1}{XY} \left\langle \left| \iint_{XY} \sigma(x,y) e^{-2\pi i(ux+vy)} dxdy \right|^2 \right\rangle , \qquad (3)$$

$$NPS_{normalized}(u,v) = \frac{NPS_{raw}(u,v)}{S_{mean}^{\ 2}} ,$$

where σ(x,y) is the difference between the average image signal and the signal at point (x,y), X and Y is a distance in the x and the y directions, the symbol <A> means the ensemble average of A, and S_{mean} represents the mean signal of the region-of-interest (ROI). The two-dimensional (2D) NPS was obtained from the acquired white image by using Eq. (3), and an estimate of the one-dimensional (1D) NPS from the 2D NPS was performed using radial-averaging technique. **Fig. 8** and **9** show the resultant 2D and 1D NPS, respectively, obtained with (a) the ^{75}Se γ-ray and (b) the microfocus X-ray sources. The 1D NPS gradually decreased with the spatial frequency, and the NPS value at zero frequency with the ^{75}Se γ-ray source was about 6.3x10^{-5} mm^2, about 1.3 times larger than with the microfocus X-ray source.

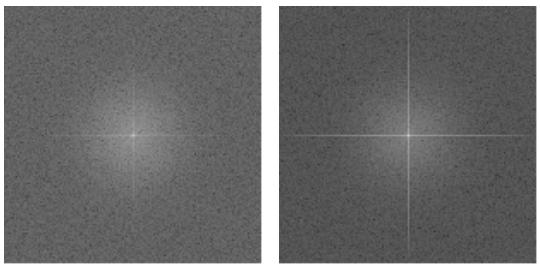

Fig. 8 2D noise power spectrums (NPS) obtained with (a) the ^{75}Se γ-ray and (b) the microfocus X-ray sources.

6. Detective Quantum Efficiency (DQE)

The detective quantum efficiency (DQE) is generally regarded as the most useful measure of sensitivity and noise performance of an imaging system and can be understood as the fraction of the quantum number entering the imaging system effectively used by the system to produce an image. As defined in Eq. (4), it can be deduced from the measured MTF, NPS, and the photon fluence Φ (photons/mm^2)[7]:

$$DQE(u) = \left(\frac{SNR_{out}}{SNR_{in}} \right)^2 = \frac{MTF^2(u)}{\Phi \cdot NPS_{normalized}(u)} , \qquad (4)$$

where SNR_{in} and SNR_{out} are the signal-to-noise ratios of the quantum field at the sensor input and of the image at the sensor output, respectively. **Fig. 10** shows the deduced 1D

DQE obtained with the ^{75}Se γ-ray and the microfocus X-ray sources. The DQE value at zero frequency with the ^{75}Se γ-ray source was about 0.26, about 1.6 times smaller than with the microfocus X-ray source.

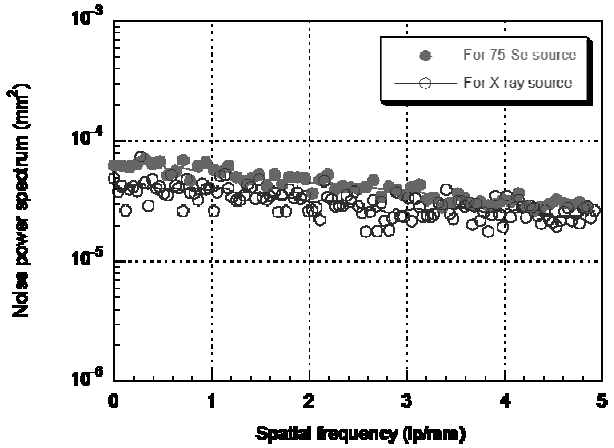

Fig. 9 1D noise power spectrums (NPS) obtained with the ^{75}Se γ-ray and the microfocus x-ray sources.

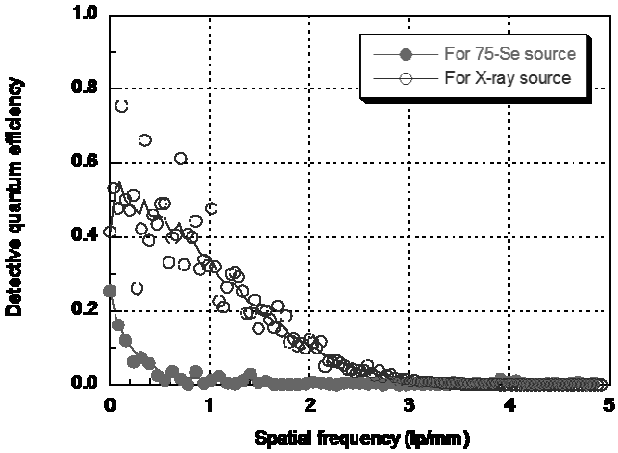

Fig. 10 1D detective quantum efficiency (DQE) obtained with the ^{75}Se γ-ray and the microfocus X-ray sources.

III. Conclusion

We have developed a digital radiographic system based upon the cadmium-telluride (CdTe) photoconductor for our ongoing application of nondestructive testings with a ^{75}Se radioisotope. The imaging system consists of a commercially-available CMOS pixel array of a 100 x 100 mm^2 pixel size and a 5.4 (in the scan direction) x 151.0 (in the vertical direction) mm^2 active area, coupled with a 750-μm-thick CdTe photoconductor for high absorption efficiency (~52% at a photon energy of 100 keV) and removal of the significant optical blurring (~0.14 mm FWHM with a microfocus X-ray tube of an about 5 μm focal spot size). We, for the first time, succeeded in obtaining useful gamma images from the imaging system with a ^{75}Se radioisotope (~ 62.8 Ci, ~ϕ 3 mm) and evaluated its imaging performance. For comparison, we also evaluated the X-ray imaging performance with the microfocus X-ray tube. With the ^{75}Se radioisotope, the FWHM of the LSF was about 0.86 mm, the spatial frequency measured at 10% MTF was about 0.87 lp/mm, the NPS value at zero frequency was about 6.3×10^{-5} mm^2, and DQE value at zero frequency was about 0.26. According to the test results with the microfocus X-ray source, these performance characteristics are thought to be significantly improved, provided that the effective source size of the ^{75}Se radioisotope can be further limited. Thus the designed gamma imaging system in this study seems to be promising for our ongoing application of nondestructive testings.

Acknowledgement

This work was supported by the Basic Atomic Energy Research Institute (BAERI) program of the Ministry of Science and Technology (MOST) under contract No. M2-0376-03-0000.

References

1) H. S. Cho, M. H. Jeong, B.S. Han, et al., "Development of a Portable Digital Radiographic System Based on FOP-coupled CMOS Image Sensor and Its Performance Evaluation," IEEE Trans. on Nucl. Sci., **52 (5)**, 1766 (2005).
2) M. P. Andre, B. Spivey, P. Martin, et al., "An Integrated CMOS-selenium X-ray Detector for Digital Mammography," Proc. SPIE, **3336**, 204 (1998).
3) M. F. Stone, W. Zhao, B. V. Jacak, et al., "The X-ray Sensitivity of Amorphous Selenium for Mammography," Med. Phys., **29 (3)**, 319 (2002).
4) C. Scheiber, "CdTe and CdZnTe Gamma Ray Detectors in Nuclear Medicine," Nucl. Instr. Meth., **A 448**, 513 (2000).
5) http://physics.nist.gov/PhysRefData/X-rayMassCoeff/tab4.html.
6) E. Samei and M. J. Flynn, "A Method for Measuring the Presampled MTF of Digital Radiographic Systems Using an Edge Test Device," Med. Phys., **25**, 102 (1998).
7) E. Samei, M. J. Flynn, H. G. Chotas, et al., "DQE of Direct and Indirect Digital Radiographic Systems," Proc. SPIE, **4320**, 189 (2001).

Journal of NUCLEAR SCIENCE and TECHNOLOGY, Supplement 5, p. 399–402 (June 2008)

Performance of Carbon-interspaced Antiscatter Grids Tested with the IEC Standard Fixture

K. Y. KIM[1], H. S. CHO[1*], J. E. OH[1], S. I. CHOI[1], S. Y. LEE[1], J. S. KIM[2], N. G. JEONG[2], J. G. KIM[2], and J. H. LEE[2]

[1]*Department of Radiological Science, Yonsei University, Wonju 220-710, Korea*
[2]*R&D Center, Jungwon Precision Ind. Co., Ltd., Ansan 690-756, Korea*

Jungwon Precision Ind. Co., Ltd. has recently developed precise carbon-interspaced antiscatter grids by adopting the sawing process in order to employ them to digital radiographic (DR) systems. Twelve grid samples of strip densities ranging from 40 to 85 lines/cm at a fixed grid ratio of 5:1 and of grid ratios from 5:1 to 10:1 at a fixed strip density of 80 lines/cm were prepared and their physical characteristics were examined under a well-controlled test condition with the IEC standard fixture, in terms of the transmission of primary radiation, the transmission of scattered radiation, the transmission of total radiation, the contrast improvement factor, and the Bucky factor. We expect that these experimental results will be useful for the selection of antiscatter grids in the applications of DR imaging as well as for the improvement of grid design.

KEYWORDS: Antiscatter grid, carbon interspace, IEC fixture, contrast improvement factor, Bucky factor

I. Introduction

In radiography, the image contrast is normally degraded by scattered radiation arriving at the image receptor, depending on the object size and composition and the radiation quality used. The use of antiscatter grids as well as the air gap and the slit techniques is well established to reduce the amount of scattered radiation [1)]. Although aluminum (Z: 13, ρ_{Al}: 2.70 g/cm^3) interspaced grids are typically used, this kind of grids may not be available enough to be applied to digital radiographic (DR) systems mainly due to the rough lead-strip uniformity caused by the manufacturing process and the relatively inferior performance of the Al interspace in the improvement of the image contrast with a Bucky factor as low as possible, as compared with an air or organic interspace, due to the appreciable absorption of the primary radiation penetrating the interspace. In order to overcome these difficulties, Jungwon Precision Ind. (JPI) Co., Ltd. [2)] has recently developed precise carbon (Z: 6, ρ_C: 2.27 g/cm^3) interspaced grids by adopting the sawing process. In this study, we prepared twelve samples of the carbon-interspaced grids with strip densities ranging from 40 to 85 lines/cm at a fixed grid ratio of 5:1 and with grid ratios from 5:1 to 10:1 at a fixed strip density of 80 lines/cm. By using the IEC standard fixture [3)] we fabricated for this study, we evaluated their performance characteristics in terms of the transmission of primary radiation (T_p), the transmission of scattered radiation (T_s), the transmission of total radiation (T_t), the contrast improvement factor (C_{if}), and the Bucky factor (B). We expect that these experimental results will be useful for the selection of antiscatter grids in the applications of DR imaging as well as for the improvement of grid design.

*Corresponding Author, Tel No: +82-33-760-2428, Fax No: +82-33-760-2815, E-mail: hscho1@yonsei.ac.kr

II. Methods and Results

1. Grid Samples

Fig. 1 and Table 1 show the geometrical characteristics of the carbon-interspaced grids we designed. The grids are linearly focused with a focal spot distance (f_o) of 100 cm. **Fig. 2** shows (a) a side view and (b) a top view of a grid sample having a grid ratio of 5:1 and a strip density of 80 lines/cm (i.e., Grid No. C5/80), indicating precise strip uniformity. **Fig. 3** shows the twelve grid samples we prepared for this study. Here the front and the back sides of the grids were coated with a thin carbon-plastic layer, each of which has an about 250 μm thickness.

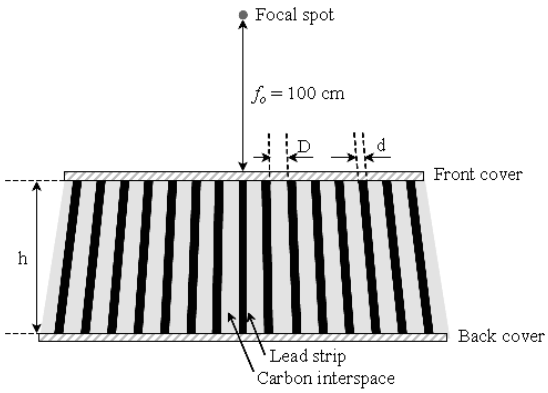

Fig. 1 Geometrical characteristics of the carbon-interspaced grids which are linearly focused with a focal spot distance of 100 cm.

Lead (Z: 81, ρ_{Pb}: 11.85 g/cm^3) is the most commonly used material for the X-ray absorbing strips in the grid, and the interspace material varies from air or organic fiber to light metal such as Al. The air is the ideal interspace material with no absorption of any primary X-rays penetrating the inter-

Table 1. Geometrical parameters of the carbon-interspaced grids.

	Strip density (lines/cm)						
	40	43	51	60	70	80	85
Thickness of lead strip, d (μm)	45	45	45	45	40	25	25
Thickness of interspace, D (μm)	202	186	150	124	103	102	93
Lead-to-interspace ratio, d/D	1/4.5	1/4.1	1/3.3	1/2.8	1/2.6	1/4.1	1/3.7
Grid height*, h (μm), for grid ratios (r) of							
5:1	1,008	930	752	622	514	510	466
6:1						612	
7:1						714	
8:1						816	
9:1						918	
10:1						1,020	

*Actual grid thickness should include two thin carbon-plastic covers, each of which has an about 250 μm thickness (not included here).

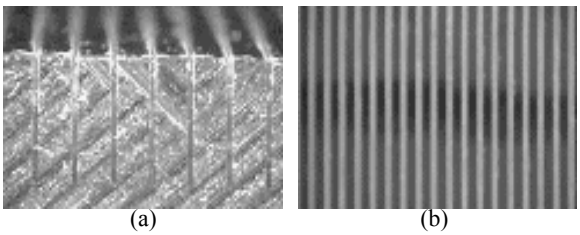

(a) (b)

Fig. 2 (a) a side view and (b) a top view of the carbon-interspaced grid having a grid ratio of 5:1 and a strip density of 80 lines/cm (i.e., Grid No. C5/80).

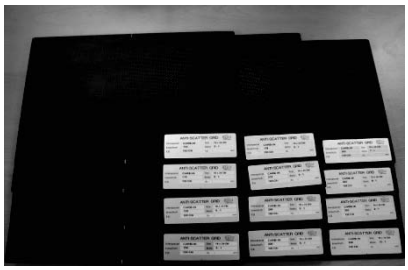

Fig. 3 12 samples of the carbon-interspaced grids we tested in this study.

space, whereas the Al may be the heaviest interspace material which has been typically used, even though it gives relatively inferior performance in the improvement of the image contrast with a Bucky factor as low as possible [4,5]. In the aspects of the benefit and sacrifice of the grid usage, the carbon is certainly advantageous as interspace material than the aluminum.

2. Experimentals

To evaluate the performance characteristics of the grid samples, we built a standard test fixture which was conformed to the IEC publication 60627 defined the design and material requirements necessary to measure the performance of general-purpose antiscatter grids, as shown in **Fig. 4**. It was designed to be able to test with both narrow- and broad-beam conditions. We measured the grid characteristics including T_p, T_s, T_t, C_{if}, and B, according to their definitions (Table 2), at a given test condition (100 kV_p, 32 mAs) by using a calibrated ion chamber (RTI Electronics, Piranha 657). The detailed measurement procedures are well described in the IEC publication 60627. Table 3 shows the resultant performance characteristics of the grid samples we measured. In the following sections, the dependence of the T_p and the T_s on the grid parameters and the relationship between the C_{if} and the Bucky factor are presented.

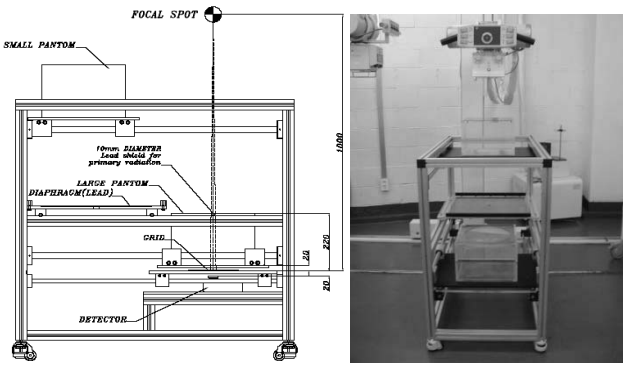

Fig. 4 IEC standard fixture we fabricated which was designed to be able to test with both narrow- and broad-beam conditions.

Table 2. Definitions of grid performance factors.

Factors	Definition
grid ratio (r)	r = h/D
T_p	the ratio of the intensity of the primary radiation with the grid in place to the corresponding intensity without grid
T_s	the ratio of the intensity of the scatter radiation with the grid in place to the corresponding intensity without grid
T_t	the ratio of the intensity of the total radiation with the grid in place to the corresponding intensity without grid
C_{if}	T_p / T_t
B	$1 / T_t$

Table 3. Performance characteristics of the grid samples we tested.

Grid No.	Grid ratio	Strip density (lines/cm)	T_p (%)	T_s (%)	T_t (%)	C_{if}	B
C5/40	5	40	74.8	37.1	50.9	1.5	2.0
C5/43	5	43	74.4	36.8	50.6	1.5	2.0
C5/51	5	51	73.6	36.7	49.6	1.5	2.0
C5/60	5	60	73.1	36.5	48.0	1.5	2.1
C5/70	5	70	67.6	34.9	49.9	1.4	2.1
C5/80	5	80	73.0	35.1	47.7	1.5	2.1
C5/85	5	85	72.9	34.5	47.3	1.5	2.1
C6/80	6	80	72.8	35.0	47.5	1.5	2.1
C7/80	7	80	72.0	34.4	47.2	1.5	2.1
C8/80	8	80	71.8	34.0	46.2	1.6	2.2
C9/80	9	80	71.5	33.8	45.7	1.6	2.2
C10/80	10	80	70.8	32.0	44.1	1.6	2.3

3. T_p and T_s vs. Grid Parameters

In order to understand the behavior of the C_{if} and the Bucky factor with the grid parameters, it is necessary to investigate the dependence of the T_p and the T_s on the grid

parameters. In practice, the T_p depends not only on the geometrical factor (i.e., D/(D+d)=1/(1+d/D)) but also on the attenuation factor of the grid and can be expressed as the following equation:

$$T_p = \frac{D}{D+d} \cdot \frac{\int_0^{E_{max}} I(E) p_{I(E)} e^{-\mu(E)h} dE}{\int_0^{E_{max}} I(E) p_{I(E)} dE}, \quad (1)$$

where I(E) the photon fluence of energy E in the spectrum of primary radiation incident on the grid, $p_{I(E)}$ is the probability that a primary photon fluence of energy E is detected by a recording system, μ(E) is the total linear attenuation coefficient of the interspace at energy E, and h is the grid height. **Fig. 5** shows the T_p measured as a function of (a) grid ratio and (b) lead-to-interspace ratio. For a given strip density of 80 lines/cm (or lead-to-interspace ratio of 1/4.1), the T_p decreases as the grid ratio increases, since the grid height increases and thus the attenuation factor increases at the same rate. Note that the geometrical factor of T_p in this case was kept constant (~80.3%). For a given grid ratio of 5:1, the T_p also decreased as the lead-to-interspace ratio increased (see the direct comparison of the samples C5/40, C5/43, C5/51, and C5/60); although the grid height decreases and hence the attenuation of the primary photons by the interspace decreases, the decrease in the geometrical factor is more dominant, resulting in a decreased T_p. The T_p value decreases from 73.0% to 70.8% when the grid ratio increases from 5:1 to 10:1. **Fig. 6** shows the similar measurements of T_s as a function of (a) grid ratio and (b) lead-to-interspace ratio. For the given strip density, the T_s decreased as the grid ratio increased because of the decrease in the solid angle defined by the space between the lead strips. The T_s value decreased from 35.1% to 32.0% when the grid ratio increased from 5:1 to 10:1. For the given grid ratio, the T_s also decreased as the lead-to-interspace ratio increased, since the thickness of the interspace decreases as well (see also the direct comparison of the samples C5/40, C5/43, C5/51, and C5/60).

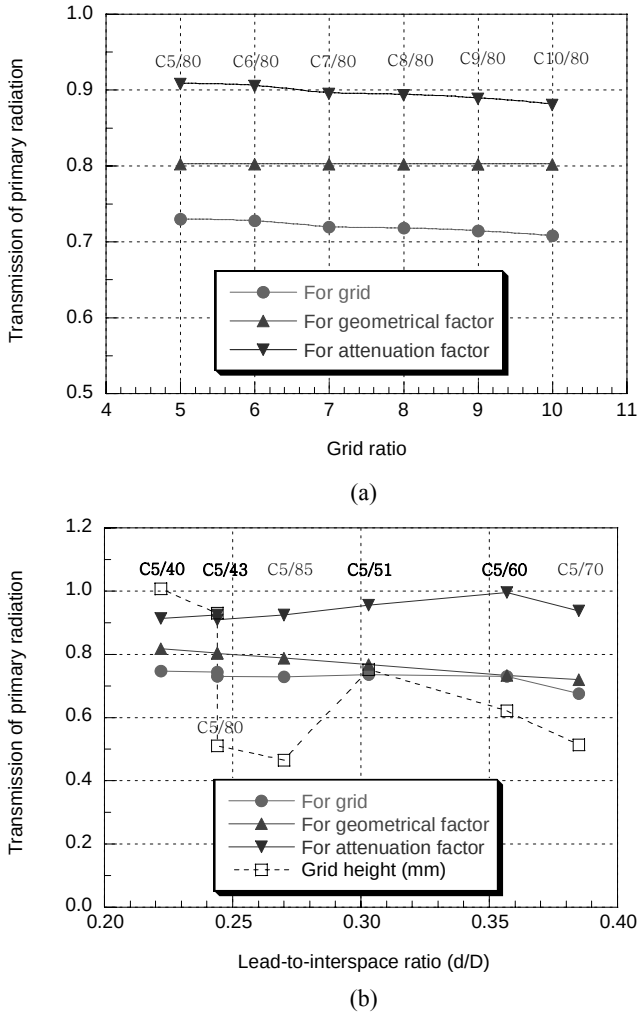

Fig. 5 Transmission of primary radiation (T_p) measured as a function of (a) grid ratio and (b) lead-to-interspace ratio.

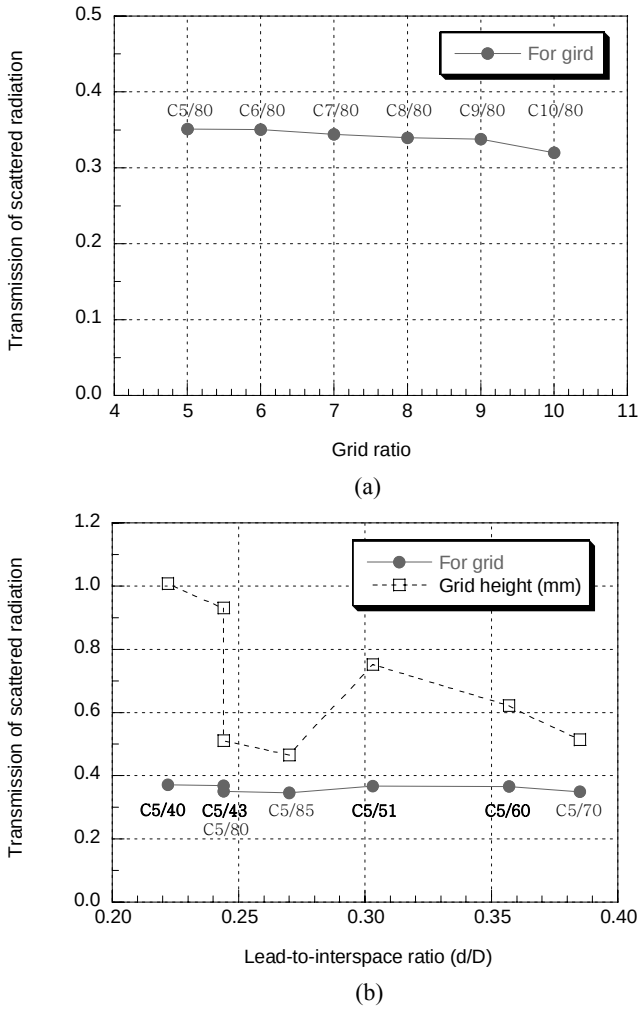

Fig. 6 Transmission of scattered radiation (T_s) measured as a function of (a) grid ratio and (b) lead-to-interspace ratio.

4. C_{if} vs. Bucky factor

The C_{if} and the Bucky factor are typically used as the benefit and cost indicators, respectively, for the evaluation of grids. As expressed in Eq. (2), the C_{if} is proportional to the T_p and the Bucky factor:

$$C_{if} = T_p \cdot B < \frac{D}{D+d} \cdot B \tag{2}$$

Since the T_p is, in practice, less than unity and furthermore D/(D+d), the fractional increase in image contrast is always less than the relative increase in the exposure. **Fig. 7** shows the C_{if} versus the Bucky factor for the tested grid samples and also for antiscatter techniques with 100% primary transmission (i.e., T_p = 1) and with D/(D+d) primary transmission, as a measure of the efficiency of antiscatter techniques [6]. As shown in **Fig. 7**, the slope of the C_{if} versus the Bucky factor is less than the constant D/(D+d) ratio. Consequently, for high contrast improvement with a Bucky factor as low as possible, a high T_p is of decisive importance, and, thus, the carbon interspace is of advantage compared with aluminum interspace. Moreover, the Bucky factors measured for the tested carbon-interspaced grids were below 2.4 less than those in a conventional aluminum-interspaced grids, possibly due to the their smaller attenuation of primary radiation.

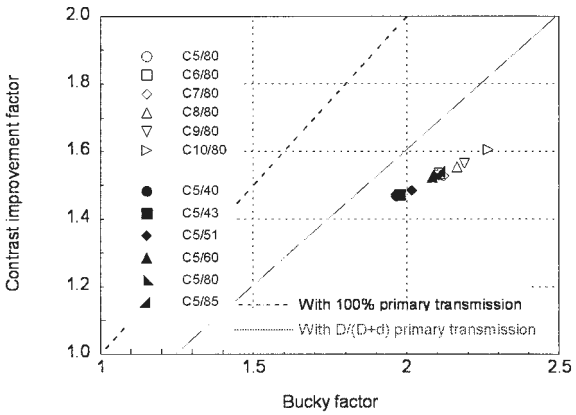

Fig. 7 C_{if} vs. Bucky factor for the tested grid samples and also for antiscatter techniques with 100% primary transmission and D/(D+d) primary transmission.

Figure **8** shows the dependence of the C_{if} on lead content, P, for the grid samples having the same strip density but different grid ratios. The lead content increases with increasing grid ratio due to the increase of the grid height:

$$P = \rho_{Pb} \frac{hd}{D+d}, \tag{3}$$

where ρ_{Pb} is the density of lead. The C_{if} increased almost linearly with the lead content. According to the **Fig. 7** and **8**, the contrast improvement capability of a grid depends strongly on the geometrical parameters of the grid and hence the distribution of lead in the strips.

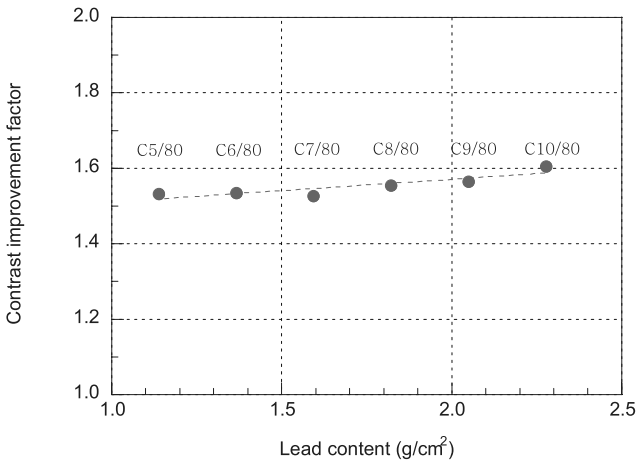

Fig. 8 Dependence of the C_{if} on lead content for the grid samples having the same strip density but different grid ratios.

III. Conclusion

In this study, we prepared twelve samples of the carbon-interspaced grids with strip densities ranging from 40 to 85 lines/cm at a fixed grid ratio of 5:1 and with grid ratios from 5:1 to 10:1 at a fixed strip density of 80 lines/cm. The T_p and T_s values decreased from 73.0% to 70.8% and 35.1% to 32.0%, respectively, when the grid ratio increased from 5:1 to 10:1 with a strip density of 80 lines/cm. For high contrast improvement with a Bucky factor as low as possible, a high T_p is of decisive importance, and the contrast improvement capability of a grid depends strongly on the geometrical parameters of the grid and hence the distribution of lead in the strips. We expect that these experimental results will be useful for the selection of antiscatter grids in the applications of DR imaging as well as for the improvement of grid design.

Acknowledgement

This work was supported by the academic-industrial cooperation program of the Yonsei University and the Jungwon Precision Ind. Co., Ltd. under contract No. YS-JPI 20070201.

References

1) Horst Aichinger, Dierker, Joite-Barfub, and Sabel, Radiation Exposure and Image Quality in X-ray Diagnostic Radiology, Springer, Berlin, 49 (2004).
2) http://www.JPI.co.kr.
3) CEI/IEC 60627:2001, Diagnostic X-ray Imaging Equipment – Characteristics of General Purpose and Mammographic Antiscatter Grids, 2nd Ed., IEC, Geneva, 21 (2001).
4) H. P. Chan and K. Doi, "Investigation of the Performance of Antiscatter Grids: Monte Carlo Simulation Studies," Phys. Med. Biol., **27**, 785 (1982).
5) P. S. Rezentes, A. Almeida, and G. Barnes, "Mammography Grid Performance," Radiology, **210 (1)**, 227 (1999).
6) H. P. Chan, P. Frank, K. Doi, et al., "Ultra-high-strip-density Radiographic Grids: a New Antiscatter Technique for Mammography," Radiology, **154**, 807 (1985).

Journal of NUCLEAR SCIENCE and TECHNOLOGY, Supplement 5, p. 403–406 (June 2008)

Digital Panoramic Tomography (DPT) and Its Realization

H. S. CHO[1*], S. I. CHOI[1], J. E. OH[1], S. Y. LEE[1], K. Y. KIM[1], B. S. LEE[2], and S. KIM[3]

[1]*Department of Radiological Science, Yonsei University, Wonju 220-710, Korea*
[2]*School of Biomedical Engineering, Konkuk University, Chunju 380-701, Korea*
[3]*Department of Nuclear and Energy Engineering, Cheju National University, Cheju 690-756, Korea*

We have developed a prototyped digital panoramic tomography (DPT) system which mainly consists of a slit-collimated X-ray generator of a 0.4-mm focal spot and a 3.5-mmAl filtration, a linear-array typed CMOS imaging sensor of a 48 x 48 μm^2 pixel size and a 128 (in the scan direction) x 3072 (in the vertical direction) pixel format, a series of microstep motors for the precise movement of the imaging system, and the designed motion control and pixel readout sequences required to make a specific plane of interest (POI) to be focused. With the several test phantoms we designed, we, for the first time, succeeded in obtaining useful DPT images by moving the X-ray generator and the CMOS imaging sensor along a continuously sliding rotation center during a continuous X-ray exposure. We demonstrated that the prototyped DPT system can be applicable to any shaped POI to be focused, provided that adequate motion control and pixel readout sequences are designed. We expect the system to be useful for our future imaging applications such as nondestructive testings and dental panoramic radiography.

KEYWORDS: digital panoramic tomography, rotation center, pixel readout sequence, nondestructive testings

I. Introduction

In a conventional X-ray imaging (i.e., 2D planar imaging) there are a few factors that limit the ability to visualize the structures within objects: (1) objects in the imaged 3D volume become superimposed on the 2D radiograph, making it difficult to detect subtle anomalies and (2) the spatial distribution of objects is obscured, making it hard to recognize the exact shape and relative position of various structures [1]. One possible method to overcome these difficulties is with geometrical tomography which utilizes geometrical focusing techniques to achieve a higher contrast in one specific plane of interest (POI) within the imaged object and blur out object structures outside of this focal plane due to parallax [2-5]. However, this imaging technique is only applicable to a *planar* POI to be focused, not to *any shaped* POI such as a circular or parabolic plane, limiting its applications in the field. Sometimes, it is necessary to focus a circular or a parabolic plane within an object, especially, for the nondestructive testings of pipes in industries or for the dental arch radiography in dentistry [6, 7].

In this study, we have developed a prototyped digital panoramic tomography (DPT) system which can focus any shaped POI within an object by moving the X-ray generator and the imaging sensor along a continuously sliding rotation center during a continuous X-ray exposure. With the adequate motion control and pixel readout sequences we designed, we, for the first time, succeeded in obtaining promising DPT images with several test phantoms and expect the system to be useful for our future imaging applications such as nondestructive testings and dental panoramic radiography.

*Corresponding Author, Tel No: +82-33-760-2428, Fax. No: +82-33-760-2815, E-mail: hscho1@yonsei.ac.kr

II. Experimental Methods and Results

1. Digital Panoramic Tomography

Fig. 1 shows a schematic illustration of the DPT principle. As shown in **Fig. 1**, the DPT system mainly consists of a slit-collimated X-ray generator, a linear-array typed imaging sensor, a series of microstep motors for the precise movement of the imaging system, and the designed motion control and pixel readout sequences required to make a specific POI to be focused. Here the X-ray generator is connected to the imaging sensor through a mechanical support, keeping the source-to-detector distance (SDD) constant. The DPT is unique in that the focus of the projection in the horizontal dimension (i.e., in the scan direction) is different from the focus of the vertical projection due to the introduction of a rotation center; the rotation center serves as the effective focus in the horizontal

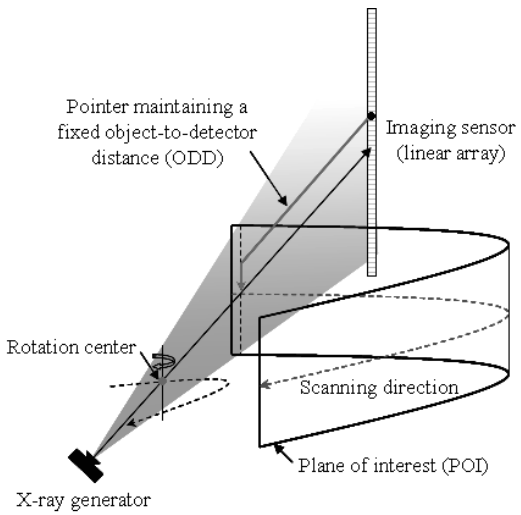

Fig. 1 Schematic illustration of the principle of the digital panoramic tomography (DPT).

projection, whereas the X-ray source does in the vertical projection. This makes the magnification factor much greater in the horizontal dimension (M_H = distance between source and detector / distance between source and POI) than in the vertical dimension (M_V = distance between rotation center and detector / distance between rotation center and POI), leading to geometrical distortion. Thus, proper magnification correction should be made in the design of the pixel readout sequence. **Fig. 2** shows a schematic illustration for the design of pixel readout sequence for a specific POI. The pixel readout frequency, *f*, required to focus the chosen POI can be calculated as the following equation:

$$f[Hz] = \frac{lM_V}{pt}, \tag{1}$$

where *l* is the total scan length, *p* is the pixel size, and *t* is the total scan time. Note that the M_V is used in Eq. (1), instead of M_H, for the magnification correction. The resultant pixel readout sequence is then determined proportionally to the scan speed.

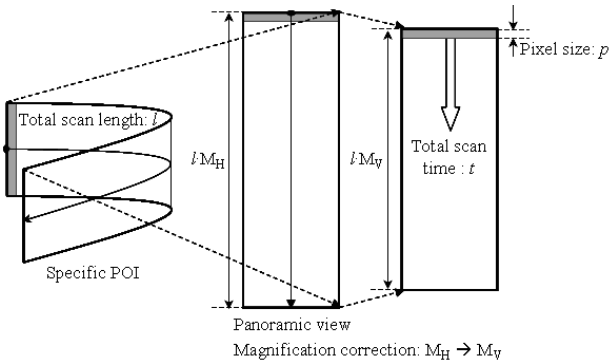

Fig. 2 Schematic illustration for the design of the pixel readout sequence for a specific POI.

Another important factor to be considered is that the rotation center should move in a fashion that the chosen POI has a fixed M_H, which definitely determines the motion control sequence. One easy method to do so is, as shown in **Fig. 1**, to use an imaginary pointer attached to the imaging sensor which maintains a fixed object-to-detector distance (ODD); the combined X-ray generator and the imaging sensor just move as the pointer scans the POI surface, giving a constant M_H to the POI. **Fig. 3** shows a schematic illustration for the design of the motor control sequence for a given POI. A set of coordinates ($\theta_{n,rotation}$, $x_{n,rotation}$) of the rotation center to be moved, as a function of the predetermined point coordinates (x_n, y_n) on the POI trajectory, can be calculated as the following equation:

$$\begin{aligned} \theta_{n,rotation} &= \sin^{-1}\left(y_n / r\right), \\ x_{n,rotation} &= x_n - r\cos\theta_{n,rotation}, \end{aligned} \tag{2}$$

where the meanings of $\theta_{n,rotation}$, $x_{n,rotation}$, x_n, and y_n are described in **Fig. 3**, and *r* is the fixed ODD.

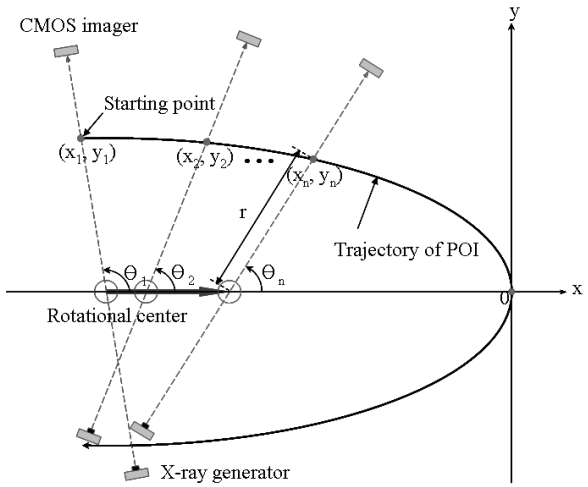

Fig. 3 Schematic illustration for the design of the motor control sequence for a given POI.

2. Prototype DPT System

Fig. 4 shows a schematic structure of the prototype DPT system developed in this study. It consists of a slit-collimated X-ray generator (0.4-mm focal size and 3.5-mmAl filtration), a linear-array typed CMOS imaging sensor of a 48 x 48 μm^2 pixel size and a 128 (in the scan direction) x 3072 (in the vertical direction) pixel format, a series of microstep motors (3.125 μm/pulse for linear motion and 0.0032°/pulse for rotational motion), and the designed motion control and pixel readout sequences. Here the CMOS imaging sensor operates in a time-delayed integration (TDI) mode, as typically required for high scan speed, and in a 2x2 binning mode to improve the signal-to-noise ratio (SNR); thus, the effective pixel size is 96 x 96 μm^2. The geometrical

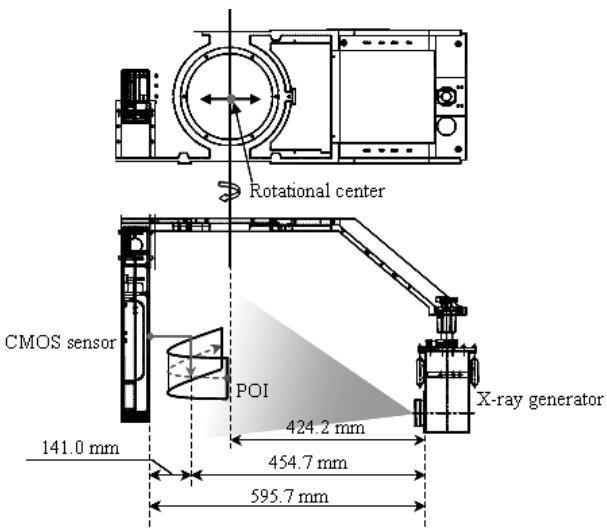

Fig. 4 Schematic structure of the prototyped DTP system.

distances among the X-ray generator, the rotation center, the chosen POI, and the imaging sensor are described as in **Fig. 4**. The vertical and horizontal magnification factors were about 1.31 and 5.62, respectively.

3. Experiments

Fig. 5 shows three test phantoms of a parabolic trajectory designed for the acquisition of DPT images with: (a) a single ball (ϕ 4 mm) layer for checking the geometrical distortion, (b) a single pin (ϕ 1 mm) layer for checking the magnification uniformity, and (c) multi-pin layers (i.e., 13 layers) for quantitative analysis of the image layer formation and its thickness. After designing the corresponding sequences of the motor control and the pixel readout for each test phantom, we acquired their DPT images by using the prototyped DPT system at a tube voltage of 68 kV_p, a tube current of 8 mA, and a scan time of 13.2 sec, as shown in **Fig. 6**. Note that in the image acquisition with the multi-pin layer phantom the middle layer (i.e., the 7^{th} layer) was designed to be focused.

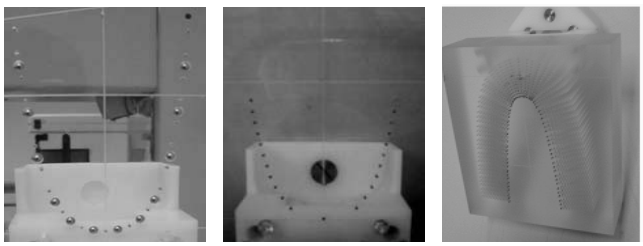

(a) (b) (c)

Fig. 5 Three test phantoms designed for the acquisition of DPT images with: (a) a single ball (ϕ 4 mm) layer, (b) a single pin (ϕ 1 mm) layer, and (c) multi-pin layers.

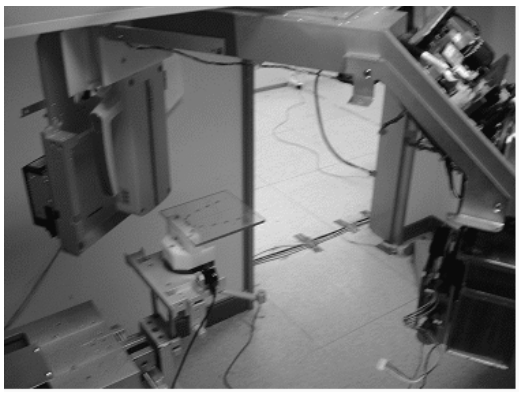

Fig. 6 Experimental setup for the acquisition of DPT images of the test phantoms.

4. Preliminary Test Results

Fig. 7 shows the DPT images acquired with the three test phantoms. As shown in **Fig. 7** (a), the balls placed on the POI trajectory were well focused, as we expected, indicating the motion control and the pixel readout sequences were precisely designed. However, the shapes of the balls became slightly distorted as being placed outside from the middle point of the POI trajectory. This may be explained by the parallax effect that occurs as the incidence angle of the X-ray beam into an object is oblique. **Fig. 8** shows the trajectories of the sliding rotation center and the POI, and the corresponding X-ray beam tracings calculated by using Eq.

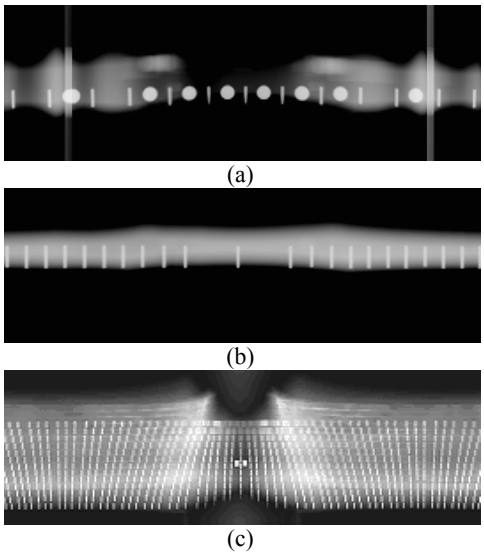

(a)

(b)

(c)

Fig. 7 DPT images acquired with the three test phantoms at a tube voltage of 68 kV_p, a tube current of 8 mA, and a scan time of 13.2 sec.

(2) for the test phantom of a single ball layer. As shown in **Fig. 8**, the X-ray beam tracings near the middle point are almost perpendicular to the POI trajectory, otherwise oblique. Thus, the shape distortion due to the parallax effect will be effectively removed, provided that the motion control sequence is designed to make the POI to be exposed perpendicularly to the X-ray beam.

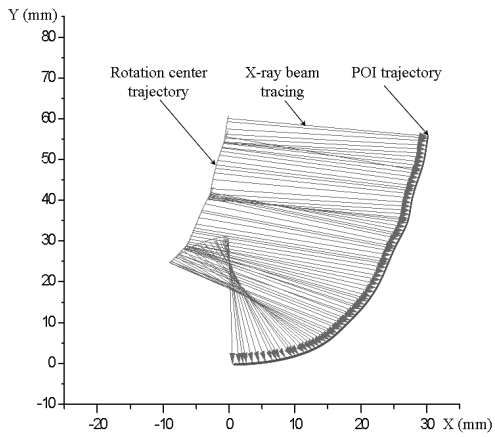

Fig. 8 Trajectories of the sliding rotation center and the POI, and the corresponding X-ray beam tracings for the test phantom of a single ball layer.

Fig. 9 shows the measurement of magnification uniformity over the POI in the scan direction, by comparing the pin distances measured from the original phantom data designed and the acquired DPT image. As shown in **Fig. 9**, there was no noticeable discrepancy in the pin distances measured, except for the pin distance *a* in the middle point; less than 5% for the pin distance *a*. In fact, since the starting

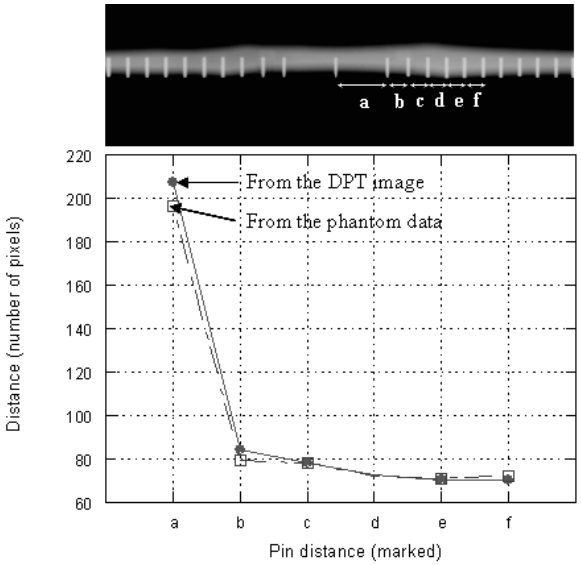

Fig. 9 Magnification uniformity over the POI in the scan direction, by measuring the pin distances from the original phantom data designed and the acquired DPT image.

point on the POI trajectory in the image acquisition, as indicated in **Fig. 3**, gradually moves forward to the middle point, the magnification uniformity may become degraded due to the accumulating rounding-off error in the calculation of the motor control sequence. Note that a ghost image appeared due to the overlapping of the blurred image of the pins on the other side, lowering the image contrast.

In **Fig. 7** (c), since the middle layer (i.e., the 7th layer) with a rectangular marker was designed to be focused in the calculation of the pixel readout sequence, this layer was well imaged with no blurring, as we expected; outer pin layers from the POI trajectory became more blurred. More quantitative analysis for the image layer formation and its thickness measurement is ongoing. Note also that a ghost image appeared due to the overlapping of the blurred image of the pins on the other side. More detailed description related to the image quality evaluation will be given in a separate paper.

III. Conclusion

As a continuation of our digital X-ray imaging sensor R&D, we have developed a prototyped digital panoramic tomography (DPT) system which can focus any shaped POI within an object. By using the imaging system incorporated with the adequate motion control and pixel readout sequences we designed, we, for the first time, succeeded in obtaining promising DPT images with several test phantoms. The designed layer to be focused was well imaged with no blurring and the other layers were blurred out. We also found that the shape distortion due to the parallax effect could be effectively removed, provided that the motion control sequence is designed to make the POI to be exposed perpendicularly to the X-ray beam. There was no noticeable discrepancy in the dimension between the original phantom data and the acquired DPT image, indicating excellent magnification uniformity over the POI in the scan direction. According to our preliminary test results, we expect the imaging system developed in this study to be useful for our future imaging applications such as nondestructive testings and dental panoramic radiography.

Acknowledgement

This work was supported by the Basic Atomic Energy Research Institute (BAERI) program of the Ministry of Science and Technology (MOST) under contract No. M2-0376-03-0000.

References

1) Albert Macovski, Medical Imaging Systems, Prentice-Hall Inc., New Jersey, 23 (1983).
2) D. Grant, "Tomosynthesis: A Three-dimensional Radiographic Imaging Technique," IEEE Trans. on Biom. Engineering, **19 (1)**, 20 (1972).
3) J. Garison, "Three dimensional Roentgenography," Am J. Roentgenol., **105**, 903 (1969).
4) J. Dobbins III and D. Godfrey, "Digital Tomosynthesis: Current State of the Art and Clinical Potential," Phys. Med. Biol., **48**, 65 (2003).
5) J. Liu, D. Nishimura, and A. Macovski, "Generalized Tomosynthesis for Focusing on an Arbitrary Surface," IEEE Trans. Med. Imaging., **8 (2)**, 168 (1989).
6) R. Halmshaw, Nondustructive Testing, 2nd Ed., E. Amold, London, 25 (1991).
7) Eric Whaites, Essentials of Dental Radiography and Radiology, 4th Ed., Churchill Livingstone, Edinburgh, 179 (2007).

Journal of NUCLEAR SCIENCE and TECHNOLOGY, Supplement 5, p. 407–409 (June 2008)

Influence of the Annealing Process for the Metal Contacts of the SiC Semiconductor Radiation Detector

Sang Mook KANG[1,2], Jang Ho HA[1], Se Hwan PARK[1], Han Soo KIM[1], Dong Hoon LEE[2] and Yong Kyun KIM[2*]

[1] *Korea Atomic Energy Research Institute, Deajon, 305-600, Korea*
[2] *Department of Nuclear Engineering, Hanyang University, Seoul, 133-791, Korea*

We have studied the radiation response of a prototype SiC radiation detector by using a 6H-SiC wafer. Metal contacts on the surface of the SiC samples were fabricated by using a thermal evaporator in a vacuum condition. Among the SiC samples, several samples were heated by a Rapid Temperature Annealing(RTA) device for 10 minutes at 300 ℃. The metal contacts on the annealed and non-annealed samples were scanned by using AFM(Atomic Force Microscope) before and after an annealing process. The current-voltage characteristics of the SiC detectors were measured by parameter analyzer and the radiation response was evaluated by ^{238}Pu with 5.5 MeV α-ray at room temperature and a atmospheric pressure. After annealing process, the surface roughness and the current-voltage characteristics decreased. The Schottky barrier heights of non-annealed and annealed SiC samples were determined as 0.638 eV and 0.688 eV, respectively. Also radiation response spectra of the annealed and non-annealed detectors were similar.

KEY WORDS: silicon carbide(SiC), radiation detector, semiconductor detector, annealing effect, alpha response

I. Introduction

Silicon carbide(SiC) has excellent properties as a semiconductor material, such as a wide bandgap, a high breakdown electric field, a high saturation velocity of electrons, a chemical inertness and a high heat conductivity. These are understood as originating from the strong bonds between silicon(Si) and carbon(C) in the SiC crystal.[1-2] Novel materials are continually researched in electronics, particularly in such applications area where the silicon properties have never been satisfactory.[3] On this score, a SiC semiconductor is an emerging material which is undergoing a rapid development for high-temperature applications in a high-level radiation field. Especially, the high temperature capability of SiC resulting from its large bandgap and high physical and chemical stability have generated significant interest in developing this material for various applications.[4] In this study, we measured the current-voltage characteristics and the radiation response of an Au/Ni/6H-SiC detector prior to and after an annealing process in an air condition.

II. Experimental Procedure

1. Fabrication Process

We used a 6H-SiC wafer of 2 inch in diameter supplied by the Dow Corning Company. The specifications of the 6H-SiC wafer are a 0.668×10^6 ohm-cm resistivity, a 387 μm thickness, and a (0001)-oriented type. We prepared 10×10 mm^2 samples by using a semiconductor diamond saw with UV tape. We also drew a line at a 100 μm depth using a diamond saw to discriminate between the Si-face and the C-face because a 6H-SiC single crystal wafer is transparent. Accordingly, the Si-face has two lines at intervals of 2.5 mm.

In the normal process, surfaces of a SiC wafer are generally etched by H_2SO_4 and H_2O_2 solutions and rinsed with de-ionized (DI) water; the removal of an oxidation layer by a HCl solution is also performed. In this study, only acetone was used during the etching process and the samples were rinsed with DI water because of their excellent chemical properties. This could shorten the work time of the etching process. Metal contacts on the surfaces were processed by a thermal evaporation under a 1.2×10^{-5} Torr vacuum condition, at 80℃ heating and a 180°/min rotation of the SiC sample holder. The final SiC samples had metal contacts of a Si-face / Ni (30 nm) / Au (300 nm) and a C-face / Ni (30 nm) / Au (300 nm). The diameter of the circular metal contact was 5 mm.

After the metallization process, several samples were annealing by using a Rapid Temperature Annealing(RTA) system at 300 ℃ for 10 minutes in Air condition. The surface roughness of samples was scanned by using an AFM(Atomic Force Microscope) before and after an annealing process.

To measure the current-voltage characteristics and radiation response, the annealed and non-annealed samples were fixed with a conducting epoxy onto a PCB layer and connected by a wire. The PCB layer was made of a FR4 substrate with a 10×10 mm^2 Au electrical contact pad.

2. Measurement of the I-V Characteristics and Radiation Response

The current-voltage characteristics of the prototype SiC radiation detectors were measured using Keithley 4200-SCS with a self voltage source. A typical measurement was

*Corresponding Author, Tel No: +82-2-2220-2354, Fax No: +82-2-2296-2354, E-Mail: ykkim4@hanyang.ac.kr

made under a biased voltage in the range -100 to 100 V. The wire terminal was connected to the high voltage power supply and the PCB electrical contact pad was connected to the ground. The biased voltage was supplied at 0.2 V intervals at the wire terminal.

The radiation response was evaluated by ^{238}Pu radioactive isotope source with 5.5 MeV at room temperature and an atmospheric pressure. Pulse height spectra were obtained by preamplifier based on Cremat's hybrid chip and its evaluation board, ORTEC's shaping amplifier, and a multi-channel analyzer.

III. Results and Discussion

1. AFM

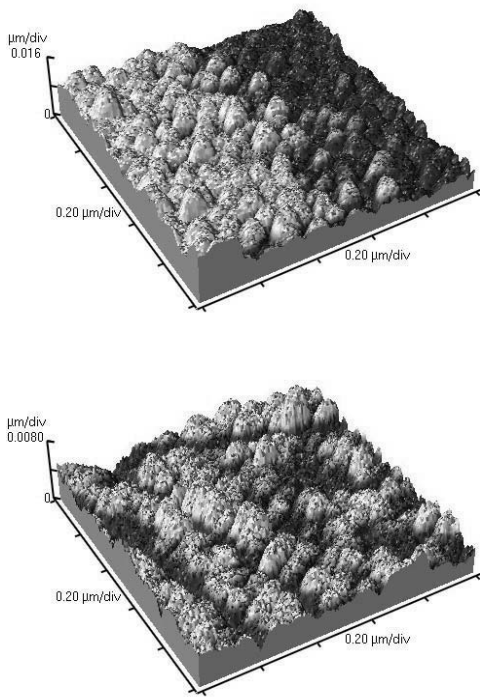

Fig. 1 AFM measurement of the surface roughness of the metal contact before and after an annealing process at 300 ℃(scan size 1x1 μm^2)

Fig. 1 shows the surface roughness of the metal contact measured by AFM before and after an annealing process at 300℃. The scan size of the images is 1x1 μm^2. After an annealing process, the maximum value of the roughness decreased to almost half value comparing with that of the non-annealed detector in non-bubble flat region. By using microscope, the surface was observed and it is showed in **Fig. 2**. A lot of bubbles with diameter around 10 to 30 µm could be observed on the surface. These bubbles cause the surface morphology change and may be formed from the sintering of Ni/Au and degrade the properties of the metal-semiconductor interface.[5] As a result, it can be understood that annealing process resulted in the increase of the surface resistance.

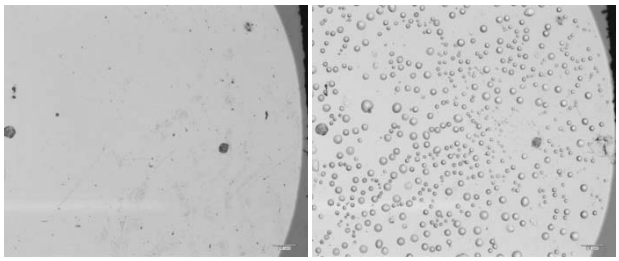

Fig. 2 Microscope images of the metal contact before(left) and after(right) a 300 ℃ annealing process(magnification 50)

2. Current-Voltage Characteristics

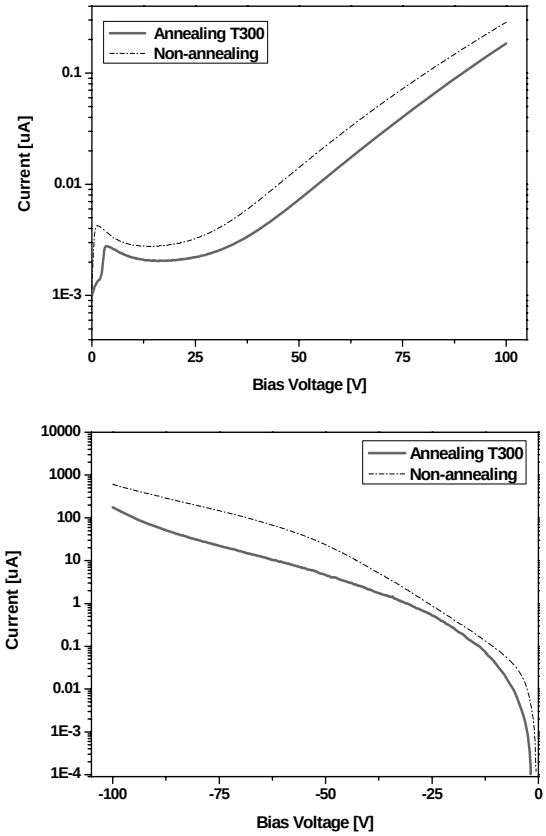

Fig. 3 The forward(top) and reverse(down) current-voltage characteristics of the annealed and non-annealed SiC detectors

The forward and reverse current-voltage characteristic of a detector prior to and after an annealing process was measured in the range from -100 to 100 V and it is presented in **Fig. 3**. The measurement was performed at room temperature and at an atmospheric pressure. The measured I-V characteristics were interpreted that the detectors were the Schottky type at the metal-semiconductor interface. After annealing at a temperature T = 300 ℃ in air, the reverse and forward currents decreased. It signified that Schottky barrier heights(SBHs) changed before and after the annealing process.

The current transport at metal-semiconductor contact is mainly due to majority carriers, in contrast to p-n junctions, where the minority carriers are responsible for it. For high-mobility semiconductors the transport can be adequately described by the thermionic emission theory. [6]

According to the thermionic emission theory, the flow is limited by the rate at which carriers try to cross the barrier; the Schottky barrier height was determined by using the forward current-voltage characteristics of the metal/semiconductor Schottky contacts. The total current density over potential barrier height is analyzed within the framework of the thermionic emission model originally described by Bethe [7]:

$$J = J_{ST} [\exp(qV/kT) - 1]$$

$$J_{ST} \equiv A^*T^2\exp[-(q\Phi_{Bn}/kT)]$$

where J_{ST} is the saturation current density, V is the biased voltage, k is the Boltzman constant, q is the carrier charge, Φ_{Bn} is the barrier height, T is temperature and A* is the effective Richardson constant for thermionic emission, neglecting the effects of optical phonon scattering and quantum mechanical reflection. By using the Richardson constant A* = 194 A/cm^2K^2 [9], the SBHs of non-annealed and annealed SiC samples were determined as 0.638 eV and 0.688 eV, respectively. Observed phenomena are determined by the defects in the interface between the metal and semiconductor, which are generated near the semiconductors' surface when the metal contact is deposited on this surface. [3]

3. Radiation Response

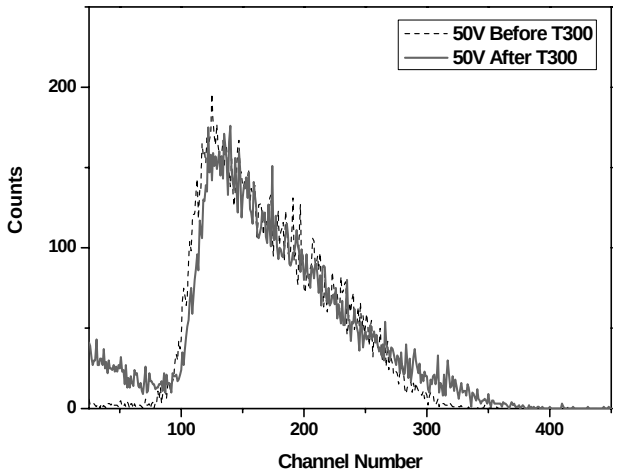

Fig. 4. Radiation response spectra before and after a 300 ℃ annealing with a biased voltage of 50 V

Fig. 4 shows the radiation response spectra of the non-annealed and annealed detectors. The radiation response spectra were evaluated by ^{238}Pu radioactive isotope source with 5.5 MeV, 6 μs shaping time, gain 60, and 600 sec collection times in an air condition and at room temperature. The radiation response spectra of the annealed and the non-annealed detector were almost similar except below energy region.

IV. Conclusions

6H-SiC semiconductor radiation detectors were fabricated with Ni/Au metal contacts and measured their current-voltage characteristic and radiation response before and after annealing process. After annealing process, the surface roughness decreased to almost half value comparing with that of the non-annealed detector and Schottky barrier heights were slightly increased. Radiation responses showed almost similar to the main energy peak before and after annealing process except for low energy region, which related electrical noise. This result meant that fabricated detector kept a good performance as a radiation detector after annealing process irrespective of the change of surface roughness and Schottky barrier heights. As a result, radiation detectors based on SiC semiconductor are available in high temperature environment.

Acknowledgement

This work has been carried out under the Nuclear R&D program of the Ministry of Science and Technology (MOST) and supported by the iTRS Science Research Center/Engineering Research Center program of MOST/ Korea Science and Engineering Foundation.

References

1) T. Ohno, "Recent Progress in SiC-Based Device Processing," Electronics and Communications in Japan, Part2, **82**[2], 128-133(1999).
2) L. Calcagno et al, "Effects of annealing temperature on the degree of inhomogeneity of nickel-silicide/SiC Schottky barrier," Journal of Applied Physics, **98**, 023713(2005).
3) M. Sochacki et al, "Influence of annealing on reverse current of 4H-SiC Schottky diodes," Diamond and Related Materials, **11**, 1263-1267(2002).
4) C. I. Harris et al, "Progress towards SiC products," Applied Surface Science, **184**, 393-398(2001).
5) C. Y. Hsu et al, "Effect of thermal annealing of Ni/Au ohmic contact on leakage current of GaN based light emitting diodes," Applied Physics Letters, **83**, 2447-2449(2003).
6) S. M. Cze, Physics of Semeconductor Device, second ed., Wiley, New York, 245-263(1981).
7) H. A. Bethe, MIT Radiat. Lab. Rep. 43-12(1942)
8) L. M. Porter, et al., "A critical review of ohmic and rectifying contacts for silicon carbide," Material Science and Engineering, **34**, 83-105(1995).

Journal of NUCLEAR SCIENCE and TECHNOLOGY, Supplement 5, p. 410–413 (June 2008)

Analysis of A Nuclear Material Accounting Uncertainty for ACP Spent Fuel Standards: MCNPX and ORIGEN-S Code Simulations

Tae-hoon LEE*, June-sik JOO, Kwang-june PARK, Hee-sung SHIN, and Ho-dong KIM

Korea Atomic Energy Research Institute, Daejeon, Korea

The target nuclide to be measured by using a neutron coincidence counter is Cm-244 for the PWR spent fuel since the dominant neutron-emitting source is Cm-244 for the spent fuel. Spent fuel standards (SFS) are usually used to calibrate the neutron coincidence counter for nuclear material measurements of spent fuel. To make the best selection and minimize the measurement uncertainty of neutron coincidence counter for the SFS, expected measurement errors for several kinds of burnups were obtained by using the ORIGEN-S code and the expected singles and doubles count rates were also acquired by using MCNPX code. The expected doubles count errors for 1 pellet of spent fuel are less than 4% for a burnup from 27 to 40 GWD/MtU. Considering everything, a higher burnup of the spent fuel seems to be better to obtain more accurate data from a nuclear material measurement by using a neutron coincidence counter than that of a lower burnup.

KEY WORDS: neutron coincidence counter, safeguards, calibration curve, MCNPX, and ORIGEN-S

I. Introduction *

Advanced spent fuel conditioning process (ACP) has been developed by Korea Atomic Energy Research Institute (KAERI) since 1997. This process is an electrolytic reduction process with which the volume, heat and radiotoxicity of the spent PWR fuel can be reduced significantly [1]. The construction of a hot cell for a lab-scale active demonstration of the ACP was completed in 2005 and all the equipments for the process and safeguards were installed in the hot cell. For the purpose of a nuclear material accounting and control (MA&C) for the ACP facility (ACPF), a neutron coincidence counter has been developed by KAERI in cooperation with LANL [2]. This paper describes the development of the ASNC, a preliminary calibration for the measurement of a dominant neutron source emitting spontaneous fission neutron and for a nuclear material accounting for the ACP nuclear materials, and an analysis of a nuclear material measurement uncertainty of the ASNC for the PWR spent fuel by using the ORIGEN-S code.

II. ACP Nuclear Materials and Neutron Measurements

There are various process materials in the ACP nuclear materials such as the rod-cuts of pressurized water reactor (PWR) spent fuel, U_3O_8 powder, uranium metal, salt waste, and hulls. In general, detection of neutrons and gamma-rays renders the quantification of special nuclear materials (SNM) like Pu or U-235 contained in the process materials. For the case of the ACP nuclear materials, the information about the gamma-rays of SNM can be distorted by the attenuation of the gamma-rays for a bulky sample as well as by the interference of the gamma-rays emitted from the fission products. On the other hand, a neutron detection method can be used for a bulky sample because of its almost negligible attenuation and it has no interference with the fission products' gamma-rays.

For the spent fuel, the neutrons are emitted by the spontaneous fission of the even-mass-number actinide nuclides and the most dominant neutron source is Cm-244 (usually more than 90% of the neutron population in the spent fuel). Because neutrons come from the induced fission of fissile nuclide such as U-235 or Pu-239 as well as from the (α, n) reaction of the α-emitting actinides with light nulides, a special technique composed of a neutron coincidence counter and a shift register is required to identify the spontaneous fission neutrons among all neutrons [3]. The neutrons emitted from a spent fuel are counted by using a neutron coincidence counter and the amount of Cm-244 in the spent fuel is measured. Usually, the ratios of Pu/Cm, U-235/Cm and U/Cm called the Cm ratios are obtained through a chemical analysis or ORIGEN code simulation and the mass of SNM can be accounted for with these Cm ratios and the results of the neutron measurements [4].

The ACP nuclear materials can be categorized into three groups according to their degree of increase of unwanted neutrons by the induced fission and (α, n) neutrons: (1) spent fuel rod cuts, U_3O_8 powder and hulls, (2) uranium metal powder and ingot, and (3) salt waste [2].

III. ACP Safeguards Neutron Counter

KAERI has completed the development of the ACP safeguards neutron counter (ASNC) for the non-destructive assay of the ACP nuclear materials. This neutron counter is a kind of neutron coincidence counter. The main parameters such as the neutron detection efficiency, die-away time and flat (or uniform) spatial efficiency in the sample holder

*Corresponding Author, Tel No: +82-42-868-8873, Fax No: +82-42-862-7313, E-Mail: typhoon@kaeri.re.kr

were calculated and optimized through MCNPX code simulations [2]. The main components of the ASNC are 24 He-3 gas detectors and amplifiers, a junction box which includes electronic parts, a neutron moderator of high-density polyethylene, a gamma-ray shield of lead blocks of a 6 cm thickness, neutron reflectors, and cadmium liners. **Fig. 1** shows the MCNPX geometry of the ASNC.

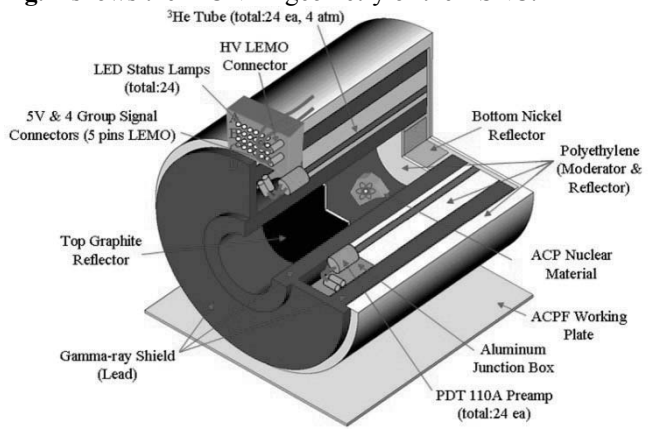

Fig. 1 MCNPX geometry of the ASNC

The main parameters of the ASNC were measured with two Cf-252 neutron sources. One is a weak source (~10^4 nps) and the other is a strong source (~10^6 nps). The strong source was cross-checked by the safeguards group of LANL. The neutron detection efficiency is 20.5% at 1650 V and the efficiency profile in the cavity of the ASNC is flat enough to obtain the coincidence counts in a short time and to reduce its spatial measurement deviation (σ: ±1.32% in the length of 33 cm). The ASNC has a special feature of a full remote maintenance capability in a high radiation environment. This was possible by adopting LEMO connectors and a horizontally-laid geometry. The broken parts can be replaced with new ones by using the remote manipulators in the hot cell. **Fig. 2** and **3** show the ASNC installed in the ACPF hot cell and its junction box and LEMO connectors.

IV. Preliminary Calibration of the ASNC

Three kinds of neutron counts are acquired from the neutron measurement of a nuclear material by using a neutron counter, shift register, and data acquisition program, called the International Neutron Coincidence Counting (INCC) program: singles (the number of single neutron events), doubles (the number of neutron pairs), and triples (the number of neutrons three at a time) rates [3]. For the case of a neutron coincidence counter, the singles and doubles rates are utilized for the measurement of nuclear materials since the measurement uncertainty of the triples rate is large and a large counting time is required.

Fig. 2 ASNC installed in the ACPF hot cell

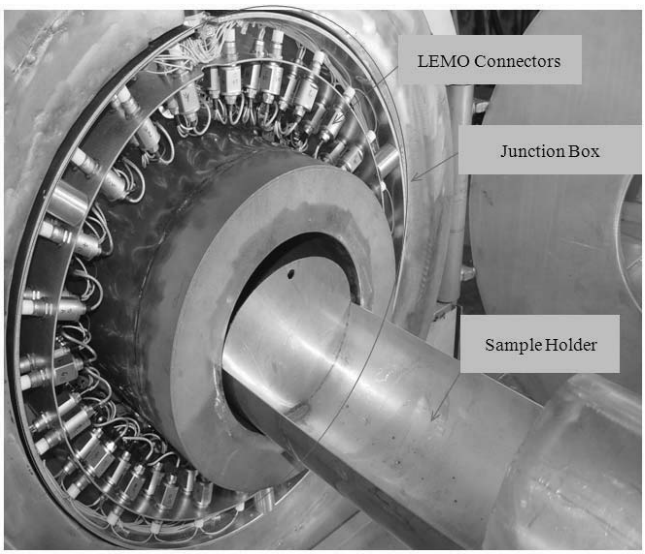

Fig. 3 Junction box and LEMO connectors of the ASNC

The relationship between the doubles rate and the amount of Cm-244 is obtained through the measurement of nuclear materials and a calibration curve is generated. A preliminary calibration coefficient for a non-multiplying sample for the ASNC was obtained by using the point model equation relationship between Cm-244 and Cf-252 [5]. A Cf-252 neutron source can be regarded as a point neutron source because its size is very small and there is almost no neutron multiplication in it. The singles, doubles, and triples rate from spontaneous fission can be obtained by using the point model equations [3]. The relationship between the doubles rates of Cm-244 and Cf-252 is described by the following equation:

$$\left(\frac{D_{Cm}}{m_{Cm}}\right)=\left(\frac{D_{Cf}}{m_{Cf}}\right)\left(\frac{F_{Cm}}{F_{Cf}}\right)\left(\frac{\varepsilon_{Cm}}{\varepsilon_{Cf}}\right)^{2}\left(\frac{(\nu_{s2})_{Cm}}{(\nu_{s2})_{Cf}}\right)=B\cdot\left(\frac{D_{Cf}}{m_{Cf}}\right)=k \quad (1)$$

where D is the doubles rate, m is the mass, F is the spontaneous fission rate, ε is the neutron detection efficiency, ν_{s2} is the second reduced *moment* of the spontaneous fission neutron distribution, and k is the calibration coefficient. Table 1 shows the values of the parameters used for the calculation of the preliminary calibration coefficient of the ASNC. The neutron detection efficiency for the Cf-252 spontaneous fission neutrons was measured by using the ASNC and that for the Cm-244 was obtained through the MCNPX code simulation. The preliminary doubles calibration coefficient for the ASNC is 2.78×10^5 [Doubles counts/s/g Cm-244]. **Fig. 4** is the preliminary calibration curve of the ASNC for the Cm-244 mass measurement [5].

Table 1 Parameters for the calculation of the preliminary calibration coefficient of the ASNC

	Cf-252	Cm-244
F	6.23×10^{11}	4.11×10^{6}
ε	0.208 (Measured)	0.211 (MCNPX)
ν_{s2}	11.962	5.939

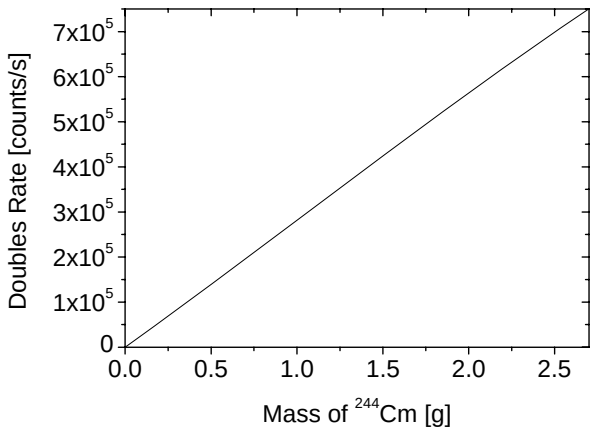

Fig. 4 Preliminary calibration curve of the ASNC for the Cm-244 mass measurement

V. Analysis of Nuclear Material Accounting Uncertainty of the ASNC for PWR Spent Fuel

Before the hot operation of the ACPF, it is necessary to test the ASNC with Spent Fuel Standards (SFS) for an examination of the hot material measurement ability of the ASNC. This will include the Cm-244 measurement in a spent fuel and produce a preliminary calibration curve of the ASNC for the spent fuel. A gamma pileup can also be checked with the SFS. KAERI has a plan to introduce the SFS into the ACPF for the hot performance test of the ASNC. The current situation is that the G23 spent fuel assembly of Kori-1 PWR which is stored in the water pool of the post-irradiation examination facility (PIEF) of KAERI is available for the hot test of the ASNC. The analyses of the spent fuels source term and the uncertainty of the doubles rate expected in the measurement by the ASNC were conducted for various fuel burnups by using the ORIGEN-S code. This data will be used to determine which burnup is optimal for the calibration of the ASNC. Table 2 shows the results of the ORIGEN-S simulation and calculated values of the parameters for the PWR spent fuels with different burnups. For a higher burnup, more amount of Cm-244 is generated and thus the measurement uncertainty of the doubles rate of the ASNC is smaller than for a lower burnup. The uncertainty of doubles rate is defined as following equation:

$$\sigma_D=(D\cdot t)^{0.5}/t \quad (2)$$

where D is the doubles rate and t is the counting time.

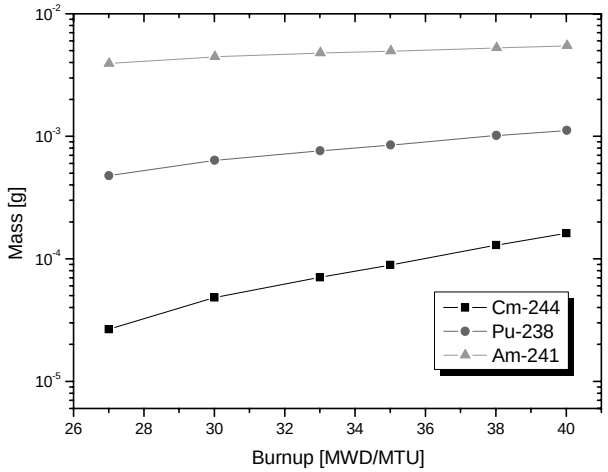

Fig. 5 Variation of mass of Cm-244, Pu-238, and Am-241 with burnup for 1 metric ton of uranium

An error caused by the assumption that all spontaneous fission neutrons are emitted from the Cm-244 nuclide is not significant because the degree of the contribution of the Cm-244's spontaneous fission neutrons to all the spontaneous neutrons is more than 94 % for all the burnup cases. As mentioned in section II, (α, n) neutrons are considered as a kind of 'noise' for the technique of a neutron coincidence counting. The main (α, n) neutron emitting nuclides of spent fuels are Cm-244, Pu-238, and Am-241. **Fig. 5** shows the variation of the mass of these nuclides with the burnup and we can see that the Cm-244 increases more rapidly compared to the other nuclides. Cm-244 nuclide is not only the most dominant spontaneous fission neutron source but also a strong (α, n) neutron emitter. The ratio of (α, n) to spontaneous fission neutron, α is an important parameter used in the neutron coincidence

counting technique. **Fig. 6** shows the variation of α value with the burnup. α decreases with increasing burnup because the increase of the Cm-244 amount has a greater influence on the increase of the spontaneous fission neutrons than on that of (α, n) neutrons. Taking everything into consideration, the PWR spent fuel of a higher burnup is better to obtain more accurate measurement data of a nuclear material of the ASNC than that of a lower burnup.

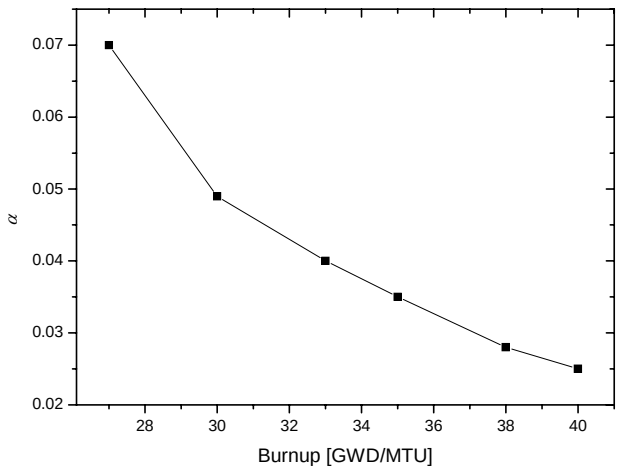

Fig. 6 Variation of α value with burnup

VI. Conclusions

The various parameters regarding a nuclear material accounting such as a measurement uncertainty of a doubles rate of the ASNC for the PWR spent fuel, the U-235 to Cm and Pu to Cm ratios, its total fissile content, and (α, n) to spontaneous fission neutron ratio were analyzed by using the ORIGEN-S code. Considering everything, a higher burnup of the PWR spent fuel seems to be better to obtain a more accurate data for the nuclear material measurement of the ASNC than that of lower burnup. The doubles count error of the ASNC with a 100 sec counting time for one pellet of PWR spent fuel is 1.5% for a 40 GWd/MtU burnup. The results of the ORIGEN-S code simulation should be compared and confirmed with actual measurement data for PWR spent fuels.

Acknowledgement

This work was performed under the long-term nuclear research and development program sponsored by Ministry of Science and Technology of Korea.

References

1) S. M. Jeong, S. B. Park, S. S. Hong, , C. S. Seo. and S. W. Park, "Electrolytic production of metallic uranium from U3O8 in a 20-kg batch scale reactor," Journal of Radioanalytical and Nuclear Chemistry, 268[2], 349 (2006).
2) T. H. Lee, H. D. Kim, K. J. Jung, and S. W. Park, "Development of a neutron coincidence counter for the Advanced Spent Fuel Conditioning Process," Journal of the Korean Physical Society, 48[2], 218 (2006).
3) N Ensslin., W. C. Harker, M. S. Krick, D. G. Langner, M. M. Pickrell, and J. E. Stewart, "Application Guide to Neutron Multiplicity Counting," LA-13422-M (1998).
4) H. O. Menlove, Y. G. Lee, H. R. Cha, W. Ko, S. Hong, and H. D. Kim, "The calibration of the DSNC for the measurement of Cm-244 and plutonium," LA-UR-99-6217 (1999).
5) H. O. Menlove, M. T. Swinhoe, and P. M. Rinard, "Calibration of Pu and Cm detectors using 252Cf," LA-13961-MS (2002).

Table 2 Various parameters regarding nuclear material measurement of PWR spent fuel as a function of their burnup (for 1 pellet of PWR spent fuel)

Burnup (GWd/MtU)	Expected Doubles Rate (counts/s)	Uncertainty of D (σ_D) for 100 sec Counting Time	Singles Rate (counts/s)	Cm-244's SF Neutron Contribut-ion (%)	Total Fissile Content (w/o)	U-235 + Pu Content (w/o)	U-235 /Cm Ratio	Pu/Cm Ratio	Activity (Ci)	α
27	7	0.26	64	94	0.61	0.77	44.3	1656.5	1.38	0.070
30	13	0.36	115	96	0.63	0.83	23.6	976.7	1.56	0.049
33	20	0.45	168	96	0.64	0.86	15.8	697.9	1.68	0.040
35	25	0.50	212	97	0.64	0.88	12.3	567.2	1.76	0.035
38	36	0.60	308	97	0.65	0.91	8.3	406.4	1.9	0.028
40	45	0.67	384	97	0.66	0.93	6.6	334.0	1.98	0.025

Journal of NUCLEAR SCIENCE and TECHNOLOGY, Supplement 5, p. 414–416 (June 2008)

A Remote Radiation Monitoring System Using an Autonomous Unmanned Helicopter for Nuclear Emergencies

Shin-ichi OKUYAMA[1*], Tatsuo TORII[1], Akihiko SUZUKI[2],
Masanori SHIBUYA[2], and Nobuyuki MIYAZAKI[3]

[1]*Tsuruga Head Office, Japan Atomic Energy Agency, 2-1 Shiraki, Tsuruga 919-1279, Japan*
[2]*Aeronautic Operations, Yamaha Motor Co., Ltd., 2500 Shingai, Iwata 438-8501, Japan*
[3]*Japan Radiation Engineering Co., Ltd., 1310 Mukaiyama, Naka 311-0102, Japan*

A feasibility study of a remote radiation monitoring system using an autonomous unmanned helicopter, mounted with a radiation detector and three CCD cameras, was carried out for surveying the dose-rate distribution of environmental radiation. This system can fly to destinations and return under automatic operation, measure radiation data during flight, and immediately transmit the data, including images, to a monitoring station on the ground. It is also possible to monitor the data on a map on a computer display in real time. Flight tests confirmed that the system can measure fluctuations of dose-rate distribution on the ground, and could be used for radiation monitoring in case of a nuclear emergency.

KEYWORDS: nuclear emergency, disaster prevention, radiation monitoring, Autonomous Unmanned Helicopter

I. Introduction

If a nuclear emergency were to occur at a nuclear installation and release a large amount of radioactive substances and/or radiation, radiation monitoring would be conducted from the sea and air as well as from the ground in the vicinity of the installation in order to estimate the dose-rate distribution around the installation, and the influence of radiation on residents. To monitor radiation from the air, manned helicopters equipped with radiation detectors could be used. However, although a manned helicopter can monitor a large area in a short time, the Aviation Law in Japan prohibits flying at an altitude lower than 300 m. This makes it difficult for a manned helicopter to measure the radiation profile near the ground and to measure the radiation level in complicated terrain. In recent years, technologies for autonomous unmanned helicopters (AUHs) for industrial use have been developed and are now being used to monitor disasters such as volcanic eruptions. We have developed a remote radiation monitoring system and investigated the possibility of using AUHs for aerial radiation monitoring during a nuclear emergency.

This paper reports the results of a feasibility experiment using an AUH equipped a radiation detector

II. Remote Radiation Monitoring System Using an Unmanned Helicopter

We have developed a radiation measurement system equipped with a large radiation detector to be mounted on an AUH, which can measure small fluctuations of the radiation. To obtain data on radiation on the ground in real time, we used a radiation distribution mapping system to display the measured data, and this system transmits the radiation data to a ground station every second.

The major specifications and the concept chart of the radiation measurement system are shown in **Table 1**, and **Fig. 1**, respectively.

Table 1 The radiation detector mounted on the AUH

Detector	Plastic scintillator (Size: 270W × 300D × 20T (mm
Dynamic range of dose rate	BG – 0.02 mSv/h
Energy range	> 60 keV
Data sampling	Every second
Weight	8.5 kg (including the cubicle)

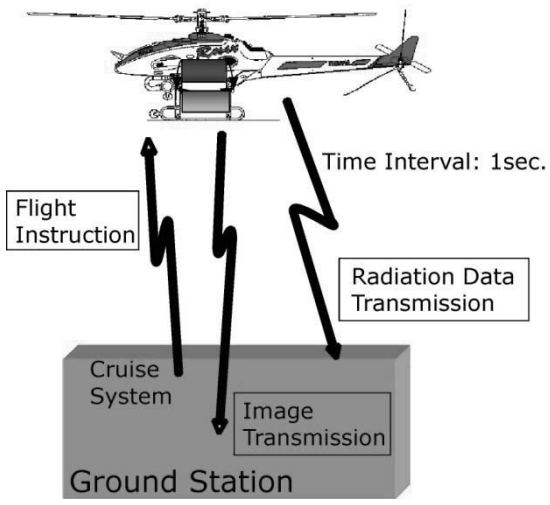

Fig. 1 Remote Radiation Monitoring System

*Corresponding Author, Tel No: +81-770-39-103, E-Mail: okuyama.shinnichi@jaea.go.jp

As the AUH, we used an industrial unmanned helicopter for crop spraying equipped with an autonomous function. In Japan where land is scarce and private houses are located close to farmland, unmanned helicopters are more useful than airplanes for crop spraying. About 2,000 helicopters are now in use and a maintenance system has been established. The main specifications of the AUH (RMAX, Yamaha Co., Ltd.) are shown in **Table 2**.

Table 2 The AUH system used in the experiment

Total length	3.63 m (including the rotor)
Weight	94 kg (main body = 58 kg)
Payload	10 kg (actually loadable weight)
Maximum flying rang	2 km (150 m in case of visual)
Flight duration	60 min. (90 min. with backup fuel tank)
Equipment	3 CCD cameras, GPS system

III. Experiment

To perform functional tests, potassium fertilizer for gardening use was placed on the ground and measurements were conducted by flying the unmanned helicopter in the air to investigate the response characteristics of the radiation measurement system. In addition, a flight test was conducted at an altitude of 30 m near the coast to measure the changes in background radiation.

1. Response to the Natural Radiation Source Put on the Ground

For the experiment, potassium fertilizer for gardening was used as a background radiation source, and the fluctuation of radiation was measured by flying the AUH over it (**Fig. 2**). Gamma rays emitted from K-40 were measured while flying the AUH at a constant altitude of about 3 m over the fertilizer (1.4 m X 1.4 m) on the ground and at a constant speed along a pre-programmed comb-shaped path in an autonomous program mode in order to investigate the response characteristics of the measurement system. The location of the fertilizer was correctly indicated on the monitor at the ground station (**Fig. 3**).

Fig. 2 The AUH flying above the fertilizer bags.

2. Measurement of Radiation Fluctuation above the Coast

The radiation fluctuation was measured while flying above the land and sea along the coast (**Figs. 4** and **5**). As shown in **Fig. 4**, the monitor at the ground station showed that the counting rate over the sea was lower than that over the ground, and thus the level of background radiation at sea is less than that on the ground. The counting rates above the land depended largely on the altitude at which the AUH was flown, while there was no significant variation in the counting rate at sea. The measured result of this experiment also shows the variation of the back ground radiation level over the land.

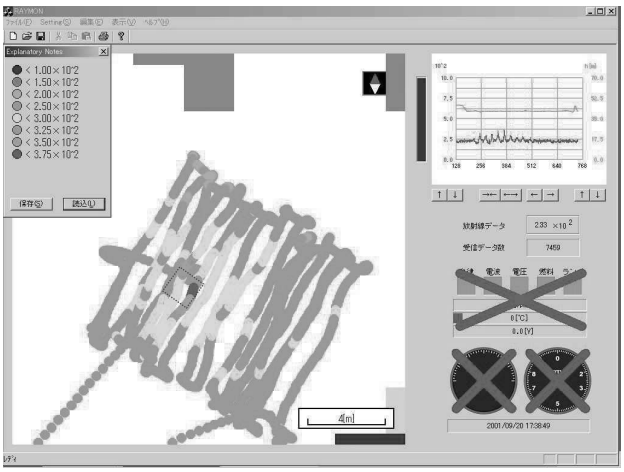

Fig. 3 A computer display showing the radiation level when flying over the fertilizers bags. A dotted line square means a rough position in which the fertilizer bags were put. The high dose-rate area seems to extend more than the region where the fertilizer bags were put, because the AUH flew at the speed of 2 m/s.

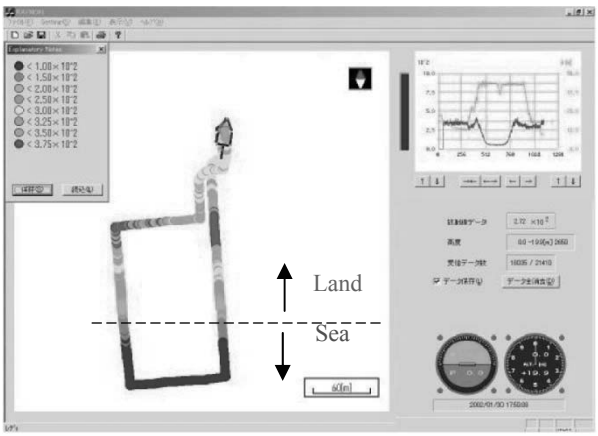

Fig. 4 Measurement result of natural radiation along the coast. The color marker shows the radiation level at each measuring point.

IV. Discussion

We have investigated the feasibility of a remote radiation monitoring system using an autonomous unmanned helicopter mounted with a radiation detector for surveying the dose-rate distribution of environmental radiation. Experiments showed that the system can quickly and

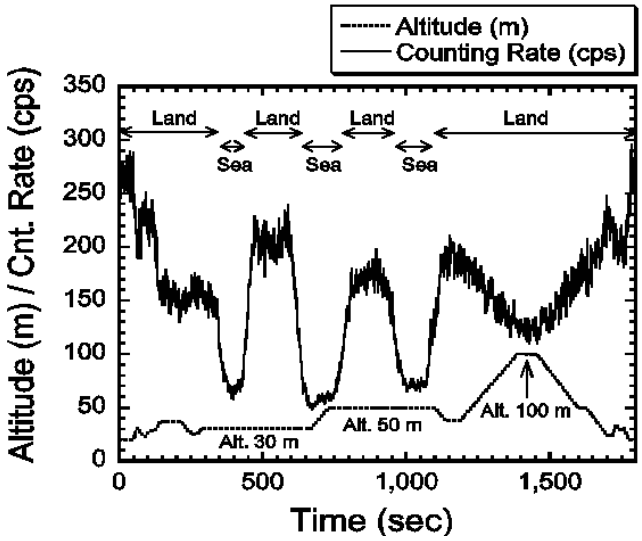

Fig. 5 The fluctuation of counting rate along the coast and the flying altitude of the AUH.

accurately measure the variation of the radiation level. In addition, we demonstrated that the ground station could generate real-time mapping of the radiation profile. Aerial radiation monitoring in a nuclear emergency using the AUH offers the following advantages:

- Measurement near the ground without being restricted by the Aviation Law
- Repeated measurements during a short time
- Radiation monitoring in complicated terrain because the flight route can be programmed in advance
- Radiation monitoring without risk of exposure by installing the ground station at a location with a lower dose-rate
- Stable operation, since the main body of the helicopter is identical to that of industrial helicopters and a maintenance system has been established

However, there are some problems to overcome before this system can be used for nuclear disaster prevention.

First, unmanned helicopters are not restricted by the Aviation Law, so controls are voluntarily imposed by manufacturers. It is necessary to clarify such restrictions on operation in case of a nuclear emergency, and to establish the system of operation in such an emergency.

Secondly, the experiment area was small, and so data transmission to an unmanned helicopter in a large area with complex structures such as nuclear power plants needs to be confirmed. Tests on the reliability of data transmission to the helicopter must be conducted, as the relay antenna is installed in such areas. It is also important to prevent radio interference, and to reduce the weight of the helicopter in case it were to crash into a building or equipment on the ground.

Acknowledgements

We thank staff of the Environmental Monitoring Section, Tsuruga Head Office, JAEA for their assistance.

References

1) Sato, A., "Research and Development and Civil Application of an Autonomous Unmanned Helicopter", *Proc. AHS International Forum*, p. 57 (2001).
2) Okuyama, S., Torii, T., Ito, Y., Suzuki, A., and Miyazaki, N., "Study on Environmental Monitoring Method using Unmanned Aerial Vehicle in Nuclear Emergency", 36th Annual Meeting of Japan Health Phys. Soc. 2002, A-6 [in Japanese]
3) Okuyama, S., Torii, T., Nawa, Y., Kinoshita, I., Suzuki, A., Shibuya, M., and Miyazaki, N., "Development of a remote radiation monitoring system using unmanned helicopter", ICS 1276, Elsevier, 422–423 (2005).

Journal of NUCLEAR SCIENCE and TECHNOLOGY, Supplement 5, p. 417–420 (June 2008)

Development of Alpha Detector Module based on Large Area PIN Photodiode

Kwang Hyun KIM[1*], Jin-Hyoung BAI[2], Joo Ho WHANG[2], and In sub JUN[3]

[1]*College of Dentistry, Chosun University, Gwangju, Korea*
[2]*Department of Nuclear Engineering, Kyunghee University, Kyunggi, Korea*
[3] *RadTek, Co., LTD, Daejeon, Korea*

Two alpha detectors based on scintillator coated PIN PD were manufactured and investigated for 3.5 MeV alpha particles. ZnO(Ga) and CsI(Tl) scintillators were coated on the large area of 1 cm x 1 cm PIN type photodiode, respectively. After connecting them with a charge sensitive preamplifier, system noise, signal output, and signal speed were measured and analyzed. Although the system noise after scintillator coating was increased, especially large in ZnO(Ga) coating, alpha detection was possible for both detectors. The output signal was relatively large in the CsI(Tl) coated detector compared with the ZnO(Ga) coated detector. In detection time test, the ZnO(Ga) coated detector showed the performance of about 3 times faster than the CsI(Tl) coated detector.

KEYWORDS: alpha detector, PIN type photodiode, CsI(Tl) scintillator, ZnO(Ga) scintillator

I. Introduction

Alpha detector is used in the associated particle sealed tube neutron generator for the Nuclear Materials Identification System (NMIS).[1), 2)] It is located in the neutron generator as a position sensitive detector with the property of fast response.[3)] Since the requirement of the detector is fast responsivity of several nanoseconds to the alpha particle generated in the neutron tube, gallium-doped zinc oxide, ZnO(Ga), of fast luminescence property has been considered as a coating material on a photosensor.[4), 5)] Generally, the ZnO(Ga), which converts an incident radiation to a light, was coated on a silicon detector or a Photomultiplier (PMT) in the alpha detector. In the research using the PMT, they used another metal film of Ni to detect only 5.5 MeV alpha particles from Americium-241 preventing other disturbances in the generator.

In our research, directly coated of ZnO(Ga) on PIN type photodiode (hereinafter "PIN PD") was investigated for 3.5 MeV alpha particles generated from accelerator, which is the same energy of the alpha particles in D-T reaction. Through the design of PIN PD by semiconductor simulation code and the design of scintillator by Monte Carlo simulation code, the alpha detector was fabricated including electronics. Thallium-doped cesium iodine (CsI:Tl) coated PIN PD was also manufactured and tested in order to compare each other as an alpha detector. Properties of the PIN PD and the scintillator coated PIN PD were investigated by measuring noise. System noise equivalent charge (NEQ) for the detectors was measured and analyzed in detail. In alpha detection at the accelerator, the output signal was analyzed for two detectors of scintillator coated PIN PDs.

II. Materials and Methods

1. Design and Fabrication of Alpha Detector

The considered scintillators to be coupled with the PIN PD were ZnO(Ga) and CsI (Tl) scintillators. The ZnO(Ga) scintillator is general for alpha particle detection since its decay time is several nanoseconds and the CsI(Tl) scintillator has the property of relatively large light yield compared with other scintillators. Since the transport distance of alpha with 3.5 MeV in any material is considerably short, the scintillators should be fabricated directly on a photodiode as a film using coating machine. Before coating of the ZnO(Ga) and the CsI(Tl) on the PIN PD, respectively, Monte Carlo simulation was performed to decide the thicknesses of the scintillator films using MCNPX code.[6)] The estimated thicknesses of each scintillator were 8.6 ㎛ and 21 ㎛, respectively to absorb fully the incident alpha energy of 3.5 MeV. In order to build up the ZnO(Ga) film on the PIN PD, the customized RF Magnetron Sputter System was used at the operating condition of 950°C temperature and increasing RF power/coating time of 80 W/2 hrs, 120 W/2 hrs, and 150 W/5 hrs gradually. The customized Thermal Evaporator was used to make the CsI (Tl) film on the PIN PD, fixed at the coating temperature of 200°C and the operating pressure of 1E-5 Torr. The target photosensor to be fabricated was large area of 1 cm x 1 cm PIN type photodiode. Using a semiconductor simulation code of ATLAS and the fabrication process parameters of Electronics and Telecommunications Research Institute (ETRI), the PIN PD was modeled.[7)] N-type silicon of (100) orientation substrate with 5 kΩ·cm resistivity and total thickness of 380 ㎛ was used in that ETRI process which provided around 0.1 ㎛ depth of P+ layer. Each PIN PD was surrounded by a P+ guard ring of 4 ㎛ width. **Fig. 1** shows two alpha detectors of the ZnO(Ga) and the CsI(Tl) coated large area PIN PDs. Each detector was mounted on ceramic substrates and two wires were connected as one for ground and the other for signal.

*Corresponding Author, Tel No: +82-62-230-6867, Fax No: +82-62-230-7451, E-Mail: radkim@chosun.ac.kr

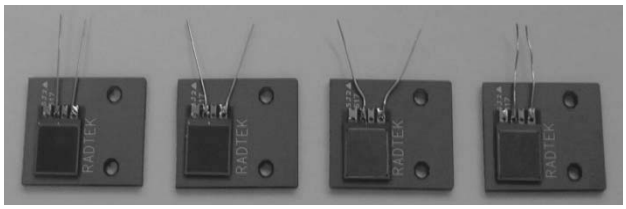

Fig. 1 Two ZnO(Ga) coated PDs (left) and two CsI(Tl) coated PDs (right).

2. Test Set-Up

For the PIN PDs, before and after scintillator coating on, the dark current to reverse bias and the terminal capacitance were measured by using a semiconductor parameter analyzer of HP-4145A since the PD is highly sensitive to the environment conditions such as temperature and impurities. A low noise charge sensitive preamplifier (CSA) of A 250F was selected to connect with each alpha detector. The noise equivalent charge (NEQ) was measured for three detectors of the PIN PD only, the ZnO(Ga) coated PIN PD, and the CsI(Tl) coated PIN PD as a function of Full Width Half Maximum (FWHM) by using a Multi Channel Analyzer (MCA) for input test pulses varying reverse biases. To measure the system noise at the output of the detectors, the sepectroscopies were performed for the known input charge of a High Voltage (H.V.) and a Low Voltage (L.V.) using the MCA. The pulses generated from the known voltages were entered into the input of the detectors through the calibration capacitor with 1 pF. The output part of the detector was connected to a shaping amplifier of 1 microsecond. Through the measured spectrum, the FWHM that is the statistical noise of the detector can be acquired. The measurement setup is shown in **Fig. 2**.

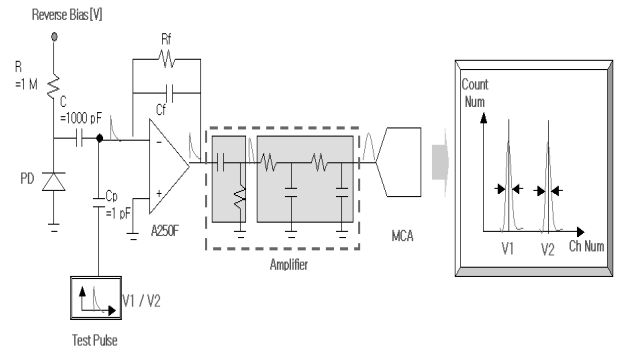

Fig. 2 NEQ measurement setup for alpha detectors using spectroscopy method.

The equations (1) and (2) give detail method to convert average voltage per a channel into the NEQ using a MCA and a test circuit including a feedback capacitor, C_f.

$$AvgV/Ch = \frac{1}{2} \times \frac{(FWHM@\,H.V + FWHM@\,LV) \times (H.V - LV)}{(PeakChannel@\,H.V - PeakChannel@\,LV)} \quad (1)$$

$$NEC\,(FWHM) = \frac{C_f \times (Avg.V/Ch.)}{q} = \frac{Q_N}{1.602 \times 10^{-19}} \quad (2)$$

Especially, Eq. (2) represents noise charge Q_N through the NEQ. The variation of the NEQ was measured as a function of reverse bias (V) for the detectors

We used a customized eletrooptical measurement system, located in the laboratory of Korea Advanced Institute of Science and Technology (KAIST), to measure the spectral response of the PDs. It consisted of a tungsten halogen lamp, a monochromator, and a set of optical powermeter and calibrated photodiode. Through a picoammeter and an automatic control system, the photocurrent generated in the PDs was measured. After each component was all integrated, the test of alpha detection was performed using He^{2+} Ion Accelerator (3.5 MeV, 0.15~0.5 nA) located in Korea Institute of Geoscience and Mineral Resources (KIGAM). Using a YOKOGAWA oscilloscope (DL9140), the variations of output voltage and pulse width from both scintillation detectors were measured for the current of 0.15 ~ 0.5 nA and the reverse bias of 0 ~ 6 V, respectively.

III. Results and Analyses

1. Property of PIN Type Photodiode

For the large area of 1 cm x 1 cm PIN PD, the dark current to reverse bias, terminal capacitance, and quantum efficiency were measured. The range of the dark currents was from ~ pico-ampere to ~ nano-ampere for near zero bias and 6 volt, respectively. The detailed values were plotted in **Fig. 5** comparing with the scintillator coated PD. The range of the terminal capacitances for the PD was 94 ~ 264 pF at the reverse bias of near zero bias and 6 volts, respectively, as shown in **Fig. 3**.

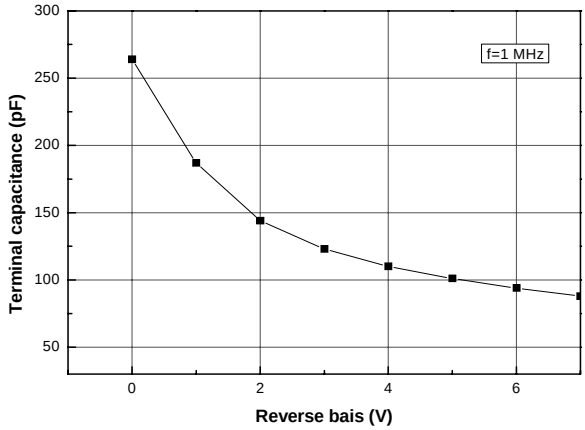

Fig. 3 Measured terminal capacitances for various reverse biases of the manufactured PIN PD.

The quantum efficiencies were compared between the simulated and the measured, and plotted in **Fig. 4**. In **Fig. 5**, while the simulated data followed general case of photodiode, the spectral response of the PD was the highest in the wavelength of 650 nm in the measured data. The spectral response of our concerned was 0.15 and 0.5 for the wavelengths of 380 and 565 nm emitted from the ZnO(Ga)

and the CsI(Tl). The reason the measured data are deviated from the simulated data may be explained by undulating light source, especially at low output power.

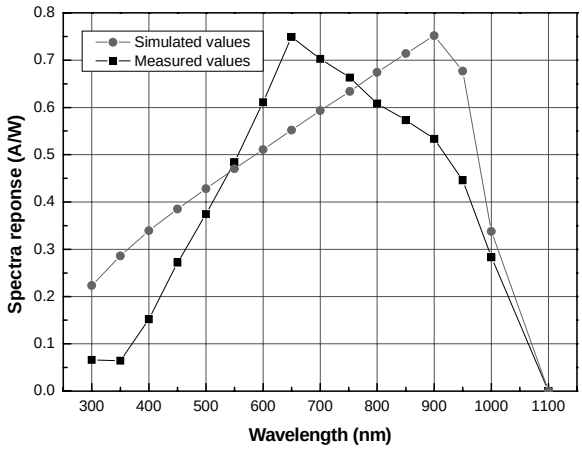

Fig. 4 Comparison of the simulated and the measured spectral responses for various wavelengths of the manufactured PIN PD.

2. Property of Scintillator Coated Photodiode

After coating each scintillator on each PIN PD, dark current to reverse bias was measured before and after scintillator coating. **Fig. 5** and **6** show the dark current variations for the ZnO(Ga) and the CsI(Tl), respectively.

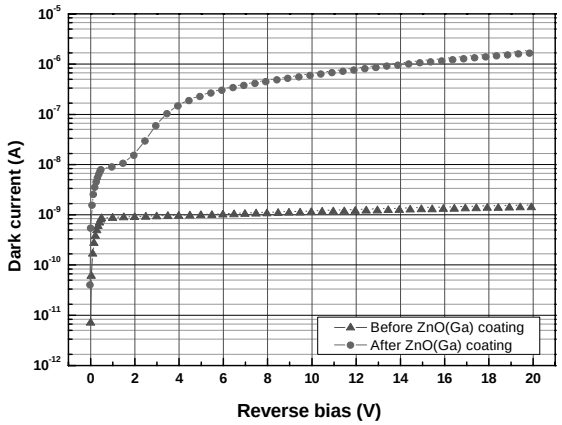

Fig. 5 Comparison of dark current variations before and after ZnO(Ga) coating on PIN PD.

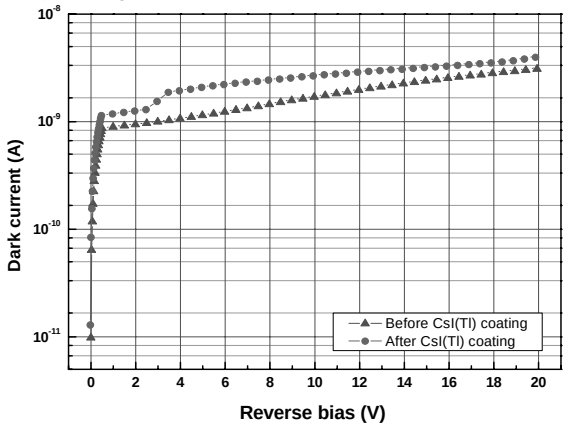

Fig. 6 Comparison of dark current variations before and after CsI(Tl) coating on PIN PD.

In both figures, there was abrupt dark current increase around 3 volts reverse bias after scintillators coating. It may be due to the reason that scintillator materials may act as inclusion of impurities on the surface of the photodiode and it reacts to a certain reverse bias. There was severe dark current increase, especially at the ZnO(Ga), and almost 100% and 47% increase at the reverse bias of 3.5 volts after the ZnO(Ga) and the CsI(Tl) coatings, respectively as shown in **Fig. 7**. It is believed that the coating temperature and the impurities of each scintillator mainly damage the photodiode.

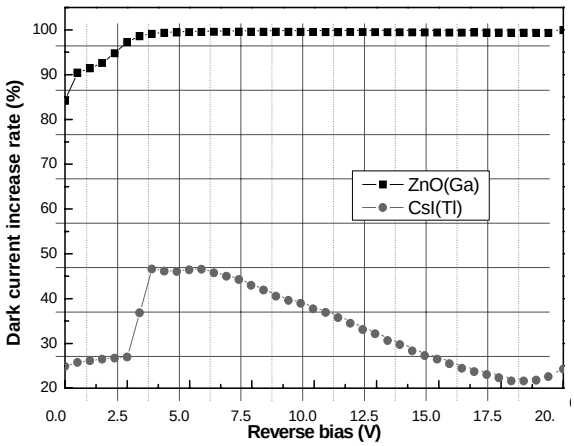

Fig. 7 Dark current increase ratio of before to after coating.

3. Noise Property of Alpha Detector

Using three detectors of bare photodiode without any scintillator, the ZnO(Ga) coated photodiode, and the CsI(Tl) coated photodiode, system noise of the NEQ was measured and displayed in **Fig. 8**. Generally, with increasingly reverse bias, its capacitance decreases and the dark current increases in a silicon photodiode. The system NEQ, however, in a semiconductor radiation detector with a CSA decreases by increasing reverse bias according to the decrease of the detector capacitance. This trend is appeared at the bare photodiode in **Fig. 8**. However, the NEQ of the CsI(Tl) coated detector showed slightly increase and there was no any variation of the NEQ for the ZnO(Ga) coated detector although the reverse bias increases. It may be due to the fact that the increment rates of the dark current after scintillator coating is relatively large as shown in **Fig. 7** and it dominates the system NEQ.

4. Alpha Detection

By increasing the accelerator current from 0.15 nA to 0.50, the output voltage (V) of the scintillator coated detector was measured as an alpha responsivity and the results were displayed in **Fig. 9**. While the early saturation of the voltage was occurred in the CsI(Tl) coated detector, the output voltage increased by the increase of the current. However, although the output voltage of the CsI(Tl) coated detector is large about 5% comparing with the ZnO(Ga) coated detector, this result didn't follow expected trend that the light efficiency of the CsI(Tl) is larger about 15 % over

the ZnO(Ga) per absorbed energy and 5 times over the ZnO(Ga) in the spectral response as shown in **Fig. 4**. It is possible to deduce two main reasons. Since the CsI(Tl) transparency was relatively bad compared with the ZnO(Ga) at a macrography, the detectible photons from the CsI(Tl) could be smaller than the ZnO(Ga). The other reason can be caused by the CsI(Tl) coverage of ~ mg/cm^2. While the ZnO(Ga) was coated by the RF sputter, the CsI(Tl) was coated by the thermal evaporator. In general, it has been known that the CsI(Tl) coverage in film type is highly dependent on the evaporation condition and the light yield per absorbed energy in the CsI(Tl) could be smaller in the unknown CsI(Tl) coverage. Unfortunately, the CsI(Tl) coverage was not measured and only the thickness of the CsI(Tl) was our concern in this study.

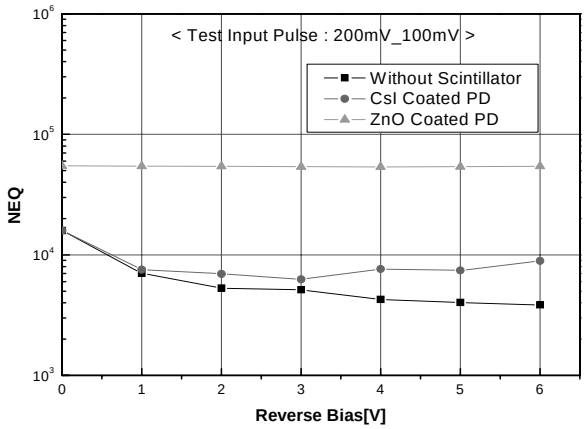

Fig. 8 Measured NEQs for two detectors and bare PIN PD.

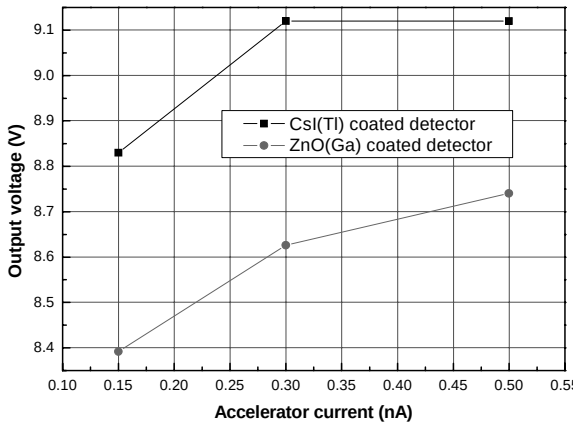

Fig. 9 Measured output signal in oscilloscope as a function of accelerator current.

Another try was to measure the response time of each detector. However, since the used oscilloscope didn't follow high speed of flash light emitted from scintillator, we failed measurement of its response time.

IV. Conclusions

In this study, the manufactured two alpha detectors based on scintillator coated PIN PD were investigated for 3.5 MeV alpha particle. The bare PIN PD without any scintillator coating showed good quality of optical and electrical properties. However, after coating the scintillators, the electrical property such as the dark current of the PIN PDs was changed and severe, especially at ZnO(Ga) coated PD.

Although the scintillator coated PIN PD showed increase of the system noise (NEQ), alpha detection was possible and the CsI(Tl) coated detector was superior to the ZnO(Ga) coated detector from the viewpoint of output signal. Both detectors showed good linearity property to alpha response up to 0.3 nA in an Ion Accelerator. Since the alpha detector in a neutron generator must satisfy event rates of up to 1 MHz [5], response time of the detectors will be measured in the next experiment even though the alpha response meets its performance.

Acknowledgement

This work was supported by the SRC/ERC program of MOST/KOSEF, and by MOCIE through EIRC program.

References

1) A. Beyerle, et al, "Design of an Associated Particle Imaging System," Nuclear Instruments and Methods in Physics Research, Vol. A299, 458-462, 1990.
2) J. T. Mihalczo et al, "Physical Description of Nuclear Materials Identification System (NMIS) Signatures," Nuclear Instruments and Methods in Physics Research, Vol. A450, 531-555, 2000.
3) J. C. Cooper et al, "Evaluation of ZnO(Ga) Coatings as Alpha Particle Transducers Within a Neutron Generator," Report No: Y/LB-16, 125, A BWXT/Bechtel Enterprise, 2002.
4) T. Batsch et al, "Timing properties of a ZnO(Ga) scintillator (NE843)," Nuclear Instruments and Methods in Physics Research, Vol. A125, 443-446, 1975.
5) J. C. Cooper et al, "Evaluation of ZnO(Ga) coatings as alpha particle transducers within a neutron generator," Nuclear Instruments and Methods in Physics Research, Vol. A505, 498–501, 2003.
6) MCNPX^{TM} User's Manual Ver. 2.5.0 April 2005 D. Pelowitz. Ed., Los Alamos Nat. Lab. Rep., Los Alamos, NM.
7) ATLAS User's Manual, Silvoco Int., Santa Clara, CA, 1998.

Journal of NUCLEAR SCIENCE and TECHNOLOGY, Supplement 5, p. 421–424 (June 2008)

Property of a CZT Semiconductor Detector for Radionuclide Identification

Sung-Dae CHUN[1,2], Se-Hwan PARK[1], Dong Hoon LEE[3], Yong Kyun KIM[3*], Jang Ho HA[1], Sang Mook KANG[1,3], Yun Ho CHO[3], Duk-Geun HONG[2], and Jong Kyung KIM[3]

[1]*Korea Atomic Energy Research Institute, Deajeon, Korea*
[2]*Department of Physics, Kangwon National University, Chuncheon, Korea*
[3]*Department of Nuclear Engineering, Hanyang University, Seoul, Korea*

Compound semiconductors of high Z value material have been studied intensively for X-ray and γ-ray spectroscopy at room temperature. CdZnTe has wide band gap energy as 1.6 eV and can provide high quantum efficiency with reasonably good energy resolution at room temperature. This study is aimed at determining radionuclide analysis ability by measuring energy resolution of CZT detector which will be applied at nuclear material identification purpose. For experiment we used a CZT detector (5 x 5 x 5 mm^3) which is manufactured by eV Products. We have performed our measurement at varied temperatures similar to the outdoor environment for the investigation about temperature dependence of energy resolution and peak centroid fluctuation of CZT detector by using gas cooling and Peltier cooling methods. In order to test radionuclide identification we used various radionuclide samples; plutonium, europium and other standard sources. Pulse height spectra were obtained by standard electronics which consists of a preamplifier, a shaping amplifier, and a multi-channel analyzer.

KEYWORDS: CdZnTe detector, Energy resolution, Peak centroid fluctuation, Temperature dependence,

I. Introduction

The cadmium zinc telluride (CdZnTe or CZT) is a semiconductor detector material which recently has received much attention because of good energy resolution, high effective atomic number for good γ-ray stopping efficiency and a wide energy bandgap(1.6 eV) for room-temperature applications. These properties made it possible to be used as X-ray or γ-ray detector which have a wide range of device applications including nuclear spectroscopy and imaging for medical and security purposes. A drawback on the other hand is the limitation on the maximum size of the semiconductor crystal, resulting in a low absolute efficiency and consequently requiring quite long measurement time in many applications [1, 2].

The CZT detectors, especially, are used in the field of nuclear safeguards to analysis radionuclide. The accurate analysis of radionuclide's spectra by using these detectors requires a correspondingly exact knowledge such as the response characteristic of CZT detector on various temperatures because gamma-ray spectrometers should have good stability versus temperature. This requirement is important if the spectral data are to be used for quantitative analysis, for example isotope identification [3, 4].

It is known that the CZT detector performance is greatly enhanced by lowering temperature of the CZT crystal. Previously, many researchers have studied the temperature dependency of the CZT detectors' performance. The variation of FWHM and peak height as function of the temperature was studied. Thermoelectrically cooled CZT detector was also studied between the temperature ranges from 30 ^oC to -40 ^oC [5, 6, 7].

In our work, the temperature dependency of the CZT detector performance was studied. The gamma-ray energy spectra such as energy resolution and peak centroid fluctuation were measured especially at the temperatures of the detector lower than room temperature from 10 to below zero degree. Therefore our study could evaluate a capacity of CZT detector's radionuclide analysis ability at the outdoor environment temperatures.

II. Method of the Study

The focus of this study was to evaluate the radionuclide analysis ability of CZT detector at various temperatures. A series of measurements were made to investigate temperature dependence of CZT detector by using two cooling method; gas cooling and Peltier cooling method.

1. Experimental Setup

(1) Measurement system by using a gas cooler

One of the detectors used for this experiment is a CZT detector probe module (model 297) which has a CZT crystal with size detector 5 x 5 x 5 mm^3 (model ev-180-5-5-5) manufactured by eV Products (USA). It contains an electronics module that houses a preamplifier, a unipolar shaping amplifier, and a bias supply optimized for use with CZT detector. We used an MCA (model 919E) made by ORTEC for this study. The experiments were carried out using standard radio-isotope (RI) sources ^{137}Cs, ^{133}Ba, ^{109}Cd, ^{57}Co, ^{238}Pu, and ^{152}Eu. The sources were placed on the front of detector window inside the cooling box. The measurement system used at this study is shown in **Fig. 1**

*Corresponding Author, Tel No: +82-2-2220-2354, Fax No: +82-2-2296-2354, E-Mail : ykkim4@hanyang.ac.kr

Table 1 FWHM and energy resolution data at room temperature for small size CZT detector (5x5x5mm^3) in the gas cooling system using various γ-ray sources

Radionuclide	Cs-137		Ba-133			Co-57		Cd-109		Eu-152			Pu-238
Energy (keV)	32	662	31	276	383	122	136	23	88	122	245	344	low energy X-ray
FWHM (keV)	2.97	11.3	2.71	7.06	7.51	3.47	1.05	2.71	3.15	3.98	4.72	6.58	7.15
Energy resolution (%)	9.28	1.71	8.74	2.56	1.96	2.84	0.77	11.8	3.58	3.27	1.93	1.91	35.7

The energy spectrum for each RI source was obtained at room temperature by measuring the gamma-rays for at least 30 minutes, sufficiently long to observe the peaks. To study the temperature dependence of the detector, we also acquired gamma-ray spectra at various temperatures using the selected radionuclide sources. To change the temperature, we used a cooling box that could easily reach temperatures down to -40℃. The cooling box housed the detector only, but RI sources and CZT probe electronic modules were placed outside the box to prevent the water vapor from condensing on them. The detector was cooled by supplying the dry ice gas into the cooling box and the temperature of detector system was measured with a thermocouple after stabilizing the temperature for half an hour. Energy spectra were taken at 25℃, 0℃, -10℃, -20℃, -40℃, and then energy resolutions at each temperature were evaluated.

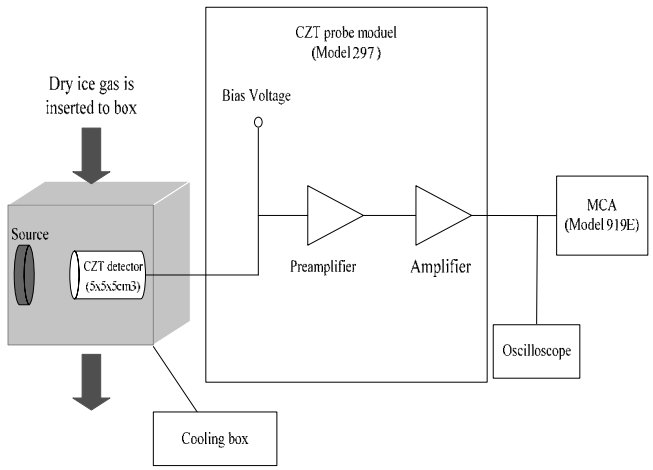

Fig. 1 Spectrum measurement system using gas cooler

(2) Measurement system by using a Peltier cooler

Another CZT detector employed in our work was a spectrum grade crystal with the dimensions of 5 × 5 × 5 mm^3. It was obtained from eV products. It was known that the Pt electrodes were deposited on both sides of the CZT detector. The signal electrode was connected to a metal plate with a conductive epoxy. The gamma rays from ^{241}Am and ^{57}Co were measured with this CZT detector. The signal from the detector was passed through the charge-sensitive preamplifier (eV products Model 550), and the amplifier (ORTEC Model 572). The shaping time of the amplifier was 1 μsec. High voltage was biased on the detector with a high voltage power supply (ORTEC Model 659). The high voltage on the detector was 200 V. Since the Peltier cooler can generate a noise in the detector signal, the detector was placed inside a metal shield box and the Peltier cooler was placed outside the box. The current on the Peltier cooler was increased to reduce the temperature of the CZT detector, and the temperature of the detector was measured with a thermocouple same to the gas cooling system. It was found that the thermocouple produced a noise in the detector signal. The thermocouple was also switched off during the measurement after stabilizing the cooled temperature.

III. Result of Experiment

1. Measurement at Room Temperature

This experiment was performed at 25℃ and with various radio-isotope standard sources. We obtained a full width at half maximum (FWHM) and energy resolution for the detector condition at room temperature. And the electronic circuit noise was estimated by measuring the FWHM of the pulser peak. We obtained a result of pulser FWHM with 1.0 keV; therefore we could ignore the circuit noise in the analysis procedure because of the small value. The typical FWHM value achieved for this detector was 11.3 keV at ^{137}Cs 662 keV peak. A summary of the FWHM and energy resolution data for this detector using various standard sources at room temperature was given in Table 1.

2. Measurement at Various Temperatures

(1) Measurement using the gas cooling system

Using the gas cooling box, we acquired energy spectra at each temperature condition. The results of measurements are shown in **Fig. 2**.

We found that the peak centroid of energy spectrum fluctuated during the cooling cycle. This fluctuation can cause a risk of peak misidentification. We evaluated the fluctuation of peak positions at each temperature for various isotope sources and acquired gain stability data. To evaluate this peak fluctuation, we used the room temperature peak positions as criterion, and temperature

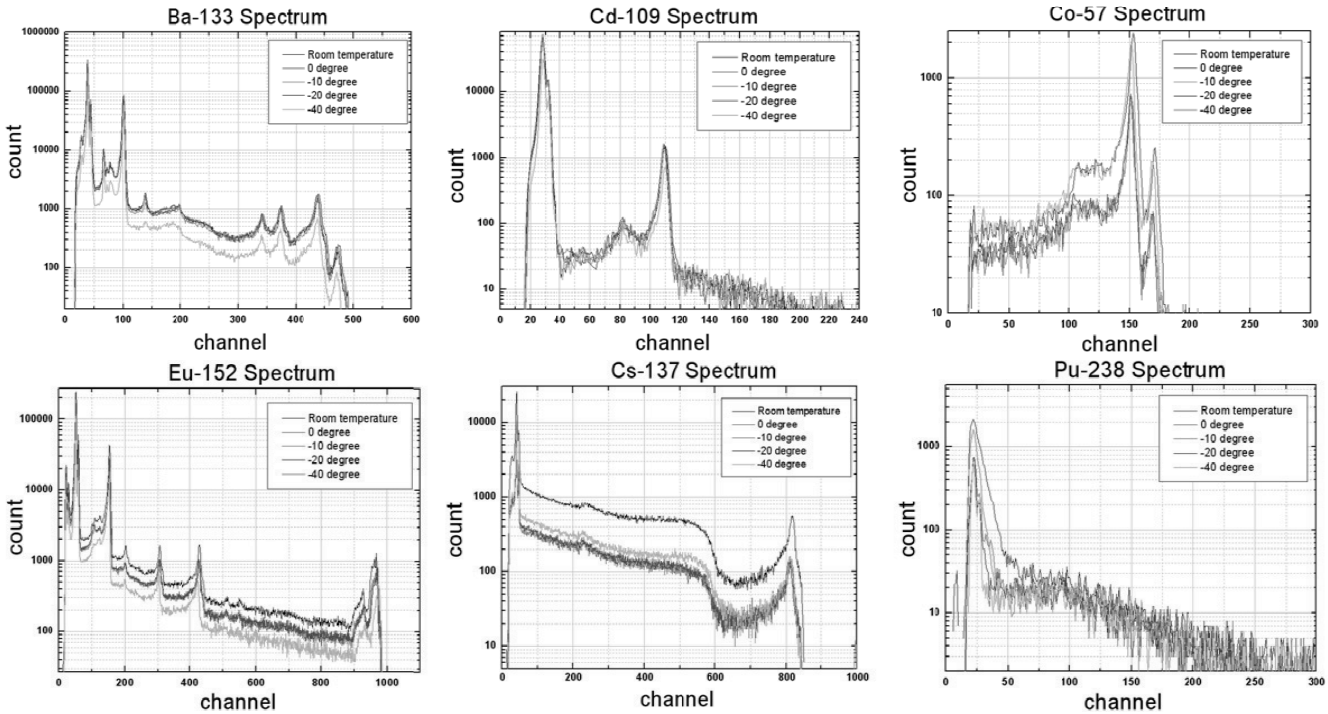

Fig. 2 Energy spectra taken with the CZT detector for each temperature condition in the gas cooling system using various standard γ -ray sources.

range was from 25℃ to -40℃. The tendencies of the peak position shift obtained from ^{57}Co RI sources are shown in **Fig. 3**. At the lower temperatures the peak position shifted to the lower channel than at the room temperature. Since these peak fluctuations depending on temperature have very small amount, there is no real risk of peak misidentification. And the peak energy resolution was also analyzed. We found that the energy resolution improved up to about 2% at the temperature range from 25℃ to -40℃ while cooling the detector.

These results show that the overall temperature effects, both in peak position and resolution, are not considerable from a practical point of view.

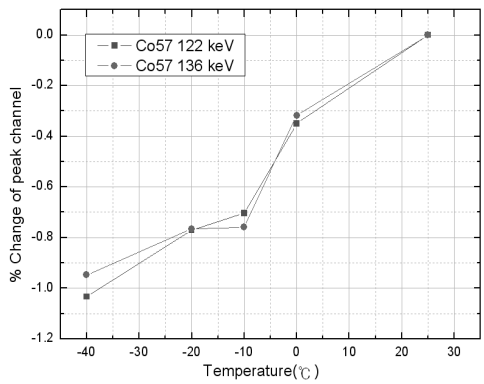

Fig. 3 Peak fluctuation data of ^{57}Co with CZT detector using the gas cooling system.

(2) Measurement in the Peltier cooling system

Using a Peltier cooling system, the energy spectra were measured at various temperatures from 32.6℃ to -9.6℃ with ^{57}Co sources. **Fig. 4** shows the measured spectra at 32.6℃ and -9.6℃ with ^{57}Co. Two spectra were measured with same bias voltages of 200V and show almost the same shape. The peak position of the energy spectrum measured at the lower temperature was shifted slightly to the lower channel than that of the energy spectrum measured at the higher temperature. **Fig. 5** shows the fluctuation of peak position for the CZT detector in the Peltier cooling system at 400V bias voltage and 0.5μs shaping time. The amount of peak fluctuation measured in the Peltier cooling system is larger than the gas cooling system's one, but the results of two systems show same aspects of peak position shift to the lower channel according to the lower temperature.

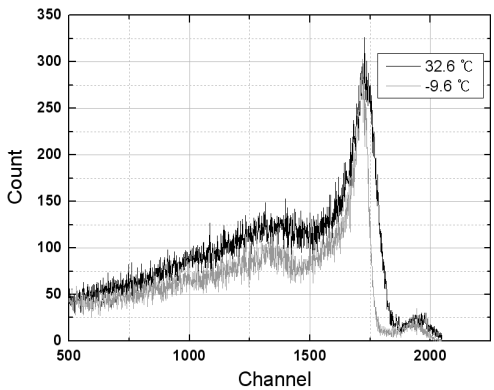

Fig. 4 ^{57}Co Gamma-ray energy spectra measured with the CZT detector at the 32.6℃ and -9.6℃ using the Peltier cooling system.

And by the temperature change from 32.6℃ to -9.6℃, the resolution was also improved about 3.54% at maximum in this system. **Fig. 6** shows the variation of FWHM values with ^{57}Co source for the CZT detector in the Peltier cooling system. It could be from a reduction of the leakage current at a lower temperature.

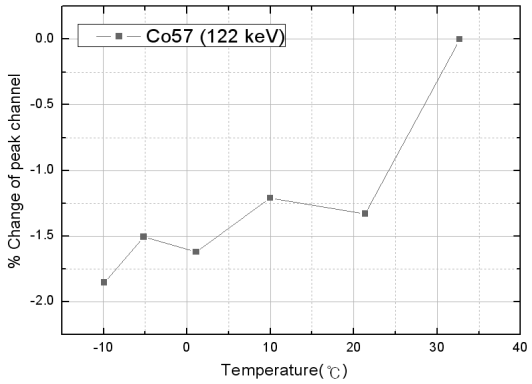

Fig. 5 Peak fluctuation of ^{57}Co with CZT detector in the Peltier cooling system.

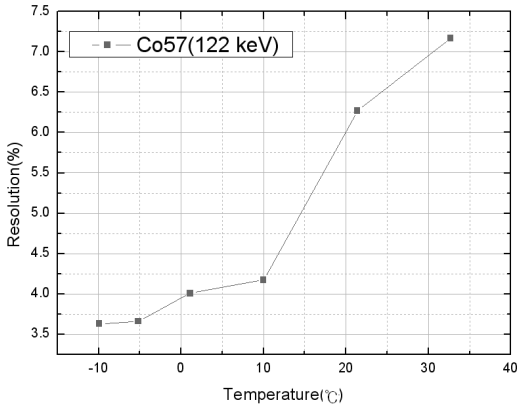

Fig. 6 Variation of FWHM values versus temperature for CZT detector in the Peltier cooling system.

IV. Summary

We have measured at various temperatures the energy resolution of a small size CZT detector (5 x 5 x 5 mm^3) manufactured by eV Products. The gas cooler and Peltier cooler were employed to lower the detector or the CZT crystal temperature. When the gamma-ray energy spectrum was measured at the same bias voltage, the results show some fluctuation of the peak position. Since this fluctuation value is very small, the energy spectra at the lowered temperature were almost the same as the energy spectrum at the room temperature.

A low crystal temperature could reduce the thermal noise of the detector. Also it could affect the charge carrier transport property inside the crystal. At the temperature changes from 32.6℃ to -9.6℃ using Peltier cooling system, the FWHM was improved about 4.1% at maximum.

In the present work, the energy spectra at different temperatures were measured at the same bias voltage and it was shown that the energy spectrum was not change significantly due to the temperature change from room temperature to -40℃. A CZT detector can be operated stably at the temperature range of the outdoor environment.

Acknowledgement

This work was performed under the nuclear research and development program by Ministry of Science and Technology of Korea, and also supported by the Innovative Technology Center for Radiation Safety (iTRS).

References

1) G. F. Knoll, *Radiation Detection and Measurement*, Wiley, New York, 353 (1989).
2) R. Arlt, M. Aparo, H. Boeck, and H. Zwickelstorfer, "Spectrum catalogue of gamma spectra taken with CdTe and CdZnTe detectors," Nuclear Instruments and Methods in Physics Research A **458**, 216-213 (2001).
3) B. W. Sturm, Z. He, T. H. Zurbuchen, P. L. Koehn, "Investigation of Asymmetric Characteristics and Temperature Effects of CdZnTe Detector," IEEE Transactions on Nuclear Science, **52**[5], 2068-2075 (2005).
4) R. Arlt, and D. E. Rundquist, "Room Temperature Semiconductor Detector for Safeguards Measurements," Nuclear Instruments and Methods in Physics Research A **380**, 455-461 (1996).
5) Y. Eisen, A. Shor, and I. Mardor, "CdZn and CdZnTe gamma ray detectors for medical and industrial imaging systems," Nuclear Instruments and Methods in Physics Research A **428**, 158-170 (1999).
6) G. Bale, A. Holland, P. Seller, and B. Lowe, "Cooled CdZnTe detectors for X-ray astronomy," Nuclear Instruments and Methods in Physics Research A **436**, 150-154 (1999).
7) W. Quam, "Cadmium-Zinc-Telluride (CZT) Gamma Ray Spectroscopy", DOE/NV/117-654 (2001).

Journal of NUCLEAR SCIENCE and TECHNOLOGY, Supplement 5, p. 425–427 (June 2008)

Beam Loss Monitor System for SSRF Storage Ring

Lei HOU[1*], Ming ZENG[1], Guanghua GONG[1], Beibei SHAO[1], and Yuxiong LI[2]

[1]*Department of Engineering Physics, Tsinghua University, Beijing 100084, P.R.China*
[2]*National Synchrotron Radiation Laboratory, University of Science and Technology of China, Hefei 230000, P.R.China*

A Beam Loss Monitor (BLM) system has been designed for Shanghai Synchrotron Radiation Facility (SSRF). The BLM system is utilized to detect beam loss around the electron storage ring. It will be helpful to find out the position of vacuum leakage, regulate the machine operation parameters, and study the beam lifetime. This paper will discuss some considerations in the BLM system design, including the detector selection, the beam loss mechanism, the detector location along the ring, and the structure of BLM system.

KEYWORDS: BLM system, SSRF, PIN diode detector, loss mechanism, shower electrons, ethernet

I. Introduction

Shanghai Synchrotron Radiation Facility (SSRF), a third-generation synchrotron radiation light source, is under construction now in Shanghai, China. SSRF consists of a 150-MeV LINAC, a booster that accelerates the electron bundles from 150 MeV to 3.5 GeV in 0.5 second, and a 3.5-GeV electron storage ring. **Fig. 1** is the structure map of SSRF.

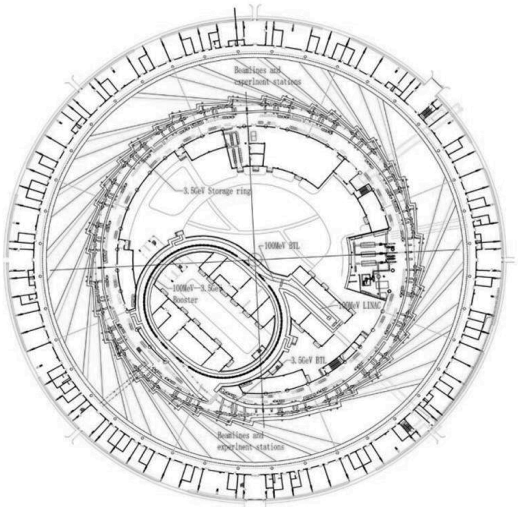

Fig. 1 The structure map of SSRF

During the construction, a beam loss monitor (BLM) system will be installed to detect the beam loss along the storage ring. This system will help tuning the machine in the commissioning and regulating the operation parameters, and also contribute to physics study like the beam lifetime research.

II. Detector Selection

From the mechanism of beam's losing particles, shower occurs when electrons hit the vacuum chamber wall [1]. During this process, shower electrons are generated which carry more distinct position information of lost particles than the generated photons and neutrons do [4]. So it is decided to monitor the beam losses by detecting the generated shower electrons.

In this case, the PIN photodiode detector originally designed at DESY is employed. This detector is sensitive to shower electrons (the detection efficiency to the shower electron whose energy higher than the minimum ionizing particle is over 30 %), but nearly has no response to photons and neutrons (its sensitivity to gamma is lower than 0.06 %) [4].

III. Loss Mechanism

In the design of the BLM system, the beam loss mechanism needs to be carefully studied. Mainly three effects will determine the lifetime of beam under normal situation. They are the quantum effect, the Touschek effect, and the inelastic scattering [5].

1. Quantum Effect

The beam in the storage ring appears in Gaussian particle distribution. Since the beam transverse apertures and the energy acceptance would never range unlimited, the quantum effect always exists. If the RF voltage is large enough, the quantum lifetime is mainly dominated from the horizontal aperture. [5] Since the horizontal aperture of the SSRF beam pipe is large enough, the quantum effect can be omitted.

2. Touschek Effect

The Touschek effect is from the collision of inner-bunch particles, which is elastic and may make large momentum changes [4]. This kind of loss always involves a pair of electrons. When the collision happens and an electron loses a certain amount of longitudinal momentum, there must be another electron that gains the same energy in opposite directory [6]. So the chances to hit inner or outer wall of the vacuum chamber are equal.

*Corresponding Author, Tel No: +86-10-6278-2026, Fax No: +86-10-6278-2026, E-Mail: houlei00@mails.tsinghua.edu.cn

3. Inelastic Scattering

When the electrons collide with residual gas molecules, they may lose energy and change their orbit. If the energy loss exceeds a certain amount, the losers will hit the inward wall of the chamber during or after passing dipoles. [4]

The three loss mechanisms above are what the BLM system aims to. Generally, for high energy machines, the quantum effect and the Touschek effect are not as serious as inelastic scattering. In many high energy machines, the BLM detectors are only equipped in the inner side to detect inelastic scattering.

The electron beam energy is 3.4 GeV in SSRF. It is not high enough to neglect the Touschek effect. Thus a pair of detectors will be placed at both the inner and outer sides of the chamber.

IV. Detector Location

To find out the best location to place detectors, it is necessary to calculate the position of the shower electrons induced by lost particles.

When the electrons lose energy, they will deviate from the normal orbit. The deviation mostly depends on the dispersion (η) function, the β function, and the lost energy (ΔE). When the lost energy exceeds a certain value, the electrons will hit the inward wall of the chamber and get lost. [3]

Thus the η and the β functions will give a clue where the electrons will most possibly get lost. The peak positions of the η and the β functions are the most interesting places for loss monitor.

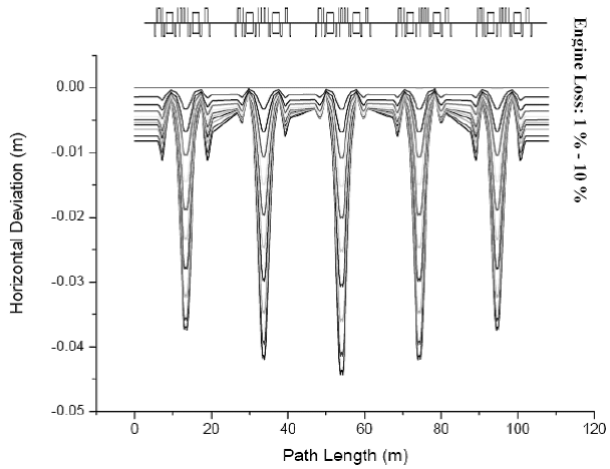

Fig. 2 The path of electrons in SSRF storage ring with loss energy from 1 to 10 % [2]

Fig. 2 shows the path calculated for electrons in SSRF storage ring with an energy loss from 1 to 10 %. Since the critical horizontal deviation of the SSRF beam is about 2.5 cm, the electrons with energy loss more than 6 % will hit the inward wall of the chamber and get lost. This figure also shows the most possibly lose position of particles. Then we can get the rough place for loss monitor. [3, 5, 7]

V. System Structure

The BLM system is a distributed data acquisition system

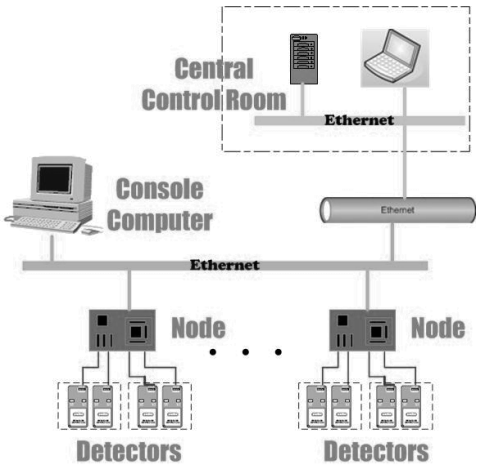

Fig. 3 The structure of BLM system

based on Ethernet. It is composed of detecting nodes and the console computer, as shown in **Fig. 3**.

Installed after all the dipoles and the injecting point, 43 monitor points will be set up along the storage ring, each with detectors in both sides.

The data collector node is able to record signals from 4 detector channels. Hence two monitor points, each consisting of two detectors, share a data collector. The data collector counts pulse signals from all the four detectors, buffers the data inside, and transfers the data when receiving an acquisition command from the console computer.

The console computer is the master in the distributed system. It broadcasts time stamp packets in certain frequency to synchronize all the nodes, sends out data acquisition command to fetch data log from all the nodes, and shows users the beam loss information of data log. The console computer also provides a general data access interface via Ethernet. Then the central control room can access the console computer through Ethernet and integrate the beam loss log data into the whole control system database.

VI. Experiments at HLS and Conclusions

Because the construction of SSRF storage ring is not finished, several testing experiments have been carried out in Hefei Light Source (HLS).

HLS is a second-generation dedicated light source at National Synchrotron Radiation Laboratory (NSRL), which has an 800-MeV electron storage ring.

Fig. 4 shows a beam loss monitor example on HLS. During injection, because of operation parameter regulating and beam ramping, the beam loss is very large. After injection, the beam loss falls immediately. Then it goes down slightly, just like the beam current does. The curve is very similar as an exponential function of time. At the point

of beam extraction, the entire beam gets lost suddenly, which makes the monitor get another large loss value. In the whole process, the detected beam loss matches the machine's operation very well.

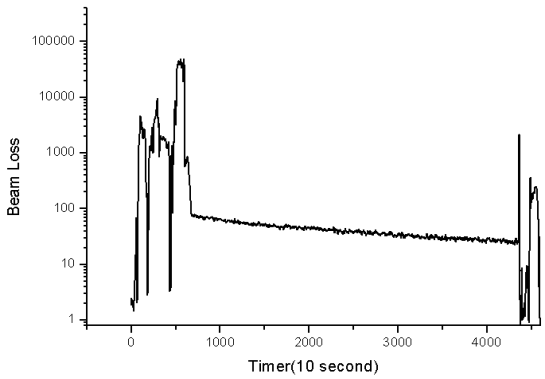

Fig. 4 Beam loss monitor on HLS

In the experiments at HLS, the detectors, the data collector nodes, and the software of the console machine work well as expected. The whole system is proved sensitive and steady enough for beam loss monitor.

References

1) K. Wittenburg, 'Beam Loss Detection,' Proceedings of 1st DIPAC93, Montreux, CERN PS/93-95, 1993.
2) Z. Dai, G. Liu, N. Huang, et al., 'Design of the SSRF Storage Ring Magnet Lattice,' Nuclear Science And Techniques, vol.14, pp.89-92, 2003.
3) Y. Cui, et al., 'Design of Beam Loss Monitor System for an 800MeV Synchrotron Facility,' Proceedings of the International Workshop on PCs and Particle Accelerator Controls, 1999.
4) Y. Li, et al., 'A New Tool for Beam-life Research at HLS Storage Ring,' Proceedings of the 2003 Particle Accelerator Conference, 2003.
5) J. Cui, L. Ma, et al., 'BEPC Storage Ring Beam Loss Monitor System Design,' Proceedings of the Second Asian Particle Accelerator Conference, 2001.
6) K. Wittenburg, 'Beam Loss Monitoring and Control,' Proceedings of EPAC, 2002.
7) W. Bialowons, F. Ridoutt, K. Wittenburg, 'Electron Beam Loss Monitors for HERA,' Proceedings of 4th EPAC, 1994.

Journal of NUCLEAR SCIENCE and TECHNOLOGY, Supplement 5, p. 428–431 (June 2008)

Development of Portable Thyroid Monitoring System for ^{131}I and ^{133}I in Nuclear Emergency

Mee JANG*, Hyun Ki KIM, and Chang Woon CHOI

National Radiation Emergency Medical Center, Korea Institute of Radiological and Medical Science, Seoul, Korea

In the event of emergency situation such as leakage of radionuclides from nuclear power plant, it has the potential for significant radiation exposure in large populations. ^{131}I and ^{133}I are major release radionuclides in a nuclear emergency and they are accumulated in the human thyroid. Therefore it is important to measure the iodine including short-lived radioiodine rapidly in the case of large casualties. The purpose of this study is to establish a thyroid monitoring system for emergency situation and to evaluate the factors influencing counting efficiency using Monte Carlo simulation of radiation transport in the mathematical phantom and the radiation detector.

KEYWORDS: thyroid, radioiodine, NaI detector, Monte Carlo simulation

I. Introduction

Accidental releases of radionuclides at the plant have the potential for significant radiation exposure in large population. ^{131}I and ^{133}I are major release radionuclides in a nuclear emergency, and they are accumulated in thyroid. Especially short-lived radioiodine ^{133}I should be accounted for the assessment of thyroid health effects because of higher radiobiological effectiveness by higher dose rate. For example it has been reported that the increased incidence of childhood thyroid cancer in Chernobyl accident area is due to the contribution of the short-lived radioiodine and ^{131}I to thyroid dose.[1)]

Because a fast identification of the population with radioiodine uptake is very important for subsequent measures, it is necessary to develop a thyroid monitoring system to be used for the estimation of the radiation dose by ^{131}I and ^{133}I in the nuclear emergency situation. For this purpose the thyroid monitoring system should have portability and the ability of fast examination, prompt data acquisition and dose estimation.[2)] Also it is necessary to establish the counting geometry and to investigate the factors that lead to errors and uncertainties related to counting geometry.

II. Methodology

1. Monitoring System

The monitoring system is for in-situ examination of the population in ^{131}I and ^{133}I released areas for fast screening of those with radioiodine uptake in a radiological emergency. The system would be operationally simpler and lighter than the conventional thyroid uptake monitoring system stationed in hospitals. It consists of scintillation detector NaI Model 8024(Canberra) with the most common sizes (51mm×51mm and 76mm×76mm) and Unispec multi channel analyzer. We use the Genie-2000 basic spectroscopy software for data acquisition, display and analysis.

2. Monte Carlo Simulation

To prevent the interference of the background radiation as well as the radionuclides deposited externally and internally in other part of the human body, a lead shielding and a collimator were designed. The thickness of the wrapping shield and the length of the collimator were to be determined by MCNPX simulation. The thickness of shielding wrapping around NaI is 0.5, 1, 1.5 and 2 cm and we assumed that background radionuclides are ^{40}K, ^{226}Ra, ^{228}U series and ^{232}Th series.[3)] The length of collimator is 0, 5, 10, 12 and 15 cm and we assumed that the radionuclides from body are ^{85}Kr, ^{133}Xe, ^{134}Cs, ^{137}Cs and ^{132}Te.[4)]

The factors influencing the counting efficiency were simulated for optimization of thyroid counting geometry. The detector was placed at 0, 5, 10 and 15 cm from the neck and then repositioned horizontally (on the x-axis) by 1 cm intervals from –4 to 4 cm. Also it was placed vertically (on the z-axis) by 1 cm intervals from 0 to 4 cm on both sides. Next, the response of detector was simulated as a function of the detection angle.

3. Mathematical Phantom

A primary step of the simulation was the modeling of the NaI(TI) detector. To experimentally check the detector model, simple detection geometry using physical thyroid phantom was used. However it is difficult to design the detector's shielding and to investigate the response under variable geometric conditions using physical thyroid phantom.[5)] So we used the mathematical phantom for shielding design and counting geometry, except for detector model's validation. We used adult phantom of the ORNL mathematical phantom series (1996). The dimensions of the thyroid and neck of ORNL mathematical phantom are listed in Table1.

*Corresponding Author, Tel No: +82-2-970-1425, Fax No: +82-2-970-2404, E-Mail: mjang@kirams.re.kr

Table 1. Characteristics of the thyroid and neck of ORNL mathematical phantom

Parameter	Adult male
Neck diameter (cm)	10.8
Neck height (cm)	8.40
Thyroid height (cm)	5.0
Thyroid volume (cm^3)	19.9

III. Results

1. Validation of Detector Model

To check the mathematical model of detector experimentally, ANSI neck phantom as physical thyroid phantom was used. This phantom consists of acrylic cylinder with one source vial channel to simulate the thyroid. The detector was calibrated about energy and efficiency using the standard gamma source. We used the ^{131}I source vial, and checked the validation of detector model comparing the calculation and measured values. A comparison of calculated results with experimental data at different distances is shown in **Fig. 1**. Because the calculated values agree with the measured ones, the detector model was simulated properly.

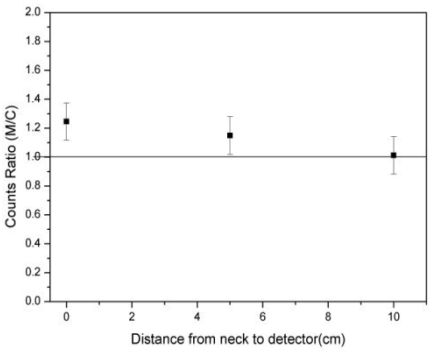

Fig. 1 Ratio of measured values (M) to calculation values(C) for ^{131}I at various distances from the neck

2. Design of Thyroid Monitoring System

Portable thyroid monitoring system should have higher counting efficiency for radioiodine from thyroid and lower counting efficiency for background radiation and other radionuclides from the body. The cross-sectional view of the detector model and a geometrical arrangement of the mathematical neck phantom including thyroid and detector are shown in **Fig. 2**.

(1) Crystal Size

We assumed that the detector has collimator (12 cm length of lead, truncated right angle cone shape) and the detector was placed at 0, 5, 10 and 15 cm. As seen in **Fig. 3**, the detector with larger crystal size has higher counting efficiency for ^{131}I and ^{133}I. As the distance between neck and detector increases, the counting efficiency and the difference of the counting efficiency decrease. Because shielding size increases with the crystal size, it is necessary to decide the crystal size considering total weight of the system as well as counting efficiency.

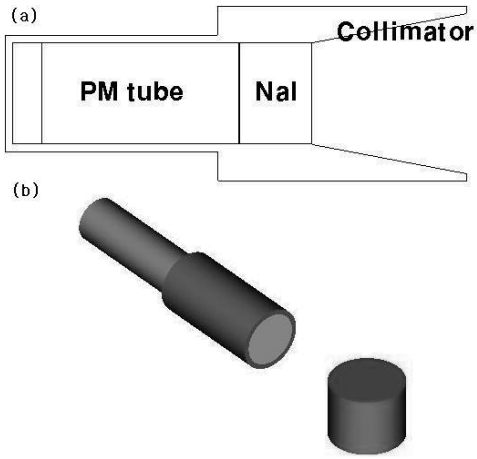

Fig. 2 Cross-sectional view of detector model (a) and a geometrical arrangement of the mathematical neck phantom including thyroid and detector (b)

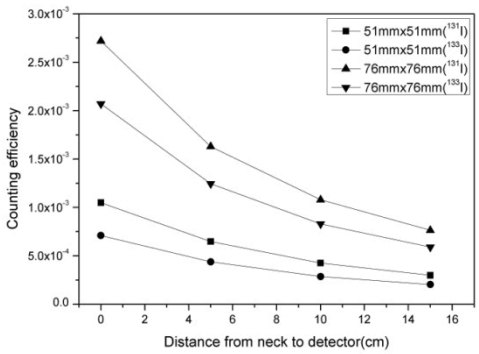

Fig. 3 Counting efficiency of the 51mm×51mm and 76mm× 76mm detectors at various distances from the neck

(2) Shielding Thickness

It is necessary to shield NaI crystal from background radiation properly. 0.5, 1, 1.5 and 2 cm thickness were simulated at 10 cm distance and the results are presented in **Fig. 4**. A similar shielding efficiency is showed at low energy (<0.25 MeV) for all of shielding, and shielding of 1.5 and 2 cm thickness has analogous shielding efficiency at the energy bin including energy of ^{131}I(364 keV) and ^{133}I(530 keV). As the photon energy increases, shielding of 2 cm thickness is more effective.

(3) Collimator Length

In the event of nuclear accident or radiological emergency, there is the potential for external and internal contamination of the human body by radionuclides such as ^{85}Kr, ^{133}Xe, ^{134}Cs, ^{137}Cs and ^{132}Te. We assumed that the chest of body is contaminated by these radionuclides and the detector was located at 10 cm from the neck. As seen in **Fig. 5**, shielding efficiency increases with the collimator length. But as the collimator length decreases, counting efficiency increases as shown in **Fig. 6**.

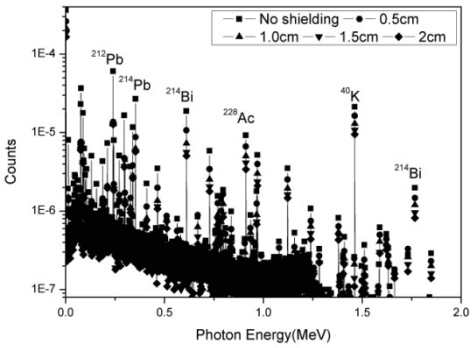

Fig. 4 Spectrum of the detector with Pb shielding of various thicknesses at 10 cm distance from the neck

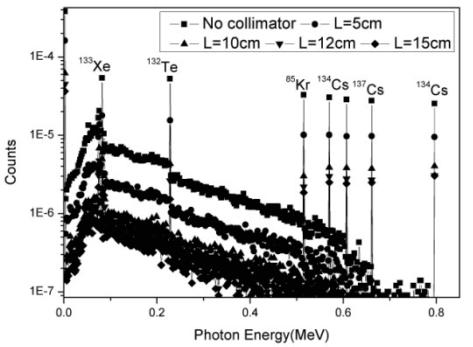

Fig. 5 Spectrum of the detector with collimator of various lengths at 10 cm distance from the neck

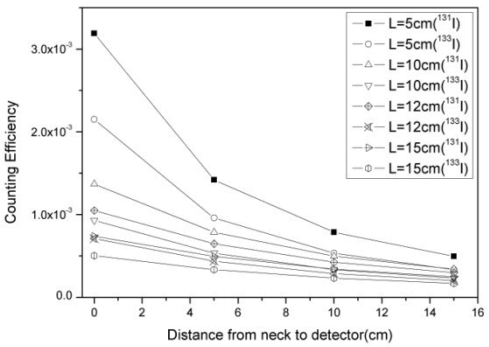

Fig. 6 Counting efficiency of the detector with collimator of various lengths at various distances from the neck

3. Effect of Counting Geometry to Counting Efficiency

Monitoring should be carried out having higher counting efficiency and lower uncertainty. The higher counting efficiency is obtained by arranging the detector at a shorter distance from the neck, however the short distance causes larger uncertainty. We assumed that the detector has collimator of 12 cm length.

(1) Distance from Neck to Detector

As the distance between neck and detector increases, counting efficiency and the errors of counting efficiency by shift decreases. For example distance "neck-detector" is changed from –1 to 1 cm at the 10 cm distance, the range of errors is from –7.26 to 8.03% in the case of ^{131}I. However the range of errors is from –8.83 to 9.72% at 5 cm distance.

(2) Detector Offset

Detector offset is defined as the positioning error of a detector on the x (horizontal plane) and z (vertical plane) direction.[6] As the distance from neck to detector increases, the errors by horizontal and vertical displacement decrease. **Fig. 7** and **8** show the variation of counting efficiency by horizontal and vertical displacement at 0, 5, 10, 15 cm distance from the neck.

When the limit of deviation for horizontal displacement is 2 cm at 10 cm distance, the range of errors is from –2.35 to –1.17% for ^{131}I. And assuming the vertical displacement changes from –2 to 2 cm at 10 cm distance, the range of errors is from –4.46 to –0.7% for ^{131}I. The errors by vertical displacement are larger than by horizontal displacement. This is due to the position of thyroid.

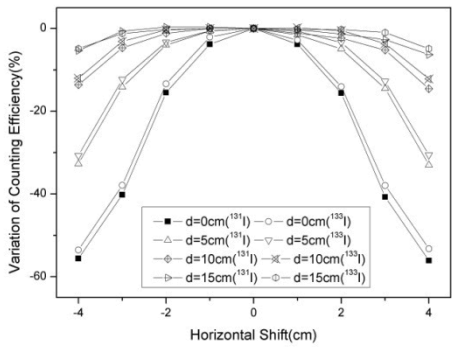

Fig. 7 Variation of counting efficiency by horizontal displacement at various distances from the neck

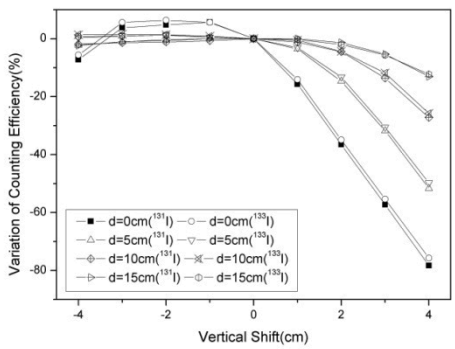

Fig. 8 Variation of counting efficiency by vertical displacement at various distances from the neck

(3) Detection Angle

Fig. 9 presents the variation of counting efficiency by detection angle in horizontal plane. In practice the deviation of angle in horizontal plane is not large, the range of errors is –3.76 to –1.17% for ^{131}I when the limit of

deviation for detection angle is from -20 to 20° at 10 cm distance.

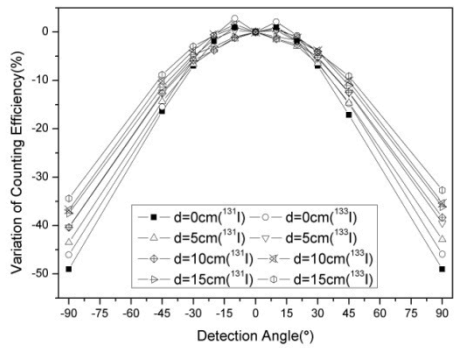

Fig. 9 Variation of counting efficiency by detection angles at various distances from the neck

IV. Simulation Results and Conclusions

To establish the transportable thyroid monitoring system, crystal size, shielding thickness and collimator length were simulated. If the difference of counting efficiency is small, smaller crystal size is more proper to system considering the total weight of the system. And lead shielding of 1.5 cm thickness is proper thickness, which protects the background radiation in the energy region of interest. Considering both shielding efficiency and counting efficiency, the collimator of 12 cm length is optimum. If the thyroid monitoring system consists of lead shielding of 1.5 cm thickness and collimator of 12 cm length, total weight of shielding and collimator is under 10 kg.

To establish the counting geometry, we investigated the counting efficiency and errors related to the positioning of the detector using computational simulation. Monitoring should be conducted under conditions of higher counting efficiency and lower uncertainty. The optimum detection distance is above 10 cm considering the counting efficiency and errors. **Table 2** lists the type of deviation and range of errors at the 10 cm distance. The largest error is associated with the variation in the distance between neck and detector.

Table 2. Range of errors by the deviation of detector positioning

Type of deviation and limit	Range of errors (%)	
	^{131}I	^{133}I
Distance from neck to detector (-1 to 1 cm)	-7.26 to 8.03	-7.0 to 8.11
Horizontal displacement (-2 to 2 cm)	-2.35 to -1.17	-0.52 to 0.17
Vertical displacement (-2 to 2 cm)	-4.46 to -0.7	-4.36 to 1.39
Angle in horizontal plane (-20 to 20°)	-3.76 to -1.17	-1.22 to 1.57

Assuming that the errors are independent all geometrical errors is added to estimate the range of uncertainty for the measured activity of ^{131}I and ^{133}I in the thyroid. The resulting error due to misplacement is equal to –17.83 to 4.99 % for ^{131}I. This represents either an underestimate of a factor of 1.22 or an overestimate of a factor of 1.05 in the activity of the thyroid. The range of errors is –13.1 to 11.24 % for ^{133}I, and this represents either an underestimate of a factor of 1.15 or an overestimate of a factor of 1.11 in the activity of the thyroid.

The methodology used in this study, including the mathematical models of detector and thyroid, will be applied further investigation the factors influencing the counting efficiency of ^{131}I and ^{133}I by the thyroid characteristics of individual such as thyroid volume and prethyroid tissue thickness.

References

1) M. Balonov, G. Kaidanovsky, I. Zvonova, A. Kovtun, A. Bouville, N. Luckyanov and P. Voilleque, 'Contribution of Short-Lived Radioiodine to Thyroid Doses Received by Evacuees from the Chernobyl Area Estimated using Early In Vivo Activity Measurements', Radiation Protection Dosimetry, Vol.105, No.1-4, pp.593-599, 2003.
2) IAEA, 'Rapid Monitoring of Large Groups of Internally Contaminated People Following a Radiation Accident', IAEA-TECDOC-746, 1994.
3) UNSCEAR, 'Exposures from Natural Radiation Sources', UNSCEAR 2000 Report, Vol. I : Annex B, 2001
4) U.S. Nuclear Regulatory Commission, 'Accident Source Terms for Light-Water Nuclear Power Plant', NUREG-1465, 1995
5) Alexander V. Ulanovsky, Victor F. Minenko and Sergey V. Korneev, "Influence of Measurement Geometry on the Estimate of 131I Activity in the Thyroid: Monte Carlo Simulation of a Detector and a Phantom", Health Physics, Vol. 72, No. 1, pp.34-41, 1996
6) Gary H. Kramer, Suzanne Yiu, 'Examination of the Effect of Counting Geometry on ^{125}I Monitoring using MCNP', Health Physics, Vol.72, No.3, pp.465-470, 1997

Journal of NUCLEAR SCIENCE and TECHNOLOGY, Supplement 5, p. 432–434 (June 2008)

Radiation Monitoring System of Pohang Light Source(PLS)

Sukmo HONG*, Kyunghoon KWAK, and Heeseok LEE

Pohang Accelerator Laboratory, Pohang, Korea

Ion chambers for photon, BF_3 proportional counters for neutron and local displayers for indication of dose level and alarm are installed at 24 posts. There are 13 monitoring posts in the storage ring, 9 posts in the linear accelerator(linac) and 2 posts in the site boundary for environment monitoring. Monitored data from storage ring and linac are transferred to the computer installed at the control room via CAN communication, and those from the site boundary are stored in computer at each post via RS232 communication. Modbus protocol is used to gather data from each computer via network of Pohang Accelerator Laboratory. The radiation monitoring system is interlocked with the personnel safety system, which stops the beam operation when the dose level exceeds the prescript limits.

KEYWORDS: radiation monitoring system, PLS, ion chamber, BF3 proportional counter, digital display

I. Introduction

Pohang Light Source is the facility which produces synchrotron radiation to accelerate the electron. When the high energy electrons strike the components of accelerator, high energy photons and neutrons are produced. To reduce the radiation, the accelerator is installed in a room shielded with 40 cm – 3 m thick concrete. But high energy photons and neutrons leak out the outer concrete wall, and the personnel who works in experimental area can be exposed to the leaked radiation. The radiation monitoring system is installed to monitor radiation level continuously, and to protect those personnel and environment. The monitors are manufactured by IHEP in China. The local displayer which displays radiation level in local area and the control software are developed in Pohang Accelerator Laboratory.

II. Outline of Radiation Monitoring System

Ion chambers for photon, BF_3 proportional counters for neutron and Local displayers for indication of dose level and alarm are installed at 24 posts. In the storage ring, 3 monitoring posts are installed around the injection area for the radiation leaked out the outer shielding wall during the injection of electron beam, 5 posts for the radiation of experimental hall during the normal operation, 3 posts around the inner shielding wall of the control shed which the control system is installed, and 1 post for low energy X-ray of RF cavity room. In linac, 6 monitoring posts are installed around the klystron gallery for low energy X-ray from klystron and the radiation leaked out the shielding tunnel with 3m concrete thickness, and 3 posts around the 100 MeV test linac which is used for the nuclear reaction experiment. For environment monitoring 2 posts is installed in the site boundary. The radiation monitoring system is interlocked with the personnel safety system, which stops the beam operation when the dose level exceeds the prescript limits and the local displayers are failed. The limits of alert alarm and high alarm are 25 μSv and 125 μSv except injection area and test linac, in which those are 25 μSv and 250 μSv.

A schematic block diagram of the radiation monitoring system is shown in **Fig. 1**. The data from the local displayers are collected to the client personnel computer via CAN or RS232 communication. The server personnel computer collects the data from the 4 client PC via LAN and wireless LAN using modbus protocol.

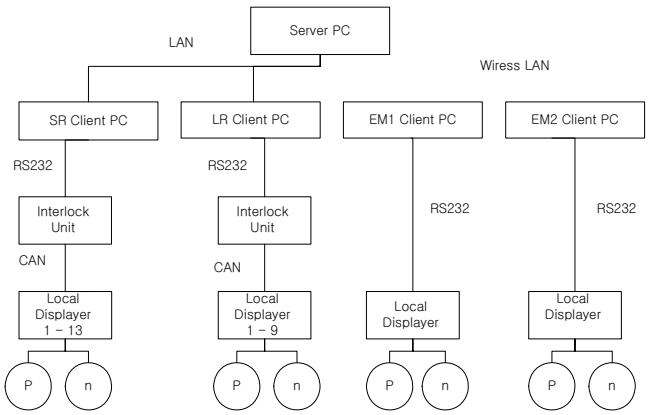

Fig. 1 Schematic block diagram of Radiation Monitoring System

III. Monitor[1,2)]

The area gamma monitor consists of high pressure argon filled ion chamber, an I-F converter and power supply board. The ion chamber is a Φ 155 X 120mm stainless steel cylinder with a hemispheric back end. The wall thickness is 2.5mm and the volume is about 3l . The sensitivity of that is about 1.25 X 10 A/μSv/hr. The area neutron monitor is made of BF3 proportional counter (Φ 25mm X 75mm, pressurized with 500mHg), which is placed at the center of rem construction. The output pulse from BF3 counter go through a preamplifier, main amplifier, pulse amplitude discriminator and shaping circuit to produce current pulse. It's sensitivity is about 200

*Corresponding Author, Tel No: +82-54-279-1858, Fax No: +82-54-279-1799, E-Mail: mo@postech.ac.kr

cps/mSv/hr. Environmental Gamma Monitor use a spherical, high pressure ion chamber with 260mm diameter and 2.5 mm stainless wall thickness. It's volume is 8.5l and filled with 25 atm, of pure argon. The sensitivity is about 3.05 X 10 μSv/hr. The environmental neutron monitor is that a BF3 proportional counter tube (Φ 50mm X 350mm, pressurized to 600mmHg) was placed at the center of 6.5cm thick polyethylene cylinder. Those monitors are manufactured by IHEP in China.

IV. Local Displayer

The output pulse from photon and neutron monitor is counted by the counter of the local displayer and calculated by 89C52 microcomputer. The calculated data is stored in 128 KB RAM and is transferred to a personnel computer. The data is refreshed on the time selected by user (default 5 seconds) and the counting time is continuously varied depending on a fixed statistical accuracy. The sum of photon dose and neutron's integrated during 1 hour is used for high alarm and alert alarm limits.

In front panel 1 display, 1 keypad, 5 status LED is installed. 20 characters, 2channel VFD (Very fluorescent display) is used to show gamma and neutron radiation level. 18 keypad is used for entering calibration constants, alarm limit etc. In rear panel 2 monitor connectors and 9 pin port which has a select switch for CAN and RS232 are installed. 2 output ports are used for alarm/buzzer and interlock. **Fig. 2** shows the photograph and the block diagram of the local displayer.

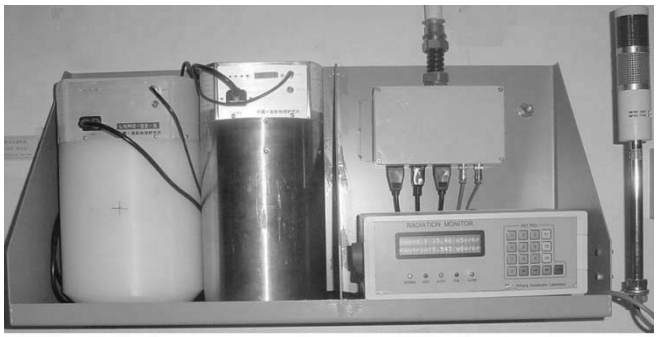

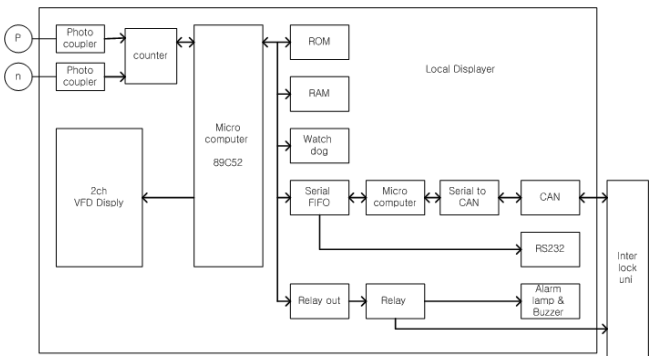

Fig. 2 Photograph and Block diagram of Local Displayer

V. Interlock Unit

The interlock unit connects the data cables and converts CAN signal to serial signal by CAN/RS232 converter for communication with a personnel computer. High alarm LED is connected to the relay output of each local displayer directly. And it is turned on when high alarm is activated and stops the beam operation in connection to the personnel safety interlock system. For fail safe the beam operation should be stopped when all the monitors are failed. The microcomputer of the interlock unit performs this function and is programmed to stop the beam operation when all the monitors around the injection area or the experimental hall are failed in the storage ring. The monitors of the linac are grouped into 1 GeV, 2 GeV, test lianc.

VI. Computer System

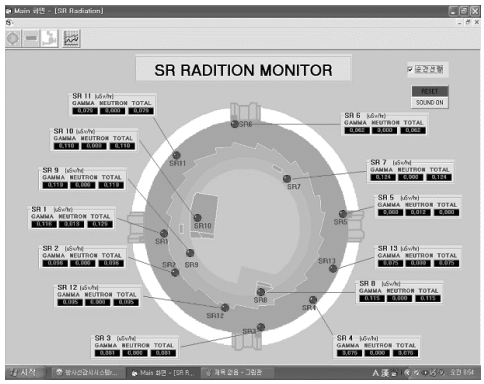

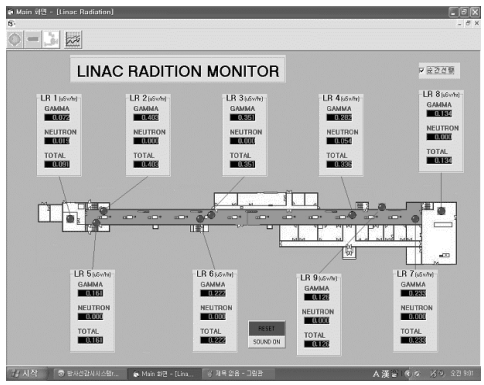

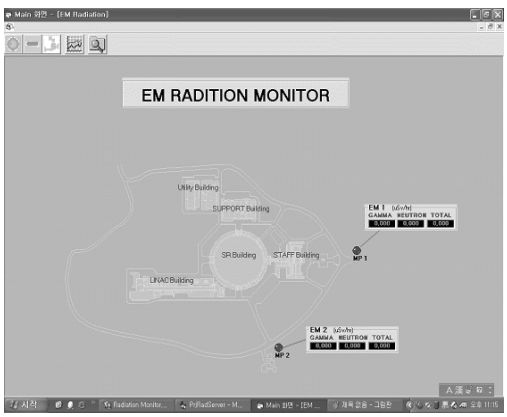

Fig. 3 Control Software

The computer system is consisted of 1 server computer and 4 client computers. The client computers collect the data from the local displayer via CAN (computer aided network) communication used in the storage ring, the linac and RS232 communication in the environmental monitoring. The server computer gathers the data from the client computers using modbus communication protocol via network of Pohang Accelerator Laboratory and wireless LAN for the environmental monitoring. The control Software is written to the visual basic language and consisted of the server program, the client program and the monitoring program. Those functions are followings.

1) Input of parameters about monitor
2) Display of current radiation level (dose rate or integrated dose)
3) Store of data
4) Graphical Display of trend during 2 hr
5) Data analysis
   – Graphical display of daily data
   – Calculation of integrated dose

Fig. 3 shows the control software of radiation monitoring system. Gamma, neutron and total dose are indicated to dose rate and integrated dose in according to the select item. When high alarm or alert alarm is activated, the color of LED is changed into red or yellow.

VII. Improvement of Local Displayer

Now the local displayer added to a wireless LAN port and a compact flash memory is being developed. It will be possible to transfer the data to a personnel computer anytime, anywhere and store the data to 2 GB.

Reference

1) Li Jian-Ping, Tang Yue-Li, Shao Bei-Bei, Liu Shu-Dong, Zhang Zhen-Gang, Qu Guo-Ying, "Intellligent environmental neutron and gamma monitoring system" , Chinese Physics, Vol.9, No.2, April-June 1989
2) Institute of High Energy Physics, Academia Sinica, " Instruction Manual for area radiation monitoring System"

Journal of NUCLEAR SCIENCE and TECHNOLOGY, Supplement 5, p. 435–438 (June 2008)

New Detector Module Design and Its Performance Estimation for Dual X-ray Baggage Inspection System

Kwang Hyun KIM[1*], Hwa Yeon YEO[2], and In Sub JUN[3]

[1]*College of Dentistry, Chosun University, Seosek-dong, Dong-gu, Gwangju, Korea*
[2]*Department of Nuclear Engineering, Chosun University Seosek-dong, Dong-gu, Gwangju, Korea*
[3]*RadTek, Co., LTD, KAERI, Daejeon, Korea*

New detector module based on screen type scintillators coupled photodiode has been proposed and estimated for the condition of dual X-ray baggage inspection. The new detector consisted of the Lanex Regular coupled photodiode for low energy detector and Lanex Fast-B coupled photodiode with copper filter of 1.1 mm thickness for high energy detector. By using simulation tools of MCNPX, DETECT 97, and ATLAS, optimum detector structure was designed and analyzed on Z-map. Compared with the commercialized detectors of Detection Technology (DT) and Electron Tube (ET), the proposed detector showed good performance property in the dual X-ray baggage inspection.

KEYWORDS: baggage inspection system (BIS), dual X-ray imaging, low energy detector (LED), high energy detector (HED).

I. Introduction

Commercialized detector modules for X-ray Baggage Inspection System (BIS) are a sandwich structure of two detectors; Low Energy Detector (LED) and High Energy Detector (HED). Each detector uses scintillator coupled linear array 16 channel photodiodes. Generally, screen film-type scintillator is coupled with the 16 channel photodiodes for the LED and 16 discrete crystal scintillators such as CsI(Tl) and CWO are coupled with each channel of the photodiode for the HED. While an incident X-ray spectrum passed fully the LED, the copper filter covered on the HED filtered low energy region of the incident X-ray spectrum. This gives an effect of double X-ray shots on the detector by only single X-ray shot. In addition to that mechanism, through the mechanism of X-ray interaction with matter, organic and inorganic matters can be distinguished.[1)] Therefore, the signal difference between each detector should be as large as possible for an incident X-ray spectrum, and that is the reason that an intrinsic difference of scintillation light on each detector should be large for a given X-ray exposure.[2)] Since Lanex^{TM} Regular and Fast-B scintillators based on GADOX material shows also relatively large difference of the scintillation light for any X-ray exposure, this combination of scintillators coupled with linear array photodiode may be available for the LED and the HED in the BIS. By using simulation tools of MCNPX, DETECT 97, and ATLAS, the signal estimation has been performed for various thicknesses of copper filter and compared with the commercialized two detectors of Detection Technology (DT) and Electron Tube (ET). Finally, the degree of separation of organic from inorganic matter was plotted by using Z-map which is general in dual X-ray imaging.

II. Materials and Methods

Generally, the conditions of X-ray generator are 160 kVp rated at 0.7 ~ 0.8 mA, but operating at 140 kVp for dual X-ray baggage inspection system, and highly depend on the specification of X-ray tube manufacturer. So as to investigate the performance of the BIS detector, sandwich type detectors and X-ray tube modeling were performed by Monte Carlo code of MCNPX.[3)] The properties of the sandwich type detectors were described in detail in Table 1.

X-ray spectra to be entered into the given detectors described in Table 1 at the incident energies of 140 and 160 kVp were acquired by the simulation for the given specifications of that tube and compared those spectra with the X-ray spectra acquired from SRS-78 X-ray simulation code.[4)] The used simulation data were for XP-ZSCAN GEN^{TM} X-ray system which is generally used in BIS. The given specifications of the X-ray tube were as follows; a Tungsten target, intrinsic filter of 0.8 mm-thick Beryllium, and 1.5 mm-thick fiber glass. In order to separate the incident X-ray spectrum into low and high energy photons at the dual X-ray BIS, it is necessary to optimize copper filter located just before the HED considering the signal difference between low energy detector and high energy detector. Using two X-ray input spectra of 140 kVp and 160 kVp and the sandwich type detectors modeled by the MCNPX, we investigated the spectra of the absorbed energies in each detector of the LED and the HED for two commercialized detectors of the DT and the ET and compared them with the spectra acquired from the proposed detector (PD). Since the performance of the detector which uses scintillator and photosensor depends on the characteristics of the scintillator, the photosensor, and

*Corresponding Author, Tel No: +82-62-230-6867, Fax No: +82-62-230-7451, E-Mail; radkim@chosun.ac.kr

Table 1. Properties of three detectors; the commercialized two detectors and the proposed detector.

		Scintillator	Thickness (mm)	Wavelength (mm)	Cu filter (mm)	Light yield (#/MeV)	X-ray	
DT	LED	Lanex-Fast-B	0.1826	545	1	-	140 kVp, 0.8 mAs	160kVp, 0.8 mAs
	HED	Csl(T1)	3.0	560		54000		
ET	LED	Lanex-Fast-B	0.1826	545	1	-		
	HED	CWO	2.0	475		15000		
PD	LED	Lanex-Regular	0.0913	545	0.7~1.3	22400		
	HED	Lanex-Fast-B	0.1826	545		-		

the combination of the scintillator and the photosensor, the light transport in the scintillators and the quantum efficiency of the photosensor for the concerned wavelengths were simulated by another Monte Carlo code of DETECT 97 and device simulation tool of ATLAS.[5) 6)] Using those simulated data, the signal generated in each detector and the signal ratio of the HED and the LED for two commercialized detectors of the DT and the ET were estimated and referenced in order to evaluate various copper thicknesses of the PD. Finally, so as to see the degree of separation of organic matter from inorganic matter in that detector combination, the Z-map was plotted by the Monte Carlo code of MCNPX and the calculated signal values in the condition that plastic and acryl were laid on the considered detector.

III. Results and Analyses

In order to evaluate the acquired X-ray spectra from the MCNPX simulation with the proven X-ray spectra the X-ray tube condition was set at 140 kVp/1 mAs and anode angle of 22° at source to detector distance (SDD) of 750 mm.[7)] Other spectra to be entered into the detectors were also acquired at the Be window of the X-ray tube by the simulation for the conditions of 140 kVp/0.8 mAs and 160 kVp/0.8 mAs at the anode angle of 25° considering real X-ray tube as mentioned before. Those all spectra were displayed in **Fig. 1**. In this Figure, the X-ray spectra between the acquired by the simulation and the proven by the SRS 78 were almost same that the spectra at the conditions of 140 kVp/0.8 mAs and 160 kVp/0.8 mAs at the anode angle of 25° were reasonable to use as real spectra generated in the X-ray tube. Using both spectra of 140 and 160 kVp, the absorbed energies in the LED and the HED of the DT and the ET were plotted as shown in **Fig. 2** concerning the spectrum filtration to know the effect of the fixed filter thickness. Compared with the LED, the HEDs of the DT and the ET showed almost same filtering low energy off.

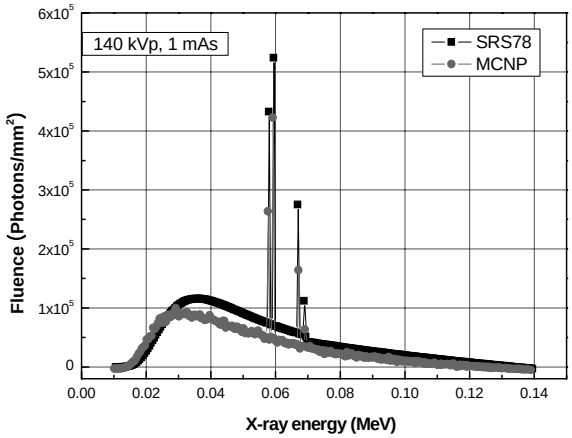

Fig. 1 Comparison of X-ray spectrum between SRS 78 and MCNPX codes.

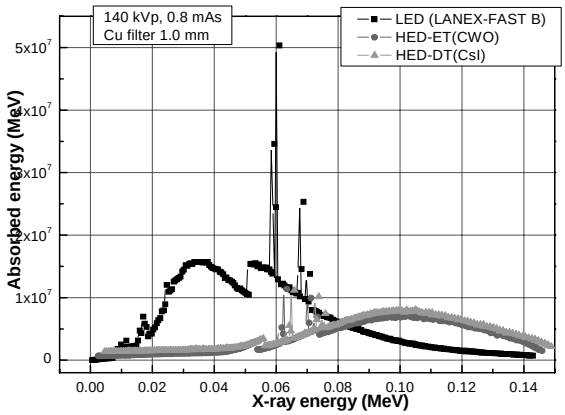

Fig. 2 Comparison of absorbed energy in high energy detector (HED) after filter for DT and ET.

The filtration of low and high energy regions at the proposed detector (PD) by the various filter thicknesses were investigated and plotted for both spectra as shown in **Fig. 3**. Compared with **Fig. 1**, the absorbed energy in the HED after the filter was low and the high energy peak near 0.1 MeV was not shown although overall spectrum was separated by the filter for the input spectrum.

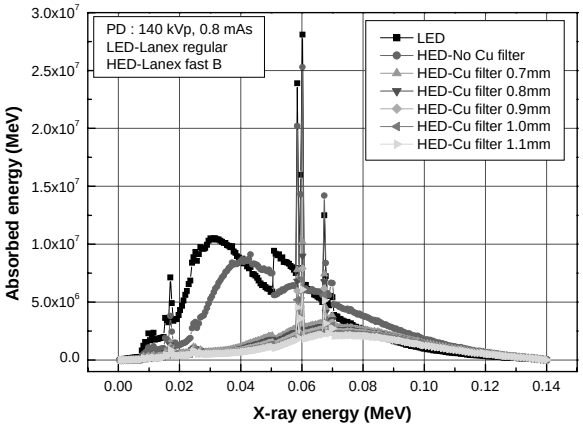

Fig. 3 Comparison of absorbed energy in HED for various filter thicknesses at PD.

Next approaches what we did were to analyze the absorbed ratio of the HED to the LED and the signal ratio of the HED to the LED. Since each detector uses different scintillator and its physical and optical properties are different for the incident X-ray spectrum, the absorbed and the signal ratio of the HED to the LED may be used to estimate the performance of dual detector. In the calculation of the signal ratio, the absorbed energies in each scintillator were simulated by the MCNPX, and multiplied by the light yields and the light transmission efficiencies (LTE) of each scintillator. Based on the assumption that all detectors use the same photodiode and electronics, only the scintillation light generated by the absorbed energy in the scintillator is considered. The LTEs were acquired by the simulation of the DETECT 97 code considering the position of the absorbed energy in the scintillator. However, since the optical properties of the Lanex^{TM} Regular and Fast-B scintillators were not clear, the 22,000 lights per MeV from the Regular multiplied by the absorbed energy in the Regular and Fast-B, acquired by the MCNPX simulation, were used, and as a result the light yield of the Fast-B was 1.67 times over the Regular.[8] The result was the same as the data measured by others.[9] The quantum efficiencies (QE) of photodiode were simulated by ATLAS code for the wavelengths of each scintillator. Each ratio of the absorbed and the signal was plotted at 140 kVp/0.8 mAs in **Fig. 4** comparing three detectors. The PD's highest value was 0.375 at 0.7 mm thickness, which was similar to the value of 0.385 at 1.0 mm thickness in the DT. In the signal ratio, the ET showed the smallest value of 0.25 at 1.0 mm thickness while it was 0.28 at 1.1 mm thickness in the PD. From the results, the absorbed and the signal ratios give only the information about the thickness of the filter in the PD; 0.7 mm for the absorbed ratio and 1.1 mm for the signal ratio. So as to select the optimum filter thickness, Z-map comparison was performed for three detectors of the DT, the ET, and the PD. Generally, the Z-map is used to see the degree of separation of organic from inorganic matter in dual X-ray imaging.[10] In the same geometries at the Monte Carlo modeling, aluminum plates of 1 ~ 4 mm and acryl plates of 10 ~ 40 mm were located on each detector. On the Z-map as shown in **Fig. 5**, the HED and the LED signals with the phantoms of the aluminum and acryl plates showed different slope which represented different effective atomic numbers of the phantoms in X-ray interaction. The angle between two different slopes is the degree of the separation between organic and inorganic materials.

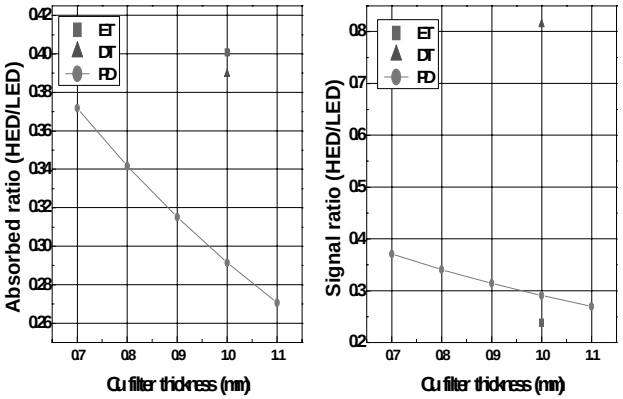

Fig. 4 Comparison of the absorbed energy and the signal ratios for three detectors.

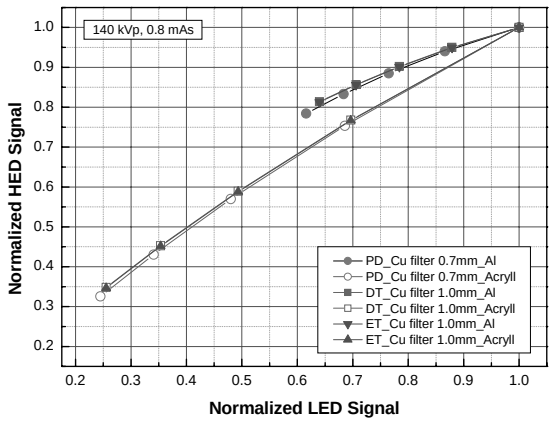

Fig. 5 Comparison of Z-map for three detectors at 140 kVp/0.8 mAs.

In the **Fig. 5**, the data were normalized and the angles between each slope were almost same for the DT and the ET. Slight difference was found in the PD compared with other detectors. However, from the Figure, it is found that the performance for proposed detector (PD) is comparable to other detectors. As a final step, the effects of the filter thickness and the incident X-ray energy were investigated and showed in **Figs. 6** and **7**. In the **Fig. 6**, they were all linear fitted and the filter thicknesses of 0.7 mm and 1.1 mm were compared in the PD's slopes for X-ray of 140 kVp/0.8 mAs and. The angles between the slopes were 12° and 13° for 0.7 mm and 1.1 mm filters, respectively. However, the angles were not different for the X-ray energies of 140 kVp/0.8 mAs and 160 kVp/0.8 mAs for the fixed filter thickness of 1.1 mm as shown in the **Fig. 7**.

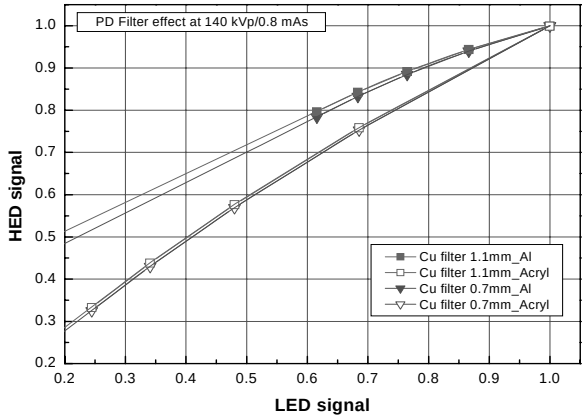

Fig. 6 Effect of filter thickness on Z-map at the fixed incident X-ray energy.

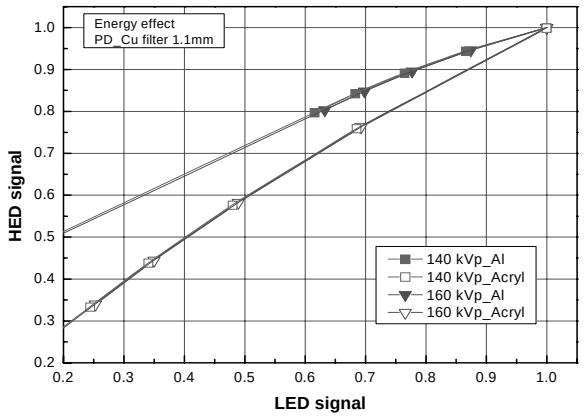

Fig. 7 Effect of incident X-ray energy on Z-map at the fixed filter thickness.

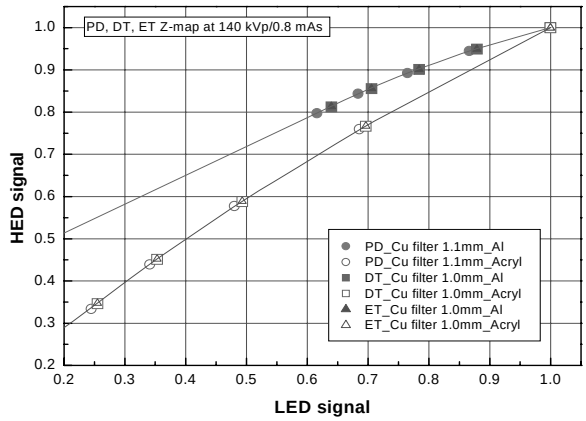

Fig. 8 Comparison of Z-map for three detectors after optimized filter thickness for PD.

Using the filter of 1.1 mm for the PD, the Z-map was plotted again at 140 kVp/ 0.8 mAs as shown in **Fig. 8**. Comparing with **Fig. 5**, the slight difference was overcome and all three detectors showed the same angle of 13° between each slope.

IV. Conclusion

For the sandwich type of low and high energy detectors in X-ray baggage inspection system, the proposed new detector using screen type scintillator for both low and high energy detectors showed the same performance as commercialized detectors of Detection Technology and Electron Tube. The performance estimation of the new detector was investigated by simulation and calculation based on Z-map. In the proposed detector, the low energy detector of Lanex Regular coupled photodiode and the high energy detector of Lanex Fast-B coupled photodiode showed comparable performance of organic-inorganic separation on Z-map. The optimized filter was copper of 1.1 mm at the incident X-ray energy of 140 kVp/0.8 mAs.

While the commercialized detector uses crystalline and segmented scintillator such as CsI(Tl) and CdWO in the high energy detector, the proposed detector uses screen type scintillator based on GADOX. Since screen type scintillator is a cost effective and there is no any effort to process accurately, the proposed detector can be used with a good performance and a competitive price for the dual X-ray baggage inspection system.

References

1) S. Singh, M. Singh, 'Review Explosives Detection System for Aviation Security,' Signal Processing, vol. 83, pp 31-55 (2003).
2) V, Rebuffel, J.M. Dinten, 'Dual-Energy X-Ray Imaging: Benefits and Limits,' ECNDT-Th.1.3.1 pp 1-12 (2006)
3) MCNPX^{TM} User's Manual Ver. 2.5.0 April 2005 D. Pelowitz. Ed., Los Alamos Nat. Lab. Rep., Los Alamos, NM
4) K Cranley et al, 'Catalogue of Diagnostic X-ray Spectra and Other Data,' Report No. 78, September, 1997.
5) G. F. Knoll and T. F. Knoll, DETECT Manual. Ann Arbor, MI: Univ. Michigan, 1996.
6) ATHENA User's Manual, Silvaco Int., Santa Clara, CA, 1998.
7) K Cranley et al, "Catalogue of Diagnostic X-ray Spectra and Other Data," Report No. 78, September, 1997.
8) H. S. Cho, et al 'Development of a Portable Digital Radiographic System Based on FOP-Coupled CMOS Image Sensor and Its Performance Evaluation,' IEEE TNS, Vol. 52, No. 5, pp. 1776-1772, 2005.
9) L. E. Antonuk, et al, 'Development of Hydrogenated Amorphous Silicon Sensors for Diagnostic X-ray Imaging,' IEEE TNS, Vol. 38, No. 2, pp. 636-640, 1991.
10) 10) R. D. Macdonald, 'Design and Implementation of a Dual-Energy X-ray Imaging System for Organic Material Detection in an Airport Security Application,' Proc. SPIE, Vol. 4301, pp. 31-41, 2001.

Journal of NUCLEAR SCIENCE and TECHNOLOGY, Supplement 5, p. 439–442 (June 2008)

Radioactive Analysis of a Spent HEPA Filter Using the Distribution Characteristics of the Captured Radionuclide

Young-Yong JI[1*], Dae Seok HONG[1], Il-Sik KANG[1], Bum-Kyoung SEO[2], and Jong-Sik SHON[1]

[1]*PIE & Radwaste Center, Korea Atomic Energy Research Institute, Daejeon, Korea*
[2]*Decommissioning Technology Development Center, Korea Atomic Energy Research Institute, Daejeon, Korea*

To investigate the species and the distribution of the captured nuclides in a HEPA filter, it was dismantled into a metal part and a filter medium part to obtain a filter medium. From the nuclide analysis results for a filter medium part through pre-treatment of it, it was possible to obtain three kinds of typical distributions in view of the distribution of the captured nuclides in the filter medium. When considering these distribution characteristics of the captured radionuclide, the region showing the high concentration of the captured nuclides was the intake or the outlet part of the HEPA filter. On the other side, the middle part generally represented a uniform distribution below the average concentration of the captured nuclides. Therefore, in the event of taking a representative sample of a HEPA filter at the intake and the outlet part, the results of a nuclide analysis for that sample could be estimated as existing in the range from 1.0 to 1.5 times the real concentration of the nuclides captured by a filter medium. As a result, to conduct a radionuclide assessment of a spent HEPA filter without a dismantlement of it, the analysis results for a representative sample taken from both the intake and the outlet part of a spent HEPA filter could be regarded as an average value for the corresponding HEPA filter.

KEYWORDS: HEPA filter, filter medium, glass fiber, representative sample, nuclide analysis

I. Introduction

According to the operation of nuclear facilities and a continuous construction of them, a great amount of used high efficiency particulate air (HEPA) filters which are widely used in a ventilation system in the nuclear industry have been generated as spent filter waste. These spent HEPA filters at KAERI generally consist of those after filtering of all the contaminants in the air stream generated during the operation of the HANARO research reactor and the nuclear fuel cycle facilities.

In order to dispose of these spent HEPA filters, it is first necessary to conduct a radionuclide assessment of them. However, it is difficult to directly measure a radioactive concentration of the nuclides existing in a HEPA filter because of its great bulk and specific shape. Therefore, after taking a representative sample from a HEPA filter, the analysis results for it are regarded as an average value for the corresponding HEPA filter. To use this method, it is essential to confirm the validity of the sampling procedure and the average value.

The methods for taking a representative sample from a HEPA filter can be divided into two methods. First, after dismantling a HEPA filter into a metal (frame and separator) part and a filter medium part, one can take a sample from the filter medium. It is not, however, desirable to use this method because of the possibility of a radioactive contamination during a dismantlement and an excessive preparation time for taking a sample. Second, one can take a representative sample directly from the front and the rear side of a HEPA filter without a dismantlement. Using the second method, the HEPA filter should have a regular tendency for the distribution of the captured nuclides in both sides. If a regular tendency for the distribution of the captured nuclides is maintained in a HEPA filter, it is possible to utilize this distribution as a guide for taking a representative sample.

To investigate the species and the distribution of the captured nuclides in a HEPA filter, a spent HEPA filter was dismantled into a metal part and a filter medium part to obtain a filter medium. From the nuclide analysis results for the filter medium part, it was possible to divide the filter medium into three specific regions in respect of the nuclide distribution. As a result, these three regions could be a sampling guide to take a representative sample from a spent HEPA filter. And also, it was possible to use the result of a radioactive analysis from a representative sample obtained by using the distribution characteristics of the captured radionuclide as an average value of a spent HEPA filter.

II. Materials and Methods

1. The Captured Particles in a HEPA Filter

The shape of a HEPA filter is a rectangular parallelepiped form filled extensively with a pleated filter medium made from a mixture of glass fibers in the metal filter case. A filter medium consists of glass fibers with an average diameter range from 0.2 to 0.5 ㎛ and its whole size is about 57 ㎝ (H) × 57 ㎝ (W) × 26.4 ㎝ (D). It is known that a HEPA filter has a minimum particle removal efficiency of no less than 99.97 % for 0.3 ㎛ particles which are the most penetrating sized particles for a filtering[1-2]. **Fig. 1** shows the assembled components of a

*Corresponding Author, Tel No: +82-42-868-2561, Fax No: +82-42-868-8221, E-Mail; yyji@kaeri.re.kr

HEPA filter with corrugated separators and a schematic diagram of the flow and capture of the particles in the passages which are produced by the separators.

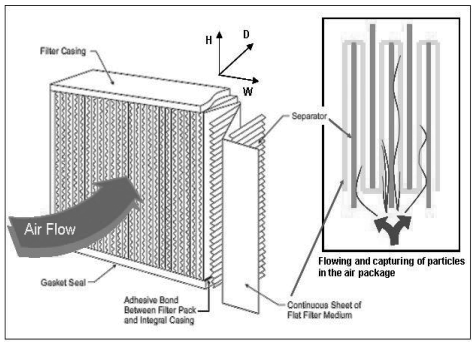

Fig. 1 The composition of a HEPA filter and the schematic diagram of capture of the particles

As a rule, process-generated particles are divided into two fields which mean a mechanical field produced by a machining, grinding, polishing, and other mechanical operations and a chemical field produced by an evaporation, condensation, and so on. These particles sometimes become radioactive by an adsorption of radioactive vapors or gases or by an agglomeration with already radioactive particles. **Fig. 2** shows SEM images for the filter medium of a HEPA filter before use and after capturing particles generated in nuclear facilities. A filter medium caused by a mechanical process showed a very light gray color and a considerable amount of dust when dismantling a HEPA filter. On the other hand, a filter medium mainly caused by a chemical process showed a dark gray color and there was no dust because of an agglomeration with the vapor.

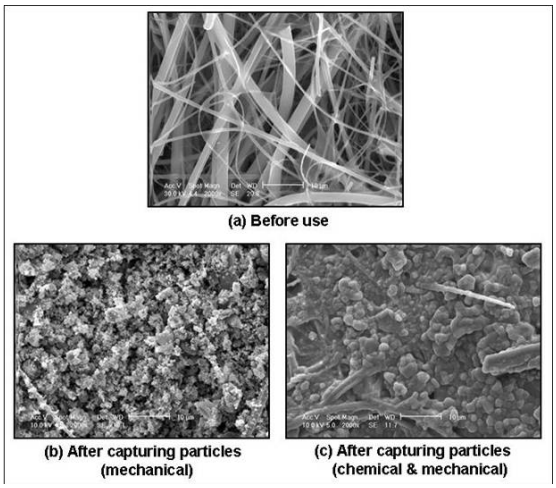

Fig. 2 The SEM images for the filter medium of a HEPA filter

2. The Distribution of the Captured Nuclides

There are some researches on a radionuclide assessment of a HEPA filter by using a leach system and a waste assay system [3-4]. In this study, to investigate the species as well as the distribution of the captured radionuclide in a HEPA filter, the spent HEPA filter was dismantled into a metal part and a filter medium part. After marking the filter medium in the direction of the air flow, it was cut into 12 pieces in the direction from the intake to the outlet. And then, these 12 pieces of the filter medium were individually put into Marinelli beakers which had a 1 liter volume (**Fig. 3**). In the case of conducting a quantitative analysis of the nuclide existing in the Marinelli beakers, it is possible to establish the radionuclide distribution in a filter medium because each piece has depth information regarding that filter.

First of all, to establish the distribution of the gamma emitters existing in a filter medium, an analysis of the gamma nuclides for 12 units of Marinelli beakers was conducted by using a HPGe detector. And then, to take a sample for an analysis of the alpha and beta emitters in each Marinelli beaker, pieces of the filter medium in each beaker were poured into a tray, as shown in **Fig. 3**.

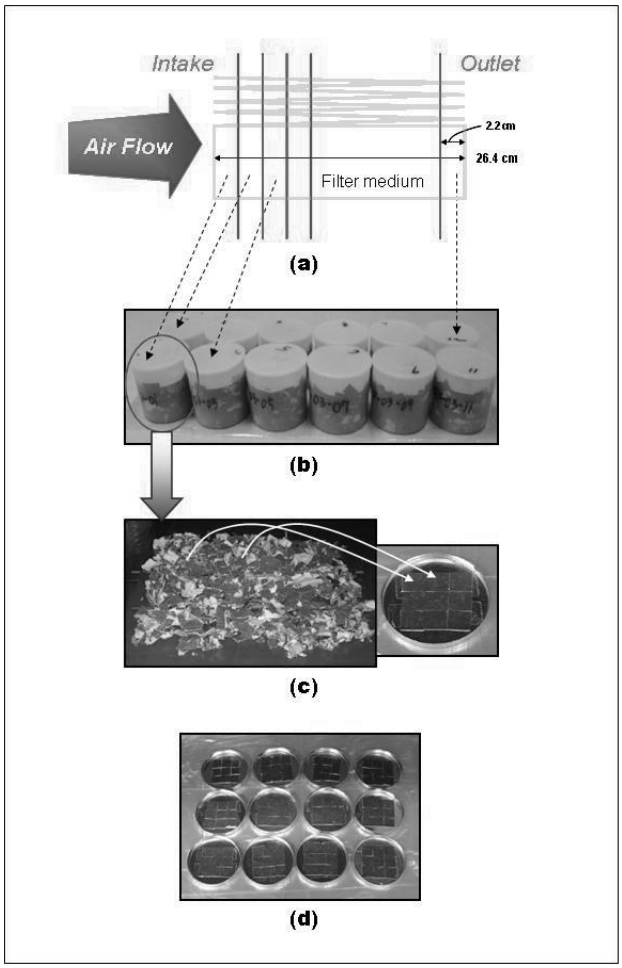

Fig. 3 The procedure for taking a sample to investigate the distribution of the captured radionuclide in a filter medium

After uniformly distributing the pieces of the filter medium by measuring the dose rate, samples were respectively taken at 9 segments and cut into the same size, 1 ㎝ × 1 ㎝. And then, these 9 samples were attached to a planchet with a regular geometry of the planchet. In this way, 12 units of planchets to analyze the alpha and beta

emitters in the filter medium were made and finally analyzed by using a gross alpha and beta counter.

III. Results and Discussion

After selecting several HEPA filters generated in the HANARO research reactor, the RIPF (RI Production Facility), the IMEF (Irradiated Material Examination Facility), the PIEF (Post Irradiation Examination Facility) and the RWTF (Radioactive Waste Treatment Facility), a nuclide assessment for a filter medium was conducted according to the depth of a HEPA filter. **Fig. 4** shows the results for the nuclide assessment. The dotted lines mean the average specific activity of each nuclide, i represents the nuclides existing in a filter medium, and j represents the region of a filter medium from the intake to the outlet (j=1~12). So, one region of a filter medium accounts for about 2.2 ㎝ in total depth from the intake to the outlet, about 26.4 ㎝. Gross alpha and beta in a HEPA filter generated in the HANARO and the RIPF were not detected because of their low activity levels. And also, in the RWTF and the RIPF, only three gamma emitters, Co-60, Cs-134, and Cs-137, were detected. In most of the HEPA filters, the specific activity of the Cs-137 was higher than the other detected nuclides, and the distributions of the gross alpha and beta were similar to that of the gamma emitters because the alpha and beta decays were mainly accompanied by a gamma decay. That means that pure alpha and beta emitters seldom exist in the filter medium or the amount of their contribution to the gross alpha and beta is small.

In view of the geometry of a HEPA filter, the intake and the outlet part will show a high dispersion of the air flow and have a large area directly contacting the air flow, when compared with the middle part of a filter medium. Therefore, the concentration of the captured nuclides was generally higher at the intake part or the outlet part because of the high probability of a collision of the particles with the glass fiber in the filter medium in those regions. The middle part generally represented a uniform distribution below the average specific activities of each nuclide.

In the case of taking samples from a HEPA filter without a dismantlement to conduct a nuclide analyze of it, it is possible to consider samples individually taken from the intake and the outlet part which are easy to access as a representative sample of a HEPA filter. To confirm the validity of this sampling method, one should obtain the ratio of the concentration of the nuclides in each region of the filter medium from the intake to the outlet, to the average concentration of the nuclides in the whole region of a filter medium. The results for the ratio of the concentration of the nuclides are shown in Table 1 and **Fig. 5**. The region from 1 to 3 represents the intake part with a depth of about 6 ㎝, and the region from 10 to 12 represents the outlet part with the same depth as the intake part.

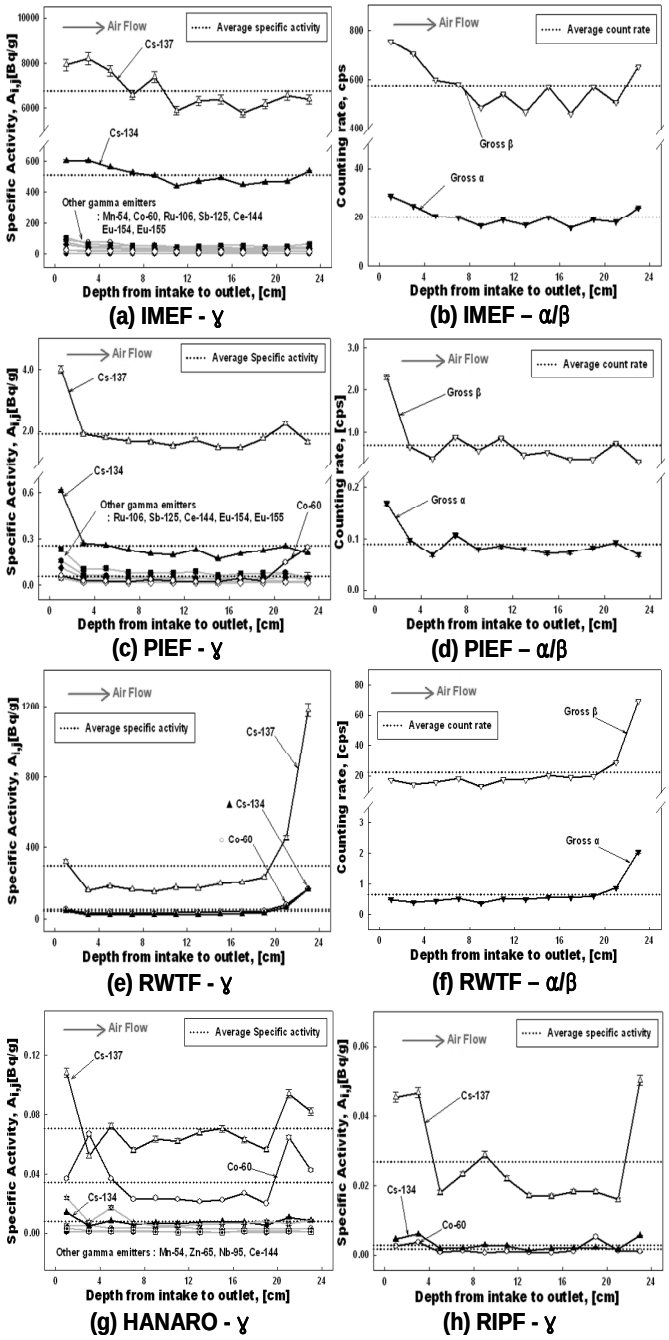

Fig. 4 The distribution of captured nuclides in the filter medium generated in the nuclear facilities

As a consequence, it was possible to obtain three kinds of typical distributions in view of the distribution of the captured nuclides in the filter medium, as shown in **Fig. 5**. First, the concentration of the captured nuclide in the intake part of the air flow was higher than the middle or the outlet part in the filter medium (Type A). Second, contrary to the first, the concentration of the captured nuclide in the outlet part was higher than any other part (Type B). And third, a mixture of the first and the second, the concentration of the captured nuclide in the intake and the outlet part was higher than the middle part (Type C).

Table 1 The ratio of the concentration of the nuclides in the each part of the filter medium to the average concentration of the nuclides for the whole part

	Nuclide	Average($A_{i,j} \sim A_{i,j+2}$) / Average(A_i)			
		j = 1~3	j = 4~6	j = 7~9	j = 10~12
IM EF	Mn-54	1.51	0.98	0.78	0.73
	Co-60	1.56	0.91	0.78	0.75
	Ru-106	1.30	0.86	0.92	0.91
	Sb-125	1.18	0.92	0.90	1.00
	Cs-134	1.16	0.96	0.92	0.96
	Cs-137	1.17	0.98	0.91	0.94
	Ce-144	1.32	0.78	0.79	0.93
	Eu-154	1.35	0.83	0.83	0.99
	Eu-155	1.33	0.90	0.83	0.94
	Gloss α	1.22	0.91	0.87	1.00
	Gloss β	1.20	0.93	0.87	1.00
RW TF	Co-60	0.77	0.62	0.72	1.89
	Cs-134	0.73	0.55	0.63	2.08
	Cs-137	0.73	0.55	0.63	2.09
	Gloss α	0.68	0.72	0.82	1.78
	Gloss β	0.70	0.72	0.84	1.74
HA NA RO	Co-60	1.38	0.68	0.69	1.25
	Zn-65	1.27	1.07	0.83	0.84
	Nb-95	1.38	0.89	0.79	0.94
	Cs-134	1.16	0.83	0.96	1.05
	Cs-137	1.10	0.86	0.95	1.10

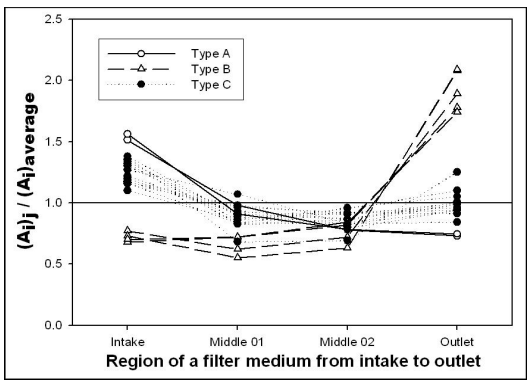

Fig. 5 The typical distribution forms of captured nuclides in the filter medium

For a type A distribution, the average values for the concentration of the nuclides at the intake and the outlet part were about 1.00 to 1.20 times the average concentration of the nuclides for the whole region of the filter medium, $(A_i)_{average}$. For a type B distribution, the average concentration of the nuclides at the intake and the outlet part were about 1.20 to 1.50 times $(A_i)_{average}$. And for a type C distribution, the average concentration of the nuclides at the intake and the outlet part were about 1.00 to 1.40 times $(A_i)_{average}$. Therefore, in the event of taking a representative sample of a HEPA filter both at the intake and at the outlet part, the results of a nuclide analysis for that sample can be estimated as existing in the range from 1.0 to 1.5 times the real concentration of the nuclides captured by a filter medium.

As shown in **Fig. 6**, a punch device with a diameter of 2 inch was developed for cutting a part of a filter medium as a regular size without a dismantlement of a HEPA filter. So, circular samples of a 2 inch diameter from a filter medium were obtained for the intake and the outlet part by using this punch device. And then, after placing every circular sample into a plastic cylindrical bottle, 20 cc, this bottle could be considered as a representative sample of a HEPA filter for a radioactive analysis.

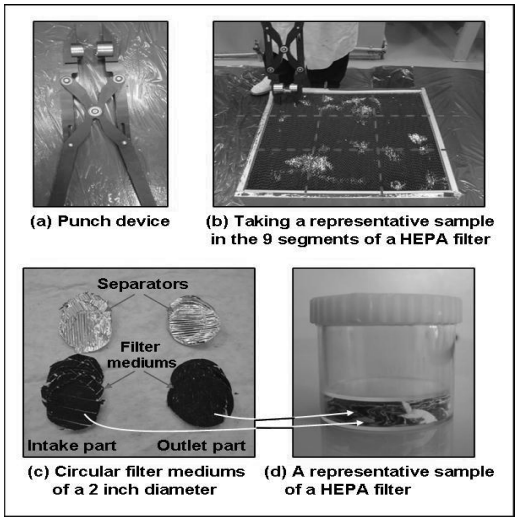

Fig. 6 The method for taking a representative sample using a punch device without dismantlement of a HEPA filter

IV. Conclusions

The nuclide assessments for several filter mediums were conducted according to the depth of a HEPA filter. As a result, it was possible to obtain three kinds of typical distribution characteristics in view of the distribution of the captured nuclides in the filter medium; First, a type A distribution which represents a high concentration of the nuclides at the intake part, then a type B distribution which is contrary to a type A distribution, and finally a type C distribution which is a mixture of the type A and the type B distributions. From these distribution characteristics, the region that showed the highest concentration of the captured nuclides was the intake or the outlet part of the HEPA filter. Therefore, the nuclide analysis results for a representative sample taken from both the intake and the outlet part could be regarded as an average value for the corresponding HEPA filter and also, that value could be estimated as existing in the range from 1.0 to 1.5 times the real concentration of the nuclides captured by the filter medium.

References

1) DOE handbook, "Nuclear Air Cleaning Handbook", DOE-HDBK-1169-2003, (2003).
2) DOE Standard, "Specification for HEPA Filters Used by DOE Contractors", DOE-STD-3020-97, (1997).
3) M. Argyle, R. Demmer, K. Archibald, K. Pierson, K. Shackelford, and K. Kline, "INEEL HEPA Filter Leach System: A Mixed Waste Solution", INEEL/CON-98-00795, (1999).
4) V.R. Casella and R.A. Dewberry, "Verification of HEPA Filter Analysis for the Canberra Q2 Waste Assay System", WSRC-TR-2002-00423, (2002).

Journal of NUCLEAR SCIENCE and TECHNOLOGY, Supplement 5, p. 443–446 (June 2008)

Measurements of keV-Neutron Capture Cross-Sections and Capture γ-rays of ^{105}Pd

Tae-Ik RO[1], Byeong Ryong PARK[1], Won-Chung CHUNG[1], Guinyun KIM[2*], Youngdo OH[3], Samyol LEE[4], Masayuki IGASHIRA[5], and Toshiro OHSAKI[5]

[1]*Department of Physics, Dong-A University, Busan 604-714, Korea*
[2]*Department of Physics, Kyungpook National University, Daegu 702-701, Korea*
[3]*Pohang Accelerator Laboratory, Pohang University of Science and Technology, Pohang 790-784, Korea*
[4]*Department of Radiological Science, Nambu University, Gwangju 506-824, Korea*
[5]*Research Laboratory for Nuclear Reactors, Tokyo Institute of Technology, Tokyo 152-8550, Japan*

The neutron capture cross-sections and capture γ-rays of ^{105}Pd were measured for keV-neutron using the 3-MV Pelletron accelerator of the Research Laboratory for Nuclear Reactors at the Tokyo Institute of Technology. Pulsed neutrons were produced from the ^{7}Li(p,n)^{7}Be reaction, and the incident neutron spectrum on a capture sample was measured by neutron time-of-flight method with a ^{6}Li-glass detector. The capture γ-rays were detected with a large anti-Compton NaI(Tl) γ-ray spectrometer. A pulse-height weighting technique was applied to measure the capture γ-ray pulse-height spectra to derive capture yields. The capture cross-sections were obtained by using the standard capture cross-section of ^{197}Au. And we obtained the γ-ray energy spectrum of capture γ-ray by the pulse-height unfolding method. The present results were compared with the previous measurements and the evaluated data of ENDF/B-VII, JEFF-3.1, and JENDL-3.3.

KEYWORDS: Pelletron accelerator, pulsed keV-neutron, neutron capture cross-section, time-of-flight method, pulse-height weighting technique, anti-Compton NaI(Tl) spectrometer

I. Introduction

The neutron capture cross-sections of Palladium (Pd) isotopes in keV-neutron energy region are important in the design of reactors as well as in the nuclear and astrophysics studies. Since the major portion of the natural Pd capture cross-sections is due to ^{105}Pd, the accurate knowledge of the cross-sections for these isotopes is also of importance to the calculation of the reactor characteristics when Pd is used as burnable poison in light water reactors. In addition, the data are also important to examine the availability of Pd as a control material of the fast reactors.

We have measured the neutron capture cross-sections of ^{105}Pd in the neutron energy region from 10 to 90 keV and at 550 keV by using a high efficient capture γ-ray spectrometer. Pulsed keV neutrons were produced from the ^{7}Li(p,n)^{7}Be reaction by bombarding a lithium target with the 1.5-ns bunched proton beam from the Pelletron accelerator of the Research Laboratory for Nuclear Reactors at the Tokyo Institute of Technology (Titech). The measurement of neutron capture cross-sections of ^{105}Pd in the neutron energy region of 10 to 90 keV was published in elsewhere[1)]. In the present paper, we report the neutron capture cross-sections of ^{105}Pd in the neutron energy of 550 keV and the capture gamma-ray spectra in the neutron energy region both in 10-90 keV and in 550 keV. We have compared the present results with the previous ones[2,3)] and with the evaluated values of ENDF/B-VII[4)], JEF-3.1[5)], and JENDL-3.3[6)].

*Corresponding Author, Tel No: +82-53-950-5320, Fax No: +82-53-955-5356, E-mail: gnkim@knu.ac.kr

II. Experimental Procedure

The experimental procedure has been described in detail elsewhere[7,8)], so only a general description of the experiment is given here. An experimental arrangement is shown in **Fig. 1**. Pulsed keV-neutrons were produced via ^{7}Li(p,n)^{7}Be reaction by bombarding metallic lithium target with the 1.5-ns bunched proton beam. The pulse repetition rate was 4 MHz, and the average proton beam current was about 8.4 μA. The incident neutron spectrum on a capture sample was measured by means of a time-of-flight (TOF) method with ^{6}Li-glass scintillation detector. A 5.0-mm diameter and a 5.0 mm thick ^{6}Li-glass detector placed at 40 degrees with respect to the proton-beam direction and 0.50 m from the neutron target was used for the neutron detector in the 10-90 keV region, and a ^{6}Li-glass detector with a diameter of 102.0 mm and a thickness of 6.4 mm, located 4.6 m from the neutron target and at 1.4 degrees with respect to the proton beam direction was used for those at 550 keV.

The samples have been prepared from isotopically enriched Pd powder in carbon case. A gold disk with a diameter of 15 mm and a thickness of 1.0 mm was used as a standard sample. The characteristics of samples are summarized in **Table 1**. Each capture sample was aligned at zero degrees with respect to the proton beam direction. The distance between the Li target and the sample was 12 cm for the measurements in the 10-90 keV region and 20 cm for those at 550 keV. The prompt γ-rays emitted from the sample were detected by using an anti-Compton NaI(Tl) spectrometer located 86 cm from the sample and at an angle of 125 degrees with respect to the proton-beam direction. The main detector of the spectrometer was a

15.2-cm diameter by 20.3-cm long NaI(Tl) detector and was centered in a large hollow Compton-suppression NaI(Tl) detector with an outer diameter of 33.0 cm and a length of 35.6 cm. The spectrometer was set in a heavy shield consisting of borated paraffin, borated polyethylene, cadmium, and potassium free lead[9]. The capture events detected by the spectrometer were stored into a computer as two-dimensional data based on the TOF and the pulse height.

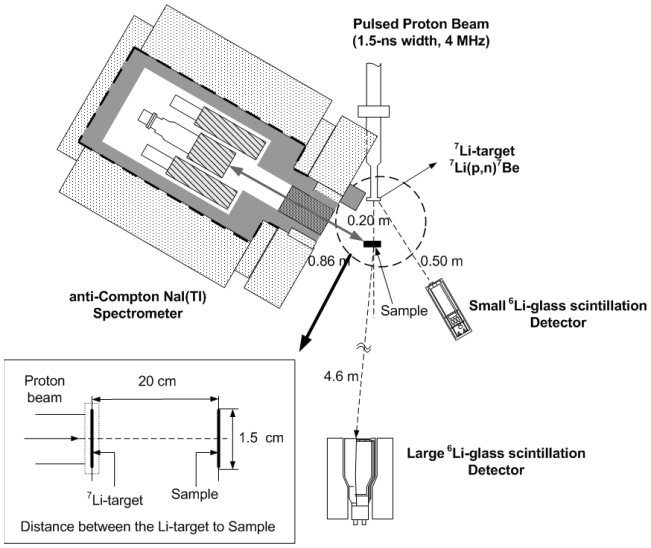

Fig. 1 Experimental arrangement for 550 keV measurements

Table 1. Characteristics of samples

Sample	^{105}Pd	^{197}Au
Weight [g]	0.426	3.430
Thickness [mm]	0.675	1.0
Size [mm^2]	176.71	176.71
Composition(%)		
^{197}Au	-	99.99
^{104}Pd	1.90	
^{105}Pd	90.90	
^{106}Pd	6.30	
^{108}Pd	0.90	

The runs with and without the sample (sample run and open run) and the run with standard gold sample (gold run) were made cyclically in each measurement to average changes in the experimental conditions, such as the incident neutron spectrum. Since the measurements were carried out cyclically, systematic changes in the experimental conditions could be corrected for. The open run was performed in order to determine the background and to monitor any changes in the incident neutron energy and the thickness of the ^{7}Li neutron-target. The three runs were normalized with the neutron counts of a small the ^{6}Li-glass neutron detector. The total measuring times for this experiment were about 79 hours: 38, 9 and 32 hours for the sample, gold and open runs, respectively.

III. Data Process

The data processing was given in detail elsewhere[7], so only a brief description is given in the present paper. The incident neutron energy spectrum on the sample was derived from the TOF spectra observed with the ^{6}Li-glass detector for the blank run. Typical normalized spectra are shown in **Fig. 2**.

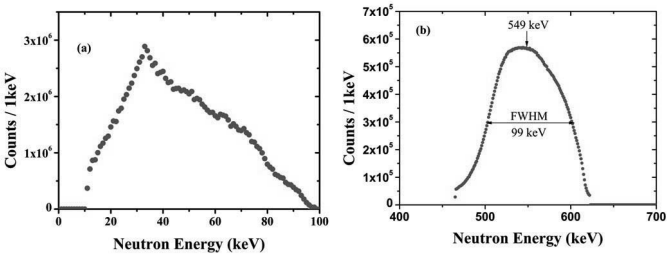

Fig. 2. Typical normalized energy spectra of incident neutrons in the (a) 10 - 90 keV and (b) 550 keV measurements with the ^{6}Li-glass detector for a blank run.

In order to obtain the capture yields of individual samples and the ^{197}Au sample, a pulse-height weighting technique[10] was applied to the observed net capture gamma-ray pulse-height spectra as shown in **Fig. 3**. The number of incident neutrons in the ^{197}Au run was determined by the capture yield of ^{197}Au and the averaged capture cross-section of ^{197}Au, which was obtained from the capture cross-sections of ENDF/B-VI[11] and the neutron energy spectrum.

The number of incident neutrons in the ^{105}Pd sample was derived from that in the gold run and the neutron monitor counts of the ^{6}Li-glass detector. The averaged neutron capture cross-section of each ^{105}Pd isotope was derived from the number of incident neutrons and the capture yield of each sample. Corrections for the neutron self-shielding and multiple-scattering in the sample were made by a Monte Carlo method[12], taking account of impurities in the sample. Moreover, other corrections were made for the gamma-ray scattering and absorption in the sample, for the effect of chemical and isotopic impurities in the sample on the capture yields.

The capture gamma-ray spectra were derived by unfolding the net capture gamma-ray pulse-height spectra with a computer code, FERDOR[13], and the response matrix of the gamma-ray spectrometer.

IV. Results and Discussion

The capture cross-sections of ^{105}Pd were measured in the incident neutron energy region of 10 to 90 keV and at 550 keV. In addition to the statistical error (0.3 – 0.6 %), the

following systematic errors were taken into account for the capture cross-section measurements: errors in the number of target nuclei (< 1%), in the standard capture cross-sections of ^{197}Au (3%), in the weighting function of γ-ray spectrometer (1%), in the extrapolation of net capture γ-ray pulse height spectrum below the discrimination level (0.6 MeV) in the deriving the capture yield with the pulse-height weighting technique (2%), and in the estimate of correction factor (1-2%). Consequently, they were added according to the error propagation formula to obtain the combined error. The combined error was about 4 %.

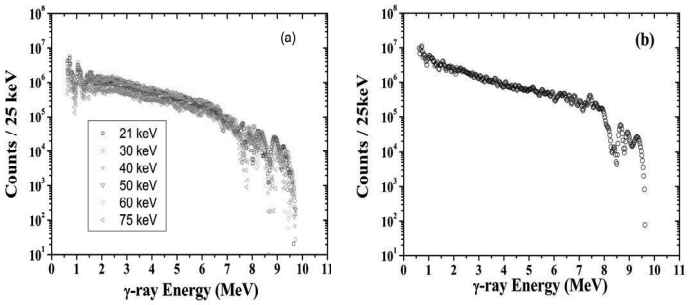

Fig. 3. Observed net gamma-ray spectra for (a) 10-100 keV and (b) 550 keV.

The present result for ^{105}Pd is shown in **Table 2** and in **Fig. 4**, respectively, and is compared with the previous measurements[2, 3] and with the evaluations of ENDF/B-VII[4], JEF-3.1[5], and JENDL-3.3[6]. Macklin *et al.*[2] presented the neutron capture cross-sections for ^{104,105,106,108,110}Pd without errors measured at the Oak Ridge Electron Linear Accelerator (ORELA) in the neutron energy region from 2.6 to 700 keV. Cornelis *et al.*[3] reported the capture cross-sections of ^{104,105,106,108,110}Pd without errors measured at the 30-m TOF path length of GEEL. The present result of ^{105}Pd is in general good agreement with the previous results[2, 3] and with the all evaluated values.

Table 2. Neutron Capture Cross-section of ^{105}Pd

Average neutron Energy [Energy region] (keV)	Capture cross-section (barn)	
	^{105}Pd	^{197}Au^{+}
21 [15 ~ 25]	1.558 ± 0.063 [4.02%]	0.717
30 [25 ~ 35]	1.313 ± 0.053 [4.02%]	0.567
40 [35 ~ 45]	1.167 ± 0.047 [4.02%]	0.494
50 [45 ~ 55]	1.025 ± 0.041 [4.03%]	0.439
60 [55 ~ 65]	0.906 ± 0.037 [4.04%]	0.399
75 [65 ~ 90]	0.818 ± 0.033 [4.04%]	0.356
550 [FWHM : 99keV]	0.232 ± 0.009 [4.00%]	0.123

+ Data from ENDF/B-VII

V. Conclusion

The neutron capture cross-sections and capture gamma-ray spectra of ^{105}Pd have been measured in the incident neutron energy region from 10 to 100 keV and at 550 keV. These data will provide important information on nuclear reaction mecanisms and the information will be used for accurate evaluations of the neutron capture cross-sections of ^{105}Pd.

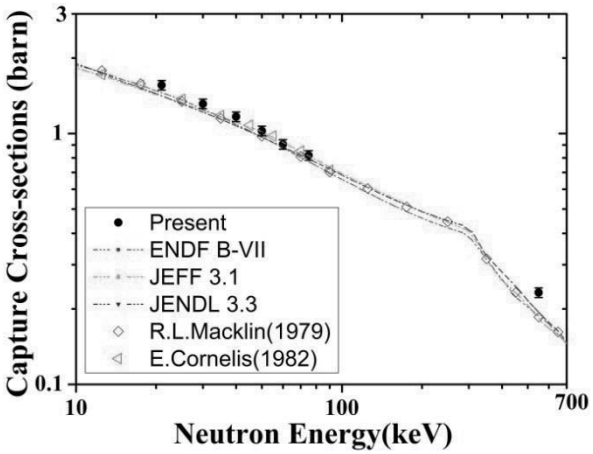

Fig. 4. Neutron Capture Cross-sections of ^{105}Pd

Acknowledgment

The authors would like to express their sincere thanks to the staff of the Research Laboratory for Nuclear Reactors, Tokyo Institute of Technology (Titech) for the excellent accelerator operation. This work was partly supported by the Korea Science and Engineering Foundation (KOSEF) through a grant provided by the Korean Ministry of Science and Technology (MOST) in 2007 (Project No. M2 07B090010810). One of authors (G. N. Kim) is partly supported by the Science Research Center (SRC) program of the Institute of High Energy Physics, Kyungpook National University.

References

1) Tae-Ik Ro, Byeong Ryong Park, Yeong-Rok Kang, Won-Chung Chung, Guinyun Kim, Youngdo Oh, Samyol Lee, Masayuki Igashira and Toshiro Ohsaki, J. Korean Phys. Soc., **50**, 1598 (2007).
2) R. L. Macklin, J. Halperin, R. R. Winters, Nucl. Sci. Eng. **71**, 182 (1979).
3) E. Cornelis, G. J. Vanpraet, C. Bastian, G. Rohr, R. Shelley, T. Van Der Veen, in *Proceedings of the International Conference on Nuclear Data for Science and Technology*, edited by K. H. Bockhoff (Antwerp, 1982), p.222.
4) R. E. Schenter and F. Schmittroth, ENDF/B-VII data file for ^{105}Pd (MAT=4634) (2006).
5) E. Menapace *et. al*, JEF 3.1 data file for ^{105}Pd (MAT=4634) (2006).
6) Japan Nuclear Data Center Fission Parameter Nuclear Data Working Group, http://www.nndc.bnl.gov/exfor2/ endf00.htm, JENDL 3.3 data file for ^{105}Pd (MAT=4634) (2002)
7) S. Mizuno, M. Igashira, and K. Masuda, J. Nucl. Sci. Tech. **36**,

855 (1999).
8) H. Kim, E. Jung, J. K. Ahn, D. Lee, G. N. Kim, T. I. Ro, Y. K. Min, M. Igashira, T. Ohsaki, and S. Mizuno, J. Korean Phys. Soc. 41, 655 (2002); H. Kim, J. K. Ahn, G. N. Kim, T. I. Ro, W. C. Chung, M. Igashira, T. Ohsaki, and S. Mizuno, J. Korean Phys. Soc. **45**, 1474 (2004).
9) M. Igashira, H. Kitazawa, and M. Yamamuro, Nucl. Instr. Meth**. A 245**, 432 (1986).
10) R. L. Macklin, and J. H. Gibbons, Phys. Rev. **159**, 1007 (1967).
11) P. G. Young, ENDF/B-VII data file for ^{197}Au (MAT=7925) http://www.nndc.bnl.gov/nndc/endf/ (2006).
12) K. Senoo, Y. Nagai, T. Shima, T. Ohsaki and M. Igashira, Nucl. Instr. Meth. **A 339**, 556 (1994).
13) H. Kendrick and S. M. Sperling, "An Introduction to the Principles and Use of the FERDOR code," Gulf Radiation Technology, GA 9882 (1970).

Journal of NUCLEAR SCIENCE and TECHNOLOGY, Supplement 5, p. 447–450 (June 2008)

Detection of the Scintillation Light Emitted from Direct-Bandgap Compound Semiconductors by a Si Avalanche Photodiode at 150 mK

Takashi YASUMUNE[1*], Nobuyasu TAKAYAMA[1], Keisuke MAEHATA[1], Kenji ISHIBASHI[1], and Takahiro UMENO[1, 2]

[1]*Department of Applied Quantum Physics and Nuclear Engineering, Kyushu University, 744, Motooka, Nisi-ku, Fukuoka, 819-0395, Japan*
[2]*Taiyo Nippon Sanso Corporation, 1-3-26, Koyama, Sinagawa-ku, Tokyo, 142-8558, Japan*

In this work, the direct-bandgap compound semiconductor materials are irradiated by α particles emitted from ^{241}Am for the detection of scintillation light at the temperature of 150 mK. For the irradiation experiment, two disk shaped samples were fabricated from an epoxy resin mixed with the powder of PbI_2 and CuI, respectively. Each disk-samples was cooled down to 150 mK by a compact liquid helium-free dilution refrigerator. A Si avalanche photodiode (APD) was employed for detecting the scintillation light emitted from the disk-sample inside the refrigerator. The detection signal current of Si APD was converted into the voltage pulses by a charge sensitive preamplifier. The voltage pulses of the scintillation light emitted from the direct-bandgap semiconductors were observed at the temperature of 150 mK.

KEYWORDS: direct-bandgap semiconductor, scintillation light, avalanche photodiode, low temperature

I. Introduction

Inorganic scintillators are used to detect gamma-rays because of its high detection efficiency. However, most inorganic scintillators have long scintillation decay time. For example, values of the efficiency and the decay time constant of NaI(Tl) are 38000 photons/MeV and 230 ns, respectively. Although GSO(Tl) exhibits a fast decay time constant of 56 ns, the efficiency of 9000 photons/MeV is lower than that of NaI(Tl)[1)].

Direct-bandgap compound semiconductors have a potential for a fast scintillation detector because of their fast scintillation processes. Intensity of scintillation light emitted from the direct-bandgap compound semiconductors has been found to increase with decreasing temperatures from 300 K. In this work, the direct-bandgap compound semiconductor materials are irradiated by α particles emitted from ^{241}Am for the detection of scintillation light at the temperature of 150 mK.

II. Direct-Bandgap Compound Semiconductors

In usual inorganic scintillators, scintillation photons are emitted through the transition between a valence band and impurity levels. On the other hand, the photon emission of pure compound semiconductors arises from exciton recombination transition. The life time of exciton recombination is shorter than other recombination processes. If they have a direct bandgap, Very fast transition for scintillation photon emission has been observed in a direct bandgap semiconductors[2)]. The scintillation decay time of the direct-gap semiconductors have found to be a few nanosecond or less[3)]. Unfortunately they have small scintillation efficiency at room temperature since the thermal energy breaks excitons for scintillation photon emission. For this reason, direct-gap semiconductors have not been used for the scintillation detector. Recently, the scintillation efficiency of some compound semiconductors was found to increase with decreasing temperatures down to 10 K by Derenzo et al[3,4)]. The direct-bandgap compound semiconductor material is expected to exhibit high scintillation efficiency in the low temperature region. Scintillation light from compound semiconductor has not been observed in low temperatures below 1 K.

III. Experiment

For the irradiation experiment, two disk shaped samples were fabricated from an epoxy resin mixed with the compound semiconductor powder of PbI_2 and CuI, respectively. The purity of CuI and PbI_2 were 99.5 % and 95 %, respectively. The powder was mixed with an epoxy resin. After shaping into a disk, the sample was warmed up to the temperature of 400 K for 30 min. Specifications of samples are listed in **Table 1**. The fabricated disk sample was wrapped with aluminum foil and white TPFE tape for increase of light collection efficiency.

Table 1 Specifications of sample

	Powder	Radius	Hight	Weiht
Sample 1	CuI	11.8 mm	5.1 mm	0.8 g
Sample 2	PbI_2	11.7 mm	5.6 mm	0.9 g

A Si avalanche photodiode (APD, Hamamatu Photonics S5344) was employed for detecting scintillation light from the disk-sample of the direct-gap semiconductor. The typical internal gain of the APD was 10-100 or more. The S/N ratio is improved in the low temperature region because of a reduction in the leakage current of the APD. For obtaining the relationship between the leakage current and the bias voltage in low temperatures, the APD was cooled down to

*Corresponding Author, Tel No. and Fax No.: 092-802-3484, E-mail: yasumune@kune2a.nucl.kyushu-u.ac.jp

150 mK by operating a liquid-helium-free ^{3}He-^{4}He dilution refrigerator. **Fig. 1** shows the relationship between the leakage current and the bias voltage of the APD measured at 150 mK, 3.6 K and 298 K. The large decrease in the leakage current was observed at low temperatures. Because of the leakage current smaller than 1 pA, the APD is expected to operate with improved S/N ratio at low temperatures.

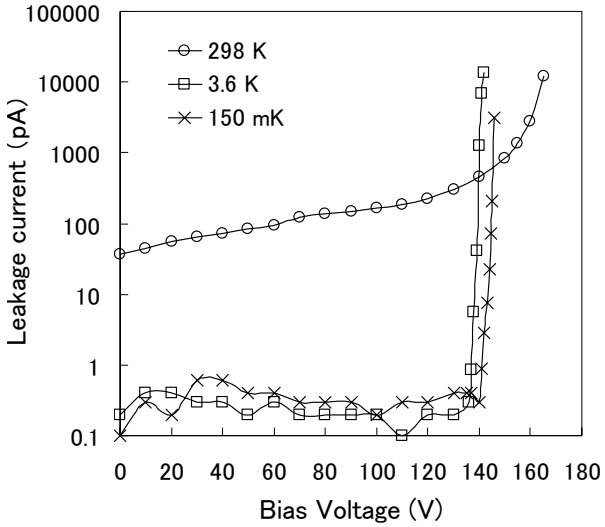

Fig. 1 The relationship between the leakage current and the bias voltage at several temperatures (S5344)

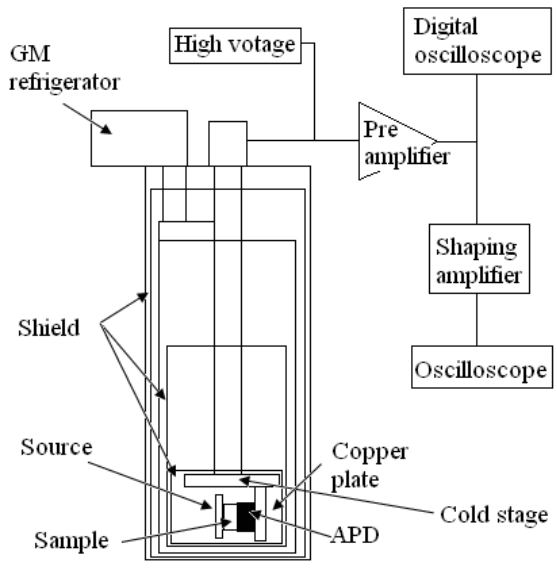

Fig. 2 A schematic diagram of the measurement system

Fig. 2 shows a schematic diagram of the measurement system. The APD was mounted on the holder of a copper plate attached on the cold stage. A sensitive area of the APD was irradiated by γ-rays of 60 keV emitted from ^{241}Am source placed in front of the APD. The current signal of the APD was converted into voltage pulse signal by a charge sensitive preamplifier. **Fig. 3** shows an example of the voltage signal pulse of the γ-ray detection by the APD operated at 150 mK. The signal pulse had a rise time constant of 120 ns.

The APD was irradiated with continuous light emmited by a LED for the photocurrent measurement. **Fig. 4** shows the relationship between the relative gain and the bias voltage at 150 mK, 4 K, 13 K and 40 K. An avalanche multiplication was observed at low temperatures. Judging from the above, the APD can be operated in the range of 150 mK to 40 K.

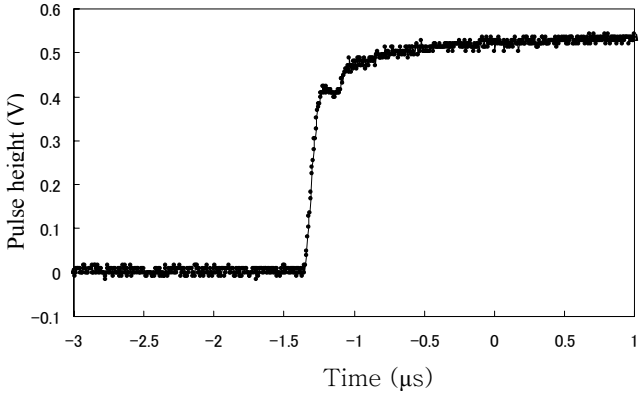

Fig. 3 Example of the voltage signal pulse

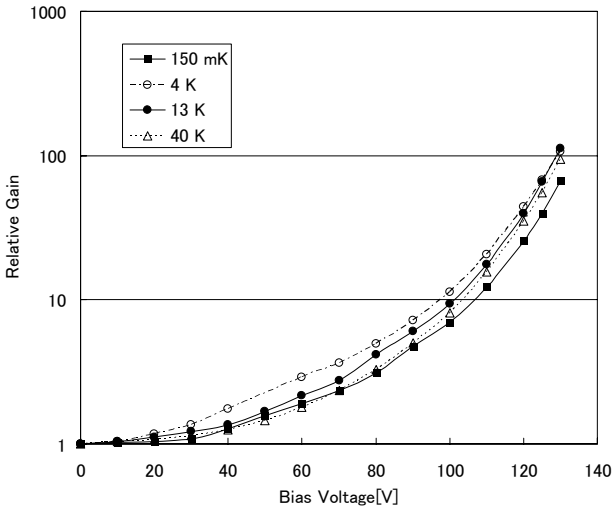

Fig. 4 The relationship between the relative gain and the bias voltage at several temperatures (S5344)

The fabricated disk sample with wrapping was mounted on the APD in the dilution refrigerator as shown in **Fig.2**. The disk sample was irradiated by α particles emitted from ^{241}Am through a hole 2mm diameter at the center of the wrapping. Scintillation light was transmitted to the APD from the sample through a hole of 2 mm in diameter located at the center of the wrapping. The detection signal current of Si APD was converted into the voltage pulses by a charge sensitive preamplifier (CANBERRA 2003BT), and fed to the shaping amplifier (ORTEC 572). The voltage pulses of the preamplifier and the shaping amplifier were accumulated into a digital oscilloscope (Tektronix DPO7000) for analyzing the pulse shape of the detection signal. The temperature of the disk sample and the Si APD was maintained at 150 mK by operating the refrigerator.

IV. Results

1. Measurement of CuI

Fig. 5 shows the voltage signal pulses of the charge sensitive amplifier in the case of mounting the disk sample fabricated from CuI powder. Two types of signal voltage pulses were observed with different rise time constants. The signal pulses with fast rise time constant of 120 ns correspond to the current generated by the γ-rays absorbed in the depletion layer of the APD by referring **Fig. 3**. Therefore, detection of scintillation light by the APD is attributed to the signal pulses with slow rise time constant of 500 ns.

The decay time constant of scintillation light of the CuI sample is obtained by differentiating the rise part of the slow voltage signal pulse in **Fig. 5**. **Fig. 6** shows the differentiating result. The decay time constant of the CuI sample is estimated to be 130 ns. The estimated time constant is much longer than our expectation. Various impurities contained in the sample may contribute to lengthen the decay time.

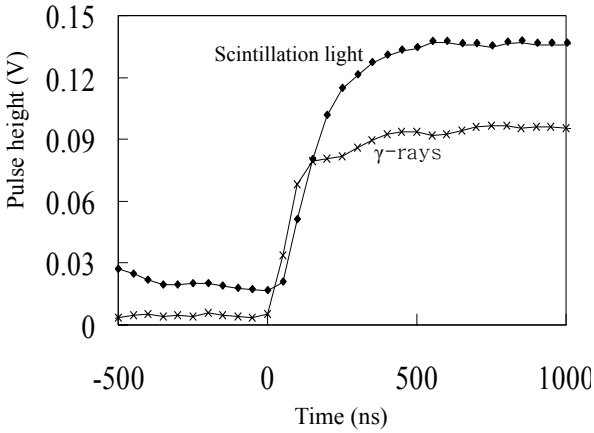

Fig. 5 The signal pluses from the preamplifier (CuI)

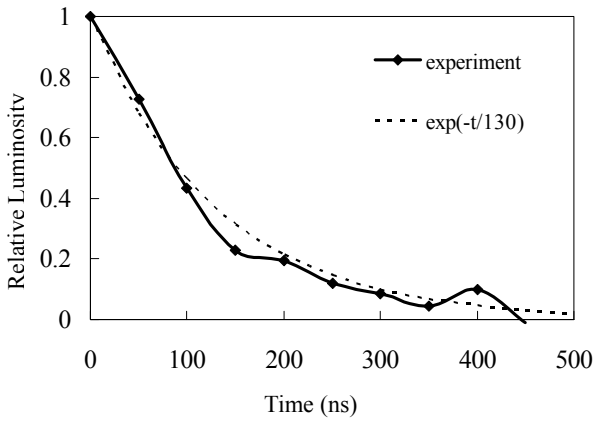

Fig. 6 The differential signal pulse from scintillation light of CuI

2. Measurement of PbI_2

Fig. 7 shows the voltage signal pulses of the charge sensitive amplifier in the case of mounting the disk sample fabricated from PbI_2 powder. The signal pulse with rise time constant of 400 ns correspond to the detection of the scintillation light by the APD, while a direct γ-ray detection by the APD generates the fast signal with the rise time constant of 120 ns.

Fig. 8 shows the result of differentiating the rise time part of the slow signal in **Fig. 7**. The decay time of PbI_2 was estimated to be 110 ns much longer than our expectation.

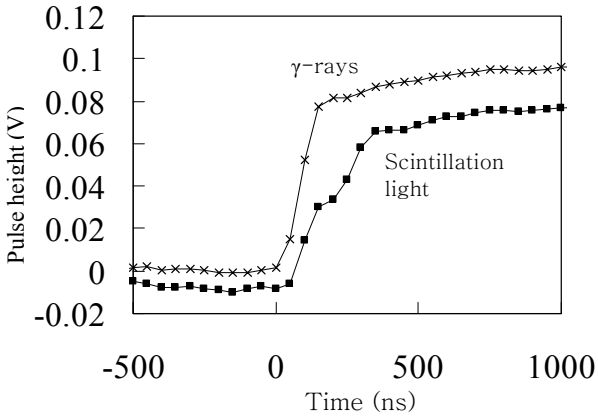

Fig. 7 The signal pluses from the preamplifier (PbI_2)

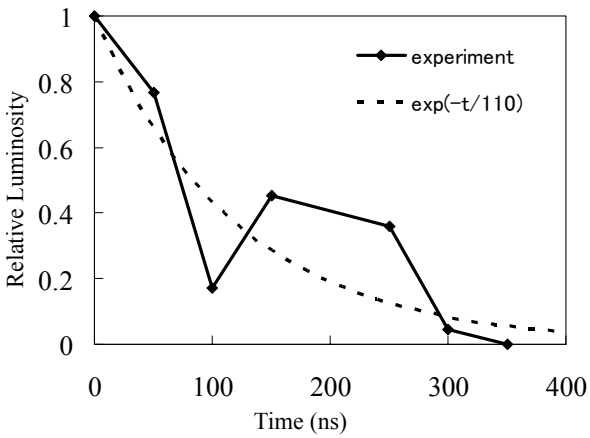

Fig. 8 The differential signal pulse from scintillation light of PbI_2

V. Conclusion

The scintillation light emitted from direct band-gap semiconductors of CuI and PbI_2 was detected by the APD at the temperature of 150 mK. By analyzing the rise part of the voltage signal pulse of the preamplifier, the decay time constants of scintillation light of CuI and PbI_2 were obtained to be 130 ns, 110 ns, respectively. They were much slower than we have expected. The impurities in the semiconductor may disturb the scintillation processes and the life time of an excited state is lengthened.

Reference

1) Glenn F. Knoll, Radiation Detection and Measurement,third edition, JohnWiley & Sons, Inc., 235
2) J.I.Pankove, Optical Processes in Semiconductors, Dover Publications, New York, 114
3) S.E. Derenzo, M.J. Weber, M.K. Klintenberg, Temperature dependence of the fast, near-band-edge scintillation from CuI,

HgI_2, PbI_2, ZnO:Ga and CdS:In, Nucl. Instr. and Meth. A486, 214, (2002)
4) M.K. Klintenberg, M.J. Weber, S.E. Derenzo, Luminescence and scintillation of PbI_2 and HgI_2, Journal of luminescence 102-103, 287, (2003)

Journal of NUCLEAR SCIENCE and TECHNOLOGY, Supplement 5, p. 451–454 (June 2008)

Influence of Tomographic Parameters on the Image Quality of Digital X-ray Tomosynthesis

J. E. OH[1], H. S. CHO[1*], S. I. CHOI[1], K. Y. KIM[1], S. Y. LEE[1], B. S. LEE[2], and S. KIM[3]

[1]*Department of Radiological Science, Yonsei University, Wonju 220-710, Korea*
[2]*School of Biomedical Engineering, Konkuk University, Chungju 380-701, Korea*
[3]*Department of Nuclear and Energy Engineering, Cheju National University, Cheju 690-756, Korea*

In this study, by using the MATLAB® 7.0 program, we investigated the fundamental principle of digital X-ray tomosynthesis (DTS) and, furthermore, the influence of tomographic parameters associated with the acquisition and reconstruction processes for the isocenter motion, including the tomographic angle (θ) and the angle increment between each projection (Δθ) on the reconstructed images. A proper compensation for the ununiform magnification for the isocenter motion was made in the tomographic algorithm to remove the geometrical distortion in the acquired projections. A simple tomographic algorithm, the so-called the modified shift-and-add (MSAA), was also studied in order to reduce effectively the blurring artifact that occurs typically in the conventional reconstruction algorithm of SAA. We expect that the simulation results we obtained in this study will be useful for the optimal design of a digital X-ray tomosynthesis system for our ongoing application of nondestruction testings.

KEYWORDS: Tomosynthesis, tomographic parameters, image quality, projection, shift-and-add (SAA)

I. Introduction

The principle of tomosynthesis is not new, but recently digital X-ray tomosynthesis (DTS) has gained popularity in many areas of medical and industrial applications such as mammography, dental radiography, and nondestructive testings owing to the recent digital revolution in imaging [1-3]. The DTS is a three-dimensional (3D) imaging technique that has the ability to address shortcomings of conventional X-ray imaging modalities in which all structures in the imaged 3D volume become superimposed onto a two-dimensional (2D) radiograph. It refers to a limited-angle technique of 3D image reconstruction with a low X-ray exposure, in which a set of projection data acquired within a limited-tomographic angle are subsequently used to synthesize the image of whole object, basically by using the reconstruction algorithm of shift-and-add (SAA) [4-6]. **Fig. 1** shows a schematic illustration of the DTS principle. Here a sequence of projections are acquired by moving the X-ray tube and the detector around a fulcrum on a specific plane within a limited angle and then all the projection data are properly shifted-and-added such that only a specific plane is focused and others are blurred out. The common way to achieve this is to use a parallel-path geometry and thus to move the X-ray tube and the detector in a linear fashion in an opposite direction. However, it requires a very precise control in the movement of the X-ray tube and the detector, especially, in the direction of the X-ray tube. In this study, as shown in **Fig. 1**, we used the isocenter motion just as in the C-arm, in which a proper compensation for the ununiform magnification should be made to remove geometrical distortion in the acquired projections. In this paper, by using the MATLAB® 7.0 program, we investigated the fundamental principle of DTS and, furthermore, the influence of tomographic parameters associated with the acquisition and reconstruction processes, including the tomographic angle (θ) and the angle increment between each projection (Δθ) on the reconstructed images. A simple tomographic algorithm, the so-called the modified shift-and-add (MSAA), was also studied to reduce effectively the blurring artifact that typically occurs in the SAA.

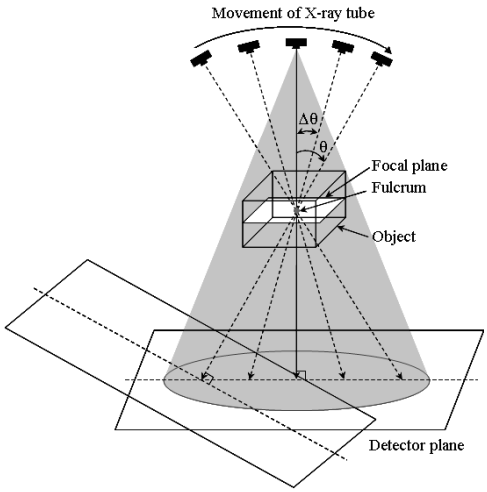

Fig. 1 Schematic illustration of the principle of the digital X-ray tomosynthesis (DTS) with the isocenter motion.

II. Methods and Results

1. Simulation Geometry

Fig. 2 shows a schematic illustration of the geometrical structure used in the simulation study emulated with the MATLAB® 7.0 program. Three different patterns with a

*Corresponding Author, Tel No: +82-33-760-2428, Fax No: +82-33-760-2815, E-mail: hscho1@yonsei.ac.kr

cross-, a horizontal-, and a vertical-shaped rectangles were placed in order on each plane-of-interest (POI) of a 128 x 128 pixel size and designed to have a linear attenuation coefficient (μ) of unity (arbitrarily); zero for the remaining structures. To emulate a cone-beam exposure, we used a built-in function, *fanbeam( ),* in the MATLAB® 7.0 program, being translated step by step perpendicularly to the fanbeam direction; thus no parallex effect occurs in the translation direction of the fanbeam. In order to examine the influence

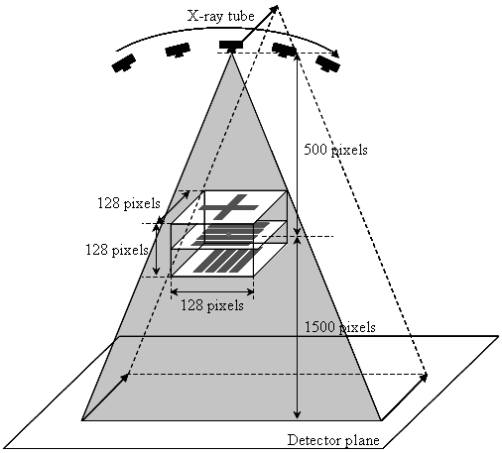

Fig. 2 Schematic illustration of the geometrical structure used in the simulation emulated with the MATLAB® 7.0 program.

of tomographic parameters associated with the acquisition and reconstruction processes on the final images reconstructed, we acquired a sequence of projections around a fulcrum selected for each POI with θ = ± 20°, ± 30°, and ± 40° at a fixed angle increment of 10° and with the angle increments between each projection of 5°, 10°, and 15° at a fixed θ = ± 30°. After being applied a proper compensation for the ununiform magnification in the isocenter motion described in the next section, the resultant projections were shifted-and-added with the corresponding shift length.

2. Magnification Compensation

For the isocenter motion in which the X-ray tube and the detector move concentrically around the fulcrum in an opposite direction but the object is stationary, a proper compensation for the ununiform magnification should be made in order to remove geometrical distortion in the acquired projections due to the different distance from each point of the POI to the X-ray tube, as shown in **Fig. 3**. In **Fig. 3**, the point *P* located at $x = d$ is imaged to the point *P'* at *x'=d'* with a geometrical magnification of *M'(d,θ)* as the following equation:

$$M'(d,\theta)=\frac{H}{h+d\sin\theta},\quad d'(d,\theta)=\frac{Hd\cos\theta}{h+d\sin\theta}. \tag{1}$$

Thus the proper magnification compensation for each point of the POI can be made by dividing *M'(d,θ)* into the magnification of the point *O* on the POI (i.e., *H/d*).

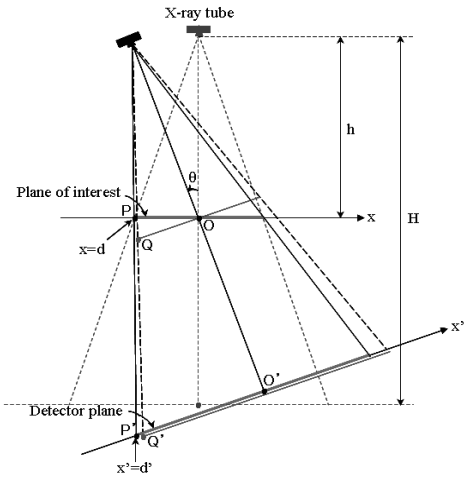

Fig. 3 Magnification compensation for the isocenter motion required to remove geometrical distortion in the projections.

Fig. 4 and **5** show the tomographic images obtained with the phantom having only the third POI in **Fig. 2** (a) before and (b) after making the magnification compensation and the grayscale distribution along the migration of **Fig. 4**, respectively.

(a) (b)

Fig. 4 Tomographic images (a) before and (b) after making the magnification compensation for the isocenter motion.

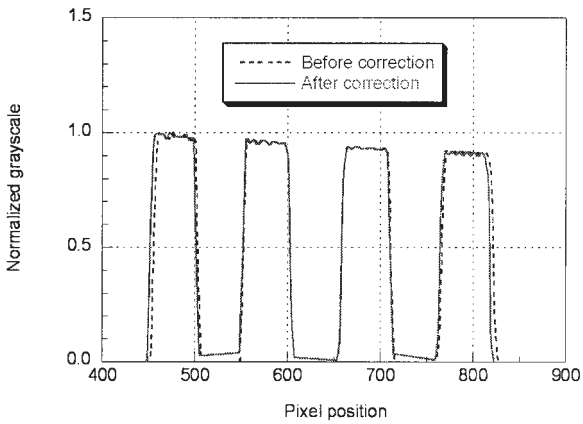

Fig. 5 Distribution of the grayscales measured along the migration of **Fig. 4**.

3. Modified Shift-And-Add (MSAA)

We studied a simple reconstruction algorithm, MSAA, to reduce the blurring artifact effectively. **Fig. 6** shows the simplified principle of the MSAA algorithm to enhance the image sharpness. The MSAA is fundamentally based upon the SAA but has a correction procedure by extracting the blurring artifact (i.e., $f_{SAA(POI=0)}(x,y;z)$) from the firstly-

reconstructed image data for the whole POIs and then subtracting it from the firstly-reconstructed image data of the specific POI (i.e., $f_{SAA(POI)}(x,y,z)$). Here the first step of the correction procedure is performed just by replacing the original image data for the specific POI with zeros.

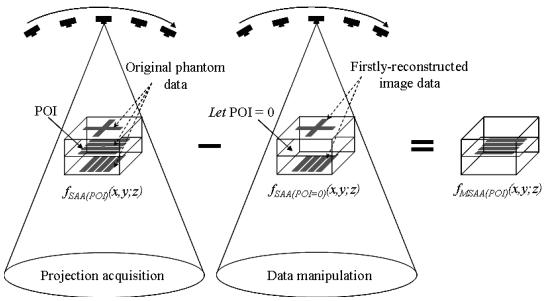

Fig. 6 Simplified principle of MSAA algorithm to enhance the image sharpness in the conventional DTS based upon the SAA.

4. Simulation Results

Fig. 7 shows the projections obtained around the fulcrum at the second POI with a tomographic angle of ± 30° at a fixed angle increment of 10°: at (a) θ = -30°, (b) θ = -20°, (c) θ = -10°, and (d) θ = 0°.

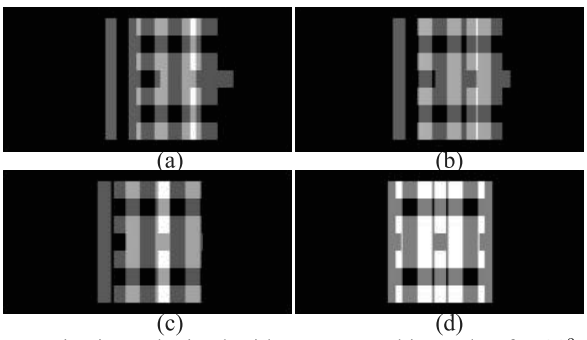

Fig. 7 Projections obtained with a tomographic angle of ± 30° at a fixed angle increment of 10°: at (a) θ = -30°, (b) θ = -20°, (c) θ = -10°, and (d) θ = 0°.

Fig. 8 and **9** show the reconstructed images for each POI by using (a) the SAA and (b) the MSAA algorithms with a tomographic angle of ± 30° at a fixed angle increment of 10° and the grayscale distribution along the migration of **Fig. 8**, respectively, indicating the effectiveness of the MSAA algorithm. **Fig. 10** shows the reconstructed images for the second POI obtained with tomographic angles of (a) ± 20°, (b) ± 30°, and (c) ± 40° at a fixed angle increment of 10° by using the SAA and the MSAA algorithms. **Fig. 11** also shows the grayscale distribution measured along the migration of **Fig. 10**, indicating the higher image sharpness for the larger tomographic angle. **Fig. 12** and **13** show the similar images for the third POI obtained with a tomographic angle of ± 30° at a fixed angle increment of 15°, 10°, and 5° by using the SAA and the MSAA algorithms and the grayscale distribution along the migration of **Fig. 12**.

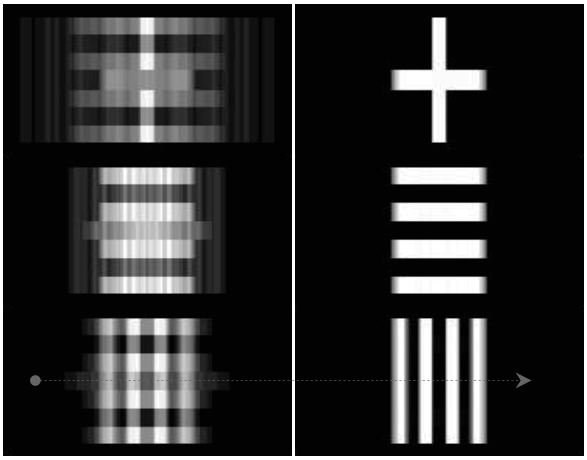

Fig. 8 Reconstructed images for each POI by using (a) the SAA and (b) the MSAA algorithms.

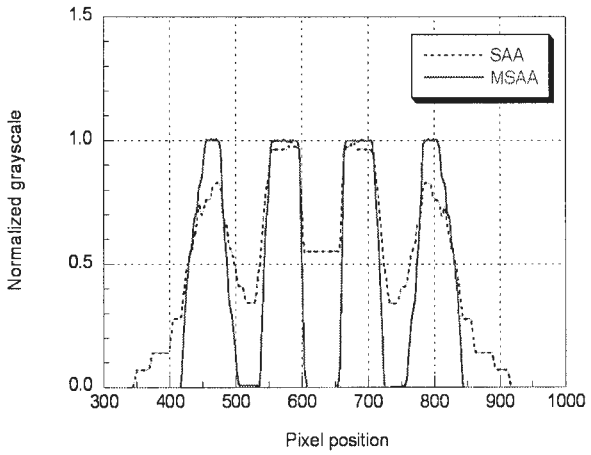

Fig. 9 Grayscale distribution measured along the migration of **Fig. 8**, showing the enhancement of the image sharpness with the MSAA.

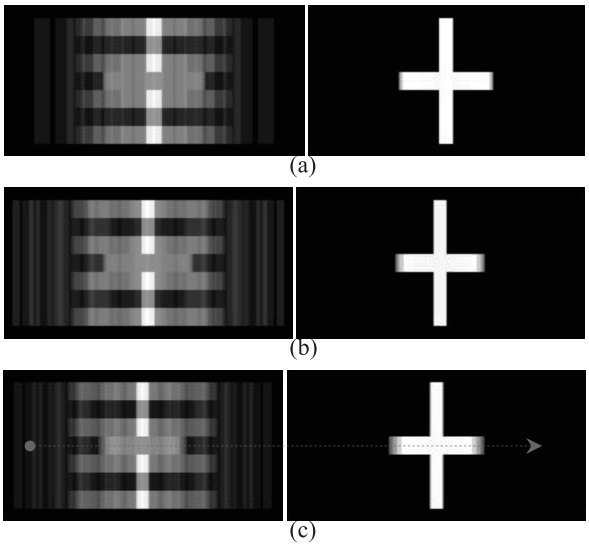

Fig. 10 Reconstructed images for the second POI obtained with tomographic angles of (a) ± 20°, (b) ± 30°, and (c) ± 40° at a fixed angle increment of 10° by using the SAA and the MSAA algorithms.

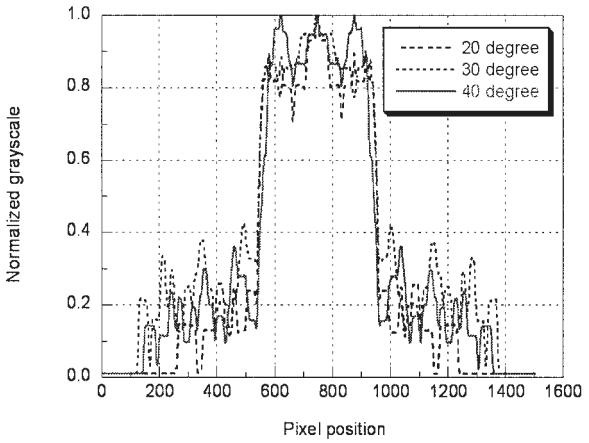

Fig. 11 Grayscale distribution along the migration of **Fig. 10**.

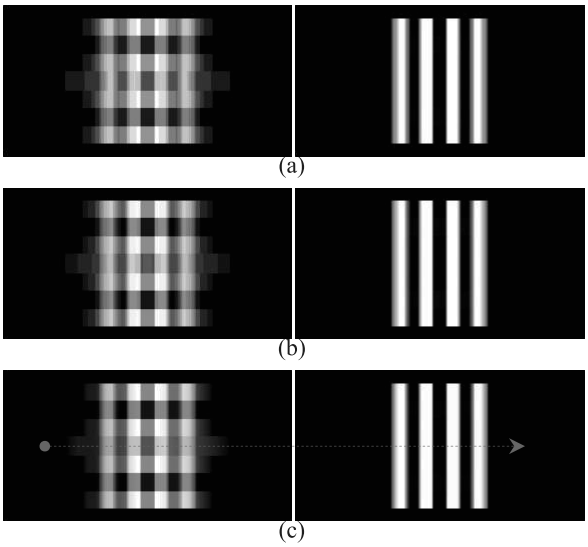

Fig. 12 Reconstructed images for the third POI obtained with a tomographic angle of ± 30° at a fixed angle increment of (a) 15°, (b) 10°, and (c) 5°, respectively.

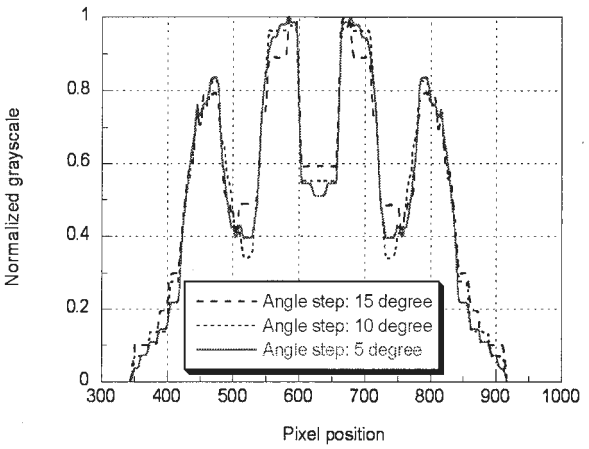

Fig. 13 Grayscale distribution along the migration of **Fig.12**.

III. Conclusion

For the optimal design of a digital X-ray tomosynthesis system in our ongoing application of nondestruction testings, we first studied the fundamental principles of DTS and, furthermore, the influence of tomographic parameters associated with the acquisition and reconstruction processes for the isocenter motion, including the tomographic angle and the angle increment between each projection on the reconstructed images by using the MATLAB® 7.0 program. A proper magnification compensation for the isocenter motion was made in the tomographic algorithm to remove the geometrical distortion in the acquired projections. A simple tomographic algorithm, MSAA, reduced the blurring artifact effectively. The image quality of the DTS improved as the tomographic angle increased and the angle increment decreased. More quantitative evaluation of the effect of the tomographic parameters and the related experiments are being performed.

Acknowledgement

This work was supported by the Basic Atomic Energy Research Institute (BAERI) program of the Ministry of Science and Technology (MOST) under contract No. M2-0376-03-0000.

References

1) G. M. Stevens, R. L. Birdwell, C. F. Beaulieu, et al., "Circular Tomosynthesis: Potential in Imaging of Breast and Upper Cervical Spine-Preliminary Phantom and in Vitro Study," Radiology, **228**, 569 (2003).
2) J. Dobbins III and D. Godfrey, "Digital Tomosynthesis: Current State of the Art and Clinical Potential," Phys. Med. Biol., **48**, 65 (2003).
3) J. Liu, D. Nishimura, and A. Macovski, "Generalized Tomosynthesis for Focusing on an Arbitrary Surface," IEEE Trans. Med. Imaging., **8 (2)**, 168 (1989).
4) L. T. Niklason, "Digital Tomosynthesis in Breast Imaging," Radiology, **205**, 399 (1997).
5) R. J. Warp, D. J. Godfrey, and J. Dobbins III, "Applications of Matrix Inverse Tomosynthesis," Proc. SPIE, **3977**, 376 (2000).
6) J. Duryea, J. Dobbins III, and J.A. Lynch, "Digital Tomosynthesis of Hand joints for arthritis assessment," Med. Phys., **30**, 325 (2003).

Journal of NUCLEAR SCIENCE and TECHNOLOGY, Supplement 5, p. 455–457 (June 2008)

Urethral Alarm Probe for Permanent Prostate Implants

D.CUTAJAR[1], M.LERCH[1], G.TAKACS[1], B.LEE[2**], Y.S.CHIN[3], J.BUCCI[3], M. ZAIDER[4], M. ZELEFSKY[4], J.YAMADA[4], G.N. COHEN[4], V.L.PEREVERTAYLO[5] and A.B. ROSENFELD[1*]

[1]*Centre for Medical Radiation Physics, University of Wollongong, Australia*
[2]*Department of Biomedical Engineering, College of Biomedical & Health Science, Konkuk University, South Korea*
[3]*St George Cancer Care Centre, Kogarah, Australia*
[4]*Memorial Sloan Kettering Cancer Center, New York, USA*
[5]*SPA BIT, Ukraine*

We have developed a urethral dosimetry system for real time dose verification along the urethra during permanent implant prostate brachytherapy. The urethral alarm probe uses "spectroscopic dosimetry" to calculate the dose rate along the urethra in real time. The application of spectroscopic dosimetry for the urethral alarm probe was verified using Monte Carlo calculations. In phantom depth dose measurements as well as isotropy measurements were performed to verify the usefulness of the urethra alarm probe as an in vivo real time dosimeter.

KEYWORDS: permanent implant, brachytherapy, prostate, real time, spectroscopic dosimetry, Monte Carlo

I. Introduction

Permanent prostate implants are a common treatment modality for early stage prostate cancer. Reducing the risk of complications, whilst at the same time maintaining good dosimetric coverage of the tumor, is a major concern in prostate brachytherapy. We have developed a probe which measures in real time the dose delivered along the urethra and may be used by the physicians during seed implantation to monitor for excessive doses. In vivo dosimetry is commonly performed with miniature radiation detectors such as MOSFETs or diodes[1)]. The main disadvantages of such systems are energy dependence and low sensitivity. The urethral alarm probe circumvents these problems by measuring the energy spectrum of the treatment radiation field. The dose rate at the point of measurement is proportional to the magnitude of the measured photopeaks. The urethral alarm probe consists of a silicon mini-detector connected to a shaping amplifier and discriminator, located inside a cable small enough to be inserted within a urethral catheter. A portable data acquisition system provides real time dose calculations and extrapolated total treatment doses. The following reports on Monte Carlo calculations and physical experiments to confirm the suitability of spectroscopic dosimetry as a tool for low dose rate in vivo measurements.

II. Methodology

1. Monte Carlo Simulations

EGSnrc v4[2)] was used for the following Monte Carlo simulations. The user code DOSRZnrc was used to score doses in a water phantom whereas the user code FLURZnrc was used to score particle fluence in a water phantom.

An iodine 125 based brachytherapy seed, model 6711 from Amersham Health, was modeled in a large liquid water phantom. The dose deposited in the phantom was recorded at 5 mm intervals up to 5cm from the seed along the transverse axis and normalized to 1 at 1cm. The particle fluence was also recorded at 5mm intervals up to 5cm from the seed long the transverse axis. The number of events in the photopeaks were counted for each of the spectra and normalized to 1 at 1cm, to simulate the application of spectroscopic dosimetry, calibrated at a distance of 1cm from the seed. The two depth-dose curves were plotted to compare the DOSRZnrc predicted dose and the spectroscopic dosimetry predicted dose.

2. Phantom Measurements

1) Depth dose measurements

An iodine 125 based seed was placed inside a gel phantom. The urethral alarm probe was used to measure the extrapolated treatment dose at various distances from the seed along the transverse axis. These doses were plotted in comparison with TG43 (3) calculated doses.

2) Isotropy measurements

An iodine 125 based seed was placed inside a gel phantom. The urethral probe was placed 1cm from the seed on the transverse axis of the seed. The probe was rotated 360° with measurement taken every 30° to measure the azimuth isotropy of the detector. The probe was then moved parallel to the seed with measurements taken every 5mm. Each step of 5mm increased the polar angle of measurement, but also increased the source to detector distance. The measured dose vs. expected dose was plotted to investigate the polar isotropy of the detector.

III Results

1. Monte Carlo Simulations

*Corresponding Author, Tel No: +61-2-4221-4574, Fax No: +61-2-4221-4954, E-Mail: anatoly @uow.edu.au
**B. Lee is currently a visiting fellow at CMRP on sabbatical

The application of spectroscopic dosimetry has been simulated using FLURZnrc. **Fig. 1** shows the comparison of spectra measured at 0.5cm and 5cm from an iodine 125 based seed. It can be seen from **Fig. 1** that the shape of the spectrum does not change significantly with distance, although the fluence has greatly decreased. This indicates that spectroscopic dosimetry may be viable over a large range of depths (up to 5cm from sources).

a)

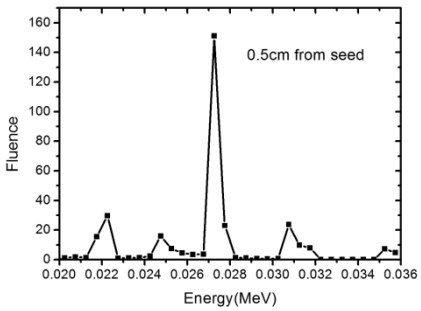

b)

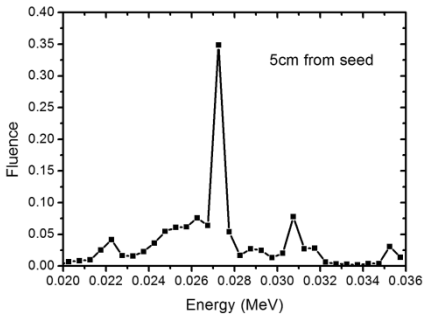

Fig.1 Spectra at depths of a) 0.5cm and b) 5cm from an iodine 125 seed.

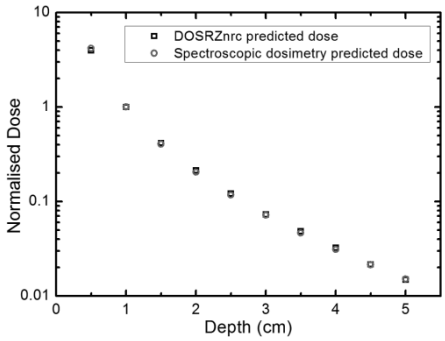

Fig. 2 Spectroscopic dosimetry predicted dose and DOSRZnrc predicted dose vs. depth

Fig. 2 shows the depth dose curves for both the spectroscopic dosimetry predicted doses and calculated doses, up to 5cm from an iodine 125 based seed. Spectroscopic dosimetry has predicted the dose to within 2% of the calculated dose for each point of measurement.

2. Phantom Measurements

The measured spectrum of an iodine 125 based seed in free air is shown in **Fig. 3**. Several peaks are well resolved, indicating the urethral alarm probe is adequate for performing spectroscopy based dose calculations.

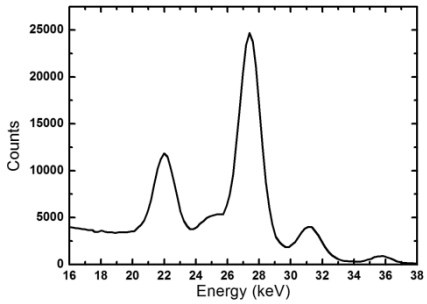

Fig. 3 Iodine 125 based seed spectrum as measured by the urethral alarm probe at a distance of 1cm in free air.

Depth dose curves for an iodine 125 based seed in a gel phantom as measured by the urethral alarm probe and as calculated by TG43 are shown in **Fig. 4**. The urethral alarm probe has measured the doses to within 5% of the expected doses.

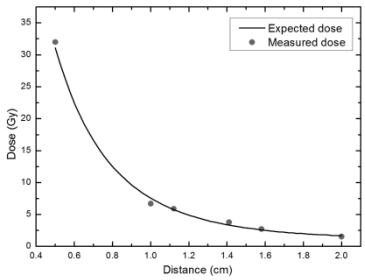

Fig. 4 Depth dose curve from an Iodine 125 based seed in a gel phantom as measured by the urethral alarm probe and calculated using TG43[3].

The azimuthal isotropy of the urethral alarm probe is represented in **Fig. 5**. The urethral alarm probe has an isotropy within 4% of the mean response for 360° about the detector azimuth.

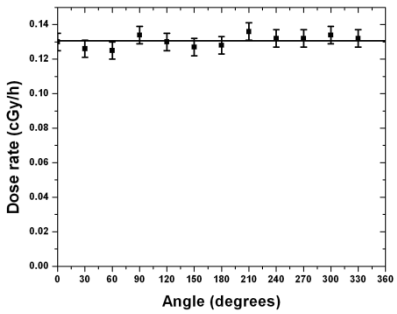

Fig. 5 Azimuthal isotropy of the urethral alarm probe

The polar isotropy of the urethra alarm probe is represented in **Fig. 6**. The decrease in dose with an increase of angle between transverse axis of the seed and direction from the seed center to the detector is due to the increasing source to detector distance. The measured doses were within 5% of the calculated doses. The urethral alarm probe exhibits a polar isotropy to within 5% for angles up to 80° from the polar axis.

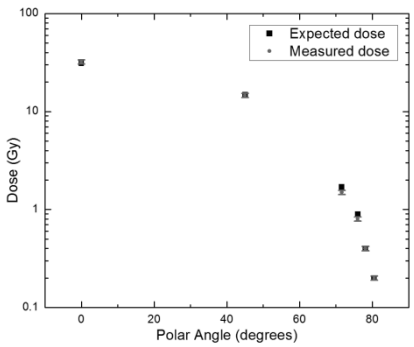

Fig. 6 Polar isotropy of the urethral alarm probe

IV. Conclusion

The urethral alarm probe has been developed to provide real time dosimetry for permanent implant prostate brachytherapy. Monte Carlo calculations have shown spectroscopic dosimetry to be accurate to within 2% up to 5cm from low energy x-ray sources with distinct emission spectra. The urethra alarm probe uses spectroscopic dosimetry to measure low dose rates to an accuracy of within 5% of calculated doses, up to 5cm from sources, and for all angles of incidence about the detector (for both azimuth and polar angles).

The urethral alarm probe demonstrates the ability for real time in vivo dose measurements using spectroscopic dosimetry. The patented urethral alarm probe will be a very useful tool in clinical dose verification both during seed implantation and post implant.

References

1) A.B. Rosenfeld, D.L. Cutajar, M.L.F. Lerch, G.J. Takacs, J. Brady, T.Braddock, V.L. Perevertaylo, J. Bucci, J. Kearsley, Zaider M, Zelefsky, In vivo dosimetry and seed localization in prostate brachytherapy with permanent implants. IEEE Trans. Nucl. Science, 51: 3013-3018 (2004).
2) I. Kawrakow and D. W. O. Rogers, "The EGSnrc code system," NRC, Ottawa, ON, Canada, NRC Rep. PIRS-701, (2000)
3) R. Nath, L. L. Anderson, G. Luxton, K. A. Weaver, J. F. Williamson, A. S. Meigooni, "Dosimetry of interstitial brachytherapy sources: Recommendations of the AAPM Radiation Therapy Committee Task Group No. 43," Med Phys, 22 (2), Feb, pp 209-234 (1995)

Journal of NUCLEAR SCIENCE and TECHNOLOGY, Supplement 5, p. 458–461 (June 2008)

A Dual Scintillator – Dual Silicon Photodiode Detector Module for Intraoperative Gamma\Beta Probe and Portable Anti-Compton Spectrometer

A.B. ROSENFELD[1*], M.L.F. LERCH[1], M. CHAN[1], D. INWOOD[1], G.J. TAKACS[1], D. INWOOD[1], B. LEE[2**], A.F. GEKTIN[3], and V.L. PEREVERTAYLO[4]

[1]*Centre for Medical Radiation Physics, University of Wollongong, NSW 2522 Australia*
[2]*Department of Biomedical Engineering, Research Institute of Biomedical Engineering, College of Biomedical and Health Science, Konkuk University, Korea*
[3]*AMCRYS-H, Kharkov, Ukraine*
[4]*SPO BIT, Ukraine*

A new approach has been investigated for the miniaturization and simplification of intraoperative gamma and beta probes that have recently found application in radioguided surgery and sentinel lymph node biopsy. The probe design that is based on dual annular scintillators coupled to specially designed silicon concentric dual photodiode (CDPD). This approach allows us to avoid fiber optics coupling and PMTs. Two channels readout front-end electronics including shaper amplifier attached directly to the back of the detector module has been proposed. Two geometries of Si dual photodiodes coupled to CsI(Tl) annular scintillators with light masking between them were fabricated and investigated. CDPDs have size 10 and 6 mm as well as 6 and 3 mm outer and inner diameters respectively. The spectroscopy properties of CDPD separately and coupled to CsI(Tl) dual scintillator were investigated on I-125, Co-57 and Na-22 photon sources. Both detectors have demonstrated acceptable energy resolution (10% for 511-keV) for the proposed application with FDG isotopes. In the smaller detector the amplitude of the 511 keV photopeak from outer detector was less than in inner and is related to the light collection in the current geometry. When used in coincidence mode operation we observe a significant reduction in the measured Compton continuum level relative to the photopeak which is not significantly attenuated. The spatial resolution of detector module measured in the horizontal plane was 2-mm FWHM using a 0.5-mm collimated Tc-99m source.

KEYWORDS: photodetector, anti-Compton, lymphoscintigraphy

I. Introduction

Intraoperative gamma and beta probes have found application in radioguided surgery and sentinel lymph node biopsy. The development of a portable beta probe suitable for endoscopic procedures is also of great interest. Coupling of the miniature radiation probe with an endoscopic device may eliminate the need of multiple biopsy samples thus providing minimally invasive determination and treatment of cancer.

The most widely used isotopes for cancer targeting are Tc-99m gamma emitter with energy 140 keV and F-18 (FDG) positron emitting isotope with annihilation 511-keV photons. In both cases the finding of the cancer requires the ability of the detection device to distinguish the increased uptake on a radiation background of normal tissue uptake. The situation is even more complicated in the case of FDG tracers because high energy 511-keV photons are producing an essential contribution to the beta channel which makes it difficult to distinguish the spot (often quite small in size) with the highest uptake. The development of unique probe, which will be suitable both for pure gamma emitters and FDG isotopes with excellent spatial resolution, is a challenge.

The traditional approach that utilizes passive collimation and scintillator coupled to PMT is not suitable in a 511-keV photon field. Essential increasing of the thickness of the passive protection leads to increasing the size of the probe, making difficult for intraoperative use. Using concentric scintillators separated by layer of lead or steel and coupled to the two separate PMTs via fiber optics demonstrated improvements in the spatial resolution. The improvement was due to the suppression of the 511-keV gamma background in the beta channel (core detector) in case of an FDG isotope or reducing the contribution of scattered gamma radiation to the core detector in case of Tc-99m.[1,2)] A detector module for beta activity detection with gamma suppression in case of FDG isotope, which is based on two back-to-back 0.5-mm thick Si SBD detectors with 3-mm diameter of active region, also has been proposed.[3)] For full depletion of such detectors 150 V bias is required.

The current paper describes the proposed at CMRP, manufactured and tested prototype of a patented detector module, which will be suitable for gamma/beta activity detection with high spatial resolution on a background of high energy gamma radiation. This module is based on concentric, optically isolated CsI(Tl) scintillators coupled to a dual single crystal PD, optimized and fabricated for this application.

In this paper we report on the technical characteristics of the dual, circular, concentric photodiodes of different

*Corresponding Author, Tel No: +61-2-42214574, Fax No: +61-2-42215944, E-Mail; anatoly@uow.edu.au
**B. Lee is currently a visiting fellow at CMRP on sabbatical

geometry that incorporates dual scintillator technology and the spectroscopic characteristics of dual scintillator-dual photodiode module for Co-57 (122 keV), Tc-99m (140 keV), Na-22 (511 keV) and Cs-137 (662 keV). Some comparisons are also made with a currently available commercial probe that is based on a solid state CdZnTe detector configuration.

II. Detectors, Materials and Methods

Fig. 1a and **1b** show the principle of the detector module with dual concentric PDs. The advantage of this approach is in identical readout electronics due to the same nature of detectors, possibility of miniaturization with readout miniature front-end electronics attached directly at the back of the detector, low voltage operation (25V), utilizing of coincidence technique for improvement of spread function of probe in case of beta/gamma or pure gamma isotope activity mapping.

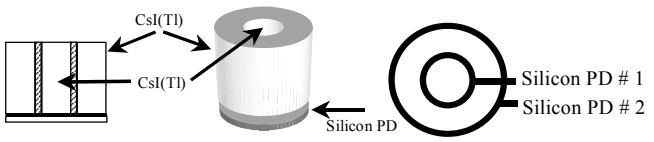

Fig. 1 schematic diagram of (a) the concentric PD coupled to dual scintillator and (b) the concentric PD design

To evaluate the detector module properties, the module was mounted on a computer controlled rotating/translating gantry (shown in **Fig. 2a**) designed and built at CMRP labs. A lead block as shown in **Fig. 2b** was used to collimate a variety of radiation sources. In the case of Tc-99m, which was used to determine the spatial resolution of the probe, the radioactive source was sealed in a fine plastic tube, which then positioned inside the block. The probe was positioned 1.9 mm above the point source defined by the block. The probe was moved in x-direction and acquisition time for the inner detector was 300 s with Tc-99m (140 keV). Response using the inner detector was measured, with the acquisition time being 30 s. The spatial resolution is the FWHM of the experimentally measured line spread function.

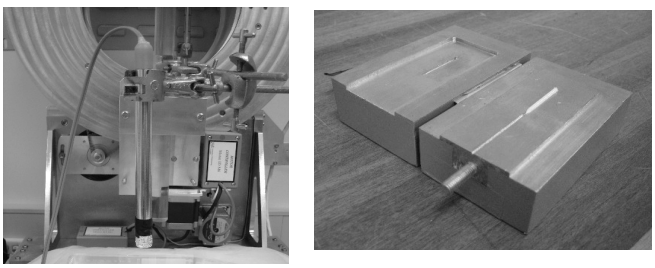

Fig. 2 Photo of (a) the dual probe mounted on the scanning gantry and (b) the two piece lead collimator used in the experiments.

III. Results and Discussion

Two different geometries of dual concentric photodiodes were manufactured and investigated. One dual PD had an inner and outer diameter of 3 and 6mm , respectively. The other dual PD had a 6 mm inner diameter and a square 10x10 mm^2 outer PD design. The results presented in this article focus on the 3 mm 6 mm geometry photodetector.

One important issue investigated here is signal crosstalk. In this case charge created within the diameter of the inner detector may be registered in the outer detector. Such cross-talk can lead to much confusion when carrying out pulse height analysis techniques. To investigate the significance of cross talk in our detector we exposed the photodetector to a 0.5 mm collimated I-125 source. **Fig. 3** shows the response of the inner Si PD to photons from I-125 source (21 and 27 keV are the main peaks observed) measured with an in-house designed miniature charge sensitive preamplifier respectively, under 25 ^{0}C. The two main lines are clearly observed and resolved when the collimated source was exposed to the inner photodetector. However when the collimated source is moved onto the outer detector an insignificant number of counts are measured on the inner detector.

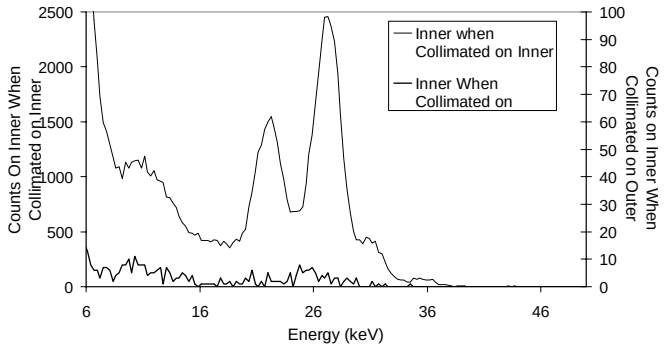

Fig. 3 The response of inner 6mm PD on I-125.

The results clearly indicate that the level of cross-talk between the inner and the outer detector is insignificant. What few counts are measured are most likely due to the imperfect collimation of the source. It should also be noted that the cross-talk results displayed here were independently verified using a much more accurate technique (Ion Beam Induced Charge Collection), however this is not discussed here.

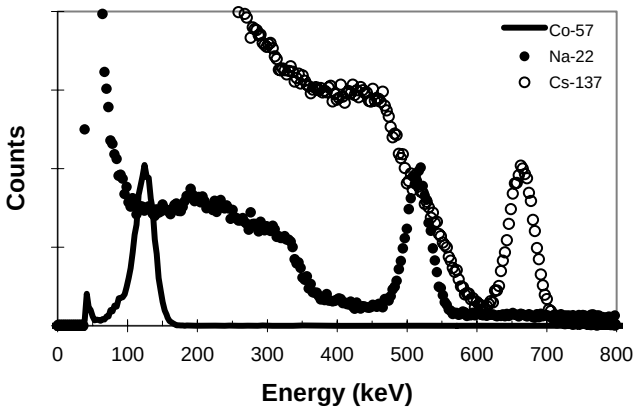

Fig. 4 The response of the inner scintillator detector of the module with a 3mm diameter core optically coupled to CsI(Tl) excited by 122 keV photons from a Co-57 source, 511 keV photons from a Na-22 source and 662 keV photons from a Cs-137 source.

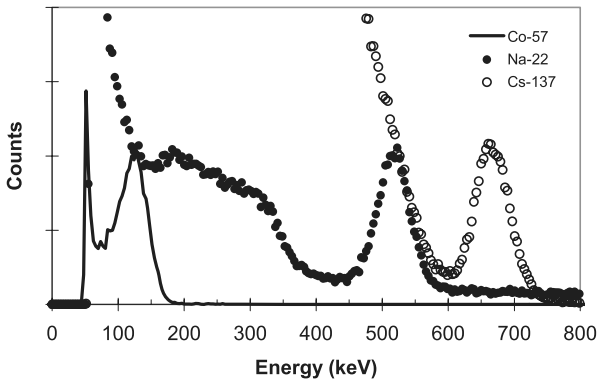

Fig. 5 The response of the outer scintillator detector of the module with a 6mm diameter core optically coupled to CsI(Tl) excited by 122 keV photons from a Co-57 source, 511 keV photons from a Na-22 source and 662 keV photons from a Cs-137 source.

Fig. 4 and **5** show the response of the inner and outer PD design coupled to a dual CsI(Tl) scintillator excited by collimated gamma sources Co-57, Cs-137 and Na-22 measured under the same experimental conditions respectively. The ADC was set to 1024 channels for these two spectra. These results may be improved by better geometry of the scintillator, improved optical coupling of the scintillator and optimization of the antireflective coating for 540nm light. Taking into account that gap between annular photodiodes is about 0.3 mm any small misalignment also can lead to a reduction of the number of photons reaching the active area of the photodiode. Special technology of alignment of the scintillator with the PD is currently under development.

Table 1 shows the measured energy resolution of the two concentric scintillator-PD detectors that make up the probe. The data indicates that the probe can be utilized with both low energy and high energy gamma emitting isotopes. The inner detector displays the best energy resolution, which is important in the case where the probe is used in high spatial resolution mode. In this case the counts measured in the outer probe are discarded. Excellent energy resolution is not a high priority, but is important when the probe is used in anti-Compton suppression mode.

Table. 1 Measured energy resolution of the inner and outer detectors that make up the probe.

	Cs-137	Na-22	Co-57
Energy Resolution [%] Inner Detector	5 ± 3	6 ± 3	25 ± 5
Energy Resolution [%] Outer Detector	10 ± 3	10 ± 3	33 ± 5

Fig. 6 shows the spatial resolution of the CMRP probe in comparison with a current commercial probe. In this experiment a collimated Tc-99m source was used and the CMRP probe was used in high spatial resolution mode. In this case only the counts from the inner scintillation detector were used and the spatial resolution of the CMRP probe is clearly superior. The spatial resolution is determined by the geometrical configuration of the probe.

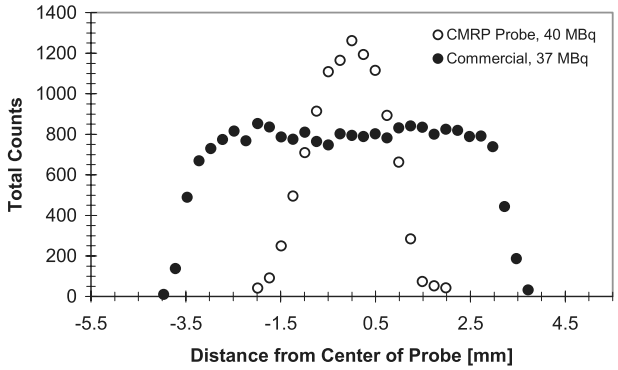

Fig. 6 Measured linear spatial resolution of the CMRP probe in comparison with a current commercial probe in a Tc-99m radiation field.

We also investigated the angular resolution of the CMRP probe in comparison to the same commercial probe. In this case the tip of the probe was placed at the centre of rotation of the collimated source. **Fig. 7a** and 7**b** show the results of this experiment for two separate source activity levels. The CMRP probe displays better angular resolution for both source activity levels used.

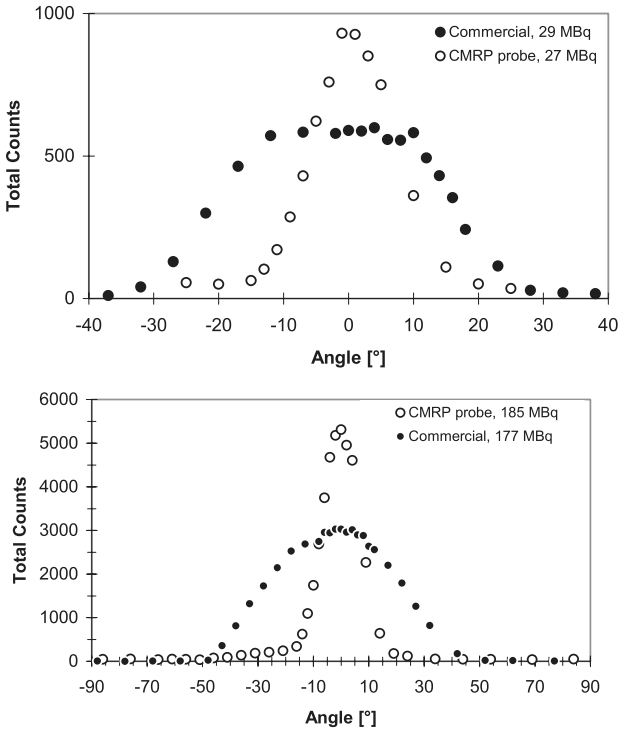

Fig. 7 Measured spatial resolution of the CMRP probe in comparison with a standard, commercially available probe using a relatively (a) weak and (b) strong Tc-99m source.

The final experiment carried out in this study investigated the Compton suppression capabilities of the CMRP detector probe. **Fig. 8** shows the effect of running the probe in anti-Compton mode with a Cs-137 source. Without Compton

suppression the level of Compton contribution to the measured pulse height spectrum is clearly much more significant. Such Compton suppression may have very valuable contribution if dual energy radiotracers are utilized as part of the radioguided surgery procedure.

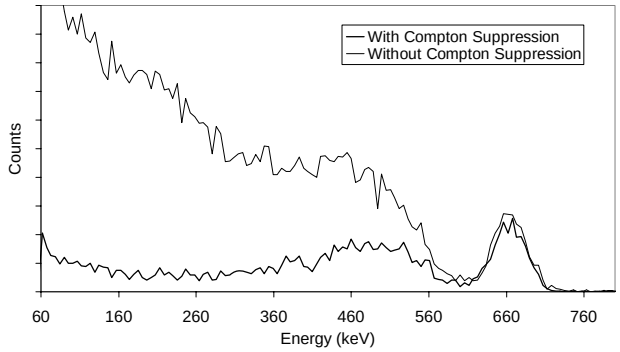

Fig. 8 Measured pulse height spectrum of a Cs-137 source with the CMRP probe operated with and without Compton suppression mode.

IV. Conclusions

We have characterized the readout performance of a new dual photodetector, dual scintillator probe for radioguided surgery. The obtained energy resolution is enough to realize beta probe in count mode for use with PET isotopes using weighted counts from the outer detector for substraction of gamma 511 keV background from the core detector. In contrast to Si back-to-back detector module[3] the sensitivity to 511 keV gamma photons is much higher and can be used additionally to increase the sensitivity of the probe using the core detector for beta and gamma radiations simultaneously. In this case counts due to scattered 511 keV gamma photons will be eliminated using a coincidence technique.

Study with collimated gamma beam demonstrated that no cross talk effect related to charge division between two PDs or light penetration between two concentric scintillators. Readout front–end electronics including shaper amplifier for both channels placed on 10×25×0.2 mm PC board and anti-Compton application of the probe will be investigated and presented along with detailed characterization of proposed module.

Refferences

1) T.S.Hionkernel et al “Dual detector for surgical tumor staging” , J.Nucl. Med. , 29, 1101, (1988).
2) F.Daghighian, E.J.Hofman et al “Intraoperative beta probe: a device for detecting tissue labelled with positron or electron emitting isotopes during surgery” , Med Phys, 21, 153, (1994).
3) R.R.Raylman et al “A Dual surface barrier detector unit for beta sensitive endoscopic probes” , IEEE Trans on Nucl Sci., 51, N1, 117,(2004).

Journal of NUCLEAR SCIENCE and TECHNOLOGY, Supplement 5, p. 462–465 (June 2008)

Monitoring Methodologies and Chronology of Radioactive Airborne Releases from Tokai Reprocessing Plant

Jun KOARASHI*, Satoshi MIKAMI, Akira NAKADA, Kiyomitsu AKIYAMA, Hirohide KOBAYASHI, Hiroki FUJITA, and Minoru TAKEISHI

Japan Atomic Energy Agency, 4-33 Muramatsu, Tokai-mura, Naka-gun, Ibaraki 319-1194, Japan

Tokai reprocessing plant (TRP) has released radionuclides such as ^{3}H, ^{14}C, ^{85}Kr and ^{129}I into the atmosphere since the start of operation in 1977. We have established the monitoring methodologies for these nuclides, to realize an appropriate and continuous radioactive discharge control. The methodologies having various special technical considerations for matching the monitoring of reprocessing off-gas, were summarized in this paper. Briefly, ^{3}H was collected by a cold-trap technique and the concentration was evaluated being independent of the water collection efficiency; ^{14}C was collected by a monoethanolamine bubbler and then measured by liquid scintillation counting without any interferences from ^{3}H and ^{85}Kr; ^{85}Kr was continuously measured by combination of two kinds of detectors to cover very wide range of the concentration; and ^{129}I was collected by a charcoal filter and a charcoal cartridge in series with a relatively high collecting performance. The monitoring records over the period from the start of operation to fiscal 2006, the end of contract-based reprocessing, certainly ensured that the releases of these nuclides from the TRP have never exceeded the authorized discharge limits.

KEYWORDS: monitoring methodology, airborne release, Tokai reprocessing plant (TRP), tritium (^{3}H), carbon-14 (^{14}C), krypton-85 (^{85}Kr), iodine-129 (^{129}I)

I. Introduction

Nuclear energy is one of the significant options for meeting dramatically growing energy needs throughout the industrialized and developing world, and countering the serious problem of global warming. A closed nuclear fuel cycle in which the reprocessing of spent fuels plays a central role, will lead to a sustainable energy supply for the future.

Tokai Reprocessing Plant (TRP) of Japan Atomic Energy Agency (JAEA), constructed as the first reprocessing plant in Tokai-mura, Japan, started operation in 1977. The TRP has the design-base annual reprocessing capacity of 210 tons of spent fuels with the average burn-up of 28,000 MWd/MTU and the cooling time of more than 180 days. The TRP has successfully reprocessed the total amount of 1,100 tons of spent fuels used at PWRs, BWRs and an advanced thermal reactor (ATR, called FUGEN) as of March 2006 when JAEA has completed the contract-based reprocessing with nuclear power companies. The reprocessing processes have resulted in releases of radionuclides into the atmosphere via three 90-m high stacks. The nuclides of specific interest are ^{3}H, ^{14}C, ^{85}Kr and ^{129}I, with relatively long half-lives. Therefore, JAEA has developed and improved the monitoring methodologies for these nuclides to realize an appropriate and continuous radioactive discharge control.

Synchronously, in March 2006, the first commercial large-scale fuel reprocessing plant, built in Rokkasho-mura, Aomori, Japan, began test runs using actual spent fuels, thereby still more increasing public concerns regarding the discharge of radionuclides into the environment from the fuel reprocessing plant. Our knowledge on the monitoring for airborne releases at the TRP thus would be very useful for the radioactive discharge control in the fuel reprocessing plant. This paper summarizes: (1) our monitoring methodologies for these nuclides and their special technical characteristics; and (2) the 30-year history of radioactive airborne releases from the TRP since its emergence.

II. Methodologies with Special Technical Features

Selecting suitable monitoring methodologies for radionuclides of interest requires special considerations on their activity level in the target gas and radiation emission types. Two different categories of methodologies were applied to accomplish the continuous monitoring of radionuclides in airborne release from the TRP: an online real-time measuring method for ^{85}Kr; a batch-sampling method for ^{3}H and ^{14}C; and the combination of both for ^{129}I.

1. Tritium

(1) Sampling

To determine the concentration of tritiated water (HTO), a portion of the airborne effluent from the stack was introduced into a tritium-collecting unit after passing through a dust filter. The sampling was made at a constant flow rate of 2 $l \cdot min^{-1}$ normally for a week. Temperature and relative humidity of the sampled air were measured carefully at an early stage of the sampling line. In the collecting unit, water vapor including HTO was condensed with a cold trap at -32 ^{o}C under pressure of 2.2 $kg \cdot cm^{-2}$. At the end of sampling, the water condensed in the cold trap was recovered completely by heating. This cold trap technique is very suitable for a routine-based monitoring because of its easy procedure for

*Corresponding Author, E-mail: koarashi.jun@jaea.go.jp

recovering water sample.

(2) Activity measurement and discharge evaluation

One milliliter of the recovered water was mixed with 15 ml of liquid scintillator (Aquasol 2, Packard BioScience B.V.) in a 20 ml glass vial. The activity of ^{3}H in the prepared sample was measured with a liquid scintillation counter (LSC; Tri-Curb Model 2550TR/AB, Packard) with 60 minutes counting time. The weekly-averaged concentration of ^{3}H in airborne release, C_T (Bq·m^{-3}), was determined by

$$C_T = A_T \cdot \rho(T) \cdot H / 100 , \quad (1)$$

where A_T is the ^{3}H activity per unit volume of water (Bq·l^{-1}), $\rho(T)$ the saturated water vapor density as a function of air temperature (l·m^{-3}), T the air temperature (^{o}C) and H the relative humidity of air (%). The total activity discharged from the stack was evaluated by multiplying the ^{3}H concentration by air throughput of the stack.

Careful measurements of temperature and relative humidity allow us to estimate the total amount of water in the sampled air. In this case, the water collection efficiency of the unit is not an essential parameter for evaluating the ^{3}H concentration of the sampled air. The tritium-collecting unit, however, requires the small changeability of collection efficiency during the sampling when the water content and the ^{3}H specific activity in the airborne effluent largely change as is often the case in the TRP. Our sampling system with the high and stable collection efficiency of more than 90% at least for one-week sampling, answers well the airborne ^{3}H monitoring purpose.[1)]

The detectable concentration of this method was below 3.0 Bq·m^{-3} for the airborne release from the TRP, considering that the temperature and relative humidity of it were normally less than 40^{o}C and 50%, respectively.[2)] This concentration was sufficiently lower than one required for the routine monitoring of ^{3}H in the TRP (37 Bq·m^{-3}).

2. Carbon-14

(1) Sampling

The stack air was sampled at a flow rate of 0.4 l·min^{-1} for a week. The sampled air was first passed through a dust filter. Carbon monoxide and hydrocarbons in the sampled air were converted into CO_2 with a CuO catalyst kept at 700^{o}C. The CO_2 that was present and formed, was then absorbed in 200 ml of monoethanolamine (MEA; 2-aminoethanol) in a bubbler-type trap (CO_2 trap), after removing water vapor in the air. The oxidation and CO_2 collection efficiencies were >99.3 % and >97.5%, respectively.[2)]

Krypton-85, a major radionuclide contained in the airborne effluent from the TRP, is not absorbed by the MEA solution because it is a noble gas nuclide. However, there is a possibility that ^{85}Kr interferes with the measurement of ^{14}C due to the overlapping β-energy range of ^{85}Kr (687 keV) with ^{14}C (156 keV), when ^{85}Kr is remained as minute bubbles in the MEA solution after sampling. The ^{14}C sampling system was therefore equipped with a line for purging ^{85}Kr off the MEA solution by room air with relatively low ^{14}C concentration after sampling.

(2) Activity measurement and discharge evaluation

After the sampling, a 2 ml aliquot of the ^{14}C-absorbing MEA was added to a 20 ml glass vial containing 10 ml of the liquid scintillator, and 4 ml of methanol was also added to make it thoroughly miscible. The ^{14}C activity of the sample was then measured using the LSC with measurement time of 60 min. The weekly-averaged ^{14}C concentration in airborne release, C_C (Bq·m^{-3}), was evaluated by

$$C_C = A_C \cdot V_0 \cdot (100 / E_{ox}) \cdot (100 / E_a) / U , \quad (2)$$

where A_C is the ^{14}C activity per unit volume of ^{14}C-absorbing MEA (Bq·ml^{-1}), V_0 the volume of MEA used for ^{14}C absorption (ml), E_{ox} the oxidation efficiency of carbon-compounds into CO_2 (%), E_a the CO_2 absorption efficiency of the CO_2 trap (%) and U the total volume of air sampled for a given period (m^{3}). The total activity discharged from the stack was estimated by multiplying the ^{14}C concentration by air throughput of the stack.

In the LSC measurement, a ^{14}C-counting channel was set to determine accurately ^{14}C activity even in the case that ^{3}H (18.6 keV) was incorporated into the prepared sample. Setting of the ^{14}C-counting channel naturally reduced the counting efficiency of ^{14}C to some degree because a portion of the ^{14}C spectra was located in the area below the lower discrimination channel, but it made possible to detect ^{14}C at more than 40% efficiency without any interference from ^{3}H contamination.[2)] The detectable ^{14}C concentration in airborne release was estimated to be about 1.6 Bq·m^{-3}, which was one order of magnitude lower than one required for the routine-base monitoring of ^{14}C in the TRP (40 Bq·m^{-3}).[2)] The simple MEA technique presented here made it feasible to reduce the time required for sample preparation and the complications in the monitoring procedure.

3. Krypton-85

A portion of airborne effluent in the stack was introduced into a krypton monitor at a flow rate of 70 l·min^{-1}. The krypton monitor consisted mainly of two kinds of detectors, a GM counter for measuring the lower concentration range and a NaI(Tl) scintillation detector for the higher one, settled in a gas ventilation tank (14 m^{3}). Beta radiations observed with the GM counter was all regarded as those from ^{85}Kr because ^{85}Kr was the dominant β-emitter in the effluent. The count rates were continuously stored in a data processor and recorded on a trend-recording chart on real time. The hourly averaged concentration, C_K (Bq·m^{-3}), was computed by

$$C_K = K \cdot C_n \cdot 760 / (760 - p) / 60 , \quad (3)$$

where K is the conversion coefficient from count rate to ^{85}Kr concentration (Bq·m^{-3}/cpm), C_n the hourly net counts that is obtained by integrating net counts per minute and p the negative pressure in the ventilation tank (mmHg). The conversion coefficient was determined by using pure ^{85}Kr gas and a standard ionization chamber once a year. The hourly, daily, monthly and also annually discharged activities of ^{85}Kr were then evaluated based on the hourly-averaged concentration. The detectable concentration of this technique was approximately 3×10^{2} Bq·m^{-3} (depending directly on the conversion coefficient for the GM counter), which was lower

than the required detectable concentration of 2.4×10^{3} Bq·m^{-3}. Using two kinds of detectors as a krypton monitor enabled us to measure the wide range ^{85}Kr concentration varying from 10^{2} to 10^{8} Bq·m^{-3}.

4. Iodine-129

(1) Sampling

An activated charcoal-impregnated filter paper and an activated charcoal cartridge (Haruna Co., Ltd., Japan) were used for collecting ^{129}I in airborne effluent. Both media were impregnated with 10 wt.% of triethylendiamine (TEDA).

The stack gas was introduced into a sampling unit at a flow rate of 50 l·min^{-1} for a week. The sampling unit contained the charcoal filter paper and the charcoal cartridge in series. The high collecting performance of charcoal filter papers and cartridges is well-known, but it is only for a low-flow-rate and short-term sampling.[3,4] Our *in situ* investigations derived a more practical finding that the combined use of the charcoal filter paper and charcoal cartridge gave a collection efficiency of more than 90% even for the high-flow-rate and relatively long-term sampling.[5]

(2) Activity measurement and discharge evaluation

After sampling, ^{129}I activities were measured for both collecting media with a Ge(Li) γ-spectrometer with 3000 seconds measurement time. As for the charcoal cartridge, measurements were made at both front (upstream) and back (downstream) surfaces of it, taking into account the thickness of the cartridge (20 mm) and weak energy of γ-rays from ^{129}I. A preliminary experiment showed that the simple arithmetic mean of activities measured at the front and back surfaces leads to a reasonable quantification of ^{129}I trapped in the cartridge.[5] The averaged-concentration of ^{129}I in the airborne release, C_I (Bq·m^{-3}), was evaluated as

$$C_I = \{A_F + (A_{Cf} + A_{Cb})/2\}\cdot(100/E)/U\,, \qquad (4)$$

where A_F, A_{Cf} and A_{Cb} are the ^{129}I activities measured for the filter paper, the front surface of the cartridge and the back surface of the cartridge (Bq), respectively. The variables E and U are the ^{129}I collection efficiency of the collecting unit (%) and the total volume of air sampled (m^3), respectively. The concentration will not be underestimated using a constant collection efficiency of 90%. The total ^{129}I activity discharged was calculated by multiplying the concentration by the exhaust air from the stack. The detection limit of activity never exceeded 5 Bq for each measurement, giving the detectable ^{129}I concentration of about 2.2×10^{-2} Bq·m^{-3} or better in this method. This concentration was lower than the required detectable concentration of 3.7×10^{-2} Bq·m^{-3}.

(3) Real-time monitoring

In addition to the weekly-based quantitative evaluation of ^{129}I discharge by the batch-sampling method, we have made a real-time monitoring of the trend of ^{129}I discharge during the sampling, using a system mainly including a high purity Ge detector for γ-spectrometry, a single charcoal cartridge, a pulse height analyzer and a data processor. The integrated counts for a region of interest were obtained at 5-minute interval, and then the integrated amounts of ^{129}I discharged were calculated for every one-hour since the set of the charcoal cartridge. The cartridge was renewed once a week. This system enabled us to recognize quickly an unexpected ^{129}I discharge in the reprocessing operation.[6]

III. Chronology of radioactive airborne releases

Fig. 1 shows the 30-year record of annual radioactive releases from the TRP. In the TRP, all nuclides except for ^{14}C have been monitored since 1977. Reporting the data of ^{14}C discharge was officially started in 1991. The annual releases from the TRP were in orders of 10^{0}, 10^{-1}, 10^{3}-10^{4} and 10^{-4} TBq for ^{3}H, ^{14}C, ^{85}Kr and ^{129}I, respectively, which were always less than the authorized annual discharge limits in the Safety Regulation for the TRP: 560, 5.1, 8.9×10^{4} and 1.7 TBq, respectively. The figure also plots the discharge data from Cap de La Hague (France) up to 1997[7] and from Sellafield (United Kingdom) up to 2004.[7-9] For all nuclides, the annual discharges from the TRP were, in general, one or two orders of magnitude lower than those from other two reprocessing plants. From the data obtained at the TRP after 2000, the ratios of the discharge to the inventory of nuclide in the fuel were estimated to be <1.0%, 3.7-24.1%, >70% and <0.5% for ^{3}H, ^{14}C, ^{85}Kr and ^{129}I, respectively.

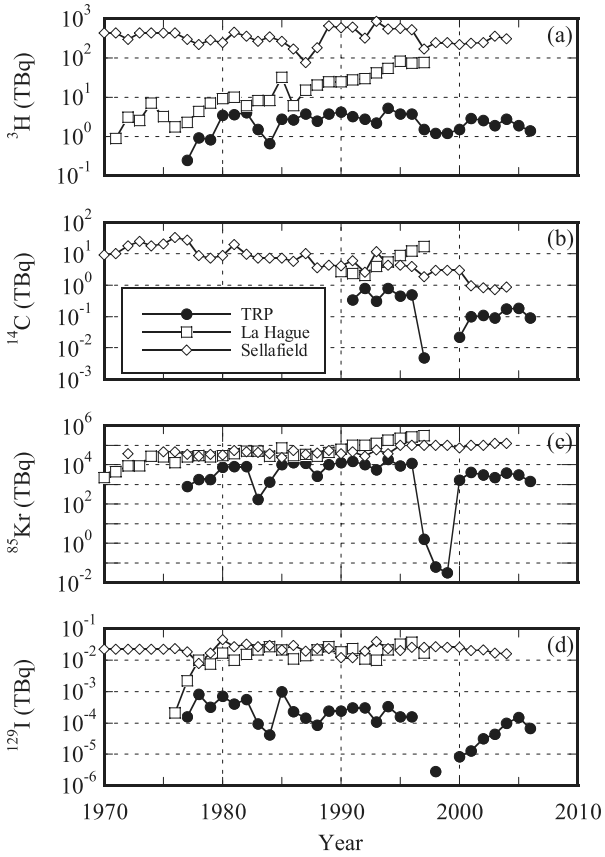

Fig. 1 Annual releases of radionuclides from the TRP, with those from La Hague and Sellafield reprocessing plants: (a) ^{3}H; (b) ^{14}C; (c) ^{85}Kr; and (d) ^{129}I

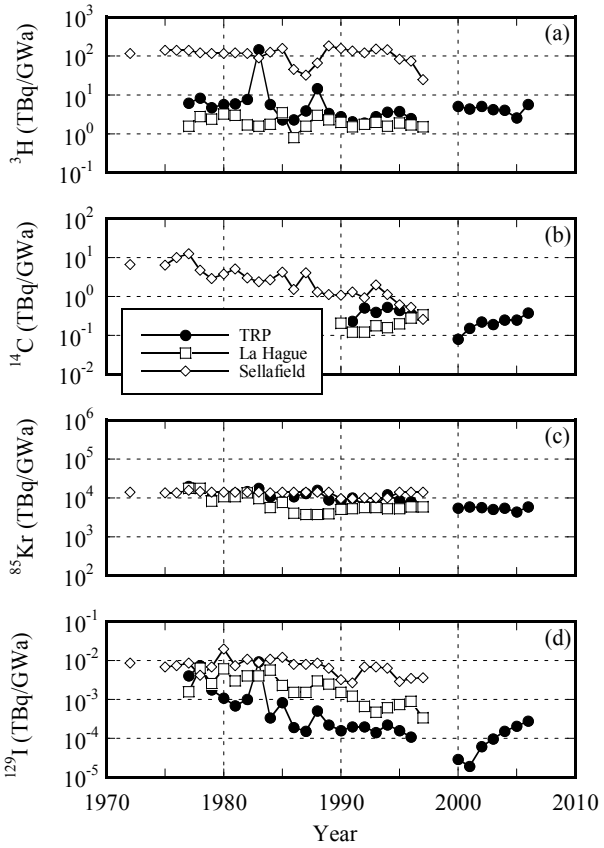

Fig. 2 Normalized releases of radionuclides from the TRP, with those from La Hague and Sellafield reprocessing plants: (a) ^{3}H; (b) ^{14}C; (c) ^{85}Kr; and (d) ^{129}I

Fig. 2 gives the normalized releases (in TBq/GWa) from three reprocessing plants per unit of energy generated (*i.e.* energy equivalent of fuel reprocessed).[7] One GWa (gigawatt-year) corresponds to the energy generated by the power plant operating at 1 GW for 1 year. The normalized releases of ^{3}H from the TRP were comparable to those from La Hague, but were significantly lower than those from Sellafield plant. We have demonstrated that (1) ^{3}H in tritiated hydrogen (HT) form is also released from the TRP during reprocessing operation, the amount of which reaches approximately one-third of the amount of HTO; and (2) a small quantity of ^{3}H is released even in non-reprocessing period, but only in HTO form.[1] The high normalized ^{3}H release obtained in 1983 was thus attributed to the considerably small amount of fuel reprocessed. No consistent difference in the normalized ^{14}C releases was observed among three reprocessing plants in 1990s, implying that the airborne ^{14}C discharge was relatively proportional to the amount of fuel reprocessed. Recent investigations using a ^{14}C-speciation-sampler have shown that more than 97% of ^{14}C discharge from the TRP is apportioned to the CO_2 form.[10] The normalized releases of ^{85}Kr from three plants were almost in the same level, suggesting the technical difficulty of recovering ^{85}Kr, a noble gas nuclide, in the plants, as shown by the high ratio of discharge to the inventory. In contrast, the normalized release of ^{129}I from the TRP has decreased since the early time of the operation. This may reflect our effective discharge control by the installation of silver-exchanged zeolite (AgX) filters in the off-gas treatment process and the careful adjustment of pH in solutions in the reprocessing processes.

IV. Conclusions

We have established the integrated-monitoring-system that includes the methodologies considering the situations to be applied and feedbacks of our practical experiences. The system has successfully provided the long-term monitoring of ^{3}H, ^{14}C, ^{85}Kr and ^{129}I in airborne release from the TRP. The update methodologies, or some parts of them, would be applicable to the monitoring not only in the coming reprocessing plants but also in nuclear power plants. Our monitoring data certainly ensure that the TRP has never given a significant radiation dose to public during the 30-year operation.

References

1) J. Koarashi, S. Mikami, K. Akiyama, *et al*., "Determination of chemical forms of ^{3}H released to the atmosphere from the Tokai reprocessing plant," *J. Radioanal. Nucl. Chem.*, 262[3], 569 (2004).
2) J. Koarashi, S. Mikami, K. Akiyama, *et al*., "A simple and reliable monitoring system for ^{3}H and ^{14}C in radioactive airborne effluent," *J. Radioanal. Nucl. Chem.*, 268[3], 475 (2006).
3) M. Naritomi, Y. Yoshida, S. Fukuda, "Method for improving the collection performance of iodine samplers under high relative humidity," *J. Nucl. Sci. Tech.*, 10[5], 292 (1973).
4) Japanese Standards Association, *JIS Z 4336: 1995, Radioactive iodine samplers*, 2004, Japan.
5) J. Koarashi, S. Mikami, K. Akiyama, *et al*., "A practical method for monitoring ^{129}I concentration in airborne release," *J. Radioanal. Nucl. Chem.*, 267[1], 155 (2006).
6) S. Mikami, J. Koarashi, T. Miyauchi, *et al.*, "Airborne radioiodine monitoring at Tokai reprocessing plant," *Proc. 2nd Asian and Oceanic IRPA Cong. Radiological Protection*, Beijing, China, Oct. 9-13, (2006) [in CD-ROM].
7) United Nations Scientific Committee on the Effects of Atomic Radiation, *Sources and Effects of Ionizing Radiation UNSCEAR Report to the General Assembly with Scientific Annexes, Volume I Sources, 2000*, United Nations, New York.
8) British Nuclear Fuels plc., *BNFL Annual Report 2002, Discharges and Monitoring of the Environment in the UK*, Warrington, UK.
9) British Nuclear Fuels plc., *BNFL Annual Report 2004, Discharges and Monitoring of the Environment in the UK*, Warrington, UK.
10) J. Koarashi, K. Akiyama, T. Asano, *et al*., "Chemical composition of ^{14}C in airborne release from the Tokai reprocessing plant," *Radiat. Prot. Dosim.*, 114[4], 551 (2005).

Journal of NUCLEAR SCIENCE and TECHNOLOGY, Supplement 5, p. 466–469 (June 2008)

Development of Two-dimensional Fiber-optic Radiation Sensor for High Energy Photon Beam Therapy Dosimetry

Kyoung Won JANG[1], Dong Hyun CHO[1], Wook Jae YOO[1], Sang Hun SHIN[1], Hyung Sik KIM[1], Soon Cheol CHUNG[1], Bongsoo LEE[1*], Hyosung CHO[2] and Sin KIM[3]

[1]*Department of Biomedical Engineering, Research Institute of Biomedical Engineering, College of Biomedical & Health Science, Konkuk University, Chungju 380-701, Korea*
[2]*Basic Atomic Energy Research Institute and Department of Radiological Science, Yonsei University, Wonju 220-710, Korea*
[3]*Department of Nuclear & Energy Engineering, Applied Radiological Science Research Institute Cheju National University, Cheju 690-756, Korea*

In this study, we have developed two-dimensional fiber-optic radiation sensors using organic scintillators and plastic optical fibers for high energy photon beam therapy dosimetry. The scintillating lights generated from each organic sensor probe embedded and arrayed in a polymethylmethacrylate phantom are guided by 10 m plastic optical fibers to the light-measuring devices such as 25 channel photodiode-amplifiers system. Two-dimensional photon beam distributions in a polymethylmethacrylate phantom are measured with different energies and field sizes of photon beam. Also, percent depth dose curves for 6 and 15 MV photon beams are obtained using a two-dimensional fiber-optic sensor. This sensor has many advantages such as high resolution, real-time measurement, two-dimensional dose measurement and ease calibration over conventional radiation measurement devices.

KEYWORDS: fiber-optic radiation sensor, two-dimensional, dosimetry, photon beam

I. Introduction

Recent radiotherapy treatment such as image guided radiation therapy (IGRT) or intensity modulated radiation therapy (IMRT) deals with complex dose distributions and requires more accurate dose measurements. For this purpose, sensors for radiotherapy dosimetry should have a small sensitive volume for high resolution measurements and be made of water-equivalent material for exact dose measurements without complicated calibration processes.[1)]

Small sized dosimeters for radiotherapy use such as ion chambers, silicon photodiodes, diamond detectors, and liquid ion chamber have been developed and used for dose measurements.[2-5)] However, they have some problems as a rather large sensitive volume, dose rate dependence, complicated construction and high cost.[6)] And it is difficult to measure depth dose curves and beam profiles with conventional detectors due to the loss of lateral electronic equilibrium and volume averaging.[7)]

In recent years, a fiber-optic radiation sensor based on an organic scintillator was developed.[8,9)] This sensor can minimize dose distribution perturbation in a plastic phantom or water because the sensitive volume of the sensor is very small and it is nearly water-equivalent. Also it is possible to measure the one or two-dimensional dose distributions and percent depth dose (PDD) curves by arraying these sensors freely in a polymethylmethacrylate (PMMA) or water phantom.

In this study, we have developed a two-dimensional fiber-optic radiation sensor using organic scintillators and plastic optical fibers (POF) for high energy photon beam therapy dosimetry. The scintillating lights generated from each organic sensor probes embedded and arrayed in PMMA phantom are guided by 10 m POFs to the light-measuring devices such as 25 channel photodiode-amplifiers system. The objectives of this study are to measure and obtain the surface dose distributions and PDD curves in a water-equivalent plastic phantom using a two-dimensional fiber-optic radiation sensor. Two-dimensional photon beam distributions in a PMMA phantom are measured as functions of different energy and field size of the photon beam from a clinical linear accelerator (CLINAC). Also, averaged PDD curves for 6 and 15 MV photon beams are obtained. This sensor has many advantages such as high resolution, real-time measurement, two-dimensional dose measurement and ease calibration over conventional radiation measurement devices.

II. Materials and Methods

As the sensor probe material, commercially available organic scintillators (BCF-20, Saint-Gobain Crystals) made out of a polyvinyltoluene (PVT) base with wavelength-shifting fluors are used. The emission color and peak wave length of this organic scintillator is blue and 492 nm, respectively. The number of emitted photons per 1 MeV energy ionizing particle which interacts with this scintillator is about 8000. These scintillators are cylindrically shaped with a 1 mm diameter and a 10 mm length, and both surfaces of the scintillator are polished with various polishing pads in

*Corresponding Author, Tel No: +82-43-856-0976, Fax No: +82-43-851-0620, E-mail: bslee@kku.ac.kr

a regular sequence. An organic scintillator is glued to the POF fiber using an optical-cement (DP-100 Plus, 3M). Both surfaces of the scintillator and plastic optical fiber are also polished using polishing pads.

Commercial grade plastic multimode optical fibers (CK-40, Mitsubishi Ltd.) are used to guide scintillating lights from the sensor probes to the photodiode (S1336-18BK, Hamamatsu Photonics)-amplifiers system. The outer diameter of these fibers is 1.0 mm, and the cladding thickness is 0.02 mm. The refractive indices of the core and the cladding are 1.49 and 1.402, respectively, and the numerical aperture (NA) is 0.504. **Fig. 1** shows a schematic diagram of the fiber-optic radiation sensor which is fabricated with a POF and an organic scintillator. The surface of the sensor probe as shown in **Fig. 1** is surrounded by reflective paint based titanium oxide (TiO_2) to increase scintillating light collection efficiency and to intercept the light noise from outside. Two-dimensional fiber-optic radiation sensor arrays with gaps of 2 cm and with depth of 1 cm embedded in PMMA phantoms are shown in **Fig. 2**.

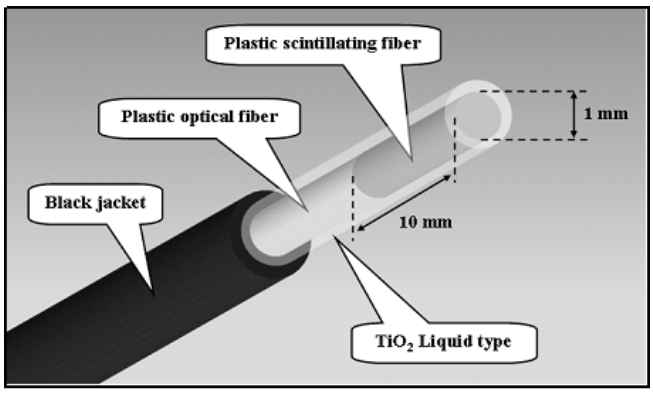

Fig. 1 Fiber-optic radiation sensor

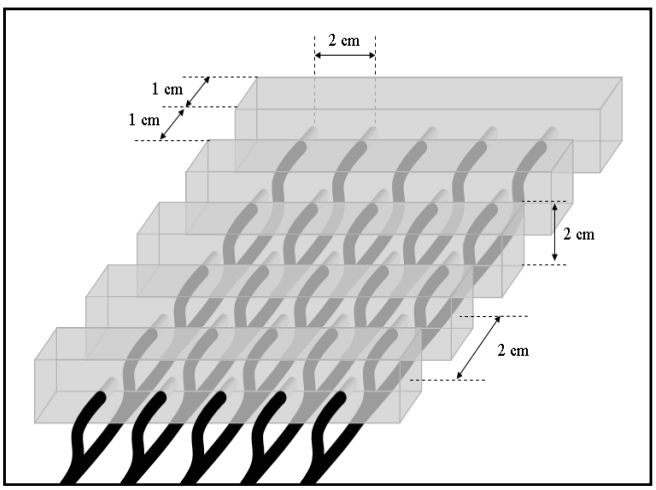

Fig. 2 Two-dimensional fiber-optic radiation sensor

Fig. 3 shows experimental setup to measure two-dimensional dose distribution of photon beams from a CLINAC. Throughout this study, photon beams are provided with a Varian CLINAC 2100CD and two kinds of photon beam energies such as 6 and 15 MV are used and the field sizes of photon beam are 5 × 5 and 10 × 10 cm^2. The scintillating light measurements are made with 25 channel photodiodes amplification system.

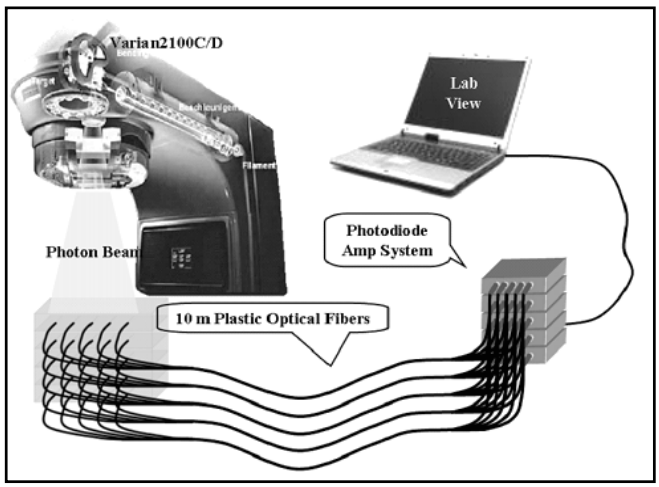

Fig. 3 Experimental setup

III. Experimental Results

Fig. 4 shows two-dimensional photon beam distributions in a polymethylmethacrylate phantom using fiber-optic sensor arrays. The field size of photon beam is 10 × 10 cm^2 and the energies of the photon beam are 6 and 15 MV. 25 individual fiber-optic sensors are arrayed with the same gap of 2 cm and embedded in PMMA phantom with 1 cm depth. Each light signal from the fiber-optic sensors is guided to the 25-channel photodiode array which can converts light into electrical signal.

Before measurements, we have arrayed 25 fiber-optic sensors two-dimensionally on the center of 20 x 20 cm^2 radiation field with gaps of 5 mm. Because the amount of dose in the center part of the radiation field is considered to be uniform, we have measured scintillating light signals from 25 sensors and have obtained average value of those light signals. Using the average value, we have decided the correction factor of each sensor and have calibrated the measured results.

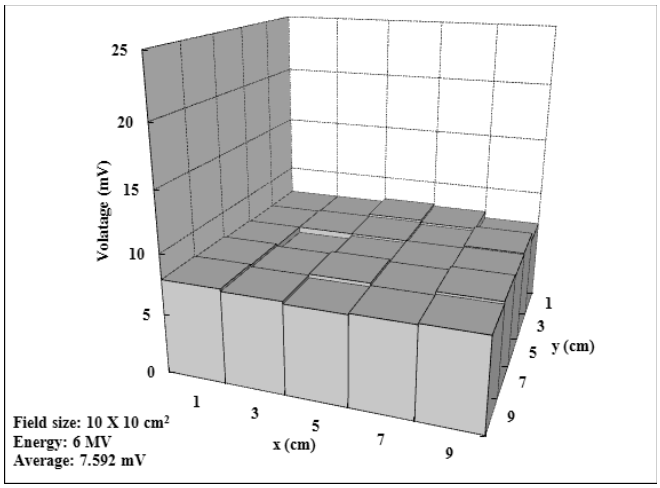

(a)

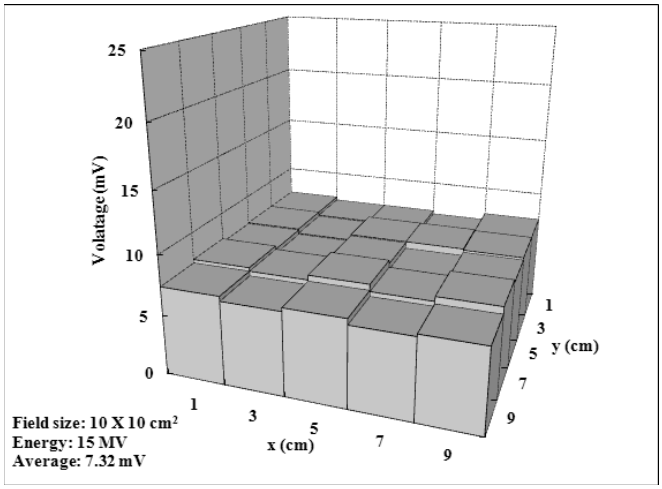

(b)

Fig. 4 Measurements of scintillating lights using two-dimensional fiber-optic radiation sensor array for (a) 6 MV, and (b) 15 MV photon beams with 10 × 10 cm^2 field size

The measured light signals show almost same values and are distributed uniformly in the field size of 10 × 10 cm^2 for two different photon beam energies. The scintillating light signals induced by 6 MV photon beam are higher than those by 15 MV photon beam because the maximum depth doses of 6 and 15 MV photon beam are occurred about 1.5 and 3 cm in water phantom respectively.[10)]

Fig. 5 also shows two-dimensional photon beam distributions in a polymethylmethacrylate phantom with 5 × 5 cm^2 field size of photon beam. The maximum light signal from 9 fiber-optic sensors in the radiation field are obtained and other 16 sensors which are outside of the field size cannot detect valid signals due to the reduced field size.

Measured PDD curves using a two-dimensional fiber-optic sensor array for 6 and 15 MV photon beams are shown in **Fig. 6** and **7**, respectively. **Fig. 6-(a)** and **7-(a)** show one-dimensional PDD curves in a PMMA phantom. 5 individual fiber-optic sensors of the two-dimensional sensor array are located at the same depth and are used to measure scintillating light signals simultaneously.

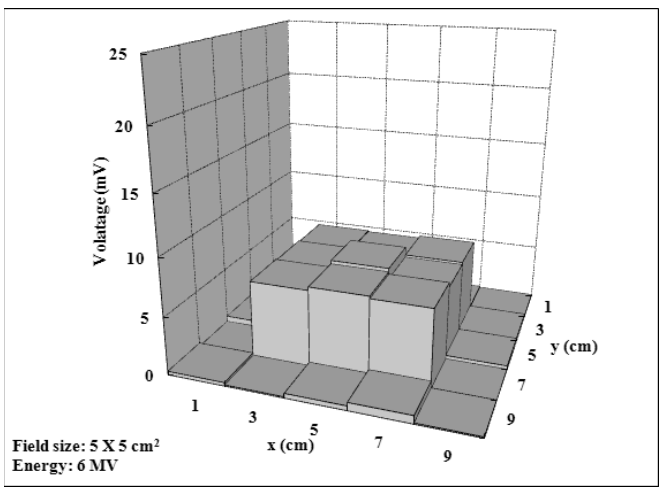

(a)

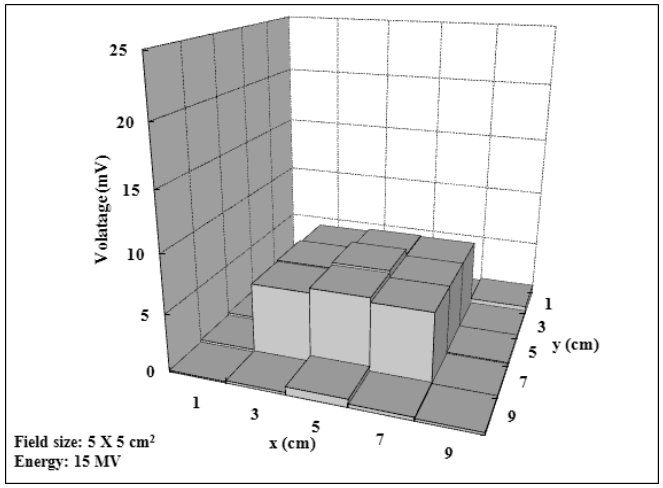

(b)

Fig. 5 Measurements of scintillating lights using two-dimensional fiber-optic radiation sensor array for (a) 6 MV, and (b) 15 MV photon beams with 5 × 5 cm^2 field size

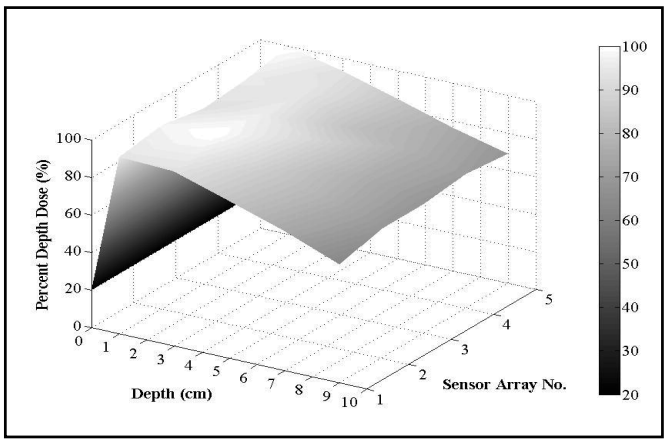

(a)

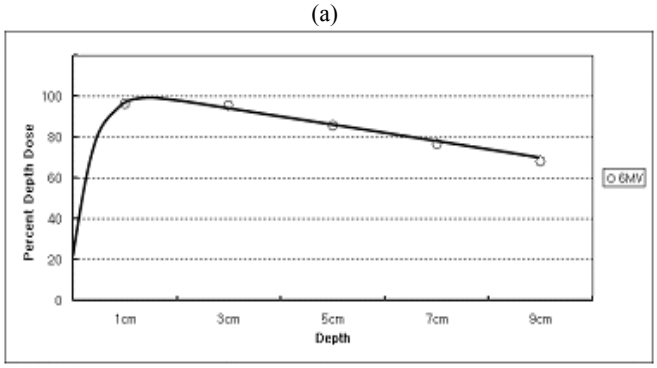

(b)

Fig. 6 PDD curves in a PMMA phantom for 6 MV photon beam using a two-dimensional fiber-optic sensor array with (a) measured scintillating light signals, and (b) averaged values

The curves in **Fig. 6-(b)** and **7-(b)** also show that PDD curves for 6 and 15 MV photon beams, which are obtained by the average value of the measured light signals using 5 individual fiber-optic sensors at the same depths as shown in **Fig. 6-(a)** and **7-(a)**. These PDD curves show that the maximum depth doses are at about 1.5 cm and 3 cm depths of a PMMA phantom respectively and they are consistent

with previous results which are obtained using an ion chamber.[10)]

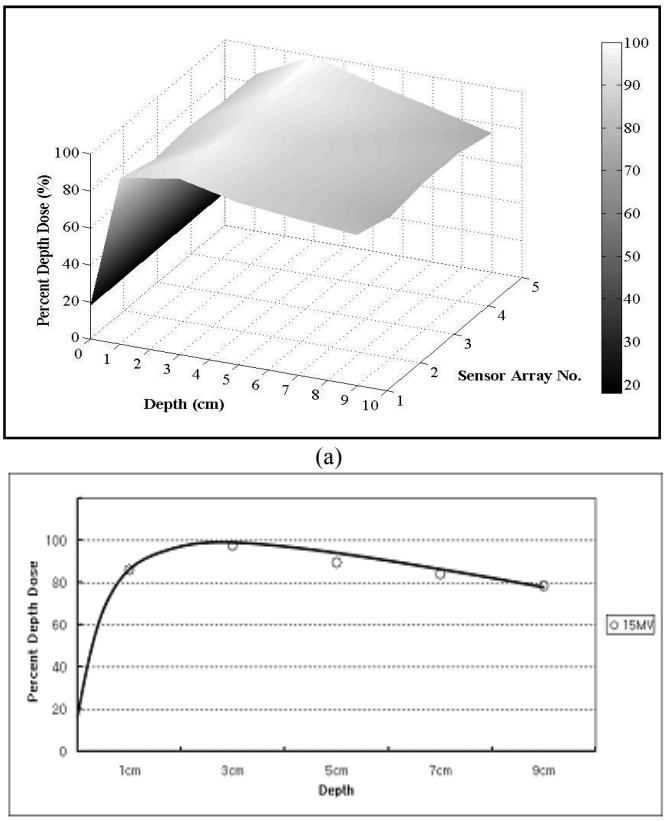

(a)

(b)

Fig. 7 PDD curves in a PMMA phantom for 15 MV photon beam using a two-dimensional fiber-optic sensor array with (a) measured scintillating light signals, and (b) averaged values

IV. Conclusions

In this study, we have fabricated a fiber-optic radiation sensor with an organic scintillator and two-dimensional sensor array to measure high-energy photon beam distributions for radiotherapy dosimetry. Two-dimensional, high resolution and real-time dose measurements in the water-equivalent plastic phantom could be possible using this two-dimensional fiber-optic sensor array. Two-dimensional photon beam distributions in a PMMA phantom are measured with different energies and field sizes of photon beam. Also, PDD curves in a PMMA phantom for 6 and 15 MV photon beams are obtained using two-dimensional sensor array. Further studies will be carried out to measure the spatial resolution of a two-dimensional fiber-optic sensor array and to fabricate three-dimensional fiber-optic sensor array which can measure surface dose distribution and PPD simultaneously.

Acknowledgement

This study was supported by the Basic Atomic Energy Research Institute (BAERI) program of the Ministry of Science & Technology (MOST) (M20376030002-04B0505-00210).

References

1) A-M. Frelin, J-M. Fontbonne G. Ban, J. Colin, and M. Labalme, "Spectral discrimination of Cerenkov radiation in scintillating dosimeters", Medical Physics, **32**, 3000 (2005).
2) Francisco Sánchez-Doblado, Roberto Capote, Joan V. Roselló, Antonio Leal, Juan I. Lagares, Rafael Arráns and Günther H. Hartmann, "Micro ionization chamber dosimetry in IMRT verification:Clinical implications of dosimetric errors in the PTV", Radiotherapy and Oncology, **75**, 342 (2005).
3) Robert L. Dixon and K. E. Ekstrand, "Silicon diode dosimetry", The International Journal of Applied Radiation and Isotopes, **33**, 1171 (1982).
4) B. Planskoy, "Evaluation of diamond radiation dosemeters" Phy. Med. Biol. **25**, 519 (1980).
5) K Eberle, J Engler, G Hartmann, R Hofmann and J R Horandel1, "First tests of a liquid ionization chamber to monitor intensity modulated radiation beams", Phys. Med. Biol. **48**, 3555 (2003).
6) T. Aoyama, S. Koyama, and H. Maekoshi, "A scintillator-optical fiber detector with photodiode redout for dosimetry in small irradiation fields", VI Int. Conference on Med. Phys., Patras, Greece, Sept. 1-4, 1999, p.117 (1999).
7) D. Letourneau, J. Pouliot, and R. Roy, "Miniature scintillating detector for small field radiation therapy", Med. Phys., **26**, 2555 (1999).
8) A. S. Beddar, T. R. Mackie, and F. H. Attix, "Water-equivalent plastic scintillation detectors for high-energy beam dosimetry: I. Physical characteristics and theoretical considerations", Phys. Med. Biol., **37**, 1883 (1992).
9) A. S. Beddar, T. R. Mackie, and F. H. Attix, "Water-equivalent plastic scintillation detectors for high-energy beam dosimetry: II. Properties and measurements", Phys. Med. Biol., **37**, 1901 (1992).
10) Faiz M. Khan, "The physics of radiation therapy", 2nd ed., Williams & Wilkins, Baltimore, 131 (1994).

Journal of NUCLEAR SCIENCE and TECHNOLOGY, Supplement 5, p. 470–473 (June 2008)

Light Output Characteristic of Inorganic Scintillators to Intermediate-energy Charged Particles

Yusuke KOBA[1*], Minoru IMAMURA[1], Takuro SHIMAZU[1], Hiroki IWAMOTO[1], Genichiro WAKABAYAHI[1], Yusuke UOZUMI[1], and Naruhiro MATSUFUJI[2]

[1]*Department of Applied Quantum Physics and Nuclear Engineering, Kyushu University, 744 Motooka Nishi-ku, Fukuoka 812-0395, Japan*
[2]*National Institute of Radiological Sciences, 4-9-1 Anakawa Inage-ku, Chiba 263-8555, Japan*

In order to convert the light output of an inorganic scintillator to the deposited energy, the study of light output curves is very important due to its non linearity. We carried out experiments to investigate the light output response of NaI(Tl), CsI(Tl), GSO(Ce) and LYSO(Ce) crystals to intermediate-energy ^{4}He and ^{12}C beams from HIMAC at National Institute of Radiological Sciences. Scintillation efficiency was obtained in the wide energy range. It was found that a light output curve is represented using the peculiar scintillation efficiency despite it greatly changes its shape with different particles. In addition, it was found that scintillation efficiency was a function of the stopping power. Using the measured scintillation efficiency, the light output curves of the crystals were systematically reproduced

KEYWORDS: inorganic scintillator, light output, scintillation efficiency, NaI(Tl), CsI(Tl), GSO(Ce), LYSO(Ce)

I. Introduction

In high energy experiments, various scintillators have been developed strenuously with the advancement of energy and beam intensity of accelerators. The performance requested for these scintillators is heavier, faster and more tolerant to radiation damage. GSO(Ce) and LYSO(Ce) are one of the scintillators which have been developed for these requests. In order to use them as high precision calorimeters, it is necessary to investigate the light output characteristics of these scintillators. Especially, it is very important to define a light output curve which is the relation between the energy deposited in crystals and the amount of the luminescence.

The light output curves of scintillators are generally nonlinear. This is one of the undesirable problems when we use scintillators as calorimeters. In order to represent the light output curves of organic scintillators, Birks showed the following equation on the assumption that the amount of the luminescence per unit length is described by a function of its stopping power,

$$\frac{dL}{dx} = \frac{S\left(dE/dx\right)}{1+kB\left(dE/dx\right)}, \quad (1)$$

where S is the absolute scintillation efficiency and kB is the Birks parameter[1)]. Eq. (1) shows that the amount of the luminescence per unit length decreases by the quenching effect in high dE/dx region. Eq. (1) reproduced light output curves of organic scintillators appropriately. Then this equation has been applied to inorganic crystals, and also reproduced their light output curve roughly. However, in recent high energy experiments, it is reported that the light output curve in the low dE/dx region, for example that of high-energy proton, cannot be represented by the Birks equation. We carried out experiments on the light output characteristics of several scintillators for intermediate-energy (several hundred MeV/u) charged particles. Focusing attention on the relation between the scintillation efficiency (dL/dE) which is the amount of the luminescence per unit energy, and the stopping power (dE/dx), we investigated the light output characteristics of four kinds of crystals, NaI(Tl), CsI(Tl), GSO(Ce), and LYSO(Ce). The light output curves of these crystals were systematically reproduced.

II. Experiment

Measurements were performed at the PH1 course of HIMAC (Heavy Ion Medical Accelerator in Chiba) in the National Institute of Radiological Sciences. Monochromatic ^{4}He and ^{12}C particles accelerated up to 720 MeV and 3.48 GeV were used in the experiments. **Fig. 1** shows the schematic view of present measurement system. It was composed of, from upstream, a degrader changer, an active collimator, a thin plastic scintillator with the thickness of 2 mm, and two inorganic scintillators. The active collimator has an aperture of 5 mm diameter as an active slit to determine the solid angle of the spectrometer. The thin plastic scintillator generated the trigger signals by the coincidence method with the signal of the inorganic crystal. The dimensions of inorganic scintillators are NaI(Tl) : 50.8 mm, CsI(Tl) : 43 mm, GSO(Ce) : 43 mm, and LYSO(Ce) : 20 mm cube on a side. The light output of crystals was collected using a photomultiplier tube. In order to change incident energy to the inorganic scintillators we used some degraders made of aluminum or copper. The measured energy region was 150~700 MeV for ^{4}He, 500~3400 MeV for ^{12}C. The light output of scintillators was normalized with a LED and standard radiation sources.

*Corresponding Author, Tel No:092-802-3479, Fax No: 092-802-3479, E-mail: yusemi@nucl.kyushu-u.ac.jp

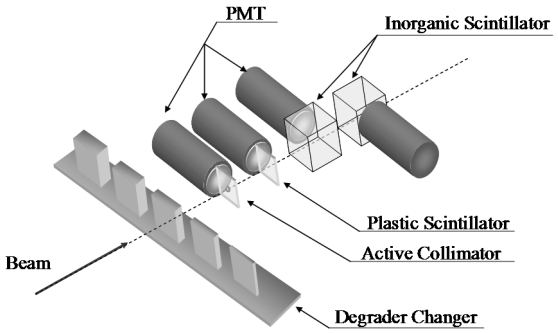

Fig.1. The schematic view of present measurement system. Each scintillator was attached a photomultiplier tube

The deposit energy in crystals or degraders was calculated by the following equation,

$$-\frac{dE}{dx} = 4\pi r_0^2 z^2 \frac{m_e c^2}{\beta^2} NZ\left[\ln\left(\frac{2m_e c^2}{I}\right) - \ln\left(1-\beta^2\right) - \beta^2\right], \quad (2)$$

where r_0 is the classical electron radius, z is charge of incident particles, $m_e c^2$ is the rest mass energy of electron, Z is atomic number of material, N is atomic density of material, I is the mean excitation potential. In the measured energy range Eq. (2) calculates the stopping power with satisfactory accuracy.

III. Result and Discussion

1. Light Output

Fig 2 shows the light output of NaI(Tl) as a function of deposit energy for several charged particles. These data contains not only the present experimental result but also the result derived from references[2,3]. The solid lines in Figure tied each data of same particle. **Fig.3~5** shows CsI(Tl), GSO(Ce), and LYSO(Ce). Because it hardly reports for LYSO(Ce), the data is only present results. In comparatively

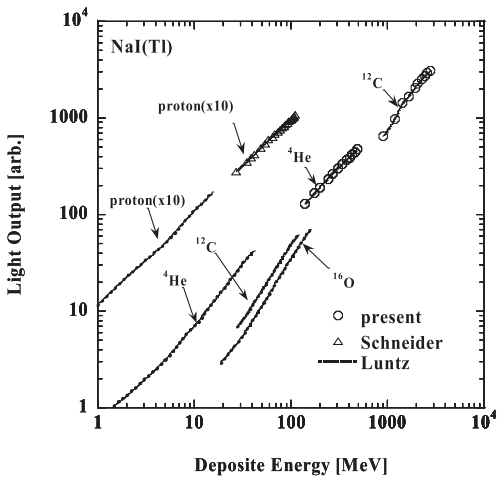

Fig.2. The light output of NaI(Tl) as a function of deposit energy to several charged particles.

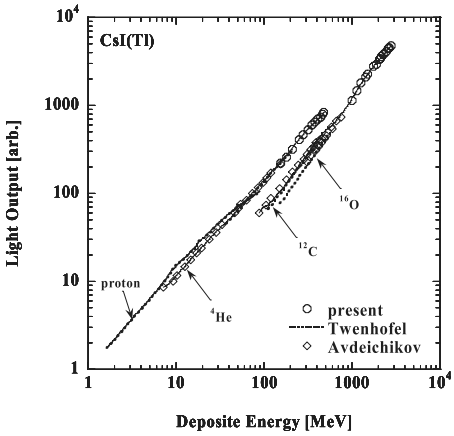

Fig.3. The light output of CsI(Tl) as a function of deposit energy to several charged particles[4,5].

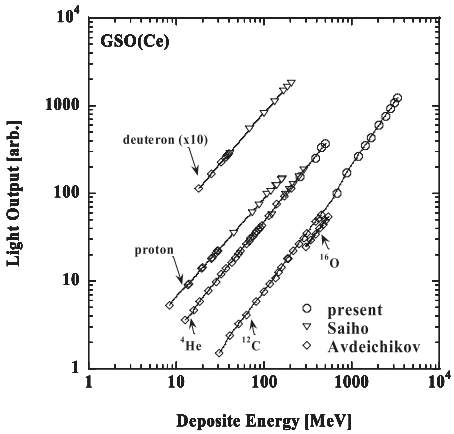

Fig.4. The light output of GSO(Ce) as a function of deposit energy to several charged particles[6].

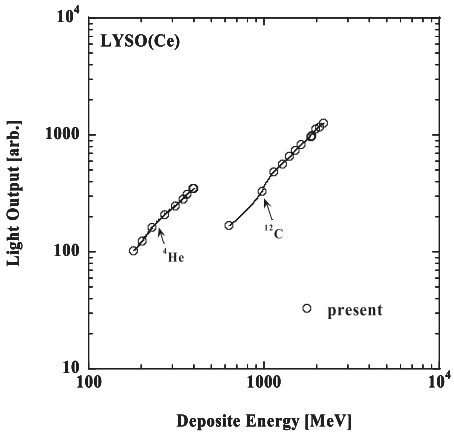

Fig.5. The light output of LYSO(Ce) as a function of deposit energy to several charged particles.

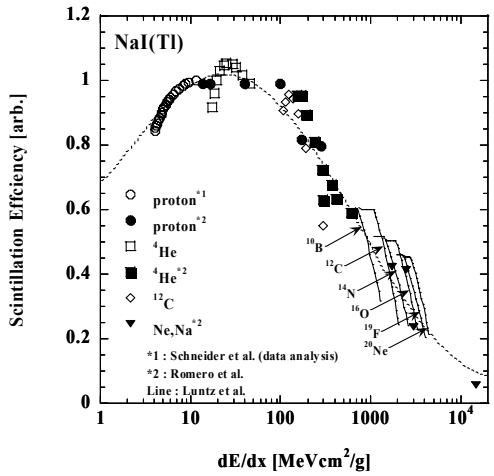

Fig.6. The scintillation efficiency of NaI(Tl) as a function of the stopping power. The broken line is the calculation using Eq. (3).

row energy region, the larger the atomic number of incident particle is, the smaller the light output of same deposit energy is. But in comparatively high energy region, this tendency is not shown.

2. Scintllation Efficiency

As described above, the light output curves considerably change its shape with the measured particle. Therefore it is difficult that the light output (L) is represented by the unified equation with the deposit energy (E). So we focused attention on the relation between scintillation efficiency (dL/dE) and stopping power (dE/dx). At first, the scintillation efficiency is defined approximate slope of the light output curve on each measurement. The stopping power on incident particles is calculated with Eq. (2). **Fig. 6~8** show the relation between the scintillation efficiency and the stopping power of NaI(Tl), CsI(Tl) and GSO(Ce). In all region of the stopping power the scintillation efficiency of GSO(Ce) decreases monotonically, but that of NaI(Tl) and CsI(Tl) become lowering in the region of the low stopping power.

The scintillation efficiency of NaI(Tl) for several charged particles was reported by Romero et al.[7]. Romero et al. represented the scintillation efficiency of NaI(Tl) as the following equation,

$$\frac{dL}{dE} = \sum_{t=0}^{5} a_t \left(\ln \frac{dE}{dx} \right)^t , \tag{3}$$

where this parameter set is a_0= 0.68, a_1= 0.12, a_2= 0.045, a_3= -0.022, a_4= 0.0023, a_5= -0.000073. The solid line in **Fig. 6** shows the calculation result by Eq. (3), and represents the scintillation efficiency of NaI(Tl) approximately. In the other hand, the scintillation efficiency of CsI(Tl) depends on a kind of particles strongly.

In order to represent the scintillation efficiency of GSO(Ce), we applied the following equation derived by **Eq. (1)**.

$$\frac{dL}{dE} = \frac{S}{1 + kB\left(dE/dx\right)} . \tag{4}$$

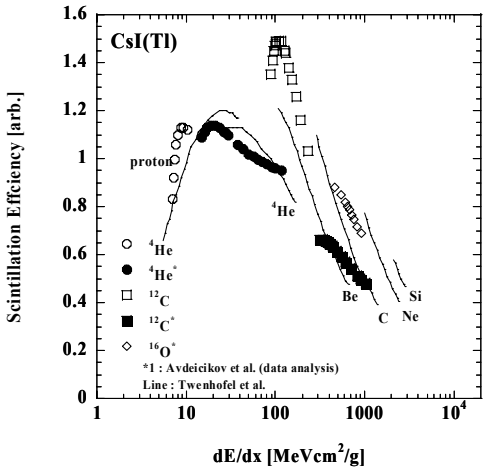

Fig.7. The scintillation efficiency of CsI(Tl) as a function of the stopping power.

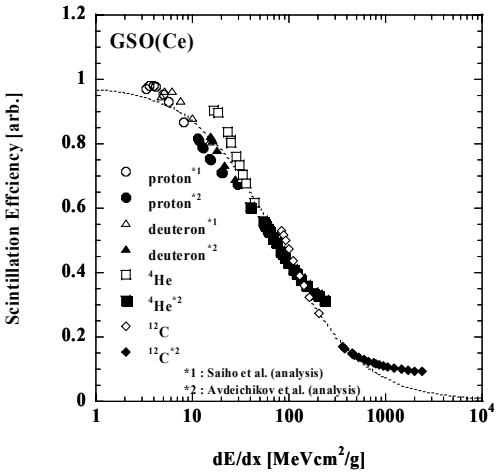

Fig.8. The scintillation efficiency of GSO(Ce) as a function of the stopping power. The broken line is the calculation using Eq. (4).

The parameters were used the following value, S = 1.0[arb.], $kB = 1.14\times10^{-2}$[g/MeVcm^2]. The solid line in **Fig. 8** shows the calculation result by Eq. (4), and represents the scintillation efficiency of GSO(Ce) moderately. Because of data deficiency the scintillation efficiency of LYSO(Ce) is not analyzed.

The light output curves calculated by Eq. (3) and (4) are shown as the solid line in **Fig. 9** and **10**. In **Fig. 9** and **10**, curves of small atomic number particle are reproduced by calculation well. But curves of large atomic number particle cannot be reproduced. It is because that Eq. (3) and (4) cannot represent the scintillation efficiency of these particles.

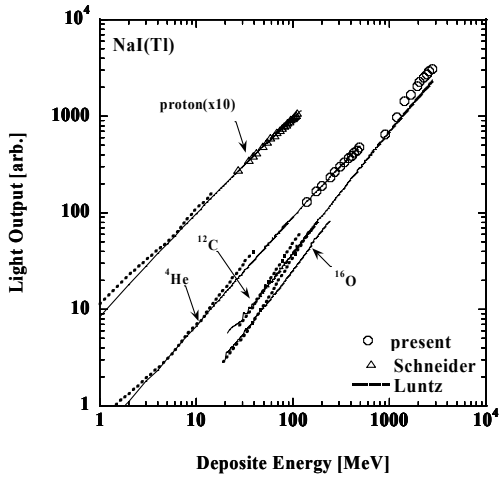

Fig.9. The light output curves of NaI(Tl) as a function of thedeposit energy. The solid lines are the calculation using Eq. (3).

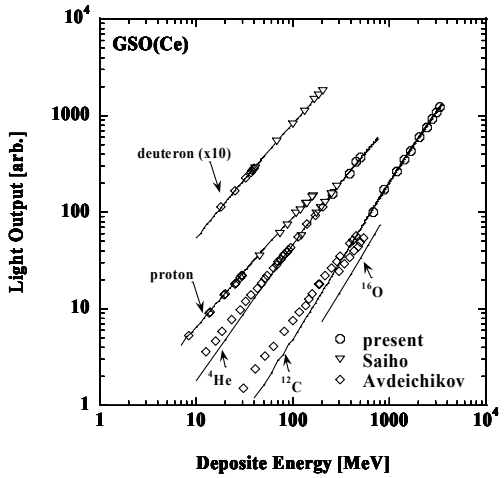

Fig.10. The light output curves of GSO(Ce) as a function of the deposit energy. The solid lines are the calculation using Eq. (4).

V. Conclusion

In order to investigate the light output characteristics of inorganic scintillators, we carried out experiments at PH1 course of HIMAC (Heavy Ion Medical Accelerator in Chiba) in National Institute of Radiological Sciences. By measurements of the wide range of intermediate energy, the scintillation efficiency for the wide range of the stopping power was measured. The scintillation efficiency of NaI(Tl) and GSO(Ce) could be represented by Eq. (3) and (4), and the calculations using these equations could represent the light output curve of these crystals. This study shows that the scintillation efficiency is a function of the stopping power. The more accurate scintillation efficiency is represented, the more strictly the light output curve may be represented. It is anticipated that the more refined researches of scintillation efficiency clear up the light output characteristics of inorganic scintillators.

Acknowledgement

The authors are grateful to staff members of the National Institute of Radiological Sciences. This work was performed as the Research Project with Heavy Ions at the NIRS-HIMAC, 18 P 214.

Refferences

1) J. B. Birks, “The Theory and Particle of Scintillation Counting “, Pergamon, New York, (1964)
2) U. Schneider, D. Renker, “Proton energy measurements using a NaI(Tl) scintillator”, Nucl. Instr. & Meth. **A 388,** 199 (1997).
3) M. Luntz, “Track-Effect Theory of Scintillation Efficiency”, Phys. Rev. **B4-9**, 2857 (1971).
4) C. J. W. Twenhofel, P. F. Box et al., “The Response Function of a CsI(Tl) scintillator with Photodiode Readout to Light and Heavy Ions in the Intermediate Energy Range”, Nucl. Instr. & Meth. **B 51**, 58 (1990)
5) V. Avdeichikov, B. Jakobsson et al., “On-beam calibration of the □E(Si)-Sci/PD charged particle telescope”, Nucl. Instr. & Meth. **A 466,** 427 (2001)
6) F. Saiho, T. Kin et al., “Response and efficiency of stacked GSO(Ce) spectrometer to intermediate-energy deuterons”, Nucl. Instr. & Meth. **A 537**, 594 (2005).
7) J. L. Romero, G. A. Needham et al., “The response of NaI(Tl) to 30-60 MeV Z=1 particles”, Nucl. Instr. & Meth. **A 301,** 241 (1991).

Journal of NUCLEAR SCIENCE and TECHNOLOGY, Supplement 5, p. 474–476 (June 2008)

Development of MRG10 Mobile Roadway Gamma Monitor

DENG Changming*, CHENG Chang, DU Xiangyang, SONG Chenxin,
REN Yi, MENG Dan, WANG Zhigang, LIU Yun, and HAN Shuping

China Institute for Radiation Protection, Taiyuan, Shanxi 030006, China

The MRG10 mobile roadway gamma monitor is described in this paper. This system is developed to meet requirements to survey roadways for gamma contamination in nuclear power plants and other nuclear facilities. The system consists of a four wheel electric utility vehicle, two detector modules and a MCU based controller. The detector module consists of a lead shielded large area plastic scintillator(1000×500×50 mm), a PMT and amplifier unit, a MCU based counting unit, and a semiconductor cooler. The detector module and controller unit are connected with RS-485 bus. When a survey starts, the controller unit takes control of the vehicle speed, displays the measurement data, and will switch on the semiconductor cooler when the temperature of detector module is higher than a set point.

KEYWORDS: roadway gamma monitor, plastic scintillator, detector, alarm

I. Introduction

Fig. 1 Appearance

The MRG10 mobile roadway gamma monitor is a vehicle radiation measurement equipment which can be used for roadway and surroundings radioactive contamination survey in nuclear plants and other nuclear facilities. It can survey the contaminated spots caused by the diffusion of gas and water and little things dropped from cargoes in time. It consists of these parts: electric vehicle, gamma sensitive radiation detector modules, data processing and alarm device, power supply, DC-AC converter and charger. Gamma sensitive radiation detector modules have two detectors, one faces to the ground for roadway survey, the other one stands sideways for surroundings survey. Signals generated by the two detectors are processed by the amplification-shape circuit and the MCU circuit, and then transmitted by RS485 to the data processing and alarm device that give out the counting rate of each detector. The unit has many kinds of functions, such as timing, calculation, data storage, communication, alarm and so on. It also has two levels of alarms: low and high background alarms. Sound and light signals, will be given off to warn person on the spot when alarming. The records can be transmitted by RS-232 cable to the management computer. Color LCD displays the main information of measurement. The threshold of alarm and the voltage value can be set through the keyboard on the alarm device. The original data, fault records can be read and printed by management software, and all kinds of values can also be set. When measuring, the monitor runs at three levels of speed (0.9 km/h, 1.8 km/h, 3.6 km/h) by switches.

II. Design

1. System Frame

As **Fig. 2** shows, the device of data processing and alarming is the core of the monitor. The device receives signals produced by detector unit through RS-485 cable. It shows and saves the measurement data, and gives off sound and light alarms. The measurement data are shown on color LCD in cab at the same time through the other RS-485 cable. During measurement, the data processing and alarm device receives signals from the speed-stable switch and then output corresponding voltage to control the mobile speed.

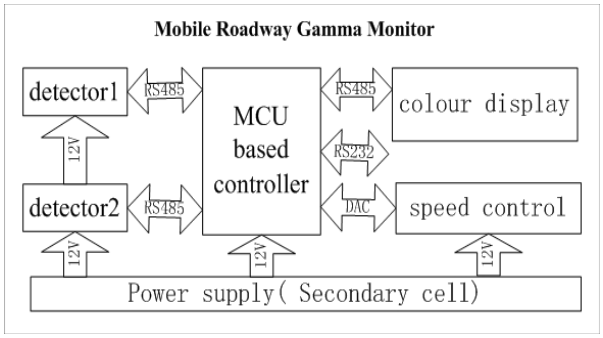

Fig. 2 Whole circuit frame

2. Detector

*Corresponding Author, Tel No: +86 351 2202150, Fax No: +86 351 2202147, E-mail: dengchangming@cirp.org.cn

The monitor equips with two plastic scintillators of EJ-200 type produced by the ELJEN company of America. The size of the detector is 1000 mm×500 mm×50 mm. The emitting peak is 425nm. Emission efficiency is 10000 photons /MeV. The matched PMT is CR-150 produced by HAMAMATSU company of Japan. The diameter of PMT is 51mm. Its cathode is made of two kinds of alkaline materials. The typical anode gain is 2.5×10^7. The risetime is 7 ns.

Using special light coupling piece can enhance the light conduction efficiency. The PMT and its divider are set in a shell pressed by a spring onto the detector and sealed. The bottom of detectors has lead plates shielding the background.

3. Circuit Design

The monitor consists of detection circuit and alarm circuit. Detection circuit consists of PMT divider, follower and amplifier.

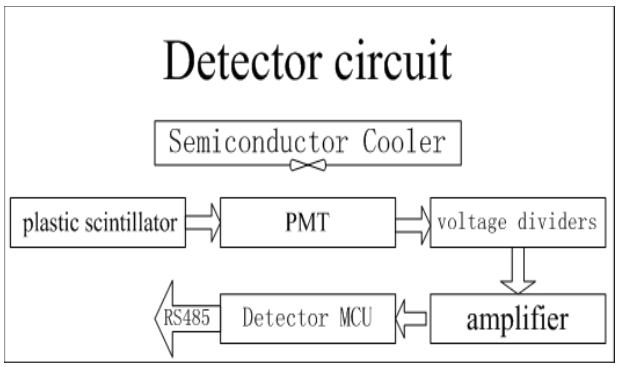

Fig. 3 Detector circuit frame

Detector unit circuit described in **Fig. 3**: rays enter the plastic scintillators and hit out photons on the cathode of PMT. Then the electron-photon system amplifies the photons. Later the anode of PMT selects the multiplied photons and forms anode current. The follower and amplifier make the current signals larger than original value. Then the MCU circuit processes and sends it through RS-485 cable. Semiconductor coolers whose cold sections face to PMT are controlled by temperature controller. To make sure the equipment works well, coolers start as long as the temperature goes beyond the normal range.

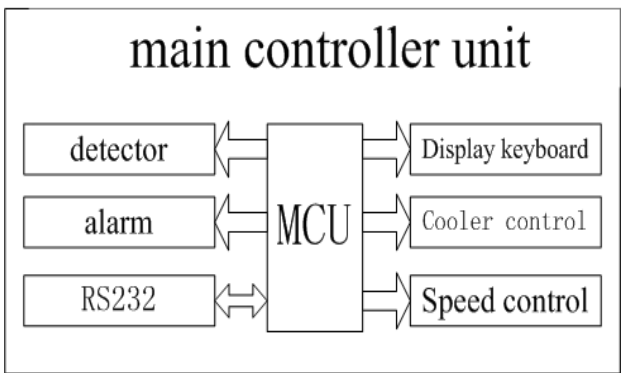

Fig. 4 Alarm unit frame

Main control unit circuit is shown in **Fig 4**. The alarm device is the core of the monitor. Measurement signals from the detectors are transmitted by RS-485 cable to the MCU unit, and processed by the control unit. The unit has such functions as alarming, displaying in two screens, speed controls and cooling controls. Alarm thresholds and timing period can be set through the keyboard of the unit. The capacity of the FLASH memorizer is 128MB. The data can be transmitted via RS-232 bus to the software.

4. Speed stable Survey

Responding to survey requirement, this system has speed controller which can make the mobile speed stable in three levels: 0.9 km/h, 1.8 km/h and 3.6 km/h. The sensor sends the rotation counts to control unit circuit which can output adjusted voltage to control the mobile speed. Using PID arithmetic on program can ensure the precision of the rate and the measurement.

5. Semiconductor Cooling

In order to make the detectors work well, we use semiconductor coolers. They consist of semiconductor chips, temperature sensors, fans and temperature controller. According to the operation setting, it is suggested that to the coolers be started when the temperature is up to 35 °C. Total power is 100 W.

III. Software

This management software adopts Visual C++ 6.0. The measuring data in main controller unit can be downloaded to a PC via this software. This program performs several functions such as setting alarm values, adjusting parameters, looking over records, making average report forms and graphs.

IV. Characteristics

The main characteristic of this instrument is surface detection efficiency. The efficiencies in different distance were measured for the two detectors. The check source is ^{60}Co, 23.7 kBq.

Table 1 Surface detection efficiency

Distance	1 m	30 cm	1 cm
Side detector	1.26%	6.03%	47.37%
Ground detector	-	1.26%	41.17%

The Ground detector is shielded by the floor of vehicle, so the efficiency of Ground detector is lower than Side detector.

V. Conclusion

The MRG10 mobile roadway gamma monitor is suitable for surveying the radioactive contaminated spots on roadway and surroundings in real time. It has been used in a nuclear power plant in China since December 2006, and satisfies the

demands of measurement in workplace on account of its fashion style and advanced functions such as digital signal transmission, stability and well EMC.

References

1) LUO, Xiaobin, et al., "The measurement of the fluorescence response of plastic scintillator ST1422 to neutron," Nuclear Electronics & Detection Technology., 24 [2] 186 (2004).
2) ZHOU, Jianbin, et al., "Applying of C8051 MCU in nuclear spectrum acquisition system," Nuclear Electronics & Detection Technology., 25 [5] 515 (2005).
3) TIAN, Xin, et al., "Design of the detector for vehicle nuclear material monitors," Nuclear Electronics & Detection Technology, 26 [5] 609 (2006).

Journal of NUCLEAR SCIENCE and TECHNOLOGY, Supplement 5, p. 477–480 (June 2008)

Performance Evaluation of One-dimensional Fiber-optic Radiation Sensor for Measuring High Energy Electron Beam Using a Charge-coupled Device

Dong Hyun CHO[1], Kyoung Won JANG[1], Wook Jae YOO[1], Soon Cheol CHUNG[1], Gye Rae TACK[1], Gwang Moon EOM[1], Bongsoo LEE[1*], Hyosung CHO[2], and Sin KIM[3]

[1]*Department of Biomedical Engineering, Research Institute of Biomedical Engineering, College of Biomedical & Health Science, Konkuk University, Chungju 380-701, Korea*
[2]*Basic Atomic Energy Research Institute and Department of Radiological Science, Yonsei University, Wonju 220-710, Korea*
[3]*Department of Nuclear & Energy Engineering, Applied Radiological Science Research Institute Cheju National University, Cheju 690-756, Korea*

In this study, we have fabricated one-dimensional fiber-optic radiation sensor array for high energy electron beam therapy dosimetry. Fiber-optic radiation sensor comprises an organic scintillator as a sensing volume, optical fiber as a light guider and photo-detector as a light measuring device. Usually, photomultiplier tube or photodiode is used as a photo-detector however we have tried to use a charge-coupled device as a scintillating light measuring system for one-dimensional fiber-optic radiation sensor array. This system can take an image of the proximal ends of one-dimensional fiber-optic sensor array and can measure light intensities of individual image of optical fibers simultaneously using simple imaging software. Charge-coupled device as a light measuring detector has many advantages which are easy in multi-dimensional measurements, high spatial resolution and relatively low cost. We have measured one-dimensional electron beam distributions in a PMMA phantom with different energies and field sizes of electron beam using a fiber-optic sensor and a charge-coupled device. Also, the percentage depth dose curves for high energy electron beams are obtained.

KEYWORDS: fiber-optic radiation sensor, one-dimensional, electron beam, CCD

I. Introduction

Typically, a fiber-optic radiation sensor for radiotherapy dosimetry applications uses an organic scintillator probe, an optical fiber and a light-measuring device.[1,2)] An optical fiber is usually made of plastic or glass, which is used to guide the light signal from a scintillator to light measuring device such as a photomultiplier tube (PMT), photodiode or optical power-meter. PMT is commonly used to measure scintillating light due to its high internal gain and reasonable quantum efficiency however it has some drawbacks such as gain change with time, high cost, relatively large volume and difficulty in using multi-channel measurements. Photodiodes can be the preferred solution because they are relatively cheap, compact and very easy to make an array, but the problem is that they work efficiently with higher wavelength visible light, whereas most organic scintillators emit light with lower wavelengths in visible light or ultraviolet range.[3)] Optical power-meter is rarely used to measure scintillating light due to its lack of stability in measurement and high cost.

In this study, we have used a charge-coupled device (CCD) as a scintillating light measuring system for one-dimensional fiber-optic radiation sensor array. This system can take an image of the proximal ends of one-dimensional fiber-optic sensor array and can measure light intensities of individual image of optical fibers simultaneously using simple imaging software. CCD as a light measuring device has many advantages which are easy in multi-dimensional measurements, high spatial resolution and relatively low cost.[4)]

We have measured one-dimensional electron beam distributions in a polymethylmethacrylate (PMMA) phantom with different energies and field sizes of electron beam using a fiber-optic sensor and a CCD. Also, the percentage depth dose (PDD) curves for high energy electron beams are obtained.

II. Materials and Experimental Setup

As a fiber-optic sensor probe, an organic scintillator which is made out of a polyvinyltoluene (PVT) base with wavelength-shifting fluors is used. It has a cylindrical shape and commercially available (BCF-20, Saint Gobain Crystals). This scintillator emits green light whose peak wavelength is 492 nm and the decay time is 2.7 nsec. About 8000 photons are emitted when 1 MeV ionizing particle interacts with this scintillator. An organic scintillator of 1 mm diameter and 10 mm length is glued to the 10 m length plastic optical fiber (POF) with an optical-cement. Optical polishing should be done both surfaces of an organic scintillator and POF before gluing. POF has many advantages as a scintillating light guider in fiber-optic radiation sensor. First, POF is flexible and able to withstand a bend radius of up to 20 mm with no change in transmission. Second, POF can be used in the high radiation environment because it does not create any electromagnetic interference. Third, POF itself or its

*Corresponding Author, Tel No: +82-43-856-0976, Fax. No: +82-43-851-0620, E-mail: bslee@kku.ac.kr

connector is cheaper and its surface is easily polished compared to the glass optical fiber. The outer diameter of POF (CK-40, Mitsubishi) which is used in this study is 1.0 mm, and the cladding thickness is 0.02 mm. The refractive indices of the core and the cladding are 1.49 and 1.402, respectively, and the numerical aperture (NA) is 0.504. The NA stands for the light-gathering power and more lights can be guided by a POF with a high NA.

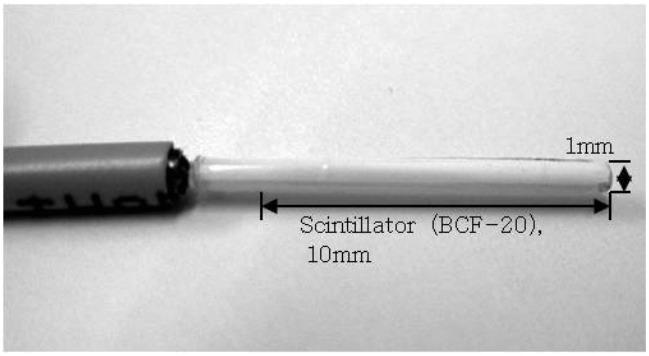

Fig. 1 Fiber-optic radiation sensor with organic scintillator probe

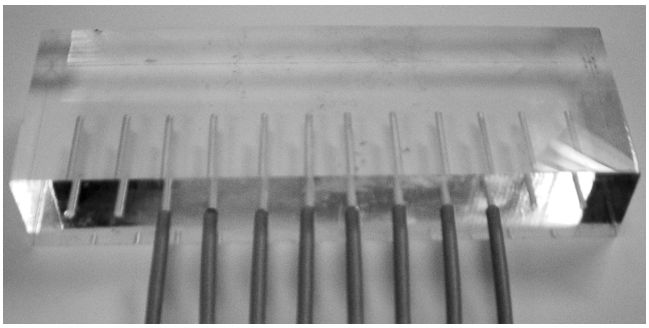

Fig. 2 One-dimensional fiber-optic radiation sensor array embedded in PMMA phantom

Fig. 1 shows a fiber-optic radiation sensor which consists of an organic scintillator probe and a general POF. The surface of the sensor probe is surrounded by reflective paint based Titanium Oxide (TiO_2) to increase scintillating light collection efficiency and to intercept the light noise from outside. And one-dimensional fiber-optic radiation sensor array with a gap of 1 cm, which is embedded in PMMA phantom are shown in **Fig. 2**. There is no air gap between fiber-optic sensor probe and every hole in PMMA phantom to maintain the water-equivalency of each sensor probe and a phantom.

Fig. 3 shows experimental setup to measure one-dimensional distributions of electron beam in a PMMA phantom which has water or tissue-equivalent material characteristics. Electron beams are provided with a Varian clinical linear accelerator (CLINAC) 2100CD and 6 and 12 MeV energies electron beam with 4 × 4 and 10 × 10 cm^2 field sizes are used.

The images of the proximal ends of one-dimensional fiber-optic sensor array are taken using a CCD (SDZ-160, Samsung) with an image capturing software (FlashBus MV ver. 3.91, Integral Technologies, Inc.). The light intensities of those images are measured with a Matlab (version 7.3.0.267(R2006b), MathWorks, Inc.) The SDZ-160 Color CCD Camera has 1/4 inch image format with 410,000 Pixels and has a built-in lens in a compact package. The maximum zoom ratio of this CCD is 128 times with 16 times optical and 8 times digital zoom.

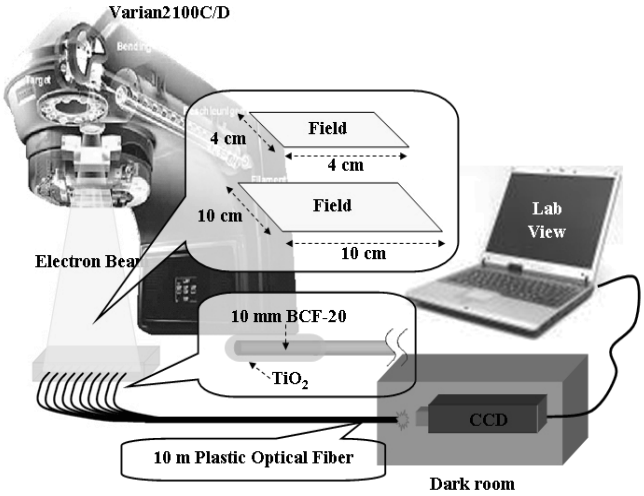

Fig. 3 Experimental setup

III. Experimental Results

Fig. 4 and **5** show the measured scintillating light signals from a one-dimensional fiber-optic sensor array with different electron energies and field sizes. The fiber-optic sensors are embedded in a PMMA phantom with 1 cm depth and arrayed with the same gap of 1 cm. The measured light signals show almost same values and are distributed uniformly in the field size of 4 × 4 and 10 × 10 cm^2 for two different electron beam energies.

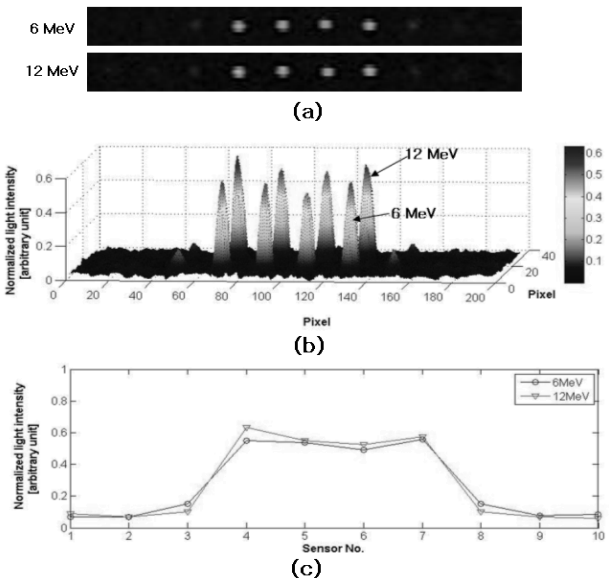

Fig. 4 Measured scintillating light signals of one-dimensional fiber-optic sensor array irradiated by 6 and 12 MeV electron energies with field size of 4 x 4 cm^2

To calibrate each fiber-optic sensor we have arrayed 10 fiber-optic sensors one-dimensionally on the center of 20 x 20 cm^2 electron field with gaps of 5 mm. Because the amount of dose in the center part of the electron field is considered to be uniform, we have taken 10 images of proximal ends of fiber-optic sensors and measured light intensities of those images. Also, we have obtained average value of measured light intensities and we have decided the correction factor of each sensor using the average value. Finally, we have calibrated and corrected the measured results.

Fig. 4-(a) and **5-(a)** show the images of proximal ends of fiber-optic sensor array, which are taken by CCD when the scintillating probes of fiber-optic sensor array are irradiated by 6 and 12 MeV electron beam, respectively. The light intensities of the proximal end images are measured using imaging software and the results are shown in **Fig. 4-(b)** and **5-(b)** with different field sizes.

The scintillating light signals induced by 6 MeV electron beam are almost same as those by 12 MeV electron beam as shown in **Fig. 4-(c)** and **5-(c)** because the percent depth dose curves of 6 and 12 MeV electron beam show the same value at the depth of 1.0 cm in a water phantom.[5] In **Fig. 4-(c)**, only 4 scintillating light signals are detected because the field size is 4 × 4 cm^2 and every 10 light signals are measured by fiber-optic sensor array with increased field size of 10 x 10 cm^2 in **Fig. 5-(c)**.

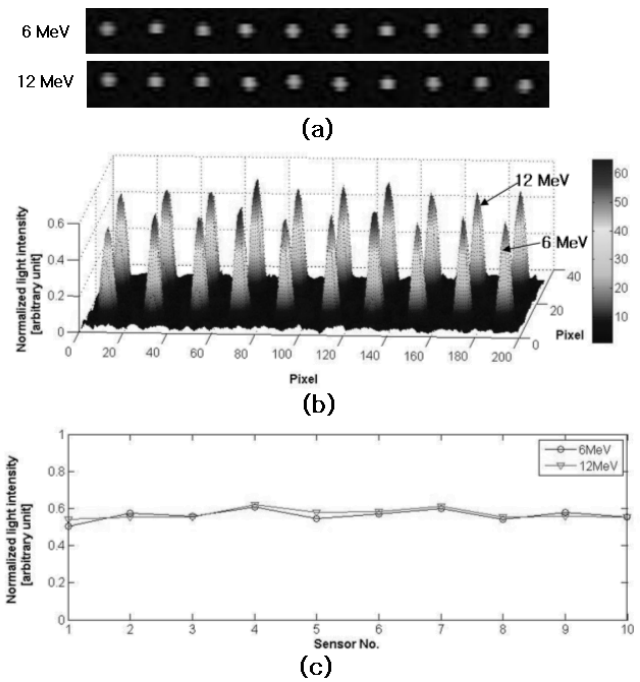

Fig. 5 Measured scintillating light signals of one-dimensional fiber-optic sensor array irradiated by 6 and 12 MeV electron energies with field size of 10 x 10 cm^2

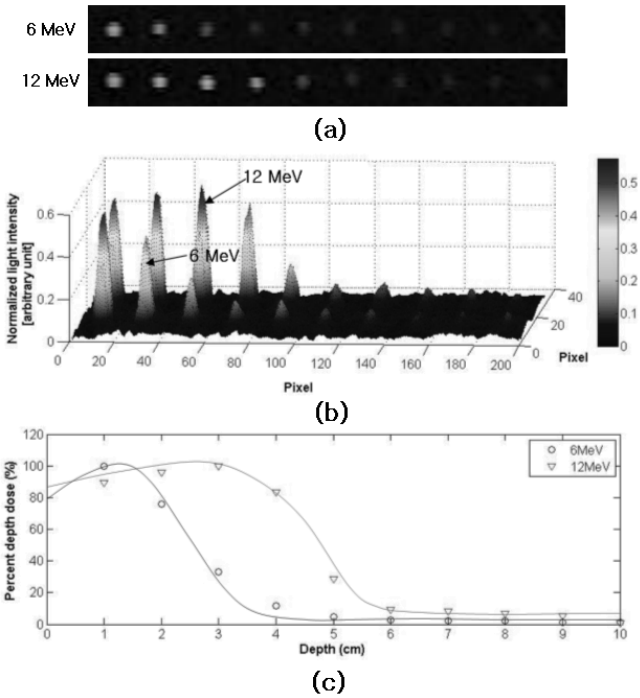

Fig. 6 Measured depth doses curves in PMMA phantom for 6 and 12 MeV electron energies using one-dimensional fiber-optic sensor array

Fig. 6 shows the one-dimensional percent depth dose curves using a one-dimensional fiber-optic sensor array for 6 and 12 MeV electron beams. Also, the images of the proximal ends of fiber-optic sensor taken by CCD are shown in **Fig. 6-(a)** and the measured light intensities of the images are shown in **Fig. 6-(b)**.

Fig. 6-(c) shows that the percent depth dose curves for 6 and 12 MeV electron beams are maximized at about 1.5 cm and 3.0 cm depth of a PMMA phantom respectively. These are consistent with known results that the maximum depth doses are measured at 1.3 cm for 6 MeV and at 2.8 cm for 12 MeV electron beams using an ion chamber in a water phantom.[5]

IV. Conclusions

In this study, we have fabricated one-dimensional fiber-optic sensor arrays and developed a method to measure scintillating light signals using a CCD for high energy electron beam therapy dosimetry. We have measured one-dimensional electron beam distributions in a PMMA phantom with different energies and field sizes of electron beam using a fiber-optic sensor and a CCD. Also, the PDD curves for high energy electron beams are obtained. Further studies will be carried out to measure the spatial resolution of a one-dimensional fiber-optic sensor array and Cerenkov lights induced by fiber-optic sensor array embedded in a phantom. Also, angular dependence of fiber-optic sensor array will be investigated. It is expected that multi-dimensional fiber-optic sensor array and CCD system as a light measuring device can be used for electron beam therapy dosimetry with high accuracy and spatial resolution.

Acknowledgement

This study was supported by the Basic Atomic Energy Research Institute (BAERI) program of the Ministry of Science & Technology (MOST) (M20376030002-04B0505-00210).

References

1) B.M. Rogine, and Vojnovic, "Application of optical fiber sensors for radiation dosimetry" Radiation Measurements, Vol. 26, No. 4, pp 599-602, (1996).
2) E. Takada, A. Komura, T. Hosono, H. Takahashi, and M. Nakazawa "Radiation distribution sensor with optical fibers for high radiation fields" J. of Nucl. Sci. and Tech Vol. 36, No. 8, pp 641-645, (1999).
3) T. Aoyama, S. Koyama, M. Tsuzaka, H. Maekoshi, "Depth-dose measuring device using a multichannel scintillating fiber array for electron beam therapy". Nagoya University College of Medical Technology, Daikokminai, Higashi-ku, Nagoys 461, Japan, pp 1235-1239, (1997).
4) A.M. Chugg, R. Jones, P. jones, P. Nieminen, A. Mohammadzadeh, M.S. Robbins, and K. Lovell, "A CCD Miniature Radiation Monitor", Nuclear sci. Vol. 49, No. 3, pp 1327-1332, (June 2002).
5) Faiz M. Khan, "The Physics of Radiation Therapy", 2nd ed. Williams & Wilkins, Baltimore, pp. 365, (1994)

Journal of NUCLEAR SCIENCE and TECHNOLOGY, Supplement 5, p. 481–484 (June 2008)

Measurement of Rectal Dose during HDR Brachytherapy using the new MO*Skin* Dosimeter

Ian KWAN[1], Andrew HOWIE[2], Michael LERCH[1], Bongsoo LEE[3**], Yaw Sinn CHIN[2], Joseph BUCCI[2], Vladimir PEREVERTAYLO[4] and Anatoly ROSENFELD[1*]

[1]*Centre for Medical Radiation Physics, University of Wollongong, New South Wales, 2500, Australia*
[2]*St. George Cancer Care Centre, Kogarah, New South Wales, Australia*
[3]*Department of Biomedical Engineering, College of Biomedical & Health Science, Konkuk University, South Korea*
[4]*SPA BIT, Ukraine*

In HDR prostate brachytherapy, post-treatment complications occur due to overdosing the rectum wall and urethra. An area of concern regarding treatment is related to how the rectal wall dose is calculated using treatment planning systems. Treatment planning systems can calculate the dose delivered to the rectal wall, assuming that the rectum is filled with water equivalent material. This assumption is not always correct, as the rectum is emptied before treatment begins. The aim of this research is to quantify the difference in the dose measured in an 'empty' rectal phantom, and in a rectal phantom filled with water equivalent material. Results indicate that the dose measured by the MO*Skin* and RadFET in an empty rectum is approximately 10–15% lower than the dose measured dose in a full rectum, and the dose calculated by the PLATO TPS, which assumes that the rectum is full. This could have implications on the design of HDR treatment plans.

KEY WORDS: high dose rate brachytherapy, prostate cancer, rectum, rectal dose

I. Introduction

The use of metal oxide semiconductor field effect transistors (MOSFETs) in dosimetry has gained acceptance for dosimetry in high energy photon and electron beam fields. Traditionally, patient dose verification is performed using thermoluminescence dosimeters (TLD). While the small size of TLDs is desirable, they do not allow for real-time, *in-vivo* dose information to be obtained during a clinical treatment. Also, stringent handling and annealing procedures must be followed to acquire accurate, reproducible results with TLDs. The sensitive volume of detectors such as TLDs and fiber optic dosimeters is on the millimeter scale, and would only allow for volume averaging of the absorbed dose, providing poor spatial resolution. In regions with a steep dose gradient, such as that experienced near a high dose rate (HDR) brachytherapy source, thinner sensitive volumes are required to measure the absorbed dose in steep dose gradient conditions. Radiochromic films, such as EBT GAFCHROMIC® film from International Specialty Products (USA), have 34 μm thick active volumes (two 17 μm layers combined) that allow for high spatial resolution measurements to be made, but require 6–24 hours to develop[1)], and therefore, cannot offer real-time dose information to clinicians during a treatment. In HDR prostate brachytherapy, post-treatment complications occur due to overdosing the rectum wall and urethra. At St. George Cancer Care Centre in Sydney, Australia, careful planning is conducted so that the rectal wall receives a dose no higher than 75% of the dose delivered to the prostate gland[2)]. The close proximity of the rectum to the prostate leads to a high probability of delivering too much dose to the rectum. Quality Assurance (QA) during an HDR brachytherapy treatment session is required to ensure that slight movements of the prostate and catheter during treatment don't lead to rectal damage. By monitoring the dose delivered to the rectum during treatment, the treatment can be altered or stopped before too much dose is delivered to the rectum or corrected during the next fraction. The popularity of MOSFET-based detectors is increasing in this field due to their small size, reusability, and their ability to offer real-time dose information. While other detector systems, such as fiber optic dosimeters, meet these requirements, MOSFET-based dosimeters are also capable of high spatial resolution due to their sensitive volume, which is typically less than 1 μm thick.

An area of concern is related to how the rectal wall dose is calculated using treatment planning systems. Treatment planning systems (TPS) can calculate the dose delivered to the rectal wall, but typically assumes that the rectum is filled with water equivalent material. This is likely not necessary correct assumption by the TPS, as the rectum is emptied before HDR brachytherapy treatment begins. The rectal wall dose measured in an empty rectum should be lower than the dose measured in a "full" rectum due to the lack of backscatter material in an empty rectum. The aim of this research is to quantify the difference in the dose measured in an empty rectal phantom, and a full rectal phantom. The results were compared to the dose calculated by the PLATO TPS, developed by Nucletron.

*Corresponding Author, Tel No: +61-2-4221-4574, Fax No: +61-2-4221-5944, E-Mail: anatoly@uow.edu.au
**B. Lee is currently a visiting fellow at CMRP on sabbatical

II. Materials and Methodology

1. MOSkin Design

Measurements in the rectal phantom were taken using the newly designed MOSkin™ detector, developed by the Centre of Medical Radiation Physics (CMRP) at the University of Wollongong, Australia. The MO*Skin*™ is designed to measure the dose at an air-tissue interface, such as the skin dose, or the dose along the rectal wall. What makes the MO*Skin*™ unique is the design of the packaging. It does not incorporate neither an epoxy 'bubble' to encapsulate and protect the MOSFET sensor nor wire bonding of MOSFET chip. Instead, a thin, flexible, and reproducible polyamide film is used to protect the MOSFET sensor rather than epoxy. **Fig. 1** illustrates the design differences between a MOSFET-based detector that uses an epoxy 'bubble' for encapsulation, and the MO*Skin*. The film is acting as controllable build-up region and chip protection from external environment simultaneously , and is thin enough (7 mg/cm^2) to allow for skin dose measurements at the basal cell layer, which is the first important radiosensitive layer of the skin. According to the International Commission on Radiological Protection (ICRP), the estimated depth of the basal cell layer depth is 0.07mm [4]). When looking at MOSFET detectors that utilise an epoxy bulb, none have proven to be adequate at measuring dose at an air-tissue interface such as the rectal wall.

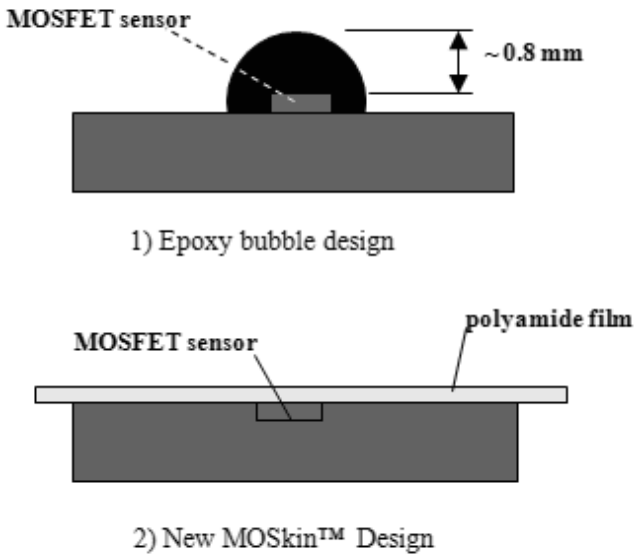

Fig. 1 Illustrates the difference in the packaging design of a MOSFET detector with epoxy bubble, and a MO*Skin*.

A second MOSFET detector used for comparison is the commercially available RadFET™ detector, designed by REM Oxford in the UK. In this design, the sensor is mounted to a thin PCB carrier and encapsulated by a black epoxy 'bubble' that physically protects the sensor and acts as a build-up region. The PCB of the RadFET is 55 mm long and 9 mm wide; the epoxy bubble is approximately 1 mm thick. The packaged MO*Skin* detector is 1 x 2.5 mm^2 in area. The MOSFET chip itself is only 350 μm thick, with overall thickness less than 1 mm.

Both the MOSkin™ and RadFET™ detectors are read out by a portable, battery-powered reader designed by the CMRP. The reader allows ten MOSFET detectors to be attached simultaneously, and read out individually. Measurements presented here were obtained with the reader set to 12 V bias; however, the reader is also capable of applying a 5 V bias voltage if desired or without bias.

2. MOSkin Calibration

To convert the voltage readings reported by the reader into a dose value, a dose conversion factor was required for the MOSkin™ and RadFET™ detectors. The dose calibration factor was determined using a 6 MV x-ray beam with a 10×10 cm field size, produced by a Varian 2100EX linear accelerator (LINAC). The two detectors were positioned at the depth of maximum dose (d_{max}), or 15 mm, with the source-to-surface distance (SSD) set to 100 cm. A two minute wait period was incorporated between the irradiation and readout in order to minimise the effects of creep-up[5]) and keep readout condition for both detector the same.

This calibration factor was also compared to a calibration factor obtained by irradiating the MO*Skin* in-phantom at a depth of 20 mm using a Nucletron microSelection Ir-192 PDR source.

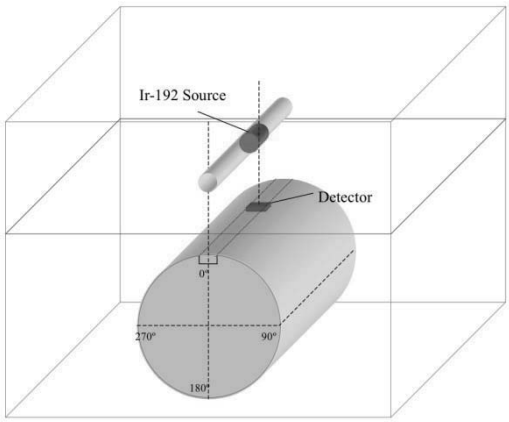

Fig. 2 The phantom setup used to measure the dose delivered to the anterior side of a full rectal phantom.

3. Phantom Design

The dose was measured using a rectal phantom made of Plastic Water™ purchased from Gammasonics Pty. The phantom is comprised of numerous solid water slabs in a stacked configuration, each slab designed to serve a particular purpose. During irradiation, the afterloader sends the Ir-192 source down the source cable and into the catheter, which is inserted into a phantom slab designed to hold the catheter. The rectal phantom slab is 30 mm thick, with a 21 mm diameter hole that acts to simulate an empty rectum. A cylindrical piece of plastic water was designed to fit the hole of the rectal phantom and simulate the conditions of a full rectum. This special cylindrical piece was designed with a

groove etched along the surface, and allows the MO*Skin*™ to fit snugly within the groove. The groove runs parallel to the central axis of the cylinder. The phantom was designed to ensure that the Ir-192 source was positioned along the perpendicular bisector of the detector.

4. Angular Response Comparison of MO*Skin* and RadFET Detectors

To measure the dose delivered to the inner wall of a rectal phantom when it is filled with water equivalent material, the MO*Skin*™ is first placed within the groove of the cylindrical piece, which is inserted into the hole of the rectal phantom slab. By rotating the cylinder clockwise or anti-clockwise, the MO*Skin*™ can be positioned at any point along the inner wall of the phantom. In this experiment, measurements were taken with the detector positioned at the "anterior" side of the rectal phantom. In this discussion, the "anterior" wall of the phantom is defined to be the point on the rectal wall closest to the Ir-192 source. The relative position of the Ir-192 source and the detector is illustrated in **Fig. 2**. The distance between the source and anterior wall was kept at a constant 18.6 mm distance. A moderate distance was chosen because placing the detector closer to the source would mean that the detector is located in a steeper dose gradient, where a slight uncertainty in our detector placement, or distance measurement may have a large effect on the absorbed dose. Placing the detector further away would decrease the uncertainty of the measurement.

To measure the dose delivered to the anterior wall of an empty rectal phantom, the detector was carefully positioned at the inner wall of the phantom, held in place using an adhesive tape. The dose was measured without the cylindrical piece inserted into the phantom.

III. Results

1. Detector Calibration

A dose calibration factor was found for six individual MOSkin detectors, along with the RadFET. The MO*Skin* was found to have a mean dose calibration factor of 402.4±15 cGy/V. The variation in the calibration factor calculated for each MO*Skin* detectors was very small. The RadFET had a mean calibration factor of 662.7±26 cGy/V.

2. Absorbed Dose in Full and an Empty Rectum

First, the dose delivered to the wall of the rectal phantom was measured when the cylinder was inserted. With the cylindrical piece inserted into the rectal phantom, the MO*Skin* and RadFET detectors measured a rectal wall dose of 35.9 and 33.7 cGy, respectively. The PLATO TPS, which assumes that the rectum is filled with water, empirically calculated the dose to be 37.1 cGy. When comparing the experimental results to the PLATO TPS, a discrepancy of -3.1±2% and -9.1±2% was observed using the MO*Skin* and RadFET, respectively. Ideally, the dose measured by the two detectors should be identical to the dose determined by the TPS, since measuring the dose in a full rectal phantom is analogous to using the detectors to simply measure the depth dose in a block of solid water.

Next, the dose delivered to the wall of an empty rectal phantom was measured. The dose measured at the anterior wall using the MOSkin and RadFET was 30.4 and 29.2 cGy, respectively. The MO*Skin* dose measurement was 18.1±2% less than the dose calculated by PLATO, while the RadFET result was 21.2±2% less. The results indicate that the dose measured by the MO*Skin* and RadFET in an empty rectum is approximately 10-15% less than the dose measured dose in a full rectum, and the dose calculated by the PLATO TPS, which assumes that the rectum is full. A summary of the results is shown in **Table 1**.

Table 1 Absorbed dose measured in an empty rectal phantom, and in a rectal phantom filled with a water-equivalent material.

	CMRP MOSFET		RadFET		PLATO
	Measured (cGy)	% Diff. from PLATO	Measured (cGy)	% Diff. from PLATO	Dose (cGy)
Empty	30.4	-18.0%	29.2	-21.2%	37.1
Full	35.9	-3.1%	33.7	-9.1%	37.1

These measurements were performed without considering an important factor regarding the RadFET design. The distance from the Ir-192 source to the anterior side of the rectal wall is 18.6 mm, but the RadFET is only capable of measuring dose at 19.6 mm distance away from the source due to the 1 mm of epoxy material covering the RadFET's sensor. The 1 mm difference in the source-to-detector distance should account for the smaller dose value obtained using the RadFET in the full rectum, which was 9.1% lower than the dose calculated by the PLATO TPS.

To verify that the extra 1 mm distance, rather than a poorly performing RadFET, was the cause of the low reading, PLATO TPS was used to determine the dose at a distance of 19.6 mm. This value was then compared to the RadFET dose obtained earlier at a distance of 18.6 mm. At 19.6 mm, PLATO calculates the dose to be 33.4 cGy, which is very similar to the 33.7 cGy obtained earlier by the RadFET. The 1 mm of epoxy material appears to be the cause of the discrepancy between the RadFET and the TPS. It is confirmation of importance in HDR brachytherapy QA to have detector with minimal build up in conjunction with very high spatial resolution that was achieved in MO*Skin*.

IV. Conclusions

Results indicate that the dose measured by the MOSkin and RadFET in an empty rectum is approximately 10–15% lower than the dose measured in a full rectum, and the dose calculated by the PLATO TPS. This could have implications on the design of HDR treatment plans, as treatment planning systems have likely overestimated the dose to the rectum, since patients are treated with empty bowels rather than completely full.

Furthermore, MOSFET-based detectors packaged in an epoxy bubble resin appear less suitable for rectal wall

dosimetry in HDR brachytherapy due to the thick for existing dose gradient and not reproducible epoxy build-up material that encapsulates the MOSFET sensor. As a result of the epoxy material, the RadFET is unable to accurately measure the absorbed dose at the depth of interest because the sensitive part of the sensor cannot be moved to the proper position without removing the epoxy material. This can be mentioned about most detectors used *in vivo* for rectal wall dosimetry due to failing of requirements of packaging design or small size of the dosimetric volume. The MO*Skin* is appeared the most suitable dosimeter for such QA.

Acknowledgement

This work was made possible because of the generous support provided by the Australian Rotary Health Research Fund/Districts 9650 scholarship. This work was also supported by Australian government NHMRC grant 354114 the Korea Research Foundation Grant funded by the Korean Government (MOEHRD, Ministry of Education and Human Resource Development) (KRF-2007-013 D00117).

References

1) ISP, "GAFCHROMIC EBT: Self-developing film for radiotherapy dosimetry", International Specialty Products (2005).
2) Dr Joseph Bucci, Private Communication .
3) A. Rosenfeld, "MOSFET dosimetry in modern radiation oncology modalities" Radiation Protection Dosimetry, 101[1-4], 393 (2002).
4) ICRP (International Commission on Radiological Protection), "The biological basis for dose limitation in the skin", ICRP Publication 59 (1991).
5) R. Rameseshan, S. Russell, P. O'Brien, "Clinical Dosimetry Using MOSFETs", Int. J. Radiation Oncology Biol. Phys. 37[4], 959 (1997)

Journal of NUCLEAR SCIENCE and TECHNOLOGY, Supplement 5, p. 485–488 (June 2008)

Monte Carlo Study on Optimization of Reflectors in Pixelated CsI Film for Mammographic Application

Chae hun LEE, Gyuseong CHO*, Bo Kyung CHA, and Hosang JEON

Korea Advanced Institute of Science and Technology
Guseong-dong, Yuseong-gu, Daejeon, Korea

Isotropic light spread in the scintillator film decreases the spatial resolution of scintillator-based digital X-ray imaging systems such as digital radiography and mammography. Pixelation of the scintillator film could be a good solution to overcome this limitation. This has been demonstrated with pixilated CsI:Tl layers which was made by thermal evaporation process on a pre-patterned substrate or which was post-patterned by laser after preparation. Additionally, in order to minimize cross-talk between pixels and to maximize light collection efficiency, a reflection material can be coated on the top and side surfaces of each pixilated scintillator block. In This paper, several materials such as Al, and quarter-wave multilayer reflector with SiO_2 and TiO_2 were considered as the reflector materials of pixilated CsI:Tl scintillator blocks. Through a serious of simulations given below on these simple 2-dimensional scintillator blocks coated by a reflector, reflectivity, cross-talk, and modulation transfer function were calculated to find the optimum reflector.

KEY WORDS: Modulation Transfer Function, pixelated CsI:Tl, reflectors, quarter-wave multilayer reflector, Digital Mammography

I. Introduction

Digital Mammography is one of the diagnostic methods for breast cancers in women. Digital Mammographic imaging detectors are usually based on scintillators and photo-sensors. The quantum efficiency of the detectors can be improved by adding scintillating materials which have a high x-ray absorption coefficient and convert x-ray photons into visible light.[1,2] However, isotropic light spread in the scintillator film decreases the spatial resolution of scintillator-based digital X-ray imaging systems such as digital radiography and mammography. Pixelation of the scintillator film could be a good solution to overcome this limitation.[3,4] This has been demonstrated with pixilated CsI:Tl layers which was made by thermal evaporation process on a pre-patterned substrate or which was post-patterned by laser after preparation. Additionally, in order to minimize cross-talk between pixels and to maximize light collection efficiency, a reflection material can be coated on the top and side surfaces of each pixilated scintillator block by using chemical vapor deposition (CVD), Atomic Layer Deposition (ALD), etc. However its thickness should be optimized i.e., thick enough to work as reflector but thin enough not to absorb much incident X-rays.

SiO_2, TiO_2, Al, and the combination of SiO_2 and TiO_2[5] are commonly used as optical reflectors. The refractive index of SiO_2, TiO_2, and Al in visible wavelength is 1.46, 2.4, and 1.3, respectively. SiO_2 and TiO_2 are dielectric coating materials while Al is a metallic coating material which reflects or absorbs visible light. Physical characteristics of these reflectors and CsI:Tl scintillator are listed on **Table 1**.

Table 1 characteristics of reflectors and CsI:Tl

	Aluminum	SiO_2	TiO_2	CsI:Tl
Density (g/cm^3)	2.7	2.2	4	4.51
Refractive index (at 550 nm)	1.3	1.46	2.4	1.8
Quarter-wave thickness-λ/4n (nm)	105	94	57	.

The aim of this paper is to model the characteristics of pixelated CsI:Tl having reflectors with Monte Carlo simulation tools such as MCNPX[6] and DETECT[7] for x-ray and visible photon transport, and optimize reflectors for performance improvement in pixilated CsI:Tl scintillator.

II. Methodology

Overall simulation diagram in this study was shown as **Fig. 1** in which the upper-right figure is a cross-section view of pixilated CsI with side reflectors and the bottom-right figure is a side view of CsI pixel with top reflector. The source-to-detector distance (SDD) was 65 cm and the focal spot size of Mo target was 0.3 mm. The CsI:Tl scintillator pixel width is 50 μm and reflector width between pixels is 10 μm as shown in **Fig. 1**. Reflectors can be SiO_2, TiO_2, and Al on the top of CsI:Tl or gap between pixels. Quarter-wave thickness, 94 nm and 57 nm of SiO_2 and TiO_2 were used for a stack of multilayer reflector. 25 × 25 array of pixilated CsI:Tl scintillator was designed for MTF calculation. 1.5 mm thick 5˚ tiled tungsten edge for over-sampling was used MTF measurement.

X-ray source for mammography is different from conventional chest radiography. So, X-ray source spectrum for mammography was calculated with SRS-78 program.[8]

*Corresponding Author, Tel No: +82-42-869-3821, Fax No: +82-42-869-3810, E-Mail: gscho@kaist.ac.kr

Molybdenum whose characteristic X-ray energy is 17.5 and 19.6 keV, was used for the target and filter of X-ray tube. Its average of X-ray energy is 17 keV. Additionally, a 500 μm thick Beryllium window was used. **Fig. 2** is the X-ray spectra used in MCNPX simulation.

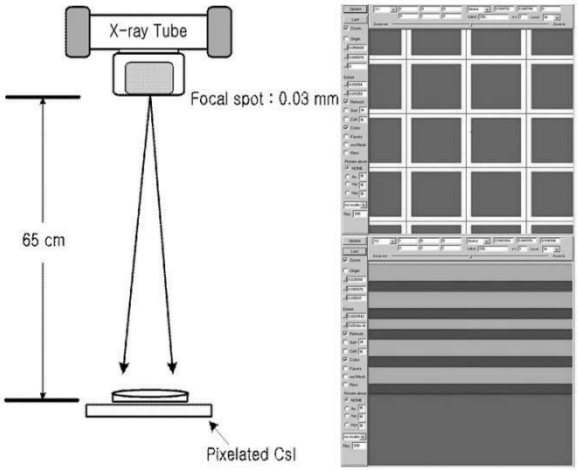

Fig. 1 Simulation diagram and pixelated CsI:Tl pixel structure

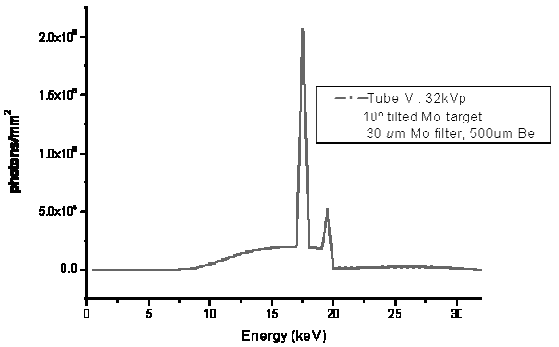

Fig. 2 X-ray spectra calculated by SRS-78 for mammography

In MCNPX simulation, deposited X-ray energy in each pixel was calculated and light photons as much as deposited energy were generated in DETECT in which light spread was applied. Finally, 25 × 25 edge images were obtained for MTF calculation.

III. Result

1. Determination of CsI:Tl Thickness

Fig. 3 shows absorbed X-ray energy with respect to the thickness of CsI:Tl scintillator. Absorption of 17.5 keV X-ray energy is saturated at thinner CsI:Tl thickness rather than 19.6 keV. And used X-ray spectra is almost absorbed at 200 μm. In this study, the thickness of CsI:Tl scintillator was determined as 150 μm which absorbs more than 90 % X-ray energy.

2. X-ray Transmission through Reflectors

X-ray photons are transmitted through materials or absorbed by the Lambert-Beer law,

$$I = I_0^{(-\mu/\rho)\rho x} \quad (1)$$

Where ρ is material density, μ/ρ is the mass absorption coefficient. The transmission of the X-rays through reflectors was calculated for thicknesses to 1.5 μm with different X-ray energy. Higher than 15 keV X-ray penetrates almost 100 % through 1.5 μm thick Al, SiO_2, and TiO_2, but low X-ray energy was absorbed due to K-edge. At used mammographic X-ray spectra, more than 99 % was transmitted through them.

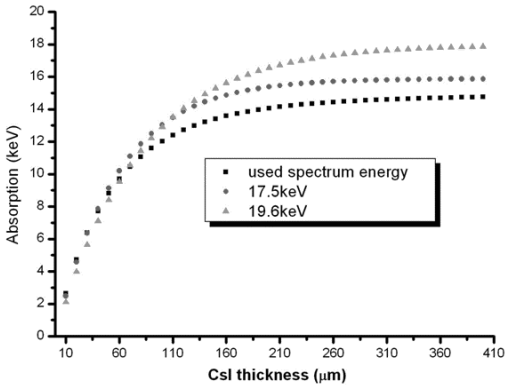

Fig. 3 Absorbed X-ray energy with different CsI:Tl scintillator thickness

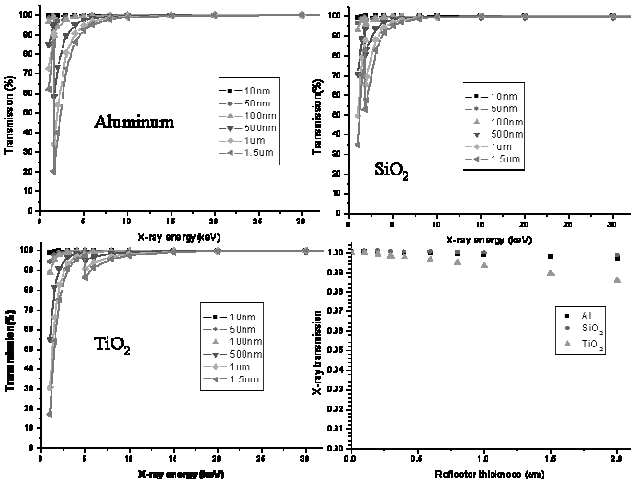

Fig. 4 Transmission with different X-ray energy

3. Reflectivity

Aluminum is usually used as a metallic coating material, while SiO_2 and TiO_2 are dielectric coating thin films. Al is a common reflection material which is used for visible light reflection. If optical thickness, t = nd in which n is refractive index and d is physical thickness, is bigger than λ/4, it's enough thickness for optical reflectors. On the other hand, SiO_2 and TiO_2 reflect or refract visible light photons on their interface with other materials in which reflection and refraction depends on refractive indices of interface and incident angles of visible photons. So, SiO_2 or TiO_2 solely can not be a good reflection material. But SiO_2/TiO_2 multilayer can behave as a good reflector in quarter-wavelength thickness (λ/4n). Quarter-wave thickness of SiO_2 and TiO_2 is 94 nm and 57 nm.

Fig. 5 shows the reflectivity of aluminum with respect to incident angles, when aluminum thickness is 105 nm and the material of incident interface and substrate are CsI:Tl whose refractive index is 1.8. As shown in **Fig. 5**, reflectivity is higher than 86 % in all incident angles and about 87 % in average. And at incident angle higher than 80˚ the reflectivity heavily increases.

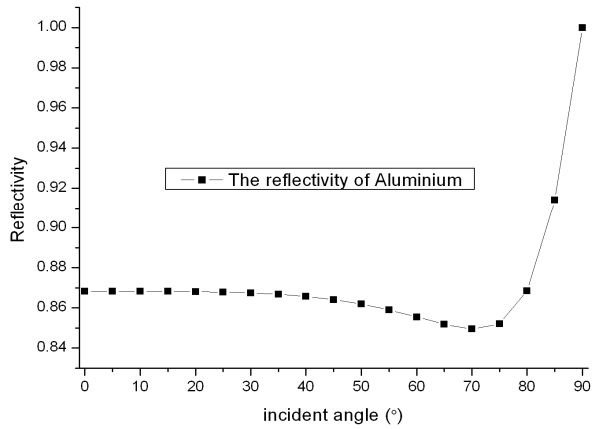

Fig. 5 Reflectivity of aluminum with respect to incident angles of visible photons

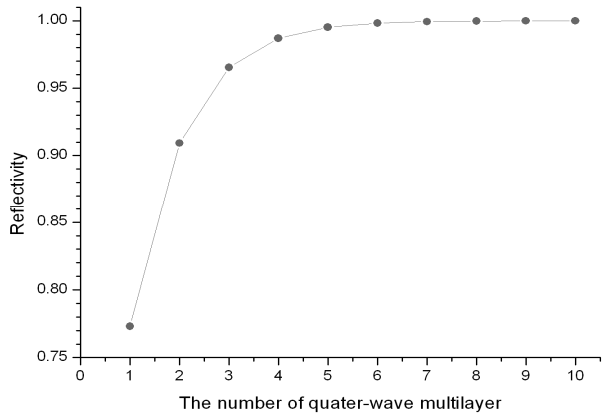

Fig. 6 Reflectivity of SiO_2/TiO_2 multilayer with respect to the number of quarter-wave layer

The reflectivity of SiO_2/TiO_2 multilayer follows the equation below ;

$$R = \left(\frac{1-(n_H/n_L)^{2m}(n_H{}^2/n_s)}{1+(n_H/n_L)^{2m}(n_H{}^2/n_s)}\right)^2 \qquad (2)$$

in which n_H, n_L and n_S are High refractive index and low refractive index, and refractive index of the substrate, respectively. m is the number of multilayer.

Fig. 6 shows the reflectivity of SiO_2/TiO_2 multilayer. As the number of SiO_2/TiO_2 multilayer increases, the reflectivity also increases and is almost constant after 5 layers.

Light collection efficiency in different reflector types was shown in **Fig. 7**. The side reflector of Al has the best light collection efficiency. SiO_2/TiO_2 quarter-wave multilayers (M3~M6) as a top reflector have better light collection efficiency than solely used SiO_2, TiO_2, and Al.

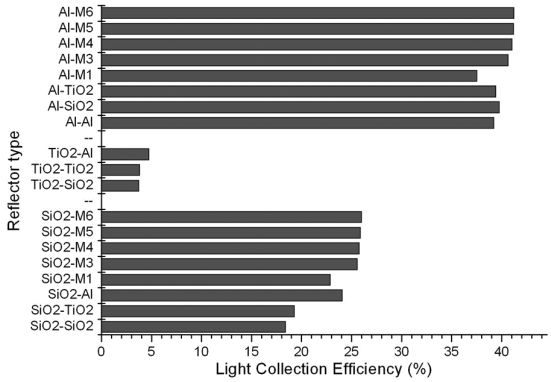

Fig. 7 Light collection Efficiency with respect to different reflectors

4. Modulation Transfer Function (MTF) Calculation

First of all, in order to decide the side reflector, MTF of side reflectors SiO_2, and TiO_2 were calculated without top reflectors. It is no doubts that aluminum is the best for the side reflector because Al reflects or absorbs visible photons and rarely transmits photons which mean minimum cross-talk. But there's no thin film fabrication processes having good step coverage characteristics to fill Al between CsI:Tl pixels, so Al was excepted as a side reflector.

5˚ tilted tungsten was used for MTF measurements to obtain pre-sampled Edge Spread Function (ESF). **Fig. 8** is an obtained 25 x 25 image and shows how to calculate MTF. 11 lines (≈1/tanθ) of 5˚ tilted tungsten images were sampled and differentiated to obtain pre-sampled Line Spread Function (LSF) which will be Fourier-transformed for MTF calculation.

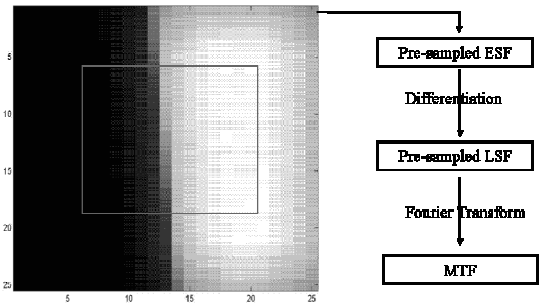

Fig. 8 Obtained 25 x 25 images and the method to calculate MTF

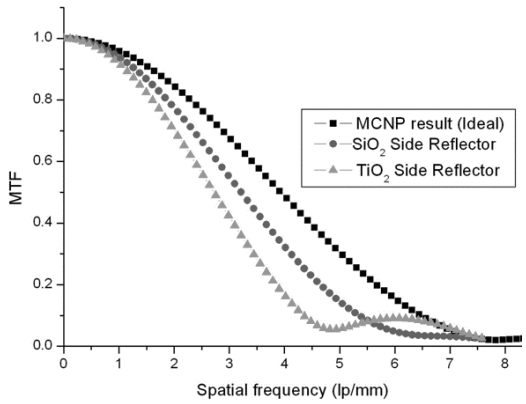

Fig. 9 MTF with SiO2 and TiO2 side reflectors

As shown in **Fig. 9**, MTF of SiO_2 is higher than TiO_2 in overall spatial frequency. It means that SiO_2 is a better side reflector than TiO_2.

After deciding SiO_2 as a side reflector, MTF was calculated with different top reflectors such as Al, and SiO_2/TiO_2 quarter-wave multilayer (M1~M6). The result was shown in **Fig. 10**. MTFs were not much different between the types of top reflectors. Top reflectors did not affect spatial resolution of the detector.

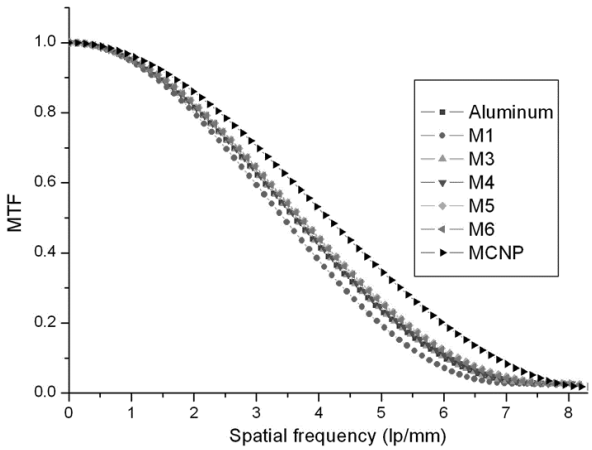

Fig. 10 MTF in different top reflectors in SiO2 side reflector

IV. Conclusions

In this study, Pixilated CsI:Tl scintillator with reflectors for mammographic application was modeled with Monte Carlo method and its characteristics were analyzed with MTF calculation. Al is a good reflector solely, however there's no Al filling method having good step coverage characteristics in thin film fabrication process. Pixelatd CsI:Tl with the side reflector of SiO_2 has the better MTF than TiO_2.

Top reflectors rarely affected spatial resolution as seen by MTF, but will affect light collection efficiency which can improve Signal-to-Noise Ratio (SNR). 3 to 6 stacks of SiO_2/TiO_2 multilayer reflector can be used for top reflector which can improve Detective Quantum Efficiency (DQE) of detector systems.

Acknowledgement

This work was supported by KOSEF (M20704030002-07M0403-00210).

References

1) C. Frojdh, H.E. Nilson, P. Nelvig, C.S. Petersson, 'Simulation of the X-ray response of scintillator coated silicon CCDs' IEEE Trans. Nucl. Sci. NS-45 (3), pp. 374-378, 1998.
2) P. Kleymann, et al., 'An X-ray Imaging Pixel Detector Based on A Scintillating Guides Screen,' IEEE Trans. Nucl. Sci., NS-47, pp.1483-1486, 2000.
3) J. G. Rocha, J. H. Correia, 'A high-performance scintillator-silicon-well X-ray microdetector based on DRIE techniques' sSensors and Actuators A(92), pp. 203-207, 2001.
4) M. Hjelm, et al., 'Monte Carlo simulation of the imaging properties of scintillator-coated X-ray pixel detectors,' NIM-A(509), pp. 76-85, 2003
5) Minghong Yang, et al, 'Optical thin films with high reflectance, low thickness and low stress for the spectral range from vacuum UV to near IR' J. Opt. A: Pure Appl. Opt.(8), pp.327-332, 2006.
6) J. F. Briesmeister, Ed., 'MCNP-A General Monte Carlo N-Particle Transport Code Version 4C.' LA-13709-M, Los Alamos National Laboratory, 2000.
7) G. F. Knoll, et al., 'Light collection in scintillating detector compsites for neutron detection,' IEEE Trans Nucl. Sci., NS-35, pp. 872-875, 1998.
8) K. Carney, et al., 'catalogue of Diagnostic X-ray Spectra and Other Data: Report No 78,' Institute of Physics and Engineering in Medicine, 1998.

Journal of NUCLEAR SCIENCE and TECHNOLOGY, Supplement 5, p. 489–491 (June 2008)

Development of a Radiation Detector Based on Silicon Carbide

I. ISHIKAWA[1*], W. KADA[1], F. SATO[1], Y. KATO[1], T. TANAKA[2], T. IIDA[1]

[1]*Division of Electrical, Electronic and Information Engineering, Graduate School of Engineering, Osaka University, 2-1 Yamada-oka, Suita, Osaka 565-0871, Japan*
[2]*Fusion Engineering Research Center, National Institute for Fusion Science, 322-6 Oroshi, Toki, Gifu 509-5292, Japan*

Five alpha particle detectors based on a 4H semi-insulating SiC substrate wafer were made for the fusion diagnostics of the burning plasma. About 50 nm thick aluminum films were made as the ohmic-contact type electrodes on the 380 μm thick substrate by an evaporation process. The characteristics of the detectors were examined by using a standard Am-241 alpha source. Each detector was irradiated with alpha particles and the electric charge induced in the detector was measured in the temperature range from room temperature up to 573 K. For all the detectors, the alpha particle detection signals were clearly observed with an oscilloscope at the bias-voltage higher than 500 volt. Two of the present detectors measured alpha particles with an energy resolution of about 25% at the temperature beyond 550 K and they are to be used for the measurement of escaping particles in plasma experiments.

KEYWORDS: silicon carbide, alpha particle detector, high temperature operation, plasma diagnostics

I. Introduction

The fusion energy has the potential to solve many of the world's energy problems and many researchers and engineers have made efforts to develop a fusion reactor. The self-heating by alpha particles due to the fusion reaction is the key to maintain the self-sustainable thermonuclear plasma in a fusion reactor. It is, therefore, important to measure confined/escaping alpha particles under high temperature of the burning plasma. A radiation detector made of a diamond with wide bandgap has been used for fusion diagnostics[1,2]. The diamond detector has very good features of high-temperature operation, high radiation resistance and others. However, it is not easy to have a high-purity crystal, and such a large crystal is very expensive.

The silicon carbide (SiC) has good thermal stability and is expected as one of the particle detection materials used at high temperature. The detector characteristics of ohmic contact[3], Schottky contact[4-6], p-n junction[7] and pin junction[8,9] have been examined to develop a SiC radiation detector. The purpose of this paper is to show fundamental data from some experiments at high temperature for the development of the SiC detector. At first, this paper describes the way of making an ohmic-contact type SiC detector and then shows results on the response of the detector to alpha particles at high temperature.

II. Experimental

The 4H semi-insulating SiC wafer (Cree Inc.) of 380 μm in thickness was cut into plates of 10×10 mm^2. About 50 nm thick aluminum films were made as the ohmic-contact type electrode on the SiC plate by an evaporation process. The aluminum was deposited on both sides of the SiC plate and the area of each aluminum-deposited circular electrode was 6mm in the diameter.

A schematic illustration of the SiC radiation detector is shown in **Fig. 1**. The SiC substrate was placed on a ceramic plate (MACOR, Corning Inc.) with a built-in heater. The aluminum films of 300 nm in thickness were made as the ground electrode on the ceramic plate by an evaporation process. A silver paste was used for the electric contact. To monitor the temperature of the detector, the thermocouple was attached on the ceramic plate. The SiC radiation detector with the ceramic heater was set in the vacuum chamber for the examination of its response to alpha particles.

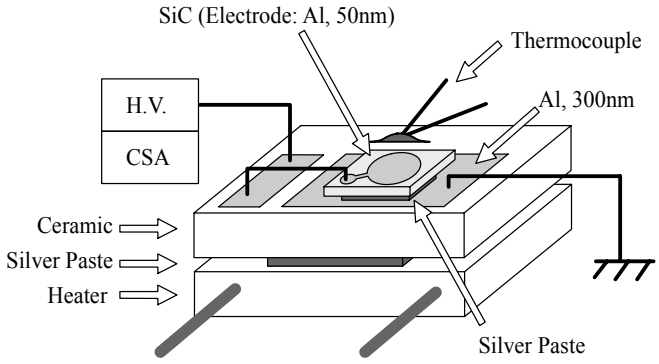

Fig.1 Schematic illustration of SiC radiation detector

Fig. 2 shows a schematic drawing of the experimental setup for the measurement of the response of the SiC detector to alpha particles. The measurement system is composed of a high voltage power supply (HV), a charge-sensitive preamplifier (CSA), a linear amplifier (LA), a multi-channel pulse height analyzer (PHA) with a personal computer (PC) and a digital oscilloscope (DO) to observe waveforms of output signals from the CSA. The vacuum chamber was evacuated with a rotary pump and it was

*Corresponding Author, Tel No: +81-6-6879-7909, Fax No: +81-6-6879-7363, E-mail: ishikawa@nf.eie.eng.osaka-u.ac.jp

stopped during the measurement. The ceramic heater was driven by a DC power supply and the temperature of the SiC detector was monitored with a thermocouple followed by a thermometer.

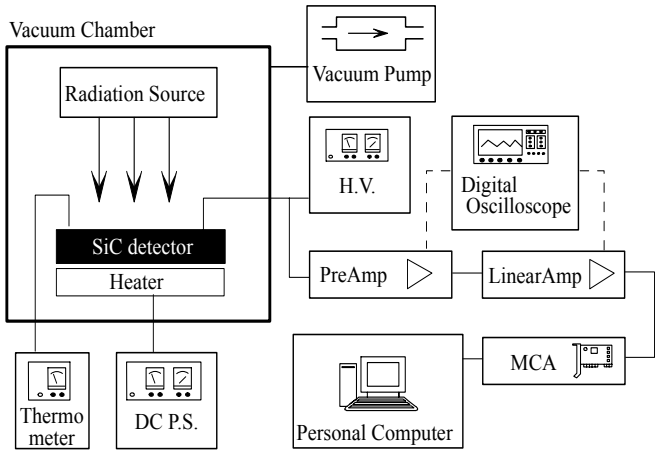

Fig. 2 Schematic drawing of experimental setup for measurement of response of SiC detector to alpha particles

The relation between the bias voltage and leakage current was measured for the examination of the ohmic characteristics of the SiC detectors. All the SiC detectors showed almost linear I-V characteristics in the voltage region from -500 V to 500 V and were ascertained to have good ohmic-contact. The resistance of the SiC detectors ranged from 1 to 3 $\times 10^{12}$ Ω at room temperature.

The standard Am-214 alpha source was set in the vacuum chamber and the pulse height distributions of the SiC detectors for alpha particles were measured with the system shown in **Fig.2**. The bias voltage was changed from –500 V to 1000 V.

III. Results and Discussions

For all the detectors, the alpha particle detection signals were clearly observed with the digital oscilloscope at the bias-voltage higher than 500 V. Larger pulse signals were obseved for the positive bias voltage.

Fig. 3 shows the relation between the bias voltage and the charge collection efficiency (CCE). The CCE was relatively calculated from the peak position of alpha particles in the pulse height distributions. The CCE increased with the bias voltage and became saturated in the high voltage region. It is clear from the figure that the loss of charge carrier is sufficiently reduced in the voltage region over 700 V. Large noises due to the local breakdown were occasionally observed for the three SiC detectors in the voltage region over 700 V. The other two SiC detectors worked well at the bias voltage of 1000 V. Thus, the bias voltage was kept at 700 V in the experiments on the temperature effect.

In order to examine the effect of the temperature, the two SiC detectors were heated from 300 to 573 K in the vacuum chamber at a pressure of 1×10^{-3} Torr.

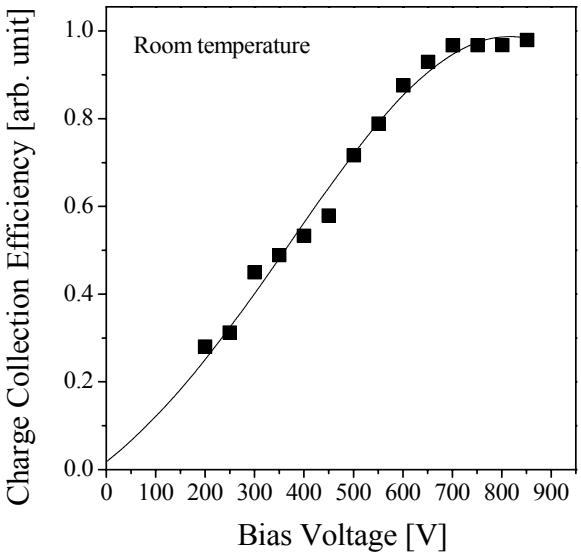

Fig. 3 Relation between bias voltage and charge collection efficiency

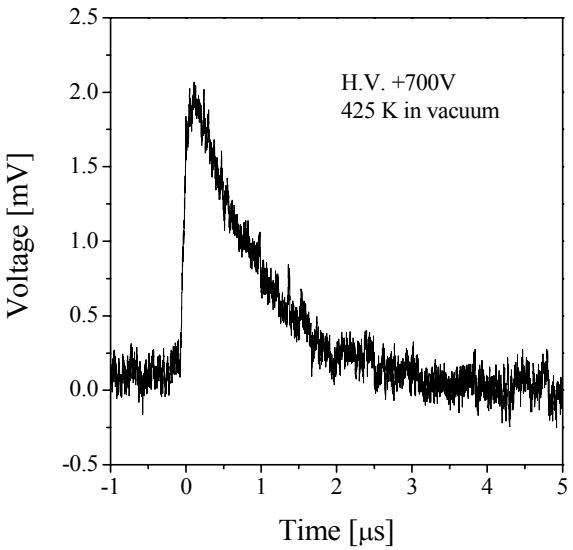

Fig. 4 Example of observed output pulse shape from CSA for alpha particle detection with SiC detector at 425 K

Fig. 4 shows an example of observed output waveforms from the fast charge-sensitive amplifier for alpha particle detections with the SiC detector at 425 K. The signal of alpha particles from the standard Am-241 source was clearly observed at 425 K.

Fig. 5 shows the pulse height distributions of the SiC detector for ^{241}Am alpha particles at high temperatures. The energy resolution hardly changed even when the temperature increased from 350 K to 425 K, though the background noise level increased at 425 K. The energy resolution was assumed to be about 25 %. Moreover, the detection signals of alpha particles were well observed even when the temperature of the SiC detector became 550 K, although the energy resolution became poor. The leakage current began to increase rapidly at 573 K.

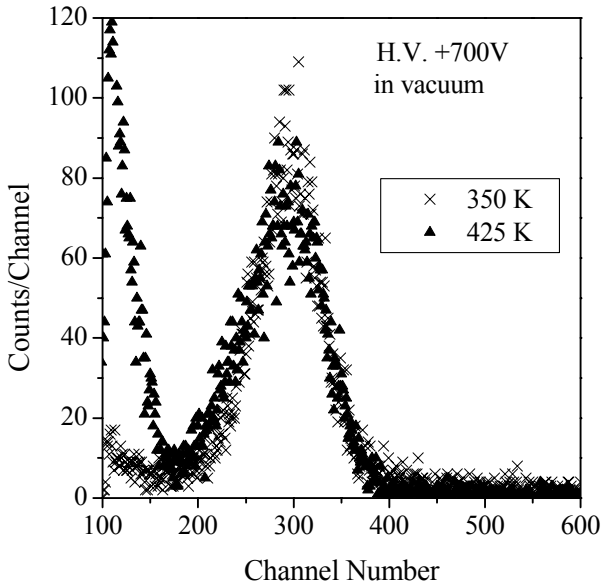

Fig. 5 Pulse height distributions of SiC detector for ^{241}Am alpha particles at high temperatures

The present SiC detectors were fairly inferior in the energy resolution to a commercially available Si surface barrier detector. However, the above results show that the SiC detector works better than the Si surface barrier detector at high temperature and is useful for the alpha diagnosis of a fusion reactor.

We have also developed the p-n junction type SiC detector. To realize higher energy resolution, the p-n junction is to be made by using our ion irradiation system with a 200 kV ion implanter[10] and simultaneous laser irradiation system[11] for the annealing.

IV. Conclusions

The ohmic-contact type alpha particle detectors based on the 4H semi-insulating SiC substrate were made for the fusion diagnostics of the burning plasma. The characteristics of the detectors were examined by using the standard alpha source. The detectors were irradiated with alpha particles and the induced charge was measured in the temperature range up to 573 K. The detection signals of alpha particles were clearly observed at the bias voltage higher than 500 V. The two SiC detectors made in this work detected Am-241 alpha particles with an energy resolution of about 25 % at the temperature beyond 550 K and they are to be used for the measurement of escaping particles in plasma experiments.

Acknowledgements

This work was supported in part by Grant-in-Aid for Scientific Research on Priority Areas (Advanced Diagnostics for Burning Plasmas: project code 442) from the Ministry of Education, Culture, Sports, Science and Technology of Japan.

References

1) J. Kaneko, Y. Ikeda, T. Nishitani,M. Katagiri, “Response function measurement of a synthetic diamond radiation detectorfor 14 MeV neutrons,” Rev. Sci. Instrum., Vol. 70, No. 1, 1100-1103, January (1999).
2) A. V. Krasilnikov, V. N. Amosova, P. van Belle et al. “Study of d–t neutron energy spectra at JET using natural diamond detectors, ” Nucl. Instr. and Meth. A 476, 500–505 (2002)
3) M. Rogalla, K. Runge, A. Söldner-Rembold, “Particle detectors based on semi-insulating Silicon Carbide,” Nuclear Physics B (Proc. Suppl.) vol.78, 516-520, (1999).
4) F. H. Ruddy, A. R. Dulloo, J. G. Seidel, S. Seshadri, and L. B. Rowland, “Development of a silicon carbide radiation detector, IEEE Trans. Nucl. Sci, vol.45, no.3, 536-541, June (1998).
5) W. Cunninghama, J. Melone, M. Horn et al., “Performance of irradiated bulk SiC detectors,” Nuclear Instruments and Methods in Physics Research A 509, 127–131 (2003).
6) F. Nava, P. Vanni, M. Bruzzi, S. Lagomarsino et al., “Minimum Ionizing and Alpha Particles Detectors Based on Epitaxial Semiconductor Silicon Carbide,” IEEE Trans. Nucl. Sci, vol.51, no.1, 238-244, February (2004).
7) F. H. Ruddy, A. R. Dulloo, B. Petrović, and J. G. Seidel, “Fast neutron spectrometry using silicon carbide detectors”, in Reactor Dosimetry in the 21st Century, J. Wagemans, H. A. Abderrahim, P. D’hondt, and C. De Raedt (Eds.), World Scientific, London, 347-355 (2003).
8) A.Kinoshita, M.Iwami, K.Kobayashi et al., “Radiation effect on pn-SiC diode as a detector,” Nucl. Instr. and Meth. A 541, 213–220 (2005).
9) Bernard F. Phlips, Karl D. Hobart, Francis J. Kub et al., “Silicon Carbide PiN Diodes as Radiation Detectors,” IEEE Nuclear Science Symposium Conference Record, 1236-1239 (2005).
10) I.Ishikawa, W.Kada, F.Sato et al.: “Development of a compact and user-friendly ion irradiation system controlled remotely through the Internet”, J. Nucl. Sci. Technol., Vol.44, No.8, 1039-1044 (2007).
11) F.Sato, T.Tanaka, T.Kagawa, T.Iida, “Simultaneous irradiation of laser and ion beams on optical materials,” Nucl. Instr. and Meth. B 210, 281–284 (2003).

Journal of NUCLEAR SCIENCE and TECHNOLOGY, Supplement 5, p. 492–495 (June 2008)

Study on a Re-verification Detection System for IAEA Safeguard to a Consolidated Spent Fuel Storage System

Jeong Hyoun YOON[1], Gyuseong CHO[1], and Chang Lak KIM[2]

Department of Nuclear and Quantum Engineering,
[1]Korea Advanced Institute of Science and Technology, Daejeon, Korea
[2]Korea Hydro&Nuclear Power Co. Nuclear Energy Technology Institute, Daejeon, Korea

A modular type storage system that has an enhanced storage density has been developed. It has storage density more than twice larger than silo type which stands alone. The storage module can accommodates 40 cylinders in 4 rows of 10, with 24 located close to periphery of the module and 16 located internally at some distance from the peripheral walls. As for IAEA Safeguards, the module is equipped with a comprehensive set of receptacles into which the IAEA can install seals and verification equipment. The Safeguards equipment, coupled with related measures for physical protection, will facilitate the timely detection of any diversion of significant quantities of nuclear material from the spent fuels stored in the modules. Nevertheless, due to its generic design feature it makes very difficult to provide re-verification of the loaded or under loaded cylinders inside module. along with an unattended monitoring system re-verification is an IAEA safeguard requirement to measure the gamma dose rate and spectrum of each irradiated fuel basket once the storage cylinders are loaded with spent fuel. The gamma profile is read by lowering a detector inside the tube so that it can be registered at the level of each basket. For the 24 peripheral storage cylinders this method of measurement is retained on the side wall of the module. However, an alternate method is required for the 16 internal dry fuel storage cylinders since they are located some distance from the module walls and thus surrounded by storage cylinders.

I. Introduction

A new module contains 40 dry fuel storage cylinders, each of which houses 10 CANDU spent fuel baskets. The storage cylinders are arranged in 4 rows of 10, with 24 located close to periphery of the module and 16 located internally at some distance from the peripheral walls. Re-verification is an IAEA safeguard requirement to measure the gamma dose rate and spectrum of each irradiated fuel basket once the storage cylinders are loaded with spent fuel. This is required to monitor the presence of spent fuel in the storage cylinders(see **Fig. 1** and **Fig. 2**). To achieve this, re-verification tube, running inside the module walls, is provided for each storage cylinder. The gamma profile is read by lowering a detector inside the tube so that it can be registered at the level of each basket. For the 24 peripheral storage cylinders this method of measurement is retained on the module. However, an alternate method is required for the 16 internal dry fuel storage cylinders since they are located some distance from the module walls and thus surrounded by storage cylinders. This paper describes the re-verification method proposed for the internal cylinders and reviews changes recommended for the peripheral re-verification tubes along with arrangement of collimation to reduce signal to noise ratio.

II. Re-verification Structure to the New Module

1 IAEA Requirements for the Re-verification System

In order for IAEA safeguards to obtain data to properly check the existence of spent fuel in module, IAEA is suggesting requirements[1)] as follows;

- Detector location relative to the basket must be reproducible, for instance by use of a tube guiding motion of the probe.
- Radiation recorded must originate from the basket and the background radiation from surrounding baskets must be negligible or corrected.

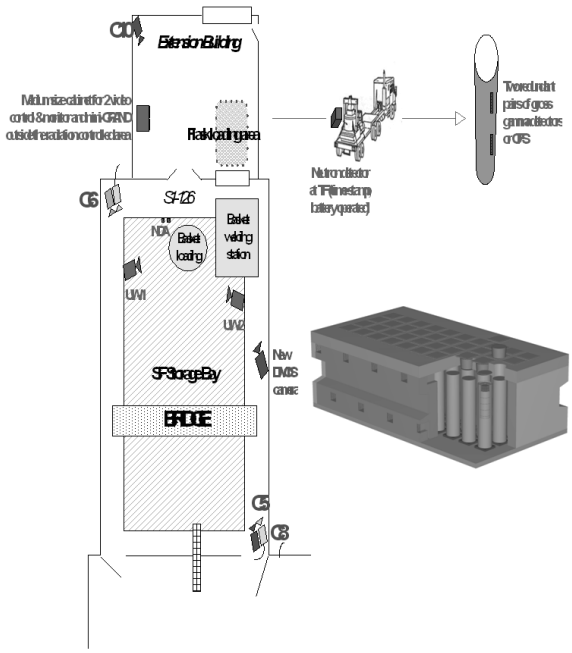

Fig. 1 Process of Spent Fuel Storage from S/F Bay to Storage Module

*Corresponding Author, Tel No: +82-42-861-5687, E-mail: yoonjh156@hanmail.net

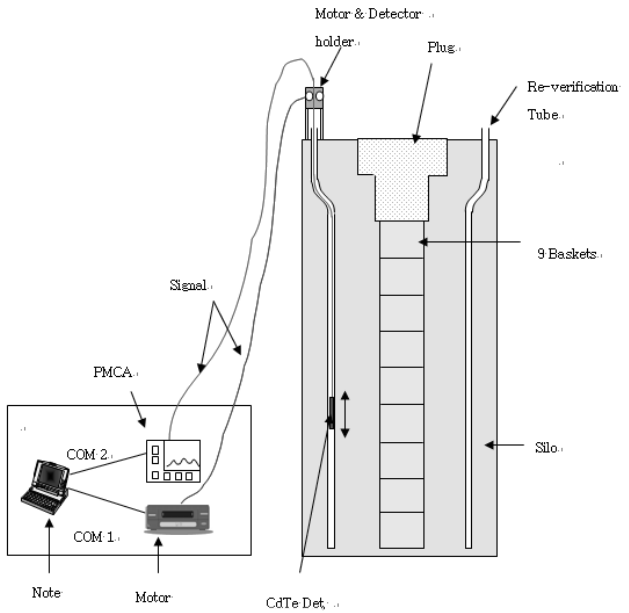

Fig. 2 Schematic Drawing of Re-verification System for S/F Storage

- Pattern indicating presence of all loaded baskets in the storage tube must be visible.
- Radiation signature should change when significant change occurs in storage tube loading (i.e. retrieval of spent fuel from a basket must result in a decrease in the recorded signal.
- Easy Motion without risk of blockage for a 25 cm long, 3 cm diameter object which is a size of typical detector IAEA inspectors carry.
- Motion of probe from bottom to top at a constant distance from the cylinder.
- Protection of interior corrosion which can block the movement of detector inside the tube. It contains water drainage system.

2 Description of the Re-verification System

There are 40 dry fuel storage cylinders with 24 located close to the walls of the module and 16 located internally. The re-verification method used for peripheral storage cylinders is a conventionally proven design and, therefore, has been retained on the new module. The central re-verification concept, as illustrated in **Fig. 3** employs 4 freestanding square columns to measure the dose rate of fuel baskets in the surrounding 16 storage cylinders. The shielding portion of each column consists of a central hollow steel column surrounded by a square concrete column(see **Fig. 4**). The re-verification tube is positioned in the concrete column at the centre of a quarto set of cylinders. In order to maximize the signal from a specific fuel basket, the columns are provided with viewing tubes, called collimators, which are used to increase the signal from the basket being measured. The collimators are fixed in a spiral manner from the bottom of the concrete column, each one aimed at the position of a designated fuel basket. The collimators provide a direct path from the designated fuel basket to a moving detector in the re-verification tube. The gamma profile is read by lowering a detector inside the re-verification tube so that it can be registered at the level of each basket. The arrangement of background shielding and direct reading via the collimators helps to maximize the radiation signal from each viewed basket while minimizing background radiation originating from the surrounding fuel baskets. The central metal shielding is necessary to reduce the overall cross section of the column so that it can fit into the available space between the storage cylinders. Various collimator configurations have been analyzed in the radiation shielding analysis report and the resulting recommendations form the basis of the present concept.

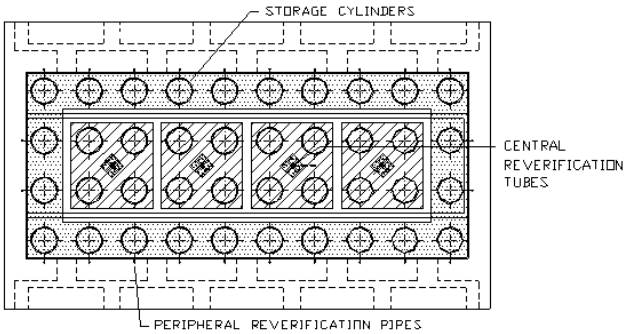

Fig. 3 Position of Re-verification Tube inside the Module

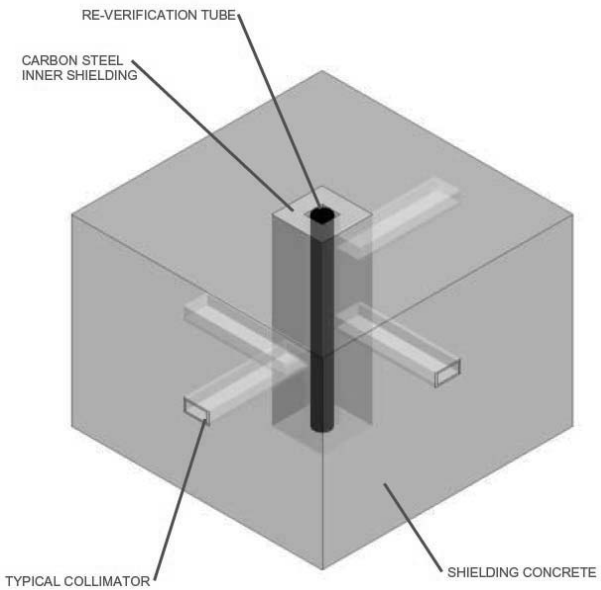

Fig. 4 Structure holding Re-verification Tube inside Concrete Column

Forty collimators, installed over the height of the concrete column, are positioned such that each one is aimed uniquely at a targeted irradiated fuel basket in the storage cylinder. The dimensions of each collimator are 7.5 x 3.8 centimetres and are made from 1.6mm thick stainless steel. The collimators pass through the concrete column and the inner steel shielding to the central re-verification tube. Except for the very thin external caps, this provides an unshielded path from the targeted fuel basket up to the detector in the re-verification tube. The gamma dose rate is read by

lowering a detector inside the central re-verification tube so that a measurement can be registered at the level of each irradiated fuel basket. The detector is lowered into the module via a 5cm schedule 40s stainless steel re-verification tube, which is embedded in the top slab and passes through the ceiling thermal insulation panel. The re-verification tube in the top slab penetrates through the ceiling thermal insulation panel (TIP) and aligns with the column re-verification tube, thus facilitating insertion and removal of the detector into and from the body of the re-verification column. The re-verification tubes protrude approximately 25cm above the top of the module to allow insertion of detector when a thick ice cover is present and are capped when not in use to prevent ingress of water.

As for peripheral re-verification, one re-verification tube, which runs inside the wall module, is provided per storage cylinder and the gamma profile is read at the level of each of the 10 baskets by lowering a detector inside the tube. However, since the peripheral wall cylinders now number 24 instead of 20 an additional 4 re-verification tubes are required in the end walls of the module. The re-verification tubes protrude approximately 25 cm above the top of the module to allow insertion of detector when a thick ice cover is present and are capped when not in use to prevent ingress of water. Moreover, all peripheral re-verification tubes are made of stainless steel.

The remaining 16 dry fuel storage cylinders, containing 160 fuel baskets, cannot be measured by this method since they are located internally, some distance from the peripheral walls.

3 Shielding Assessment For the Collimators

The signal (dose rate) at the detector when it is in front a collimator should be higher than the radiation dose rate passing through the bulk shielding of the re-verification column (noise), so that a reasonable signal-to-noise ratio can be achieved to distinguish each basket with some margin. **Fig. 5** shows a desirable fingerprint from a Re-verification of spent fuel baskets. It can be obtained after appropriate noise discrimination. In order to fulfill the requirements of IAEA inspection, the signal-to-noise ratio is needed to be increased, and a larger collimator was needed and the stray radiation coming through the bulk shielding of the re-verification column needed to be reduced by adding steel shielding and increasing the collimator size. **Table 1** shows the difference in signal-to-noise ratio between with and without heavy shielding metal shielding around the detector housing.

Estimated gamma field from basket being examined is around 19 R/hr while 1 cm thick shielding block around the detector reduces the estimated gamma field from basket to 5 R/hr. That makes it possible to achieve S/N upto 4 to 5 which is enough to determine the existence of spent fuel inside. Consequently it can be concluded that shielding above and below the detector provided by its housing will significantly reduce scatter radiation in the verification tube.

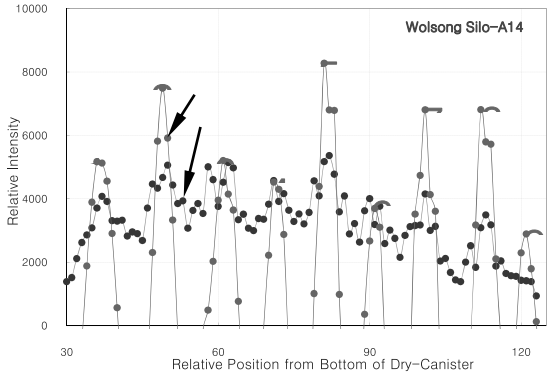

Fig. 5 Pattern of Typical Fingerprint from Re-verification of Spent Fuel Baskets

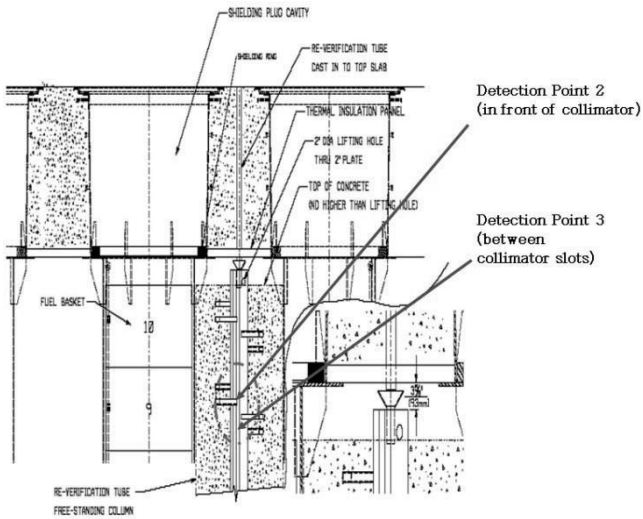

Fig. 6 Positions inside Re-verification Column To Compare S/N with and without Shielding

Table 1 Comparison Estimated Dose Rates between With and Without Shielding

	Estimated Dose Rates (rad/h) - Without Scattering		
	All Sources	Target Basket	S/N Ratio
Without Shielding	24	19	4
With Shielding	6	5	5

III. Conclusions

The proposed safeguards design can be considered to be able to meet re-verification requirements in IAEA safeguards provisions providing;

Sufficient strength of pulse with satisfactory S/N upto 5 facilitating to obtain discrimination between a designated fuel loaded basket and background radiations in the newly designed module. Confirmation of loading of a loaded basket during loading campaign in case of unattended safeguards approach by IAEA. It can also provide confirmation of presence of the original amount of fuels in case of a breach

of safeguards seal. However, there are 40 collimators in a column, discrimination of signal from noise is needed to obtain cleaner Re-verification results

References

1) D. Hanks, C. Liguori, A. Tolba, C.Olivier, and M. Aparo "Implementation of An Attended Safeguards Approach To the Transfer of the Spent Fuel into Interim Dry Storage, IAEA Vienna, Austria
2) W.M.Smith, "Analysis Report, Radiation Analysis in Support of: Re-verification Tube Design, Storage Cylinder Closure Design, & Thermal Insulation Panel Material Qualification," AECL Document, 2005

Journal of NUCLEAR SCIENCE and TECHNOLOGY, Supplement 5, p. 496–499 (June 2008)

Simulation Analysis of Ion Chambers for Area Radiation Monitoring System

Tae-Yung SONG[1*], Han Soo KIM[1], Se-Hwan PARK[1], Jang Ho HA[1], and Yong-Kyun KIM[2]

[1] *Korea Atomic Energy Research Institute, 1045 Daedeokdaero, Yuseong, Daejeon, Korea*
[2] *Hanyang University, Haengdang-dong, Seongdong-gu, Seoul, Korea*

KAERI (Korea Atomic Energy Research Institute) has been developing ion chambers which are used for an area radiation monitoring system. Those ion chambers will be placed in the area where it is necessary to monitor radiation dose all the time. The areas are nuclear plant site, research reactor site, radiation waste disposal site etc.. KAERI is developing a few different types of ion chambers for the above-mentioned purposes. One is an ion chamber having cylindrical shape with the active volume of ~1 *l*. Another one is also a cylindrical type ion chamber with the active volume of ~10 *l*. The smaller ion chamber of those 2 detectors will be installed in the place where a compact detector is required. Those ion chambers can be filled with gases such as air or Ar or Xe. The characteristics of those two ion chambers can be analyzed by simulation study. The simplified design of air-filled detectors (1.2 *l* and 13.7 *l*) was made and simulation study was performed by using the code EGSnrc. The energy of parallel radiation beam was varied from 50 keV to 1.5 MeV to analyze the expected ionization currents and dose as function of beam energy. The 100 keV and 1 MeV point source beams were adopted to investigate the angular dependence of radiation dose absorbed in the detector. We also investigated the change of characteristics of the 1.2 *l* ion chamber when the type of filled gas is changed from air. The radiation dose was obtained for the cases of Ar and Xe. The same study was also performed when the pressurized air (2 bar) was filled in the detector.

KEYWORDS: area radiation monitoring, Monte Carlo simulation, EGSnrc, ion chamber, gas radiation detector

I. Introduction

Radiation detectors can be used widely in many areas such as medical diagnosis and therapy, components analysis, gauge industry, image sensing, explosive detection and nuclear industry. Some different types of detectors are adopted according to the application area. For example, scintillation detectors and semiconductor detectors are used for the fine components analysis and spectroscopy.

Although there are some different types of detectors for the different application areas, the gas ion chamber is still popular in the field of area radiation monitoring. Since the ion chamber can be fabricated and used conveniently with stability, it is installed and operated in the nuclear power plant site or other places where the area radiation monitoring is needed for a long time.

KAERI (Korea Atomic Energy Research Institute) has been developing gas ion chambers which are used for the area radiation monitoring system[1)]. The gas ion chambers have the cylindrical shape in general. The size of active gas volume of the detector is decided based on the noise level and sensitivity. KAERI considered an air-filled gas ion chamber with the active gas volume of ~1 *l*. If the radiation monitoring area requires a higher sensitivity, a larger active volume detector can be considered. Therefore, KAERI also considered an air-filled ion chamber with the active volume of ~10 *l*. If a higher sensitivity is required for the smaller gas active volume, the pressure of the filled gas should be increased or the gas type be changed to Ar or Xe.

When gas ion chambers are developed, a simulation study is necessary to estimate the sensitivity of the detectors. We can investigate not only the sensitivity but also other detector characteristics such as dependence on the radiation beam energy and radiation source angle. The design of a detector can be optimized based on the results of the simulation analysis.

EGSnrc[2)] code was used for the simulation analysis. Based on the simulation analysis, the ion chambers for the area radiation monitoring were fabricated and tested[3)].

II. Methodology

The ion chamber consists of an anode (collecting electrode), a cathode and a filled gas. There are other detailed parts related to the supporting structure. Since the purpose of this study was to investigate the general characteristics of the ion chambers, the detailed parts were omitted and the design of detector was simplified. **Fig. 1** shows the simplified design of two detectors with different gas active volumes. The cylindrical cases are made of polyethylene with the thickness of 5 mm. The inner surface of the polyethylene case is coated with carbon and plays role of a cathode.

The anode is also made of polyethylene coated with carbon. The anode of the smaller detector has a cylindrical shape. In case of the larger detector, the anode is a cylindrical shell. The length and diameter of the anodes were

*Corresponding Author, Tel No: +82-42-868-8924, Fax No: +82-42-868-2971, E-Mail: tysong@kaeri.re.kr

decided based on the electrical field applied inside the detectors. The distance between the anode and the top of the detector was set to be 45 mm for the smaller detector so that the distance between the anode and the side of cylinder is same as the distance between the anode and the top of the detector. In case of the larger detector, the distance between the anode and the top of the detector is 80 mm. Since the diameter of the anode cylinder shell is 60 mm, the distance between the anode and the side of cylinder is 75 mm.

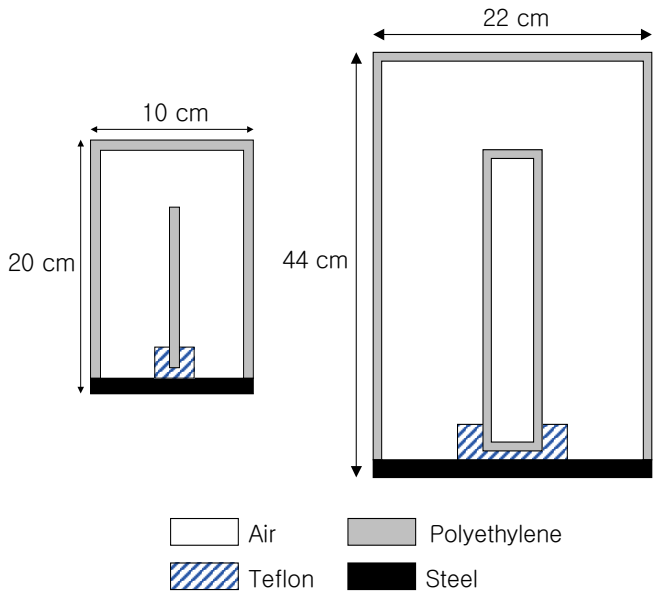

Fig. 1 The simplified design of two ion chambers for the simulation analysis

The bottom of the detector is made of stainless steel with the thickness of 10 mm. The anode is isolated from steel by introducing teflon as an insulator. The gas active volume of the detectors are 1.2 *l* and 13.7 *l* for the smaller and larger detectors respectively. Those volumes correspond to the air mass of 1.4 g and 16.5 g respectively.

A simulation code should be selected to perform a simulation analysis. We considered both EGSnrc code and MCNP[4] code. MCNP is a code developed for not only electron/photon but also neutron transport. EGSnrc is a code upgraded from EGS4 and developed for electron/photon transport. Since the analysis of ion chambers is restricted to electron/photon transport, EGSnrc was chosen for the simulation analysis. In addition, EGSnrc is well developed for the analysis of RZ geometry detectors.

The analysis was performed mainly in four aspects. Firstly, the sensitivity of the detector was investigated. The photon beam energy was set to be 50 keV, 300 keV, 750 keV and 1.5 MeV to estimate the current production in the air active volume. Secondly, an absorbed dose was calculated at different photon beam energies. The beam energy was varied from 50 keV to 1.5 MeV to estimate the relationship between the absorbed dose of the detectors and beam energy. Thirdly, the angle of the photon point source was varied from 0 degree to 90 degree to evaluate angle dependence of the absorbed dose. Finally, the gas of the 1.2 *l* detector was changed from air to Ar or Xe to estimate the effect of gas type on the absorbed dose. In addition to that, the pressure of air was changed from 1 bar to 2 bar to calculate the change of the absorbed dose.

EGSnrc was run with histories between 1,000,000 and 100,000,000 according to the simulation cases. The number of history was decided to have the statistical error less than 5%.

III. Results and Discussion

1. Sensitivity of Detectors

An ion chamber collects charges produced in the gas volume. Therefore, the signal of an ion chamber is the DC current. Since a detector has a noise, the signal should be much greater than a noise. A noise can be measured as a leakage current after a detector is fabricated. A noise level varies according to the fabrication status, but the normal noise level of the ion chamber shown in **Fig. 1** is a few tens fA[5]. The noise of the detector is assumed to be 100 fA and the radiation flux to produce the noise level current is calculated by simulation.

EGSnrc can not produce current information directly. Instead, EGSnrc produces absorbed dose information. But the absorbed dose can be converted into the current by dividing the dose by W-value which is the average energy needed to produce one electron-ion pair.

The radiation beam energy was set to be 50 keV, 300 keV, 750 keV and 1.5 MeV to estimate the current production in the air active volume. The radiation source is the parallel beam incident on the top of the detector. **Table 1** summarizes the results.

Table 1 The radiation flux needed to produce the current of the assumed noise level (100 fA)

Beam Energy (keV)	Noise Level Flux for the 1.2 *l* Detector ($cm^{-2}\cdot sec^{-1}$)	Noise Level Flux for the 13.7 *l* Detector ($cm^{-2}\cdot sec^{-1}$)
50	7.18×10^{2}	3.88×10^{1}
300	2.83×10^{2}	1.46×10^{1}
750	1.21×10^{2}	7.38×10^{0}
1500	6.54×10^{1}	4.06×10^{0}

According to the results of **Table 1**, 50 keV radiation of 7.18×10^{2} $cm^{-2}\cdot sec^{-1}$ can produce 100 fA in the 1.2 *l* detector. Since 100 fA is the assumed noise level current, the signal should be much greater than 100 fA. For example, the signal should be 10 times the noise. This means that the minimum flux to be measured by 1.2 *l* detector is 7.18×10^{3} $cm^{-2}\cdot sec^{-1}$. In case of 13.7 *l* detector, the minimum flux of 50 keV beam is 3.88×10^{2} $cm^{-2}\cdot sec^{-1}$, which is much lower than the 1.2 *l* detector case. This means that the larger detector can have a higher detector sensitivity. As the beam energy increases, the minimum flux decreases.

2. Dependence of Dose on Source Energy

A radiation beam deposits its energy in the gas active volume of the detector. The deposited energy produces electron-ion pairs to show signals as a form of current. Therefore, the deposited energy was calculated as a form of absorbed dose. The photon beam energy was varied from 50 keV to 1.5 MeV. The beam is the parallel beam coming from the top of the detector which is same as the sensitivity calculation case.

Fig. 2 shows the dose as a function of the photon beam energy. The dose was calculated as a value per unit incidence fluence, which is 1 photon per cm^2. Both 1.2 *l* and 13.7 *l* cases show the absorbed dose varies linearly as the beam energy increases. But the linearity is not shown at low beam energy region. The deposited energy can be calculated by multiplying the dose by air mass. The deposited energies are 0.22 MeV and 3.62 MeV for 1.2 *l* and 13.7 *l* detectors respectively.

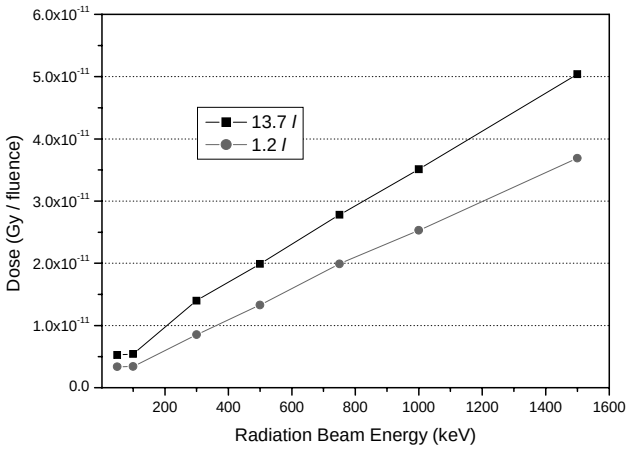

Fig. 2 The absorbed dose of 1.2 *l* and 13.7 *l* ion chambers in the active gas volume as function of photon beam energy

3. Dependence of Dose on Source Angle

The ion chamber developed by KAERI has RZ symmetry. Therefore, the signal is not changed although the radiation source is rotated around the anode axis with the fixed distance from the center of the ion chamber. But the detected signal is changed if the source is rotated in the way shown in **Fig. 3**.

To investigate the effect of source angle on the absorbed dose, we calculated the relative dose while varying source angle from 0^o to 90^o. The point radiation source is located at the same distance from the center of the ion chambers. The fixed distances were set to be 12 cm and 26 cm for 1.2 *l* and 13.7 *l* ion chambers respectively. The doses were simulated at angles of 0^o, 15^o, 30^o, 45^o, 60^o, 75^o and 90^o. The absorbed dose was calculated at two different source energies, which are 100 keV and 1 MeV.

Fig. 4 and **5** show source angle dependence of the radiation absorbed dose. The dose values are normalized to the 0^o case of each beam energy.

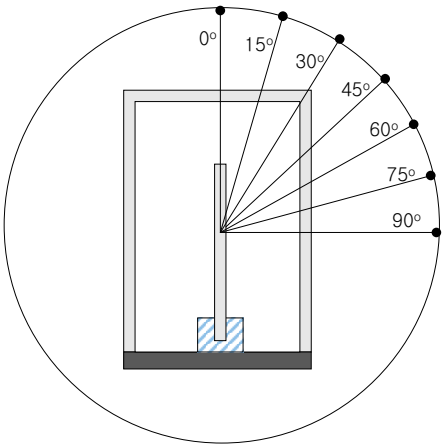

Fig. 3 Variation of point source angle from 0^o to 90^o for the simulation of dose dependence on the source angle

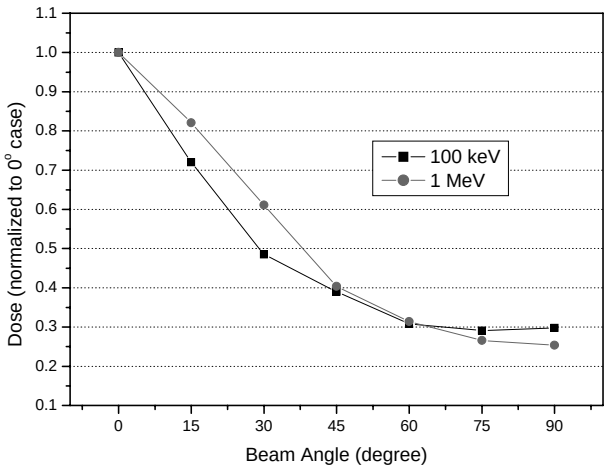

Fig. 4 Angle dependence of dose of 1.2 *l* ion chamber

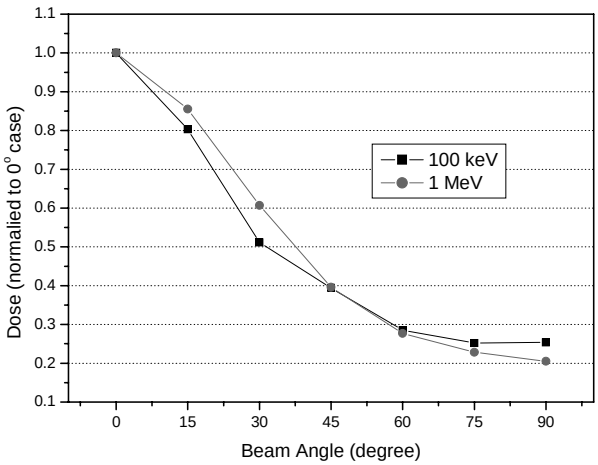

Fig. 5 Angle dependence of dose of 13.7 *l* ion chamber

In both cases, the dose decreases as the source angle increases. The decreasing rate of dose is greater for 100 keV beam than 1 MeV beam at an angle less than about 45^o. When the angle is greater than 45^o, the situation is reversed.

4. Change of Filled Gas

Table 1 shows that the sensitivity of 1.2 *l* ion chamber filled with air is much lower than 13.7 *l* ion chamber. The filled gas can be changed to improve the sensitivity of 1.2 *l* ion chamber. One method is to increase the pressure of air. The other method is to change air into denser gases like Ar or Xe.

Simulation analysis was performed to study the effect of gas change on the sensitivity of 1.2 *l* ion chamber. Three different gas types were examined, which are 2 bar air, Ar and Xe. We adopted a parallel photon beam incident on the top of the ion chamber and the beam energy was varied from 50 keV to 1.5 MeV. **Fig. 6** shows the deposited energy in the active gas volume as the function of beam energy.

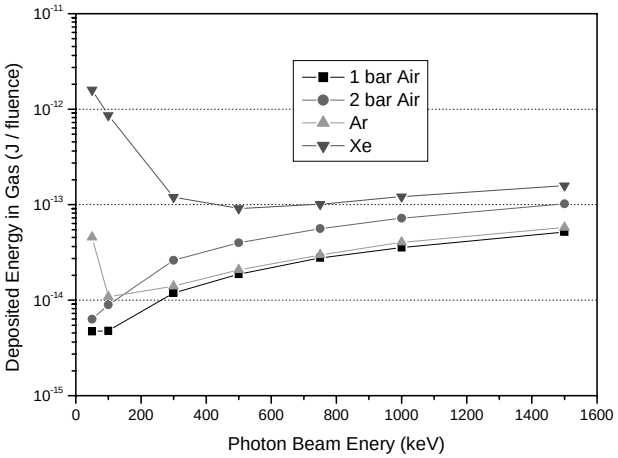

Fig. 6 Deposited energy in the active gas volume of the 1.2 *l* ion chamber according to the gas type and beam energy

The deposited energy of Ar and Xe decreases first and then increases as the beam energy increases. The same situation is expected for air, but it is not shown in **Fig. 6** since it happens at energy lower than 50 keV. According to the results, the sensitivity of Ar and Xe is especially good at the low beam energy region.

The charge production of the ion chamber can be calculated by dividing the deposited energy by W-value, which is 33.8 eV and 26.4 eV for air and Ar respectively.

IV. Conclusions

KAERI has been developing ion chambers which are used for an area radiation monitoring system. The simplified design of air-filled detectors was made and simulation study to investigate the detector characteristics was performed.

The sensitivity of the detector was investigated. It was shown that 50 keV photon of 7.18×10^{2} $cm^{-2} \cdot sec^{-1}$ could produce 100 fA in the 1.2 *l* detector. In case of 13.7 *l* detector, the needed flux to produce 100 fA was 3.88×10^{1} $cm^{-2} \cdot sec^{-1}$ for the 50 keV photon. An absorbed dose was calculated at different photon beam energies. The beam energy was varied from 50 keV to 1.5 MeV to estimate the relationship between the absorbed dose of the ion chambers and beam energy. The angle of the photon point source was varied from 0 degree to 90 degree to evaluate angle dependence of the absorbed dose. Finally, the gas of the 1.2 *l* ion chamber was changed from 1 bar air to 2 bar air or Ar/Xe to estimate the effect of gas type on the absorbed dose.

Acknowledgement

This work was performed under the long-term nuclear research and development program sponsored by Ministry of Science and Technology of Korea, and supported by the Innovative Technology Center for Radiation Safety (iTRS).

References

1) Y. K. Kim et al., 'Development of Radiation Detector Design and Fabrication Technology,' KAERI Research Report, KAERI/RR-2538/2004, 2005.
2) I. Kawrakow and D. W. O. Rogers, 'EGSnrc Code System : Monte Carlo Simulation of Electron and Photon Transport,' PIRS-701 National Research Council of Canada, 2001.
3) H. S. KIM et al., 'Characteristics of Nobel Gas-filled Ionization Chambers for a Low Dose Rate Monitoring,' Proceedings of 2007 Spring Korean Nuclear Society Meeting, 2007.
4) J. F. Briesmeister, Ed., 'MCNP-A General Monte Carlo N-Particle Transport Code Version 4C,' LA-13709-M, Los Alamos National Laboratory, 2000.
5) H. S. KIM et al., 'Characteristics of a Fabricated Ionization Chamber for Using as a Beta Gauge,' Proceedings of 2007 Spring Korean Association for Radiation Protection Meeting, 2007.

Journal of NUCLEAR SCIENCE and TECHNOLOGY, Supplement 5, p. 500–502 (June 2008)

Development of the In-situ Monitoring System for Pipe Internal Contamination Measurement in the Decommissioning Site

Bum-Kyoung SEO*, Chan-Hee PARK, Kune-Woo LEE, Dong-Gyu LEE, and Chong-Hun JUNG

Korea Atomic Energy Research Institute, Deokjin-dong 150, Yuseong-gu, Daejeon, Korea

The in-situ monitoring system of pipe internal (IMSPI) was developed for transporting a variety of survey tools into pipes. Tools available for use with the system include alpha, beta and gamma-ray detectors and video cameras. In the IMSPI, phoswich detector for simultaneous measurement of alpha- and beta-particles and CdTe detector for gamma-rays were used. The phoswich detector composed with ZnS(Ag) and plastic dual scintillator was manufactured, which could be applicable in the contamination monitoring systems. The IMSPI used a helical gear and automatic controller to transport radiation detectors and video cameras into pipes. And the membrane inserted into a pipe to transfer the characterization tools through the piping, providing a clean conduit through which the detectors and camera could travel.

KEYWORDS: pipe internal, contamination monitoring, phoswich detector, decommissioning, alpha and beta particles

I. Introduction

With respect to nuclear wastes, the amount of wastes being produced during decommissioning of nuclear facilities is much higher than the total wastes cumulated during operation. And, the process of decommissioning has a strong possibility of personal's exposure and emission to environment of the radioactive contaminants, requiring thorough monitoring and estimation of radiation and radioactivity.

Most of the wastes generated in the process of decommissioning are classified as low-level radioactive waste except those whose radionuclide contamination is confirmed. To be released from the decommissioning site, those low-level wastes must prove to be free of radionuclides. The internal surfaces of small diameter piping, however, are not accessible by conventional monitoring devices, making it hard to be monitored for contamination measurement. Therefore, this kind of particularity of piping triggered the development of new detection system that is applicable to direct measurement of radioactive contamination inside piping. So countries advanced in decommissioning technology, such as USA and Japan, has developed remote-controlled detection systems that are suitable for radioactive contamination in piping[1,2]. But there is no technology for simultaneous measurement alpha and beta particle in the pipe internal.

A detection system for monitoring the internal surface of pipe has to hold a function of detecting various radioactive contaminants including α/β particles and γ-rays as well as a function applicable to small diameter pipes, so that it is possible for the pipes to be determined whether recycled or disposed through in-situ measurement. And, as a detector unit of the system has to be movable inside pipe, the unit should not be contaminated by the contaminants or sludges inside piping during both moving and detecting processes.

In this research, a detection system that is suitable for detecting radioactive contamination inside piping is developed. The developed system is composed of both a detector unit for simultaneous detection of α/β particles and γ-rays and a transport and controlling unit for movement of the detector inside piping.

II. Methodology

The detector consists of two components, one as a phoswich detector[3] for simultaneous detection of α/β particles and the other as a CdTe detector for γ-ray detection. The phoswich detector is made of both a cylindrical type scintillation composite for alpha particles[4] and a plastic scintillator for beta particles[5]. Scintillations emitted from the two scintillators are quantified using photomultiplier tube(PMT). The signals of alpha- and beta-particles were distinguished using pulse shape discrimination(PSD) method.

The zero crossing method of PSD has widely used in the phoswich detectors. Measurement of the zero crossing time of the bipolar pulse determines the particle type. The distribution of zero crossing times can be used to determine a PSD figure of merit M.

$$M = T/(t_a + t_b) \quad (1)$$

T is the separation between the time peaks and t_a and t_b are the respective full width at half maximum (FWHM) of the zero crossing time distributions for particle a and b, respectively.

As shown in **Fig. 1**, the IMSPI consists of a inspection part to monitor inside piping, a detection part to load the detector unit, and a transportation part to move the whole system. The inspection part is composed of CCD camera for

*Corresponding Author, Tel No: +82-42-868-8210, Fax No: +82-42-868-2499, E-Mail: bumja@kaeri.re.kr

identifying contaminants such as sludge and LED for illuminating inside piping. The transporting part is manufactured to be remote controlled, using helical gear and wheels.

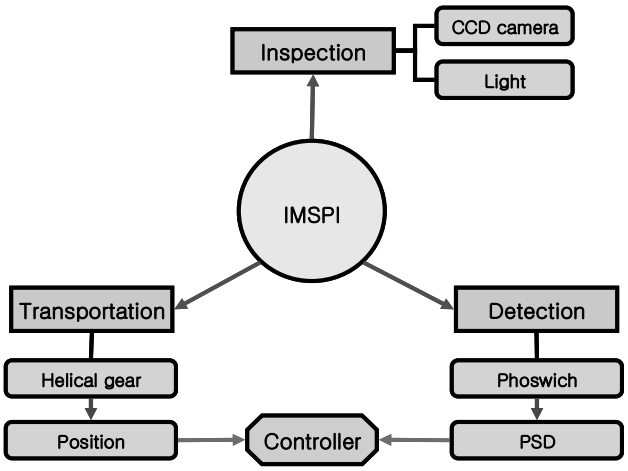

Fig. 1 Conceptual Diagram of the IMSPI

And, the gamma ray detector using CdTe semiconductor is applicable to both detection and analysis of a gamma-ray emitting nuclides. A program for automatic operation system is developed for measurement and estimation of radiological contamination, which can be controlled using a personal computer.

III. Results and Discussion

1. Phoswich Detector

Variation of detection capacity with geometric positioning of detector unit (configuration of a detector unit) is measured for designing the phoswich detector. One phoswich as shown in **Fig. 2** is formed by loading a ZnS(Ag) scintillator composite for alpha detection and a plastic scintillator for beta detection separately into a unit[3]. The other comprises a dual scintillator sheet for simultaneous detection of alpha and beta particles[6]. In the dual scintillator sheet, the thickness of the ZnS(Ag) and plastic scintillator layer was 10 mg/cm^2 and 0.25 mm, respectively.

Each radiation must be discriminated in a phoswich detector to allow simultaneous measurement of different type radiations using single-detector system. The pulse-shaped discrimination and pulse-height discrimination were generally used to discriminate each radiation. Pulse heights generated by alpha- and beta-rays were discriminated using the energy level discriminator for the pulse-height discrimination method. But, the accurate measurements can't be performed because of overlap of alpha and beta events for low level activity. Therefore, the pulse-shape discrimination method is generally used to discriminate each other. The pulse-shape discrimination is the method discriminating rise-time of scintillation formed in each scintillator. The pulse-shape distribution spectra for alpha- and beta-ray measured with the phoswich detector are shown in **Fig. 3**.

In the detection capacity for measurement of radioactive contamination, the phoswich formed by separate loading into a detector unit is superior to that prepared from one double-layer scintillator. In this case, the detection efficiencies were 1.0 and 0.5% for alpha and beta particles, respectively. And the M was 3.2.

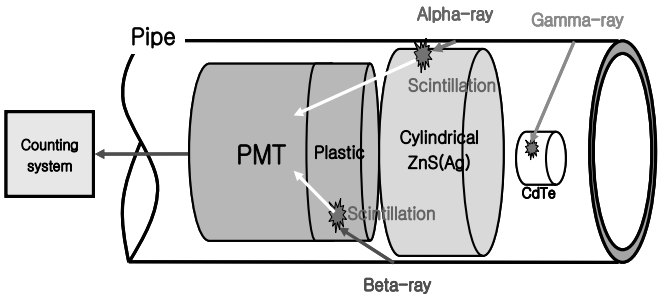

Fig. 2 Conceptual diagram of the phoswich detector for simultaneous alpha- and beta-particles counting in a pipe

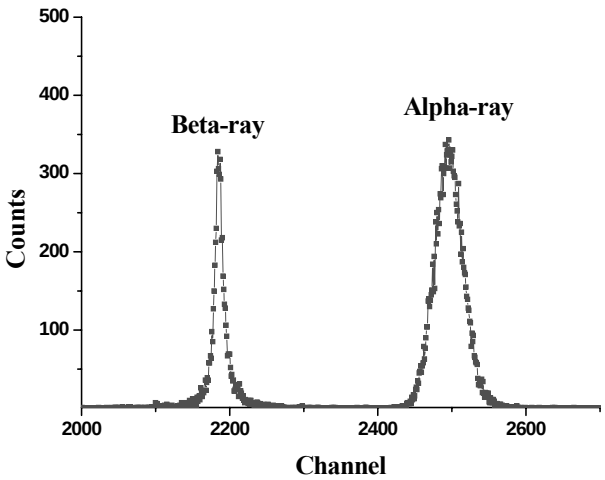

Fig. 3 Pulse-shape distribution of alpha- and beta-rays measured with phoswich detector in a pipe

2. Manufacture of the System

The transportation and detector unit is designed to be fitted into small diameter piping of 2" diameter. To reduce the size, the CdTe detector for gamma-ray detection and the monitoring part are placed side by side in the front of unit, as shown in **Fig. 4**.

- Transportation part is supported using three wheels to buttress the detector unit inside piping, and its moving is manipulated by a remote-controlled helical gear.
- Inspection part is designed for the system to be observed through a display monitor, using a CCD camera and an illuminating device, and to hold CdTe detector unit for gamma ray detection.
- Detection part is made up a detectable system that the phoswich detector is mounted on.

The transporting part measures 43 mm in diameter and 278.5 mm in length, and is composed of stainless steel and AL2024. It can also perceive and transmit video signals for monitoring inside piping. The main control unit has a built-

in digital video recorder of 20G byte, the recorder's image being transmitted to a PC.

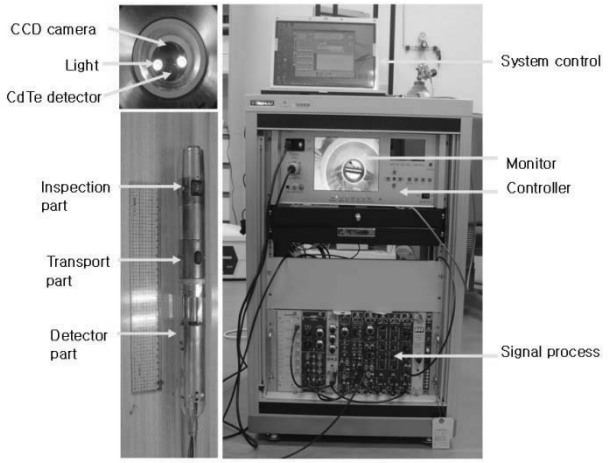

Fig. 4 Picture of the IMSPI

3. Feasibility Test in the Decommissioning Site

In a nuclear facility, piping is essential to transport of liquid substances, including wastes. Generally to evaluate the radioactive contamination, piping exposed to the outside can be cut into pieces and monitored. But, piping buried in a wall or underground has to be dug up using a core driller and monitored, which can bring out a considerable time consumption, worker's exposure to radiation, and extra cost. By using the IMSPI developed in this research, the piping buried in a wall, as constituents of the KRR 2, is characterized in terms of radioactive contamination, which is shown in **Fig. 5**.

There is possibility of the detector contamination in the pipe. So, the clean and cylindrical plastic film with thickness 4 mg/cm^2 was used for protecting the detector from the contaminants inside pipe. The detector was inserted into the cylindrical film. The decrease of the alpha efficiency was less than 20%.

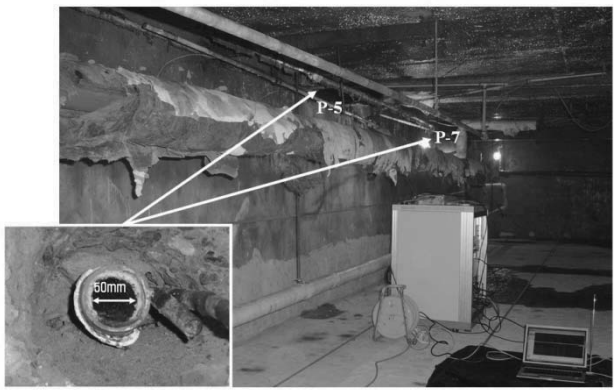

Fig. 5 The radioactive contamination measurement of the liquid waste transporting pipe in KRR-2

IV. Conclusions

A detection system that is applicable to small diameter piping is developed. The system has a cylindrical shape to be fitted into 2" piping. It consists of both a detection unit that simultaneous measurement of the alpha and beta-ray contamination as well as gamma-rays and a transporting and controlling unit for system moving.

In monitoring the contamination on the internal surfaces of small diameter pipe, the developed system is reliable, enabling both the buried and the unburied piping to be surveyed. It will be applicable to decommissioning site of the nuclear facility in the near future.

Acknowledgement

This work was performed under the long-term nuclear research and development program sponsored by Ministry of Science and Technology of Korea.

References

1) C.D. Cremer and D.T. Kendrick, "Case studies of uses of the pipe explorerTM system", International Conference on Decommissioning and Decontamination and on Nuclear and Hazardous Waste Management, Denver, CO, September 13-18 (1998).
2) R.C. Bedick, "Demonstrating and deploying private sector technologies at DOE sites – issue to be overcome", WM'02 Conference, Tucson, AZ, February 24-28 (2002).
3) Gye Hong Kim, Chan Hee Park, Chong Hun Jung, Kune Woo Lee, and Bum Kyoung Seo, "Development of the ZnS(Ag)/BC-408 phoswich detector for monitoring radioactive contamination inside pipes", J. Korea Asso. Radiat. Prot. 31 (3), pp. 1234-128 (2006).
4) Bum-Kyoung Seo, Yeon-Hee Jung, Gye-Hong Kim, Kune-Woo Lee, Chong-Hun Jung, and Myeong-Jin Han, "Study on preparation of a thin film type of ZnS(Ag) scintillator sheet for alpha-ray detection", Analytical Science & Technology 19 (5), pp. 389-393 (2006).
5) Gye-Hong Kim, Won-Jin Oh, Kune-Woo Lee and Bum-Kyoung Seo, "Fabrication and estimation of the plastic detector for measuring the contamination for beta-ray of the kind of duct waste", J. Korean Radioactive Waste Society 3(3), pp.159-165 (2005).
6) B.K. Seo, G.H. Kim, C.H. Park, Y.H. Jung, C.H. Jung, K.W. Lee, and M.J. Han, "Development of the dual scintillator sheet and phoswich detector for simultaneous alpha- and beta-rays measurement", WM'07 Conference, Tucson, AZ, February 25 – March 1 (2007).

Journal of NUCLEAR SCIENCE and TECHNOLOGY, Supplement 5, p. 503–506 (June 2008)

Fabrication and Properties Analysis of Lithium Borate Glass scintillators with Transition Metal Oxides

Jin-hyoung BAI*, Jung Ryul KIM, Jin Young CHUNG, Jung Hoon KIM, and Joo Ho WHANG

Department of Nuclear Engineering, Kyunghee University, Youngin, Kyunggi,Korea

Nonlinear optics crystals are vital fundamental materials in optoelectronic technology, and also important for other fields, such as information, energy resource, medical application, etc. Lithium borate system has attracted considerable attention because this system contains many important nonlinear optics crystals, such as $2Li_2O–3B_2O_3$, $L_2O–B_2O_3$, $Li_2O–2B_2O_3$, $Li_2O–3B_2O_3$, etc. This study fabricated a Li_2O-B_2O_3 glass scintillators with TMO (transition metal oxide) activators. The crystal structure of the fabricated Li_2O-B_2O_3 glass scintillators were confirmed, and experiments were conducted to study the absorption curve by density of the added activators, photorefractive effect, band-gap energy, emission spectrum and elemental composition. Also, the purpose of this study is to develop a glass scintillator with improved performance by improving on it through continued researches and experiments. Further researches on light efficiencies of the glass scintillator prepared in this study for neutron irradiation should be performed. In addition, by changing compositions for glass scintillator showing good performance, it will also be carried out to calculate compositional ratios for neutron glass scintillators and to prepare ones with best performance.

KEYWORDS: neutron detector, neutron glass scintillator, Lituim Borate glass

I. Introduction

Nonlinear optics crystals are vital fundamental materials in optoelectronic technology, and also important for other fields, such as information, energy resource, medical application, etc. Lithium and boron had larger neutron absorption cross-sections in the thermal neutron region. Lithium borate system has attracted considerable attention because this system contains many important nonlinear optics crystals, such as $2Li_2O–3B_2O_3$, $L_2O–B_2O_3$, $Li_2O–2B_2O_3$ (LB_2), $Li_2O–3B_2O_3$ (LB_3), etc[1-4]. In consideration of production costs and manufacturability, when the ratio between Li_2O and B_2O_3 is 8:2, it is sintered as L_20-B_2O in the phase-change curve as illustrated in Fig. 2. As shown in Table 2, it was confirmed through analysis of XPS components.

This study a Li_2O-B_2O_3 glass scintillator with TMO (transition metal oxide) added as an activator was fabricated to develop a scintillation detector for detection of neutrons. The crystal structure of the fabricated Li_2O-B_2O_3 glass scintillator was confirmed, and experiments were conducted to study the absorption curve by density of the added activators, photorefractive effect, band-gap energy, emission spectrum and elemental composition. Also, the purpose of this study is to develop a glass scintillator with improved performance by improving on it through continued researches and experiments.

II. Fabrication and Measurement of Lithium Borate Glass

In this study TMOs (Transition metal oxides), i.e. Al_2O_3, MnO_2, NiO, Fe_2O_3, TiO_2 and V_2O_5 were added as activators to the main materials, Li_2CO_3 and H_3BO_3. As for the best heating conditions, repeated experiments set the melting temperature at 950℃, and melting time at 90 minutes as shown in **Fig. 1** and similarly, the effect of heat treatments on the crystallization behavior of the glass is shown in **Fig. 2**.

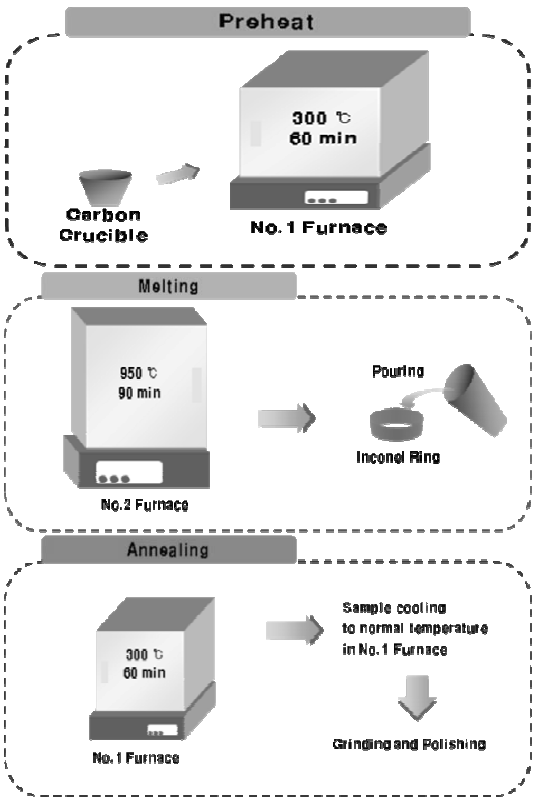

Fig. 1 Preparing procedures of glass scintillator

*Corresponding Author, Tel No +82-31-201-2913, Fax No: +82-31-202-5973, E-Mail: xray10@korea.com

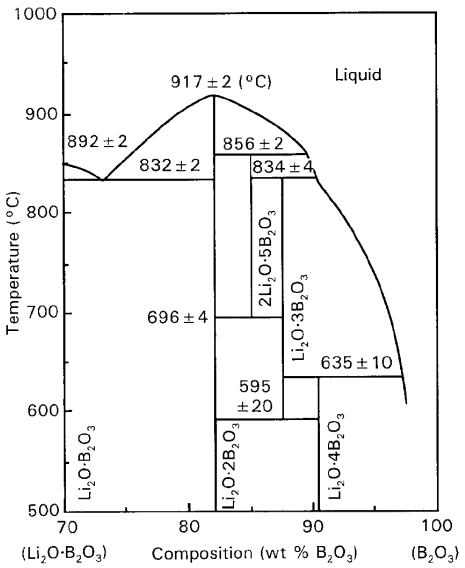

Fig. 2 The binary Li_2O-B_2O_3 phase diagram[1)]

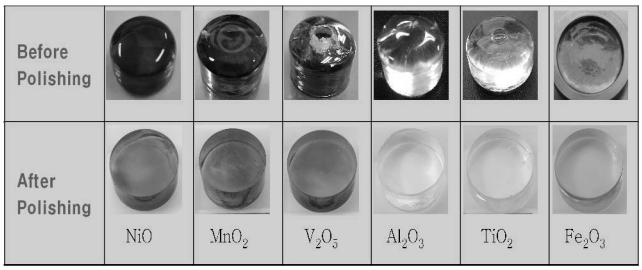

Fig. 3 Prepared glass scintillator specimen

Spectroscopic ellipsometry (V-VASE) was used to measure the transmittance and band-gap energy of the fabricated scintillator in **Fig. 3**, and a spectrophotometer (HITACH U3000) was used to measure the absorption curve. 325nm He-Cd laser light was used to measure the photoluminescence of the scintillator at normal temperature. A lens was used to concentrate the emitted light, and 1m monochromator and GaAs photomultiplier were used to analyze the spectrum. To reduce the noise of the measured signals, the standard 'Lock-in measurement method' was used, and the frequency speed of the Chopper was 300ms. The diameter of the laser beam was approximately 0.3 mm, and the intensity of light was about 20 mW.

As for the ESCA operating conditions for analysis of the element composition of the Li_2O-B_2O_3 glass scintillator, a vacuum of 5×10^{-8} torr (with x-ray on, flood gun off) was created, and corrected with the C 1s (284.5 eV) value. Monochromatic Al-*K* (15 kV, 100W, 400 micrometer) as an X-ray source was used, and the elements in the samples were simply identified with the pass energy at 50 eV, and the step size at 1.0 eV for the wide scan. To obtain detailed information about certain elements on this basis, an appropriate analysis area was selected and a narrow scan was performed. Here, for the narrow scan, the pass energy was 20 eV, and the step size was 0.1 eV. Thermo VG's analysis program called Advantage was used for analysis.

Table 1. Measured densities and Band-gap energy

No.	Scintillator	Density [g/cm^3]	Band-gap energy[eV]
1	Li_2O-B_2O_3-Al_2O_3	2.132	5.62
2	Li_2O-B_2O_3-V_2O_5	2.038	3.434
3	Li_2O-B_2O_3-TiO_2	2.153	4.93
4	Li_2O-B_2O_3-MnO_2	2.335	4.07
5	Li_2O-B_2O_3-Fe_2O_3	2.277	4.094
6	Li_2O-B_2O_3-NiO	2.070	3.37

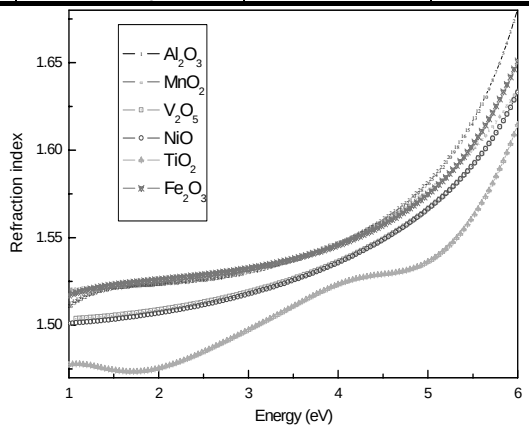

Fig. 4 Photorefractive indices

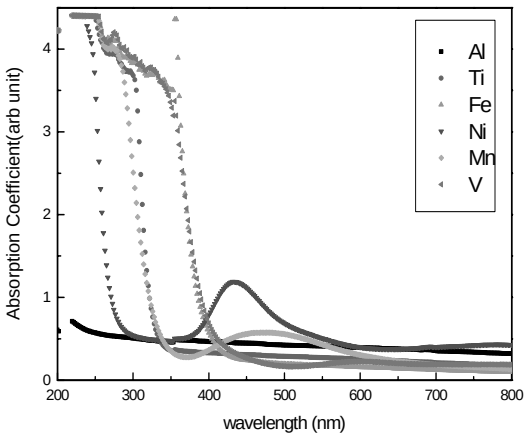

Fig. 5 Wavelength of the absorption spectrum

III. Results

The XRD analysis of the Li_2O-B_2O_3 glass scintillator fabricated in this study, and the X-ray analysis of crystallization of the samples confirmed that they were amorphous substances. The result suggests that each element is formed independently and does not have any crystal structure. The densities of Li_2O-B_2O_3 glass were systematically measured by Archimedes principle[5)]. The density was 2.0~2.3 g/cm^3 as shown in **Table 1**, and the photorefractive effect of the Li_2O-B_2O_3 glass scintillator measured by Spectroscopic ellipsometry (SE) was 1.48~1.55 as shown in **Fig. 4**. The wavelength of the absorption spectrum of the Li_2O-B_2O_3 glass scintillator measured by UV-VIS Spectrophotometry ranged between 300 and 350nm in **Fig. 5**, and the central wavelengths of the emission

spectrum pumped to the absorption edge were Al_2O_3 434nm and 592nm, MnO_2 425nm and 602nm, NiO 434nm, Fe_2O_3 434nm and 760nm, TiO_2 518nm, and V_2O_5 555nm respectively. The materials with the best emission intensity were Al_2O_3 and MnO_2, and the material with the best emission intensity near 400nm of interest to the authors was Al_2O_3, whose emission wavelength was 434nm in **Fig. 6**.

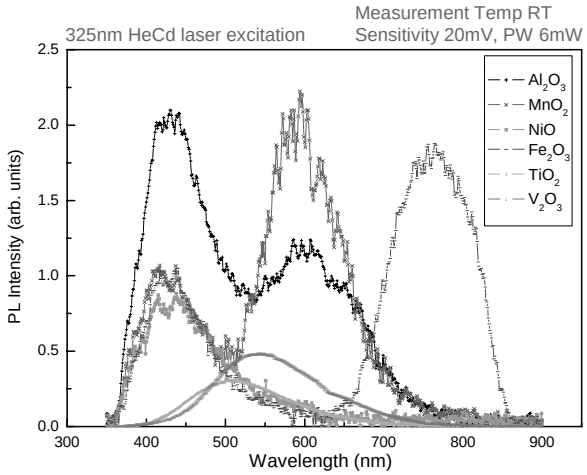

Fig. 6 Emission spectra and wavelengths

The measurements of the element composition of the Li_2O-B_2O_3 glass scintillator based on ESCA showed that Li and B, main materials, accounted for about 10% and 40% respectively, O about 50%, and the remainder was analyzed quantitatively by means of TMO as shown in **Table 2** and **Fig. 7** and **8**.

Table 2. Compositions of glass scintillator according to TMO

No.	Scintillator	Element ratio			
		O	Li	B	TMO
1	Li_2O-B_2O_3-Al_2O_3	49.79	10.98	38.8	0.44
2	Li_2O-B_2O_3-V_2O_5	51.43	12.15	36.38	0.04
3	Li_2O-B_2O_3-TiO_2	51.51	10.08	38.27	0.14
4	Li_2O-B_2O_3-MnO_2	52.12	9.92	37.85	0.12
5	Li_2O-B_2O_3-Fe_2O_3	49.16	13.17	37.67	-
6	Li_2O-B_2O_3-NiO	51.03	10.92	38.05	-

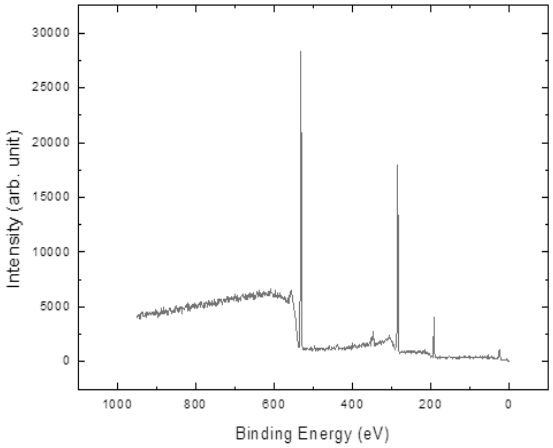

Fig. 7 Li_2O-B_2O_3-TiO_2 wide scan using ESCA

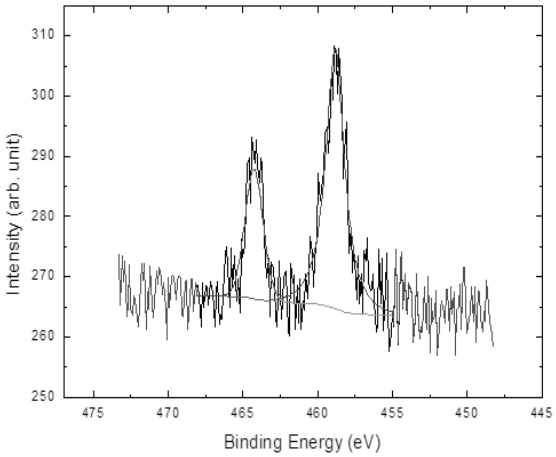

Fig. 8 Results from Ti-2p3 and Ti-2p1 narrow scan based on Li2O-B2O3-TiO2

IV. Discussions

The analysis of the characteristics of this glass scintillator and its comparison with commercial glass scintillators with lithium revealed that part of the data satisfied the requirements for a scintillator for detection of neutrons, and its performance was good enough to be used as a neutron detector. However, compared to commercial glass scintillators, its physical properties and overall performance were not sufficient. In addition, additional R&D must be dome in terms of the composition of a scintillation detector and a neutron detection system and applicability. Accordingly, if the performance of two glass scintillators were compared, and continued R&D were conducted to analyze the physical properties of Li_2O-B_2O_3 glass scintillators and improve their performance, it would be possible to develop a glass scintillator which is more economical than glass scintillators containing lithium, and performs as well. The fabrication technology and data on basic characteristics can be utilized for fabrication of several inorganic scintillators with outstanding performance. The characteristics of the Li_2O-B_2O_3 glass scintillator analyzed in this study can be used for detection of neutrons.

V. Future Works

Further researches on light efficiencies of the glass scintillator prepared in this study for neutron irradiation should be performed. In addition, by changing compositions for glass scintillator showing good performance, it will also be carried out to calculate compositional ratios for neutron glass scintillators and to prepare ones with best performance.

Acknowledgement

This work was supported by the SRC/ERC program of MOST/KOSEF, and by MOCIE through EIRC program, and supported by the Innovative Technology Center for Radiation Safety(iTRS).

References

1) I. W. DONALD, B. L. METCALFE, D. J. BRADLEY, M. J.

C.HILL, J. L. McGRATH, A. D. BYE, "The preparation and properties of some lithium borate based glasses," Journal of Materials Science 29,pp 6379-6396, 1994.
2) N. A. El-Alaily, R. M. Mohamed, "Effect of irradiation on some optical properties and density of lithium borate glass," Materials Science and Engineering B98, pp 193-203, 2003.
3) S. Y. Marzouk, N. A. Elalaily, F. M. Ezz-Eldin, W. M. Abd-Allah, "Optical absorption of gamma-irradiated lithium-borate glasses dopes with different transition metal oxides," Physica B 382, pp 340-351, 2006.
4) AST, "Lithium glass(neutron & gamma characteristics)," Applied Scintillation Technologies, Phosphor data sheet 41b, 2000.
5) X. M. Shi, Q. Wang, C. X. Li, X. J. Niu, F. P. Wang, K. Q. Lu, "Densities of Li2O–B2O3 melts," Journal of Crystal Growth 290, pp 637–641, 2006.

Journal of NUCLEAR SCIENCE and TECHNOLOGY, Supplement 5, p. 507–510 (June 2008)

Simplified Calibration Method for the Transportable Whole Body Counting System in Radiation Accidents

Wi-Ho HA*, Ji Seok KIM, Hyun Ki KIM, and Chang Woon CHOI

National Radiation Emergency Medical Center,
Korea Institute of Radiological and Medical Science, Seoul, Korea

A whole body counter is used for assessment of internal dose in the body by directly measuring the radiation emitted from the body. It is the most reliable and standard method of monitoring for internal exposure. National Radiation Emergency Medical Center in Korea Institute of Radiological and Medical Science constructed the transportable whole body counting system with chair geometry. The system uses HPGe detector as *in-vivo* monitoring device. Good energy resolution of the system was obtained with the HPGe detector. Although chair geometry used in the system has poor uniformity of the detector response, it is more suitable than other geometries as transportable system for accidental monitoring of internal contamination. In this study, relative response of the single torso detector according to position of the detector was analyzed to determine counting distance between subject and detector and to promote conventional calibration method for whole body counting system. Activities in each part of the phantom were measured to obtain detector response, and counting efficiency under various conditions was analyzed to improve performance of the *in-vivo* monitoring system. It was found that single torso detector in chair geometry is not sensitive to activity above the neck and below thighs. Therefore, transportable system can be more conveniently calibrated by using only parts of the torso and arms among whole body phantoms at the scene in the vicinity of radiation accident.

KEYWORDS: whole body counter, in-vivo monitoring, internal contamination, radiation emergency

I. Introduction

Major accidental release of radionuclides has the potential for significant radiation exposure in large populations.[1)] Rapid monitoring for internally contaminated people is required in radiation emergency. If the release contains radionuclides which emit high energy gamma ray, the most suitable mean of providing this monitoring is whole body counter (WBC).[2)] But, WBC system may be costly and time-consuming because fixed installations are usually used. These problems can be reduced appreciably by the use of mobile system.[3)]

Transportable WBC system for *in-vivo* monitoring during radiation emergency was constructed at National Radiation Emergency Medical Center in Korea Institute of Radiological and Medical Science. The system is shown in **Fig. 1**.

In this system single high purity germanium (HPGe) detector is used as torso detector. It is impossible that activity distribution in whole body is determined by only single torso detector. In order to effectively resolve this problem and optimize counting geometry in the system, an analysis of relative response of the torso detector according to position of the detector has been required. A compromise between sensitivity and uniformity of detector response is necessary in designing a WBC system.[4)] In this study, analysis on the relative response of the torso detector according to subject-detector distance was performed to determine optimal counting distance and to promote conventional calibration method for WBC system.

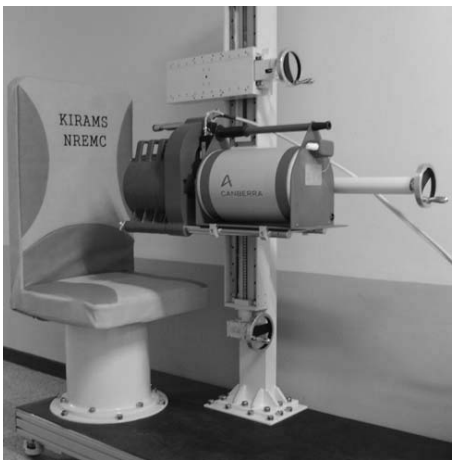

Fig. 1 Transportable WBC system.

II. Materials and Methods

1. Transportable WBC System

Bed geometry is the most widely used configuration in WBC system.[5)] In radiation accidents, the mobile system need to be relatively light and portable for access to remote regions.[4)] Chair geometry is an alternative for quick monitoring. WBC system with chair geometry has been utilized as it requires much less space than bed geometry and is easier for the subjects to access.[2)]

The single torso detector is located in position that the detector centre is 35 cm above the seat of the chair and the

*Corresponding Author, Tel No: +82-2-970-1430, Fax No: +82-2-970-2404, E-Mail: lovin@kirams.re.kr

front face is 38 cm from the backrest. This position recommended by Youngman can be used for reference adults.[2] Counting geometry of the system is shown in **Fig. 2**.

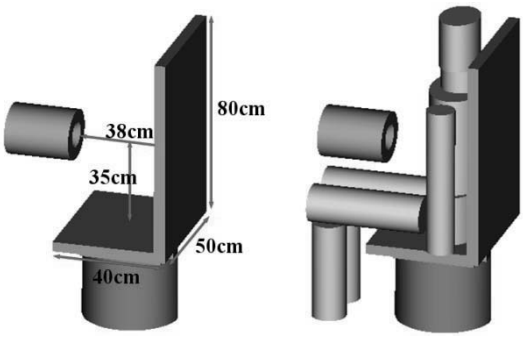

Fig. 2 Geometry of transportable WBC system.

The chair-type WBC system consists of a gamma ray spectrometer with lead shielding. The system uses p-type HPGe coaxial detector (CANBERRA Model GC9021). The use of germanium detector has improved the performance of counting system, especially the ability to distinguish among and between gamma rays that have similar energies.[6]

Relative efficiency of the HPGe detector compared with a 3×3 inch NaI(Tl) detector is 90%, and measured resolution of the detector is 2.1 keV at the 1,332 keV gamma emission. The germanium crystal is a cylinder of 80 mm in diameter and 63 mm in length.

The backrest and the seat of the chair consist of 4 cm lead in thickness. The HPGe detector is covered with the lead of 5 cm thickness. Collimator in front of the detector is also made by lead, and an opening angle of the collimator is 90°. The chair leg and frames of the system are built of steel. The total weight of the system is about 600 kg. **Table 1** shows weight of each component.

Table 1. Weight of the system components.

Component	Weight (kg)
Detector Shield	60
Chair Shield	250
Detector and Electronics	20
Body Frames	170
Bottom Frame and Wheels	100
Total	**600**

2. Background Reduction

The environmental radioactivity is the main contributor to the background of gamma spectrometry.[7] It is obvious that the evaluation of background spectrum is basically important to have an idea about minimum detectable activity (MDA) which depends on the background radiation level.[2] In order to consider the effect of background radiation as well as transportability of the system, thickness and size of the lead shield was analyzed in the previous study.[8,9] Background gamma spectra reduced by the shielding effect are shown in **Fig. 3**. Although X-ray peak of low energy was produced by lead used in the system, natural background radiation spectrum in unshielded system was considerably reduced through the lead shield of the chair and the detector.

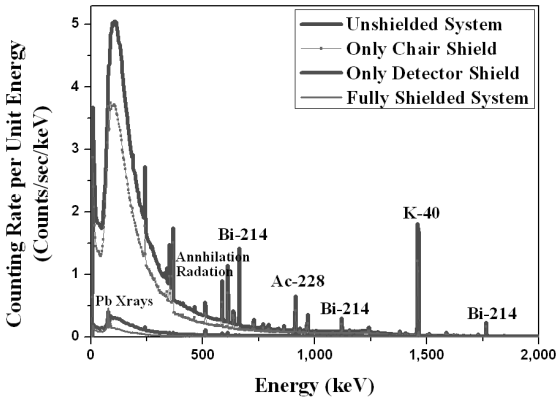

Fig. 3 Background gamma spectra under the various shielding conditions.

3. Conventional Calibration of Chair-type WBC

WBC system was calibrated using a phantom where the activity is homogenously distributed. BOMAB(Bottle Manikin Absorption) phantom have traditionally used for WBC calibration.[10] A BOMAB phantom consists of ten parts as head, neck, upper and lower torsos, 2 arms, 2 thighs and 2 shins. The walls of the BOMAB phantom are polyethylene and the interior sections are filled with a mixed radionuclide. ^{57}Co, ^{60}Co, ^{88}Y, ^{109}Cd, ^{113}Sn, ^{137}Cs, ^{139}Ce and ^{203}Hg are included in the radionuclide standard source for calibration.

The effect of moving the detector 5 cm above or below the normal position indicates that counting efficiency is not sensitive to the actual detector height in chair geometry.[2] However, the distance between subject and detector is important parameter to determine counting efficiency of the system. Therefore, counting efficiencies according to subject-detector distance were obtained through the measurements. The counting time was 86,400 seconds for calibration. The counting efficiencies for the horizontal distance of the detector are shown in **Fig. 4**.

The horizontal distance exactly represents distance between backrest of the chair and front face of the detector. It is confirmed that the counting efficiency generally decreases as the distance is increased.

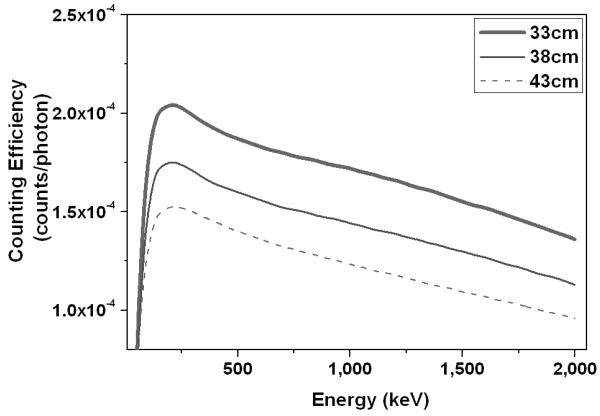

Fig. 4 Counting efficiencies for the horizontal distance of the detector.

Uniformity of the detector response is poor in chair geometry.[5] Relative response according to the horizontal distance of the detector was analyzed to evaluate detector performance at the standard position for reference adults and determine optimal position of the detector.

III. Results and Discussion

1. Detector Response

In order to evaluate contribution to counting efficiency from each part of the phantom in chair geometry, the relative response of the detector at 7 parts was considered according to position of the detector.

The relative response of the detector was analyzed by using activity in the BOMAB phantom. Activities were respectively measured at each part of the BOMAB phantom filled with standard source for calibration. Each part was replaced in every measurement. The measurements at each part were conducted for 3,600 seconds, respectively. In this result, the measurements for Cs-137 (661.7keV) were analyzed. **Table 2** shows the results of the measured activity and the detector response.

Table 2 Activity measured at the 7 parts and percentage response of the detector at the various distances.

Part of Phantom (Volume, cm^3)	Measured Activity (Bq) Uncertainty (Bq) (Percentage Response, %)		
	33 cm	38 cm	43 cm
Head (3,525)	ND*	3.84E+02 6.26E+01 (2.18)	ND
Neck (1,030)	ND	3.86E+02 6.53E+01 (2.19)	ND
Upper Torso (16,970)	1.59E+04 4.34E+02 (79.86)	1.25E+04 3.01E+02 (70.69)	1.06E+04 3.14E+02 (67.90)
Lower Torso (9,990)	1.61E+03 1.01E+02 (8.04)	1.89E+03 1.16E+02 (10.75)	2.17E+03 1.26E+02 (13.90)
Arms (7,600)	2.41E+03 1.77E+02 (12.10)	2.50E+03 1.81E+02 (14.20)	2.84E+03 1.84E+02 (18.20)
Thighs (12,100)	ND	ND	ND
Shins (7,490)	ND	ND	ND

* ND : Not Detectable

At 33 cm, percentage response in the torsos is 87.9%. On the other hand, response in other parts except the torsos is very low because of a solid angle reduced by the detector collimator. Of course, volume of the torsos is larger than others. Total torso volume is 3.5 times larger than arms. Response in the torsos is 7.3 times much higher than arms. It was found that uniformity of the detector response is poor especially at short distance in chair geometry. At 43 cm, response in the parts except the torsos is 18.2%. Response in the torsos is 4.5 times much higher than arms. It is more similar with volume ratio than other positions. It was found that the longer distance between subject and detector, the more stable uniformity of response in chair geometry. But, total measured activity in this position is lower than the others because of the low counting efficiency which causes the increase of the MDA. Therefore, this position is unsuitable in aspect of sensitivity of the detector. At 38 cm, response in the parts except the torsos is above 18.5%. In addition, activities in the head and the neck could be measured in this position. It was found that 38 cm is the most reasonable position through results compared with both relative response and counting efficiency in the other positions.

As a result of the measurements, it was confirmed that relative response of single torso detector in all parts except the torsos is relatively lower than response in the torsos. Torso detector was not sensitive to activity above the neck and below thighs. Especially, activity below thighs was not measured at all positions.

2. Calibration Method for Transportable WBC System

In this study, alternative calibration method in chair geometry was considered to more conveniently calibrate the transportable system for preparedness of radiation emergency.

It was known that relative responses of the torso and arms were relatively high. From this result, counting efficiency at 38 cm in distance was measured by using 4 different phantom arrangements containing standard source for calibration. The counting time was 86,400 seconds for each measurement. The counting efficiency under 4 different calibration conditions is shown in **Fig. 5**. The results represent the counting efficiency against total activity in whole body phantom.

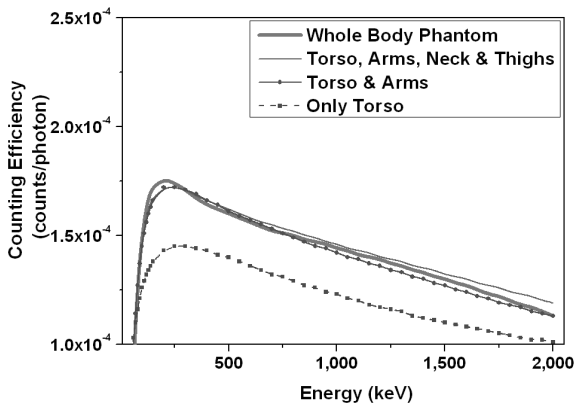

Fig. 5 Counting efficiencies under 4 phantom arrangements for calibration.

It was found that counting efficiencies under 3 conditions except calibration using only torso had very similar pattern. Consequently, it was found that all parts of the phantom were not necessary to calibrate the system in chair geometry.

The transportable system could be calibrated by using only parts of torso and arms of the BOMAB phantom.

VI. Conclusions

In this study, the relative response of the torso detector for transportable WBC system with chair geometry was analyzed through obtaining the measurements of the activities according to position of the detector. Although detector response in chair geometry has poor uniformity, it is most commonly used for accidental monitoring of internal contamination due to relatively small volume and weight. It was found that single torso detector in chair geometry was not sensitive to activity above the neck and below thighs. Therefore, all parts of phantom are not necessary to calibrate the system. The system could be calibrated by using only parts of torso and arms of the BOMAB phantom. In case that system calibration should be conducted at the scene in the vicinity of radiation accident, this method would be more convenient. But, in order to obtain efficiency curve against whole body, total activity value uniformly distributed in all parts of the phantom should be known in advance.

References

1) IAEA Technical Report, "Rapid Monitoring of Large Groups of Internally Contaminated People Following a Radiation Accident," IAEA-TECDOC-746, (1994).
2) M J Youngman, "Transportable *In vivo* Monitoring System for Accident Monitoring of Internal Contamination," NRPB-W12, (2002).
3) N Stradling, et al., "Assessment of Intake and Dose after Inhalation of Caesium-137 by Workers and Adult Members of the Public," NRPB-W51, (2003).
4) ICRU Report No 69, "Direct Determination of the Body Content of Radionuclides," Journal of the ICRU, 3[1], (2003).
5) M. A. Lopez, et al., "State of the Art Dosimetric Methods for Internal and External Exposures: Conclusions of a EURADOS Action," Radiation Protection Dosimetry, Vienna 2005 Special Issue, (2007).
6) T. Ishikawa, "Performance of a Whole-Body Counter with Five High-Purity Germanium Detectors," Applied Radiation and Isotopes, 64: pp. 386~389, (2006).
7) D. S. MRDA, et al., "Background Reduction of Using Fe and Pb Shielding," Fifth General Conference of the Balkan Physical Union, Vrnjacka Banja, Serbia and Montenegro, Aug. 25-29, (2003).
8) Wi-Ho Ha, et al., "Optimization of Shielding Design for Chair-type Whole Body Counter by the Monte Carlo Simulation," The Second Asian and Oceanic Congress for Radiation Protection, Beijing, China, Oct. 9-13, (2006).
9) Wi-Ho Ha, et al., "A Study on the Shielding Design of the HPGe Detector for Chair-type Whole Body Counter," Conference of Korea Association for Radiation Protection, Gyeongju, Korea, Nov. 23-24, (2006).
10) Gary H. Kramer, et al., "A New Phantom for Use in Whole Body Counters: A Monte Carlo Design Project," Health Physics, 88[1]: pp. 80~83, (2005).

Journal of NUCLEAR SCIENCE and TECHNOLOGY, Supplement 5, p. 511–514 (June 2008)

Design and Analysis of CMOS Single Photon Counting Avalanche Photodiodes Integrated with Active Quenching Circuits

Kwang Hyun KIM, and Young Soo KIM*

Chosun University, Seosuk-dong, Dong-gu, Gwangju, Republic of Korea

The CMOS SPADs (Single Photon Avalanche Diodes) integrated with active quenching circuits were fabricated on same chip using AMIS 0.7 μm high voltage CMOS process without any process modifications. The SPADs have N+/P-substrate structure and their diameter of photo sensing area are 25 μm, 50 μm, 100 μm, 400 μm, and 800 μm. The avalanche multiplication is occurred at 10.7 V, and the photocurrent gain at 11 V reverse bias voltage is about 1000. In zero bias condition, the maximum quantum efficiency appears at 650 nm wavelength, and it corresponds to around 30 %. The active quenching circuit is composed of a comparator, three monostable, and two MOS switch. As a circuit simulation results, the comparator and the monostable generate ~ 22 nsec and ~ 1 nsec delayed output pulse, respectively. The dead time of the active quenching circuits integrated with SPADs is about 100 nsec as a measured result.

KEYWORDS: active quenching, avalanche photodiodes, CMOS integrated circuit, photodetectors, single photon counting

I. Introduction

Single photon counting techniques are widely used in many applications and it is required that the sensor has high sensitivity or gain to detect very low light. Until recently, the most widely used detector has been the photomultiplier tube (PMT). Although PMTs are sensitive to light and have very high gain, they are bulky and fragile. In addition, the PMTs require high voltages to operate and are extremely sensitive to magnetic fields that can disturb the path of the photoelectrons.

To overcome these drawbacks of the PMTs, silicon based avalanche photodiodes (APDs) have been considered as an alternative to PMTs. Since a few years, silicon APDs are commercially available with outstanding characteristics. Therefore, the silicon based APDs are being currently replaced PMTs in nuclear imaging applications, such as positron emission tomography (PET)[1]. However, silicon APDs have also several disadvantages. Since it is fabricated using special non-planar process, the production cost is very high and it is impossible to integrate readout circuit on the same chip. So, off-chip electronics are necessary to operate the APDs, whole system become very complex. Many researchers have been trying to overcome these problems by investigating the APDs in a conventional CMOS process. The APDs fabricated in conventional CMOS process have several advantages such as possibility to integrate the driving and signal processing circuit on the same chip, low cost production, and high gain characteristics, that is, high signal to noise ratio[2, 3].

According to operation condition, APDs have two modes which are proportional mode and Geiger mode. In proportional mode, APDs are biased slightly below breakdown voltage and amplification electronics such as charge sensitive preamplifier are needed for converting and amplifying the generated signal charge to voltage. In this configuration, the sensor can be affected by noise that is generated by electronics, so the signal to noise ratio can be deteriorated. In Geiger mode, APDs are biased above the breakdown voltage and very high electric field exists in the depletion region formulated in p-n junction of the device. When a single photon enters into this region, it has enough energy and triggers a multiplication process. The avalanche current having tens of milliampere is generated and digital pulse is initiated by this current for counts. The APDs operated under such condition are called single photon avalanche diodes (SPADs). In order to detect the subsequent photon and prevent from damage by avalanche current that cause overheat, the quenching circuit lowering the bias voltage of the SPADs below the breakdown voltage is required[4,5].

In this work, several sizes of SPADs integrated with active quenching circuit on same chip that are fabricated using conventional standard CMOS process are introduced. And, the experimental results such as gain and quantum efficiency of the CMOS SPADs and timing characteristics of the active quenching circuit are shown.

II. CMOS SPADs

The CMOS SPADs were fabricated using commercially available AMIS 0.7 μm high voltage CMOS process without any process modifications. This process has three metal layers and two poly layers. Generally, the shape of the photodiode is square, but it is known that the early breakdown is occurred and the much leakage current flows at the corner in this case. So, the shape of the SPADs was designed with round. SPADs have N+/P-substrate structure as shown in **Fig. 1**, and the five kinds of pixels were

*Corresponding Author, Tel No: +82-62-230-7450, Fax No: +82-62-230-7451, E-Mail: yskim75@chosun.ac.kr

implemented. The diameters of the each pixel are as follows: 25 μm, 50 μm, 100 μm, 400 μm, and 800 μm. All of round pixels are surrounded with field terminating rings in order to isolate from another pixels or signal processing blocks. The fabricated sample of the CMOS SPADs is shown in **Fig. 2**.

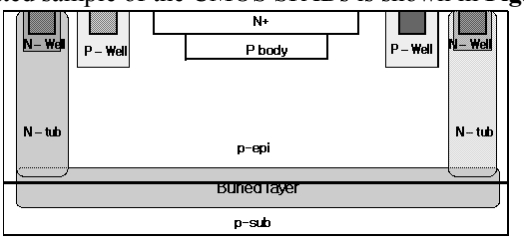

Fig. 1 The cross section of the N+/P-substrate structure CMOS SPADs.

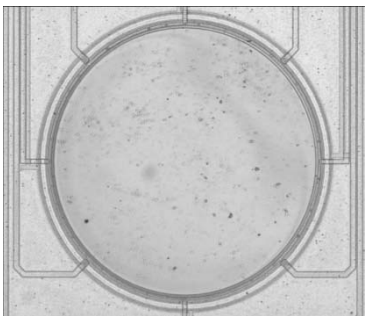

Fig. 2 Photograph of one of the test sample of CMOS SPADs fabricated using AMIS 0.7 μm high voltage process.

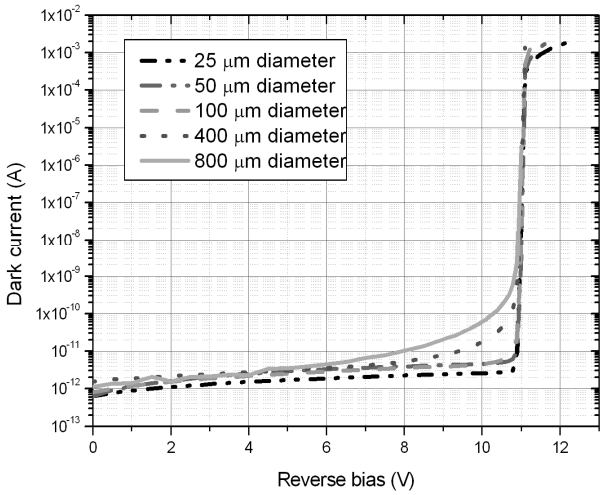

Fig. 3 Dark current for CMOS SPADs with 25 μm, 50 μm, 100 μm, 400 μm, and 800 μm diameter.

Photocurrent gain and quantum efficiency are very important factors determining the performance of the CMOS SPADs. To calculate photocurrent gain, the dark current and the photocurrent must be measured since photocurrent gain is the ratio of the photocurrent at applied reverse bias voltage to the photocurrent at zero reverse bias voltage. The dark current was measured from zero bias to breakdown voltage under reverse bias condition. In **Fig. 3**, as the bias voltage and the active area diameter of the sensor increases, the dark current also increases and the breakdown voltages decrease. The photocurrent was measured when the light source with 550 nm wavelength and 120 nW power. The measured photocurrent is sum of dark current and real photocurrent. Therefore, to calculate the photocurrent gain, the differences of the measured photocurrent and dark current were used. As shown in **Fig. 4**, the avalanche multiplication is occurred at ~ 10.7 V, and the photocurrent gain at 11 V reverse bias voltage is about 1000.

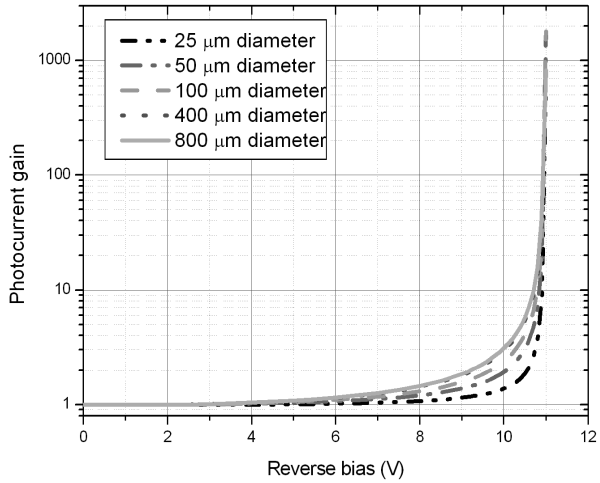

Fig. 4 Photocurrent gain for CMOS SPADs with 25 μm, 50 μm, 100 μm, 400 μm, and 800 μm diameter when the light source with 550 nm wavelength and 120 nW power is illuminated.

The quantum efficiency was measured from 400 nm to 1000 nm wavelength with 50 nm steps under zero bias condition using the monochromatic light source that consists of a tungsten halogen lamp, a monochromator, and an integrating sphere. To measure the power of the incident light to the samples, the calibrated photodiode was used. The quantum efficiency peaks at 650 nm wavelength and the value is about 30 %, since the absorption length of the light with 650 nm fits with the depth of the P body layer which is active region.

III. Integrated Active Quenching Circuit

The active quenching circuit is composed of a comparator, three monostable, and two MOS switch as shown in **Fig. 5**. When a photon enters into the SPAD biased above avalanche breakdown voltage, very large current flows through SPAD, and then passive quenching begins by quenching resistor R_Q connected to the anode of the SPAD. At the same time, a voltage pulse is generated on the load resistor R_L. This pulse enters into the input of the comparator, and the comparator outputs short pulse when the level of the pulse is higher than the reference voltage. The output pulse of the comparator inputs two monostables. One is for generation of the count pulse that is used for photon count entering SPAD. The other is for active quenching. This quenching pulse closes the MOS switch M_{quench}, and the anode of the SPAD is connected to V_{quench}. Also, this pulse inputs third monostable that is reset monostable. The reset pulse generated by reset monostable closes the MOS switch M_{reset}, the anode of the SPAD is connected to ground in order to wait the subsequent photons[6].

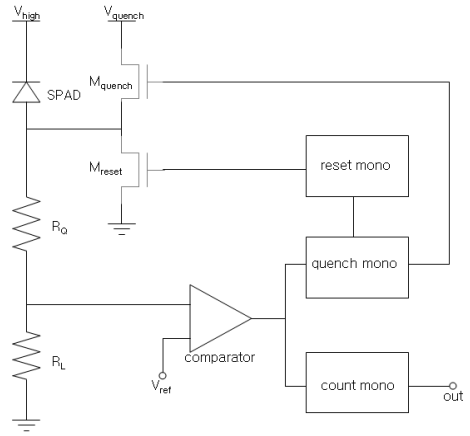

Fig. 5 Block diagram of the active quenching circuit.

The active quenching circuit was designed through circuit simulation using HSpice that is integrated circuit simulator. The model parameter supplied by process foundry was used for simulation. In **Fig. 6**, the simulation results for comparator are shown. When the rectangular pulse with 5 V amplitude and reference voltage with DC 0.8 V is entered into negative and positive input of the comparator, respectively, about 22 nsec delayed pulse outputs. **Fig. 7** shows the output of the three monostable to comparator's output. Sequentially downward, there are output of the comparator, quench monostable, count monostable, and reset monostable. The monostable generate output pulse with about 1 nsec delay for the falling edge of the input pulse.

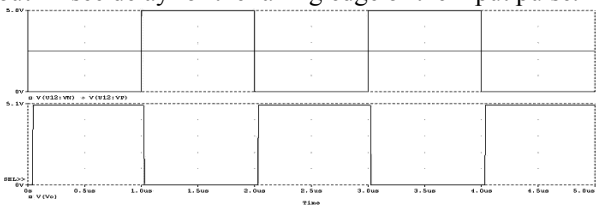

Fig. 6 Simulation results of the comparator.

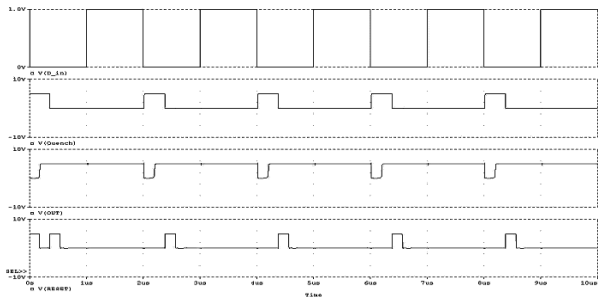

Fig. 7 Simulation results of the quench, count, and reset monostables.

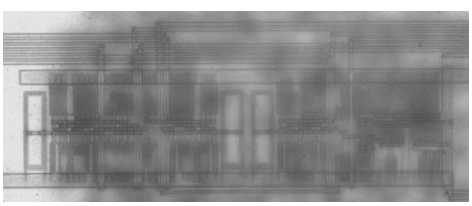

Fig. 8 Photograph of one of the test sample of active quenching circuit fabricated AMIS 0.7 μm high voltage process.

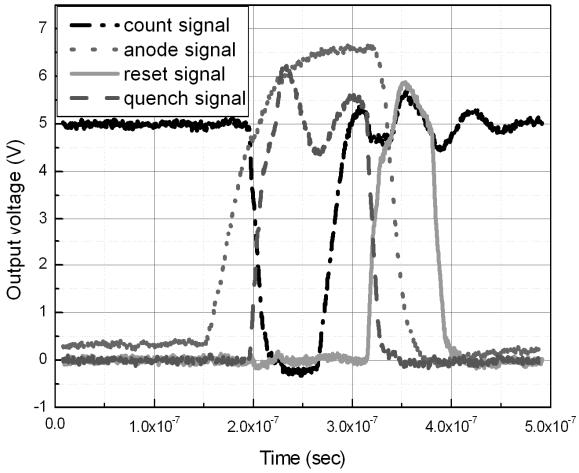

Fig. 9 Anode voltage of the SPADs with respect to the quench and reset signal.

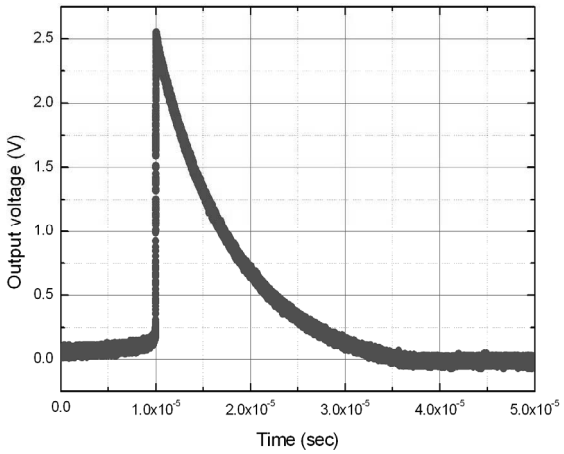

Fig. 10 Anode voltage of the SPAD using passive quenching.

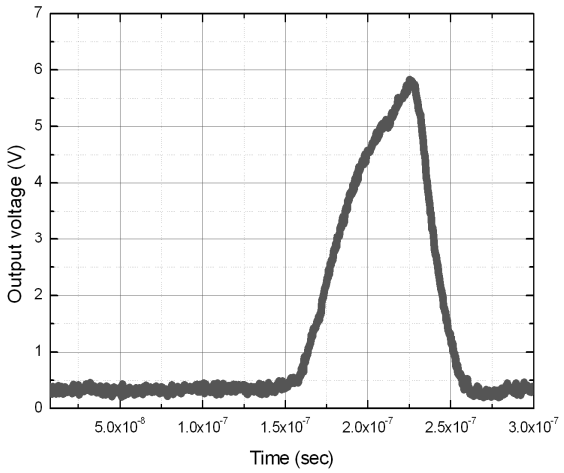

Fig. 11 Anode voltage of the SPAD using active quenching.

The fabricated active quenching circuit using AMIS 0.7 μm high voltage process is shown in **Fig. 8**. The reference voltage of the comparator and pulse width of the monostable can be controlled externally.

In **Fig. 9**, test results for anode of the SPAD, count monostable output, quench monostable output, and reset

monostable are shown. At the beginning of quenching, passive quenching is accomplished, and then active quenching is followed when quenching signal is enabled. At the last sequence, if the reset signal is enabled, the bias of the SPAD is recharged above avalanche breakdown voltage.

The result of the active quenching is compared to the passive quenching in **Fig. 10** and **Fig. 11**. The dead time of passive quenching circuit is 30 μsec, whereas that of the active quenching is 100 nsec.

IV. Conclusion

The CMOS SPADs integrated with active quenching circuits were fabricated on same chip using AMIS 0.7 μm high voltage CMOS process without any process modifications. To characterize the CMOS SPADs, dark current, photocurrent gain, and quantum efficiency were measured. The avalanche multiplication begins at 10.7 V, and the photocurrent gain at 11 V reverse bias voltage is about 1000. The wavelength of the incident light having maximum quantum efficiency is 650 nm and the quantum efficiency is around 30 %. Also, to characterize the active quenching circuits, the output signals of the functional blocks such as count monostable, quench monostable, and reset monostable were measured. And, the formation of the signal at the CMOS SPAD's anode was measured with respect to the output signals of the functional blocks using oscilloscope. The dead time of the active quenching circuits integrated with SPADs is about 100 nsec.

References

1) C. S. Levin, A. M. K. Foudray, P. D. Olcott, and F. Habte, "Investigation of position sensitive avalanche photodiodes for a new high-resolution PET detector design," IEEE Trans. Nucl. Sci., 51[3], 805-810 (2004).
2) W. J. Kindt and H. W. van Zeijl, "Modeling and fabrication of Geiger mode avalanche photodiodes," IEEE Trans. Nucl. Sci., 45[3], 715-719 (1998).
3) A. Rochas, A. R. Pauchard, P. A. Besse, D. Pantic, Z. Prijic, and R. S. Popovic, "Low-noise silicon avalanche photodiodes fabricated in conventional CMOS technologies," IEEE Trans. Electron Devices, 49[3], 387-394 (2002).
4) A. Rochas, P. A. Besse, and R. S. Popovic, "Actively recharged single photon counting avalanche photodiode integrated in an industrial CMOS process," Sensors and Actuators A, 110, 124-129 (2004).
5) C. Niclass, A. Rochas, P. A. Besse, R. Popovic, and E. Charbon, "A 4 μs integration time imager based on CMOS single photon avalanche diode technology," Sensors and Actuators A, 130-131, 273-281 (2006).
6) F. Zappa, M. Ghioni, S. Cova, C. Samori, and A. C. Giudice, "An integrated active-quenching circuit for single-photon avalanche diodes," IEEE Trans. Instrumentation and Measurement, 49[6], 1167-1175 (2000).

Journal of NUCLEAR SCIENCE and TECHNOLOGY, Supplement 5, p. 515–517 (June 2008)

Conceptual Design for Real Time Monitoring of Electron Microbeam

Ji Seok KIM[1,2*], Hyun Ki KIM[1], Gwang Min SUN[3], Mee JANG[1], Chang Woon CHOI[1], and Jai Ki LEE[2]

[1]*National Radiation Emergency Medical Center, Korea Institute of Radiological and Medical Sciences, Seoul, Korea*
[2]*Department of Nuclear Engineering, Hanyang University, Seoul, Korea*
[3]*Korea Atomic Energy Research Institute, Daejeon, Korea*

It is recognized that the microbeam is powerful system to understand the interaction of ionizing radiation with cells. Especially, electron microbeam system is useful to investigate the effect of low-LET radiation for cells. Electron microbeam has been developed in KIRAMS. It can irradiate the small volume in cell level by collimator and electromagnetic field and give local dose to individual cell by controlling the number of electrons. When the electron microbeam irradiates the individual cell, however, there is a possibility to change the current and intended trajectory of electron beam. Because this possibility introduces the uncertainty of dose, it is necessary to monitor the trajectory and current of electron beam. This study deals with development of real time monitoring device to confirm beam quality and to control if necessary during experiment. Consequently we designed dual monitoring device to solve various factors. And we optimize the design by simulation.

KEYWORDS: electron microbeam, current, trajectory, simulation, real time measuring device

I. Introduction

Microbeam system, which has been developed to study effects of low dose radiation on human body, is currently being researched actively in many countries such as USA, U.K., and Japan.[1)] The Korea Institute of Radiological and Medical Sciences (KIRAMS) has been operating a electron microbeam system since 2002. In particular, the electron microbeam system of KIRAMS deserves attention because this device can irradiate the exact volume of target cells and imitate the secondary electrons generated inside the human body. The electron microbeam system is shown in **Fig. 1**[1)].

Fig. 1 Electron microbeam system

The electron microbeam system is consisted of an electron gun, a vacuum chamber for transmission, a cell irradiating plate, and a hardware for cell image capture and cell position control. The propagation of electron microbeam is made to be parallel to the human cell irradiation. The position of electron beam and beam focusing are controlled by the electromagnet. As shown in **Fig. 2**[1)], the electron microbeam system radiates a predetermined amount on the target cell by the process of passing through the final collimator.

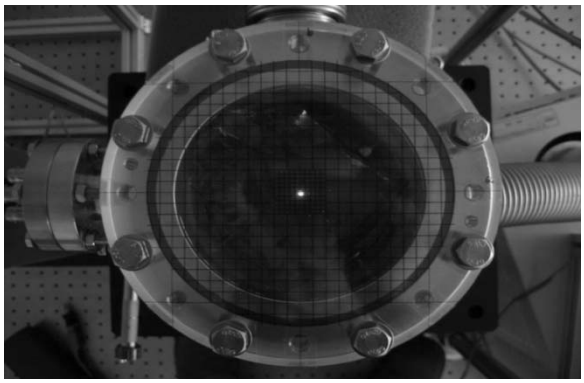

Fig. 2 Observation of the electron beam alignment by illuminating the fluorescent material

The final collimator has a 10μm-diameter pinhole. As it is very small, it is very hard to align the electron-beam to the hole while corresponding to the influence of terrestrial magnetism and the change of environment, beam current and energy. In addition, the electron-beam has its own inherent fluctuation. As time passes, the thermal effect and space-charge effect are added to them. Therefore, the prediction of the energy and the beam current level becomes very difficult.

Of course the electron-beam can be measured using a Canberra B50AM PIPS detector, but a real-time measurement is not possible during cell investigating experiment because the PIPS detector interferes with the propagation of electron-beam.

*Corresponding Author, Tel No: +82-2-970-1430, Fax No: +82-2-970-2404, E-Mail: aerobone@hanmail.net

Accordingly, KIRAMS has devised a system that can determine the energy and the beam current in the real-time, and can analyze the causes and can feedback the beam quality.

II. Design

Electrons can deviate from their intended trajectory easily because of their light mass. However, the device with a hole at the center possesses a symmetric structure, which is beneficial to solve the trajectory deviation problem.

Table 1. Factors of problem and solution in holed-device

Change	Factors	Detecting	Solution
Energy peak to noise ratio	Internal scattering	Trajectory tracking	Electromagnet control
Current	Thermal effect	Real time current measurement	Source voltage control
	Beam position	Trajectory tracking	Electromagnet control
	Beam focus	Trajectory tracking	Electromagnet control
	Space charge effect	Real time current measurement	Source voltage control

Table 1 lists a number of variables. Not only to measure the current but also to restore the current to the normal level, the causes of change should also be known. For example, in the case of a holed-device, when focal width is increased without any specification, the measured current can be misunderstood as the emission current has increased. In that case, to restore the electron-beam to the normal status, the focal width must be reduced, but sometimes the emission current may be mistakenly reduced. Accordingly, in the measurements reported in this thesis, not only the current level but also the trajectory of electron-beam will be monitored when real-time electron-beam monitoring is done.

After the electron microbeam is shot from electron gun in mono-energetic condition with the energy range of 1~100 keV, the electrons are scattered from the collimator and the structure of device, and the beam quality gradually becomes worse. When electrons undergo scattering, they are mainly scattered from collimator of the internal components and thereby the most are accumulated in the collimating material.

Therefore, the energy peak to noise ratio can be estimated based on the level of scattering by installing a Keithley 6517 electrometer, an electron measuring device, at the location of maximum scattering. In this concept, the electrons' trajectory may be inferred by analyzing the locations where the electrons get accumulated, and beam quality feedback becomes possible based on the estimated trajectory.

Fig. 3 describes the pattern of electron-beam entering the trajectory-tracking device, as well as the measurement circuits. The four divisional trajectory-tracking devices emit a signal in proportion to the incident electrons, and an increase of the signal in one direction indicates the change of the beam position toward that orientation, and increases in all the four directions indicate the enlargement of the beam focal width. Also, measurement of the beam scattering provides a good indication on the beam quality.

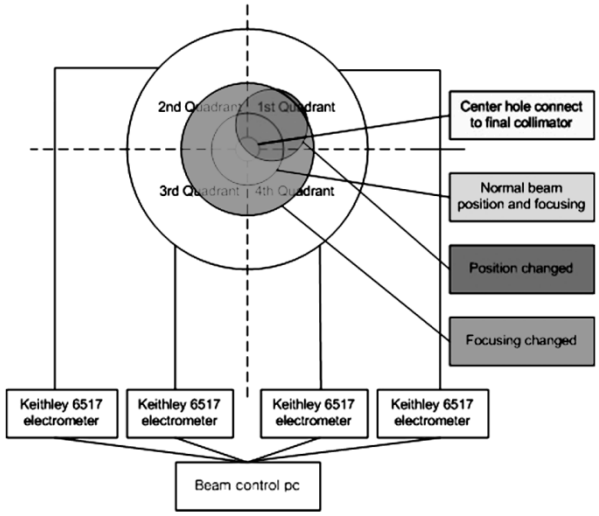

Fig. 3 Real time trajectory-tracking device

It is common to make a current measurement of the electron microbeam using Faraday Cup. However, the method is not adequate for a real-time monitoring. So, proportional values are obtained by comparing the count of the electrons incident on the final collimator against the PIPS detector's measurement, and finally the current of electron microbeam in the absence of PIPS detector is estimated.

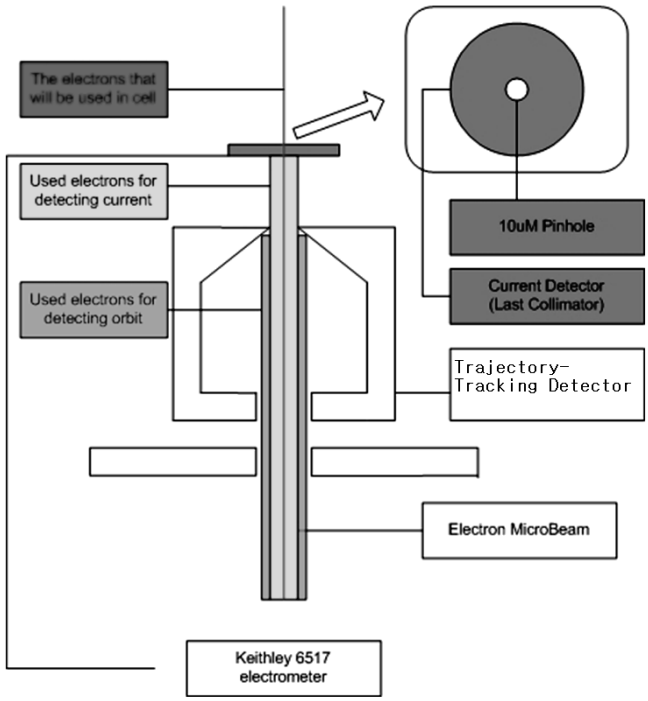

Fig. 4 Real time current measuring and trajectory tacking device

Fig. 4 shows the electron microbeam entering into the current measuring device through the orbit tracking device.

There are two important reasons in utilizing such a dual system for the current measurement.

The first reason is to measure the current of electron microbeam that is finally irradiated into the cell in a more direct way. The second reason is to control the diverse factors in order not to be generated independently or complexly. In this dual system, only after the orbit of electron-beam has been checked first and there is no abnormality in it, the current can be measured. Thus, the influence of orbital change on the current can be excluded. This kind of independent system is especially suitable in controlling the variables.

III. Optimization of design by simulation

It would be inconsistent to put some material in progress of electron microbeam in order to make a better beam. The current detecting device will not cause any problem since it is an original part of the beam device. However, the orbit-tracking device can be problematic. Accordingly, an optimum condition for the measurement employing the device in which the beam does not deteriorated was searched through a simulation.

The simulation condition was as follows: a parallel beam with 500μm diameter, 30keV, vacuum and cupper-made components. The simulation code was Beamnrc code. The size of the optimized orbit tracking device is shown in **Fig. 5**.

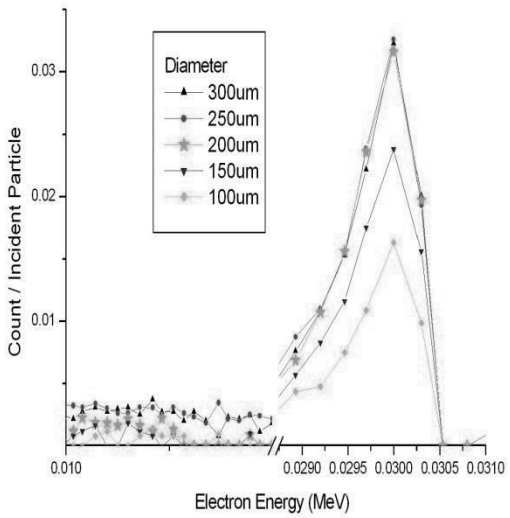

Fig. 5 Change of electron energy peak by size of hole in trajectory tracking device

Fig. 5 shows the energy peak values of electrons irradiating on the cell, in which the hole size of the trajectory tracking detector was used as the parameter. It indicates that the energy peak is lowered when the hole size is smaller than 150μm. On the other hand, the peaks are adequate when the hole size is 200μm. If the hole size is further increased the amount of the electron-beam entering is too low for the measurement. **Fig. 6** shows that the hole size should be less than a certain amount. In the case of **Fig. 6** the limit value was set at in which the minimum value readable by the electrometer was used as the base quantity, under an assumption that the measurements would be made every ten seconds. Since the minimum measurable quantity of the electrometer is 2nC when the micro-beam's emission current is about 1 nA, at least 15% of the initial emission electron value should incident on each part of the orbit tracking detector. Adequate hole size was 200μm, and the bevel angles of the device in a range of 30 to 60 degrees were all adequate.

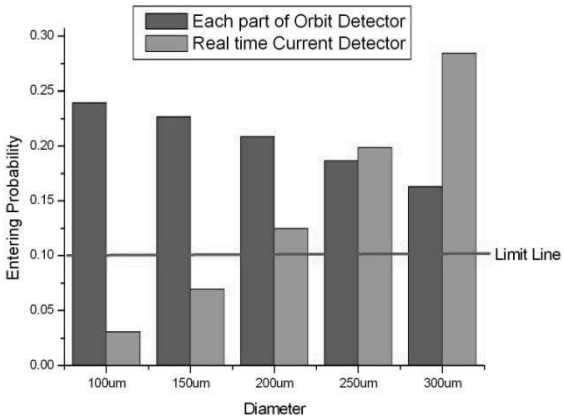

Fig. 6 Signal limit and entering probability

IV. Conclusion

The current can be measured more precisely as compared to a system measuring only the current, if the trajectory tracking device's hole size is set at 200μm and a current detector is employed at the location of the last collimator. This is because such a dual system can take care of various factors that would be overlooked in the system that measures only the current value. Also, the dual system is capable to find problems caused on the trajectory of the electron-beam, thus proving information necessary for restoring the beam back to the normality and necessary for stopping any electrons that would undesirably irradiate the cell. Errors in the simulation data do not exceed 5%.

References

1) Eun Hui Kim, et al., Microdosimetric Aspects of Low-Dose Low-LET Radiation, Final Report of Nuclear, 2004

Journal of NUCLEAR SCIENCE and TECHNOLOGY, Supplement 5, p. 518–521 (June 2008)

Comparison of the New MO*Skin* Detector and Fiber Optic Dosimetry System for Radiotherapy

Ian KWAN[1], Bongsoo LEE[2**], Wook Jae YOO[2], Donghyun CHO[2], Kyoungwon JANG[2], Sanghun SHIN[2], Martin CAROLAN[3], Michael LERCH[1], Vladimir PEREVERTAYLO[4] and Anatoly ROSENFELD[1*]

[1]*Centre for Medical Radiation Physics, University of Wollongong, New South Wales, 2500, Australia*
[2]*Department of Biomedical Engineering, College of Biomedical & Health Science, Konkuk University, South Korea*
[3]*Illawarra Cancer Care Centre, Wollongong Hospital, Wollongong, New South Wales, 2500, Australia*
[4]*SPA BIT, Ukraine.*

In radiotherapy, interest in real-time dosimetry stems from the desire to monitor the dose delivered to the target volume and the surrounding normal tissue to enable clinicians to track the progress of the treatment, and prevent surrounding tissue from receiving too much radiation dose. In this study, the dosimetric performance of the new MO*Skin* dosimeter and a Bicron BCF-20 scintillating fiber was compared to depth dose measurements taken with a Farmer-type ionization chamber. The performance of the MO*Skin* and BCF-20 detectors in the build-up region of the depth dose curve, where the dose gradient is steep, is also compared to readings taken with an Attix chamber. At depths greater than 15 mm, the MO*Skin* readings deviated from the ion chamber readings by up to 4%, while the fiber optic dosimeter always remained within 3% of the ionization chamber reading. In the build-up region, the MO*Skin* proved quite capable of measuring the dose at build up when compared to the Attix chamber results, while the fiber optic dosimeter was not able to measure the dose in this region with a high level of precision due to the thick sensitive volume of the scintillating crystal.

KEYWORDS: MOSFET detector, fiber optic dosimetry, scintillator, depth dose, Attix chamber

I. Introduction

In radiotherapy, interest in real-time dosimetry stems from the desire to monitor the dose delivered to the target volume, and the dose delivered to the surrounding normal tissue that receive unnecessary dose. The information provided by a real-time dosimetry system would enable clinicians to track the progress of the treatment, and prevent surrounding normal tissue from receiving a dangerous level of radiation dose.

Scintillator-based fiber optic dosimetry systems have gained acceptance in dosimetry because they're water equivalent, provide linear dose response, and can measure dose in real-time. The ability to acquire dose information during the treatment procedure would allow for a treatment to be adjusted or stopped if the dose was not being delivered correctly, or if the dose to the surrounding organs was higher than expected. They can be made quite small, with 1 mm thick crystals now being common. Smaller 0.5 mm thick crystals are also available, which means fiber optic dosimeters offer a sensitive volume with a thickness comparable to or better than that of TLDs[1)]. Their water equivalence is a valuable characteristic, as ion chambers introduce complicated issues related to the difference in the physical characteristics of the surrounding material, and that of the ion chamber. The main issue with fiber optic dosimetry has always been the background radiation due to Cerenkov radiation.[1,2)] Cerenkov radiation is produced when charged particles, (electrons in this case) pass through the fiber at a speed greater than the speed of light in the fiber. The Cerenkov radiation produced when a high energy photon beam is delivered from a linear accelerator (LINAC) has a wavelength in the 400–480 nm range, which is in the violet and blue end of the visible spectrum. Since the amount of Cerenkov produced in the fiber is not directly proportional to the dose delivered to the fiber, the Cerenkov contribution to the signal is considered background noise.[2, 3, 4)] Methods such as background subtraction and optical filtering are used to reduce the majority of this noise[2, 3)].

MOSFET-based dosimeters utilize a different technology to measure dose, but share many characteristics with fiber optic dosimeters such as small size, water equivalence for MV X-ray, and the ability to measure dose in real-time. MOSFET dosimeters have the added benefit of a micron-scale sensitive volume, allowing them to measure the absorbed dose in steep dose gradient conditions.[5,6)] Larger detectors can only measure a volume average dose, which lacks precision and results in a large uncertainty in the measurement like ionization chamber and TLD detectors in a build up region of MV X-ray from LINAC . In an X-ray field delivered by a medical LINAC, the thin sensitive volume of the MOSFET proves invaluable in the build-up region of the depth dose curve, where the dose gradient is very steep. MOSFETs have proven to be effective dosimeters in external beam radiotherapy, intensity modulated radiotherapy, microbeam radiotherapy, and in diagnostic radiology. They can provide accurate integrated

*Corresponding Author, Tel No: +61-2-4221-4574, Fax No: +61-2-4221-5944, E-Mail: anatoly@uow.edu.au
**B. Lee is currently a visiting fellow at CMRP on subbatical

dose readings, but their reading becomes less accurate when the mean energy spectrum of the beam is less than 250 keV. Below 200 keV, the MOSFET begins to over respond and demand calibration in the same field [6,10)]

This paper aims to investigate the performance of the new MO*Skin*™ dosimeter and a fiber optic dosimetry system when irradiated on a LINAC. The MO*Skin*™ was designed at the Centre for Medical Radiation Physics (CMRP), University of Wollongong, Australia, while the fiber optic dosimetry (FOD) system utilizes a BCF-20 scintillating crystal from Saint-Gobain Crystals (Bicron). The Korean team at Konkuk University designed and produced the FOD probe and computerized reader.

II Materials and Methods

1. MOSFET Detector Design

The MO*Skin*™ is a MOSFET-based detector with a unique design that allows it to accurately measure the dose at an air-tissue interface, such as the dose delivered to the skin during breast treatment, or the dose delivered to the rectal wall during HDR brachytherapy. What makes the MO*Skin*™ unique is the proprietary patented design of the packaging. Rather than incorporating an epoxy resin "bubble" to encapsulate and protect the MOSFET sensor, a thin, flexible, and reproducible polyamide film is placed on top of the gate oxide to seal and protect the sensor. The film acts as a build-up layer, and is thin enough and reproducible to allow for skin dose measurements at an equivalent depth of 70 μm, which is the approximated depth of the basal layer, according to the International Commission on Radiological Protection (ICRP)[7)]. The basal layer represents the first important radiosensitive layer of the skin.

The packaged MO*Skin* detector is 1 x 2.5 mm^2 in area. The MOSFET chip itself is only 350 μm thick, with overall thickness less than 1 mm. It is read out by a portable, battery-powered reader that allows ten MO*Skin* detectors to be attached simultaneously, and read out individually via five channels. Some MO*Skin* detectors actually contain two independent MOSFET sensors on one chip: a high sensitivity with a thicker oxide, and a lower sensitivity sensor with a thinner oxide similar as in a RadFET™ REM chip. The reader allows for either a 0V, 5 V or 15 V bias voltage to be applied to the gate during irradiation. MO*Skin* measurements presented here were obtained using a MO*Skin* prototype with a single thin oxide MOSFET, while the reader was set to 15 V bias.

2. Fiber Optic Dosimetry System

The optical fiber dosimeter used in this study is the Bicron BCF-20, an organic scintillator produced by Saint-Gobain Crystals. When the radiosensitive scintillating element is irradiated, it emits a green light with an emission peak at 492 nm. This signal is sent down the length of the fiber optic cable towards a photodiode or photomultiplier. The amount of light emitted by the scintillator depends on the dose rate delivered by the LINAC. The radiosensitive scintillating volume was 1 mm diameter and 10 mm in length, and is optically coupled to a 10 m long polymethylmethacrylate (PMMA) optical fiber (model CK-40) produced by Mitsubishi Inc. The cable has a refractive index of 1.49. The other end of the fiber is connected to a Hamamatsu S1336-18BK photodiode, which produces a photocurrent which is amplified by current amplifier. The output signal from the amplifier is sent to a laptop computer via a data acquisition (DAC) system based on from National Instruments card. The computer collects the data and graphically displays the average current and integral charge incoming pulse using a software program created in LabVIEW 7.

3. Depth Dose Determination

The dosimetric ability of the MOSkin and the BCF-20 fiber optic detectors were compared to dose readings taken with a CC13 ion chamber from Scanditronix. The depth dose distribution of the x-ray beam was measured in a water-equivalent phantom made from Solid Water™ material (Gammex RMI), with the detectors placed inside the phantom. The detectors were irradiated with a 6 MV photon beam delivered by a Varian 2100EX linear accelerator (LINAC). The detectors were irradiated from a direction normal to the phantom surface, with the detectors placed at the centre of the radiation field throughout the experiments. The dose was measured at depths ranging from 0 mm (at the surface of the phantom) to 100 mm, using radiation field sizes of 5×5, 10×10, 20×20, and 40×40 cm^2 and SSD of 100 cm. The ion chamber has a finite water-equivalent depth due to the thickness of the walls, so dosimetry at shallow depths (<0.5 mm) is not possible. The response of each detector was normalised to the response measured at 15 mm depth (d_{max}), where the dose is a maximum.

The dose measurements taken in the build-up region (0–15 mm) are also compared to readings taken with an Attix chamber, which is the only type of ionization chamber designed to measure dose in regions with a steep dose gradient, and better suited than the CC13 chamber in build up region. Previous research has shown that parallel plate ion chambers can over-respond by up to 30% in the build-up region when irradiated by a high energy photon beam[8)]. Gerbi has shown that Attix chambers provide surface dose results comparable to an extrapolation chamber, over-responding by less than 1% when irradiated by a 6 MV photon beam at normal incidence.

III. Results and Discussion

The depth dose measurements obtained with the MO*Skin,* fiber optic dosimeter, and the Attix chamber for the four field sizes used in this experiment are shown in **Figs. 1** to **4**. At depths greater than d_{max}, the response of the MO*Skin* is lower than the CC13 chamber, but within 4% up to the maximum measured depth of 10cm. This is related to the changing of the electron stopping power ratio of water to SiO_2 with changing of the average electron energy with depth when using a MOSFET detector. Similarly, Chuang[9)] has observed agreement with the ionization chamber to

within 3% for depths up to 340 mm. The 4% discrepancy observed here may be due to poor statistics, as the mean response was calculated using only two readings at each depth. The BCF-20 FO dosimeter over-responded when compared to the ion chamber readings within 3%.

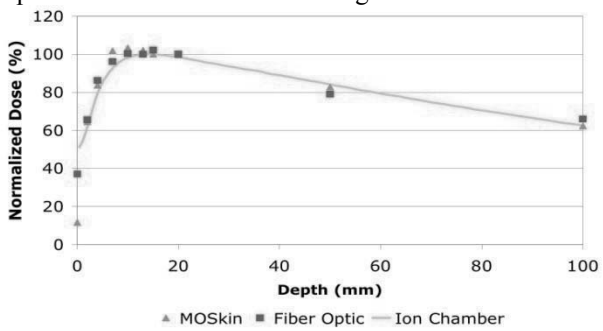

Fig. 1 Depth dose distribution measured using each detector when irradiated by a 5×5 cm photon beam.

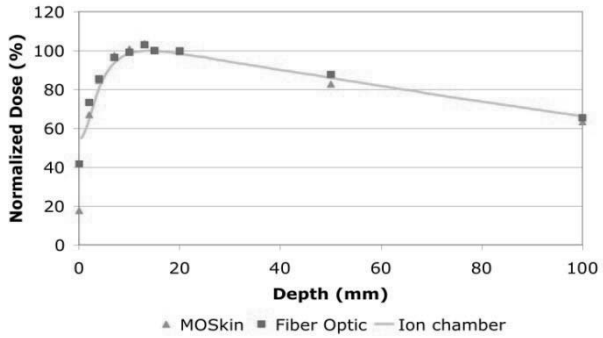

Fig. 2 Depth dose distribution measured using each detector when irradiated by a 10×10 cm photon beam.

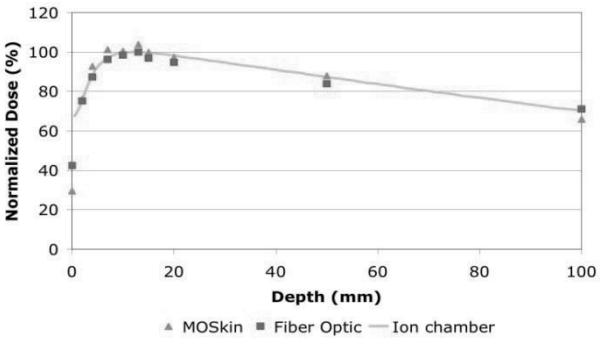

Fig. 3 Depth dose distribution measured using each detector when irradiated by a 20×20 cm photon beam.

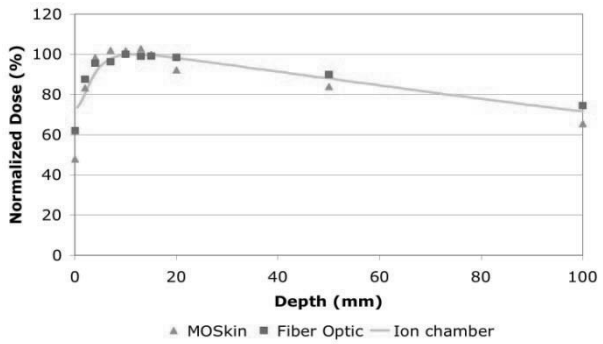

Fig. 4 Depth dose distribution measured using each detector when irradiated by a 40×40 cm photon beam.

In build up region 0–4 mm response of MO*Skin* less then FOD and both of them under-responded when compared to the ionization chamber, which is related to the large size of FOD used and Farmer IC and error associated with this. Previous comparison of Monte Carlo simulations, ATTIX IC and bare MOSFET response demonstrated perfect agreement [5,10] in a build up region that is supporting assumption above.

Table 1 shows the PDD values obtained when the MOSkin, fiber optic dosimeter, and Attix chamber were placed on the surface of the phantom and irradiated at field sizes of 5×5, 10×10, 20×20, and 40×40 cm^2. The MO*Skin* response is more comparable to the Attix chamber than the response of the FOD used in this work. This isn't unexpected, as the radiosensitive scintillator core is 1 mm in diameter, which is large for accurate surface dosimetry. For example, using a 5×5 cm^2 field size, the surface dose measured by FOD is greater than the dose delivered to the surface (0 mm) by a factor of 3 while MOSkin is accurately predicting dose at depth 0.07mm as designed. It should be noted that Attix chamber as designed provide dose at depth less then 0.07mm , i.e. closer to the surface like extrapolation chamber.

Table 1 Percentage Surface Dose values obtained using various field sizes in cm^2.

	Percentage Depth Dose (%)			
	5x5	10x10	20x20	40x40
BCF-20	37.1	41.7	42.4	61.9
MO*Skin*	11.4	17.7	29.6	47.1
Attix chamber	10	16	27	42

IV. Conclusions

In this study, the depth dose distribution within a water equivalent phantom was measured using the newly developed MO*Skin*™ detector, and a BCF-20 fiber optic dosimeter. The results were compared to the response of a Farmer-type ionization chamber. The response of the detectors in the build-up region of the depth dose curve was then compared to the results from an Attix chamber, a type of parallel plate ionization chamber capable of measuring dose in regions with a steep dose gradient.

Both the MO*Skin* and BCF-20 fiber optic dosimeter are capable of measuring depth dose and both are very useful for quality assurance in radiation therapy, but the MO*Skin* performs better within the build-up region, where the scintillator's 1 mm thick sensitive volume becomes a limiting factor in the level of precision and accuracy attainable in regions with a steep dose gradient.

Acknowledgement

This work was made possible because of the generous support provided by the Australian Rotary Health Research

Fund/Districts 9650 scholarship. This work was also supported by Australian government NHMRC grant 354114 the Korea Research Foundation Grant funded by the Korean Government (MOEHRD, Ministry of Education and Human Resource Development) (KRF-2007-013 D00117).

References

1) J. Lambert, T. Nakano, S. Law, et al., 'In vivo dosimeters for HDR brachytherapy: A comparison of a diamond detector, MOSFET, TLD, and scintillation detector,' Med. Phys. 34[5], 1759 (2007).
2) S. Boer, A. Beddar, J. A. Rawlinson, 'Optical filtering and spectral measurements of radiation-induced light in plastic scintillation dosimetry,' Phys. Med. Biol. 38, 945 (1993).
3) T. Aoyama, S. Koyama, et. al., 'A depth-dose measuring device using a multichannel scintillating fiber array for electron beam therapy,' Med. Phys. 24[8], 1235 (1997).
4) B. Justus, P. Falkenstein, A. Huston, et al., 'Elimination of Cerenkov interference in a fiber-optic-coupled radiation dosemeter,' Radiation Protection Dosimetry, 120[1-4], 20 (2006).
5) M. Butson, A. Rosenfeld, J. Mathur, et al., 'A new radiotherapy surface dose detector: the MOSFET,' Med. Phys. 23[5], 655 (1996).
6) A. Rosenfeld, 'MOSFET dosimetry in modern radiation oncology modalities,' Rad. Protection Dosimetry, 101[1-4], 393 (2002).
7) ICRP (International Commission on Radiological Protection), 'The biological basis for dose limitation in the skin,' ICRP Publication 59 (1991).
8) B. Gerbi, 'The response characteristics of a newly designed parallel-plate ionization chamber in high-energy photon and electron beams,' Med. Phys. 20[5], 1411 (1993).
9) C. Chuang, L. Verhey, P. Xia, 'Investigation of the use of MOSFET for clinical IMRT dosimetric verification,' Med. Phys. 29[6], 1109 (2002).
10) A.B.Rosenfeld, M.G. Carolan, B.J.Allen, et al "MOSFET Dosimeters: role of encapsulation in mixed gamma-neutron and megavoltage X-ray fields", IEEE Trans. on Nucl. Sci., NS-42, N6, 1870-1877, 1995

Journal of NUCLEAR SCIENCE and TECHNOLOGY, Supplement 5, p. 522–525 (June 2008)

Development of TES Microcalorimeter for high Precision Spectroscopy of LX-ray photons emitted from Transuranium Elements

Katsunori UENO[1*], Akihiro YAMAGUCHI[1], Keisuke NAKAMURA[1], Keisuke MAEHATA[1], Kenji ISHIBASHI[1], Takahiro UMENO[1, 2], Keiichi TANAKA[3], and Koji TAKASAKI[4]

[1]*Department of Applied Quantum Physics and Nuclear Engineering, Kyushu University*
[2]*Taiyo Nippon Sanso Corporation*
[3]*SII NanoTechnology Inc.*
[4]*Japan Atomic Energy Agency*

A microcalorimeter with the superconducting transition edge sensor (TES) with a Au absorber of 5.0 μm thick was fabricated for the energy dispersive measurement of LX-ray photons emitted from transuranium elements. The TES microcalorimeter and a superconducting quantum interference device (SQUID) amplifier chips were cooled by operating a compact ^{3}He-^{4}He dilution refrigerator without consuming liquid helium by loading a Gifford-McMahon (GM) cooler. Since the cold stages of the GM cooler are tightly coupled to the heat exchangers of the dilution refrigerator, the TES and SQUID chips suffered from mechanical vibrations induced by a reciprocating motion of the displacer of the GM cooler. Detection signals of LX-ray photons emitted from an ^{241}Am source were observed by operating the TES microcalorimeter in severe noise environment induced by mechanical vibrations.

KEYWORD: transition edge sensor (TES), microcalorimeter, LX-ray measurement, liquid helium free ^{3}He-^{4}He dilution refrigerator

I. Introduction

Plutonium isotopes are handled with special care in such nuclear fuel cycle plants as recycling plants, mixed oxide fuel fabrication plants. For the radiation protection of workers in such plants, it is necessary to estimate the internal exposure dose with high precision by monitoring the amount of the intake of plutonium isotopes. The in vivo counting of the LX-ray photons is employed for the direct estimation of the amount of the intake of plutonium isotopes. The emission probability of LX-ray photons in the α-decay of plutonium isotopes is one of the most important parameters for high precision estimation of the amount of the intake of plutonium isotopes by using the in vivo counting. The energies and emission probabilities of LX-ray photons emitted from plutonium and americium isotopes are listed in **Table 1**.

The value of the emission probability is estimated by analyzing an experimental energy spectrum of LX-ray photons emitted from the plutonium isotopes[1)]. The width of the full energy peaks of LX-ray photons in the energy spectrum is desired to be narrow for the precise estimation of the emission probability. It is necessary to obtain the value of the full width at the half maximum (FWHM) below 100 eV for full energy peaks in the experimental energy spectrum of LX rays emitted from the plutonium isotopes.

In this work, a microcalorimeter with a superconducting transition edge sensor (TES) with a thick energy absorber was developed for the energy dispersive measurement of X-ray photons of the energy of 10 to 20 keV with the excellent energy resolution below 50 eV of FWHM value. The TES microcalorimeter was cooled by a liquid-helium-free ^{3}He-^{4}He dilution refrigerator for detection of LX-ray photons emitted from an ^{241}Am source.

Table 1 Energies and emission probabilities of LX-ray photons emitted from ^{241}Am and ^{239}Pu.

LX-ray	^{241}Am		^{239}Pu	
	Energy[keV]	Emission probability	Energy[keV]	Emission probability
L_l	11.87	0.0104	11.62	0.001163
$L_{\alpha 1}$	13.76	0.017	13.44	0.00192
$L_{\alpha 2}$	13.95	0.149	13.62	0.01685
L_α	13.90	0.166	13.60	0.01877
L_η	15.86	0.00238	15.40	0.000393
$L_{\beta 6}$	16.11	0.00267	15.73	0.000297
$L_{\beta 15}$	16.79	0.0034	16.39	0.000386
$L_{\beta 2}$	16.84	0.0314	16.43	0.00354
$L_{\beta 4}$	17.06	0.0146	16.58	0.00115
$L_{\beta 7}$	17.27	0.001	16.84	0.000108
$L_{\beta 5}$	17.50	0.0065	17.07	0.000741
$L_{\beta 1}$	17.75	0.0837	17.22	0.01395
$L_{\beta 3}$	17.99	0.0123	17.45	0.000998
$L_{\beta 10}$	18.58	0.0007	18.03	0.000053
$L_{\beta 9}$	18.76	0.00103	18.21	0.000079
L_β	17.54	0.1573	17.06	0.0213
$L_{\gamma 5}$	20.10	0.00065	19.51	0.000107
$L_{\gamma 1}$	20.78	0.0192	20.17	0.00316
$L_{\gamma 2}$	21.10	0.004	20.49	0.00031
$L_{\gamma 8}$	21.26	0.00017	20.62	0.000027
$L_{\gamma 3}$	21.34	0.0039	20.72	0.000309
$L_{\gamma 6}$	21.49	0.0038	20.84	0.000612
$L_{\gamma 4}$	22.22	0.00193	21.53	0.000151
$L_{\gamma 13}$	22.38	0.00033	21.73	0.000026
L_γ	22.01	0.0339	20.30	0.0047

*Corresponding Author, Tel No: +81-92-802-3484, Fax. No: +81-92-802-3484,E-mail: ueno52@kune2a.nucl.kyushu-u.ac.jp

II. TES Microcalorimeter

The TES microcalorimeter is a thermal detector which measures the energy of an incident photon as a temperature rise[2]. A superconducting thin film thermometer of the TES microcalorimeter exhibits the sharp transition edge between superconducting and normal conducting states as shown in **Fig. 1**. The energy of incident X-ray photons is converted into the temperature rise in the absorber. The temperature rise induces a steep growth in the electric resistance of the thermometer.

The TES chip consists of the thin film thermometer with a bilayer structure of Au/Ti and the absorber of Au layer deposited on the thermometer film. The phase transition temperature of the TES was designed to be 200 mK by using the proximity effect between Au and Ti. The thickness of the Au absorber was designed to be 5.0 μm for absorption efficiency of 50 % and counting rate of 100 counts per second for detection of LX-ray photons with the energy from 10 to 20 keV. The geometrical dimensions of the thermometer and the absorber are 300 × 300μm^2 and 500 × 500μm^2, respectively. The TES chip was fabricated by SII NanoTechnology Inc.

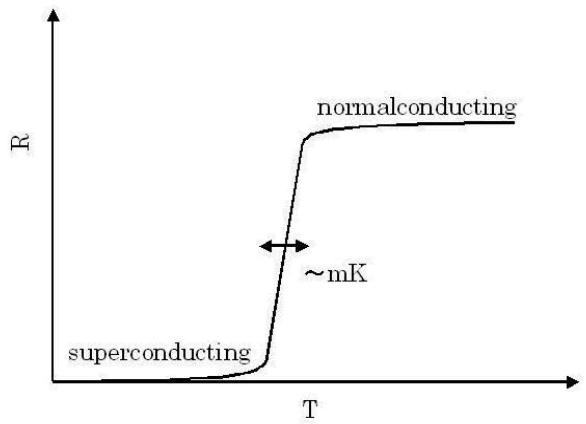

Fig. 1. Relationship between the electrical resistance R and the temperature T of typical superconductor in the phase transition region.

III. Liquid-Helium-Free ^{3}He-^{4}He Dilution Refrigerator

For achieving the excellent energy resolution, the TES microcalorimeter is operated in cryogenic temperatures below 200 mK. A ^{3}He-^{4}He dilution refrigerator is used to maintain the TES microcalorimeter at the operating temperature. Although liquid helium is consumed as a coolant in the operation of usual dilution refrigerators, it is difficult to use liquid helium in most laboratories for handling nuclear fuel and transuranium elements. Therefore, a liquid-helium-free refrigerator is desired to operate the TES microcalorimeter for the detection of LX-ray photons emitted from transuranium elements.

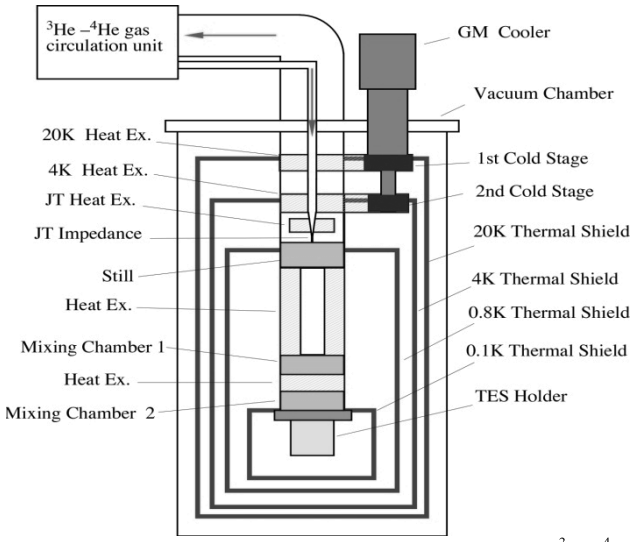

Fig. 2. Schematic drawing of the liquid-helium-free ^{3}He-^{4}He dilution refrigerator.

In this work, a liquid-helium-free ^{3}He-^{4}He dilution refrigerator was employed for operation of the TES microcalorimeter. The liquid-helium-free ^{3}He-^{4}He dilution refrigerator was manufactured by Taiyo Nippon Sanso Corporation. A schematic drawing of the liquid-helium-free ^{3}He-^{4}He dilution refrigerator is illustrated in **Fig. 2**. The ^{3}He-^{4}He dilution refrigerator is operated without consuming liquid helium by loading a Gifford-McMahon (GM) cooler. For assembling into a compact structure, the first and second cold stages of the GM cooler are tightly coupled to the 20 K and 4 K heat exchangers, respectively through copper plates in the vacuum chamber. The TES holder was attached on the base plate of the mixing chamber2. The helium-free dilution refrigerator performs the cooling power of 20 μW at 100 mK.

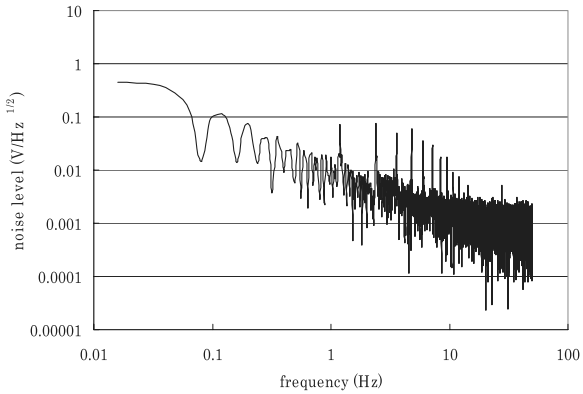

Fig. 3. Noise spectrum of the voltage signals of the SQUID amplifier.

Reciprocating motion of the displacer of the GM cooler induces mechanical vibrations of the TES holder in the operation of the dilution refrigerator. A superconducting quantum interference device (SQUID) amplifier chip was placed on the TES holder for surveying noise components induced by the mechanical vibrations. The SQUID amplifier chip was fabricated by SII NanoTechnology Inc. Voltage

output of the SQUID amplifier was analyzed by using a fast Fourier transform (FFT). **Fig. 3** shows the analyzed result of the noise spectrum. Components of 1.2 Hz and higher harmonics correspond to reciprocating motion of the displacer.

IV. Detection of LX-ray photons emitted from ^{241}Am

The fabricated TES microcalorimeter chip was mounted on the TES holder of the liquid-helium-free ^{3}He-^{4}He dilution refrigerator for the measurement of the electrical resistance and temperature (R-T) characteristics. A lock-in amplifier was employed for the electric resistance measurement with the four-wire method. The lock-in frequency was taken to be 77 Hz for reduction of the severe noise contribution. Values of the bias current were taken to be 1, 5 and 10 μA for suppressing the thermal disturbance caused by the Joule heat generation. The temperature of the TES microcalorimeter chip was controlled by using a PID controller in the temperature range from 160 to 200 mK with a 5 mK step. **Fig. 4** shows obtained R-T characteristics. Although a steep growth of the electric resistance does not appear in **Fig. 4** owing to the wide step of the temperature increment, the phase transition region is found in the temperature region from 170 to 185 mK. The TES microcalorimeter chip is found to have the electric resistance of 50 mΩ in the normal conducting state.

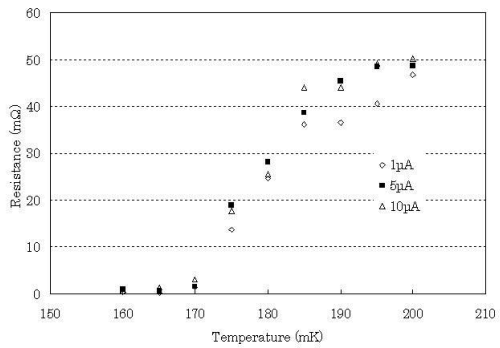

Fig. 4. R–T characteristic of the TES microcalorimeter with the absorber thickness of 5.0μm.

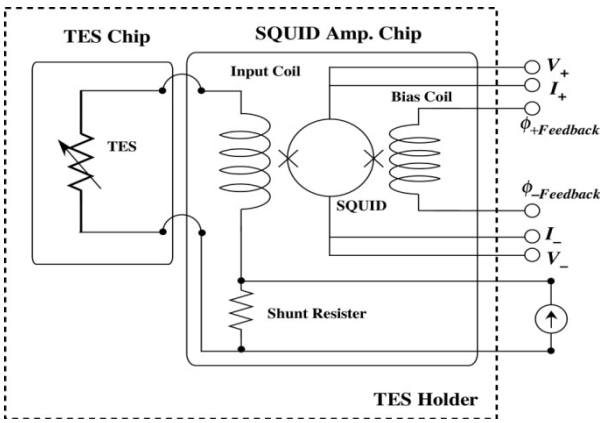

Fig. 5. Circuit diagram of the TES microcalorimeter and the SQUID amplifier chips.

The SQUID amplifier chip was placed on the TES holder with being adjacent to the TES chip for a reduction of a noise voltage generated in the wirings connected to the SQUID input. **Fig. 5** shows a circuit diagram of the TES microcalorimeter and the SQUID amplifier. A constant bias current was supplied to the TES-SQUID circuit from a precise current source outside the refrigerator, while the TES microcalorimeter was biased with a constant voltage generated by a shunt resistance of 7 mΩ.

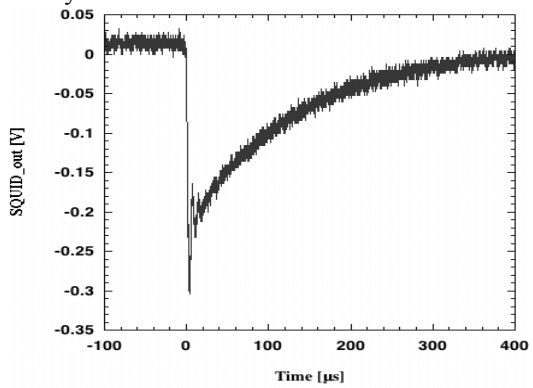

Fig. 6. Voltage signal pulse of the TES microcalorimeter in detection of LX-ray photon emitted from ^{241}Am source.

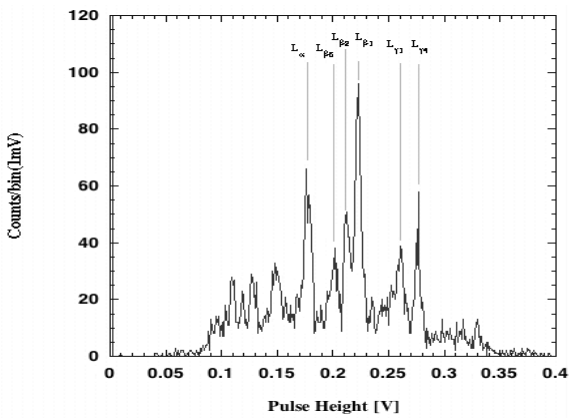

Fig. 7. The pulse height distribution of detection signal pulses of LX-ray photons emitted from ^{241}Am source.

An ^{241}Am source was placed in front of the TES microcalorimeter. The intensity of the ^{241}Am source was 3.7 MBq. The surface of the ^{241}Am source was covered with a polyimide tape with sufficient thick for stopping α particles. Voltage signal pulses of the SQUID amplifier were observed at the mixing chamber temperature of 120 mK by supplying the bias current of 600 μA as shown in **Fig. 6**. The rise- and decay time constant of the signal pulses are 3 and 160 μs, respectively. The decay time constant of 160 μs implies the electrothermal feed back operation of the TES microcalorimeter. **Fig. 7** shows a pulse height distribution of the voltage signal pulses processed through a low-pass filter with the cut-off frequency of 50 kHz. A vertical axis indicates the number of counts of a pulse height within the bin-width of 1 mV. Peaks in **Fig.7** are labeled with corresponding LX-ray photons by referring the LX-ray energy emitted from ^{241}Am listed in **Table 1**. The signal

current generated by the TES microcalorimeter is evaluated to be 2.5 μA / 10 keV by using a conversion gain of the SQUID amplifier. In the pulse height distribution, a poor energy resolution may be caused by insufficient reduction of various noise contributions in the liquid-helium-free ^{3}He-^{4}He dilution refrigerator. However, the TES microcalorimeter with the 5.0 μm thick absorber was demonstrated to operate the detection of LX-ray photons emitted from the ^{241}Am source.

V. Conclusion

The TES microcalorimeter with a Au absorber of 5.0 μm thick was fabricated for the energy dispersive measurement of LX-ray photons emitted from transuranium elements. The TES microcalorimeter and The SQUID amplifier chips were cooled by operating the liquid-helium-free ^{3}He-^{4}He dilution refrigerator with loading the GM cooler. The TES and SQUID chips suffered from mechanical vibrations induced by a reciprocating motion of the displacer of the GM cooler. Detection signals of LX-ray photons emitted from ^{241}Am source were observed by operating the TES microcalorimeter in severe noise environment induced by mechanical vibrations.

Acknowledgement

The authors would like to thank K. Kimura, T. Yasumune, H. Arakawa, Y. Nagafuchi and T. Masuda, for their support on our experiments. This work is supported in part by Grant-in-Aid for Scientific Research (A) (18206098) of the Japan Society for the Promotion of Science and the JAEA Cooperative Research Scheme on the Nuclear Fuel Cycle.

References

1) Lepy M. C., et al, Nucl. Instrum. Methods. Phys. Res. A353 (1994) 10-15
2) Moseley S. H., et al, J. Apple. Phys. 56 (1984) 1257

Journal of NUCLEAR SCIENCE and TECHNOLOGY, Supplement 5, p. 526–529 (June 2008)

Study of Recoil-Proton-Detector System Using Organic and Inorganic Scintillators for High Energy Neutron Measurement

Tsuyoshi Kajimoto[1*], Hiroyuki Arakawa[1], Shusaku Noda[1], Takehito Watanabe[1], Nobuhiro Shigyo[1], Kenji Ishibashi[1], and Robert C. Haight[2]

[1]*Kyushu University, 744 Nishi-ku, Motooka, Fukuoka 819-0395, Japan*
[2]*Los Alamos National Laboratory, Los Alamos, NM 87545, USA*

An optimized design for a recoil-proton-detector system is studied to measure (n, xn) cross sections of incident energies up to 300 MeV. The detector system is composed of a radiator to convert a neutron into a recoiled proton and a phoswich-type detector to detect the recoiled proton. The radiator is made of an NE213 liquid organic scintillator. The phoswich-type detector includes a BGO scintillator surrounded by an NE102A plastic scintillator. Optimal design is investigated by varying dimensions of the radiator and the phoswich detector. Calculations of detector properties are performed by the PHITS. The detector system is shown to have a capability to measure (n, xn) cross sections effectively.

KEYWORDS: recoil proton detector, neutron, radiator, phoswich-type detector, PHITS

I. Introduction

Evaluated nuclear data is important to research and development of spallation neutron sources and accelerator-driven systems. Nuclear data are evaluated by determining internal parameters of models to reproduce experimental values. Cross sections of proton incidence[1–3] have been measured in large energy ranges from 10-30 MeV to 3 GeV. However, the number of cross section data on neutron incidence is much less than that on proton incidence. In the energy region grearer than 100 MeV, cross sections of neutron incidence have almost never been reported yet.[4] Most nuclear data on neutron incidence have been evaluated by using calculation model parameters of proton incidence. Therefore, evaluated nuclear data on neutron incidence above 100 MeV need to be compared with experimental data.

A neutron-incident-neutron-production (n, xn) cross section using a continuous-energy neutron source has been measured at the WNR facility of the Los Alamos Neutron Science Center (LANSCE). At incident neutron energies greater than 100 MeV, a phoswich-type[5] recoil-proton-detector system has been tested. [6] The detector system is composed of a polyethylene radiator and a phoswich-type detector comprising a NaI (Tl) and plastic scintillators as the core and the surrounding materials, respectively. Cross section measurements using the detector system needed a long time to obtain a sufficient number of events because the detector system had low measurement efficiency.

In this paper, the optimal design for a high-energy neutron-detector system with a capability of neutron measurement up to 300 MeV is studied. The detector system has a structure similar to that of the former system. We search for the optimal design by varying dimensions on a radiator and a phoswich detector. Moreover, the feasibility of the detector system for measuring the (n, xn) cross section is discussed when simulating (n, xn) cross section experiment.

II. Detection Principle and Material of Detector

The detector system includes a radiator and a phoswichtype detector. A schematic of the detector system is shown in **Fig. 1**. The measurement principle is that an incident neutron is converted into a recoiled proton in a radiator, and the energy of the recoiled proton is measured by a phoswich-type detector. An NE213 liquid organic scintillator is used as a radiator, and a phoswich-type detector is adopted to the construction of a BGO scintillator surrounded by a 1.0 cm thick NE102A plastic scintillator.

To discriminate events by protons recoiled in the radiator, a scintillator is appropriate as a radiator material to obtain a signal from the radiator. The NE213 liquid organic scintillator is introduced to reduce the energy loss caused by nuclear reaction in the radiator and increase the number of hydrogen. Since BGO scintillator has a larger density, the detector system has smaller dimensions and a larger solid angle than those of the NaI (Tl) scintillator.

The unfolding method is applied to analyses of the (n, xn) cross section. If the detector response function has a peak, then the unfolding process is simplified. The peak appears in the response function while discriminating events which recoil protons fully stop in the BGO scintillator from events escaping from the BGO scintillator. It is possible to apply the phoswich structure, which is feasible for selectively analyzing full stop events, because the decay time of the BGO scintillator is much longer than that of the plastic scintillator.

*Corresponding Author, Tel. +81-092-802-3484, Fax. +81-092-802-3484, E-mail: kajimoto@kune2a.nucl.kyushu-u.ac.jp

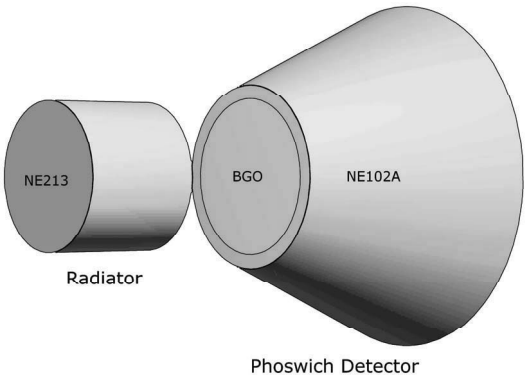

Fig. 1 Schematic of detector system.

III. Analysis of Recoil Protons from Radiator

Optimal designs of the detector system are searched by focusing attention on the number of protons produced in the radiator. The calculations are performed by the PHITS,[7] which is a three-dimensional Monte Carlo simulation code. For the sake of simplicity, the radiator has a cylinder shape and the phoswich-type detector has the shape of a sliced cone. The simulations are implemented without placing a veto and a ΔE detectors. Analyses for 300 MeV neutrons are carried out because the maximum incident neutron energy is the most important in this study.

Properties of recoil protons produced in a radiator are observed on the energy distribution and the number of recoil protons crossing the incident plane of the BGO scintillator by perpendicularly irradiating the radiator with a 300 MeV neutron beam. The neutron beam has a circular cut-plane equal to the radiator radius. In the calculation, the radiator is treated to examine characteristics of recoil protons. The optimization is carried out by varying dimensions of the radiator radius, R_r, and thickness, T_r, a distance D from the radiator to the phoswich-detector incident plane, and the BGO scintillator radius, R_b, at the incident plane. The variation ranges of dimensions and the top view of the detector system are shown in **Table 1** and **Fig.** 2, respectively. Energy distributions for recoil protons are shown in **Fig. 3**. A peak is observed at a slightly lower energy than the incident energy. The peak is attributed to forward elastic scattering of hydrogen.

The number of recoil protons is one of the essential factors used to improve neutron-detection efficiency because the number of protons corresponds to neutron detection efficiency. In measurement of (n, xn) cross sections, the number of neutrons incident upon the radiator changes according to the solid angle of the radiator. The solid angle depends on radiator radius and distance from the sample to the radiator. The distance is uncertain because collisions of neutrons with protons may occur anywhere in a radiator. For simplicity, the distance is determined by regarding points as the center of the radiator.

The radiator thickness contributes to the solid angle. The solid angle is derived from the half thickness of the radiator and the distance between the sample and the incident plane of the radiator. The distance from the sample to the incident

Table 1 Dimensions of elements of detector system.

Variation Element	Minimum[cm]	Maximum[cm]
R_r	1.5	6.5
T_r	1.0	13.0
D	0.0	10.0
R_b	1.0	10.0

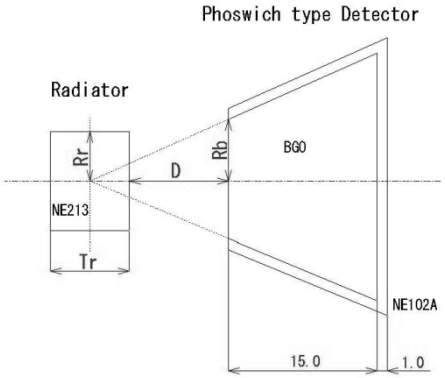

Fig. 2 Top view of detector system.

plane of the radiator is defined as the same value as that obtained in an experiment.[8] Therefore, the solid angle is obtained from the radiator radius and thickness. The effective neutron-detection efficiency is derived from the product of the neutron-detection efficiency and the solid angle for the radiator. The effective neutron-detection efficiency in the case with the R_r and T_r held constant is indicated in **Fig. 4**. Since it is possible to measure most protons crossing an incident plane of the BGO scintillator, which have various energies, response functions of the detector system depend on the proton energy distributions. In analyses of (n, xn) cross sections, the unfolding method needs to be introduced to search the neutron flux from the sample. To simplify the unfolding method, a method for evaluating peaks of proton energy distributions is needed. A Gaussian form is not suitable to fit the peak because the shape of the peak differs from that of a Gaussian form. In addition, the proton energy distributions have various spectra, as shown in **Fig. 3**.

A method to evaluate peaks is proposed for all proton energy distributions. The trend of a peak is sharper as the fraction of the peak area to the total area of the proton energy distribution is larger. The method is introduced to calculate the ratio of the area by adding the proton energy distribution from the high-energy region to the total area of the proton energy distribution. The recoil proton energy when the ratio is equal to 0.5 is used as the index of the method. The index in the case where the R_r and T_r are held constant is presented in **Fig. 5**.

The optimal design is determined by the evaluated value and the effective neutron-detection efficiency. The condition of the optimization is that dimensions of the detector have the highest effective neutron-detection efficiency when the index is greater than 250 MeV. As a result, the R_r, T_r, D, and R_b are 5.5, 9.0, 10.0, and 6.0 cm, respectively. The maximum energy of recoil protons produced in the radiator is 300 MeV

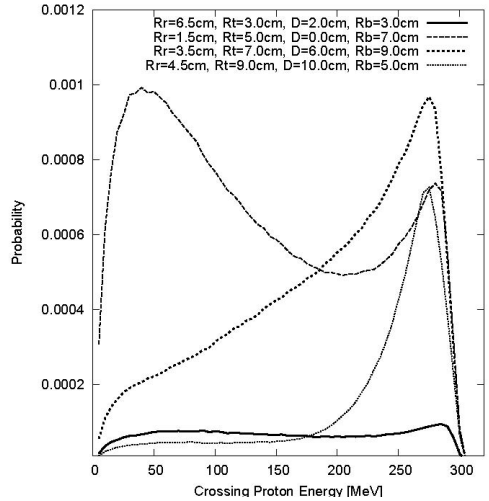

Fig. 3 The energy distribution for the proton crossing the incident plane of the BGO scintillator

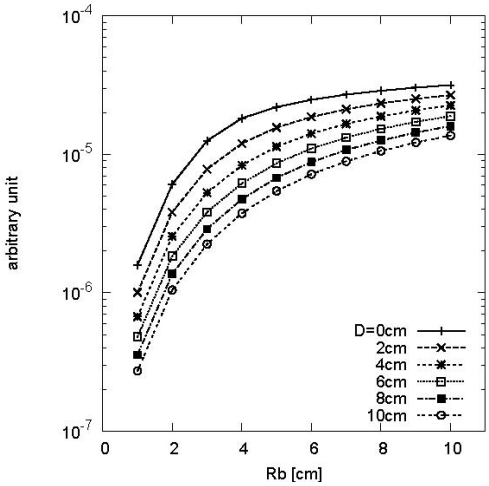

Fig. 4 The effective neutron detection efficiency in the case of R_r =3.5, T_r =9 cm

when irradiating the radiator with 300 MeV neutrons. The BGO scintillator needs to have sufficient length to fully stop 300 MeV protons. Hence, 15 cm is chosen as the length of the BGO scintillator. To detect more protons, the shape of the phoswich-type detector has a taper. The gradient of the taper is dependent on the neutron detection efficiency including the phoswich-type detector. The gradient of the taper is determined by connecting the center of the radiator and the edge of the BGO scintillator incident plane with a straight line, as shown in **Fig. 2**, because points at which recoil protons are produced in the radiator are at the center of the radiator in the derivation of the solid angle.

The neutron-measurement efficiency of the optimized detector system for full stop particles is calculated by the PHITS. The neutron-measurement efficiency of the optimized detector system and that of the existing NaI (Tl) phoswich detector system calculated by the PHITS is shown in **Fig. 6**. In the energy region less than about 80 MeV, the neutron measurement efficiency of the optimized detector system is low relative to that of the NaI (Tl) phoswich detector system. This is due to using the radiator of the

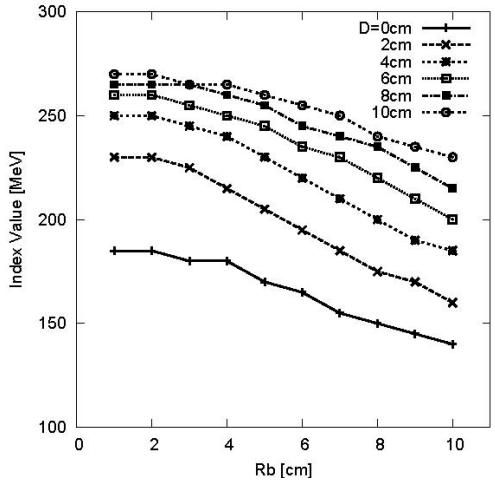

Fig. 5 Index value of peak in case of R_r = 3.5, T_r = 9 cm.

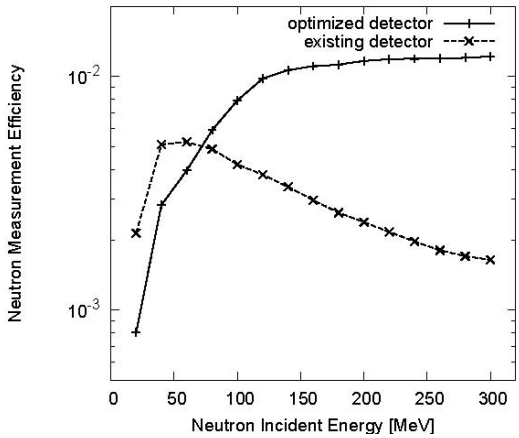

Fig. 6 Neutron-measurement efficiency of optimized detector system and that of NaI (Tl) phoswich detector system[5] calculated by PHITS.

optimized detector system, which is thicker than that of the NaI (Tl) phoswich detector system. That is because more recoil protons are stopped in the radiator in the case of low-energy incident neutrons and using a thicker radiator. In the energy region greater than 100 MeV, the optimized detector system has a larger neutron-measurement efficiency than that of the NaI (Tl) phoswich detector system. Thus, the optimized detector system is applicable to measuring neutrons that have energies from 100 to 300 MeV.

IV. Unfolding Test

To research feasibility of optimized detector system, the 300 MeV incident (n, xn) cross section measurement is simulated. Aluminum is used as a sample material because it is used as a construction material of buildings. The unfolding method is used for the derivation of the energy spectra of neutrons emitted from the sample at the (n, xn) cross section measurement. Energy spectra of the optimized detector system obtained by neutrons emitted from the sample and the response functions of the optimized detector system are needed for the unfolding test.

Calculations of the response functions are performed by irradiating the radiator of the optimized detector system with

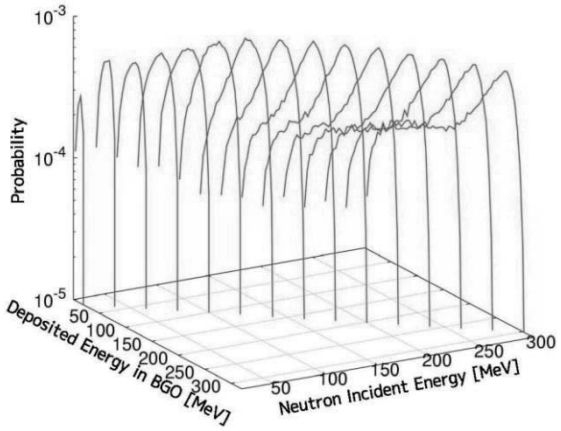

Fig. 7 Response functions of detector system.

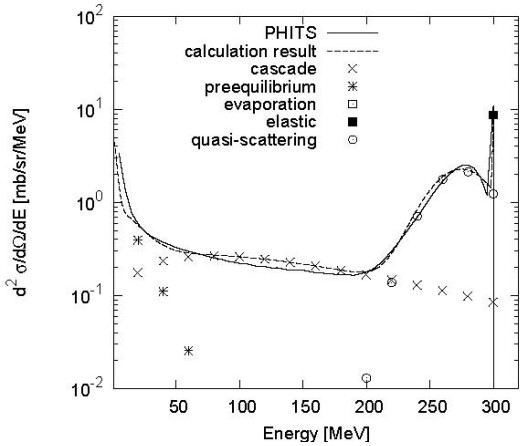

Fig. 8 300 MeV (n, xn) double-differential cross sections for aluminum calculated by simulating experiment and PHITS.

a neutron beam. Response functions are regarded as the deposited energy distribution in the BGO scintillator when recoil protons enter the scintillator. Only the recoil protons fully stopped in the BGO scintillator are discriminated by eliminating events with the deposited energy in the NE102A plastic scintillator of the phoswich detector. Response functions are calculated by varying neutron incidence energy from 20 to 300 MeV at intervals of 20 MeV. Response functions are shown in **Fig. 7**. In the experiment, the detector system was set at an angle of 15 degrees from the sample.[8] In the calculation of response functions, the response of the optimized detector system to neutrons from the sample is calculated by irradiating the center of the sample with a 300 MeV neutron beam.

The energy spectra of emitted neutrons are derived from unfolding the energy spectrum obtained by neutrons emitted from the sample. For the unfolding, the energy spectrum of neutrons emitted from the sample is,

$$\begin{pmatrix} \vdots \\ \phi_\xi \\ \vdots \end{pmatrix} = \begin{pmatrix} \ddots & \vdots & \vdots \\ \cdots & R_{\xi,E} & \cdots \\ \vdots & \vdots & \ddots \end{pmatrix} \cdot \begin{pmatrix} \vdots \\ \rho_E \\ \vdots \end{pmatrix} + \begin{pmatrix} \vdots \\ R_{\xi,E_{in}} \\ \vdots \end{pmatrix} \cdot \rho_{el}, \qquad (1)$$

where ϕ_ξ, $R_{\xi,E}$, $R_{\xi,E_{in}}$, and ρ_E stand for the response of the detector system to neutrons from the sample, response function matrix, a response function at the same incident energy as that when irradiating a sample with the neutron beam, and the energy spectra of neutrons emitted from the sample, respectively. The symbol ρ_{el} is the component of elastic scattering. Seeking the value of the ρ_{el} is difficult, so that value is treated as a constant.

The following moving source model[9] is used for the ρ_E.

$$\left(\frac{d^2\sigma}{d\Omega dE}\right) = \sum_{i=1}^{3} pA_i \exp\left[-\left(\frac{E+m-p\beta_i\cos\theta}{\sqrt{1-\beta_i^2}}-m\right)/T_i\right] + A_G \exp\left[-\frac{(E-E_G)^2}{\sigma_G^2}\right] \qquad (2)$$

where quantities E, p, and m are the kinetic energy in the laboratory system, the momentum of an emitted neutron in the laboratory system frame, and the neutron mass, respectively. Three components of i = 1 to 3 correspond to individual processes of the cascade, the preequilibrium, and the evaporation, respectively. The last term of **Eq. 2** indicates the element for the quasi-scattering. Symbols A_i, β_i, and T_i are called the amplitude, the velocity, and the temperature parameters of components i, respectively. The A_G, E_G, and σ_G are adjustment parameters for the quasi-scattering. The quasi-scattering includes quasi-elastic and quasi-inelastic scatterings.

In the process of unfolding, (n, xn) double-differential cross sections are parameterized using the moving source model running a least mean-square approximation program. Results of the unfolding test with respect to four components and the 300 MeV incident (n, xn) double-differential cross sections for aluminum calculated using the PHITS are indicated in **Fig. 8**. Good agreements are seen between the result of the unfolding test and the calculated data.

V. Summary

The optimal detector system to measure (n, xn) cross sections is searched by varying of dimensions of the detector system. The applicable energy range to measure neutrons is from 100 to 300 MeV. The optimized detector system has up to seven times as much neutron-measurement efficiency as that of the NaI (Tl) phoswich detector system. By simulating the (n, xn) cross section experiment and analyses with the unfolding method, it has been shown that the detector system has the feasibility for measuring the (n, xn) cross sections efficiently. For further work, another index for simpler unfolding method is desired to evaluate a peak of the recoil proton energy distribution.

References

1) K. Ishibashi et al., J. Nucl. Sci. Technol., 34, 529, (1997)
2) S. Leray et al., Phys. Rev., C65, 044621, (2002)
3) W.B. Amian et al., Nucl. Sci. Eng., 112 78, (1992)
4) S. Kunieda et al., AIP Conf. Proc. 769, 1058 (2005)
5) N. Shigyo et al., AIP Conf. Proc. 769, 924 (2005)
6) N. Shigyo et al., Proceedings of ISORD3, 41, (2005)
7) H. Iwase et al., J. Nucl. Sci. Technol., 39, 1142 (2002)
8) T. Watanabe et al., AIP Conf. Proc. 769,1062 (2005)
9) H. Kitsuki et al., J. Nucl. Sci. Technol., 38, 1 (2001)

Journal of NUCLEAR SCIENCE and TECHNOLOGY, Supplement 5, p. 530–533 (June 2008)

A Simulation Study on Spatial Resolution and Noise Power Spectra of a URA-based Multi-hole Collimator in a Small Gamma Camera

Hosang JEON, Hyunduk KIM, Chae Hun LEE, and Gyuseong CHO*

Department of nuclear and quantum engineering, KAIST, Yu-sung gu, Daejeon, Korea

Presently the gamma scintillation camera is widely used in various industrial, environmental and medical diagnostic fields. Two major performance parameters, spatial resolution and noise, are primarily determined by the collimator. The imaging performance of the simple collimator, single pin-hole, and a coded-aperture collimator, uniformly redundant array (URA), are analyzed in this study. Though parallel-hole collimators are used in some medical applications, in principle its performance is equivalent to that of a single-hole collimator and moreover its use is limited to the near-field application only. A coded aperture imaging (CAI) techniques have been proposed for gamma-ray imaging especially for far-field applications such as the astrophysics study or environmental monitoring in order to overcome these limitations of a pin-hole or a parallel-hole collimator.

In this study, the simulated gamma images using a monte carlo code, MCNP, were acquired with two different energy windows and two-type and four-different collimators. For the evaluation of spatial resolution and noise power spectra, modulation transfer function (MTF) and normalized noise power spectra (NNPS) were computed for all images. In the result, we found that MTF and NNPS can reflect the different properties of different gamma camera systems.

KEYWORDS: gamma camera, URA, MTF, NNPS, collimator, energy window, performance evaluation

I. Introduction

Recently the gamma scintillation camera is widely used in various industrial, environmental and medical diagnostic fields. The concerns about precise and effective evaluation of gamma imaging system performance increase as the components of those systems improve. Evaluation of gamma imaging system performance has a long history. The spatial resolution of an imaging system can be described by the full width at half maximum (FWHM) from the line spread function (LSF). The FWHM is widely used to measure the spatial resolution of a gamma scintillation system.[1] However, the FWHM has the possibility to ignore the effect of scattered radiation on spatial resolution. An alternative way to describe resolution is to use modulation transfer function (MTF). The spatial resolution can be described in spatial frequency domain by MTF.[2]

The noise power spectrum (NPS) of a scintillation camera can be described in the viewpoint of stochastic and non-stochastic terms.[3] The non-stochastic term dominates the results in the lower spatial frequencies. The stochastic term is the constant level of frequency independent white noise. When the spatial frequency increases, the total noise power spectrum decreases and approaches the level of white noise.[4]

In gamma imaging systems, the collimator is an essential component to produce images of radiating objects. The basic and widely-used types of collimators are generally pin-hole and parallel-hole. Additionally, the coded-apertures are an alternative type of collimators. Coded apertures were initially developed as a way of improving the signal to noise ratio (SNR) of collimating imagers and have already been applied in the past, mainly in astronomy and space applications, but also in physics, and nuclear medicine.[5]

In this study, the performance evaluation of a simulated gamma camera system with three pinhole (1, 2, 4mm-hole diameter) collimators and a coded aperture collimator using uniformly redundant array (URA) was performed.

II. Material and Methods

1. Gamma Camera System

The performance of a gamma camera system was described as shown in **Fig. 1** using monte carlo simulation program, MCNP. The properties of components of the gamma camera system totally influence on the image quality. In this simulation study, the influence caused only by collimators and a scintillator were studied. The position-sensitive photo-multiplier tube (PSPMT) and signal post-process were assumed as ideal processes.

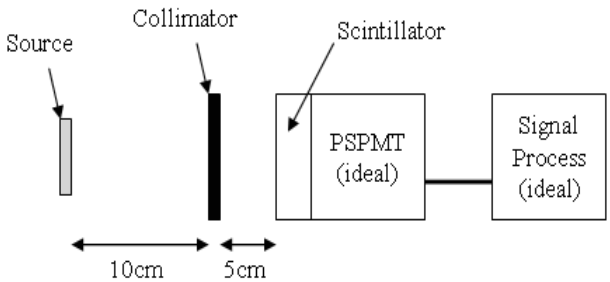

Fig. 1 Geometry for the imaging performance simulation of a gamma camera system

*Corresponding Author, Tel No: +82-42-869-3821, Fax No: +82-42-869-3810, E-Mail: gscho@kaist.ac.kr

The PSPMT is widely-used component in small gamma camera systems instead of PMTs array. The scintillator is a sodium-iodide single crystal with 100mm×100mm×10mm dimension.

2. Source

The gamma energy of sources was 140keV, which is the energy of Tc-99m. Two kinds of source geometry were used. The one is a cylinder (30mm-long and 1mm-diameter) for the acquisition of LSFs. The other is a disk (50mm-diameter and 1mm-thickness) for the acquisition of uniform flood images.

3. Collimator

The pinhole collimators with three different hole diameter (1, 2, 4mm) and a coded aperture collimator using URA were used to produce gamma images as shown in **Fig. 2**. All collimators were designed with lead (3mm thickness) and have 60mm×60mm dimension.

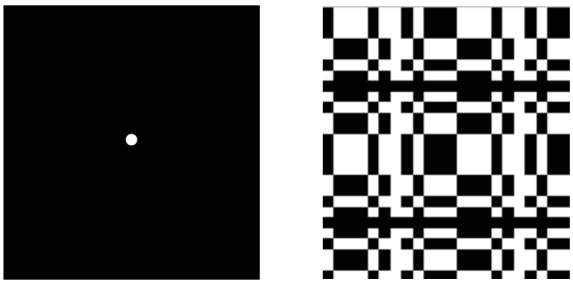

(a) (b)

Fig. 2 Geometry of (a) the pinhole and (b) URA collimator

The URA-based coded aperture had been designed by Fenimore and Cannon.[6] The governing equation of producing URA is

$$A(I,J)=\begin{cases}0 & \text{if } I=0\\ 1 & \text{if } I\neq 0, J=0\\ 1 & \text{if } C_r(I)C_s(J)=1\\ 0 & \text{if otherwise}\end{cases} \quad (1)$$

where

$$C_r(I)=\begin{cases}1 & \text{if } 1\le x<r \ \ (x:\text{integer},\ I=\text{mod}_r\, x^2)\\ -1 & \text{if otherwise}\end{cases} \quad (2)$$

The matrix A means the array of coded aperture and 1 is hole and 0 is opaque. The basic array used in this study had dimensions r=13 by s=11. The mosaic of a basic pattern was used as shown in **Fig. 2(b)**. The decoding process can be easily performed using array G, which is

$$G(I,J)=\begin{cases}1 & \text{if } A(I,J)=1\\ -1 & \text{if } A(I,J)=0\end{cases} \quad (3)$$

4. Energy Window

In the output signal of gamma camera, the wide energy spectrum is observed because of the interacting properties between gamma rays and materials though mono-energetic gamma rays are emitted from gamma sources. Therefore, band-pass filtering of output signal by the energy window influence the image quality. In this study, the comparison of image qualities between 100% (0~150keV) and 15% (130~150keV) energy window was performed.

5. MTF Computation

The line images were acquired using a cylinder source. The major steps for obtaining MTF were as follows.

(a) **LSF acquisition:** The line profile containing maximum pixel value was acquired and tail data below 10% of peak value of that profile was cut-off and linear extrapolation was performed to condition the data for spectral estimation.[7]

(b) **MTF computation**: The MTF was obtained from the fast fourier transformation (FFT) of the LSF and normalization to unity at zero spatial frequency.

6. NNPS Computation

The normalized NPS described the normalized spectral decomposition of the variance of pixel-to-pixel fluctuation[8] The uniform flood images were acquired using a disk source. We developed the program for NNPS computation using Matlab™. The major steps were as follows.

(a) **ROI definition:** The ROI is only 17×17 pixels at center. The edge data was ignored for the statistical reliability.

(b) **Normalization:** The pixel values at the ROI were converted to relative noise by dividing data by their mean value.

(c) **2D NNPS computation:** The NNPS of each ROI was obtained from the two-dimensional FFT of the data using the formula[8]

$$NNPS(u,v)=\frac{p_x p_y}{N_x N_y}E\left\{\frac{\left|FFT^{2D}\left\{\Delta d_{n_x n_y}\right\}\right|^2}{\overline{d^2}}\right\} \quad (4)$$

where p is detector pixel dimension, N is ROI dimension, and d is the pixel value.

(d) **1D NNPS computation:** For an easier comparison, one-dimensional NNPS was computed by averaging the 2D NNPS spectrum samples over circular regions of the same width and increasing radius in the frequency space.[9]

III. Results and Discussion

1. Spatial Resolution Analysis

The MTF curves with four-different collimators and two-different energy windows were given at **Fig. 3**. Using 100%

energy window, the MTF values are: 1mm-pinhole; 0.98 at 0.6 lp/cm and 0.94 at 1.2 lp/cm; 2mm-pinhole; 0.95 at 0.6 lp/cm and 0.80 at 1.2 lp/cm; 4mm-pinhole; 0.84 at 0.6 lp/cm and 0.47 at 1.2 lp/cm; URA; 0.91 at 0.6 lp/cm and 0.67 at 1.2 lp/cm. The spatial resolution, MTF value, was inversely proportional to the diameter of pinhole at the range of 0.5~2 lp/cm. We found that the spatial resolution of URA was equivalent to that of 3mm-diameter pinhole collimator. It was verified that an ideal URA collimator would not affect the MTF, as verified by Fenimore.[10] But the real URA collimator affected the measured MTF. The MTF decrease of a URA collimator was caused by scatter effect at the edges of 286 holes.

The energy window of the gamma camera system generally affects the MTF values except using URA collimator. The narrow window contributes to better spatial resolution because of the decrease of influence of scatter effect on the resultant image. These scatter effect are mainly observed in the scintillator. The comparison of MTF curves between 100% and 15% energy window were shown in **Fig. 3**. The MTF of 15% window was higher than that of 100% window except URA because of using narrow window. We found that gamma camera resolution with a URA collimator was little affected by energy window because no MTF difference was observed between different energy windows.

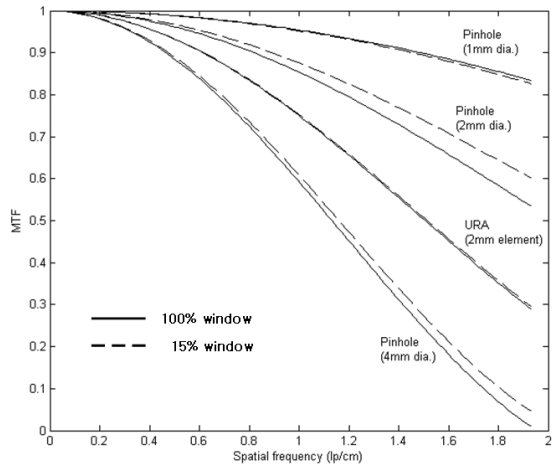

Fig. 3 Simulated MTF curves with four different collimators and two different energy windows

2. Noise Analysis

The different patterns of noise power spectra were observed for the different type collimators, pinhole and URA. In the range of 0.5~5 lp/cm, the noise power spectra of pinhole systems are flat as shown in **Fig. 4(a)** and **4(b)**. It means that the stochastic noise component is dominant at the pinhole systems. The stochastic noise of the gamma camera in this study was almost totally Poisson because of digital-type images. So the magnitude of noise decreases as pinhole diameter increases. Under the poisson assumption, the relationship between average count level and NNPS was given as follows[4]

$$NNPS(u,v) = \frac{p^2}{x} \tag{5}$$

where p is detector pixel pitch and x is average count level.

The average magnitude of noise spectra decreases as the width of energy window decreases. This means that narrow energy window contributes to lower scatter effect as previous description. The decreasing ratios of average noise are: 1mm-pinhole; 0.25; 2-mm pinhole; 0.35; 4-mm pinhole; 0.27.

In the case of URA collimator system, higher magnitude of noise was observed at lower spatial frequency. The difference of noise patterns between pinhole and URA system were caused by the existence of non-stochastic noise and higher efficiency of URA collimator. At lower frequency, non-stochastic noise component are more prominent at the URA collimator because of complex geometry of URA. Meanwhile, the stochastic noise component dramatically decreases because of higher count level. So the total noise power spectra of a URA collimator system were given as **Fig. 4**.

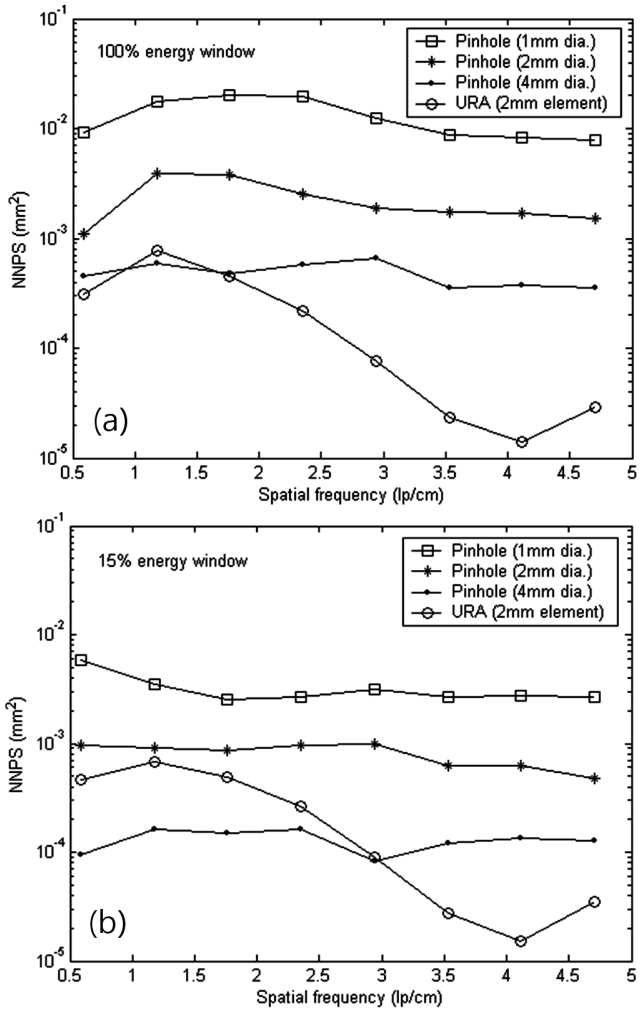

Fig. 4 Simulated NNPS curves with four different collimators using (a) 100% and (b) 15% energy window

IV. Conclusions

The objective and effective evaluation of imaging performance is more important because of technical development of gamma camera system. In this study, we computed two factors, the modulation transfer function and normalized noise power spectra, of a simulated gamma camera system with 4-different collimators. We found that these factors reflect the properties of each system quantitatively and effectively.

The ratio of output signal to noise ratio to input signal to noise ratio, detective quantum efficiency (DQE), is widely used for the evaluation of x-ray medical imager. This DQE can be obtained by simple computation with MTF, NNPS. Recently, an attempt of evaluating the performance of gamma camera systems with DQE computation was published by Starck.[4] The result of this study can be useful reference for DQE analysis of gamma camera.

Acknowledgement

This work was supported by the innovative technology center for radiation safety (iTRS), South Korea.

References

1) NEMA, "Performance measurements of scintillation cameras", Standard Publication no.Nu1-2001
2) Tyson R.K., Amtey S.R., "Practical considerations in gamma camera line spread function measurement", Med. Phys. 5 480-484
3) L.W. Grossman, M.P. Anderson, R.J. Jennings, J.B. Kruger, S.J. Lukes, R.F. Wagner, C.P. Warr, "Noise analysis of scintillation camera images: stochastic and non-stochastic effects", Phys. Med. Biol., 1986, Vol. 31, No 9, 941-953
4) S.A. Starck, M. Bath, S. Carlsson, "The use of detective quantum efficiency (DQE) in evaluating the performance of gamma camera systems", Phys. Med. Biol. 50(2005), 1601-1709
5) R. Accorsi, F. Gasparini, R.C. Lanza, "A coded aperture for high-resolution nuclear medicine planar imaging with a convensional anger camera: Experimental results", IEEE transactions on nuclear science, VOl.48, No.6, 2001, 2411-2417
6) E.E. Fenimore, T.M. Cannon, "Coded aperture imaging with uniformly redundant arrays", Applied Optics, Vol.17, No.3, 1978, 337-347
7) J.T. Dobbins, D.L. Ergun, L. Rutz. D.A. Hinshaw, H. Blume, D.C. Clark, "DQE(f) of four generations of computed radiography acquisition devices", Med. Phys. 22(10), 1995, 1581-1593
8) Ian A. Cunningham, "Ch2. Applied linear-systems theory", Handbook of medical imaging, vol. 1
9) G. Borasi, A. Nitrosi, P. Ferrari, D. Tassoni, "On site evaluation of three flat detectors for digital radiography", Med. Phys.30(7), 2003, 1719-1731
10) E.E. Fenimore, "Coded aperture imaging: the modulation transfer function for uniformly redundant arrays", Applied Optics, Vol.19, No.14, 1980, 2465-2471

Journal of NUCLEAR SCIENCE and TECHNOLOGY, Supplement 5, p. 534–537 (June 2008)

Comparative Study of a CsI and a ZnSe(Te/O) Scintillation Detector's Properties for a Gamma-ray Measurement

Yun Ho CHO[1], Se Hwan PARK[2], Woo Gyo LEE[1], Jang Ho HA[2], Han Soo KIM[2], N. STARZINSKIY[3], Dong Hoon LEE[1], Sangsoo Park[4], and Yong Kyun KIM[1*]

[1]*Department of Nuclear Engineering, Hanyang University, Seoul, 133-791, Republic of Korea*
[2]*Korea Atomic Energy Research Institute, Daejeon, 305-353, Republic of Korea*
[3]*National Academy of Sciences of Ukraine, 60 Lenin Ave., Kharkov 61001, Ukraine.*
[4]*Department of Biomedical Engineering, Eulji University, Gyeonggi, 461-713 , Republic of Korea*

A ZnSe crystal based on a Ⅱ-Ⅵ compound semiconductor has various physical properties: electroluminescent, photoelectric, luminescent and scintillation. Activated ZnSe crystals are highly-efficient scintillators, and they are already being applied to the detecting units of a X-ray introscopy and a dosimetric system. ZnSe-based scintillators have a high absolute light output, and their radiation spectra matches well with the Si-photodiode spectral sensitivity.

The present study was performed by using a polished ZnSe and CsI(Tl). ZnSe is a low-density crystal(5.42 g/cm^3). The emission wavelength of ZnSe(Te) is 610 nm and ZnSe(O) is 592 nm. We have fabricated 10x10x1 mm and 10x10x2 mm ZnSe crystals in which the activators were doped with tellurium and oxygen. ZnSe and CsI crystals were mounted on a S3590-08 HAMAMATSU PIN photodiode and an R3479 HAMAMATSU PMT. Teflon tape as a reflector for the PIN photodiode and PMT. Gamma-ray spectrum measurements were performed by using ^{241}Am, ^{57}Co, ^{133}Ba and ^{137}Cs radio isotopes. We have compared the measured spectra of ZnSe and CsI under the same conditions.

KEYWORDS: ZnSe, scintillator, PMT, photodiode, pulse height spectrum

I. Introduction

An ideal behavior of a scintillator would be characterized by a proportionality between the energy deposited in the crystal and the number of scintillation photons. The measurement of the absolute light output of a scintillator is very complex and difficult. Photons created by nuclear radiation in the scintillator are affected by many processes that reduce their number before they are converted into photoelectrons in photomultipliers(PMT) or electron-hole pairs in Si photodiodes.[1)]

One of the recent important steps is development of a new type scintillator based on zinc selenide. Development of the scintillator ZnSe has effectively filled the gap in the "scintillator-photodiode" detector series for modern radiation detector.[2)] For example, scintillators based on ZnSe crystals have conversion efficiency of semiconductor scintillator ZnSe(Te) is 1.1-1.3 times higher, and radiation stability 3-4 orders higher as compared with crystals CsI(Tl).[2-4)] Now, the ZnSe scintillators based on the II-VI compound semiconductor doped with various activators were investigated.[5)]

In our study, we measured pulse height spectrum of ZnSe doped tellurium and oxygen in PMT, large area avalanche photodiode (LAAPD) and Si-PIN-Photodiode, and compared with spectra of ZnSe and CsI crystals.

*Corresponding Author, Tel No: +82-2-2220-2345, Fax No: +82-2-2296-2354, E-Mail: ykkim4@hanyang.ac.kr

II. Experiments

All the measurements were done with CsI(Tl), ZnSe(Te) and ZnSe(O) crystal. The ZnSe crystals were delivered from the national academy of sciences of Ukraine in two samples ZnSe(Te) and ZnSe(O) : They were doped tellurium and oxygen activator in ZnSe crystal. An over-view of all the crystals used is given in **Table 1**. The light collection efficiency is a function of the crystal size and its shape.

Table 1. Tested scintillators

Crystal	Activator concentration (mass %)	Size[mm^3]	Surface finish
CsI(Tl)	-	11x12x1.77	Polished
ZnSe(Te)	0.2	10 x 10 x 1	Polished
ZnSe(Te)	0.2	10 x 10 x 2	Polished
ZnSe(Te)	0.2	10 x 10 x 3	Polished
ZnSe(O)	0.02	10 x 10 x 1	Polished
ZnSe(O)	0.02	10 x 10 x 2	Polished
ZnSe(O)	0.02	10 x 10 x 3	Polished

The all samples were polished on both large surfaces, and the crystals were glued onto the PMT and LAAPD with RX 688 silicon grease of REXON Components, Inc.. The crystals were wrapped with several layers of white Teflon tape. We have also used a 630-70-73-510 window-less silicon LAAPD of the Advanced Photonix, Inc., 19 mm diameter R3479 photomultiplier tube of Hamamatsu and S3590-08 Si-PIN-photodiode of the Hamamatsu. The R3479 PMT has range from 185 nm to 650 nm, and wave-length of maximum response is 420 nm.

The preamplifier was used for CR-150-AC-BNC board and CR-110 charge sensitive preamplifier chip of the Cremate, Inc.. CR-110 preamplifier chip is low noise charge sensitive preamplifier for use with various types of radiation detectors including semiconductor detector, PIN-photo-diodes, avalanche photodiodes(APDs) and gas-based detectors.[6] Amplifiers were used ORTEC 572A amplifier with PMT and ORTEC 673 Spectroscopy amplifier with photo-diode. Multi channel analyzer was ORTEC 919E. To prevent radiation incidence on Si-PIN-photodiode, we manufactured and used lead collimator of 5 mm thick and with hole of 2 mm diameter. Light guide of 10 x 10 x 10 mm^3 size was manufactured with lucite, and lucite was polished on all surfaces.

III. Results

The main part of the measurements was carried out for ^{57}Co radiation source. To get the best possible pulse height spectrum, the gain and the shaping time constant on the amplifier were optimized for each scintillator. ZnSe(O) and CsI(Tl) were measured at 6 μsec, and ZnSe(Te) was measured at 10 μsec shaping time constant. Detailed technical characteristics of ZnSe can be found in Table 2.[7]

Table 2. Luminescence spectrum maximum λ_{max}, absorp-tion index α, decay time τ and absolute light output S of the ZnSe-based scintillators.

Scintillator	λ_{max}, nm	α, cm^{-1}	τ, μsec	S, Photon/MeV
ZnSe(Te)	640	0.08-0.15	30-80	Up to $7 \cdot 10^4$
ZnSe(O)	600	0.05	2-8	Up to $5 \cdot 10^4$
ZnSe(Cd)	620	0.1-0.15	5-20	Up to $4 \cdot 10^4$
ZnSe(Cd,Te)	635	0.1-0.15	40-100	Up to $6 \cdot 10^4$
ZnSe(O,Al)	605	0.1-0.15	3-15	Up to $5 \cdot 10^4$

1. PMT Experiments

To measure energy spectra of CsI(Tl) and ZnSe crystals, we used for the R3479 PMT of Hamamatsu. Spectra of ^{57}Co source were measured by CsI(Tl), ZnSe(Te) and ZnSe(O) crystals, and we compared with the each spectra. These measurements were carried out at gain of 200 and negative 1500 V. Scintillators have different decay times therefore we separately measured each scintillators. The spectra of ZnSe(O) and CsI(Tl) were measured at shaping time constant of 6 μsec, and ZnSe(Te) was measured at shaping time constant of 10 μsec, respectively.

In general quantum efficiency of bialkali photocathodes in PMT is about 25 % at 400 nm, and this is lower numerical value than quantum efficiency of PIN-photodiode.[8,9] The results of PMT measurement are shown in **Fig. 1**. We found energy peaks of ^{57}Co in spectra of ZnSe(O) and CsI(Tl) crystals, but the energy peaks in ZnSe(Te) were not found except 3 mm thick. The best responses were observed from ZnSe(O) of 2 mm and 3 mm thick.

These results indicate that ZnSe(O) has better response than ZnSe(Te) or CsI(Tl) at PMT, and 122.06 and 136.47 keV energy peaks from ^{57}Co source were not separated from the spectra of ZnSe crystals.

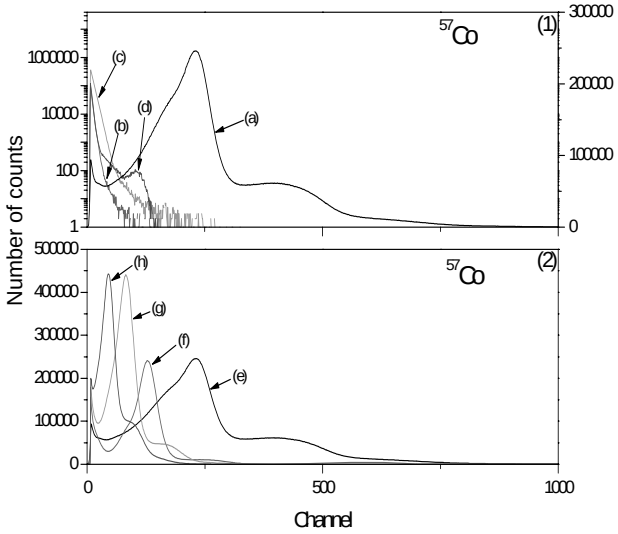

Fig. 1 Energy spectra of γ-rays from a ^{57}Co source measured with samples coupled to the R3479 PMT in the 572A amplifier. Activators of ZnSe(Te) and ZnSe(O) are 0.2 mass% and 0.02 mass%, respectively. (1) is log scale of spectra of ZnSe(Te) at 10 μsec and linear scale of spectrum of CsI(Tl) at 6μsec. (2) is linear scale of spectra of CsI(Tl) and ZnSe(O) at 6 μsec shaping time constant: (a) CsI(Tl), (b) ZnSe(Te) of 1 mm thick, (c) ZnSe(Te) of 2 mm thick, (d) ZnSe(Te) of 3 mm thick, (e) CsI(Tl), (f) ZnSe(O) of 1 mm thick, (g) ZnSe(O) of 2 mm thick and (h) ZnSe(O) of 3 mm thick.

2. LAAPD Experiments

The measurement of LAAPD carried out with the windowless 630-70-73-510 LAAPD of the Advanced Photonics, Inc.. 630-70-73-510 LAAPD has quantum efficiency of 69-77 % at 400nm, dark current of 110-269.4 nA and rise time of 11-16.2 ns.[10] The LAAPD was calibrated with 5.9 keV X-ray of ^{55}Fe source which was directly irradiated on active area of LAAPD. We used Teflon film of two layers as reflector. There experiments were carried out at positive 1800 V, gain of 100 and shaping time constant of 10 μsec. The sample crystals were coupled to a LAAPD with optical silicon grease of the Saint-Gobain.

Fig. 2 shows the energy spectra of ^{57}Co source measured with the ZnSe(Te) of 2 mm thick and ZnSe(O) of 1 mm and 2 mm thick crystals. In LAAPD experiment, we not measured ZnSe(Te) of 1 mm thick because energy peaks of ZnSe(Te) of 2 mm thick were not observed with LAAPD.

These results were indicated that ZnSe(O) has better response than ZnSe(Te), and ZnSe(O) of 2 mm thick has better light output than ZnSe(O) of 1 mm thick. With LAAPD, We measured decay time of ZnSe(Te) and had observed decay time of not less than 100 μsec. Therefore energy peaks of ^{57}Co source in ZnSe(Te) are not measured.

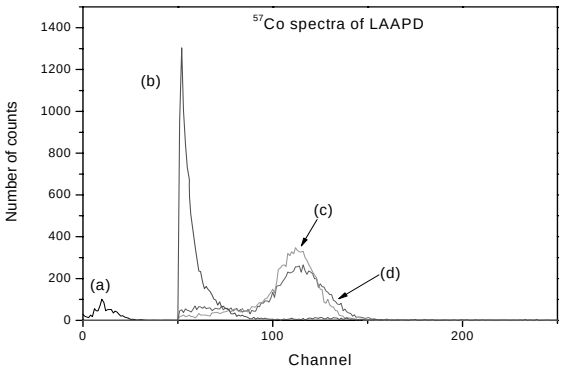

Fig. 2 Energy spectra of ^{57}Co by using a LAAPD. Activators of ZnSe(Te) and ZnSe(O) are 0.2 mass% and 0.02mass%, respectively. (a) noise of LAAPD, (b) ZnSe(Te) of 2 mm thick, (c) ZnSe(O) of 2 mm thick and (d) ZnSe(O) of 1 mm thick.

3. PIN-photodiodes Experiments

Quantum efficiency of 3590-08 PIN-photodiode is about 85 % at 540 nm.[9] With photodiode, we measured spectrum of ^{57}Co source with CsI, ZnSe(Te) and ZnSe(O), respectively. The spectrum was measured at 50 V and for live time of 10,000 sec. We manufactured lead collimator of 32□26.5 □5 mm^3 size with hole of 2 mm dia and lucite of 10□10□10 mm^3 size as light guide. Lead collimator and lucite light guide were prevent radiation from irradiating on PIN-photodiode. Refractive index of lucite is 1.5.

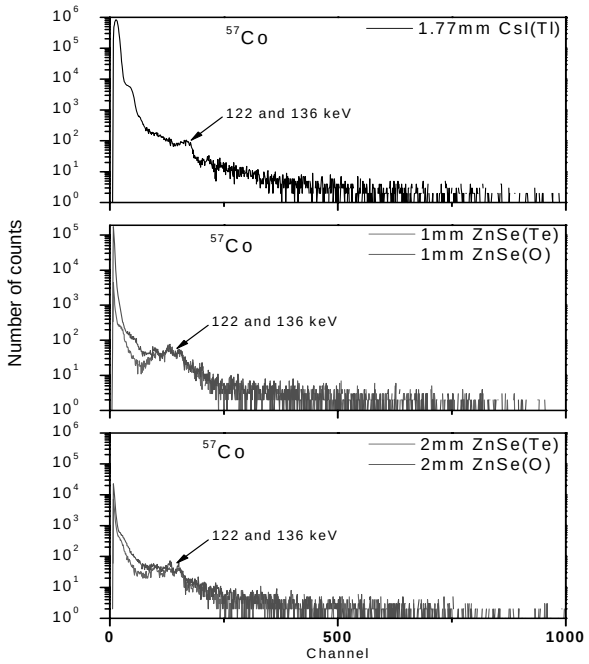

Fig. 3 Pulse height spectrum of γ-ray form a ^{57}Co source measured with CsI(Tl), ZnSe(Te) and ZnSe(O) crystal coupled to S3590-08 PIN-photodiode.

These results were shown in **Fig. 3**. The spectrum of CsI(Tl) was not separated for energy peaks of 122 and 136 keV of ^{57}Co source. This result was shown that CsI(Tl) has good light output, but the resolution of CsI(Tl) is not good. Spectra of ZnSe(Te) and ZnSe(O) were shown that the ZnSe-based scintillators have better resolution than CsI(Tl). However, light yield of used ZnSe(Te) and ZnSe(O) is not more than CsI(Tl). Thus energy peaks of ^{57}Co source were not clearly separated.

IV. Conclusions

Results form this study show that ZnSe(O) have substantial advantages for radiation detection in the 20-200 keV range as compared with CsI(Tl).

ZnSe-based scintillators have excellent properties of high conversion efficiency, low afterglow and good light yield. According to the earlier studies ZnSe(Te) exhibits a very high light output of the maximum 80,000 photons/MeV. However, measured light output of ZnSe(Te) is much lower about 40,000 photons/MeV than the 80,000 photons/MeV.[11,12]

The light collection efficiency is a function of the crystal size and its shape. It is affected by the self-absorption of the light in the crystal and by the reflector material used.[1] For increasing of thickness of ZnSe(O), light collection efficiency of ZnSe(O) was increased.

The obtained results for the ZnSe(O) scintillator have demonstrated the possibility for radiation detection coupled with PMT and PIN-photodiode.

Acknowledgement

This work was supported by the research fund of Hanyang University (HY-2006-N).

References

1) M. Moszynski, M. Kapusta, M. Mayhugh, D. Wolski and S.O. Flyck, "AbsoluteLight Output of Scintillators", IEEE, Trans. Nucl. Sci. **44[3]**, 1052 (1997).
2) A.A. Focsha, P.A. Gashin, V.D. Ryzhikov, N.G. Starzhinskiy, L.P. Gal'chinetskii and V.I. Silin, "Properties of semiconductor scintillators and combined detectors of ionizing radiation based on ZnSe(Te,O)/pZnTe-nCdSe structures", Optical materials, **19**, 213 (2002).
3) V. Ryzhikov, N. Starzhinskiy, L. Gal'chinetskii, P. Gáshin, D. Kozin and E. Danshin, "New Semiconductor Scintillators ZnSe(Te,O) and Integrated Radiation Detectors Based Thereon", IEEE, Trans. Nucl. Sci. **48[3]**, 356 (2001).
4) V. Ryzhikov,, G. Tamulaitis, N. Starzhinskiy, L. Gal'chinetskii, A. Novickovas and K. Kazlauskas, "Luminescence dynamics in ZnSeTe scintillators", J. of Luminescence, **101**, 45 (2003).
5) V. Ryzhikov, V. Chernikov, L. Gal'chinetskii, S. Galkin, E. Lisetskaya, A. Opolonin and V. Volkov, "The use of semiconductor scintillation crystals $A^{II}V^{VI}$ in radiation instruments", J. of Crystal Growth, **197**, 655 (1999).
6) Cremat catalog and http://www.cremat.com/CR-110.pdf.
7) W. G. Lee, Y. K. Kim, J. K. Kim, H. J. Seo, V. Ryzhikov, N. Starzhinskiy, O. Vyagin, K. Katrunov and O. Zelenskaya, "Particularities of ZnSe-Based Scintillatios for a Spectrometry of Charged Particles and Gamma Quanta", J. korean Phys. Soc. **48,** 47 (2006).

8) G. F. Knoll, *Radiation Detection and Measurement*, 3rd edition, Wiley, New York, 1999.
9) Hamamatsu catalog and http://jp.hamamatsu.com/resources/products /ssd/pdf/s3590_series_kpin1052e05.pdf.
10) M. Moszynski, M. Kapusta, D. Wolski, M. Szawlowski and W. Klamra, "Energy Resolution of Scintillation Detectors Readout with Large Area Avalanche Photodiodes and Photomultipliers", IEEE, Trans. Nucl. Sci. **45[3]**, 472 (1998)..
11) M. Balcerzyk, W. Klamra, M. Moszynski, M. Kapusta and M. Szawlowski, "Energy resolution and light yield non-proportionality of ZnSe:Te scintillator studied by large area avalanche photodiodes and photomultipliers", Nucl. Instr. And Meth., A **482**, 720 (2002).
12) V. Ryzhikov, L. Gal'chinetskii, K. Katrunov, E. Lisetskaya, V. Gavrilik, O. Zelenskaya, N. Starzhynskiy and V. Chernikov, "composite detector for mixed radiations based on CsI(Tl) and dispersions of small ZnSe(Te) crystals", Nucl. Instr. And Meth., A **540**, 395 (2005).

Journal of NUCLEAR SCIENCE and TECHNOLOGY, Supplement 5, p. 538–541 (June 2008)

Proton Energy Measurement Using Si(Li) and Scintillation Crystal Detector in the MC-50 Cyclotron

Kye Ryung KIM[1*], Yong Sub CHO[1], Hong Ju KIM[2], Jung Ho SO[2], and Min Yong LEE[3]

[1]*Proton Engineering Frontier Project, Korea Atomic Energy Institute, Daejeon, Korea*
[2]*Kyungpook National University, Daegu, Korea*
[3]*Korea Institute of Radiological and Medical Science, Seoul, Korea*

Absolute proton beam energy measurement with Si(Li) detector has been performed in the MC-50 cyclotron. It is known that the measurement of the absolute energy of the medium energy proton with high accuracy is very important for some experiments concerned with nuclear physics, space device test, etc. For the absolute particle energy measurement, the semiconductor detector has been recognized as a very useful tool because of their total particle energy absorbing characteristics. In the case of a scintillation detector, a part of particle energy can be lost through quenching process during penetrating the detector material and it could be a reason to increase the energy measurement error. The thicknesses of Si(Li) detector and BGO scintillation detector were 5mm and 30mm, and the sizes of active area are 75mm^2 and 49mm^2. Even though, the Si(Li) detector was originally designed and fabricated proper to the operation at the atmosphere, Si(Li) detector was installed in the vacuum chamber with the 50um thickness Al beam entrance window for more accurate measurement. The energy calibration of Si(Li) detector was done with ^{241}Am alpha sources. The proton beam energies from the cyclotron are 35MeV and 45MeV, and the beam current is below 0.5nA. The proton beam energy extracted through the 2mm thickness Al exit window was changed and controlled by Al degrader and air thickness between exit window and detector. The change of proton beam energy property such as mean energy and energy spread has been measured using Si(Li). The results are compared to the calculated results by Monte-Carlo code simulation and measured results by the BGO scintillation detector.

KEYWORDS: proton beam energy measurement, Si(Li) detector, Monte Carlo simulation, BGO scintillation detector, absolute energy measurement

I. Introduction

The PEFP (Proton Engineering Frontier Project) of KAERI (Korea Atomic Energy Research Institute) constructed a dedicated beam line at the MC-50 cyclotron of KIRAMS (Korea Institute of Radiological And Medical Sciences) in 2004 to support some basic and pilot studies of proton beam utilization in the fields of nuclear physics, biological technology and space technology. The beam line was designed to control the proton energy using degrader system which was composed of several Al sheets with various thicknesses from 0.02~2mm and to irradiate the proton beam to the samples in the air.

In some experiments, such as nuclear physics and space device test, the measurement of proton energy incident to the sample with high accuracy is very important.

The semiconductor detectors and scintillation detectors have been widely used for the particle energy measurements.[1-4)] The semiconductor detectors can be used for the absolute particle energy measurement because they absorb the full energy of the incident particle. On the other hand, in the case of scintillation detectors, the incident particle can lose their energy during penetrating the scintillation material through quenching processes. So, we have to consider the response function compare to the results of absolute energy measurement through the calibration process over the proton energy range which we interested in.

The absolute energy measurement performed at the MC-50 cyclotron using Si(Li) detectors and BGO scintillation detector. In this paper, we discuss the difference between these two cases and calculated energy using Monte Carlo simulation code, SRIM2003.

II. Experiments

1. 50 MeV Beam line at the MC-50 Cyclotron

The 50 MeV beam line was installed at the MC-50 cyclotron of KIRAMS to support basic and pilot studies on proton beam utilization technologies in 2004.[5)] It was designed to be suitable for application to space and biological technologies. The beam line is composed of a collimator, a Faraday cup, a vacuum drift tube, bellows for easy alignment, a BPM (Beam Profile Monitor), an exit window for the external beam coated with a phosphor material, a scattering system, an energy degrader, PMMA rotating modulator for SOBP (Spread-Out Bragg Peak), a target stage, an dose measurement system, an energy measurement system, etc. as shown in **Fig. 1**.

*Corresponding Author, Tel No: +82-42-868-8602, Fax No: +82-42-868-8131, E-Mail: kimkr@kaeri.re.kr

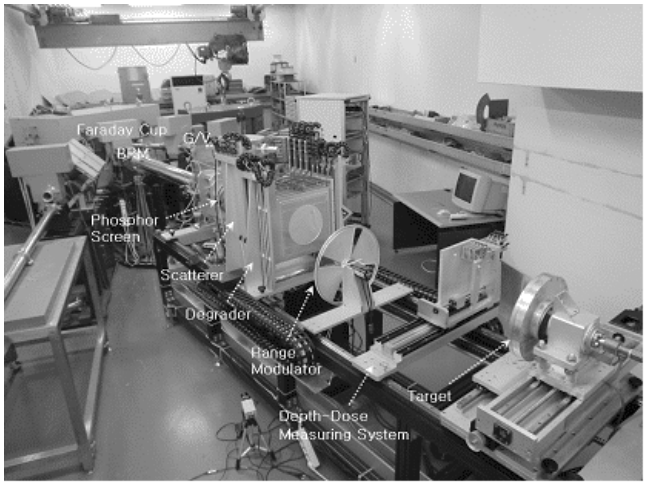

Fig. 1 Photograph of the 50 MeV proton beam line established at the MC-50 cyclotron of KIRAMS.

2. Experimental Setup for Si(Li)

The 35 MeV incoming proton beam passes through 2 mm thick Al window and loses energy down to 27.5 MeV. Then the 27.5 MeV proton beam is collimated by using 1 mm Al collimator, and passes through 44.5 cm of air, Al degrader, and 55.5 cm of air. The final energy of proton beam energy becomes 4.0~25.0 MeV with various Al thicknesses. The 45MeV incoming proton beam passes through 2 mm thick Al window and loses energy down to 39.0 MeV. Then the 39.0 MeV proton beam is collimated by using 1 mm Al collimator, and passes through 44.5 cm of air, Al degrader, and 55.5 cm of air. The final energy of proton beam energy becomes 15.6 ~ 34.7 MeV with various Al thicknesses.

The Si(Li) detector (75 mm^2 × 5 mm) was used for the proton energy measurement. The Si(Li) detector was installed in the vacuum chamber with 50 μm Al window for high resolution measurement and a high voltage of -1000 V was applied to the detector.

The analog signal from the Si(Li) detector was amplified by a pre-amplifier (ORTEC 142AH) and a spectroscopy amplifier (ORTEC 572A) and it is analyzed by the MCA installed in a PC. **Fig. 2** and **Fig. 3** depict a schematic diagram and photograph of the experimental set-up.

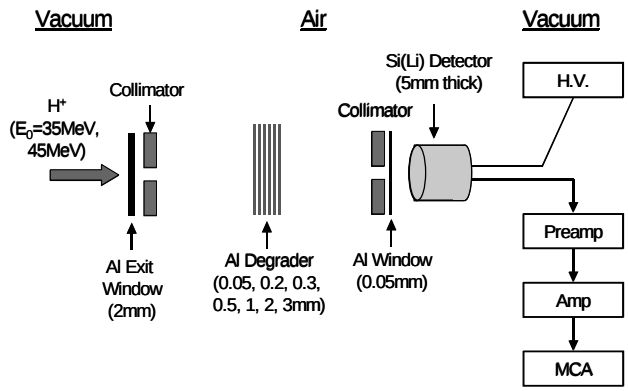

Fig. 2 Schematic diagram of the experimental set-up for energy measurement using Si(Li) detector.

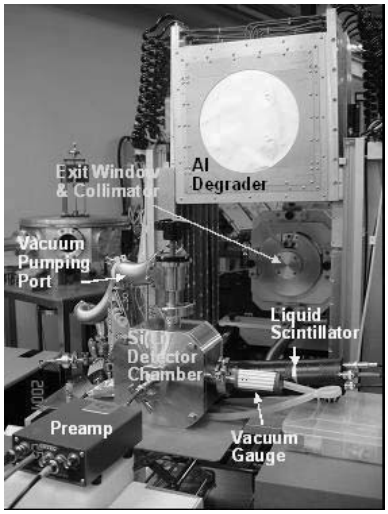

Fig. 3 Photograph of the experimental set-up for energy measurement using Si(Li) detector.

3. Experimental Setup for BGO

For the energy measurement using BGO, the air thickness of air after passing through Al degrader changed 114.5 cm.

The BGO scintillation detector (49 mm^2 × 30 mm) was used for the proton energy measurement. The BGO crystal was wrapped with Teflon followed by Al foil and a metal package E5780 PMT of 8 mm in diameter (Hamamatsu Co.) was attached to the long side of the crystal. And a high voltage of -800 V was applied to the PMT.

The longitudinal dimension of the crystal was 30mm, which was enough to stop 38 MeV protons inside the crystal. A 25 MHz USB2 based flash analog to digital converter (FADC) board was used to digitize the analog signal.[6] The analog signal from the PMT attached to the scintillator was connected into the analog input of the FADC board via a preamplifier and an ORTEC 576 shaping amplifier and the signal was also monitored by using a DSO (Digital Storage Oscilloscope). A software threshold setting was applied to trigger an event by using a self trigger algorithm on Field Programmable Gate Array (FPGA) chip of the FADC board. The FADC output was recorded into a personal computer, and the recorded data were analyzed with C++ data analysis program. **Fig. 4** shows a schematic diagram of the experimental setup for the proton energy measurement using BGO.

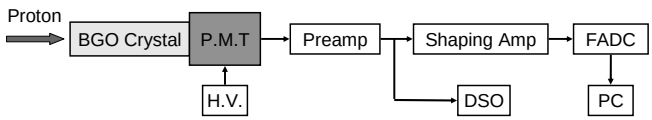

Fig. 4 Schematic diagram of the experimental set-up for energy measurement using BGO scintillation detector.

III. Results

1. Energy Measurement Using Si(Li) Detector

The pulse height spectrum measured by using Si(Li) detector is shown in **Fig. 5** for 35MeV initial proton beam. After the 35 MeV proton beam passed through 2 mm thick Al exit window, 100 cm thick air, and 50 μm thick Al

window, the energy reduced to 25.0 MeV. We obtained a 3.9 % FWHM energy straggling after a Gaussian fitting for 25.0 MeV proton beam, which is the smallest energy straggling among all of energy straggling. The energy stragglings were measured for the various Al degrader thicknesses. When the Al degrader thickness was increased up to 3 mm, the energy straggling was increased up to 91.3 %.

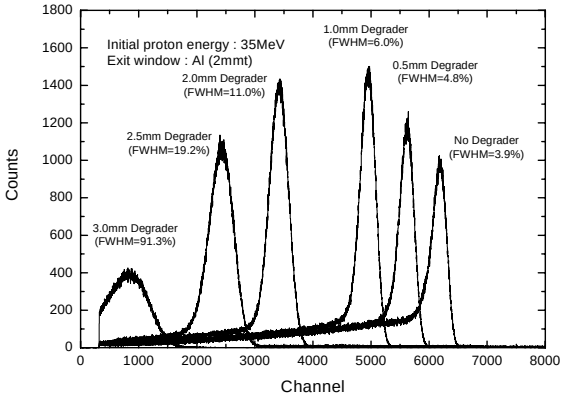

Fig. 5 Pulse height spectra of the Si(Li) with different degrader thicknesses.

The energy straggling was measured by using Si(Li) detector for 45MeV initial proton beam. After the 45 MeV proton beam passed through 2 mm thick Al exit window, 55.5 cm thick air, 2 mm thick Al degrader, 44.5 cm thick air, and 50 μm thick Al window, the energy reduced to 30.1 MeV. We obtained a 3.1 % FWHM energy straggling after a Gaussian fitting for 30.1 MeV proton beam, which is the smallest energy straggling among all of energy straggling. The energy stragglings were measured for the various Al degrader thicknesses. When the Al degrader thickness was increased up to 6.2 mm, the energy straggling was increased up to 93.9 %.

Energy degraders of 0.02, 0.05, 0.2, 0.3, 0.5, 1.0, 1.5, 2.0, 2.3, 2.5, 3.0 mm in thickness were used to reduce the proton beam of initial energy of 35 MeV. And 0.5, 1.0, 1.5, 2.0, 2.5, 3.0, 3.5, 4.0, 4.5, 5.0, 5.5, 6.0, 6.2 mm Al energy degraders were used for the 45 MeV proton beam. The mean channels with different degrader thicknesses were calculated by using Gaussian fittings. The proton energies were calculated using the SRIM2003. **Fig. 6** shows signal output versus the proton energy calculated by using the SRIM code.

The energy calibration was performed in vacuum by using ^{241}Am α-source. The energy resolution was 2.1% for 5.486 MeV alpha particles.[7)]

2. Energy Measurement Using BGO Crystal

The pulse height spectra measured by using BGO scintillation detector are shown in **Fig. 7** and **Fig. 8** for 35MeV and 45 MeV initial proton beam. The 35 MeV and 45 MeV proton beam energy reduced to 23.6 MeV and 36.2 MeV after passing through 2 mm thick Al exit window, 170cm thick air. The FWHM energy straggling of 23.6 MeV and 36.2 MeV were 5.72 % and 4.0 %.

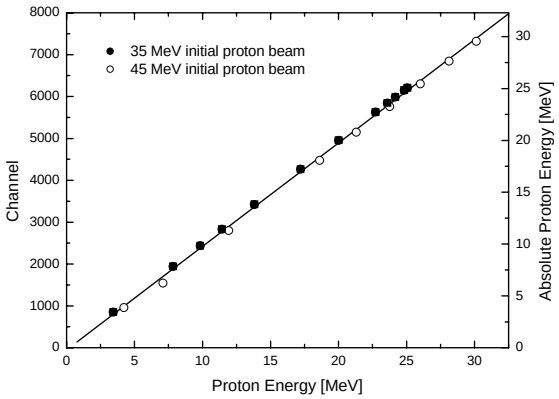

Fig. 6 Absolute energy measured by using Si(Li) versus calculated energy by using SRIM.

For the proton beam of initial energy of 35 MeV and 45 MeV, we measured the FWHM energy straggling with different Al degrader thicknesses. As shown in **Fig. 7**, when the Al degrader thickness was increased up to 2.3 mm and 5.0 mm, the energy straggling was increased up to 69.4 % and 20.6 % for 35 MeV and 45 MeV proton beam.

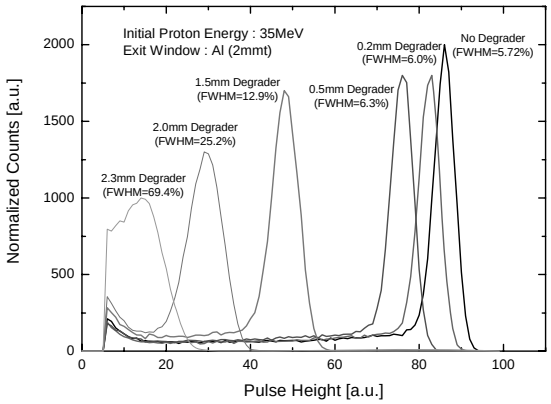

Fig. 7 Pulse height spectra of the BGO with different degrader thicknesses.

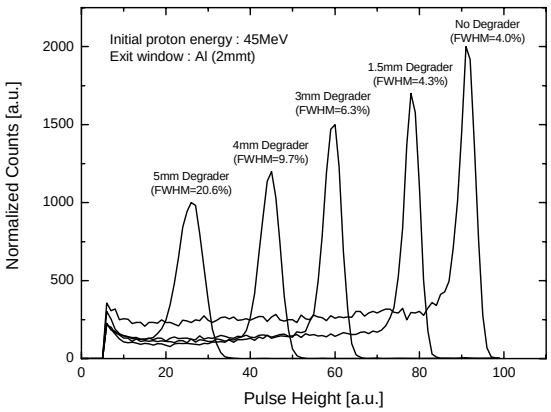

Fig. 8 Pulse height spectra of the BGO with different degrader thicknesses.

Energy degraders of 0.05, 0.2, 0.3, 0.5, 1.0, 1.5, 2.0, 2.3 mm in thickness were used to reduce the proton beam of initial energy of 35 MeV. And 0.5, 1.0, 1.5, 2.0, 2.5, 3.0, 3.5,

4.0, 4.5, 5.0 mm Al energy degraders were used for the 45 MeV proton beam. **Fig. 9** shows signal output versus the proton energy calculated by using the SRIM code.

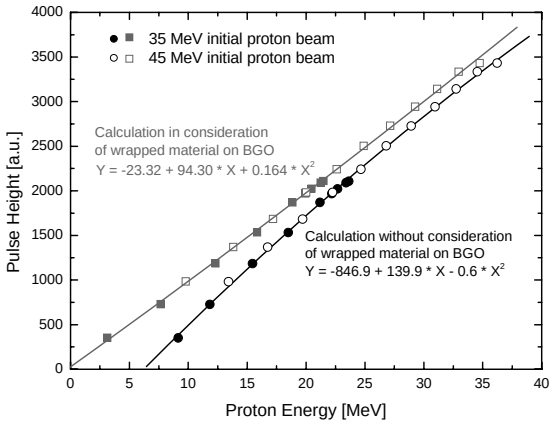

Fig. 9 Pulse height versus energy for the BGO detector.

For the electron-equivalent energy calibration, a ^{137}Cs γ-ray source of 662 keV energy was used. A clear full peak was observed, and the energy resolution was 28 % FWHM.

IV. Discussions

All of the energy straggling data measured by using Si(Li) detector and BGO scintillation detector are presented in **Fig. 10**. There's no big mismatch between the data from two detectors for the same energies.

When the BGO crystal was wrapped with 300 μm thick Teflon foil, 30 μm thick Al foil, and 200 μm thick PVC film to reduce the noise and light loss. These wrapping materials contribute the additional energy loss before the proton's incoming to BGO crystal.

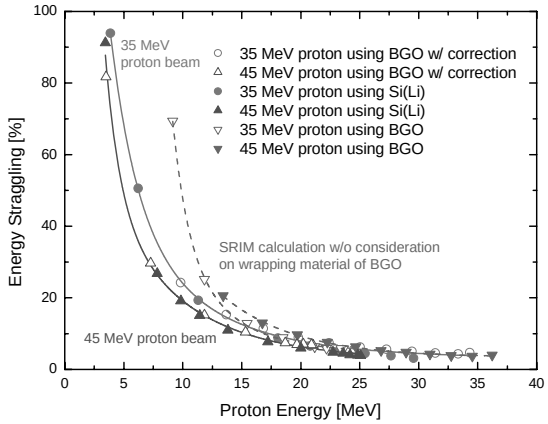

Fig. 10 Energy straggling measured by using Si(Li) detector and BGO scintillation detector.

We calculated the proton energies which are incident to BGO after passing through the wrapping material using SRIM code. These data were in good agreement with the electron equivalent calibrated data of BGO crystal with maximum 10 % error.

For the energy measurement using BGO, we have to consider the energy loss effect caused by the wrapping material of BGO.

V. Conclusions

The absolute energies measured by using Si(Li) detector coincided well with the calculated value by using SRIM code within the maximum 10 % error range.

There is no big mismatch between the data from Si(Li) and BGO detector, when we correct the energy using the calculated value by using SRIM on the reflection of the energy loss caused by wrapping material.

The initial proton energy decides the energy straggling value. The better the energy straggling is, the higher initial energy is. The mean energy information can be provided to the users through the calculation using SRIM code.

Acknowledgement

This work was performed under the support of the 21C Frontier R&D program in the MOST (Ministry of Science and Technology) of the Korean government.

References

1) J. H. Ha, J. C. Kim, Y. K. Kim, M. Youn, S. J. Chac, H. T. Chung, J. H. Choi, C. S. Lee, J. U. Kwon, C. B. Moon, J. S. Chai, Y. S. Kijm and J. D. Lee., 'Energy Measurement of 50MeV Proton Beam with NaI(Tl) Scintillator', Nucl. Intr. and Meth. A, Vol. 350, pp. 411~414, 1994.
2) U. Schneider and Dieter Renker, 'Proton Energy Measurements Using a NaI(Tl) Scintillator', Nucl. Intr. and Meth. A, Vol. 388, pp. 199~203, 1997.
3) H. J. Kim, S. C. Yang, Heedong Kang, H. Park, S. Ryu and J. H. So, 'Proton Beam Energy Monitoring with Radiation-Hard Crystal Scintillators', JKPS, vol. 50, No. 5, pp. 1534~1537, 2007.
4) R. Eisberg, D. Ingham, M. Makino, R. Cole and C. Waddell, 'Semiconductor Detector Telescopes for Measuring Proton Energies up to 300 MeV – Problems and Solutions', Nucl. Intr. and Meth., Vol. 101, pp. 85~90, 1972.
5) K. R. kim, B. S. Park, H. R. Lee, K. S. Kang, S. W. Kang and B. H. Choi, 50MeV proton beam test facility for low flux beam utilization studies of PEFP', Proc. of APAC 2004, 2004.
6) Notice Korea Co. webpage, http://www.noticekorea.com/.
7) Kye-Ryung Kim, Yong-Sub Cho, In-Seok Hong, Bum-Sik Park, Sang-Pil Yun, Han-Sung Kim, Hong-Joo Kim and Hung-Ho So, 'Proton beam energy measurement using semiconductor detectors at the 45meV test beam line of PEFP', Proc. of PAC 2007, 2007.

Journal of NUCLEAR SCIENCE and TECHNOLOGY, Supplement 5, p. 542–545 (June 2008)

A Feasibility Study for the Use of BGO Scintillator in Conjunction with a Plastic Optical Fiber for Remote Gamma Ray Dosimetry

Yong Ho KIM, Min Woo SEO, and Jae Woo PARK*

Cheju National University, 1 Ara-dong, Jeju-si, Jeju-do, Korea

A feasibility study has been carried out on a remote radiation dosimeter employing a BGO scintillator as the radiation sensing head and a plastic optical fiber as a light pipe. The sensor head is prepared in two sizes: the larger one has the size 4.7mm x 4.7mm x 10mm and the smaller one has the size 2.2mm x 2.2mm x 10mm. A low attenuation plastic optical fiber with 3mm diameter and 10m length is attached to the square surface of the larger scintillator, and the same optical fiber with 2mm diameter is attached to the smaller one. The polished scintillator is wrapped with white Teflon tape, and the fiber is shielded with a thermal shrink tube to block the ambient light. The lights generated in the sensor head are detected by a pulse-type photomultiplier tube module. Co-60 sources with radioactivity of 50μCi and 1mCi are used to test the performance of the constructed dosimeter models. The total number of pulses is measured as a function of the distance from the sensor head to the source. MCNPX simulation is also carried out for the source and dosimeter arrangements to assess the feasibility of the dosimeter model. The dosimeter model measures fairly well the change in the number of pulses as the source-to-detector distance changes, but shows poor capability to measure the pulse height spectrum and source activity.

KEYWORDS: BGO scintillator, remote radiation dosimeter, plastic optical fiber, MCNPX simulation

I. Introduction

A real-time remote monitoring of radiation doses is essential in high radiation field such as a gamma irradiator or an electron accelerator. Several methods are currently used. When a higher spatial resolution is required, for instance, the dose measurement in a human phantom for medical treatment planning, farmer-type ionization chambers or MOSFET dosimeters are frequently employed. Though very accurate, the ionization chamber is a delicate machine and hence is not robust. Most of the malfunctions occurring in the machine should be fixed by the manufacturer or original supplier, and it usually takes several weeks to have it fixed. A MOSFET dosimeter is convenient for simultaneous measurement at multiple points. The sensor head is very small so that it has an excellent spatial resolution. A big disadvantage is that its effective life time is limited and use of the dosimeter is impractical in a high radiation field.

Radiation dosimeters constructed with scintillators combined with optical fibers can be a good alternative solving these problems all together. Several scintillators with high atomic number and high density, e.g. BGO and GSO, are now commercially available. Substantial sensitivity can be achieved using one of these scintillators even with very small size. The sensor head can be as small as a MOSFET dosimeter. The light generated in the sensor head is transmitted through an optical fiber to a remote signal processing system. With a properly chosen scintillator, the life time of the dosimeter can be much longer than that of a MOSFET dosimeter. Since the sensing part consisting of the scintillator head and optical fiber is entirely passive, that means it does not have any electrical or electronic component, it will be much more robust than an ionization chamber or a MOSFET dosimeter. It can be easily modularized. If this module becomes bad, it can be simply replaced.

A number of works has been carried out in relation to this subject. Lee et al.[1] investigated the change of the optical power with different combinations of the scintillator tip and optical fiber length. Uritani et al.[2] proposed a dosimetry model based on a quartz fiber and Al_2O_3 scintillator to measure the gamma ray dose in a reactor core. Cherry[3] investigated the optical characteristics of a BGO and optical fiber combination with various different parameters. Nowotny[4] proposed a tissue equivalent dosimeter model bade on LiF:W scintillator head and plastic optical fiber to be applied in diagnostic radiology.

In this work, we present a dosimeter model employing a BGO scintillator as the radiation sensing head, a plastic optical fiber as the light pipe and a pulse type PMT module. Two different sizes of the scintillator are prepared and attached to plastic optical fibers of different diameters. The light pulses generated in the scintillators are measured with a pulse type PMT module. The dosimeter models are tested against ^{60}Co sources with activity of about 50μCi and 1mCi. MCNPX simulation is also carried out for the source and dosimeter arrangements. The simulation results and measured data are compared and the feasibility as a radiation dosimeter of the sensor models is discussed.

II. Construction of the Dosimeter Model

The dosimeter module consists of the dosimeter head, the light guiding optical fiber and, a PMT module. The dosimeter head is a BGO with chemical composition

*Corresponding Author, Tel No: +82-64-754-3645, Fax No:. +82-64-757-9276, E-Mail: jwpark@cheju.ac.kr

$Bi_4Ge_3O_{12}$, which has been purchased in a cube of 10x10x10mm^3 from Saint-Gobain Crystals. The cube is cut to prepare the sensor head in two sizes: 2.2x2.2x10mm^3 and 4.7x4.7x10mm^3. **Fig. 1** shows a picture of the cut pieces of the BGO scintillator. The surfaces of the cut pieces are polished with 0.5μm alumina powder to have the final sizes as indicated above and then wrapped with a Teflon tape.

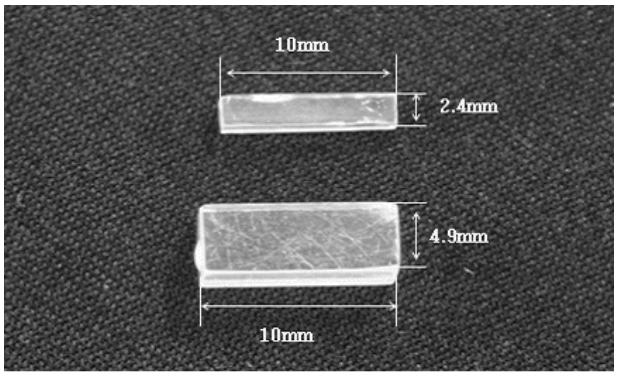

Fig.1 Picture of the cut pieces of the BGO scintillator.

The light transmitting optical fiber, which is a product of Toray Industries, is prepared in 10m length and two diameters: 2mm (PGR-FB2000) and 3mm (PGR-FB3000). The core of the fiber is made of PMMA with refractive index 1.49 and the cladding is a fluorinated polymer with refractive index 1.4. The attenuation of the fiber is less than 0.2db/m for 400-600 nm lights. The fiber end faces are also polished with the alumina powder. The constructed dosimeter module is as shown in **Fig. 2**. The fiber with 2mm diameter is attached to the smaller piece of the scintillator and the fiber with 3mm diameter is attached to the bigger piece. The coupling between the fiber tip and the scintillator is made either by bare contact or with silicon optical grease (Bicron BC-630) to see the effect of each modality. The connection between the fiber and the PMT module is made by an FC connector. The PMT module (Hamamatsu H5784), which has an optional FC adapter, is comprised of a PMT, a high voltage supply circuit and an amplifier. The electrical current from the PMT is converted to a pulse signal by the amplifier. The spectral response of the PMT is from 300 to 650nm.

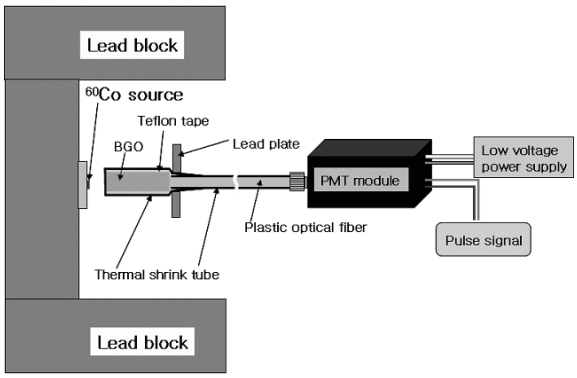

Fig.2 Configuration of dosimeter module and experimental setting.

III. Experimental Measurement and MCNPX Simulation

The voltage signal from the PMT module is amplified by a Canberra 2020 spectroscopy amplifier and then fed into an EG&G/Ortec TRUMP-8K-32 pulse height analysis (PHA) card installed with the MCA emulator MESRO II in a PC. 50 μCi and 1mCi ^{60}Co sources are used to measure pulse height spectra and total number of counts as a function of distance between the source and the dosimeter head. The experimental setting is shown in **Fig. 2**. The source is surrounded by a lead wall temporarily made with lead blocks to prevent experimenters from radiation overexposures while working. In order to minimize the interference of any possible Cerenkov radiation generated in the optical fiber, a lead plate of 5mm thickness placed between the dosimeter head and optical fiber. The measured distance is from 10cm to 50cm by 10cm increment and data are collected for 60 seconds at each point. Measurement is made three times at each point and an average is taken. The back ground data for the spectrum and total count are obtained at each point without the source and then subtracted from the data measured with the source.

For our dosimeter model to be feasible as a dosimeter, it should be at least capable of predicting the change of the total number of counts as a function of the distance between the scintillator and source. MCNPX simulation is conducted to test this capability. The volume of the scintillator is modeled as a cell, and the sources are represented by a point for the 50 μCi and by a volume for the 1mCi ^{60}Co. With F8 tally option specified, MCNPX calculates the total number of interactions scored in the scintillator. We compare the measured data with the simulated results.

IV. Results and Discussion

The pulse height spectra measured for 1mCi source with both types of scintillator at 10cm from the source are shown in **Fig. 3**. Both spectra have a couple of common features: peaks around the same position at very low energy channel and long tails over higher channels. The spectrum measured with the larger scintillator and thicker fiber shows much more counts at higher channels since it has a higher probability to absorb more of the gamma energy and can collect the lights more efficiently. Both spectra do not show the full energy peaks

The pulse height spectra obtained by MCNPX simulation for the same case are shown in **Fig. 4**. The spectrum calculated for the larger scintillator clearly shows two separate photo peaks. These peaks are used to convert the channel number into energy. The spectrum calculated for the smaller scintillator, however, does not show the photo peaks. There exist considerable differences between the calculated and measured pulse height spectra. For some reason, which should be clarified from further study, our dosimeter model may be inaccurate measuring the pulse height spectrum.

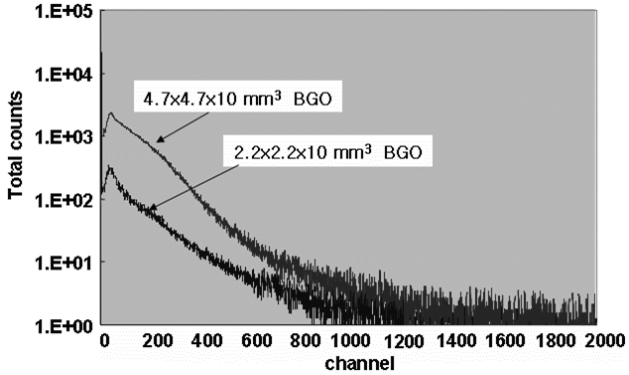

Fig. 3 Pulse height spectra measured for 1mCi source.

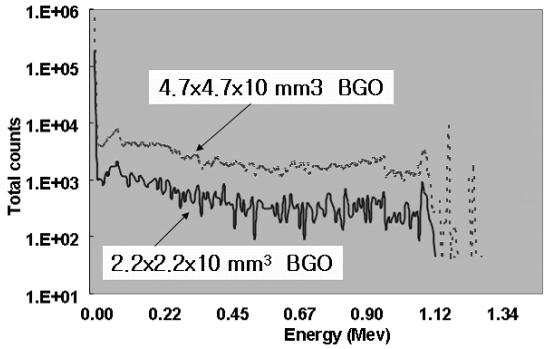

Fig. 4 Pulse height spectra obtained by MCNPX simulation for 1mCi source.

As mentioned above, the experimental data at each point are obtained from the average of 3 measurements. To look into the reliability of the dosimeter models, a simple statistical analysis is conducted for the measured data. **Table 1** shows the errors of the measured data, which is obtained by the standard deviation divided by the average, and the relative errors of the MCNPX calculation. It is found that the dosimeter model with the larger scintillator produces more reliable data. Considerable errors might be involved in the data measured by the dosimeter model with smaller scintillator.

Table 1 Errors involved in the measured and calculated data.

Distance (cm)	2.2x2.2x10mm³ BGO		4.7x4.7x10 mm³ BGO	
	Measurement errors (%)	MCNPX relative errors (%)	Measurement errors (%)	MCNPX relative errors (%)
10	2.0	1.3	0.6	0.6
20	6.1	2.3	1.6	1.2
30	10.4	3.3	2.6	1.7
40	11.9	4.5	4.2	2.3
50	2.5	5.0	5.0	2.9

The total number of particles detected in the sensor of a dosimeter is an important parameter to measure a radiation dose. In a gamma ray field with its energy known, the radiation dose delivered to a medium is directly proportional to the number of gamma rays interacting in the medium. **Fig. 5** and **Fig. 6** compare the calculated and measured changes in the number of gamma rays interacting in the scintillators as a function of distance from 50μCi and 1mCi ^{60}Co sources, respectively. The measured data are read by the right ordinate while the calculated data are read by the left ordinate.

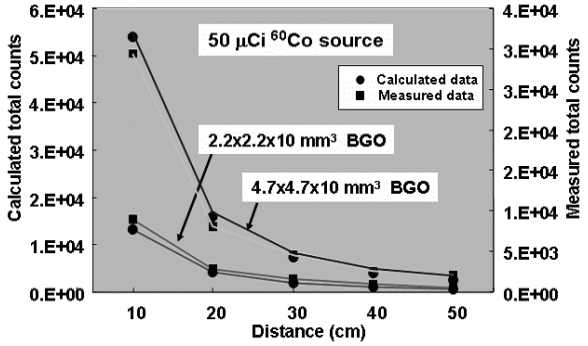

Fig. 5 The change in number of gamma rays interacting in the scintillators as a function of distance from 50μCi source.

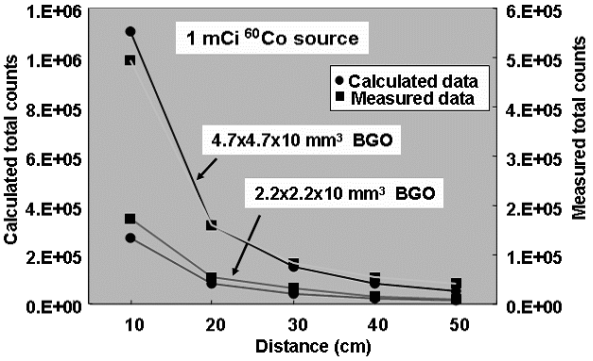

Fig. 6 The change in number of gamma rays interacting in the scintillators as a function of distance from 1mCi source.

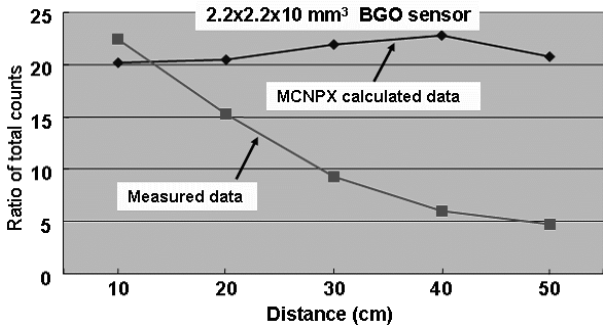

Fig. 7 Ratios in the total number of gamma rays measured and calculated for the two ^{60}Co sources with the smaller BGO.

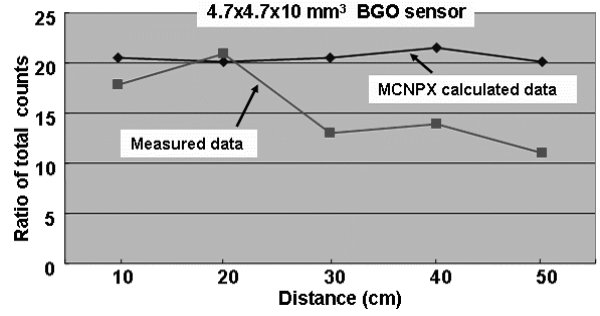

Fig. 8 Ratios in the total number of gamma rays measured and calculated for the two ^{60}Co sources with the larger BGO.

The measured total count profile obtained with the larger scintillator dosimeter model follows fairly well the calculate profiles. However, the total number of counts measured is much smaller than the calculated. Since there are substantial losses in the light collection, transmission, and conversion to electron, this decrease is deemed normal. There are some deviations between the measured and calculated profiles for the dosimeter model employing the smaller scintillator, but the overall shapes are acceptably similar.

Fig. 7 and **8** show the ratios in the total number of gamma rays of measured and calculated for the two ^{60}Co sources. **Fig. 7** is for the smaller scintillator and **Fig. 8** is for the larger scintillator. Since the activity of 1mCi source is 20 times the activity of 50μCi, this ratio should be also about that much. The MCNPX calculated results are close to this value. The congruity is better for the larger scintillator. However, the measured data fall apart from the expected value as the sensor-to-source distance increases. This tendency becomes more severe with the smaller BGO.

V. Conclusions

Two dosimeter models were constructed. One was employing 2.2x2.2x10mm^3 BGO scintillator as a gamma ray sensor attached to one end of a plastic optical fiber of 2mm diameter and 10m length which acts as a light guide to a pulse type PMT module. The other was employing 4.7x4.7x10mm^3 BGO scintillator attached to a plastic optical fiber of 3mm diameter and 10m length. The models were tested with 50μCi and 1mCi ^{60}Co sources to measure the pulse height spectra and total number of pulses as a function of sensor-to-source distance. MCNPX simulation also was performed for the source and sensor arrangement to calculate the pulse height spectra and the total number of interactions occurring in the scintillator. Compared with the simulation result, both types of dosimeter model measured fairly well the change of total number of pulses as a function of source-to-sensor distance. However, the dosimeter models did not accurately measure the change of activity, and the pulse height spectra measured with the dosimeter models remarkably differed from the calculated. The dosimeter model with the larger scintillator had generally shown superior dosimetric characteristics. In order to develop a gamma ray dosimeter, the present model, which is based on measuring the total number of pulses, should be improved. One possible alternative modality might be to replace the pulse-type PMT module with a current-type.

Acknowledgement

This work was performed under the program of Basic Atomic Energy Research Institute (BAERI) which is a part of Nuclear R&D Programs sponsored by Korea Ministry of Science and Technology, and partly supported by the Innovative Technology Center for Radiation Safety (iTRS).

References

1) B.S. Lee, Y.M. Hwang, H.S. Cho, S. Kim, and S. Cho, "Fabrication of fiber-optic radiation sensor tips with inorganic scintillator for remote sensing of X or γ – ray" Nuclear Science Symposium Conference, IEEE, Volume 2, Issue 16-22, PP:865 – 868, 2004.
2) Uritani, T. Iguchi, S. Hayashi, H., Kobayashi, Y. Takami, I. Kimura, M. Katagiri, and T. Kakuta, "Reactor Dosimetry: Radiation Metrology and Assessment" : pp769-774, 2001.
3) S. R. Cherry, Y. Shao, M.P. Tornai, S. Siegel, A. R. Ricci, M. E. Phelps, "Collection of Scintillation Light from Small BGO Crystals", IEEE Transactions on Nuclear Science, Vol. 42, No.4, pp: 1058-1063, 1995.
4) R Nowotny, "LiF:W as a scintillator for dosimetry in diagnostic Radiology", Phys. Med. Biol. 49 PP:2599–2611, 2004.

Journal of NUCLEAR SCIENCE and TECHNOLOGY, Supplement 5, p. 546–548 (June 2008)

Development of Beta-ray Spectrometer for Radiation Emergency Accidents

Toshikazu SUZUKI* and Yuji YAMADA

National Institute of Radiological Sciences, 4-9-1, Anagawa, Inage-ku, Chiba 263-8555, Japan

At the national center for radiation emergency medicine, the first step in the radiation emergency response is early identification of unknown nuclide which might be taken in the body. In such a situation, gamma emitting nuclides are relatively easy to be identified by Ge detectors. As for beta emitting nuclides, "Pico beta" has been only commercialized installed beta ray spectrometer, which consists of a gas flow type GM counter and a plastic scintillator. However, it is difficult to carry the spectrometer outdoor because it has the thick lead gamma ray shield and also Q gas supply system. Then, the detector for a portable beta ray spectrometer with gamma ray spectrometer and alpha counter was developed aiming to evaluate unknown nuclides promptly in the locale in the emergency.

KEY WORDS: decay time, plastic scintillator, ZnS(Ag), CsI(Tl), pulse shape, spectrum, light output

I. Objective

When the patient is accepted, the surface contamination monitoring is carried out with more than one survey meters by reason of detecting multiple kinds of radiation in the radiation emergency medicine. However, when the internal contamination is doubted, the rapid deployment becomes possible if it is able to identify unknown nuclides at this stage. Then, the measuring instrument which can distinguish all kinds of radiation with one detector was developed.

II. Detector

Different scintillators were adopted for detecting each kind of radiation such as ZnS(Ag) scintillator for alpha ray, plastic scintillator (EJ-204) for beta ray and CsI(Tl) scintillator for gamma ray. Light from each scintillator was detected with photomultiplier tube (7696) put in the same axis. To measure them by the same gain, it was necessary to reduce the light from ZnS(Ag) because it had 440% or more of EJ-204 light output. Therefore, ZnS(Ag) (4.0mg/cm^2) applied to substrate (polyvinylidene chloride film :2.0mg/cm^2) was optically coupled on the reflector (Teflon:8.9mg/cm^2) which was wrapped around the incident side of plastic scintillator. The shape of CsI(Tl) scintillator was processed to well type to surround ZnS(Ag) + plastic scintillator completely. The purpose of this was not only gamma detection but also gamma ray shielding to plastic scintillator. In addition, the aluminum of 500 μm thickness was inserted between CsI(Tl) and plastic scintillator as the Compton scattering electron shield.

Originally, the scintillation efficiency of CsI(Tl) is 52000 photons/MeV and that of EJ-204 is 10400 photons/MeV. On the other hand, maximum emission wavelength of CsI(Tl) is 565 nm and that of EJ-204 is 408 nm. So, the difference of scintillation efficiency was compensated within 1.6 times by the difference of quantum efficiency of the photomultiplier which had Bialkali photoelectric cathode. This means ZnS(Ag) - plastic scintillator-CsI(Tl) is almost arranged in same light output by adjusting the reflector of CsI(Tl). **Fig. 1** shows the structure of this detector and **Fig.2** shows externals of this detector.

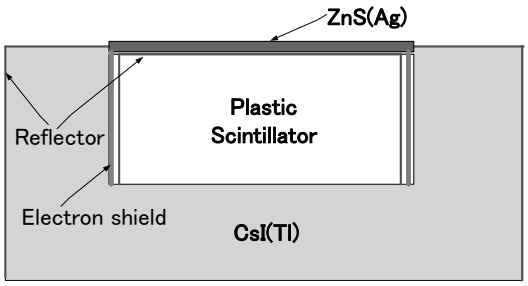

Fig. 1 Structure of detector

Fig.2 External of detector

III. System and Methods

For the discrimination of a kind of radiation, a waveform distinction technique based on the time difference until the luminescence of scintillator attenuating to 1/e was used. Among the mixture radiation of alpha, beta and gamma ray which entered from incident window (aluminized Mylar film :1mg/cm^2) that has the same diameter as the effective size of ZnS(Ag) + plastic scintillator, the alpha ray is first detected and shielded with ZnS(Ag), then only beta and gamma ray reach plastic scintillator. On the assumption that the measurement upper limit energy of beta ray is ^{90}Y (E_{max}=2.28MeV), the maximum range will be 1×10^3mg/cm^2. Here, all beta rays are absorbed in 12.5mm thick plastic

*Corresponding Author, Tel No: +81-43-206-306, E-Mail: t-suzuki@nirs.go.jp

scintillator as shown in **Fig. 1**, considering the density of EJ-204(1.023g/cm^3). Meanwhile, as the effective Z of this scintillator is 3.38, absorption to the gamma ray is relatively low. The gamma ray is detected from the direction of 4π by chiefly CsI(Tl). Though the **Fig.3** which shows a direct output from the fast filter amplifier, it is understood to exist three components in the order of plastic scintillator (decay time:1.8ns) ZnS(Ag) (200ns) and CsI(Tl) (1000ns).

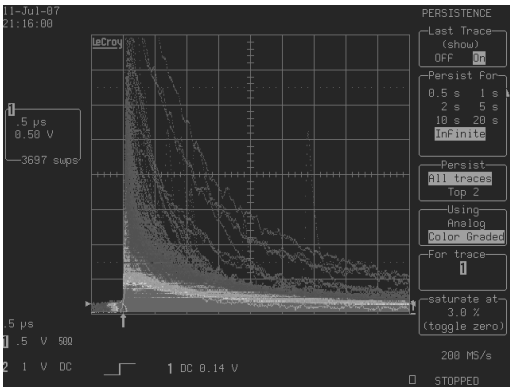

Fig.3 Wave form fast filter amp

Then, the dynode output of the photomultiplier was used for the time analysis, and the anode output was used for the energy analysis as shown in **Fig. 4**. In the time analysis system, as for linear pulse which was optimized by fast filter amplifier, the decay time difference was detected by pulse shape analyzer that consisted of two stage constant fraction timing discriminator. The difference was converted into pulse height distribution by time to pulse height converter and displayed on multi parameter M.C.A as decay time spectrum during that time. This pulse height distribution of each scintillator was separated by timing S.C.A and the gate signal was made from gate & delay generator. In the energy analysis system, linear pulse that received pulse shaping of 1.0 µs by spectroscopy amplifier was delayed for 6.5 µs by delay amp for the timing adjustment.

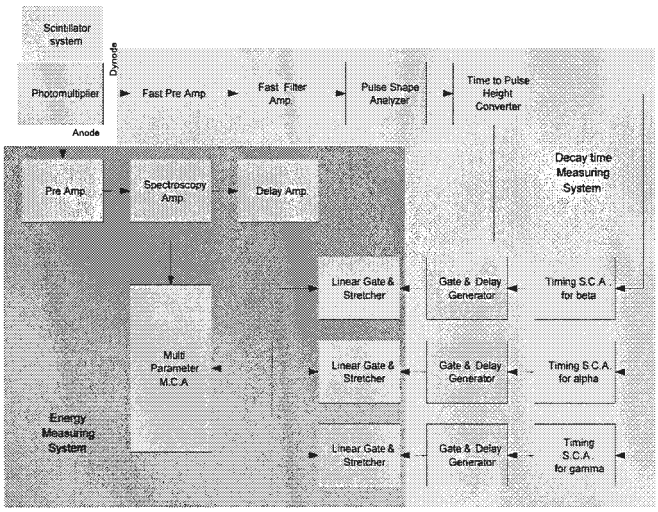

Fig. 4 System block diagram

Afterwards, the signal of each scintillator identified with linear gate & stretcher by the gate signal from the time analysis system was displayed on multi parameter M.C.A as energy spectrum.

IV. Result and Discussion

The mixture radiation source of ^{241}Am, ^{137}Cs, and ^{90}Sr-^{90}Y as a dummy source of unknown nuclide was put on the position at 5mm from the detector incident window, and the spectrum measurement was executed. It is understood that pulses from each scintillator are divided clearly in decay time spectrum obtained by the time analysis system as shown in **Fig. 5**. The width of distribution of gamma ray is wider here because CsI(Tl) has two or more decay components.

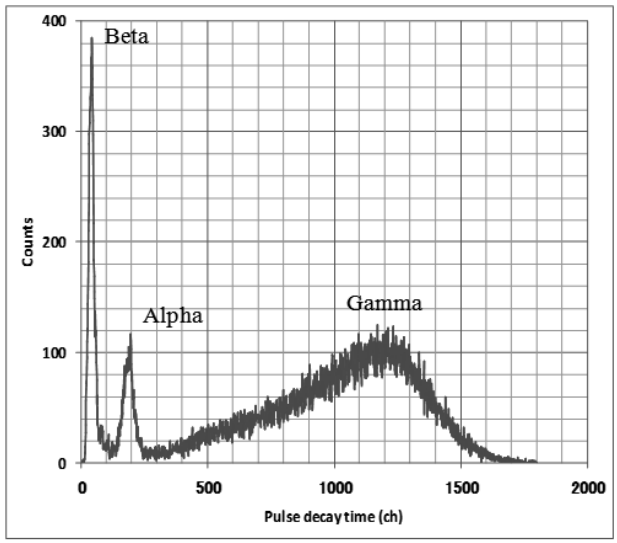

Fig. 5 Decay time spectrum

Fig. 6 shows direct pulse high distribution obtained in the energy analysis system. By taking the synchronization of each kind of radiation selected in **Fig. 5**, **Fig. 7** to **9** were obtained. **Fig. 7** does not show a direct energy distribution of the alpha ray although only the alpha radiation element mainly composed of 5.486MeV and 5.443MeV of ^{241}Am has been detected. The energy gap of several MeV or more was necessary for finding a significant difference in the pulse height distribution because the crystalline powder of ZnS(Ag) dissolved in water had just been applied on the substrate. As for **Fig. 8**, it is understood that two components of beta ray spectrum from ^{90}Sr and ^{90}Y were extracted. On the same experiment condition the pulse height of ^{14}C (E_{max}=156keV) was below the discrimination level and it was possible to obtained beta ray spectrum until ^{147}Pm (E_{max}=224keV). It seems that detection of ^{14}C will be possible according to the reduction of the system noise because the total thickness of dead layer to plastic scintillator is 15.9mg/cm^2 while maximum range of beta ray from ^{14}C is 35mg/cm^2. **Fig. 9** shows gamma ray spectrum of ^{137}Cs extracted. The part from the Compton region to the backscattering region was

transformed here, and when only CsI(Tl) scintillator was taken out, this phenomenon was not seen. When distribution exists in the decay time as CsI(Tl), it is necessary to attempt the optimization of the width of the gate further.

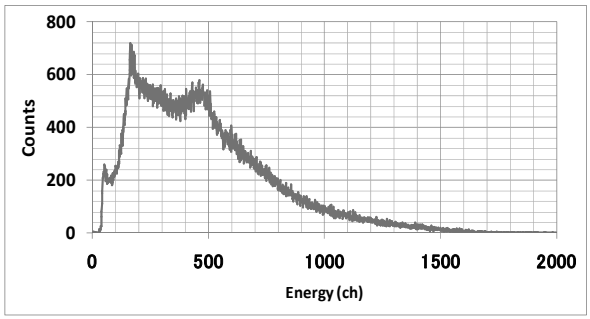

Fig. 6 Total Energy spectrum

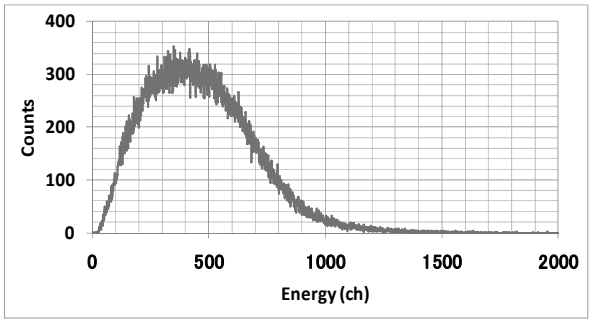

Fig. 7 ZnS(Ag) pulse height distribution

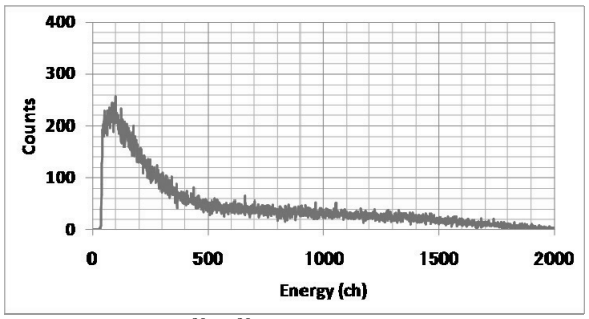

Fig. 8 ^{90}Sr-^{90}Y spectrum extracted

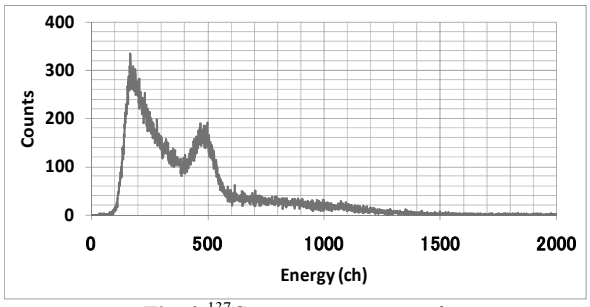

Fig. 9 ^{137}Cs spectrum extracted

V. Conclusions

Table 1 shows the background counts and the detection efficiency to the full region of alpha ray spectrum and beta ray spectrum. As for this, the efficiency is equal to or higher than that of commercially available survey meters. As a result, when a patient was contaminated by unknown nuclides, it was confirmed that the separate measurement to alpha ray, beta ray, gamma ray and the nuclide identification were possible. On the other hand, it has been improving to reduce the influence of the gamma ray background in case of beta ray measurement by using CsI(Tl) scintillator as the anti Compton detector and plastic scintillator which has slow decay time as a beta ray trigger detector.

Table 1 Background counts and detection efficiency

	alpha spectrum	beta spectrum
Back ground (natural)	0.8cps	1.64cps
Back ground (^{137}Cs)	1.0cps	3.57cps
Source	183.9cps	74.1cps
Detection efficiency	18.6%	26.0%
Source activity	1000Bq (^{241}Am)	285Bq (^{90}Sr-^{90}Y)

Acknowledgement

This work was performed under cooperation of Mr. Nishimura of APACE Science and Mr. Goto of G-tech.

References

1) A. Flammersfeld, Naturw.**33**, 280 (1946)
2) W.H. Berger, S.M. Seltzer, NASA-SP-3012 (1964)
3) Data sheet, ELJEN TECHNOLOGY (2006)
4) ICRU Report 56, pp43-45 (1997)
5) F. Liden, J Nyberg and A. Johnson, "Identification of charged particles using plastic phoswich detectors", Nucl. Inst. & Meth. in Phys. Research, A253 305-306 (1987)

Journal of NUCLEAR SCIENCE and TECHNOLOGY, Supplement 5, p. 549–552 (June 2008)

Monte Carlo Simulation of a CZT Detector

Sung Dae CHUN[1,2], Se Hwan PARK[1,], Jang Ho Ha[1], Han Soo KIM[1], Yoon Ho CHO[3], Sang Mook KANG[3], Yong Kyun KIM[3*], and Duk Geun HONG[2]

[1]*Korea Atomic Energy Research Institute, Dukjin-dong, Yuseong-gu, Daejeon, Korea*
[2]*Kangwon National University, Hyoja-dong, Chuncheon, Korea*
[3]*Hanyang University, Haengdang-dong, Seongdong-gu, Seoul, Korea*

CZT detector is one of the most promising radiation detectors for hard X-ray and γ-ray measurement. The energy spectrum of CZT detector has to be simulated to optimize the detector design. A CZT detector was fabricated with dimensions of 5×5×2 mm^3. A Peltier cooler with a size of 40×40 mm^2 was installed below the fabricated CZT detector to reduce the operation temperature of the detector. Energy spectra of were measured with 59.5 keV γ-ray from ^{241}Am. A Monte Carlo code was developed to simulate the CZT energy spectrum, which was measured with a planar-type CZT detector, and the result was compared with the measured one. The simulation was extended to the CZT detector with strip electrodes.

KEY WORDS: CZT detector, Monte-Carlo code, planar-type detector, strip electrode

I. Introduction

Cadmium Zinc Telluride (CZT) detector has been developed to obtain the high energy resolution spectrum at room temperature. It is employed in many application areas, which include medical imaging, industrial process monitoring, homeland security, environmental safety, and basic science. It was made possible with improvements in large volume crystal growth and surface treatment[1-2].

A CZT detector has high potential because of its wide band gap and high atomic number. The wide band gap enables a CZT detector to be used at room temperature without cooing system. A CZT detector is compact and easy to handle. However, tailing due to carrier trapping is still a major problem when CZT detector is used in X-ray or γ-ray spectrometry. Tailing is usually characterized by charge trappings of electrons and holes. Hence, mean free path of electrons and holes are necessary to calculate the response functions of the CZT detector[3].

In the previous works, the modeling of charge transport in CZT detector was studied. Hamel solved analytically the transport equation for charge carriers drifting in a linearly varying field[4]. Heanue first calculated the path of the change carrier and then solved numerically a one dimensional transport equation along this curve path[5]. Prettyman combined charge carrier drift and signal include computations in a two dimensional model to produce a two dimensional Charge Induction Efficiency map. It was used in a Monte Carlo calculation to the pulse height spectrum[6]. The model was developed to study the influence of material parameters; mobility, trapping, detrapping, electric field distribution. However, it was limited to the simulation of planar detectors[7]. Park developed a simulation code to calculate the energy response of the CZT detector[8]. The mean free paths of electron and hole were determined from the shape of the energy spectrum. At first, the mean free paths of the electron was extracted from the bias dependence of α-particle spectrum, and that of the hole was extracted from the comparison between the measured and the simulated γ-ray spectrum.

In this work, we measured with the γ-ray of 59.5 keV from ^{241}Am and the results were compared with simulation results. The obtained mean free paths were compared with the other group's calculated results. The simulation was extended to the energy spectrum of CZT strip detector.

II. Experiment

The CZT detector employed a spectroscopic grade crystal with the dimensions of 5×5×2 mm^3 and 5×5×5 mm^3. It was obtained from eV products and a division of II-VI incorporated. It was known that the Pt electrodes were deposited on both sides of the CZT detector. The signal electrode of 5×5×5 mm^3 dimensions was connected to a metal plate with a conductive epoxy. **Fig. 1** shows the experimental setup. A Peltier cooler with the size of 40 × 40 mm^2 was installed below the CZT detector. Water jacket was placed below the cooler to reduce the temperature. Thermocouple was placed close to the CZT detector to monitor the temperature of the CZT detector. **Fig. 2** shows experimental setup to measure the energy spectrum as the temperature of the CZT crystal was changed. The signal from the detector was passed through the charge-sensitive preamplifier (eV products Model 550), and the amplifier (ORTEC Model 572). The shaping time of amplifier was 1 μ sec. High voltage was biased on the detector with a high voltage power supply (ORTEC Model 659). The energy spectra were measured at the varying temperature. A pulse generator (ORTEC 480) was connected to the preamplifier to check the electronic noise.

*Corresponding Author, Tel. +82-2-2220-2354, Fax. +82-2-2296-2354, E-Mail; ykkim4@hanyang.ac.kr, ex-spark@kaeri.re.kr

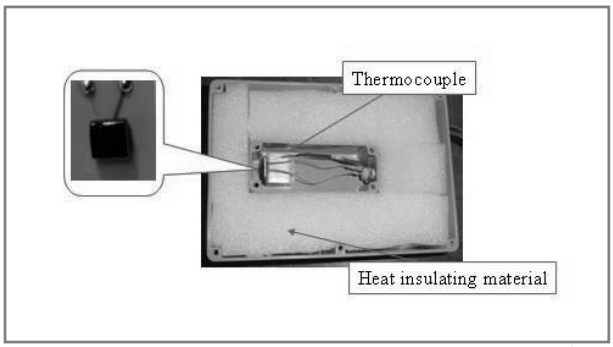

Fig. 1 The experimental setup dimensions of 5×5×2 mm^3 CZT detector

A commonly used method to study the transport properties in detectors is based on their response to α-particles. This method requires a specialized apparatus that allows the radiation source to be in close proximity to the detector, since α-particles will not penetrate more than a few microns through solid matter and will scatter inelastically even from air. Because the penetration depth of α-particles is only a few microns, the single-particle Hecht relation can be used to explain the measured circles[1]:

$$Q(V) = \frac{qVN_0(\mu\tau)_e}{d^2}\left[1-\exp\left(\frac{d^2}{(\mu\tau)_e V}\right)\right] \quad (1)$$

where N_0 is the number of charge carriers created by the incident radiation, Q the total charge collected, d the distance between the cathode and the anode. q the electronic charge, and V is the bias voltage. By measuring the charge collection with a long shaping time as a function of bias and fitting the data to the equation, $(\mu\tau)_e$ is the mobility-trapping time products for electron. Data was fitted with Eq. 1. From the fitting result, we could determine $(\mu\tau)_e$ of the CZT detector to be 1.69×10^{-3} cm^2/V.

The γ-ray energy spectrum was measured with the CZT detector. ^{241}Am with an activity of 45.6 nCi. was placed 70 cm away from the detector. Since the distance between the radiation source and the detector was quite long, it could be expected that parallel beam would be incident on the detector. The energy spectra were measured with various bias voltages. In all of the measurements, the dead times were less than 3%. **Fig. 3** shows γ-ray energy spectra measured with the CZT detector. The spectra were measured the temperature from -1.1℃ to 40℃. The energy spectrum measured with the bias voltage of 400 V showed the best energy resolution. When the bias voltage was higher than 400 V, the energy resolution got worse, and it would be from the increase of the dark current of the CZT detector. The α-spectrum was measured with the CZT detector. ^{238}Pu with an activity of 76.5 nCi. was placed 1.0 mm away from the detector. **Fig. 4** shows α-spectrum measured with the CZT detector. The spectrum was measured the temperature -4.6 ℃. The energy spectrum measured with the bias voltage of 200 V.

When the electron had to travel longer distance, the energy spectrum showed clear full energy peak. The energy spectra with the clear full peak were only employed to determine the mean free paths of the charge carriers in CZT crystal.

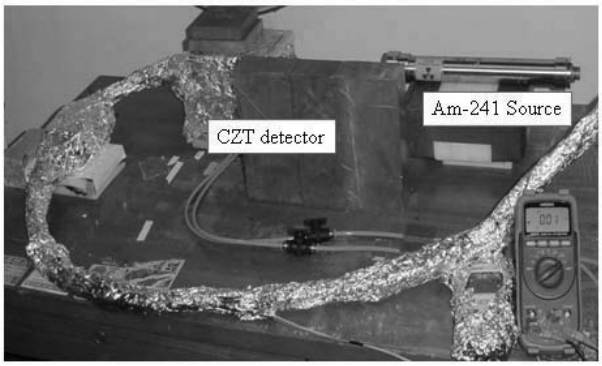

Fig. 2 Experimental setup to measure the energy spectrum as the temperature of the CZT crystal was changed

III. Simulation of the Response Function

The energy spectrum with the bias voltage of 500V was calculated with simulation, and it was fitted simultaneously to the measured ones. **Fig. 5** shows the results of the fitting.

The CZT material data was created with PEGS4 using a density of 5.86 g/cm^3. The energy limits in PEGS4[10] were chosen to be AP=0.001, UP=10.0, AE=0.512, and UE=10.0 MeV for photons and electrons, respectively. Electron-hole pairs were created whenever energy was deposited in a semiconductor. The average energy required to create an electron-hole pair was denoted as the W value, which was used 4.6 eV for CZT. The output pulse was proportional to the collected charge which was controlled primarily by mobility-lifetime products, $(\mu\tau)_e$ and $(\mu\tau)_h$ (units: cm^2/V), for electrons and holes, respectively. The mobility of charge carriers in CZT were much smaller than in Si and Ge detectors and the charge carriers were easily trapped in the crystal while they moved to the electrodes.

The charge collection efficiency was defined as the ratio of the number of charge carriers collected at the electrodes to the total number of carriers generated by radiation energy deposition. If the effect of de-trapping was neglected, the charge collection efficiency η(z) for charge carriers at depth z in a semiconductor crystal of thickness d (cm) could be expressed with Hecht equation[8].

$$\eta(z) = \frac{V(\mu\tau)_e}{d^2}\left[1-\exp\left(\frac{d^2}{(\mu\tau)_e V}\right)\right] + \frac{V(\mu\tau)_h}{d^2}\left[1-\exp\left(\frac{d^2}{(\mu\tau)_h V}\right)\right] \quad (2)$$

where both electrons and holes contributions were included, respectively. Here z is the depth into the crystal from the negatively-biased front surface.

The symmetrical peak broadening was from the electronic noise, statistics of the charge carriers, and the leakage current. The symmetrical peak broadening was approximated with the Gaussian shape. The peak broadening due to the electronic noise and the leakage current was estimated from

the pulse spectrum. The peak broadening due to the statistics of the charge carriers was included with:

$$\Gamma_{stat} = 2.35\sqrt{FWE} \quad (3)$$

where Γ_{stat} is the FWHM due to the statistics of the charge carrier, F is the Fano factor, having a value between 0.1 and 0.2 for CdZnTe[15], W the mean energy necessary to create one electron-hole pair, and E was the incident energy.

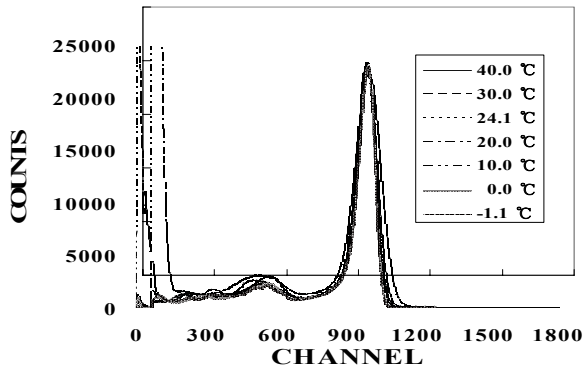

Fig. 3 γ−ray energy spectra measured with the CZT detector. The spectra were measured temperature from -1.1℃ to 40℃.

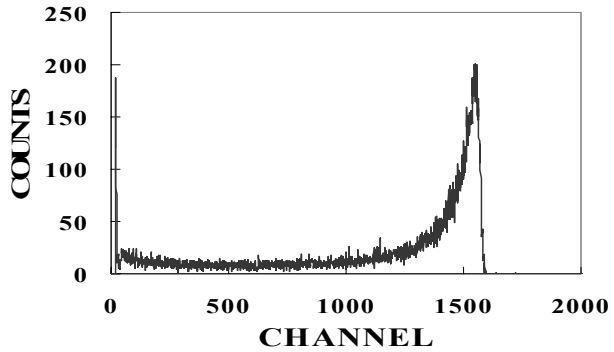

Fig. 4 α−spectrum measured with the CZT detector. The spectrum was measured temperature -4.6℃.

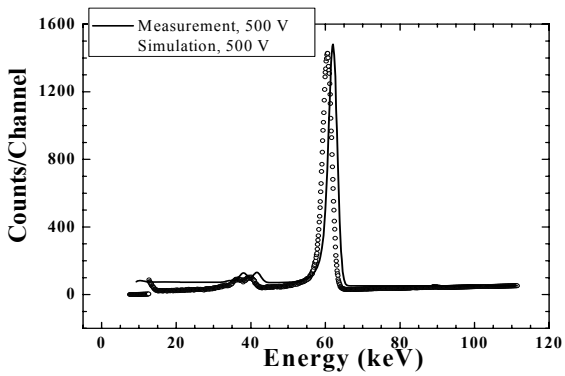

Fig. 5 The measured and the simulated energy spectra of 59.5 keV γ−ray.

From the fitting, $(\mu\tau)_h$ was determined to be 3.76×10^{-5} cm^2/V. The data obtained in our previous work was consistent with previously known values. A measure of the variations found in measured mobility is shown in Table 1., where $(\mu\tau)_e$ and $(\mu\tau)_h$ values from a number of others are presented.

The simulation was extended to the energy spectrum measured with strip-electrode CZT detector. When the CZT detector with strip electrode was used to measure the energy spectrum, more elaborate method had to be included. That is, weighting potential should be used to obtain the induced signal on the electrode. The incoming radiation generated moving charge within the detector, and charge was induced on the electrode by the movement of charge in the detector. The induced charge was amplified and shaped to the output signal. Because unique relation was established between the incoming radiation and the induced signal on the electrode, the radiation could be measured with the detector. The time dependence of the induced charge could be calculated as function of instantaneous position of moving charge in the detector. However, these processes were too tedious to be used in the real calculation. Schockley-Ramo theorem gave quite simple method to obtain the induced charge on the electrode by introducing weighting potential.

Table 1 Selected transport properties of CZT in published papers

Author	Year	$(\mu\tau)_e$ (cm^2/V)	$(\mu\tau)_h$ (cm^2/V)
Olschner[9]	1989	2.0×10^{-3}	7.0×10^{-5}
Hamilton[11]	1994	3.0×10^{-3}	
Heanue[12]	1996	2.3×10^{-3}	1.8×10^{-5}
Z. He[13]	2000	5.4×10^{-3}	
J.C. Liu[10]	2000	7.0×10^{-3}	5.0×10^{-5}
Schlesinger[1]	2001	3.30×10^{-3}	
S. Miyajima[3]	2002	1.0×10^{-1}	2.0×10^{-5}
S. H. Park[8]	2007	1.69×10^{-3}	3.76×10^{-5}

The weighting potential was calculated with the analytical expression, which was proposed by He[14]. The obtained weighting potential is shown in **Fig. 6.**

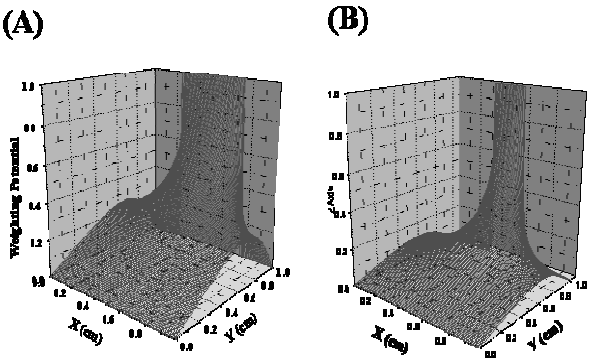

Fig. 6 Calculated weighting potentials. The right one (B) was calculated when the electrode width was 5 mm, and the left one (A) was calculated when the electrode width was 2.5 mm. As the

electrode width got thinner, the potential became steeper.

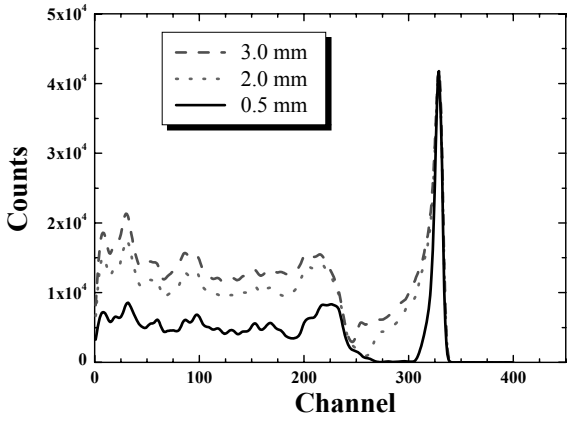

Fig. 7 The calculated energy spectra of detector with strip electrode. The size of the detector was 10×10×10 mm^3.

The number of charge carriers and the generation positions of charge carriers in the detector were calculated with EGSnrc[10]. The induced charge was obtained from the calculated weighting potential. The simulated energy spectra were shown in **Fig. 7**.

As one could see, the tail in lower energy region could be reduced when the strip electrode width got thinner. The comparison between the measurement and the simulation is underway.

IV. Conclusion

The energy resolution was improved from 12.5 % to 8.4 % when the detector temperature was changed from 40.0 ℃ to -1.1 ℃. The spectrum distortion can be characterized by the mean free path of the charge carriers. It was obtained from the measurement of the α-spectrum and γ-spectrum. A Monte Carlo simulation was developed and the result was compared with the experimental one. The simulation was extended to the case, where the energy spectrum was measured with the strip electrode. Our work could be helpful to design the CZT detector for high-resolution energy spectroscopy.

Acknowledgments

This work has been carried out under the nuclear R&D program of the Ministry of Science and Technology (MOST) of Korea. We are also supported by the iTRS Science Research Center / Engineering Research Center program of MOST / Korea Science and Engineering Foundation.

References

1) T.E. Schlesinger, J.E. Tonet, H. Yoon, E.Y. Lee, B.A. Brunett, L. Franks, and R.B. James, Materials Science and Engineering, 32 (2001) 103.
2) R. González, J.M. Perez, Z. He, Nucl. Instr. Meth. A 541 (2004) 554.
3) S. Miyajima, H. Sakuragi, M. Matsumoto, Nucl. Instr. and Meth. A 485 (2002) 533.
4) L.A. Hamel, S. Paquet, Nucl. Instr. and Meth. A 380 (1996) 238.
5) J.A. Haenue, J.K. Brown, B.H. Hasegawa, IEEE Transactions on Nuclear Science, NS-44 (3) (1997) 701.
6) T.H. Prettyman, Nucl. Instr. and Meth. A 422 (1999) 232.
7) A. Glière, M. Rosaz, L. Verger, Nucl. Instr. and Meth. A 442 (1999) 250.
8) S.H. Park, Y.K. Kim, S.D. Jeon, J.H. Ha, D.G. Hong, Nucl. Instr. Meth. A In press (2007).
9) Olschner, J.C. Lund, and I. Stern, IEEE Transactions on Nuclear Science, 36 (1989) 1176.
10) J.C. Liu, W.R. Nelson and R. Seefred, KEK proceedings 200-20 (2000) 135.
11) W.J. Hamilton, D.R. Ringer, S. Sen, M.H. Kalisher, K.James, C.P. Reid, V. Gerrish, C.O. Baccash, IEEE NS-41 (4) (1994) 989.
12) J.A. Haenue, J.K. Brown, B.H. Hasegawa, Nucl. Instr. and Meth. A 380 (1996) 392.
13) Z. He, W. Li, G.F. Knoll, D.K. Wehe, C.M. Stahle, Nucl. Instr. and Meth. A 441 (2000) 459.
14) Z. He, Nucl. Instr. Meth. A 365 (1995) 572.
15) B.P.F. Driks, C. Daly. O. Gevin, O. Limousin, F. Lugiez, Nucl. Instr. and Meth. A 567 (2006) 145.

Journal of NUCLEAR SCIENCE and TECHNOLOGY, Supplement 5, p. 553–555 (June 2008)

A Center-holed Faraday Cup Monitor for an Electron Microbeam Single Cell-irradiator

Gwang-Min SUN[1*], Mi JANG[2], Ji Seok KIM[2], Hyun Ki KIM[2], and Eun-Hee KIM[3]

[1]*Korea Atomic Energy Research Institute, 1045 Daedeokdaero, Yuseong-gu, Daejeon, Korea*
[2]*Korea Institute of Radiological and Medical Science, 215-4 Gongneung-dong, Nowon-gu, Seoul, Korea*
[3]*Seoul NationalUniversity,56-1 Sillim-dong, Gwanak-gu, Seoul, Korea*

An electron microbeam cell irradiator is used in radiation biology by using an in vitro cell irradiation. The Korea Institute of Radiological and Medical Sciences (KIRAMS) has operated such a system since 2002, when it performed its first cell irradiation experiment. But there is no appropriate real time electron beam monitoring apparatus for an electron beam. In this study, we designed a new center-holed Faraday cup monitoring system and evaluated its operation characteristics.

KEYWORDS: center-holed Faraday cup, electron microbeam

I. Introduction

Microbeam cell-irradiator has a highly localized spatial resolution corresponding to the size of a cell or a cell nucleus and has been used as a probe for the radiobiological influences induced by an exposure to a bunch of radiations. This becomes more valuable, especially in a low dose environment, since a pre-determined number of radiations can be delivered to a target with a small dimension. Microbeams adopting a low-linear energy transfer radiation such as photons and electrons have been developed in the US[1,2]. The recently constructed KIRAMS electron microbeam cell-irradiator (KEMCI) also uses electrons[3]. The electron beams from an electron gun of a 100 W power are shaped into a micrometer-sized beam through a pinhole aperture. After a startup, a beam qualification was carried out in various ways. Though this system shows good performances, a problem of monitoring a quantity of electrons incident on a target cell remains.

Though the generation of electrons in the electron gun is very stable, the low number of electrons needed in a low dose condition inevitably results in large statistical fluctuations. The relative uncertainty at about a hundred electrons in a pulse mode is over 20% while that at about a thousand electrons in a pulse mode is just several %. The lower the number of electrons is, the larger the uncertainty is. This fact requires statistical considerations for a quantification of the energies dissipated in a target cell even though electrons of a predetermined number are intended to irradiate it. Faraday cup has been used to measure the beam currents for a determination of the resultant cross-sections, which needs the ability of an absolute charge collection. Whereas the real operation of a Faraday cup as a monitor sometimes only needs a linearity between the beam currents and the other parameter of interest. For an electron microbeam with an energy range of 1~100 keV, there is no appropriate real time beam monitoring apparatus unlike for energetic heavy charged particles and alpha particle.

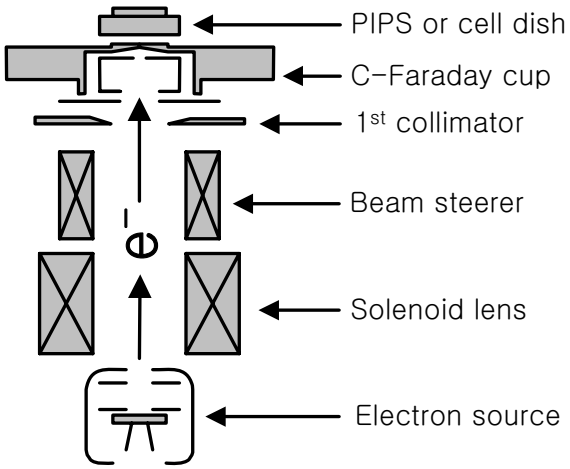

Fig. 1 Schematic view of an electron microbeam

Ion microbeam single cell irradiators employ various monitoring methods. A photo-multiplier tube can be mounted above a cell dish and a scintillator sandwiched between a collimator exit and a cell dish bottom which is the type used for an ion microbeam at the Gray Cancer Institute. A combination of a scintillator located beneath the pinhole aperture and a scintillation detector above the cell provides a real-time monitoring for an ion microbeam at Texas A&M University[4]. The transmitted particle through the cell and culture medium is detected by using a particle detector at the Radiological Research Accelerator Facility of Columbia university[5]. Electron microbeam at Texas A&M University adopted a Faraday cup inserted before and after a cell-irradiation, which doesn't yet provide a real-time monitoring.

Because the dose in a cell is heavily dependent on the number of electrons, a beam monitoring must be chosen from those methods that do not interfere with the initial electron path and their number. The conventional Faraday

*Corresponding Author, Tel No: +82-42-868-8710, Fax No: +82-42-868-8448, E-Mail: gmsun@kaeri.re.kr

cup collects an absolute beam current before and after a cell irradiation, but its use can be limited for a real time monitoring when a fluctuation or time-transience of a beam is included. We have designed a new center-holed Faraday cup (CHFC) with the provision to maintain an electron beam un-interfered with.

II. Experimental

Measurements of the CHFC performance were carried out using the electron microbeam system shown schematically in **Fig. 1**. This system has been described elsewhere[6], so only a brief description of it is included here for continuity sake. The electron microbeam was devised to shoot a pulsed beam. Beam energy can be varied from 1 to 100 keV. Beam current can be varied between 100 pA to 100 nA by adjusting the cathode current and grid voltage. This system can also be operated in a pulse mode with a pulse width of 2 μsec to DC.

Fig. 2 shows a schematic drawing of the CHFC design. A cavity is preserved for an inner cup at the lower side of the 6 inch vacuum flange. The inner diameter and depth of the cavity are 25 mm and 35 mm, respectively. The inner cup and the target made of an oxygen-free cupper were included in the cavity. The bevel angle of the target is 45°. The surface of the inner cup was cleaned by using a heating coil in an ultrahigh vacuum. A pinhole frame with a 200 μm diameter-pinhole is installed on a beam exit of the inner cup. This pinhole frame is electrically connected to the inner cup. And, another pinhole frame with a 5 μm diameter is located at the central region of the upper side of the vacuum window flange with a 1 mm diameter hole. The 2.5 μm–thick Mylar foil covers the pinhole frame and is fastened by a stainless steel ring to be airtight. Two O-rings were used for fastening the Mylar foil to the flange. One is for the stainless steel ring and another is for an additional support of the Mylar foil at the central region near the pinhole frame.

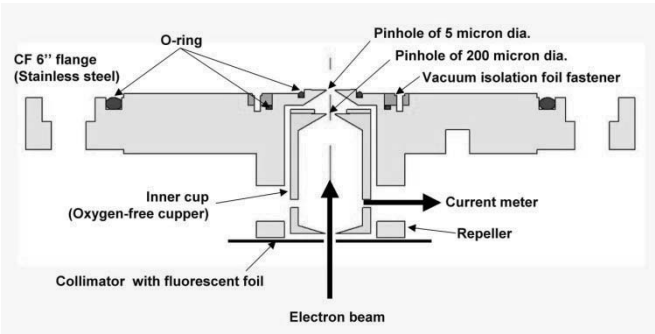

Fig. 2 Schematic drawing of a CHFC monitor design. The CHFC made of oxygen-free cupper was immersed in the vacuum window flange

Hence the electrons are generated from the electron gun, then extracted and focused by a solenoid lens to form a beam. The electrons then enter the vacuum chamber and are initially collimated by a 2 mm diameter 1st collimator and further collimated by the 200 μm and 5 μm diameter pinholes. Most of the electrons are collected at the inner cup and a very small portion is transmitted into the last pinhole frame. A Keithley 6517A digital electrometer was connected to the Inner Cup through a BNC connector. Electrons transmitted through the last pinhole were measured using the Canberra B50AM PIPS detector, of which the thickness is 500 μm. A calibration between the current at the inner cup and the number of electrons detected at the PIPS detector was carried out for various conditions. The signal from the PIPS detector is transferred to a Canberra 2008 preamplifier and an Ortec 572A amplifier through the electrical feedthrough of the vacuum chamber wall. The signal is branched into an Ortec 921E Ethernim multichannel buffer and an Ortec MCS-pci multichannel scaler. The electron pulse height spectrum is displayed on the GammaVision ver. 6.0 and the MCS-pci multichannel scaler, on a PC card, counts the number of events during a given time interval.

As shown in **Fig. 3**, a secondary electron suppressor is used to prevent an escape of the electrons from the inner cup surface and the target. The bias of the suppressor was applied by a voltage source of the Keithley 6517A electrometer of between 0 to -100 V. The dark current from the inner cup was below about 10aA without a suppressor bias and about 100aA when a suppressor bias was applied. The current from the inner cup was acquired using a DAQ software program written in Microsoft Basic 7.0. The acquisition repetition time can be varied between several nanoseconds to DC.

The energy spectrum is heavily dependent on the solenoid lens current when other parameters are fixed.

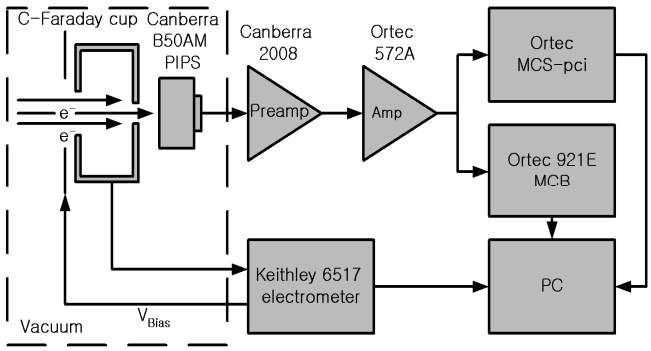

Fig. 3 Schematic diagram of a CHFC monitor. A CHFC is connected to a Keithley electrometer and a PIPS detector is connected to Ortec MCS and an MCB modules, which are controlled by a PC

III. Results and Discussion

Prior to measuring the variation of the target current according to the suppression bias of the electron repeller, the beam was scanned across the CHFC, to observe the beam energy spectrum at the PIPS detector, to elucidate the optimized operation parameters. This procedure was repeated when the beam energy or other conditions were varied. According to the solenoid lens current, the beam spot diameter without a beam collimation aperture is varied as shown in **Fig. 4**.

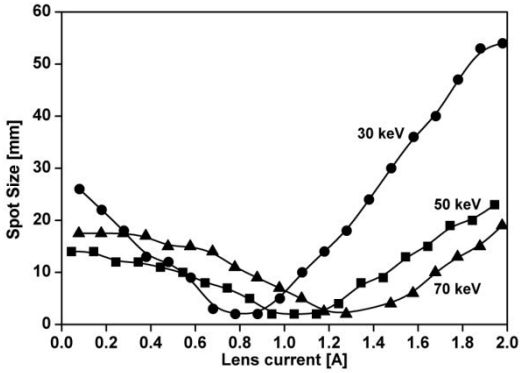

Fig. 4 Variation of the beam spot size at the sample position without a collimation aperture

The target current is mostly attributed to the primary electrons incident on the inner cup surface and the secondary electrons from the target surface and the pinhole frame. For the electrons entering the CHFC, a very small portion of those pass through the center hole (200 ㎜ diameter), and a very small portion from them also pass through the pinhole (5 ㎜ diameter).

An electron repeller is often used in front of the Faraday cup to repel stray electrons, to provide a fixed suppression bias that is not dependent upon the charge already collected by the cup, and also to retard a backscatter of primary electrons from the cup. When electrons are stopped completely in the copper stopper, and the secondary electrons from the stopper and pinhole frame are all collected in the inner cup, the accumulated charge at target Q_t measured experimentally is defined by the expression:

$$Q_t = Q_{pe} + Q_{se} + Q_{bk} \quad (1)$$

, where Q_{pe} is the charge due to the primary electrons and Q_{se} and Q_{bk} are the charges due to the secondary electrons and that due to the backscattered electron from the pinhole frame, respectively.

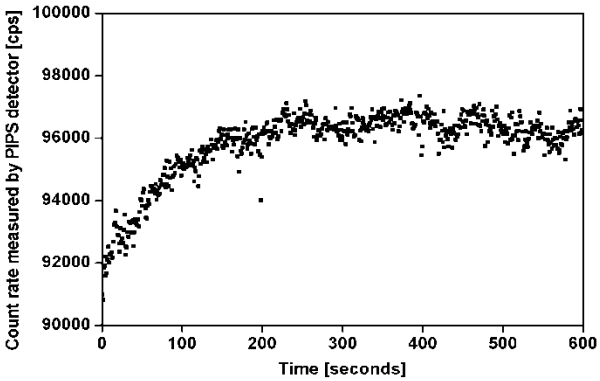

Fig. 5 Count rate measured by the PIPS detector after the start-up

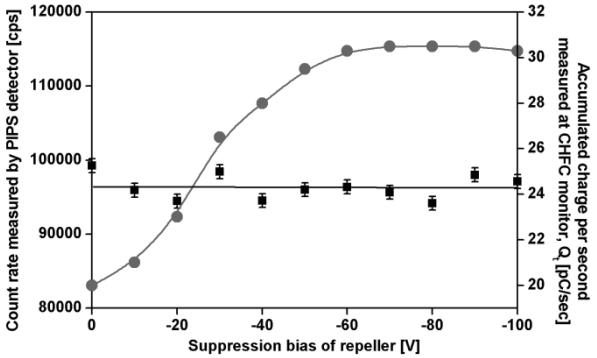

Fig. 6 Count rate measured by the PIPS detector and the accumulated charge at the CHFC monitor according to the suppression bias of the repeller

Fig. 5 shows the variation of the count rate measured by the PIPS detector, which is saturated at 200 second after a start-up. **Fig. 6** shows the count rate by the PIPS detector and the charge accumulated per second at the CHFC according to the suppression bias of the repeller. The charge rises as the bias amplitude rises and it is saturated after -60 V at which time the almost all the secondary electrons are retarded and collected in the cup.

IV. Conclusions

In this study, a new CHFC monitoring apparatus for a low energy electron beam was designed and its performance test was carried out. A real time monitoring of low energy electrons will be possible. However, more characterization studies for this apparatus will be performed in the near future.

References

1) W.E. Wilson, D.J. Lynch, L.A. and Braby, 'Microdosimery of a 25 keV Electron Microbeam', Radiat. Res. 155, 89–94, 2001.
2) M.S. Resat, and W.F. Morgan, 'Microbeam Development and Applications: A Low Linear Energy Transfer Perspective', Cancer Meta. Rev. 23, 323–331, 2004.
3) G.M. Sun, E.H. Kim, K.B. Song and M. Jang, 'Beam Characterization of the KIRAMS Electron Microbeam System', Radiat. Prot. Dosim. 121, 84–91, 2006.
4) L.A. Braby and J.R. Ford, 'Energy Deposition Patterns and the Bystander Effect', Radiat. Res. 161, 113–115 (2004).
5) G. Randers-Pehrson, C.R. Geard, G. Johnson, C.D. Elliston, and D. Brenner, 'The Columbia University Single-ion Microbeam', Radiat. Res. 156, 210–214, 2001.
6) E.H. Kim, G.M. Sun and M. Jang, 'An Microbeam Cell-irradiation System at KIRAMS: Performance and prelimary experiments', Radat. Prot. Dosim. 122, 297-300, 2006.

Journal of NUCLEAR SCIENCE and TECHNOLOGY, Supplement 5, p. 556–559 (June 2008)

Performance Tests of Developed Silicon Strip Detector by Using a 150 GeV Electron Beam

Hyojung HYUN, Sunwoo JUNG, Dongha KAH, Heedong KANG, Hongjoo KIM, and Hwanbae PARK*

Department of Physics, Kyungpook National University, Sankyuk-dong, Buk-gu, Daegu, 702-701, Korea

We manufactured and characterized a silicon micro-strip detector to be used in a beam tracker. A silicon detector features a DC-coupled silicon strip sensor with VA1_Prime2 analog readout chips.

The silicon strip sensors have been fabricated on 5-in. wafers at Electronics and Telecommunications Research Institute (Daejeon, Korea). The silicon strip sensor is single-sided and has 32 channels with a 1 mm pitch, and its active area is 3.2 by 3.2 cm^2 with 380 μm thickness. The readout electronics consists of VA hybrid, VA Interface, and FlashADC & Control boards. Analog signals from the silicon strip sensor were being processed by the analog readout chips on the VA hybrid board. Analog signals were then changed into digital signals by a 12 bit 25 MHz FlashADC. The digital signals were read out by the Linux-operating PC through the FlashADC-USB2 interface. The DAQ system and analysis programs were written in the framework of ROOT package.

The beam test with the silicon detector had been performed at CERN beam facility. We used a 150 GeV electron beam out of the SPS(Super Proton Synchrotron) H2 beam line. We present beam test setup and measurement result of signal-to-noise ratio of each strip channel.

KEYWORDS: silicon strip sensor, readout electronics, signal-to-noise ratio, electron beam

I. Introduction

Since a silicon sensor has a high position resolution compared to other detectors such as a proportional chamber, a drift chamber, etc.[1], it has been used in a variety of fields, for example, medical imaging, high energy experiment, and space science. We designed[2] a silicon strip sensor by dividing a large area diode into narrow strip, each of which has a separate electronic readout channel. We fabricated DC-coupled single-sided silicon strip sensors in a 5-in. fabrication line and developed readout electronics system. In this paper, results of a beam test performed with a silicon strip sensor including readout electronics at CERN (European Organization for Nuclear Research) beam facility by using a 150 GeV electron beam in October 2006 are presented.

II. Silicon Strip Position Sensor

When charged particles penetrate silicon bulk that is fully depleted by an applied reverse bias voltage, electron-hole pairs are produced. The produced electrons and holes in the silicon sensor are swept by the electric field to opposite sides of the sensor. The electrons are collected in the n-side and holes are collected in the p-side[3].

The DC-coupled single-sided silicon strip sensors were fabricated on 5-in., 380 μm thick, high resistivity (> 5 kΩ·cm), <100>-oriented, and n-type silicon wafers at Electronics and Telecommunications Research Institute (ETRI)[4]. A specification of the fabricated silicon strip sensors is shown in **Table 1**. They are single-sided and have 32 channels with a 1 mm pitch, and the active area is 3.2 cm by 3.2 cm with a thickness of 380 μm. **Fig. 1** is a photograph of the corner in the fabricated sensor. The p+ implanted strips, pads for signal readout, contact structure between p+ implanted and Al, and guard-ring structures are clearly seen in the photograph.

Table 1 A specification of the fabricated DC-coupled single-sided silicon strip sensor.

high resistivity (> 5 kΩ·cm), <100>-oriented, and n-type silicon wafers	
sensor area (μm^2)	35,000 × 35,000
sensor thickness (μm)	380
strip pitch (μm)	1,000
implanted strip width (μm)	400
Readout strip width (μm)	420

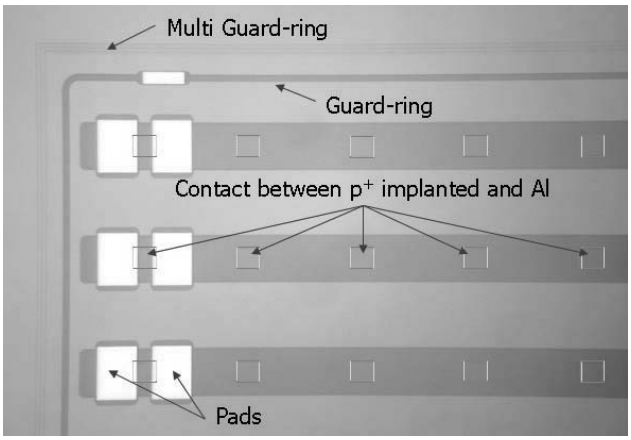

Fig. 1 Photograph of the fabricated DC-coupled single-sided silicon strip sensor

*Corresponding Author, Tel No: +82-53-950-7351, Fax. No: +82-53-953-7351, E-Mail: sunshine@knu.ac.kr

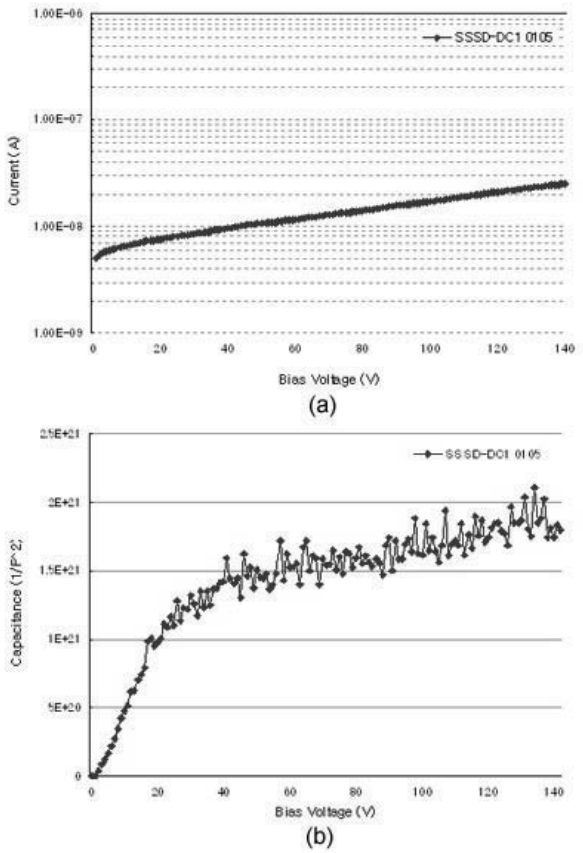

Fig. 2 The electrical characteristics measurement results, (a) leakage current and (b) capacitance as a function of reverse bias voltage, of the fabricated silicon sensor.

Measurements of the electrical characteristics such as leakage currents and capacitances provide us with information on the bulk characteristics and quality of the fabricated sensors[5]. The leakage current and capacitance of silicon bulk were measured with Keithley 6517 picoameter and HP 4277A LCZ meter as a function of reverse bias voltage, respectively (**Fig. 2**). Full depletion can be determined experimentally by measuring the capacitance of the sensor. In current prototype, the capacitance levels are expected theoretically[3] to be 60 ~ 80 volts,

$$V_{dep} = \frac{qN_D}{\varepsilon\varepsilon_0}\frac{d^2}{2} \quad (1)$$

where N_D is the doping concentration, ε is the dielectric constant, and d is the sensor thickness. To be considered as a good sensor[6], we required the leakage current of the bulk sensor should be less than 10 nA/single strip at the full depletion voltage. The leakage current of a single strip was measured to be about 0.3 nA at 100 volts and the capacitance value showed flatness from above 50 volts.

We chose silicon strip sensors for electron beam test which met the requirements of leakage current and bulk capacitance.

III. Readout Electronics System

The readout electronics system consists of VA Hybrid, VA Interface, and FlashADC & Control boards. Analog signals from the silicon strip sensor were processed by an analog readout chip, VA1_prime2 (VA for short hereafter) from IDEAS[7] on VA Hybrid board. VA has 128 channels with a low noise charge sensitive preamplifier, a shaper, and a sample and hold. Signals of readout channels are serially clocked out by control via 128-bit shift register. After that, the signals were changed into digital signals by a 12 bit 25 MHz FlashADC[8]. The digital signals were read out by the Linux-operating PC through the FlashADC-USB2 interface. Control signals from Xilinx on FlashADC & Control board were passed through logic converters on VA Interface board and distributed to VA on VA Hybrid board. Many kinds of regulators on VA Interface board make and supply various voltages for silicon strip sensor, VA chips, and amplifiers. The DAQ system and the analysis program were written in the framework of ROOT package[9].

The silicon strip sensor and readout electronics were assembled in an aluminum light-tight box as shown in **Fig. 3**.

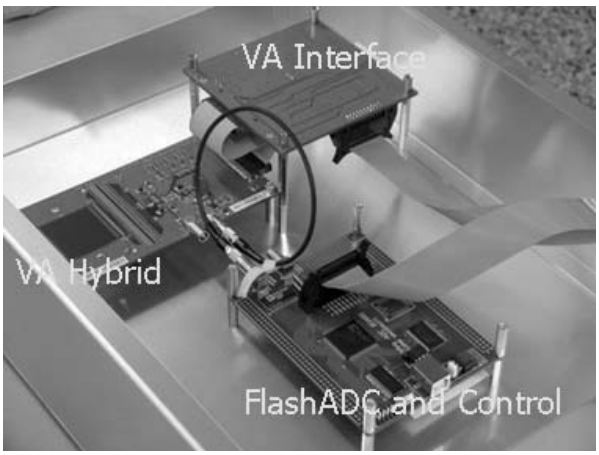

Fig. 3 Assembly of the silicon strip sensor and readout electronics in an aluminum light-tight box.

IV. Electron Beam Test

1. Experimental Set-up

The beam test with the silicon strip detector had been performed at CERN beam facility. We used a beam out of SPS (Super Proton Synchrotron) H2 beam line. A primary proton of 400 GeV from the SPS interacts with a Beryllium target of 30.0 cm thickness, called T2. As a result, many kinds of particles, such as electron, pion, muon, etc. are produced with various energies. We used a 150 GeV electron beam for the silicon strip detector test.

Fig. 4 shows the experiment setup for the beam test. Coincidence signals from three scintillators were used to trigger signals. Bias, about 60 volts, was applied to the silicon strip sensor during the irradiation and signal processes are the same as described in the previous section. The digital signals were read out by the Linux-operating PC through the FlashADC-USB2 interface. Maximum readout of the VA is 10 MHz[7], so over-sampling was used. A Linux-

operating PC which has digitized signal data was communicated with a control computer in the control booth through an Ethernet connection.

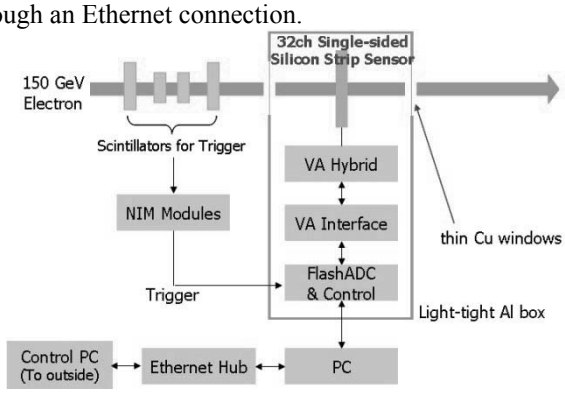

Fig. 4 Experimental setup for the electron beam test at CERN.

2. Measurement and Data Analysis Results

During the irradiation, we monitored and checked status of the silicon strip detector and beam profile. From beam profile measurement, the alignment of the detector to the electron beam was checked and corrected. **Fig. 5** shows two beam profiles: top and bottom plots are before and after correcting the alignment of the silicon strip detector to the electron beam, respectively.

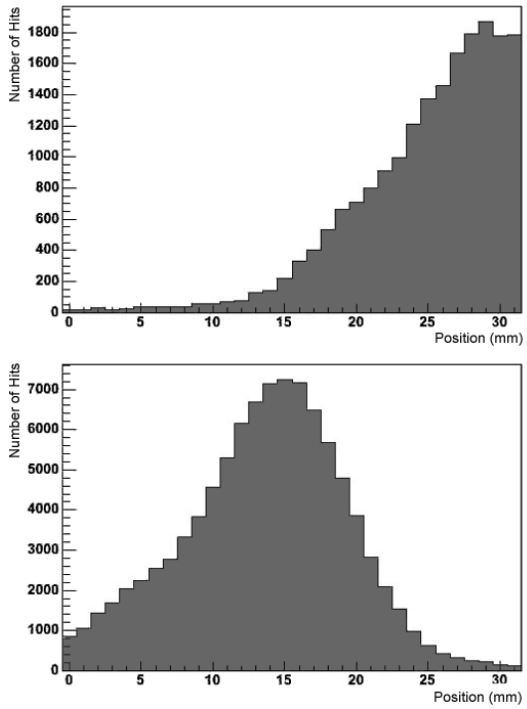

Fig. 5 Electron beam profile distributions before (top) and after (bottom) correcting alignment of the silicon detector to the electron beam.

The signal-to-noise ratio (SNR) of each channel was measured after coherent noise was subtracted. The SNR measurement result of a single channel is shown in **Fig. 6**. Pedestal and signal was fitted by a Gaussian function and a Landau-Gaussian convolution function, respectively. The SNR was measured to be 18.5. The SNRs of all channels were measured as good as 14.2 ~ 19.0 for a 150 GeV electron and are shown in **Fig. 7**. Channels 26 ~ 31 have large errors due to low statistics of triggered signal events as shown in **Fig. 5** (bottom) and a tendency of the SNR curve comes from trace routes of board layout. From simulation study[10], absorbed energy of a 150 GeV electron by a 380 μm silicon sensor is 0.11 MeV (**Fig. 8**), which corresponds to energy deposition of a minimum ionizing particle (MIP).

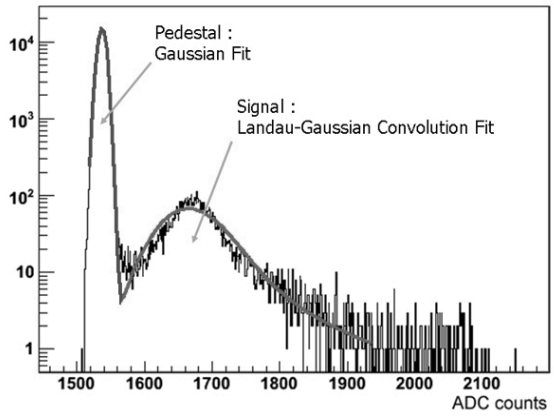

Fig. 6 Pedestal and signal distribution of a single strip channel for a 150 GeV electron beam.

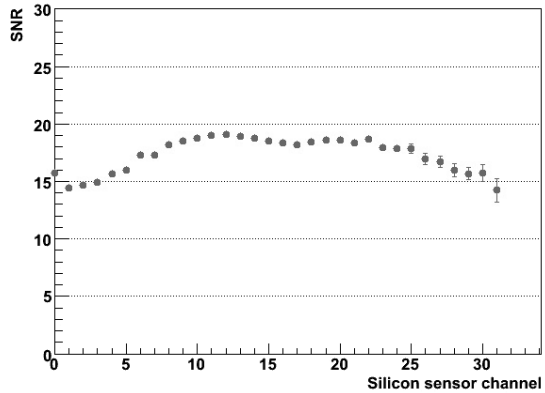

Fig. 7 Signal-to-noise ratios of all channels for a 150 GeV electron beam after coherent noise was subtracted.

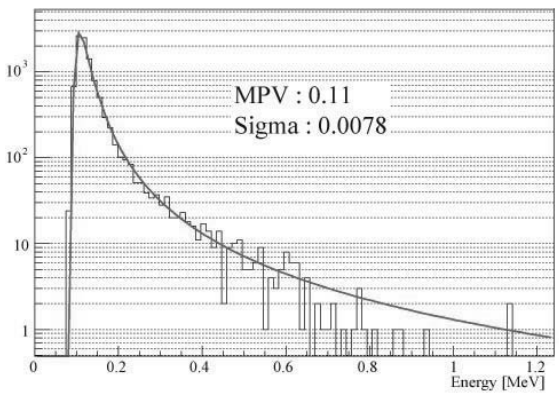

Fig. 8 Energy deposition on a 380 μm silicon sensor by a 150 GeV electron from GEANT simulation study.

V. Conclusions

We developed the silicon strip detector including DC-coupled, single-sided silicon strip sensor, and readout electronics. The fabricated silicon sensor showed a good quality in terms of electrical characteristics measurement results. We present the beam profile and the signal-to-noise ratio measurements with a 150 GeV electron beam at CERN. The measurement results show that the silicon strip detector can be used for beam tracker and the signal-to-noise ratio of the silicon strip detector is measured to be 14.2 ~ 19.0 for a MIP.

Acknowledgement

The authors wish to thank E.S. Seo, M.H. Lee, and A. Malinin for their help in beam usage and data taking at CERN beam facility. We acknowledge the support by Korea Science and Engineering Foundation under the Basic Atomic Energy Research Institute (BAERI) program, by a Korea Research Foundation grant funded by the Korean Government (MOEHRD) (KRF-2005-070-C00032), and by the International Cooperation program (M6-0404-00-0006) of the Korea Science.

References

1) W. M. Yao et al. (Particle Data Group), "Review of Particle Physics", J. Phys. G, **33**[1], 271 (2006)
2) S. Ryu, J. B. Bae, H. J. Hyun, D. H. Kah, Y. I. Kim, H. D. Kang, H. J. Kim, H. Park, and K. Y. Kim, "Signal-to-Noise Ratio Measurement for Silicon Strip Sensors with a Proton Beam", J. Korean Phys. Soc., **50**[5], 1477-1481 (2007)
3) Gerhard Lutz, Semiconductor Radiation Detectors, Springer, New York, 100-120 (2001)
4) see http://www.etri.re.kr/
5) H. Park, J. B. Bae, S. W. Jung, H. J. Hyun, D. H. Kah, H. D. Kang, H. J. Kim, Y. I. Kim, Y. J. Kim, S. Ryu, D. H. Shim, J. Lee, S. H. Doh, and D. S. Kim, "Fabrication and Beta-Ray Source Test of Double-Sided Silicon Strip Sensor", Jan. J. Appl. Phys., **46**[3A], 892--896 (2007)
6) H. Park, H. J. Hyun, D. H. Kah, H. D. Kang, H. J. Kim, Y. I. Kim, Y. J. Kim, D. H. Shim, Y. I. Choi, Y. K. Choi, J. Lee, J. M. Park, and K. S. Park, "Design and Fabrication of the Double-Sided Silicon Microstrip Sensor", J. Korean Phys. Soc., **49**[4], 1401--1406 (2006)
7) IDEAS, VA1_Prime2 version 0.9 Data-sheet, http://www.ideas.no (1999)
8) see http://www.noticekorea.com/
9) see http://root.cern.ch/
10) see http://geant4.web.cern.ch/geant4/

Journal of NUCLEAR SCIENCE and TECHNOLOGY, Supplement 5, p. 560–563 (June 2008)

Fabrication and Measurement Result of Silicon Strip Sensors

Dong Ha KAH[1], Jae Beom BAE[1], Heedong KANG[1], Hong Joo KIM[1], Hwanbae PARK[1*], Jong-Moon PARK[2], and Kun-Sik PARK[2]

[1]*Kyungpook National University, Sankyuk-dong, Buk-gu, Daegu, Korea*
[2] *Electronics and Telecommunications Research Institute, Gajeong-dong, Yuseong-gu, Daejeon, Korea*

A silicon sensor is very attractive material for medical imaging due to its intrinsic high resolution and fast readout. Silicon sensors of various types were fabricated on a 380 μm-thick n-type, float zone, 5 in. wafer which has high resistivity, <100> orientation, and is double-sided polished. We manufactured not only DC- and AC-coupled strip sensors but also pixel sensors and RC chips. The RC chips were fabricated for the purpose of using signal readout of the DC-coupled strip sensors. Electrical characteristics of the fabricated silicon sensors, leakage current and capacitance as a function of reverse bias voltage, were measured. Coupling capacitors and biasing resistors in the AC-coupled strip sensors were made by separating implantation from metallization strips with a thin oxide layer and made of polysilicons, respectively. The capacitance and resistance of each channel in the AC-coupled sensor were measured and compared with target values. The signal-to-noise ratio of the fabricated large pixel sensor was also measured by using a ^{90}Sr radioactive source.

KEYWORDS: sensor fabrication, silicon strip sensor, AC-coupled sensor, DC-coupled sensor, RC chip

I. Introduction

Silicon radiation sensors are used for detection of light, X-rays, high-energy particles and ions. Since silicon sensors provide high intrinsic position and energy resolutions, they are now used in a large variety of fields in science and technology, including nuclear physics, elementary particle physics and medicine. Even though a number of applications are growing fast and continuously, only few facilities in the world can fabricate and provide quality of silicon sensors which satisfy performance requirements.

We designed DC- and AC-coupled single-sided silicon strip (SSS) sensors, pixel sensors, and RC chips on the same n-type silicon wafer. The sensors were fabricated on 5 in. float zone (FZ), 380 μm-thick, <100>-oriented and high resistivity (> 5 kΩ·cm) silicon wafers. The RC chips were fabricated for the purpose of reading sensor signals out from the DC-coupled SSS sensor.

The details of the silicon sensors, test patterns, and RC chip designs are described in section II. Measurements of the electrical characteristics of the fabricated sensor, including coupling capacitance and biasing resistance of each channel in the AC-coupled SSS sensor, are presented in Section III. A signal-to-noise ratio (SNR) of a large pixel (PAD) sensor 1cm × 1cm size was measured by using a ^{90}Sr radioactive source and the measurement result is described in Section IV. In Section V, we summarize our measurement results and make a comparison between measured and target values of coupling capacitance and biasing resistance.

*Corresponding Author, Tel No: +82-53-950-7351, Fax No:. +82-53-953-7351, E-Mail: sunshine@knu.ac.kr

II. Silicon Sensor Design and Fabrication

The designed strip and pixel sensors are diode types, which consist of a highly doped shallow p^+ region on an n-substrate. The backside of the substrate is doped with high n^+ to provide a good ohmic contact and allow the sensor in depleted mode. The strip sensor is designed by dividing the large area diode into many small strip regions[1)].

Irradiation with light on a silicon sensor generates electron-hole pairs. A width of the space-charge region is increased by applying reverse bias voltage and the silicon bulk can be used as an active sensor volume in full depletion mode. Electron-hole pairs generated in the space-charge region are separated by the electric field. Sensor signals are then read out when charges are collected at the electrodes.

We designed not only DC-type SSS sensors[2)] but also AC-type SSS sensors which have capacitively coupled readout. PAD and pixels sensors were also designed with a main purpose of monitoring fabrication process. The RC chips were designed to be used to read signals out of the DC-type sensor.

1. AC-coupled Single-sided Strip Sensor

Capacitively coupled readout, which is called as AC-coupled, has an advantage of shielding the electronics from sensor leakage current which can lead to pedestal shifts and a reduction of the dynamic range[3)]. In the AC-coupled SSS sensor, we integrated coupling capacitors and high ohmic resistors into the silicon bulk. The coupling capacitor was manufactured by interleaving a thin oxide layer between implantation and metallization. The high ohmic biasing resistor was made of the p-doped polysilicon. A cross-sectional view of the AC-coupled SSS sensor and a top view of the biasing resistor in the sensor are shown in **Fig. 1**.

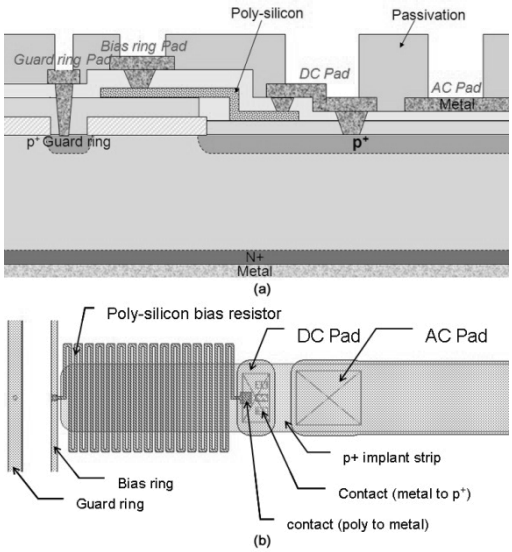

Fig. 1 (a) Cross-sectional view and (b) design layout of the AC-coupling single-sided silicon strip sensor.

Each strip has two AC-pads and one DC-pad. The AC-pads are connected to an ASIC chip by using wire bonding for signal readout. Meanwhile, the DC-pad is to measure leakage current of the strip. The thickness of the SiO_2 layer was optimized to be 500 nm to provide a proper capacitance (target value is 175 pF). The sensor was depleted by biasing resistors, which were made with p-doped polysilicon by low-pressure chemical vapor deposition (LPCVD). The length and width of the polysilicon was optimized to make the resistance of the resistor to be 20 MΩ. Specifications of the AC-coupled SSS sensors are summarized in **Table 1**.

Table 1 A specification of the AC-coupled single-sided silicon strip sensors.

	AC1	AC2
area (cm^2)	3.8 × 2.8	
number of strips	128	256
strip pitch (μm)	200	100
implant strip width (μm)	80	40
SiO_2 layer thickness (nm)	500	
polysilicon length (μm)	10000	
polysilicon width (μm)	10	

A total of 6 photo-masks were used for the sensor fabrication and each of them was designed to provide optimized fabrication process. The prototype sensors on the wafer are shown in **Fig. 2**.

2. Test Patterns

RC chips were fabricated on the same wafer to be used for signal readout from the DC-coupled SSS sensor. PAD and pixel sensors were also fabricated on the same wafer. Not only they provide a way of monitoring fabrication process but also can be used as a sensor component in a silicon detector for energy measurement and X-ray imaging.

The RC chip consists of resistors and capacitors as shown in **Fig. 3.**

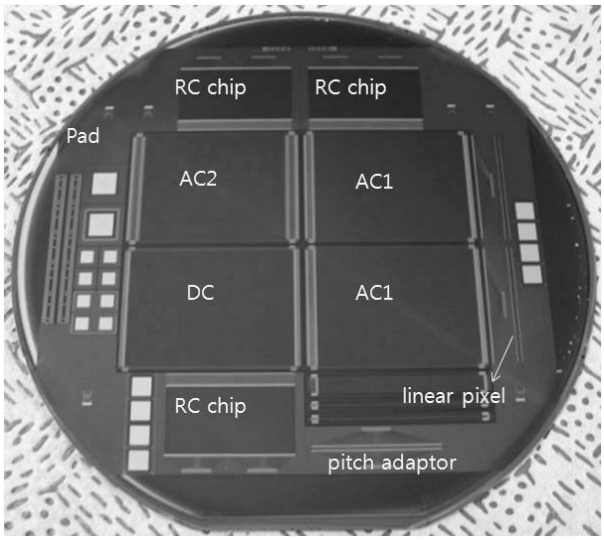

Fig. 2 The photograph of the fabricated AC-coupled sensors and various test patterns on the 5-in. wafer.

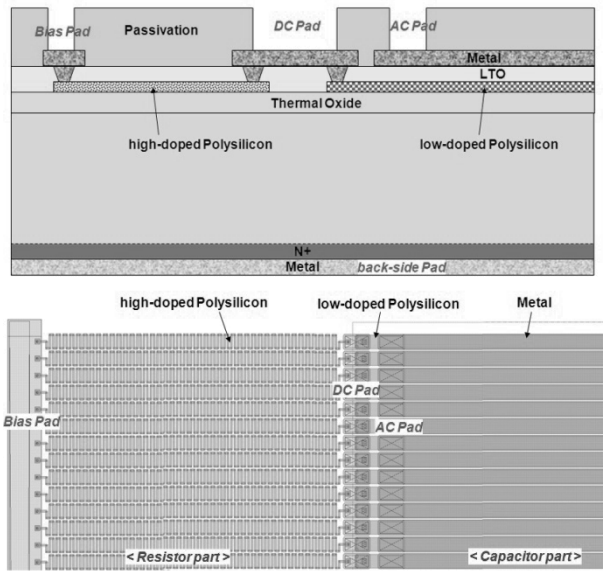

Fig. 3 Cross-sectional view and design layout of the RC chip.

The biasing structure helps to isolate each strip and will be used to bias sensors easily. The capacitor was constructed by separating high boron doped polysilicon and metal by an oxide layer. The capacitance is determined by the oxide thickness.

The qualities of RC chips were checked by measuring capacitance and resistance of the chips. Measurement results are shown in **Table 2** and show good uniformity in resistance and capacitance.

Table 2 Capacitance and resistance of a RC chip.

	Average	RMS	Target
coupling capacitance (pF)	194	18.41	200
biasing resistance (MΩ)	16	0.56	15

Table 3 shows the measured resistance values of the various test patterns. Measurement results show that we

controlled and understood fabrication process of the biasing resistor very well.

Table 3 Resistance of various test patterns for biasing resistor.

	R1	R2	R4	R4
sheet resistance (kΩ)		20		
width (μm)		10		
length (μm)	12400	16400	20400	24400
expected (MΩ)	24.8	32.8	40.8	48.8
measurement (MΩ)	25.0	33.0	39.0	47.0

An advantage of array pixel sensors provides two-dimensional position information with single-sided processing[4]. One of the PAD sensors was used for SNR measurement with a radioactive source.

The linear pixel sensor has an array of 2 × 128 pixels, the size of each pixel is 200 μm × 200 μm. The DC-pads at the both edges were designed to read signal out from each pixel. The specifications of the fabricated large and small pixel sensors are summarized in **Table 4**.

Table 4 Specifications of large and small pixel sensors.

	PAD sensor	Pixel sensor
area (cm^2)	1 × 1	2.7 × 0.3
number of channels	1	256
pixel size	1 (cm)	200 (μm)

III. Electrical Test

A direct check of the sensor quality is to measure the leakage current of the fabricated sensor. We measured the leakage current and capacitance of the bulk sensor as a function of the reverse bias voltage. A distribution of capacitance provides information of the depletion voltage,

$$V_{dep} = \frac{qN_D}{\varepsilon\varepsilon_0}\frac{d^2}{2} \quad (1)$$

where N_D is the doping concentration, ε is the dielectric constant, and d is the sensor thickness[5]. We expected the full depletion voltage to be 90 V with our silicon wafer. The leakage current and the bulk capacitance were measured[6] by using a Keithley 6517 picoammeter and a HP 4277A LCZ meter.

Fig. 4 shows the leakage currents and the bulk capacitances as a function of the reverse bias voltage. The $1/C^2$ -V distribution shows that the sensor is fully depleted well below 90 V, which means the resistivity of the silicon wafer is higher (> 8 kΩ·cm) than 5 kΩ·cm. We classified a sensor as a good quality if its leakage current at the operation voltage (80 V) is less than 10 nA/strip.

The coupling capacitances of the sensors were measured by applying the bias between the DC-pad and AC-pad. The measured (target) capacitance values were 127 (175) pF. These differences are understood due to permittivity dependence on fabrication process for oxide layer and fabrication limitation for oxide layer thickness. The resistances of the polysilicon were measured by probing the bias-ring pad and the DC-pad. The measured resistance values shows resistances of the biasing resistors of channels are very uniform.

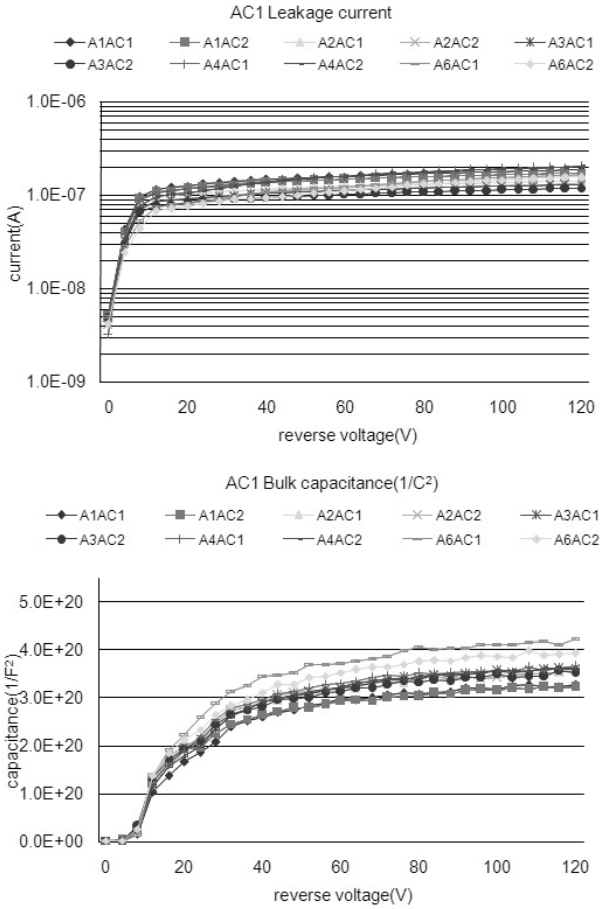

Fig. 4 The leakage current and bulk capacitance distributions of the AC-coupled silicon strip sensors.

IV. Beta Source Test

A sensor performance test of a PAD sensor was carried out by using a ^{90}Sr radioactive source.

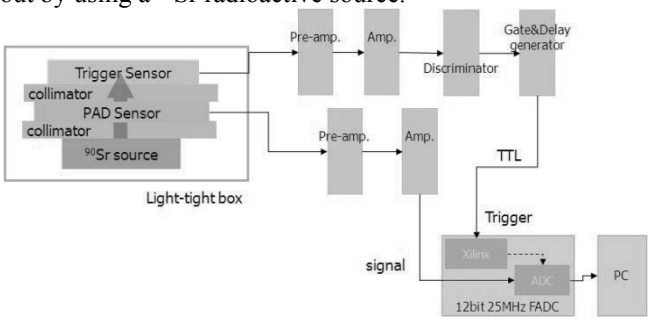

Fig. 5 A ^{90}Sr radioactive source test setup of a large pixel sensor.

Fig. 5 shows experimental set-up[7]. We used 1 × 1 cm^2 PAD sensor of process monitoring purpose. The PAD sensor and the front-end electronics were assembled in an aluminum light-tight box. A commercial photodiode[8] (called as "trigger sensor") was used to signal events. An analog

signal from the silicon sensor was connected into the analog input of a 12 bit, 25 MHz FADC board via a preamplifier and an amplifier. A signal from the trigger sensor was connected into the trigger input of the FADC board via a preamplifier, an amplifier, a discriminator, and gate & delay generator. The FADC output was recorded into a personal computer (PC) and data was analyzed with ROOT[9] based data analysis program.

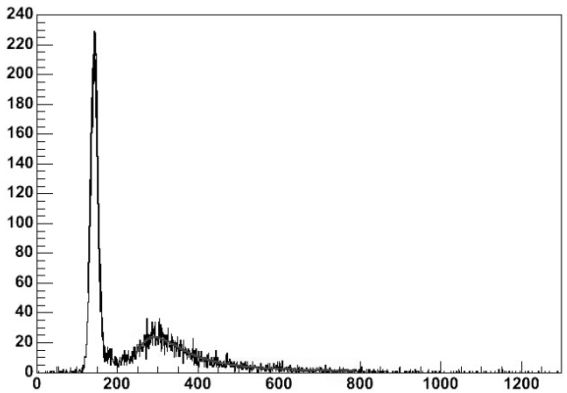

Fig. 6 A pulse height spectrum of the PAD sensor by using a ^{90}Sr radioactive source.

The measurement result is shown in **Fig. 6** to be 17.37±0.40.

V. Conclusions

The DC- and AC-coupled single-sided strip sensor with different strip pitches, large and small pixel sensors, and test patterns were designed, fabricated and their performances were tested. These sensors can be used in various fields such as medical imaging, nuclear, and high energy experiment. The sensors were fabricated on high resistivity, <100>-oriented, and n-type silicon wafer of 380 μm thickness. The prototype AC-coupled silicon strip sensor typically exhibits the full depletion voltage to be about 60 V, which is consistent with the specification for the resistivity (> 8 kΩ·cm) of the bare silicon wafers. The leakage current measurements show that the leakage current of the sensor is less than 10 nA/strip. From measurement results of resistances of the biasing resistors, we concluded that we understood fabrication process of the biasing resistor very well. The difference between measured and target capacitance values is understood due to permittivity dependence on fabrication process for oxide layer and fabrication limitation for oxide layer thickness. We also measured the signal-to-noise ratio of the fabricated PAD sensor to be about 17.0 with a ^{90}Sr radioactive source. We also fabricated RC chips and pixel sensors which showed good electrical qualities.

Acknowledgement

We acknowledge the support by the Korea Science and Engineering Foundation under the Basic Atomic Energy Research Institute (BAERI) program, by a Korea Research Foundation grant funded by the Korean Government (MOEHRD) (KRF-2005-070-C00032), and the SRC/ERC program of MOST/KOSEF (R11-2000-067-02002-0).

References

1) H. Park, H. J. Hyun, D. H. Kah, H. D. Kang, H. J. Kim, Y. I. Kim, Y. J. Kim, D. H. Shim, Y. I. Choi, Y. K. Choi, J. Lee, J. M. Park, and K. S. Park, 'Design and Fabrication of the Double-Sided Silicon Microstrip Sensor', J. Korean Phys. Soc., **49**[4], 1401-1402 (2006).
2) H. J. Hyun et al., 'Performance Tests of Developed Silicon Strip Detector by Using a 150 GeV Electron Beam', The Fourth International Symposium on Radiation Safety and Detection Technology, Hanyang University, Seoul, Korea, July 18-20, 2007.
3) G. Lutz, Semiconductor Radiation Detector, Springer, New York, 120 (1999).
4) G. F. Dalla Betta, G. U. Pignatel, G. Verzellesi, M. Boscardin, 'Si-PIN X-ray detector technology', Nucl. Instr. and Meth. A, **395**, 344-348 (1997).
5) J. Kemmer, D. Hauff, N. Krause, Ch. Krieglmeyer and Yang Yinxiang 'Current and capacitance measurements as a fast diagnostic tool for evaluation of semiconductor parameters', Nucl. Instr. and Meth. A, **439**, 199 (2000).
6) Jik Lee, D. H. Kah, H. J. Kim, H. Park and J. H. So, 'Radiation Hardness Study for Silicon Strip Sensors Using the 35-MeV Proton Beam from the MC-50 Cyclotron at the Korea Institute of Radiological and Medical Sciences', J. Korean Phys. Soc., **48**[4], 850-854 (2006).
7) H. Park, J. B. Bae, S. W. Jung, H. J. Hyun, D. H. Kah, H. D. Kang, H. J. Kim, Y. I. Kim, Y. J. Kim, S. Ryu, D. H. Shim, J. Lee, S. H. Doh, and D. S. Kim, 'Fabrication and Beta-Ray Source Test of Double-Sided Silicon Strip Sensor', Jap J. Appl. Phys., **46**[3A], 892-896 (2007).
8) Hamamatsu Photonics, K.K. 1126-Ichino Cho, Hamamatsu City, Japan.
9) see http://root.cern.ch/

Journal of NUCLEAR SCIENCE and TECHNOLOGY, Supplement 5, p. 564–567 (June 2008)

A Study on a Radiation Hardening of an Infrared Detector

Nam Ho LEE[1*], Jai Wan CHO[1], Seung Ho KIM[1], Jang Ho HA[1], and Young Ho KIM[2]

[1]*Korea Atomic Energy Research Institute, Tajeon, Korea*
[2]*i3 System, Tajeon, Korea*

In this work, radiation hardening of a infrared photo-voltaic detector which is the core component of thermal image system was studied. The device with ZnS surface passivation shows the degradation of RoA value by 1/100 after 10kGy gamma radiation. It is believed that the accumulated charge in the ZnS increases the surface leakage current and degrades the RoA value. To improve the irradiation characteristics, thermally evaporated CdTe was developed. The characteristics of CdTe passivated device was tested with various test patterns. It was found that the device with CdTe passivation shows radiation immunity for 10kGy gamma radiation.

KEYWORDS: radiation field analysis, Monte Carlo simulation, neutron spectrum, KORI nuclear power plant

I. Introduction

The infrared thermal imaging systems are used in many civil applications such as medical diagnosis which measures the temperature changes of human body, natural resources exploration from the satellite, earth observation for weather survey, non-contact measurement of product failure, crack of building, and insulating status of building. It has also been proposed that the thermal imaging system could have many applications in nuclear power plant. The malfunction of calandria located in front of nuclear reactor can be monitored by thermal imaging system and the leakage in tritium pipeline can be located by the non-contact measurement of thermal profile in the pipe.

Though the radiation hardening of thermal imaging system is essential for the nuclear application and satellite application and has been largely studied by the advanced country in Europe and U.S., the detailed technical results have hardly been reported because of the possible diversion of those technologies to military applications.

In this work, the radiation hardening of infrared detector which is the core component of radiation hardened thermal imaging system which can be applied for the monitoring of important instrument in the high radiation area in nuclear plant and for the satellite application has been studied. The degradation mechanism of infrared detector is analyzed by the radiation test and the improved process for radiation hardening is suggested and developed.

II. Radiation characteristics of Infrared detector

1. Fig. of Merits of Infrared Detector.

The performance of infrared detector is affected by the noise. In limiting case when the noise generated in the device itself is negligible, the photon noise generated by the radiation from the background limits the performance. The R_oA value which is the product of detector dynamic resistance at 0 V and the area determines the noise of the photo-voltaic detector and is generally used for the simple figure of merits of photo-voltaic detector. The R_oA value of the photo-voltaic detector can be expressed as the equation 1 if the diffusion current is the dominant current mechanism.

$$R_0 A = \frac{kTp\tau}{e^2 n_i^2 t} \quad (1)$$

(k : Boltzmann constant, T : temperature, p : hole concentration, τ: generation lifetime, e : electron charge, n_i : intrinsic electron concentration, t : device thickness)

2. Radiation Hardness of ZnS passivated HgCdTe Detector.

A sample with ZnS passivation was tested for the radiation hardness. The specifications of the tested sample are summarized in **Table 1**. This detector is developed and fabricated by i3system co. in Korea and the opto-electric performance shows the state-of-the-art characteristics. It was also chosen because the device structure as well as the process can be modified for the radiation hardness. Because its working temperature is 80 K. It is placed in the dewar which is cooled at the temperature of liquid nitrogen. **Fig. 1 (a)** shows the figure of dewar and **Fig. 1 (b)** shows the sample mounted in the dewar.

Table 1 The specification of a MCT IR device with a ZnS passivation layer

	Sample A	Sample B
Material	$Hg_{1-x}Cd_xTe$	$Hg_{1-x}Cd_xTe$
Composition	X = 0.29	X = 0.21
Cut-off Wavelength	5.1μm at 77K	11.5μm at 77K
Conduction Type	p-type	p-type
EPD	< 5e5/cm^2	< 5e5/cm^2
Junction Area	200μm X 200μm	150μm X 150μm
R_oA	1e6 Ωcm^2	10 Ωcm^2

*Corresponding Author, Tel No: +82-10-6744-1026, E-Mail: nhlee@kaeri.re.kr

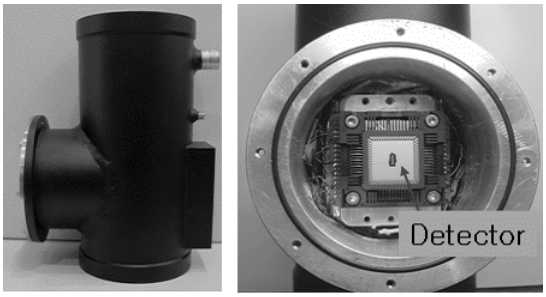

(a) Outer shape of a Dewar (b) IR detector in a Dewar

Fig. 1 The MCT IR device used in a test

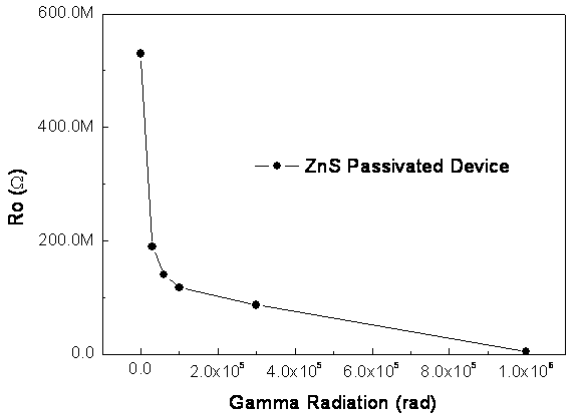

Fig. 2 The variation of R_O values to the gamma-ray dose

To measure the change of characteristics by the gamma radiation, high dose gamma source was used. Co-60 in KAERI were used for the high dose gamma source. The dose rate was 2 kGy / hour and the samples were radiated for 5 hours. **Fig. 2** shows the R_0 value changes with the gamma radiation. It is shown that the R_o value reduces by 1/5 with 1 kGy gamma radiation, which means the 2 times increased noise and degradation of opto-electric performance by 1/2. The R_o value reduces to 1/100 after 1 Mrad radiation and it is supposed that the performance will be degraded by 1/10.

The reason for the reduced R_o value by gamma radiation is supposed to be the increased surface leakage current. The surface leakage current increases by the surface fixed charge, which is accumulated in the ZnS during the irradiation of gamma ray.

When the large fixed charge appears on the surface of the device, the surface state changes as is shown in **Fig. 3**. **Fig. 3 (a)** shows the surface state when the positive fixed charge is accumulated on the surface and the current channel is generated between the p and n area. The surface current can flow through the surface channel and the R_o value reduces by the current. When the negative fixed charges are accumulated, the surface state changes as is shown in **Fig. 3 (b)**. This figure shows possible tunneling current through the reduced depletion region especially when the bandgap is small, which is the nominal condition for HgCdTe. **Fig. 3** shows that reducing the accumulation of fixed charge during the gamma ray irradiation is important for radiation hardening of HgCdTe photo-voltaic detector.

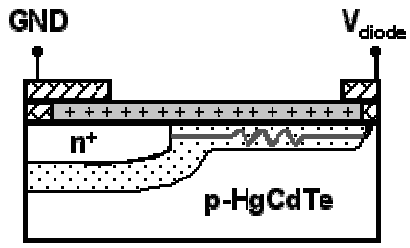

(a) In case of fixed positive charges at surface

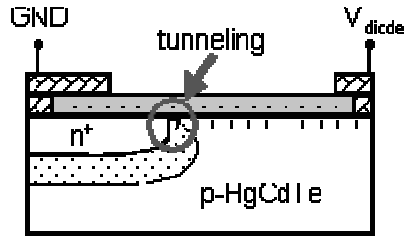

(b) In case of fixed negative charges at surface

Fig. 3 The charges of surface state to the fixed charges

III. Radiation Hardening by CdTe Surface Passivation

1. CdTe Surface Passivation

The degradation of device made with ZnS surface passivation by gamma radiation was attributed to the accumulated surface fixed charge during irradiation, which generates large surface leakage current and reduces R_o value. To reduce the surface leakage current generated by the fixed charge, CdTe passivation was proposed. It is supposed that the CdTe has small cross section of electron trapping and the inter-diffusion of CdTe and HgCdTe will increase the bandgap on top of the HgCdTe surface.

Fig. 4 shows the expected band diagram of HgCdTe/CdTe interface after HgCdTe and CdTe inter-diffusion. It is supposed that the increased bandgap on the surface of HgCdTe as is shown in figure 4 could reduce surface leakage current for large surface fixed charge and radiation hardness could be achieved.

Fig. 5 shows the R_oA value changes versus surface fixed charge. It is shown that the CdTe passivated device shows better immunity to the fixed charge as was expected by the band diagram in **Fig. 4**.

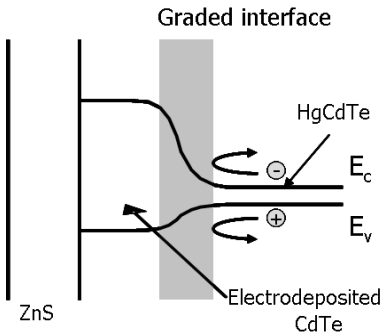

Fig. 4 An expected band diagram

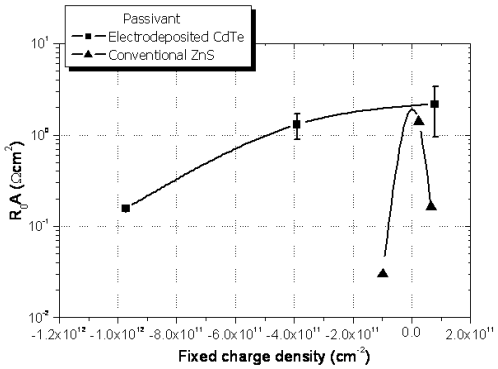

Fig. 5 R_OA value changes to the surface fixed charges

2. The Development of CdTe Passivation Layer

CdTe was formed by the thermal evaporation in the thermal evaporator which was used for ZnS evaporation and modified for CdTe evaporation. Pallet type CdTe of 2 ~ 3 mm diameter with 99.999% purity was used for the evaporation source. **Fig. 6** shows the SEM image of evaporated CdTe on Si wafer. It is shown that the evaporated CdTe has thickness of 7200 Å and columnar structure which could be generally found in the thermally evaporated ZnS. **Fig. 7** shows the surface morphology. It is shown that the evaporated CdTe has dense structure and can be applied for the passivation layer.

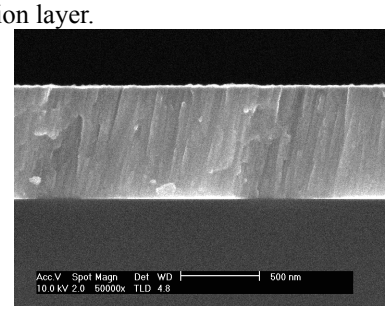

Fig. 6 The SEM image of evaporated CdTe (crosssection)

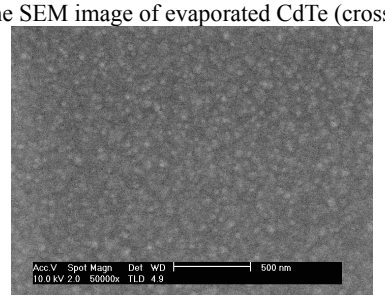

Fig. 7 The SEM image of evaporated CdTe (surface)

EDAX analysis result of thermally evaporated CdTe is summarized in **Table 2**. The atomic composition of Cd and Te is 49.7% : 50 .29%, which is believed to be the best for insulation.

Table 2 EDMX analysis result of thermally evaporated CdTe

Element (atomic no.)	Weight Percent	Normalized Wt Percent	Atomic Percent	Count Err. (sigma wt %)
Cd (48)	46.2506	46.5457	49.7089	0.5623
Te (52)	53.1153	53.4543	50.2911	0.7297

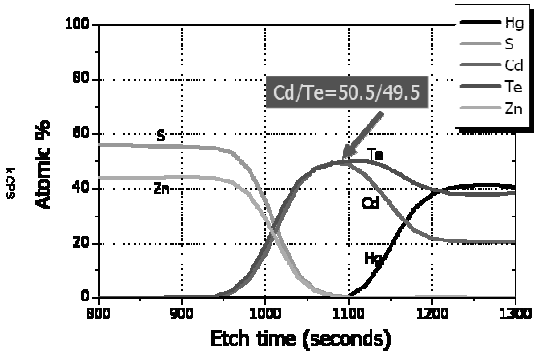

Fig. 8 AES depth profile of an evaporated of ZnS/CdTe on HgCdTe

Fig. 8 shows the AES depth profile of evaporated ZnS/CdTe on HgCdTe. It is shown that the composition of Cd : Te is 1 : 1 and 2000 Å of inter-diffused layer was formed between CdTe and HgCdTe. To characterize the insulating characteristics and interface characteristics of CdTe layer before the fabrication of photovoltaic device, C-V MIS(Metal Insulator Semiconductor) Pattern was fabricated.

Fig. 9 shows the cross-sectional view of C-V pattern. To find the insulation characteristics, the I-V characteristics between two gate metal electrode was measured. The capacitance between the gate electrode and contact electrode varying the gate electrode potential was also measured to characterize the C-V characteristics. HP4156 was used for I-V measurement and HP4280 was used for C-V measurement. **Fig. 10** shows the current density vs. voltage converted by the I-V measurement. It was found that negligible current flows between -5V and 5V and the insulating characteristics are good for possible use of CdTe to the insulator.

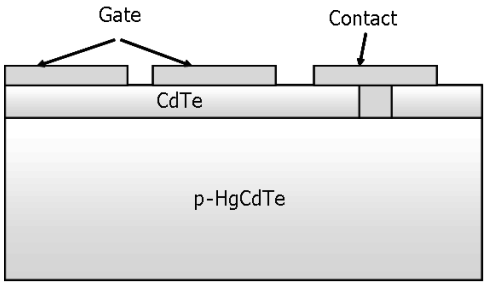

Fig. 9 A cross-sectional view of a C-V pattern

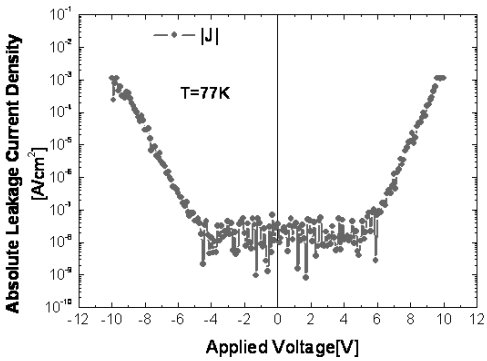

Fig. 10 I-V characteristics at a gate bias

3. Radiation Characteristics of CdTe passivated Device

The radiation hardness of fabricated diode was tested the same radiation condition as the ZnS passivated device for the comparison. **Fig. 11** shows the R_o values to the gamma radiation doses. For the comparison, the characteristics of ZnS passivated device were also shown. It is found that the CdTe passivated device did not show degradation for 1 Mrad gamma radiation. The initial improvement of R_o value of CdTe passivated device seems to result from the defect annealing by the "shaking" of crystal during the irradiation of gamma ray.

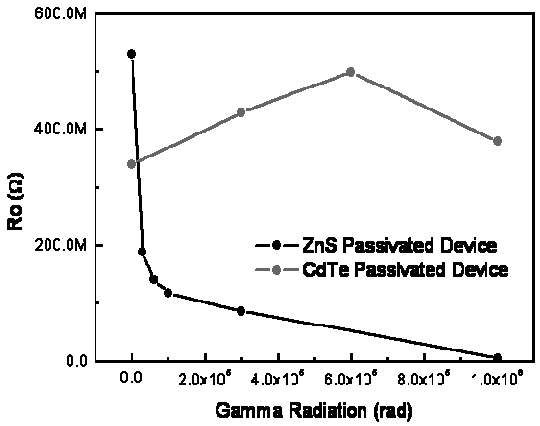

Fig. 11 R_o value changes by the gamma radiation

IV. Result

In this work, radiation hardening of infrared sensor which is the core component of infrared thermal imaging system is studied. To understand the mechanism of device degradation, the radiation hardness of usual ZnS passivated device was analyzed. It was found that the ZnS passivated device shows the reduction of R_o value by 1/100 after 1 Mrad of gamma radiation, which increases the device noise by 10 and degrades the device performance at the same ratio. It seems that the degradation results from the surface leakage current produced by surface fixed charge accumulated during the radiation bombardment. It is supposed that the radiation bombardment produces electrons and holes and the generated carriers are trapped in the defects. To avoid the accumulation of carriers and surface leakage current, thermal evaporation of CdTe was developed for the passivation of HgCdTe device. The insulting property, fixed charge density, and mobile charge density of the thermally evaporated CdTe show that CdTe is adequate for the passivation of HgCdTe. The fabricated HgCdTe device with CdTe passivation shows radiation hardness for 1 Mrad gamma radiation. It is expected that this radiation hardening technology can be applied to the development of the thermal imaging system that can be used to observe the high radiation area, space and earth in the satellite.

References

1) E.L.Dereniak, G.D. Boreman, Infrared Detectors and Systems, 1st Ed., John Wiley & Sons, New York (1996), chap. 1.
2) R.S. Muller, T.I. Kamins, Device Electronics for Integrated Circuits, 2nd Ed. Wiley, New York, (1986).
3) R. Adar, "Spatial integration of direct band‐to‐band tunneling currents in general device structures", IEEE Trans. Electron. Device 39, 976, (1992).
4) R.K.Willardson and A.C.Beer, Semiconductors and semimetals, Vol.5, New York, (1970).
5) S.P.Langly, “The bolometer”, Nature 25, 14 (1881).
6) J.H.Ludlow, W.M.Mitchell, E.H.Putley, N.Shaw, J. Sci. Instrum. 44, 694 (1967).
7) S.M.Sze, Physics of Semiconductor Device, 2nd Ed. Wiley, New York, (1981).

Journal of NUCLEAR SCIENCE and TECHNOLOGY, Supplement 5, p. 568–571 (June 2008)

Scintillation Properties of $Ba_{0.20}Sr_{0.80}Cl_2$ Single Crystal

Jungin KIM[1], Heedong KANG[1*], H.J. KIM[1], H. PARK[1], Sih-Hong DOH[2], and Sunghwan KIM[3]

[1]*Kyungpook National University, Daegu 702-701, Korea*
[2]*Pukyong National University, Busan 608-737, Korea*
[3]*Daegu Health College, Daegu 702-722, Korea*

New scintillation crystal of a $Ba_{0.20}Sr_{0.80}Cl_2$ grown by the Czochralski technique is reported. The grown crystal was cut into a size of 10×10×10 mm^3. The lattice parameter of the grown crystal is a = b = c = 7.041 Å and the crystal structure is cubic. The luminescence and scintillation properties of the $Ba_{0.20}Sr_{0.80}Cl_2$ crystal were studied. The luminescent characteristics were measured with ultraviolet (UV) light and X-ray source to study the emission spectra of the crystal. Scintillation properties of the crystal such as pulse height spectra, energy resolution, α/β ratio, light output, proportionality curve, and fluorescence decay time were measured with the various radioactive γ-ray sources and α-source at room temperature. The light output of the crystal was compared with that of the CsI(Tl) crystal and the absolute light output was measured with avalanche photodiode (APD). While the light output of the crystal was less than that of the CsI(Tl), the energy resolution was approximately 6.9% for ^{137}Cs 662 keV γ-ray with PMT which is similar to that of the CsI(Tl) crystal for ^{137}Cs γ-rays.

KEY WORDS: $Ba_{0.20}Sr_{0.80}Cl_2$, Czochralski, scintillation properties, scintillator

I. Introduction

Recently, various new and improved inorganic scintillators have been investigated with the goal of finding heavy, fast, and more efficient materials with a high light output and good energy resolution for applications as X- and γ-ray radiation detectors. Applications include medical imaging, industrial systems like security systems at airport, and those are also useful in nuclear physics, high energy physics, and astrophysics.[1)]

Alkaline earth halides have attracted researcher's attention since the pioneering reports on the possibility of modifying the optical properties of single crystals by doping with different impurities such as Ce or Eu.[2,3)] On the other hand, mixed alkaline earth halides were not dedicated much to explore their mixtures and very few systems have been grown to explore the entire range of concentrations.

The mixed $Ba_{0.20}Sr_{0.80}Cl_2$ single crystal was investigated with the purpose of obtaining new materials. The luminescent characteristics were studied and we present the scintillation properties such as pulse height spectra, energy resolution, α/β ratio, light output, proportionality, and fluorescence decay time, which were measured with the various radioactive γ-ray sources at room temperature.

II. Experiments

1. Crystal Growth

A $Ba_{0.20}Sr_{0.80}Cl_2$ single crystal was grown using the Czochralski technique under an induction heating platinum crucible with the diameter of 30 mm. The growing process was performed in the Ar-gas atmosphere with the pulling rate of 2~2.5 mm/h and the rotation rate of 20~25 rpm. To reduce crystal cracks, a low thermal gradient was setup in the furnace. The raw materials for the growth of $Ba_{0.20}Sr_{0.80}Cl_2$ were synthesized by melted-state reaction. The $BaCl_2$ powder (99.95%, Sigma-Aldrich) of 20% for molar weight and the $SrCl_2$ powder (99.99+%, Sigma-Aldrich) of 80% for molar weight were mixed for chemicals to grow the crystal. The transparent and uniform $Ba_{0.20}Sr_{0.80}Cl_2$ single crystal of 20 mm in diameter and 30 mm in height was grown as shown in **Fig. 1**. The sample of $Ba_{0.20}Sr_{0.80}Cl_2$ crystal with the dimension of 10×10×10 mm^3 was cut from the grown crystal and polished using mixed Al_2O_3 powder (grain size of 0.02 μm) in mineral oil on a polishing cloth (Buehler, No.40-7218). The CsI(Tl) single crystal as a reference was grown by using the same methods and circumstances.

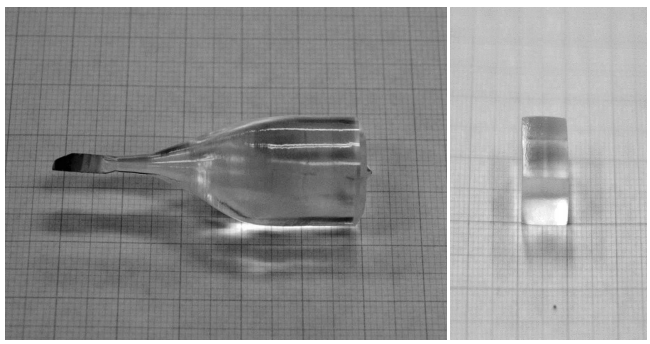

Fig. 1 The grown $Ba_{0.20}Sr_{0.80}Cl_2$ single crystal and the polished sample.

*Corresponding Author, Tel No: +82-53-320-1319, Fax. No: +82-53-320-1449, E-Mail: kimsh@mail.thc.ac.kr

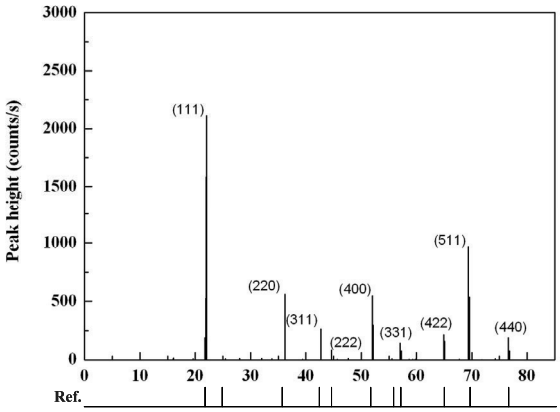

Fig. 2 X-ray diffraction patterns of the $Ba_{0.20}Sr_{0.80}Cl_2$ single crystal.

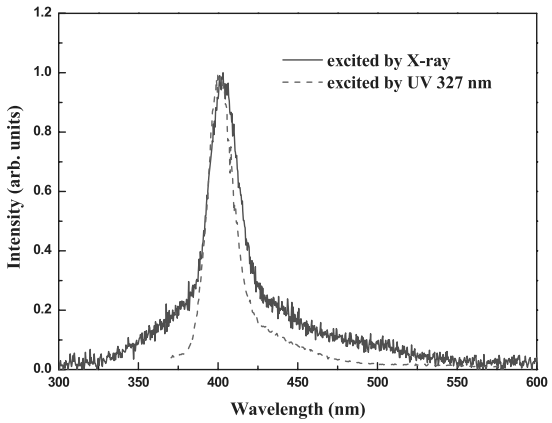

Fig. 3 Emission spectra of the $Ba_{0.20}Sr_{0.80}Cl_2$ single crystal.

2. XRD and Density

The $Ba_{0.20}Sr_{0.80}Cl_2$ mixed crystal was characterized by X-ray diffraction System (X'Pert-MPD, Philips). The $Ba_{0.20}Sr_{0.80}Cl_2$ crystal belongs to a cubic system of space group $Fm\bar{3}m(225)$ with parameter a = 7.041 Å.[4] Powder diffractorgrams of the mixed $Ba_{0.20}Sr_{0.80}Cl_2$ crystals showed single phase patterns indicating complete miscibility and it is visualized in **Fig. 2**.[5] The positions of the other peaks match with small variations in peak intensities which might be related to changes in composition introduced by the structural modification and disorder during the crystal growing process.[6]

Density of the $Ba_{0.20}Sr_{0.80}Cl_2$ crystal was determined to an accurate 3.640 g/ml performed with gas deposition method to define volumes (NOVA-2000, Quantachrome).[7]

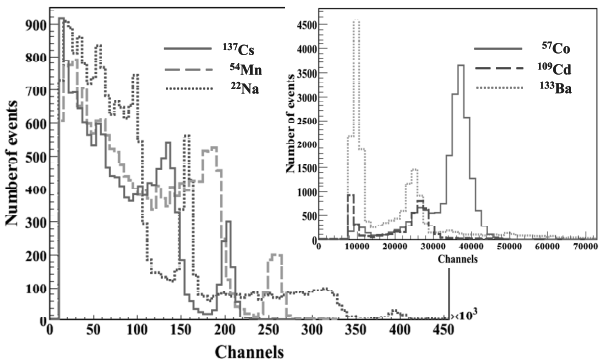

Fig. 4 Pulse height spectra of the $Ba_{0.20}Sr_{0.80}Cl_2$ crystal for various radioisotopes.

III. Results and Discussion

1. Emission Spectra

Emission spectra of the $Ba_{0.20}Sr_{0.80}Cl_2$ crystal have been measured with UV and X-ray excitation at room temperature. The emission measurements were performed with luminescence spectrometer (LS50-B, Perkin Elmer) equipped with a Xe flash lamp. The crystal was excited at 250, 260, 265, 327, 343 and 363 nm wavelength. Measurements of the emission spectra excited by X-ray were done using an X-ray generator with operated at 100 kV and 5 mA and monitored with photodiode (USB2000, Oceanoptics).[8] Apparently, both UV and X-ray emission spectra show similar results located in the range of 375 ~ 500 nm peaking at 400 nm as shown in **Fig. 3**.

2. Light Output and Energy Resolution

The crystal was wrapped in a few layers of Teflon tape and optically coupled with 2 inches bialkali photomultiplier tube (9208B, Electron tube Ltd.).[9] Signals from the PMT were fed into a 400 MHz FADC (flash analog-to-digital converter).[10] We analyzed the data using ROOT package.[11] The signal photoelectron was identified by using clustering algorithm since 400 MHz FADC was used for the signal digitization. The pulse height spectra of the $Ba_{0.20}Sr_{0.80}Cl_2$ crystal excited by various γ-ray sources are shown in **Fig. 4**.

Fig. 5 shows a typical pulse height spectra irradiated with 662 keV γ-rays in the $Ba_{0.20}Sr_{0.80}Cl_2$ single crystal and compared with that of the CsI(Tl) crystal. The energy resolution of the $Ba_{0.20}Sr_{0.80}Cl_2$ crystal was 6.9% ^{137}Cs γ-rays. It was similar to that of CsI(Tl) crystal to be 7.1%.[3,12] Relative light output of the $Ba_{0.20}Sr_{0.80}Cl_2$ compared with that of the CsI(Tl) was 77% with PMT. Relative light output was measured with comparing photo-peak channels in **Fig. 5**, which directly related with light output.

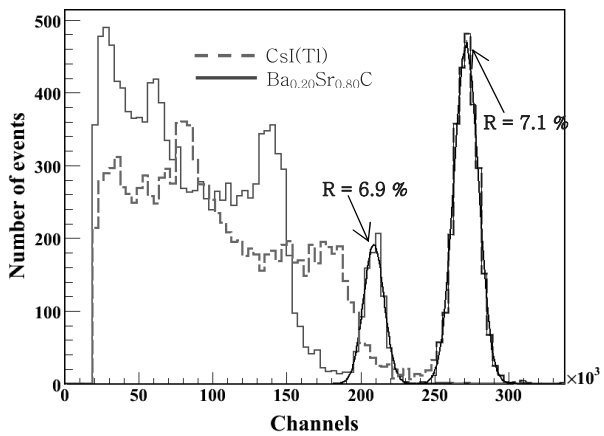

Fig. 5 Pulse height spectra of 662 keV γ-ray detected in the $Ba_{0.20}Sr_{0.80}Cl_2$ single crystal compared with CsI(Tl) crystal.

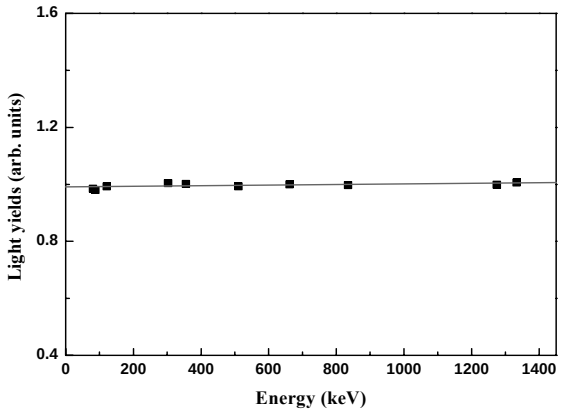

Fig. 6 Proportionality response for the $Ba_{0.20}Sr_{0.80}Cl_2$ crystal.

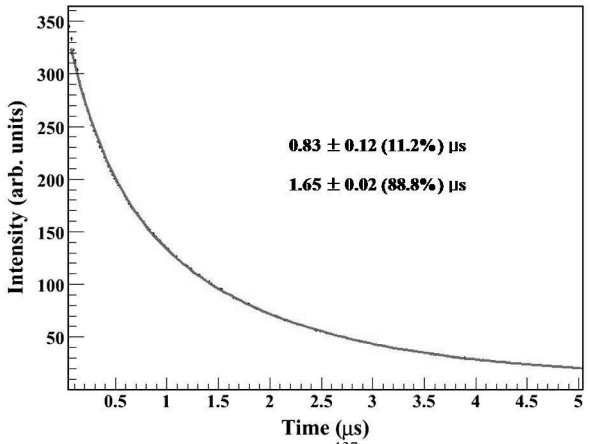

(a) Excited by ^{137}Cs γ-source

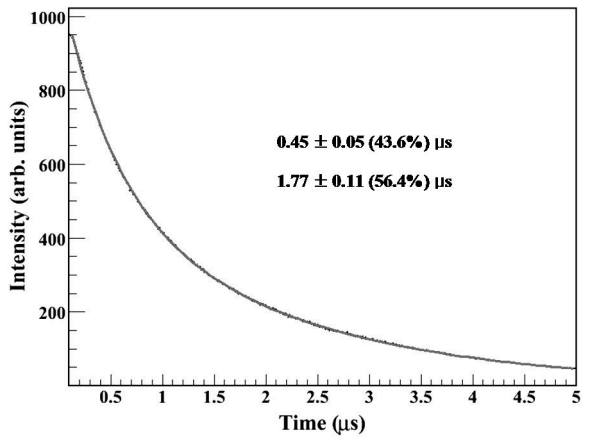

(b) Excited by ^{210}Po α-source

Fig. 7 Decay curves of the fluorescence in the $Ba_{0.20}Sr_{0.80}Cl_2$ single crystal.

Absolute light output, 23,000 phs/MeV, was measured with avalanche photodiode (APD, 630-70-73-500,Photonics) which has higher quantum efficiency and the detail procedure is described in Reference.[13)]

The proportionality is defined as the ratio of the photoelectron output measured for photo-peaks at a specific γ-ray energy relative the output at 662 keV γ-peak. This proportionality response of γ-rays is directly related to the energy resolution.[14)] **Fig. 6** shows good proportionality response for the $Ba_{0.20}Sr_{0.80}Cl_2$ crystal in the energy between 81 keV and 1,275 keV.

3. Fluorescence Decay Curve

The fluorescence decay curves of the $Ba_{0.20}Sr_{0.80}Cl_2$ crystal were recorded at room temperature under ^{137}Cs γ-rays and ^{210}Po α-source excitation by using a single photon counting technique, and were shown in **Fig. 7**. The decay time constants of the $Ba_{0.20}Sr_{0.80}Cl_2$ single crystal consist of a fast decay component of ~0.55 μs and a slow decay component of ~1.7 μs. The fast decay component shows difference in the case of a ^{210}Po α source and a ^{137}Cs γ-source. This disagreement is due to the very high ionizing power of charged particles which induces ionization as it is called quenching effect.[15)] A smaller fraction of the kinetic energy of α particle is converted into fluorescent light in the scintillator. It is associated with a difference in the transport mechanism of electron-holes towards the luminescence centers but the luminescence mechanism of the $Ba_{0.20}Sr_{0.80}Cl_2$ crystals is not well understood yet. The fast decay of the scintillation pulse by α particles and its small light output indicate that some quenching mechanism is active.

4. α/β Ratio

The α/β ratio, in other words quenching factor, is a widely used parameter to describe the different light output for scintillation between electrons and heavy charged particles. The α/β ratio is always less than 1 since the light output for electrons is always higher than that for heavy charged particles of the same kinetic energy.[16)]

Energy spectra of the $Ba_{0.20}Sr_{0.80}Cl_2$ crystal that irradiated with 5.4 MeV α particles with ^{210}Po source, simultaneously with ^{137}Cs γ-source is shown in **Fig. 8**. The α/β ratio measured to be 0.18, which indicates that 82% of the light was quenched and the light produced by α-particles was only 18%.

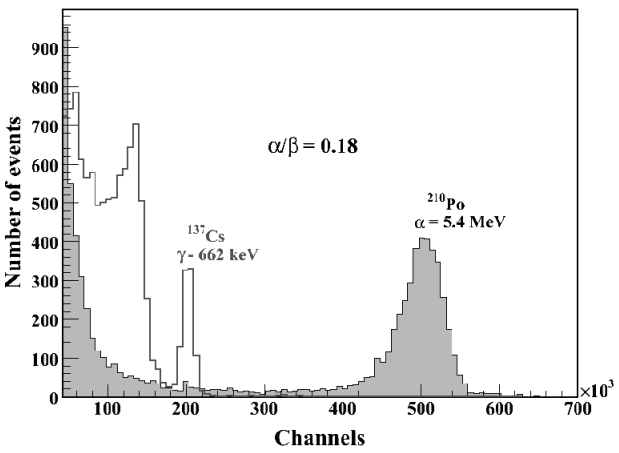

Fig. 8 α /β ratio of the $Ba_{0.20}Sr_{0.80}Cl_2$ crystal.

IV. Conclusions

We have used Czochralski technique to grow new high quality $Ba_{0.20}Sr_{0.80}Cl_2$ crystal. The emission spectrum is located in the range of 375 ~ 500 nm, peaking at 400 nm.

The scintillation properties such as energy resolution, fluorescence decay time, α/β ratio, relative light output proportionality were measured. The relative light output of $Ba_{0.20}Sr_{0.80}Cl_2$ single crystal matched with PMT is about 77% of that of CsI(Tl) and the absolute light output with APD is 23,000 photons/MeV.

The energy resolution of $Ba_{0.20}Sr_{0.80}Cl_2$ single crystal is about 6.9% for the ^{137}Cs γ-rays which is similar to that of CsI(Tl) to be 7.1%. Proportionality curve for $Ba_{0.20}Sr_{0.80}Cl_2$ single crystal shows linearity in energy range 81 keV to 1,275 keV.

A response to charged particle was obviously indicated that the increase of the fast component of fluorescence decay time is related to the α/β ratio, which means that small fraction of charged particles kinetic energy converted into fluorescent light in the scintillators. We need more to study of the luminescence of the $Ba_{0.20}Sr_{0.80}Cl_2$ single crystals to understand of scintillation mechanism of α-particles and γ-rays.

The energy resolution of $Ba_{0.20}Sr_{0.80}Cl_2$ crystal was similar to that of the CsI(Tl) measured in the same condition. The $Ba_{0.20}Sr_{0.80}Cl_2$ crystal shows promisingly scintillation materials because of its good energy resolution at room temperature.

Acknowledgement

This work was supported by the SRC/ERC program of MOST/KOSEF (R11-2000-067-02002-0) and by the Korea Science and Engineering Foundation under the BAERI program.

References

1) J. A. Mares, M. Nikl, N. Solovieva, C. D'Ambrosio, F. de Notaristefani, K. Blazek, P. Maly, K. Nejezchleb, P. Fabeni, and G. P. Pazzi, 'Scintillation and spectroscopic properties of Ce^{3+}-doped $YAlO_3$ and $Lu_x(RE)_{1-x}AlO_3$(RE=Y^{3+} and Gd^{3+}) scintillators,' *Nucl. Instr. and Meth*., **498**, 312~327 (2003).
2) S. Makino and H. Yokota, 'Scintillation properties of cerium-doped gadolinium silicate with γ-rays from ^{137}Cs,' *Nucl. Instr. and Meth*., **548**, 446~454 (2005).
3) J. Moon, H. Kang, J. Kim, W. Kim, H. Park, S. Kim, D. Kim, and S. H. Doh, 'Scintillation properties of $SrCl_2:Eu^{2+}$ crystals,' *J. Korean Phys. Soc*., **49**, 637~641 (2006).
4) JCPDS –International Center for Diffraction Data. All rights reserved PCPDFWIN v. 2.01 (1998).
5) K. G. Subhadra, E. Balaiah, and D. B. Sirdeshmukh, 'Systematic hardness measurements on $CsCl_xBr_{(1-x)}$ and $NH_4Cl_xBr_{(1-x)}$ mixed crystals,' *Bull. Mater. Sci.*, **25**, 31~35 (2002).
6) O. Karabulut, M. Parlak, and G. M. Mamedov, 'Structural and electrical properties of $TlGa(S_xSe_{1-x})_2$ mixed crystals,' *J. Alloys and Compounds*, **429**, 50-55 (2007).
7) Quantachrome Co. ; http://www.quantachrome.com/
8) Ocean Optics Co. ; http://www.oceanoptics.com/
9) Electron tubes Co. ; http://www.electrontubes.com/
10) Notice Korea Co. ; http://www.noticekorea.com/
11) R. Brun, A. Gheata, and M. Gheata, 'The ROOT geometry package,' *Nucl.Instr. and Meth*., **502**, 676~680 (2003).
12) C. W. E. van Eijk, P. Dorenbos, E. V. D. van Loef, K. Kr. amerb, and H. U. Gudel, 'Energy resolution of some new inorganic-scintillator gamma-ray detectors,' *Radiat. Meas*., **33**, 521~525 (2001).
13) Minjeong Kim, Heedong Kang, H. J. Kim, H. Park, and Sunghwan Kim, 'A Study of CsI(Tl) Scintillator with Optimized Condition of Large Area Avalanche Photodiode,' ISORD-4, submitted for publication.
14) P. Dorenbos, J. T. M. de Haas, and C. W. E Van Eijk, 'Non-linear response in the scintillation yield of $Lu_2SiO_5:Ce^{3+}$,' *IEEE Trans. Nucl. Sci.*, **41**, 735~737 (1994).
15) L. E. Dinca, P. Dorenbos, J. T. M. de Haas, V. R. Bom, C. W. E Van Eijk, 'Alpha-gamma pulse shape discrimination in CsI:Tl, CsI:Na and BaF_2 scintillators,' *Nucl. Instr. and Meth.*, **486**, 141~145 (2002).
16) Glenn F. Knoll, *Radiation detection and measurement*, Wiley, 2nd Ed., 224 (1989).

Journal of NUCLEAR SCIENCE and TECHNOLOGY, Supplement 5, p. 572–574 (June 2008)

Growth and Characteristics of Gd_2SiO_5 Crystal Doped Ce^{3+}

Woo Gyo LEE[1], Dong Hoon LEE[2], Yong Kyun KIM[2*], Jong Kyung KIM[2], and Jae Woo PARK[3]

[1]*Innovative Technology Center for Radiation Safety, Hanyang University, 17 Hangdang, Sungdong, Seoul 133-791, Korea*
[2]*Department of Nuclear Engineering, Hanyang University, 17 Hangdang, Sungdong, Seoul 133-791, Korea*
[3]*Department of Nuclear & Energy Engineering, Cheju National University, Jeju, Korea*

Gadolinium oxyorthsilicate doped with cerium, Gd_2SiO_5:Ce (GSO:Ce), is a scintillator crystal discovered in 1983, which has excellent properties, high light yield, fast decay time, and good radiation hardness. The Gd_2SiO_5 (GSO) and GSO:Ce (0.5 mole%) single crystals were grown by Czochralski method under argon atmosphere. After the growth, thermal treatment of the GSO crystals was carried out at 1780K for 3 hours under argon atmosphere. The maximum wavelength of the emission spectrum of the GSO:Ce scintillator was 430 nm. The energy resolution of the GSO:Ce scintillator was 9.1 % with PMT, when it was exposed to ^{137}Cs γ-ray. The luminescence decay time of the GSO:Ce scintillator has two exponential components with 68.7 ns and 754 ns time constant.

KEYWORDS: GSO, inorganic scintillator, absorption, emission, pulse height spectrum

I. Introduction

Inorganic scintillators have high density, Gadolinium oxyorthsilicate doped with cerium, Gd_2SiO_5:Ce (GSO:Ce), is a scintillator crystal discovered in 1983[1)], which has excellent properties, high light yield, fast decay time, and good radiation hardness[2)]. The light output of Ce:GSO is twice as high, and the decay time is 1/5 of that of BGO. Moreover, irradiation hardness of the Ce:GSO crystal is quite prominent, so it can be widely used in a variety of applications of high energy physics, nuclear physics, nuclear medical imaging (PET), and oil well survey, etc[3)].

The Gd_2SiO_5 (GSO) and GSO:Ce (0.5 mole%) single crystals were grown by Czochralski method under argon atmosphere.

In this work, GSO and Ce doped GSO (GSO:Ce) single crystals were grown by a Czochralski method, and their absorption, transmittance, excitation, emission, decay time, and pulse height spectra were investigated.

II. Experiment

GSO single crystals were grown by the Czochralski method in iridium crucible under an argon atmosphere to prevent oxidization of the crucible. The pure dried Gd_2O_3 (99.999%), SiO_2 (99.995%), and CeO_2 (99.99%) powders were weighed out in mole ratios. The powders were totally mixed and pressed into the platinum crucible. The mixed powders were sintered at 1100°C for 4 h in air, and then loaded into the mortar. And then sintered powders pulverized and pressed into the iridium crucible in the Czochralski furnace for crystal growth. The growth atmosphere was highly pure and dried argon gas (99.9999%) with a static state at 1.5 atm pressure in the furnace. In our experiment, the optimal growth parameters for GSO:Ce crystal were growth rate of 1.5 mm/h and rotation rate of 30 RPM. The concentration of Ce activator was 0.5 mole%.

The sample of GSO:Ce crystal was cut from the grown crystal and polished using Al_2O_3 powder (grain size of 0.05 μm) on a polishing cloth (microcloth supreme, Buehler). The size of the GSO:Ce specimen was 10x9x5 mm^3. Pulse height spectra were measured with the gamma emitting radio-isotopes ^{137}Cs (0.662 MeV), ^{22}Na (1.275 MeV), ^{54}Mn (0.835 MeV), and ^{60}Co (1.173 MeV, 1.333 MeV). GSO:Ce scintillator is attached to a 2 inches bialkali PMT (9208B, Electron tube Ltd.) and 16 mm LAAPD (Large Area Avalanche Photodiode) made by Advanced Photonix Inc. (API) to measure the pulse height spectra. Signals from PMT and LAAPD is fed to a low noise preamplifier and then shaping amplifier. The portable 25 MHz flash analog to digital converter (FADC) board is used for signal digitization, and digitized signal was readout by Linux based computer through USB2. The data are analyzed with the C^{++} based data analysis program, ROOT package[4)]. We use object oriented ROOT package for the data taking and analysis.

III. Result and Discussion

The absorption spectra of the GSO:Ce crystal were measured from 200 nm to 800 nm with a double-beam spectrophotometer (Cary-300, Varian, Australia). **Fig. 1** shows the absorption spectrum of the GSO:Ce crystal. The peaks (3.28 eV, 4.17 eV, and 4.51 eV) in UV region are possibly an evidence of structural transformations of the color centers[5)].

The transmittance curve of the GSO crystal was measured from 400 nm to 900 nm with a double-beam spectrophotometer (Cary-300, Varian, Australia). The transmittance coefficient of the GSO:Ce crystal was 81.4 % at 430 nm.

The excitation emission spectra of the GSO:Ce is shown in **Fig. 2**. The maximum wavelength of the emission

*Corresponding Author, Tel No: +82-2-2220-2354, Fax No: +82-2-2220-4450, E-Mail: ykkim4@hanyang.ac.kr

spectrum was 430 nm. The excitation spectrum for the emission at 430 nm has the three peaks at 250 nm, 284 nm, and 340 nm. The maximum excitation peak at 340 nm originates from the direct excitation of the 4f–5d transition of Ce^{3+}.

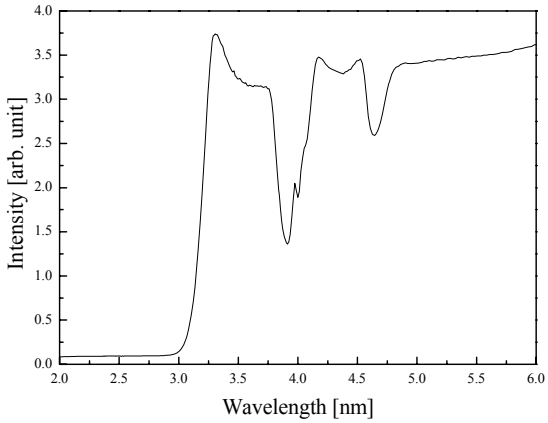

Fig. 1 Absorption spectrum of the GSO:Ce crystal.

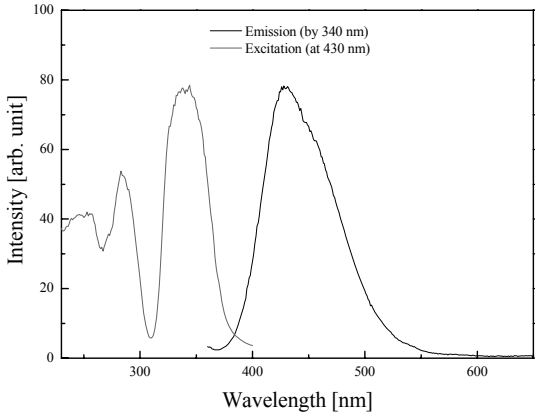

Fig. 2 Excitation and emission spectra of the GSO:Ce crystal at the room temperature.

The second excitation peak at 284 nm is probably due to the split of the 5d state, or to defects in GSO:Ce. The excitation peak at 250 nm is due to defects in GSO:Ce. The emission spectrum can be decomposed into two bands peaked at 423 and 452 nm, which assign to 5d-4f($^2F_{5/2}$) and 5d-4f($^2F_{7/2}$) transitions of Ce^{3+}, respectively. **Fig. 3** shows the decomposed into two bands.

The pulse height spectrum of the GSO:Ce scintillator is shown in **Fig. 4**. Pulse height spectra were measured with the radio-isotopes ^{137}Cs (0.662 MeV), ^{60}Co (1.173 MeV, 1.333 MeV), ^{22}Na (1.275 MeV), and ^{54}Mn (0.835 MeV). The energy resolutions of the GSO:Ce scintillator are listed in **Table 1**. The energy resolution of the GSO:Ce scintillator was attached to the PMT was 9.1% when it was exposed to ^{137}Cs 662 keV γ-rays.

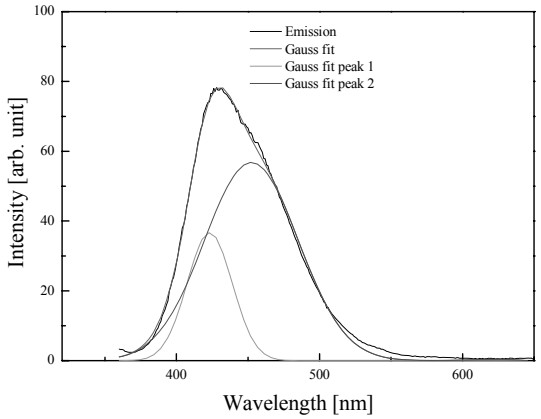

Fig. 3 Decomposed emission spectra of the GSO:Ce scintillator.

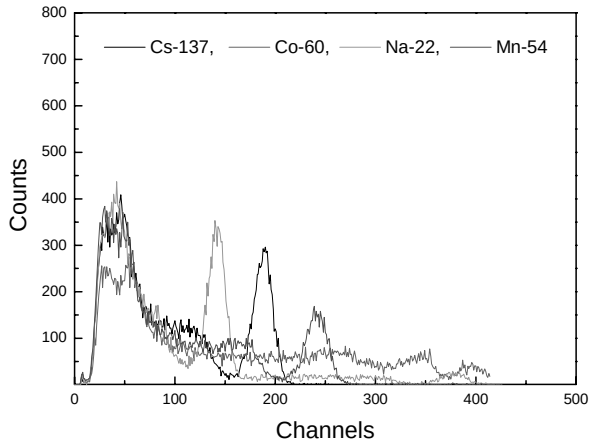

Fig. 4 Pulse height spectra of the GSO:Ce scintillator to ^{137}Cs, ^{60}Co, ^{22}Na, and ^{54}Mn gamma radiation.

Table 1 Energy resolutions of the GSO:Ce scintillator.

	^{22}Na 0.511	^{137}Cs 0.662	^{54}Mn 0.835	^{60}Co 1.173	^{22}Na 1.275	^{60}Co 1.333
PMT	14.1	9.1	10.1	11.1	7.4	6.9
APD	10.1	8.3	11.1	5.9	6.4	6.25

Fig. 5 shows the decay time curve of the GSO:Ce scintillator. The decay time curve of the GSO:Ce scintillator has two components, their values being 68.7 ns and 754 ns. The relative percentages of these decay components are 98.5% and 1.5%, respectively. The slow is due to the defects in GSO:Ce crystal.

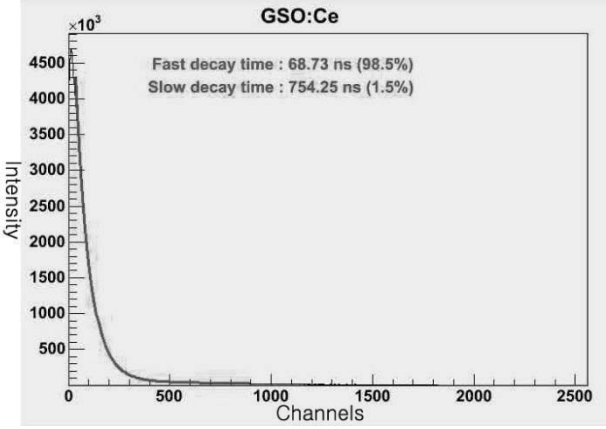

Fig. 5 Decay time curve of the GSO:Ce scintillator.

IV. Summary

The GSO:Ce (0.5 mole%) single crystals were grown by Czochralski method. The maximum wavelength of the emission of the GSO:Ce scintillator was 430 nm, which coincides with the response wavelength of PMT. The transmittance of the maximum emission of GSO:Ce scintillator was 81.4% at 430 nm. The energy resolution of the GSO:Ce scintillator was 9.1 % with PMT, when it was exposed to ^{137}Cs γ-ray. The GSO:Ce scintillator can be used the detector of the medical image system.

Acknowledgement

This work has been supported financially by the Science Research Center (SRC) / Engineering Research Center (ERC) program of MOST/KOSEF (Korea Science and Engineering Foundation, grant # R11-2000-067-01001-0).

References

1) K. Takagi, T. Fukazawa, Appl. Physc. Letters, 42, p43 (1983)
2) M. Kobayashi and M. Ishii, Nucl. Instr. Meth., B 61, 591 (1994)
3) M. Tanaka, K. Hara, K. Kondo, Nucl. Instr. And Meth. A 404, 283 (1998)
4) R. Brun, A. Gheata, and M. Gheata, Nucl. Instr. and Meth in Physics Tesearch, 502, 676 (2003)
5) P. Dorenbos, J. C. van't Spijker, C. W. E. van Eijk, Proceedings of the Internatiuonal Conference SCINT 97, Delft, The Netherlands, p. 307, (1997)

Journal of NUCLEAR SCIENCE and TECHNOLOGY, Supplement 5, p. 575–578 (June 2008)

Thermoluminescence Properties of a $CeBr_3$ Single Crystal

Sunghwan KIM[1], H.J. KIM[2], H. PARK[2], Heedong KANG[2*], S.H. LEE[2], and Sihhong DOH[3]

[1]*Daegu Health College, Daegu 702-722, Korea*
[2]*Kyungpook National University, Daegu 702-701, Korea*
[3]*Pukyong National University, Busan 608-737, Korea*

Cerium doped scintillators are characterized by an excellent energy resolution, a very high light yield and fast timing properties. In this work, we grew a $CeBr_3$ (ρ = 5.18 g/cm^3) single crystal by the Bridgman method using a two-zone transparent vertical furnace. The $CeBr_3$ is crystallized in the hexagonal structure of the UCl_3 type. We investigated the thermoluminescence (TL) of the $CeBr_3$ such as glow curve, dose response, fading etc. TL is a convenient technique to understand the charge trapping and detrapping mechanisms that result from the interaction of the radiation with the existing defects in material, which may interfere with the scintillator response. We determined the kinetic parameters of the TL traps of the $CeBr_3$ scintillator such as activation energy, frequency factor, and kinetic order by using peak shape method, variable heating rate method, and initialize method.

KEYWORDS: Bridgman, $CeBr_3$, scintillator, thermoluminescence

I. Introduction

Cerium is one of the most interesting materials for scintillation material[1-3], because cerium doped scintillators are characterized by an excellent energy resolution, a very high light yield and fast timing properties. For instance, $YAlO_3$:Ce and Lu_2SiO_5:Ce show high light yield and fast fluorescence decay time for γ-ray excitation[4,5]. The light yield of K_2LaCl_5:Ce and $RbGd_2Br_7$:Ce show close to the theoretical maximum scintillation light yield[6,7]. The energy resolution of $LaBr_3$:Ce is about 3%[8] for ^{137}Cs 662 keV γ–ray.

Thermoluminescence (TL) is a useful technique to understand the charge trapping and detrapping mechanisms that result from the interaction of the radiation with the existing defects in material, which may interfere with the scintillator response. The characteristics of TL material depend on trapped charged carriers produced after irradiation. The traps are caused by crystal defects or impurities. In many experiments the TL phenomenon was studied to investigate the characteristics of some scintillators[9,10]. Selles et al. were studied for the relationship between the role of the traps and the influence of the afterglow in lanthanum halide scintillators[11].

In this paper, we grew a $CeBr_3$ single crystal by the Bridgman method using a two-zone transparent vertical furnace and investigated the TL of the $CeBr_3$ such as glow curve, dose response, fading etc. We determined the kinetic parameters of the TL traps of the $CeBr_3$ scintillator such as activation energy, frequency factor, and kinetic order by using the peak shape method, the variable heating rate method and the initialize method.

II. Experiments

1. Crystal Growth and Sample Preparation

A pure $CeBr_3$ crystal was grown by Bridgman method using a two-zone transparent vertical furnace. The $CeBr_3$ powder (99.99%, Aldrich) was prepared and put into a quartz ampoule of 12 mm dia. × 70 mm. The quartz ampoule was sealed under 10^{-6} torr. During the crystal growing, the temperature gradient of the furnace was 10 K/cm and the falling rate of the quartz ampoule was 0.3 mm/hr. The $CeBr_3$ is crystallized in the hexagonal structure of the UCl_3 type. Space group of the $CeBr_3$ is $P6_{3/m}$. **Fig. 1** shows a sample of the grown $CeBr_3$ single crystal. The cylindrical shape of the $CeBr_3$ crystal was cut into pieces. The $CeBr_3$ crystal was polished using mixed Al_2O_3 powder (grain size 0.02 μm) in mineral oil on a polishing cloth (No.40-7218, Buehler) because of its hygroscopic property. We obtained a size of 10 mm dia. × 10 mm crystal. To prevent the influence of humidity of air during TL measurements, we smashed up the $CeBr_3$ single crystal and put it into a capillary tube. The ends of the capillary tube were sealed. The inner diameter was 1 mm and the length was 5 mm of the sealed capillary tube. The tube was put into the TL analyzer for the TL measurements.

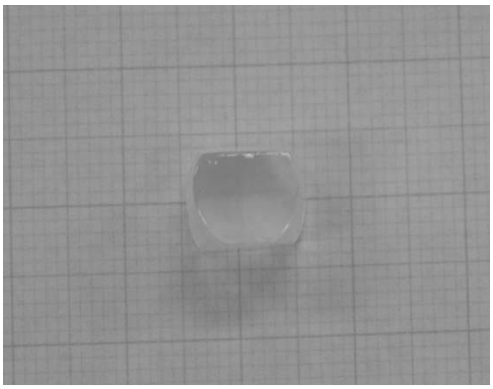

Fig. 1 Photograph of the grown $CeBr_3$ single crystal.

*Corresponding Author, Tel No: +82-53-320-1319, Fax No: +82-53-320-1449, E-Mail: kimsh@mail.thc.ac.kr

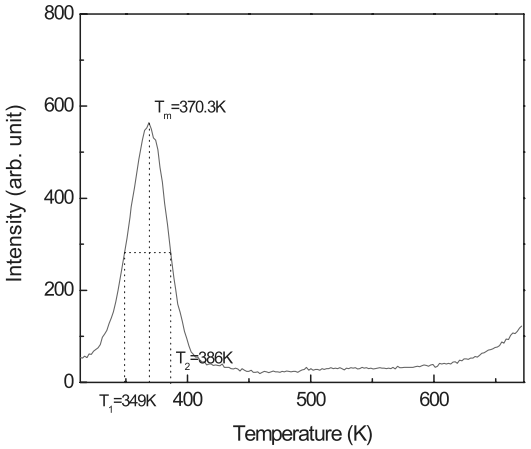

Fig. 2 Typical glow curve of the grown CeBr3 single crystal observed after X-ray irradiation with a heating rate of 4 K/s. $\omega=T_2-T_1$, $\delta=T_m-T_1$, and $\tau=T_2-T_m$.

2. Measurements of Thermoluminescence Properties

TL measurements were performed from 313 K up to 673 K using the TL analyzer (TLD 4000, Harshaw Inc.). Heating rates from 2 K/s to 10 K/s were employed. The irradiation of the samples prior to the TL measurements was done using a 6 MV X-ray (Siemens KD) at room temperature.

III. Results and Discussion

1. Typical Glow Curve

The typical glow curve of this sample exposed to 6 MV X-rays at room temperature is shown in **Fig. 2**. The TL glow curve has a single glow peak in the range from 313 K to 673 K. For a linear heating rate of 4 K/s, the maximum intensity of the glow peak occurred at about 369 K. By subtracting the intensity of a background from the TL glow curve, the isolated peak was determined. As shown in **Fig. 2**, the peak temperature was defined as T_m and a full width at half maximum (FWHM) of a glow peak was defined as ω. The low temperature part, T_m-T_1, was defined as δ and the high temperature part, T_2-T_m, was defined as τ. The symmetry factor (μ_g) was defined by the value of δ/ω. The symmetry factor of the $CeBr_3$ crystal is 0.43. It means that the TL of the $CeBr_3$ is caused by a 1st kinetic order[12].

2. Determination of the TL Kinetic Parameters

In order to determine the TL parameters of the traps of the $CeBr_3$ single crystal, we used the variable heating rate method, the initialize method, and the peak shape method.

(1) Variable Heating Rate Method

The variable heating rate method[13] was used to determine the activation energy (trap depth) associated with the glow peak in this sample. The samples were heated at linear heating rates (β) from 2 to 10 K/s. The variable heating rate method based on the shift of the maximum temperature T_m of the TL glow peak as a function of heating rate β. As shown in **Fig. 3(a)**, the more the heating rate is increased, the more the peak temperature and intensity of the glow peak is increased[13]. Chen[14] have shown that

$$\frac{\beta}{T_m^2}=\frac{ks}{E}\exp\left(-\frac{E}{kT_m}\right) \tag{1}$$

where T_m is the peak temperature of a glow curve, β is the heating rate, E is the activation energy, k is the Boltzman constant, and s is the frequency factor.

Fig. 3(b) shows, the plots of $\ln(\beta/T_m^2)$ versus $1/T_m$ for the glow peak. The activation energy of the TL trapping center found from the slopes (-E/k) was about 0.44 eV. The frequency factor of the TL trapping center found from the y-intercept was about $1.65\times10^5\ s^{-1}$.

(2) Initialize Method

The initialize method is based on the fact that the initial part of the TL glow curve is an exponential function of the temperature[15]. At the part, the TL intensity is define as

$$I(T)\propto\exp\left(-\frac{E}{kT}\right) \tag{2}$$

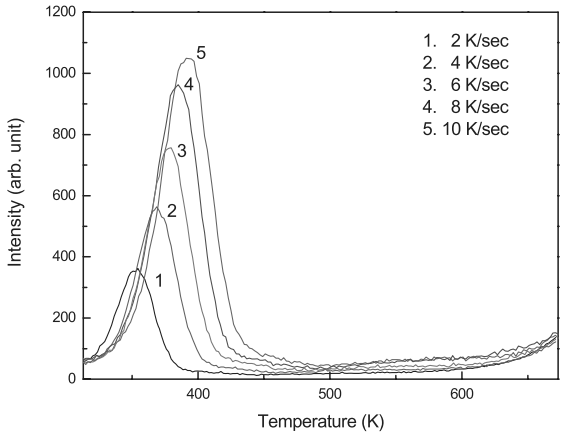

(a) Glow curves according to the heating rate

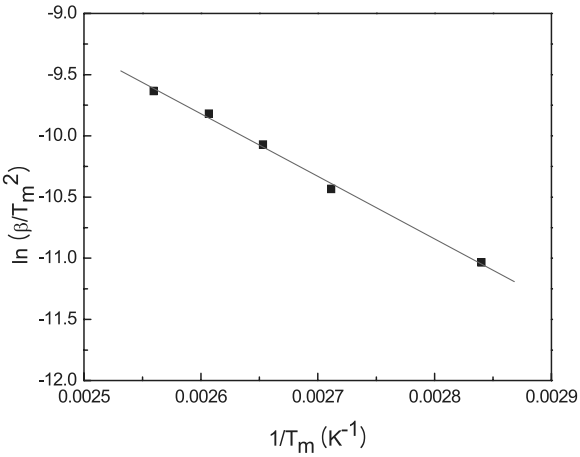

(b) Plot of $\ln(\beta/T_m^2)$ vs. $1/T_m$

Fig. 3 Determined kinetic parameters of the $CeBr_3$ crystal using the variable heating rate method.

Fig. 4 shows the plot of ln(I) as a function of 1/T. The activation energy of the TL trap can be determined from the slope (-E/k) of the curve. The activation energy of the crystal is determined to be 0.40 eV by the initialize method.

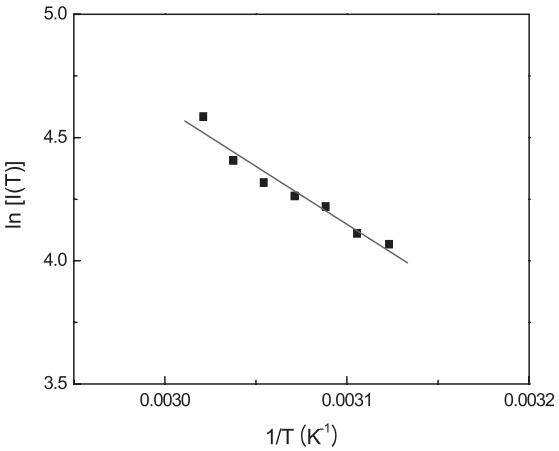

Fig. 4 Plot of ln(I) versus 1/T for the initialize method.

(3) Peak Shape Method

The TL parameters could be determined by the peak shape method using a single glow peak parameter such as T_m, ω, τ, and δ as shown in **Fig. 2**. According to Chen's equation[15], the activation energy of the TL traps was defined as

$$E_\omega = [2.52 + 10.2(\mu_g - 0.42)]\frac{kT_m^2}{\varpi} - 2kT_m \quad (3)$$

$$E_\tau = [1.51 + 3(\mu_g - 0.42)]\frac{kT_m^2}{\tau} - [1.58 + 4.2(\mu_g - 0.42)](2kT_m) \quad (4)$$

$$E_\delta = [0.976 + 7.3(\mu_g - 0.42)]\frac{kT_m^2}{\delta} \quad (5)$$

The activation energy of the crystal is determined to be 0.42 eV by the peak shape method.

Table 1 shows the value of the TL trap parameters of the crystal. The activation energy that was calculated by the peak shaping method, differed from the other values which were calculated by the initialize method and the various heating rate method. We think that the afterglow of the $CeBr_3$ scintillator had an influence on the shape of the TL glow peak[11]. The trapped charge carrier after irradiation and the radiative recombination efficiency of these charge carriers had influence on the afterglow of the scintillator[11].

Table 1. Calculated TL trap parameters of the $CeBr_3$ crystal.

Parameters	Method of Analysis	Value
Activation Energy (eV)	Various Heating Rate Method	0.44
	Initialize Method	0.40
	Peak Shape Method	0.42
Symmetry Factor	μ_g	0.43
Frequency Factor (s^{-1})	Various Heating Rate Method	1.65×10^5

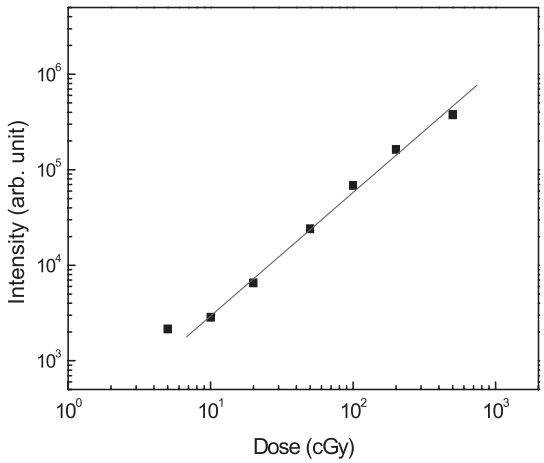

Fig. 5 Dose response of the $CeBr_3$ crystal for 6 MV X-ray.

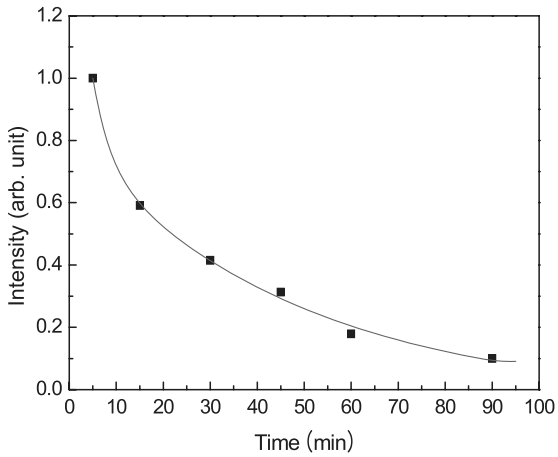

Fig. 6 Fading characteristic of the $CeBr_3$ crystal under 6 MV X-ray irradiation at room temperature.

3. Dose Response

Fig. 5 shows the TL response of the crystal as a function of the irradiated dose at room temperature. The crystal was irradiated with 6 MV X-ray. In the dose range between 10 cGy and 500 cGy, we observed the linear dose response characteristic. However, we observed a superlinear dose response at lower doses (below 10 cGy). It indicated the saturation effect associated with the available number of traps.

4. Fading Characteristics

Fig. 6 shows the fading of the integrated TL signal as a function of the elapsed time after irradiation at room temperature. The crystal was irradiated with 6 MV X-ray (100 cGy) and then the TL signal was measured at different times after irradiation. The crystal had a strong fading characteristic. The TL signal of the crystal was reduced by 40% in the first 15 min and by 90% in the first 1 hour from the initial value at room temperature. The fading curve of the crystal was composed of two components with decay constants of 3.7 min and 47.5 min, respectively.

IV. Conclusions

In this work, we discussed and presented the thermoluminescence properties of the grown $CeBr_3$ single crystal. A glow peak was observed at 370.3 K when the heating rate was 4 K/s. The trap parameters of average activation energy (E), frequency factor (s) and kinetic order (n) were 0.42 eV, 1.65×10^5 s^{-1}, and 0.43, respectively using three TL analyzing methods. The TL peak was decayed rapidly at room temperature. The fading of the crystal was composed of two components with decay constants of 3.7 min and 47.5 min. The non-linear dose response was observed under 10 cGy irradiation with 6 MV X-ray source. We think that the TL emission was also due to the transitions of 4f → 5d of the trapped electrons after irradiation and the trapped electrons had an influence to the afterglow of the scintillator.

Acknowledgement

This work was supported by the SRC/ERC program of MOST/KOSEF (R11-2000-067-02002-0).

References

1) J. Chen, L. Zhang, and R. Zhu, 'Large size LSO and LYSO crystal scintillators for future high-energy physics and nuclear physics experiments,' Nucl. Instr. and Meth., 572, 218-224 (2007).
2) V. Pankratov, L. Grigorjeva, D. Millers, and T. Chudoba, 'Luminescence of cerium doped YAG nanopowders,' Radiat. Meas., 42, 679-682 (2007).
3) W. Drozdowski, P. Dorenbos, A. J. J. Bos, A. Owens, and F. G. A. Quarati, '$CeBr_3$ scintillator development for space missions,' IEEE 9th Int. Conf. on Inorganic Scintillators and their Applications, Winston Salem, USA, Jun., 121 (2007).
4) S. Baccaro, K. Blazek, F. de Notaristefani, P. Malyb, J. A. Mares, R. Pani, R. Pellegrini, and A. Soluri, 'Scintillation Properties of YAP:Ce,' Nucl. Instr. and Meth., 361, 209-215 (1995).
5) G. Ren, L. Qin, S. Lu, and H. Li, 'Scintillation Characteristics of Lutetium Oxyorthosilicate (Lu_2SiO_5:Ce) Crystals doped with Cerium Ions,' Nucl. Instr. and Meth., 531, 560-565 (2004).
6) J. C. van 't Spijker, P. Dorenbos, C. W. E. van Eijk, K. Krämer, and H. U. Güdel, 'Scintillation and Luminescence Properties of Ce^{3+} doped K_2LaCl_5,' J. Lumin., 85, 1-10 (1999).
7) P. Dorenbos, J. C. van't Spijker, O. W. V. Frijns, C. W. E. van Eijk, K. Krämer, H. U. Güdel, and A. Ellens, 'Scintillation Properties of $RbGd_2Br_7$:Ce^{3+} Crystals; fast, efficient, and high density scintillators,' Nucl. Instr. and Meth., 132, 728-731 (1997).
8) C. W. E. van Eijk, P. Dorenbos, E. V. D. van Loef, K. Krämer, and H. U. Güdel, 'Energy resolution of some new inorganic-scintillator gamma-ray detectors,' Radiat. Meas., 33, 521-525 (2001).
9) L. Pidol, B. Viana, A. Kahn-Harari, B. Ferrand, P. Dorenbos, and C. W. E. van Eijk, 'Scintillation and thermoluminescence properties of $Lu_2Si_2O_7$:Ce^{3+} crystals,' Nucl. Instr. and Meth., 537, 256-260 (2005).
10) R. S. da Silva, Z. S. Macedo, A. L. Martinez, A. C. Hernandes, and M. E. G. Valerio, 'Thermoluminescence kinetic parameters of $Bi_4Ge_3O_{12}$ single crystals,' Nucl. Instr. and Meth., 250, 390-395 (2006).
11) O. Selles, Adrie J. J. Boss, P. Dorenbos, and D. Gourier, 'Thermally stimulated luminescence study of afterglow in cerium doped lanthanum halides,' Proc. 8th Int. Conf. on Inorganic Scintillators and their Use in Scientific and Industrial Applications, Alushta, Ukraine, Sept. 175-177 (2005).
12) R. Chen, 'Glow curves with general order kinetics,' J. Electrochem. Soc., 116[9], 1254-1257 (1969).
13) G. C. Tayler and E. Lilley, 'The analysis of thermoluminescent glow peaks in LiF(TLD-100),' J. Appl. Phys., 11, 567-580 (1978).
14) A. Halperin and A. A. Braner, 'Evaluation of thermal activation energies from glow curves,' Phys. Rev., 117[2], 408-415 (1960).
15) R. Chen and Y. Kirsh, Analysis of Thermally Stimulated Processes. Vol. 1, Pergamon Press, Oxford, 1 (1981).

Journal of NUCLEAR SCIENCE and TECHNOLOGY, Supplement 5, p. 579–581 (June 2008)

Properties of ZnSe:Te,O Crystals Grown by Bridgman-Stockbarger Method

Woo Gyo LEE[1], Yong Kyun KIM[2*], Jong Kyung KIM[2], Nicolai STARZHINSKIY[3], Vladimir RYZHIKOV[3], and Boris GRINYOV[3]

[1]*Innovative Technology Center for Radiation Safety, Hanyang University, Haengdang-dong, Seongdong, 133-791 Seoul, Korea*
[2]*Department of Nuclear Engineering, Hanyang University, Haengdang-dong, Seongdong, 133-791 Seoul, Korea*
[3]*Institute for Scintillation Material of Science-Technology Concern "Institute for Single Crystals" National Academy of Science of Ukraine, 60 Lenin Ave., Kharkov 61006, Ukraine*

Zinc selenide crystals were grown in graphite crucibles by the Bridgman–Stockbarger method in a vertical compression furnace under argon pressure of $5x10^6$ Pa. From the absorption spectra, the band gap energies of the ZnSe single crystals were calculated by a linear fitting process. The maximum wavelength of the emission spectrum of the ZnSe:Te,O scintillator was 630 nm, which was well matched with the response wavelength of the Si photodiode. The energy resolution of the ZnSe:Te,O scintillator was 11.9 % when it was exposed to ^{137}Cs γ-ray. Its size was 10x10x1 mm^3. The afterglow level of the ZnSe:Te,O scintillator after 5 ms was 0.023%. The relative light output of the ZnSe:Te,O scintillator was 2.167 times higher than CsI:Tl. The luminescence decay time of the ZnSe:Te,O scintillator has two exponential components with 27 and 84 μs time constant.

KEYWORDS: ZnSe, semiconductor scintillator, absorption, emission, afterglow

I. Introduction

II-VI compound semiconductors have various physical properties. Recently, they have been used as the radiation sensors due to the advance of the single crystal growth technique [1,2)].

The relative light output of the scintillators based on ZnSe crystals is about one and a half times higher than that of CsI:Tl. Their afterglow level after 10 ms is about three orders lower than that of CsI:Tl [3)]. Scintillators based on ZnSe crystals are quite acceptable for use in X-ray introscopy detectors because their radiation stability is relatively good and their light output is about four times higher than the oxide scintillators ($CdWO_4$, $Bi_4Ge_3O_{12}$, Gd_2SiO_5) used for similar purposes [4,5)].

In our work, ZnSe single crystals based on the II-VI compound semiconductors were grown by a modified Bridgman–Stockbarger technique. The doping effects on ZnSe single crystals were observed and are discussed. The scintillation and other physical properties of ZnSe single crystals such as X-Ray diffraction, transmittance, radioluminescence, afterglow, light output, pulse height spectrum, and decay time were also investigated.

II. Experiment

ZnSe and ZnSe:Te,O crystals were grown by a ZnSe and ZnSe:Te,O crystals were grown by a modified Bridgman–Stockbarger technique in a vertical compression furnace under argon atmosphere. During growth, the inert gas pressure of Ar was ~5×10^6 Pa and the crystallization rate was 2~5 mm/h. In this study, the size of the ZnSe specimen was 10x10x1 mm^3.

Pulse height spectra were measured with the gamma emitting radio-isotope ^{137}Cs (662 keV). An R1307 (Hamamatsu) PMT was used to measure the pulse height spectrum of the ZnSe:Te,O scintillator.

In order to obtain the decay time of the ZnSe:Te,O scintillator at room temperature, a pulsed Nd:YAG laser was employed as an excitation source. The repetition rate of the pulsed laser was 10 Hz with 6 ns duration.

III. Result and Discussion

1. Source Term Calculation

The absorption spectra of the ZnSe crystals were measured from 300 nm to 800 nm with a double-beam spectrophotometer (Cary-300, Varian, Australia). **Fig. 1** shows the absorption spectra of the ZnSe and ZnSe:Te,O crystals. Assuming that the absorption coefficient α corresponds to the direct band gap of the zinc blend structure, the band gap energy is calculated by linear fit when the absorption spectrum is plotted with $[\alpha*(h\nu)]^2$ versus the photon energy hν. In these results, the optical band gap energies of ZnSe and ZnSe:Te,O crystals were 2.608 eV and 2.555 eV, respectively. The decrease of band gap energy is assumed to result from the impurities defect level in ZnSe:Te,O crystals.

Radioluminescence provides the information on the wavelength of the emission light of the scintillators when the radiation energy is absorbed. An X-ray generator was the radiation source. **Fig. 2** shows the radioluminescence spectra of the ZnSe and that of the ZnSe:Te,O crystals. The wavelengths at maximum luminescence of the ZnSe and the ZnSe:Te,O crystals were 625 nm and 630 nm, respectively. The radioluminescence intensity of the ZnSe:Te,O crystal is clearly much higher than that of the ZnSe crystal.

*Corresponding Author, Tel No +82-2-2220-2354, Fax No +82-2-2220-4450, E-Mail: ykkim4@nural.hanyang.ac.kr

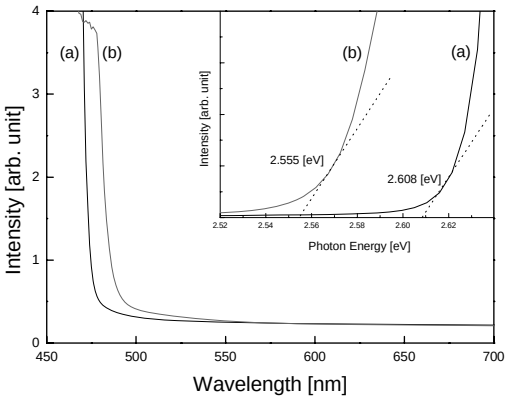

Fig. 1 Asorption spectra of (a) the ZnSe and (b) the ZnSe:Te,O crystals

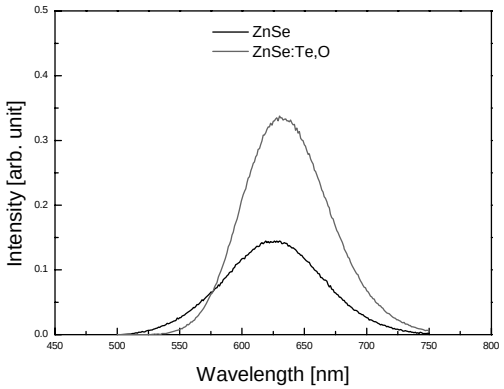

Fig. 2 Radioluminescence spectrs of the ZnSe and the ZnSe:Te,O crystals at the room temperature.

The transmittance curves of the ZnSe crystals were measured from 400 nm to 900 nm with a double-beam spectrophotometer (Cary-300, Varian, Australia). The transmittance coefficient of the annealed ZnSe:Te,O crystal was 62.5 % at 630 nm.

The relative light output of the annealed ZnSe:Te,O scintillator, compared with a CsI:Tl scintillator, was measured with a Si photodiode (S3590, Hamamatsu) under 100 kV X-rays. The relative light output of the annealed ZnSe:Te.O scintillator is about 2.167 times higher than that of the CsI:Tl scintillator.

In order to obtain the decay time of the ZnSe:O scintillator at room temperature, the data were acquired over 1,000 times. **Fig. 3** shows the decay time curve of the ZnSe:Te,O scintillator. The decay curves of the ZnSe:Te,O scintillator has two components, 27 μs and 83 μs.

The pulse height spectrum of the annealed ZnSe:Te,O scintillator is shown in **Fig. 4**. Pulse height spectrum was measured with the radio-isotope ^{137}Cs (662 keV). The energy resolution of the annealed ZnSe:Te,O scintillator was 11.9% when it was exposed to ^{137}Cs 662 keV γ-rays.

Another important physical property the afterglow was measured with a photodiode as a function of time after the X-ray generator was switched off. The afterglow levels of the ZnSe:Te,O scintillator is 0.023% (after 5 ms). This means that the afterglow level of the annealed ZnSe:Te,O scintillator is less than that of the CsI:Tl.

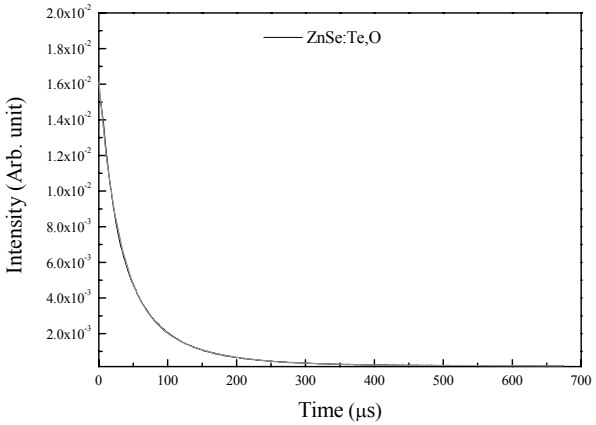

Fig. 3 Decay time curve of the ZnSe:Te,O scintillator.

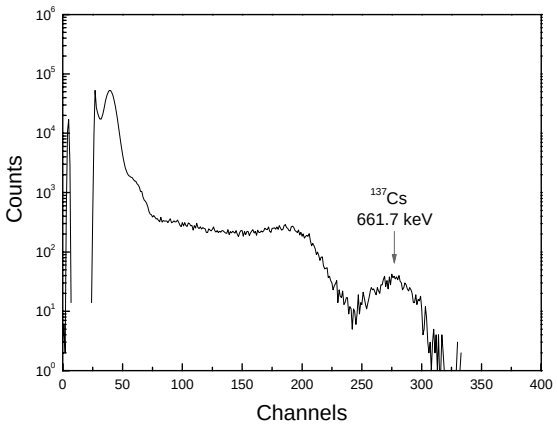

Fig. **4** Pulse height spectrum of the ZnSe:Te,O scintillator to ^{137}Cs gamma radiation.

IV. Summary

Well-structured crystals of ZnSe based on the II-VI semiconductor were grown by a modified Bridgman–Stockbarger technique. The scintillation and other physical properties of ZnSe:Te,O single crystals were investigated. The relative light output, and afterglow level of the ZnSe:Te,O scintillator is better than that of the CsI:Tl. The timing properties of the ZnSe:Te,O scintillator are especially suitable for the detectors of an introscopy system. It is expected that the ZnSe:Te,O scintillator based on the II-VI compound semiconductor can also be used for the X-ray detectors of security inspection systems.

Acknowledgment

This work has been supported financially by the Science Research Center (SRC) / Engineering Research Center (ERC) program of MOST/KOSEF (Korea Science and Engineering Foundation, grant # R11-2000-067-01001-0).

References

1) W. G. Lee, Y. K. Kim, J. K. Kim, H. J. Seo, V. Ryzhikov, N. Starzhinskiy, O. Vyagin, K. Katrunov, and O. Zelenskaya, Journal of the Korean Physical Society, 48 (2006) 47.
2) P. Schotanus, P. Dorenbos, and V. D. Ryzhikov, IEEE Trans. Nucl. Sci., 39 (1992) 546.
3) V. D. Ryzhikov, N. G. Starzhinskiy, and V. I. Silin, Nucl. Traces Radiat. Meas., 2 (1993) 53.
4) Sung-Woo Kwak, Gyuseong Cho, Bong-Hwan kim, Insu Kim, and Moo Sung Jae, Nucl. Instru. And Meth., 537 (2005) 449.
5) V. D. Ryzhikov, A. D. Opolonin, P. V. Pashko, V. M. Svishch, V. G. Volkov, E. K. Lysetskaya, D. N. kozin, and C. Smith, Nucl. Instru. And Meth., A537 (2005) 424.

Journal of NUCLEAR SCIENCE and TECHNOLOGY, Supplement 5, p. 582–585 (June 2008)

Development of Embedded DAQ System for Flux Counting

Yong Seok HWANG[1], H.J. KIM[1*], H. PARK[1], Heedong KANG[1], Wan KIM[1], Sunghwan KIM[2]

[1]*Kyungpook National University, Daegu 702-701, Korea*
[2]*Daegu Health College, Daegu 702-722, Korea*

A portable data acquisition (DAQ) system with embedded microcontroller was developed for radiation detection and environment monitoring purpose. The developed DAQ system consists of an ATMEGA128 of high performance, low-power 8-bit AVR microcontroller made by ATMEL and a AD7746 24-bit capacitance to digital converter. A software based Universal Serial Bus (USB) and a RS-232 serial port is used for the communication between the developed system with a main computer. The developed DAQ system has 8-channels analog to digital converter (ADC) with 10-bit resolution. The ADC has singled ended mode, differential mode using inside amplifier and it has maximum signals sampling rate 50-Kbit per second. It has discriminator capability with an analog comparator and signal counter capability with a 16-bit timer/counter. It can also measure precious capacitance, temperature and voltage with the functionality of the AD7746. The developed embedded DAQ system was tested with scintillation crystal irradiated with in radioactive sources. This embedded DAQ system is simple but portable and useful for radiation and environment monitoring.

KEYWORDS: ATMEGA128, AVR, AD7746, embedded, DAQ, radiation monitoring

I. Introduction

Scintillator, gas chambers and semiconductor detectors are widely used in monitoring radiation fields. Scintillator emits light when it is exposed to ionizing radiation like X-rays and gamma-rays. Scintillator converts a fraction of the energy deposited by the incident gamma-ray or X-ray into visible or ultraviolet photons. The scintillation lights are then converted into an electrical signal by using a photomultiplier tube (PMT) or a photodiode optically coupled to the scintillator[1)]. The PMT signal is digitized with conventional DAQ systems.

We have developed an embedded DAQ system for the radiation flux monitoring. The analog signals from various detectors can be put into the embedded DAQ board. These data are recorded into the personal computer or the laptop with a Linux operating system in real time through the serial connection. This module has many advantages as a DAQ system. First, developed embedded DAQ system has multifunctional capability such as ADC, timer, counter, discriminator, capacitor measurement and temperature sensing. Second, it is simple but compact and inexpensive. The size of developed board is 13 cm × 16 cm. Third, it is easy for the data transfer from the board to the main computer with a help of USART (Universal ASynchronous Receiver/Transmitter) or USB serial communication.

II. Experiments

1. Hardware and Software Description

As shown in **Fig. 1,** the embedded DAQ board consist of a ATMEGA128 microcontroller, an USB port, a LED, an USART communication serial port, an AVR ISP (In System Programming) port, a 12 MHz clock source for software based USB communication, system reset button, extra I/O ports and a AD7746 (24-bit capacitance to digital converter with temperature sensor).

First we made the board schematic with drawing of devices and connections by Cadence PSD. This schematic converted into the PCB (Printed Circuit Board) layout file by OrCad. A PCB file is a standard file format used by printed circuit board fabrication houses that contains information necessary for computer controlled machines to draw exact patterns for circuit boards. The patterns usually contain features such as land patterns, signal traces, drilled holes, milling and cutting information. **Fig. 2** shows, the schematic and the PCB layout of the embedded DAQ board. Finally we applied solder to the component as shown in **Fig. 1**.

Software program was made by the Procyon AVRlib[2)] and the AVR ATMEGA128 Master[3)]. Program was compiled by AVR-gcc[4)] compiler. The program include the functions such as I2C (Inter-Integrated Circuit) communication with AD7746, USART serial communication, USB communication, counter, ADC and voltage comparator. The compiled program was converted to HEX (file format for conveying binary information for applications like programming microcontrollers and other kinds of chips) format. This file was put into the ATMEGA128 with ISP download port.

2. Embedded DAQ Board Specification

The ATMEGA128 contains 128-Kbytes reprogrammable flash memory for program storage in system, 4-Kbytes internal SRAM (Static Random-Access Memory) and 4-Kbytes EEPROM (Electrically Erasable and Programmable Read Only Memory) for data storage. The ATMEGA128 contains additional functions as follows. The 16-bit

*Corresponding Author, Tel No: +82-53-950-5323, Fax No: +82-53-952-1739, E-Mail: hongjoo@knu.ac.kr

Timer/Counter unit allows accurate program execution timing (event management), wave generation and signal timing measurement. The analog comparator compares the input values. Then analog comparator checks digital values to determine whether they are within predetermined upper and lower limits. The successive approximation ADC converts an analog input voltage to a 10-bit digital value through successive approximation. The minimum value represents ground and the maximum value represents the voltage on the ADC reference pin minus 1 Least Significant Bit. The ADC has singled ended mode, differential mode using inside amplifier and it has maximum signals sampling 50-Kbytes sampling per second. Finally the ATMEGA128 have 53 programmable Input /Output lines[5].

The embedded DAQ board also contains the AD7746 for measured capacitance, temperature and voltage. The AD7746 capacitance input range is ±4 pF, while it can accept up to 17 pF common mode capacitance. The parts have an on-chip temperature sensor with a resolution of 0.1 ℃ and accuracy of ±2 ℃ and the measurement range have -40 ℃ to +125 ℃[6].

As shown in **Fig. 3**, this embedded DAQ board has variously communication lines with the other devices. Data monitoring and control of the embedded DAQ board is done through the USART and the USB lines. The MCU transmit or receive the data to the AD7746 through the I2C bus protocol. The software of MCU can be modified memory through the ISP.

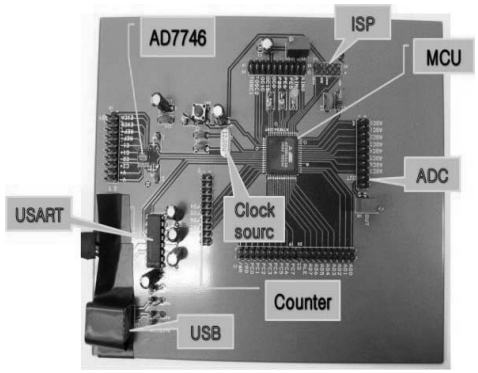

Fig. 1 A picture of embedded DAQ board.

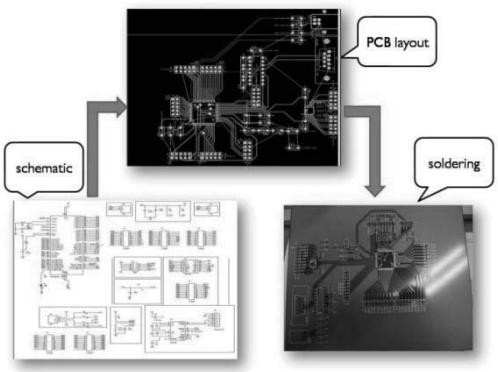

Fig. 2 A diagram of embedded DAQ board design procedure.

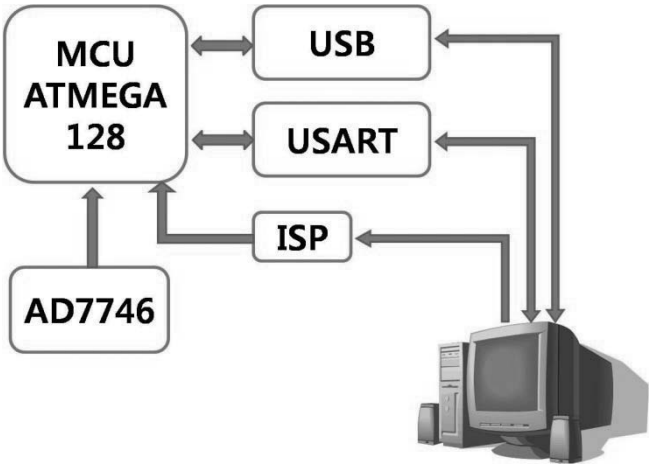

Fig. 3 A diagram of data flow.

III. Results

1. Embedded DAQ Board Test

As shown in F**ig. 4,** each of applications such as the ADC, the AD7746, the Analog Comparator (AC), the I2C and USART were tested with simple programming. This test was performed on the Windows XP operation system.

```
Welcome to ad7746 Test!
AD7746 detected and initialized!
Cap DAC A register set to : 0xAB
Common Cap value found: +0.1338582
Common residual Cap value found: -3.8749270

Welcome to ADC test!
ad ch#7 initialized!
voltage is hex=011A
ad ch#7 voltage is = +1.3769531

Welcome to AC test!
counts of over voltage is = 21507
```

Fig. 4 AD7746, ADC and Analog Comparator test results.

Fig. 4 shows the test result in the HyperTerminal through the USART. First data is an example of measured capacitance by the AD7746. Second data is measured voltage which fed into the ADC. Third data is the counts of the pulse signal which is higher than +1.25 V by analog comparator. The software based USB communication is in the process of development.

We tested the ADC functionality by Linux operation system. The various voltage signals which fed into the ADC were measured in real time. **Fig. 5** shows measurements of voltage variation with different voltage input.

The T1 counter of embedded DAQ board was tested with the Function-Generator (Agilent 33250A). As shown in **Fig. 6**, the number of counts agrees well with given frequency below 6 MHz, because the maximum allowed frequency is the half of system frequency. However, the

counter malfunction if given frequency is above 6 MHz as shown in **Fig. 6** since it is above counting capability.

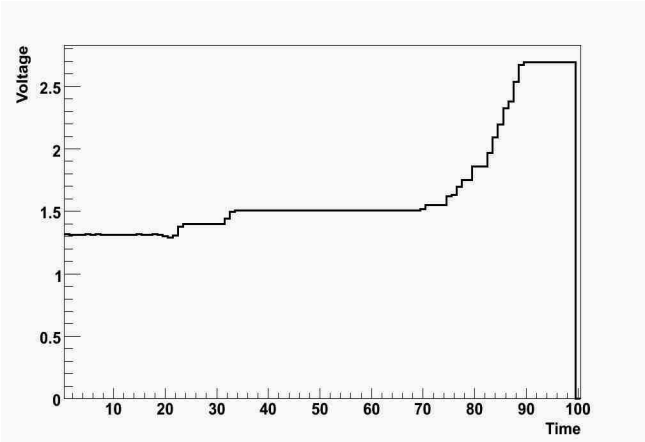

Fig. 5 ADC test with different voltage input.

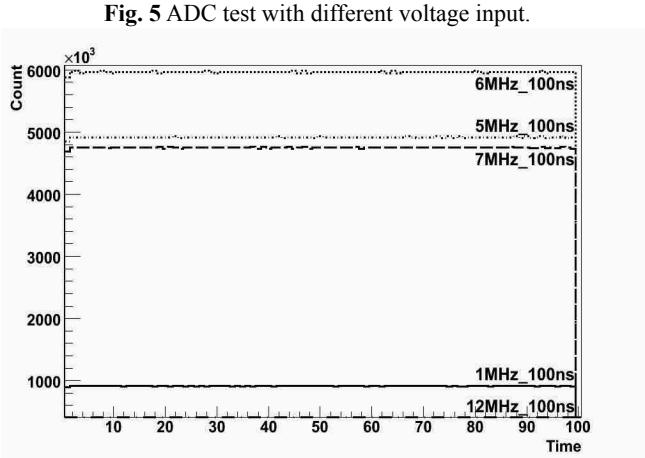

Fig. 6 Counter frequency test results.

2. Radiation Count Test by Gamma-ray Source

A $CdWO_4$ crystal scintillator was prepared for the ^{137}Cs radiation monitoring[7]. A 2-inch PMT (Hamamatsu Co.) was attached to the $CdWO_4$ crystal scintillator for the light conversion to the electric signal. This electric signal was fed to the preamplifier for the current signal conversion to the voltage signal. After amplification the signals were put into the discriminator for conversion to the NIM (Nuclear Instrument Modules) logic signal, this NIM logic signal was fed to the gate generator for conversion to the TTL (Transistor-Transistor Logic) signal[8]. This TTL signal was fed into the embedded DAQ board that has a counting capability. The counting information is recorded into the personal computer with a Linux operating system in real time through the serial connection. The data were analyzed with the C++-based data analysis program, ROOT package[9]. A schematic diagram of experimental setup is shown in **Fig. 7**[8]**.**

By using the embedded DAQ system the gamma-ray flux were measured with $CdWO_4$ crystal irradiate by 1 μCi and 5 μCi ^{137}Cs radioactive source under the natural radiation environment as shown in **Fig. 8**.

As shown in **Fig. 9,** the number of counts was decreased when the distance between the radioactive source and the crystal was increased.

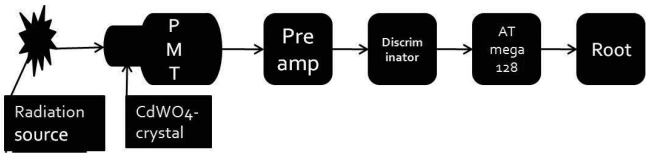

Fig. 7 A diagram of ^{137}Cs radiation flux monitoring system.

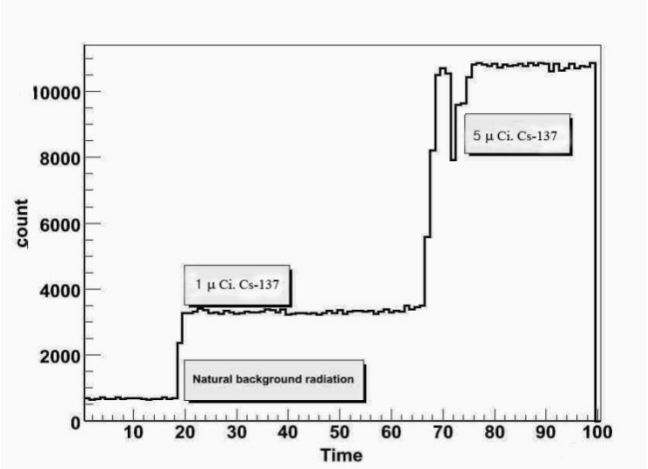

Fig. 8 Gamma-ray monitoring with ^{137}Cs sources.

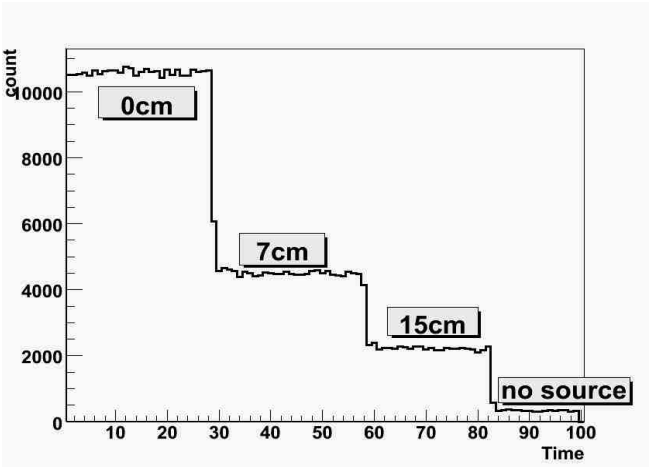

Fig. 9 Gamma-ray counting with different distance between the 5 μCi ^{137}Cs source and the $CdWO_4$ detector.

IV. Summary

A portable data acquisition (DAQ) system with embedded microcontroller was developed for radiation detection and environment monitoring purpose.

An analog voltage signal can be measured with embedded DAQ board using functionality of the ADC. It also has discrimination capability with an analog comparator and signal counter capability with a 16-bit timer/counter. The capacitance and temperature can be precious few measured with the functionality of the AD7746 in the board. The developed embedded DAQ system was tested with scintillation crystal irradiated with radioactive sources.

This embedded DAQ system is portable and useful for radiation, environment monitoring as well as proton and electron beam flux monitoring.

Acknowledgement

This work was supported by the SRC/ERC program of MOST/KOSEF (R11-2000-067-02002-0) and by the user program of Proton Engineering Frontier Project the KOMAC program.

References

1) G. F. Knoll, "*Radiation Detection and Measurement,"* John Willey and Sons, New York (1999).
2) P. Stang, *"C-Language Function Library for Atmel AVR Processors,"* URL:http://www.mil.ufl.edu/~chrisarnold/components/microcontrollerBoard/AVR/avrlib/.
3) Duck-yong Yoon, *"AVR ATMEGA128 MASTER,"* Ohm publishing Co., Korea, 85-268 (2006).
4) GNU General Public License. URL:http://www.gnu.org.
5) ATMEL Co. Ltd. URL:http://atmel.com.
6) Analog Device INC. URL:http://www.analog.com.
7) H.J. KIM, Heedong KANG, H. PARK, Sihong DOH, Sunghwn KIM and Sang Jun KANG, *"Large Size $CdWO_4$ Crystral for Energetic X-and Gamma-Ray Detection,"* ISORD-4, submitted for publication.
8) J.H. SO, H.J. KIM, Heedong KANG, H. PARK, S. RYU, and S.W. Jung, Sihong DOH, Sunghwn KIM, Kyeryung KIM *"Development of Lquid Scintillator System for Proton Flux Monitoring," J. Korean Phys. Soc*., 50,1506-1509,(2007).
9) R. Brun and F. Rademakers, *Nucl. Instr. Meth*., A389, 111 (1997), URL: http://root.cern.ch.

Journal of NUCLEAR SCIENCE and TECHNOLOGY, Supplement 5, p. 586–589 (June 2008)

A Study of CsI(Tl) Scintillator with Optimized Conditions of Large Area Avalanche Photodiode

Minjeong KIM[1], Heedong KANG[1], H.J. KIM[1*], Wan KIM[1], H. PARK[1], and Sunghwan KIM[2]

[1]*Department of Physics, Kyungpook National University, Daegu 702-701, Korea*
[2]*Department of Radiology Technology, Daegu Health College, Daegu 702-722, Korea*

Avalanche photodiode (APD) is a kind of photodiode that internally amplifies the photocurrent by an avalanche effect. The quantum efficiency of the APD is about 80% which is five times higher than that of typical photomultiplier tube (PMT). A 16 mm diameter of beveled-edge large area avalanche photodiode (LAAPD) made by Advanced Photonics was used for the CsI(Tl) scintillator characterization. A CsI(Tl) crystal was attached to LAAPD and energy spectra were measured with various γ-ray sources. Measurements of energy spectra of the CsI(Tl) crystal to optimize the energy resolutions were performed with different shaping time constants by shaping amplifier and with different gains by high voltage variation. The absolute light yield and energy resolution of CsI(Tl) crystals were measured with the LAAPD for 662 keV γ-rays from a ^{137}Cs source. The LAAPD was calibrated with X-ray of ^{55}Fe source for the calibration of the number of e-h pairs per channel. The absolute light yield of newly developed $SrCl_2$ scintillation crystal is determined by this method. This study shows that it is possible to use the LAAPD for the characterization of newly developed scintillation crystal and for the photo-sensor of scintillation detector.

KEYWORDS: avalanche photodiode, quantum efficiency, CsI(Tl) scintillator, absolute light yield

I. Introduction

For many years, scintillation detection has been based almost exclusively on the light readout by photomultiplier tube (PMT). Its internal gain is very high and sufficient signal-to-noise ratio is available. Several disadvantages of using PMTs are that it is sensitive to magnetic field, has relatively low quantum efficiency for input light signal (10-20%), and power consumption is rather high. Photodiodes are semiconductors that generate a current or voltage when illuminated by light. They can operate at much higher light levels than other detectors. Also, they have an excellent quantum efficiency (close to 80%) in the visible and near infrared wave length region. However they have no internal gain that significant noise contribution to the signal is the serious drawback of photodiode[1)].

Avalanche photodiode combines the benefits of both the PMT and photodiode. The quantum efficiency close to the 80% in the visible and near infrared. And gain of up to several hundred in the total collected charge is possible[2-4)].

We measure absolute light yield of CsI(Tl) and newly developed $SrCl_2$ crystal using 16 mm LAAPD (Large Area Avalanche Photodiode) made by Advanced Photonix Inc.(API) .

II. Large Area Avalanche Photodiode

The silicon avalanche photodiode (Si APD) is a photon detection device that offers high internal gain. It is ideal for use in high speed, low light level applications. API also offers several patented large area configurations (LAAPD) enhanced for a variety of regions of the spectrum. These are available with built-in thermoelectric coolers to reduce the dark current and enhance performance. Package options include hermetically sealed windows or windowless configurations[3)].

The "beveled-edge" diode is a p^+n junction in which the n-type resistivity is chosen so as to make the breakdown voltage very high, typically 2,000 V. APDs developed by Advanced Photonix Inc. belong to this type. This type of APDs yields a wide depletion layer and high avalanche gain (≥100). APDs produced by API allowed getting the best energy resolutions mentioned ever obtained with different scintillators. Furthermore, its wide depletion layer of ≥ 50 μm depth, it can be used in direct detection of soft X-rays in the device. The internal construction of LAAPD produced by API is shown schematically in **Fig. 1**. **Fig. 2** shows the quantum efficiency of windowed and windowless LAAPD[3)].

III. Experimental Setup

This study is performed with the CsI(Tl) (φ17 ㎜×34 ㎜) made by Bicron. The scintillator crystal properties are presented in **Table 1.**

A CsI(Tl) crystal is attached to 16 mm blue sensitive windowed (630-70-74-501) or UV sensitive windowless (630-70-73-510) LAAPD and pulse height spectra are measured with ^{57}Co (122 keV), ^{137}Cs (662 keV), ^{22}Na (511 keV and 1,275 keV) and ^{60}Co (1,173 keV and 1,333 keV) γ-ray sources. Signals from 16 mm LAAPD is fed to a low noise preamplifier (TENNELEC TC175B) and then shaping amplifier (Ortec 570) . The portable 25 MHz flash analog to digital converter (FADC) board is used for signal

*Corresponding Author, Tel No: +82-53-950-5323, Fax No: +82-53-952-1739, E-Mail: hongjoo@knu.ac.kr

digitization, and digitized signal was readout by Linux based computer through USB2. The data are analyzed with the C++ based data analysis program, ROOT package[5]. We use object oriented ROOT package for the data taking and analysis. The schematic diagram is shown in **Fig. 3.**

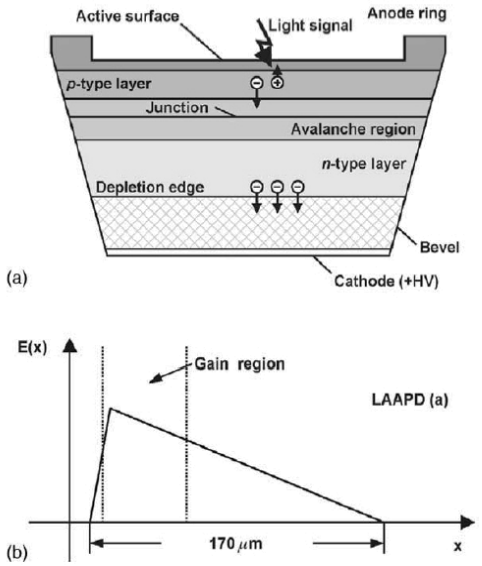

Fig. 1 Schematic cross-section of a LAAPD (a) and electric field profile (b), according to Advanced Photonix, Inc.[2].

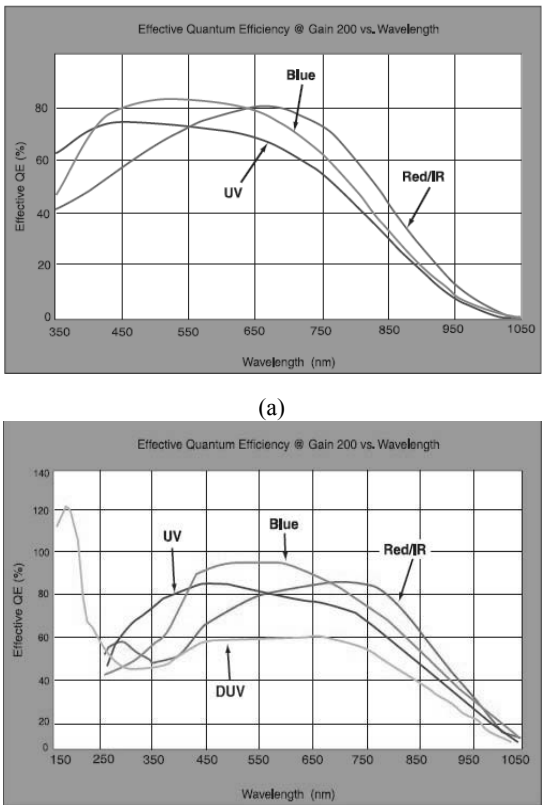

Fig. 2 The quantum efficiency of (a) windowed LAAPD (b) windowless LAAPD[3].

Table 1. Properties of CsI(Tl) crystal.

Property	Value
Light yield (Photons/MeV)	40,000 ~ 60,000
Density (g/cm^3)	4.53
Decay Time (ns)	~1,050
Peak Emission (nm)	550
Hygroscopicity	slight

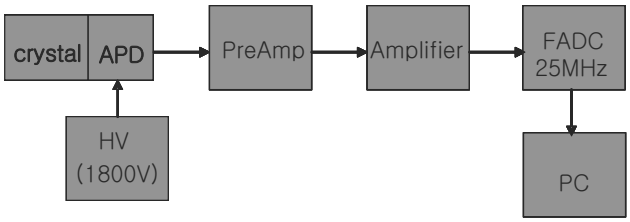

Fig. 3 Schematic diagram of the experimental setup.

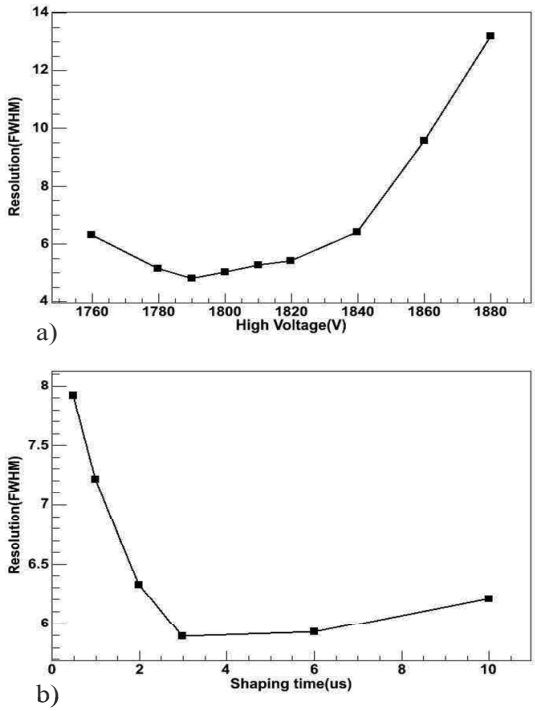

Fig. 4 Energy resolution of CsI(Tl) crystal with a) different HV and b) different shaping time constant.

IV. Results

1. Optimization Test of LAAPD

The contribution of LAAPD noise depends on device parameters such as LAAPD leakage current, capacitance, operating gain by high voltage (HV), and shaping time constant. A higher gain obtained by higher HV power allows reducing preamplifier noise while increases excess noise factor. Shorter shaping time in the spectroscopy amplifier (AMP) reduced the noise due to the LAAPD dark

current while too short shaping time will affect to the signal-to-noise ratio since it may not allow a full integration of the signal from the scintillator. Thus optimization of gain by HV and shaping time constant are necessary for good energy resolution of the crystal.

First, we performed the gain optimization of LAAPD by changing HV from 1,760 V to 1,880 V with a shaping time of 4 μs. The energy resolution of CsI(Tl) with LAAPD is determined by 662 keV γ-ray from a ^{137}Cs source. The best energy resolution of CsI(Tl) crystal is obtained in the HV range of 1,780 ~ 1,820 V as shown in **Fig. 4-a)**. Then, shaping time is changed from 0.5 to 10 μs with HV of 1,800 V. The energy resolution of CsI(Tl) with different shaping time is shown in **Fig. 4-b)** and optimized shaping time constant is in the range of 3 ~ 5 μs. The HV of 1,800 V and the shaping time constant of 4 μs are used for further study.

2. Number of Electron-hole Pairs and Absolute Light Yield

The absolute light yield of CsI(Tl) crystal is measured with the LAAPD for 662 keV γ-ray from a ^{137}Cs source. The LAAPD is calibrated with X-ray of ^{55}Fe source for the calculation of the number of electron-hole (e-h) pairs per channel. The X-ray, directly observed with the LAAPD, allows using the X-ray peak as a good reference to measure number of e-h pairs. **Fig. 5** shows the pulse height distribution of 5.9 keV X-ray from ^{55}Fe source using the amplifier gain of 100 and shaping time constant of 4 μs. The number of e-h pairs per channel is determined to be 3.34 and noise is measured to be 250 electrons rms.

The 662 keV γ-ray detection in the CsI(Tl) crystal with the LAAPD is carried out by the amplifier gain of 20 and shaping time constant of 4 μs. Then number of e-h pairs per MeV is determined by

$$Y_{e-h} = \frac{P_{peak}}{P_{X-ray}} \frac{E_{X-ray}}{E_{ion}} \frac{1}{E_\gamma}$$

where P_{peak} is 662keV energy peak position(channel) from a ^{137}Cs γ-ray source. $P_{x\text{-}ray}$ is 5.9 keV peak position from a ^{55}Fe X-ray. E_{ion} is 3.6 eV which is needed to make one e-h pair in LAAPD. **Table 2** presents the number of e-h pairs measured with CsI(Tl) scintillator coupled to the LAAPD.

To obtain the absolute light yield Y_{ph}, we use

$$Y_{ph,APD} = \frac{Y_{e-h}}{R_{PTFE}} \frac{1}{Q.E}$$

where Q.E is the quantum efficiency and R_{PTFE} is the reflection coefficient of teflon layer wrapping. The Q.E of 0.8 and the R_{PTFE} of 0.9 is used for the absolute light yield determination.

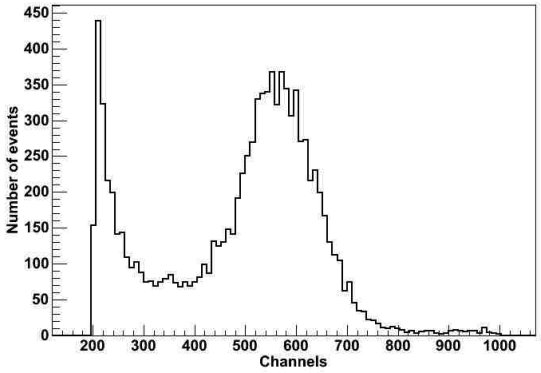

Fig. 5 Pulse height spectrum detected directly in LAAPD by 5.9 keV X-ray from a ^{55}Fe source.

Table 2. The number of e-h pairs and absolute light yield by 662 keV γ-ray irradiation for CsI(Tl) crystal.

Property	Value
Number of e-h pairs (e-h/MeV)	37,000
Absolute light yield (ph/MeV)	52,000

3. Energy Resolution

The energy resolution study was carried out with γ-rays from ^{137}Cs, ^{22}Na and ^{60}Co radioactive sources. To get the best energy resolution, optimized conditions are determined by previous section is used. **Fig. 6** shows the energy spectra of various γ-rays measured using CsI(Tl) crystal coupled to the UV-enhanced LAAPD. The energy resolution of CsI(Tl) crystal is obtained to be 4.9% ± 0.18% (FWHM) with 662 keV γ-rays as shown in **Fig. 6**. This result is comparable to those reported in Reference[6,7].

4. $SrCl_2$ Crystal Test

It is possible to use the LAAPD for the characterization of newly developed scintillation crystal. A single $SrCl_2$ crystal was grown by the Czochralski method and detailed description can be found in Reference[8]. We measure the number of e-h pairs and absolute light yield of this crystal coupled to the UV-enhanced LAAPD with 4 μs shaping time constant. **Fig. 7** shows the pulse height spectrum of $SrCl_2$ crystal irradiated with the 662 keV γ-rays from a ^{137}Cs source. The number of e-h pairs of $SrCl_2$ is determined to be 14,000 e-h/MeV and the absolute light yield is obtained to be 20,000 ph/MeV. The relative light yield of $SrCl_2$ crystal is approximately 40% of CsI(Tl) crystal. The energy resolution of the crystal is obtained to be 9.6% by LAAPD for 662 keV ^{137}Cs γ-ray source. If we use the green extended PMT, a little worse energy resolution of 10.5% is obtained.

Also newly developed $Ba_{0.20}Sr_{0.80}Cl_2$ scintillation crystal is characterized by this method and absolute light yield of the crystal is measured to be 23,000 ph/MeV. The detail description of this crystal is described in Reference[9].

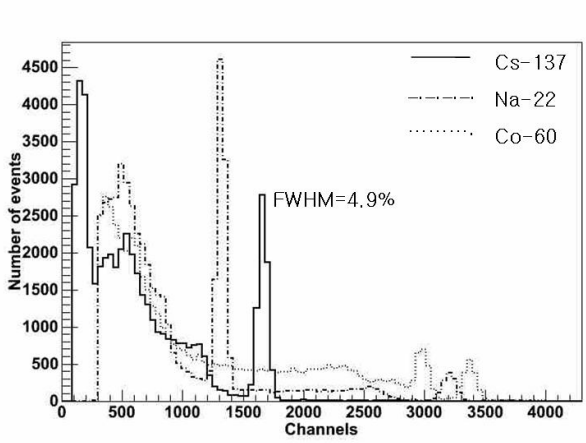

Fig. 6 Pulse height spectra of CsI(Tl) crystal irradiate with various γ-ray source.

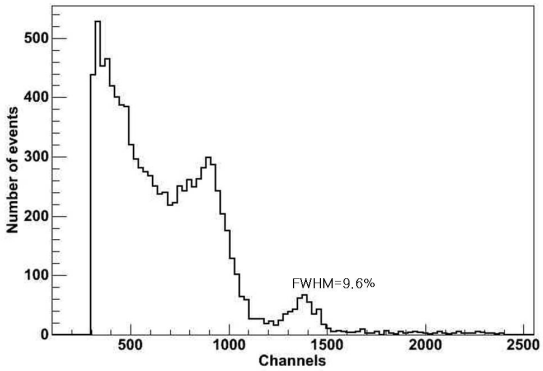

Fig. 7 Pulse height spectrum of $SrCl_2$ crystal irradiate with ^{137}Cs γ-ray source.

V. Conclusions

In this study, we measured the number of e-h pairs and the absolute light yield of scintillators using optimized conditions of LAAPD. The number of e-h pairs of CsI(Tl) is obtained to be about 37,000 e-h/MeV and the absolute light yield is obtained to be about 52,000 ph/MeV for 662 keV ^{137}Cs γ-ray source. Energy resolution of CsI(Tl) is 4.9% using LAAPD for 662 keV ^{137}Cs γ-ray source while it was 7% if a green extended PMT is used in place of APD.

We determine the number of e-h pairs of newly developed $SrCl_2$ scintillation crystal to be 14,000 e-h/MeV and the absolute light yield to be 20,000 ph/MeV.

This study shows that it is possible to use the LAAPD for the characterization of newly developed scintillation crystal and for the photo-sensor of scintillation detector.

Acknowledgement

This work was supported by the SRC/ERC program of MOST/KOSEF (R11-2000-067-02002-0) and by the Korea Science and Engineering Foundation under the BAERI program.

References

1) G. F. Knoll, Radiation Detection and measurement, John Willey and Sons, New York, (1999)
2) M. Moszyński, M. Szawlowski, M. Kapusta, and M. Balcerzyk, 'Large area avalanche photodiodes in scintillation and X-rays detection,' Nucl. Instr. and Meth. in Physics Research, 485, 504-521 (2002).
3) See http://www.advancedphotonix.com/
4) T. Ikagawa, J. kataoka, Y. Yatsu, N. Kawai, K.Mori, T. Kamae, H. Tajima, T. Mizuno, Y. Fukazawa, Y. Ishikawa, N. Kawabata, and T. Inutsuka, 'Performance of large-area avalanche photodiode for low-energy X-rays and γ-rays scintillation detection,' Nucl. Instr. and Meth. in Physics Research, 515, 671-679 (2003).
5) R. Brun, A. Gheata, and M. Gheata, 'The ROOT geometry package,' Nucl.Instr. and Meth. in Physics Research, 502, 676-680 (2003)
6) M. Moszyński, M. Kapusta, J. Zalipska, M. Balcerzyk, D. Wolski, M. Szawlowski, and W. Klamra, 'Low Energy γ-rays Scintillation Detection with Large Area Avalanche Photodiodes,' IEEE Trans. Nucl. Sci. 46[4], 880-885 (1999).
7) M. Moszyński, M. Kapusta, D. Wolski, M. Szawlowski, and W. Klamra, 'Energy Resolution of Scintillation Detectors Readout with Large Area Avalanche Photodiodes and Photomultipliers,' IEEE Trans. Nucl. Sci. 45[3], 472-477 (1998).
8) Gul Rooh, Heedong Kang, H.J. Kim, H. Park, and Sih-Hong Doh, 'Scintillation Characteristics of the SrCl2 single Crystal for the Neutrinoless β+/EC Decay Search,' IEEE Trans. Nucl. Sci., submitted for publication.
9) Jungin KIM, Heedong KANG, H.J. KIM, H. PARK, Sih-Hong DOH and Sunghwan KIM, 'Scintillation Properties of $Ba_{0.20}Sr_{0.80}Cl_2$ Single Crystal,' ISORD-4, submitted for publication.

Journal of NUCLEAR SCIENCE and TECHNOLOGY, Supplement 5, p. 590–593 (June 2008)

Measurement of the Neutron Total Cross Sections of Natural Palladium by Using Pulsed Neutrons at Pohang Neutron Facility

Youngdo OH[1], Hengsik KANG[1], Moo-Hyun CHO[1], In Soo KO[1], and Won NAMKUNG[1]
Taofeng WANG[2], Md. Shakilur RAHMAN[2], Manwoo LEE[2], and Guinyun KIM[2*]

[1]*Pohang Accelerator Laboratory, POSTECH, Hyoja-dong, Nam-gu, Pohang 790-784, Korea*
[2]*Department of Physics, Kyungpook National University, 1370 Sankyok-dong, Buk-gu, Daegu 702-701, Korea*

The neutron total cross-sections of palladiums are measured in the neutron energy region from 0.1 eV to 500 eV by using time of flight method at the Pohang Neutron Facility. The Pohang Neutron Facility consists of an electron linac, a water-cooled tantalum target with a water moderator, and a 12 m long time-of-flight path, and is producing pulsed neutron beam from 65 MeV electron as 10~15 Hz repetition rate. The neutron detector is using a ^{6}Li-ZnS(Ag) scintillator with a diameter of 12.5 cm and a thickness of 1.6 cm. Natural palladium metal plates with 5 × 5 cm^2 in area and 0.5 mm, 1 mm in thickness, are used for the neutron transmission measurement. The background level is determined by using a notch-filter of Co, In, and Cd sheets. The measurements are compared with other measurements and the evaluated data in ENDF/B-VII.0.

KEYWORDS: Pohang neutron facility, pulsed neutron, total cross section, natural palladium, electron linac, time of flight

I. Introduction

The neutron cross-sections provide basic information about the internal structure of atomic nuclei and their constituents. Accurate knowledge of the neutron cross-sections is of great importance for the safety design of nuclear reactors and for the evaluation of the neutron flux density and energy spectrum around a reactor. Precise measurements of neutron cross-sections substantially provide the quantitative nuclear data requisite to various applications of the nuclear engineering. Neutron resonance parameters are finding an increasingly important role in practical applications that are concerned with computations of reactor temperature coefficients, neutron reaction yields, self-shielding effects and related matters. Particularly in reactor design, the individual resonances can be very important. Neutron resonance data also provide reliable information on nuclear level densities.

The total cross-sections and the resonance parameters of Pd at low energy were measured in the energy region: 0.004 eV to 9.3 eV by Teich[1)], 1.2 eV to 10 eV by Biel[1)], 0.002 eV to 0.06 eV by Duggal[1)], 8.2 eV to 1.8 KeV by Vladimirskij[1)]. Although these measurements have been reported, discrepancies exist among the data, especially in the resonance energy region. Thus, there is a need to measure the total cross-sections in these relevant energy ranges.

The total cross-sections of natural Pd have been measured in the neutron energy region between 0.1 and 500 eV by using the TOF method at the Pohang Neutron Facility (PNF). The PNF based on a 100 MeV electron linac was proposed in 1997 and was constructed at the Pohang Accelerator Laboratory on December 1999[2)]. The PNF consists of an electron linac, a water-cooled Ta target and a 12 m long TOF path. The characteristics of the PNF are described elsewhere[3)]. The present measurements are compared with other measurements and the evaluated data in ENDF/B-VII.0[4)].

*Corresponding Author, Tel No: +82-53-950-5320, Fax No +82-53-952-1739, E-Mail: gnkim@knu.ac.kr

II. Experimental Overview and Procedure

1. Experimental Arrangement at the Pohang Neutron Facility

The experimental arrangement for the transmission measurements, which is similar to the previous works[5-7)], is shown in **Fig. 1**. The neutron target is located in a position where electron beam hits its center. To reduce the gamma-flash generated by the electron burst in the target, we placed the target 5.5 cm away from the center of the neutron guide tube. The neutron guide tubes were constructed of stainless steel with two different diameters, 15 cm and 20 cm, and were placed perpendicularly to the electron beam. The neutron collimation system was mainly composed of H_3BO_3, Pb and Fe collimators, which were symmetrically tapered from a 10-cm diameter at the beginning to a 5-cm diameter in the middle position where the sample changer was located, to an 8-cm diameter at the end of the guide tube where the neutron detector was placed. There was a 1.8 m thick concrete slab between the target and the detector room. The transmission samples were placed at the midpoint of the flight path and were cycled into the neutron beam by using a CAMAC module. The neutron detector was located at a distance of about 12 m from the neutron target. A ^{6}Li-ZnS(Ag) scintillator(BC702) with a diameter of 12.5 cm and a thickness of 1.6 cm was used as the neutron detector. This BC702 is good for thermal and epithermal neutrons and is

quite insensitive to gamma radiation; thus, it is suited for applications where the gamma background is high.

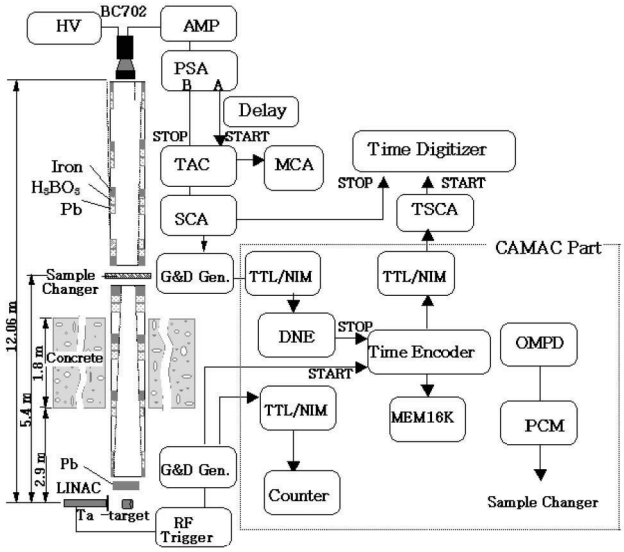

Fig. 1 Experiment setup and data acquisition system

2. Pulsed Neutron Source

Pulsed neutrons are produced by photonuclear reactions in the target nuclei by the bremsstrahlung radiation that is produced when high-energy electrons hit the target nuclei. We designed a water-cooled Ta target by using the Electron Gamma Shower simulation code, EGS4[8]. The target was composed of ten Ta plates with a diameter of 4.9 cm and an effective thickness of 7.4 cm. There was a 0.15 cm water gap between the Ta plates in order to cool the target effectively. The housing of the target was made of titanium. The estimated neutron yield per kW of beam power at the Ta target was 2.0×10^{12} n/sec[9]. The target was located in the center of a cylindrical water moderator contained in an aluminum cylinder with a thickness of 0.5 cm, a diameter of 30 cm, and a height of 30 cm. The water level in the moderator was 3 cm above the target surface.

During the transmission measurement, the electron linac was operated with a repetition rate of 15 Hz, a pulse width of 1.6 μs, and an electron energy of 65 MeV. The peak current in the beam current monitor located at the end of the second accelerator section was greater than 30mA, which was almost the same as that in the target.

3. Data Acquisition System

The configuration of the data acquisition system used in this measurement is shown in **Fig. 1**. Two different data acquisition systems were used for the neutron TOF spectra measurements: one for a NIM-based system and the other for a CAMAC-based system. The main purpose of the NIM-based system is neutron-gamma separation and parallel accumulation of the neutron TOF spectra, if necessary. The dynode signal from a BC702 scintillator is connected through an ORTEC-571 amplifier (AMP) to an ORTEC-552 pulse-shape analyzer (PSA) for neutron-gamma separation. A first NIM signal from the "A" output of the PSA is delayed by 60 ns and is used as the start signal of an ORTEC-567 time-to-amplitude converter (TAC). The "B" output signal from the PSA is used as a stop signal of the TAC. The TAC output is connected to an ORTEC-550A single-channel analyzer (SCA). One of the SCA output signals is used as the stop signal of a 150-MHz Turbo MCS (Time Digitizer); the other is sent to a CAMAC-based system. The start signal of the Time Digitizer signal comes from an RF trigger. The Time Digitizer was operated in a 16384 channel mode with a 0.5 μs width per channel.

The CAMAC-based system consists of a data acquisition part and the control part of a sample changer (SC). The SCA output signal of the NIM-based system is connected to the detector number encoder (DNE) through an NIM/TTL converter. The DNE allows the data to be taken from up to four detectors simultaneously. The output of the DNE is the stop signal for the time encoder, which operates with 4096 channels and a minimal dwell time of 0.5 μs in width per channel.

The 15 Hz RF trigger signal for the modulator of the electron linac is connected to a gate and delay generator (G&D Gen.); the output signal is used as the start signal of the time encoder. One of signals from the time encoder is sent to a 16K capacity memory module (MEM 16K), which collects the TOF data during the measurement.

The control of the SC is done by using the operating module of a physical device (OMPD), which operates the SC from a distance of 1 km. The signal from this unit is delivered on request to the position control module (PCM) to change the sample and interrupts the measurement until the next sample reaches its position. The PCM can be operated automatically (normal mode), as well as manually (manual mode). It also sets the number of full turnovers of the SC and provides a data record from the MEM16K to the relevant files for future processing. Parallel data acquisition with both the NIM system and the CAMAC system may be used if one desires to optimize the dwell time for different regions of the TOF spectra. A command file written in special script language synchronizes the CAMAC and the NIM systems.

4. Samples and Data Taking

In the total cross-section measurements, natural Pd metal plates, 5×5 cm^2 in area by 0.5 mm and 1.0 mm thickness, were used. A set of notch filters of Co, In and Cd plates, 0.5 mm, 0.2 mm and 0.5 mm in thickness, respectively, were used for the background measurement and the energy calibration. The transmission samples were placed at the midpoint of the flight path and were cycled into the neutron beam by using the automatic sample changer with four samples positions. The measurements were performed with two Pd samples with different thickness simultaneously. The two other positions of the sample changer were empty to collect the neutron TOF spectra without a sample (open beam). The positions of the samples were chosen in the

following sequence: sample, open, sample, open. The exposure time for each sample position was 500 seconds and for each open position it was 250 seconds. The interleaving sequence of open positions in the sample changer was chosen to minimize the influence of slow and/or small variations in the neutron beam intensity. If the beam intensity variation or its drift was fast and/or large, then the partial measurements were excluded from the total statistics. The total data taking time for the Pd samples was 70 hours and 35 hours for open beam.

III. Data Analysis and Results

The total cross-section is determined by measuring the transmission of neutrons through the sample. The transmission rate of neutrons at i-th group energy E_i is defined as the fraction of incident neutrons passing through the sample compared to that in the open beam. Thus, the neutron total cross-section is related to the neutron transmission rate $T(E_i)$ as follows:

$$\sigma(E_i) = -\frac{1}{t\Sigma_j N_j} \ln T(E_i), \quad (1)$$

$$T(E_i) = \frac{\{I(E_i) - IB(E_i)\}/M_I}{\{O(E_i) - OB(E_i)\}/M_O}, \quad (2)$$

where N_j is the atomic density per cm^2 of the j-th isotope in the sample, t is sample thickness. $I(E_i)$ and $O(E_i)$ are the foreground counts for the sample-in and the open-beam, $IB(E_i)$ and $OB(E_i)$ are the background counts for the sample-in and the open-beam, and M_I and M_O are monitor counts for the sample-in and open beam, respectively. In this measurement, we assumed the monitor counts to be constant during the measurement. The neutron TOF spectra for the sample-in and for the open beam are shown in **Fig. 2**, together with the estimated background level, which is indicated by a solid line

The background level was estimated by using the resonance energies of the neutron TOF spectra of notch filters of Co, In and Cd. The magnitude of the background level was calculated between the black resonances by fitting the function $y=A_1 \exp(-t_1*I)+y_0$, where A_1, t_1 and y_0 are constants and I is the channel number of the time digitizer, as shown in **Fig. 3**.

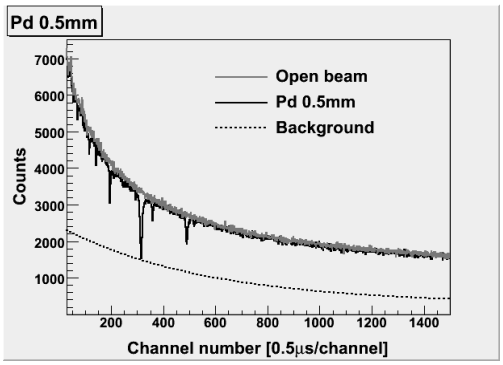

Fig. 2 Neutron TOF spectra for Pd sample, open beam and background level

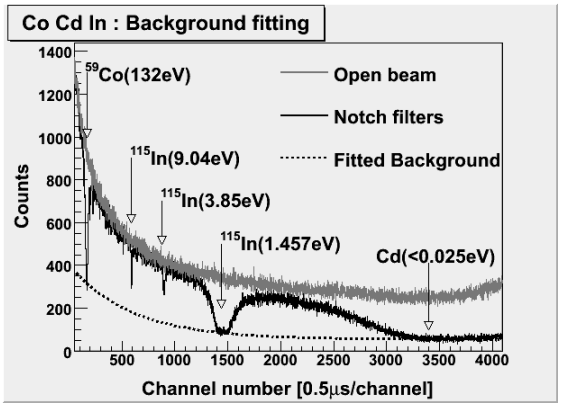

Fig. 3 Determination of the background level. The resonance energies of Co, In, Cd were fitted to $y=A_1 \exp(-t_1*I)+y_0$, A_1=347.7 , t_1=0.0017, y_0=54.7.

We obtained the flight path length L in meters from the resonance energy E in eV corresponding to the channel number I, as indicated in **Fig. 4** by using the following fitting function.

$$I = \frac{72.3 \times L}{\Delta W \times \sqrt{E}} + \frac{\tau}{\Delta W}, \quad (3)$$

where ΔW is the channel width of the time digitizer, 0.5 μs, and τ is the time difference between the start time from the RF trigger and the real time zero when the neutron burst is produced. We found L =11.87±0.012m and τ = 7.69±0.47 μs as shown in **Fig. 4**.

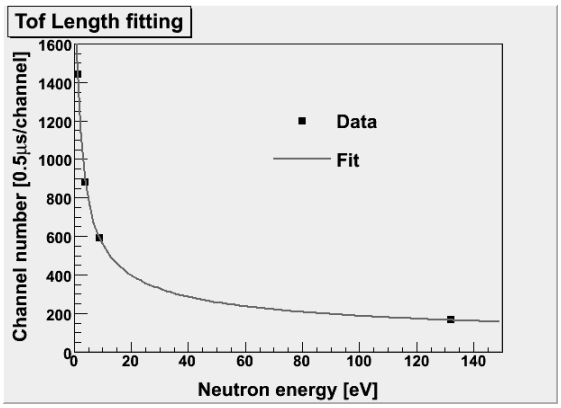

Fig. 4 TOF length was fitted using resonance channel number and corresponding resonance energy.

Then the energy resolution can be written as

$$\frac{\Delta E}{E} = 2\frac{\Delta t}{t}, \quad (4)$$

where the uncertainty (Δt) of the neutron TOF(t) is composed of uncertainties due to the flight path(1cm), the moderator thickness(3cm), the pulse width of the electron beam(1.6 μs), the channel width of the time encode(0.5 μs) and the time jitter(negligibly small) from the neutron detector. The energy resolutions for neutron energies of

0.01, 0.1, 1, 10 and 100 eV are 0.59 %, 0.60 %, 0.65 %, 1.01 % and 2.63 %, respectively.

The total cross-sections of natural Pd were obtained in the neutron energy range from 0.1 to 500 eV by using equation (1) and (2). Then we have calculated the effective total cross-sections for the same energy interval as follows:

$$\sigma_{eff}(E) = \frac{\int_{E_i}^{E_f} \sigma(E) E dE}{\int_{E_i}^{E_f} E dE}, \quad (5)$$

The systematic uncertainties came from the following sources: uncertainties from a) the flight path measurements (1 %), b) the background estimate (0.04 %) and c) the dead time, the normalization, *etc*. (2 %). Thus, the total systematic error of the present measurement is less than 3 %.

The present measurement is generally in good agreement with other data and with the evaluated data, as shown in **Figs. 5** and **6.**

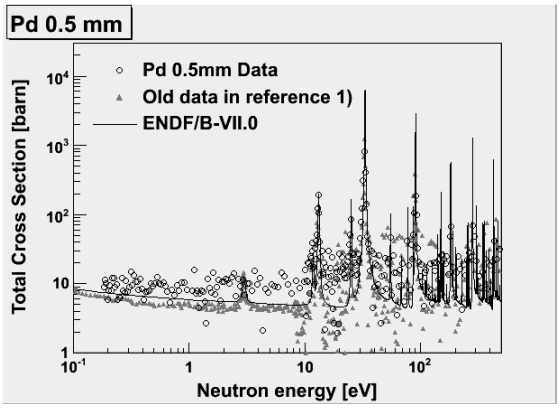

Fig. 5 Measured total cross section and ENDF evaluated value for Pd, thickenss = 0.5 mm.

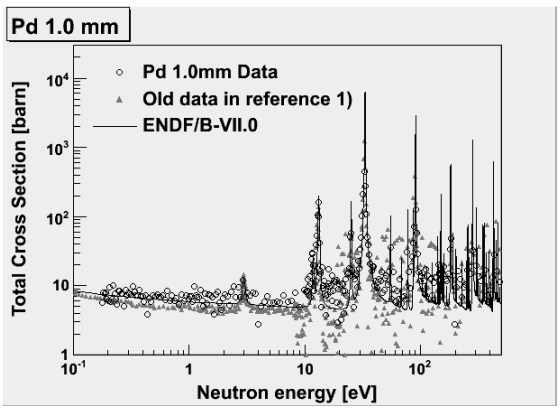

Fig. 6 Measured total cross section and ENDF evaluated value for Pd, thickness = 1.0 mm.

IV. Conclusions

The total cross-sections of natural Pd were measured at the Pohang Neutron Facility in the neutron energy from 0.1eV to 500eV by using the TOF method and a ^{6}Li-ZnS(Ag) glass scintillator as a neutron detector. The present measurement is in good agreement with other experiment data as well as the evaluated data in ENDF/B-VII.0.

Acknowledgments

The authors would like to express their sincere thanks to the staff of the Pohang Accelerator Laboratory for the excellent operation of the electron linac and their strong support. This work is supported by the Korea Research Foundation Grant funded by Korea Government (KRF-2006-353-C00014) and by the Korea Science and Engineering Foundation (KOSEF) through a grant provided by the Korean Ministry of Science & Technology (MOST) in 2007 (Project No. M20709000108-07B0900-10810).

References

1) EXFOR data: http://www.nndc.bnl.gov/exfor7/exfor00.htm.
2) G. N. Kim etc, in Proceedings International Conference on Nuclear Data for Science and Technology, edited by G. Reffo, A. Ventura and C. Grandi (Trieste, 1997), p. 556; G. N. Kim etc, in Proceedings of First Asian Particle Accelerator Conference, edited by Y. H. Chin, M. Kihara, H. Kobayashi, N. Akasaka, K. Nigorikawa and M. Tobiyama (Tsukuba, 1998), p. 743.
3) G. N. Kim et al., J. Korean Phys. Soc. 38, 14 (2001); G. N. Kim etc, Nucl. Instr. Meth. A 485, 458 (2002).
4) Evaluated Nuclear Data File, ENDF/B-VII.0, <http: //www.nndc.bnl.gov/exfor7/endf00.htm>.
5) G. N. Kim, R. Machrafi, H. Ahmed, D. Son, V. Skoy, Y. S. Lee, H. S. Kang, M. H. Cho, I. S. Ko and W. Namkung, J. Korean Phys. Soc. 43, 479 (2003).
6) G. N. Kim, Y. S. Lee, R. Machrafi, H. Ahmed, D. Son,V. Skoy, H. S. Kang, M. H. Cho, I. S. Ko, W. Namkung, J. H. Chang and K. J. Yoo, J. Nucl. Sci. Tech. S 4, 388 (2004).
7) A. K. M. M. H. Meaze, H. Ahmed, G. N. Kim, D. Son, Y. S. Lee, H. S. Kang, M. H. Cho, I. S. Ko, W. Namkung, T. I. Ro, W. Chung, Y. A. Kim, K. J. Yoo and J. H.Chang, J. Korean Phys. Soc. 46, 401 (2005).
8) W. R. Nelson, H. Hirayama and D. W. O. Rogers, The EGS4 Code System, SLAC Report, 1985.
9) W. Y. Baek, G. N. Kim, M. H. Cho, I. S. Ko and W. Namkung, in Proceedings of the Workshop on Nuclear Data Production and Evaluation, edited by J. Chang and G. N. Kim (Pohang, 1998).